

Hydraulic performance of stepped spillway aerators and related downstream flow features

THÈSE N° 6989 (2016)

PRÉSENTÉE LE 27 MAI 2016

À LA FACULTÉ DE L'ENVIRONNEMENT NATUREL, ARCHITECTURAL ET CONSTRUIT
LABORATOIRE DE CONSTRUCTIONS HYDRAULIQUES
PROGRAMME DOCTORAL EN GÉNIE CIVIL ET ENVIRONNEMENT

ÉCOLE POLYTECHNIQUE FÉDÉRALE DE LAUSANNE

POUR L'OBTENTION DU GRADE DE DOCTEUR ÈS SCIENCES

PAR

Stéphane Christian Olivier TERRIER

acceptée sur proposition du jury:

Prof. B. Merminod, président du jury
Prof. A. Schleiss, Dr M. Pfister, directeurs de thèse
Prof. M. Aufleger, rapporteur
Prof. J. Matos, rapporteur
Prof. W. H. Hager, rapporteur



ÉCOLE POLYTECHNIQUE
FÉDÉRALE DE LAUSANNE

Suisse
2016

Abstract

To protect spillways against cavitation damage, adding a small air concentration to the flow close to the invert is efficient. Aerator performance on smooth chutes was therefore well studied in terms of air entrainment and downstream air concentration development. Since bottom aerators are built upstream of regions exposed to cavitation, no damages have been observed on spillways.

The introduction of roller compacted concrete (RCC) dams in the 1980s promoted the use of stepped spillways rarely used until then. Compared to conventional smooth spillways, they have the advantage of a higher energy dissipation rate, and of a self-aeration point located higher upstream. However, the non-aerated flow upstream of the inception point is exposed to an increased cavitation risk due to flow separation on the steps. Until recently, the uncertainty about the conditions required for cavitation inception motivated conservative unit discharges. Today, the cavitation potential on stepped spillways is better known and is significant, so that techniques are necessary to safely use stepped spillways under increased unit discharges.

This research includes a physical model investigation of a deflector aerator on a stepped spillway. The key parameters influencing aerator performance and stepped spillway flow are systematically varied. These are: (i) the chute angle, (ii) the step height, (iii) the approach flow Froude number, (iv) the approach flow depth, (v) the deflector angle, and (vi) the deflector height. Large sections are used in the air supply system to keep the cavity subpressure near atmospheric conditions and thus obtain optimal aerator performance. The air concentration downstream of the aerator is measured at regularly spaced profiles by means of a fiber optical probe.

The flow field downstream of the stepped spillway aerator can be described in three main zones: (i) the *jet zone* where air is entrained on the lower and upper surfaces, (ii) the *spray and reattachment zone* where spray is produced by the jet impact and where there are rapid variations of the average and bottom air concentrations, and (iii) the *far-field zone* where the flow depth as well as the average and bottom air concentrations gradually tend towards quasi-uniform conditions.

The lower and upper surfaces of the jet issued by the deflector were considered to derive the effective takeoff angles. With the takeoff velocity, it allows to describe the lower and upper jet surfaces with ballistic trajectories. The maximum jet elevation, the jet length, and the jet impact angle on the pseudo-bottom can then be determined.

Similarly to smooth spillways, the air entrainment coefficient of the aerator is described as a function of the relative jet length. Besides, a relation for the air entrainment coefficient in function of the

Froude number and the deflector geometry is presented. The average and bottom air concentration developments show a minimum shortly after the jet impact, followed by a maximum in the spray zone. These extrema are quantified and are related to the relative jet length. In the far-field zone, unlike smooth chutes, no continuous detrainment is observed for the bottom air concentration. Both the average and the bottom air concentrations gradually converge to quasi-uniform flow values.

Tests with an increased approach flow bottom roughness showed a large increase of air entrainment due to the higher flow turbulence, but only small average and bottom air concentration differences downstream of the jet impact result. A pre-aerated approach flow leads to slightly higher average and bottom air concentrations downstream of the aerator.

The design of a stepped spillway aerator is presented in the end to summarize the results obtained and their practical application.

Key words: Aeration, Aerator, Air concentration, Air entrainment, Cavitation protection, Deflector, Hydraulic structures, Jet, Physical model, Skimming flow, Stepped chute, Stepped spillway

Résumé

Pour protéger les évacuateurs de crue de dommages dus à la cavitation, l'ajout d'une faible concentration d'air proche du fond est efficace. La performance des aérateurs sur des évacuateurs à fond lisse a donc été abondamment étudiée en termes d'entraînement d'air et de développement de la concentration d'air à l'aval. Depuis que les aérateurs de fond sont construits à l'amont des parties exposées à la cavitation, aucun dommage n'a été observé sur les évacuateurs de crue.

L'émergence des barrages en béton compacté au rouleau (BCR) dans les années 1980 a favorisé l'utilisation des évacuateurs en marches d'escalier rarement utilisés auparavant. Comparés aux évacuateurs conventionnels lisses, ils offrent l'avantage d'un taux de dissipation d'énergie plus élevé, et un début d'aération superficielle situé plus en amont. Cependant, l'écoulement non-aéré à l'amont du point initial est exposé à un risque de cavitation plus élevé dû au détachement de l'écoulement le long des marches. Jusqu'à récemment, l'incertitude quant aux conditions nécessaires pour l'apparition de la cavitation a mené à un dimensionnement d'évacuateurs en marches d'escalier avec des débits spécifiques conservateurs. Aujourd'hui, le potentiel de cavitation sur les évacuateurs en marches d'escalier est mieux établi et des techniques sont nécessaires pour accroître les débits spécifiques de manière sûre.

Cette recherche inclut l'étude sur modèle physique d'un aérateur comprenant un déflecteur sur un évacuateur en marches d'escalier. Les paramètres clés influençant la performance d'un aérateur et l'écoulement sur un évacuateur en marches d'escalier sont systématiquement variés. Ces paramètres sont : (i) l'angle du coursier, (ii) la hauteur de marche, (iii) le nombre de Froude de l'écoulement d'approche, (iv) la hauteur d'eau d'approche, (v) l'angle du déflecteur et (vi) la hauteur du déflecteur. De grandes sections sont utilisées dans le système d'approvisionnement en air afin de maintenir une sous-pression dans la cavité sous le jet proche des conditions atmosphériques, et ainsi obtenir une performance optimale de l'aérateur. La concentration d'air à l'aval de l'aérateur est mesurée à des profils régulièrement espacés par une sonde à fibre optique.

L'écoulement à l'aval de l'aérateur sur évacuateur en marches d'escalier peut être décrit selon trois zones : (i) la *zone du jet* où l'entraînement d'air se produit sur les surfaces inférieure et supérieure, (ii) la *zone de spray et de ré-attachement* où le spray est engendré par l'impact du jet et où les concentrations d'air moyenne et au fond varient rapidement, et (iii), la *zone lointaine* où la hauteur d'eau ainsi que les concentrations d'air moyenne et au fond tendent graduellement vers des conditions quasi-uniformes.

Les surfaces inférieure et supérieure du jet engendré par le déflecteur sont analysées, et des équations sont établies pour les angles d'envol inférieur et supérieur. Cela permet, à l'aide d'une équation pour obtenir la vitesse d'envol, de décrire les surfaces inférieure et supérieure du jet par des trajectoires balistiques. La hauteur maximale du jet, la longueur du jet et l'angle d'impact du jet sur le pseudo-fond peuvent alors être déterminés.

De façon similaire aux évacuateurs lisses, le coefficient d'entraînement d'air de l'aérateur est décrit en fonction de la longueur relative du jet. De plus, une équation pour déterminer le coefficient d'entraînement d'air en fonction du nombre de Froude de l'écoulement d'approche et de la géométrie du déflecteur est présentée. Les concentrations moyenne et au fond montrent un minimum peu après l'impact du jet, suivi d'un maximum dans la zone de spray. Ces extrêmes sont quantifiés et sont liés à la longueur relative du jet. Contrairement aux évacuateurs lisses, dans la zone lointaine, aucun déentraînement continu n'est observé pour la concentration d'air au fond. Autant la concentration moyenne que la concentration au fond convergent graduellement vers leur valeur en écoulement quasi-uniforme.

Des expériences avec un fond plus rugueux dans la zone d'approche montrent une grande augmentation de l'entraînement d'air due à une turbulence plus élevée de l'écoulement, mais seulement de faibles différences résultent dans les concentrations d'air moyenne et au fond à l'aval de l'impact du jet. Un écoulement pré-aéré mène à des concentrations d'air moyenne et au fond plus élevées à l'aval de l'aérateur.

Un exemple de dimensionnement résumant les résultats obtenus est donné à la fin pour montrer leur application pratique.

Mot-clés : Aération, Aérateur, Concentration d'air, Déflecteur, Déversoir en marches d'escaliers, Entraînement d'air, Évacuateur en marches d'escaliers, Jet, Modèle physique, Ouvrage hydraulique, Protection contre la cavitation

Contents

Abstract	i
Résumé	iii
Contents	v
List of Symbols	xi
1 Introduction	1
1.1 Problem outline	1
1.2 Stepped spillway aerators	2
1.3 Objectives	5
1.4 Structure of the report	6
2 Literature Review	7
2.1 Stepped spillways	8
2.1.1 Overview	8
2.1.2 Non-aerated flow	10
2.1.3 Inception point of free-surface aeration	11
2.1.4 Aerated flow	14
2.1.5 Quasi-uniform flow	15
2.1.6 Air concentration profiles	17
2.1.7 Pressure on the steps	18
2.1.8 Control section and transition steps	19
2.1.9 Flow velocity profile	20
2.1.10 Friction factor and energy dissipation	20
2.1.11 Step surface roughness and macro-roughness elements	21
2.1.12 Air-water flow properties	22
2.1.13 Lateral constriction	23
2.2 Cavitation	23
2.2.1 Overview	23
2.2.2 Cavitation damages and prevention	24
2.2.3 Cavitation potential on stepped chutes	26

2.3	Smooth chute aerators	29
2.3.1	Overview	29
2.3.2	Air entrainment coefficient	32
2.3.3	Aerator jets	35
2.3.4	Air transport	42
2.4	Stepped chute aerators	45
2.4.1	Deflector aerator	46
2.4.2	Step aerator	47
2.4.3	Comparison of stepped chute aerators	48
3	Experimental setup	49
3.1	Channel description	49
3.1.1	Jetbox	50
3.1.2	Steps	51
3.2	Aerator design	52
3.3	Dimensional analysis	54
3.4	Parameters and test program	56
3.5	Instrumentation	59
3.5.1	Fiber optical probe	59
3.5.2	Automatic positioning system	61
3.5.3	Flowmeter	61
3.5.4	Anemometer	62
3.5.5	Pressure transducers	63
3.5.6	Point gauge	63
3.5.7	Manometer	64
3.5.8	Observed jet length	64
3.6	Test procedure	64
3.7	Scale effects	65
4	Reference tests	69
4.1	Overview	69
4.2	Inception point of self-aeration characteristics	71
4.3	Flow depth development	73
4.4	Average air concentration development	75
4.5	Bottom air concentration development	77
4.6	Air concentration profiles	79
4.7	Summary	81
5	Aerator tests	83
5.1	Overview	83
5.2	Flow zones and general results	85
5.3	Air entrainment coefficient	88

5.3.1	Relative jet length approach	89
5.3.2	Froude number approach	89
5.4	Summary	91
6	Deflector jet characteristics	93
6.1	Jet trajectories	94
6.1.1	Normalized jet trajectories	94
6.1.2	Takeoff defined jet trajectories	94
6.2	Jet takeoff flow depth	98
6.3	Jet takeoff angles	99
6.3.1	Datasets used for the analysis	99
6.3.2	Selection of jet trajectory method	100
6.3.3	Comparison with the takeoff angle relations of Steiner et al. (2008)	101
6.3.4	Jet spread difference compared to Pfister (2008)	103
6.3.5	Lower takeoff angle relation	104
6.3.6	Upper takeoff angle relation	105
6.4	Jet spread angle	105
6.5	Jet length	107
6.5.1	Jet trajectory approach	107
6.5.2	Empirical approach	108
6.6	Jet impact angle on pseudo-bottom	110
6.7	Maximum jet elevation	111
6.8	Cavity subpressure	111
6.9	Jet blackwater core length	111
6.10	Design example	113
6.11	Summary	114
7	Air transport characteristics	117
7.1	Average air concentration development	117
7.1.1	Jet maximum and jet air entrainment	117
7.1.2	Jet impact minimum	119
7.1.3	Spray maximum	120
7.2	Bottom air concentration development	122
7.2.1	Minimum bottom air concentration	123
7.2.2	Maximum bottom air concentration	125
7.2.3	Scale effects on bottom air concentration	126
7.2.4	Correlation of extrema	126
7.2.5	Effect of Froude number	127
7.2.6	Effect of chute geometry	128
7.2.7	Effect of deflector	129
7.3	Comparison with the preliminary research of Pfister et al. (2006a)	129
7.4	Air concentration profiles	132

7.5	Summary	133
8	Effect of turbulence and pre-aeration	137
8.1	Tests characteristics	137
8.1.1	Grid tests	137
8.1.2	Pre-aerated tests	138
8.2	Reference tests with a grid	139
8.3	Aerator tests with a grid or pre-aerated approach flow	139
8.3.1	Visual comparison	139
8.3.2	Jet length and air entrainment coefficient	141
8.3.3	Flow development	143
8.4	Summary	145
9	Design example	147
9.1	Spillway drawdown curve and cavitation index	147
9.2	Aerator and jet characteristics	150
9.3	Air concentration development	152
10	Conclusions	155
10.1	Results	155
10.2	Limitations of the study	157
10.3	Outlook	158
A	Air entrainment coefficient	159
A.1	Relations based on the jet length	159
A.2	Relations based on the Froude number	160
A.2.1	Inclusion of the relative deflector height	160
A.2.2	Inclusion of the relative step height	161
A.2.3	Smooth and stepped chute common relation	161
B	Subpressure effect on jet trajectories	163
C	Pressure measurements	169
C.1	Average pressure	169
C.1.1	Influence of jetbox	169
C.1.2	Influence of deflector	170
C.2	Pressure fluctuations	171
C.3	Normal fluctuating velocity	171
C.4	Turbulence intensity	172
C.5	Influence of grid and pre-aerated approach flow	172
D	Flow development of aerator tests	175
E	Parameter influence	183

E.1	Air entrainment coefficient	184
E.2	Lower takeoff velocity	185
E.3	Lower takeoff angle	186
E.4	Upper takeoff angle	187
E.5	Jet spread angle	188
E.6	Blackwater core length	189
E.7	Approach flow bottom pressure	190
E.8	Approach flow bottom pressure fluctuations	191
E.9	Deflector overpressure	192
E.10	Approach flow normal fluctuating velocity	193
E.11	Approach flow turbulence intensity	194
F	Testsheets	195
	References	316
	Acknowledgments	317
	Curriculum Vitae	319

List of Symbols

Roman letters

A_A	Transverse area of aerator slot under the deflector		[m ²]
b	Chute width		[m]
C	Local air concentration		[-]
C_a	Average air concentration	eq. (2.1)	[-]
C_{a1-a3}	Average air concentration extrema	Figure 7.1	[-]
C_{ai}	Average air concentration at inception point		[-]
C_{ao}	Approach flow average air concentration		[-]
C_{au}	Quasi-uniform average air concentration		[-]
C_b	Bottom air concentration		[-]
C_{b4-b5}	Bottom air concentration extrema	Figure 7.7	[-]
C_{bu}	Quasi-uniform bottom air concentration		[-]
C_d	Coefficient of discharge		[-]
C_p	Coefficient of pressure	eq. (2.49)	[-]
d	Diameter		[m]
d_h	Hydraulic diameter		[m]
D	Air detrainment at jet impact	eq. (2.85)	[-]
D'	Dimensionless turbulent diffusivity		[-]
e	Root mean square error		[mm]
E	Euler number	$E = \rho u^2 / \Delta p$	[-]
f	Friction coefficient		[-]
F	Froude number	$F = u / (gh)^{0.5}$	[-]
F_i	Inception Froude number	eq. (2.8)	[-]
F_k	Step roughness Froude number	eq. (2.7)	[-]
F_o	Approach flow Froude number	Figure 3.9	[-]
F_p	Froude number at pressure sensor		[-]
F_s	Step roughness Froude number	eq. (2.9)	[-]
F_{wo}	Pre-aerated approach flow Froude number		[-]
g	Gravitational acceleration		[m/s ²]
h	Flow depth		[m]
h_{90}	Mixture flow depth up to $C = 0.90$		[m]

List of Symbols

h_{90o}	Pre-aerated approach flow mixture depth		[m]
h_{90u}	Quasi-uniform mixture flow depth		[m]
h_c	Critical flow depth		[m]
h_i	Mixture flow depth at the inception point		[m]
h_{jb}	Jetbox opening		[m]
h_o	Approach flow depth	Figure 3.9	[m]
h_p	Flow depth at pressure transducer		[m]
h_t	Takeoff flow depth	Figure 2.13	[m]
h_w	Equivalent blackwater flow depth	eq. (2.2)	[m]
h_{wi}	Equivalent blackwater flow depth at the inception point		[m]
h_{wo}	Approach flow equivalent blackwater flow depth		[m]
h_{wu}	Quasi-uniform equivalent blackwater flow depth		[m]
H	Energy head		[m]
H_D	Design head for ogee		[m]
H_{max}	Head of the upstream reservoir		[m]
J	Energy gradient slope		[-]
k	Step roughness	$k = s \cos(\varphi)$	[m]
k_s	Surface roughness		[m]
K	Constant		[-]
K'	Constant		[-]
K''	Constant		[-]
L	Jet length	Figures 2.13 and 3.9	[m]
L_{bwc}	Blackwater core length	Figure 2.13	[m]
L_d	Length of deflector	$L_d = t / \tan \alpha$	[m]
L_i	Inclined distance from ogee crest to inception point	Figure 2.1	[m]
L_{max}	Jet length without subpressure		[m]
L_{obs}	Visually derived jet length		[m]
L_s	Inclined distance between step edges	$L_s = h / \sin \varphi$	[m]
N	Exponent of velocity power law	eq. (2.45)	[-]
o	Offset height of aerator perpendicular to chute	Figure 2.13	[m]
p	Pressure		[Pa]
p'	Root mean square of pressure fluctuations		[Pa]
p_a	Atmospheric pressure		[Pa]
p_d	Pressure induced by a deflector		[Pa]
$p_{d,max}$	Maximum pressure induced by a deflector		[Pa]
p_v	Vapor pressure		[Pa]
P	Probability		[-]
q	Unit discharge		[m ² /s]
q_A	Unit air discharge		[m ² /s]
q_{Ao}	Pre-aerated flow unit air discharge		[m ² /s]
q_D	Design unit discharge of ogee		[m ² /s]

Q	Discharge		[m ³ /s]
Q_A	Air discharge		[m ³ /s]
r^2	Coefficient of determination		[-]
R	Reynolds number	$R = uh/\nu$	[-]
R_A	Reynolds number in the air duct		[-]
s	Step height	Figures 2.1 and 3.9	[m]
u	Velocity		[m/s]
u'	Root mean square of normal fluctuating velocity		[m/s]
u^*	Shear velocity	$u^* = \sqrt{ghJ}$	[m/s]
u_∞	Flow velocity outside of the boundary layer		[m/s]
u_A	Average air velocity in the air duct		[m/s]
$u_{A,max}$	Maximum air velocity in the center of the air duct		[m/s]
u_t	Jet takeoff velocity		[m/s]
u_{topt}	Optimal jet takeoff velocity (method M3)		[m/s]
$u_t\alpha$	Jet takeoff velocity (method M2)	eq. (6.2)	[m/s]
$u_t\varphi$	Jet takeoff velocity (method M1)	eq. (6.1)	[m/s]
t	Deflector height	Figure 3.9	[m]
T	Time		[s]
T_{jet}	Flight time of jet from takeoff to impact		[s]
T_{max}	Flight time of jet from takeoff to maximum elevation		[s]
T_u	Turbulence intensity	$T_u = u'/u$	[-]
W	Weber number	$W = u/(\sigma/\rho/h)^{0.5}$	[-]
W_o	Approach flow Weber number		[-]
x	Streamwise coordinate (inclined)	Figures 2.13 and 3.9	[m]
x'	Horizontal coordinate	Figure 2.13	[m]
x_{1-5}	Streamwise coordinate of extrema	Figures 7.1 and 7.7	[m]
x_c	Streamwise coordinate from ogee crest	Figure 2.1	[m]
x_d	Streamwise coordinate of the deflector start	$x_d = -L_d$	[m]
x_i	Streamwise coordinate of the inception point		[m]
x_o	Streamwise coordinate of approach flow point		[m]
X_c	Normalized streamwise distance from ogee crest		[m]
X_d	Normalized streamwise coordinate for drawdown		[m]
X_j	Normalized streamwise jet coordinate	eq. (2.64a)	[-]
z	Coordinate perpendicular to pseudo-bottom	Figures 2.13 and 3.9	[m]
z'	Vertical coordinate	Figure 2.13	[m]
z_{90}	Surface elevation where $C = 0.90$		[m]
z_{90l}	Lower jet surface elevation where $C = 0.90$		[m]
z_c	Vertical coordinate from ogee crest	Figure 2.1	[m]
z_{cu}	Vertical drop from ogee crest until quasi-uniform flow		[m]
z_{max}	Maximum elevation of jet trajectory		[m]
Z	Normalized depth coordinate	$Z = z/z_{90}$	[-]

List of Symbols

Z_d	Normalized depth coordinate for drawdown		[m]
Z_j	Normalized depth coordinate	eq. (2.64b)	[-]

Greek letters

α	Geometrical deflector angle	Figures 2.13 and 3.9	[°]
α_k	Kinetic energy correction coefficient		[°]
α_t	Jet takeoff angle		[°]
α_{tl}	Lower jet surface takeoff angle	Figure 2.13	[°]
α_{top}	Optimal jet takeoff angle (method M3)		[°]
α_{tu}	Upper jet surface takeoff angle	Figure 2.13	[°]
$\alpha_{t\alpha}$	Jet takeoff angle (method M2)		[°]
$\alpha_{t\varphi}$	Jet takeoff angle (method M1)		[°]
α'_t	Jet takeoff angle measured from horizontal		[°]
β	Air entrainment coefficient	$\beta = Q_A/Q$	[-]
γ	Jet impact angle	Figure 2.13	[°]
δ_{bl}	Thickness of boundary layer	Figure 2.1	[m]
δ_i	Inner jet spread	Figure 2.16	[m]
δ_o	Outer jet spread	Figure 2.16	[m]
δ_s	Jet spread angle		[°]
Δp	Air cavity subpressure		[Pa]
Δx	Streamwise measurement spacing		[m]
Δz	Depth wise measurement spacing		[m]
$\Delta z'$	Vertical elevation difference between approach flow and takeoff		[m]
ε	Relative roughness	$\varepsilon = k_s/d$	[-]
λ	Scale factor		[-]
μ	Dynamic viscosity		[Pa·s]
ν	Kinematic viscosity		[m ² /s]
ξ	Head loss coefficient		[-]
ρ	Density		[kg/m ³]
σ	Cavitation index	eq. (2.48)	[-]
σ_w	Surface tension of water		[N/m]
φ	Chute angle	Figures 2.1, 2.13 and 3.9	[°]
Φ	Cumulative distribution function		[-]
Ψ	Regression function		[-]

Subscripts

a	Average
A	Air
b	Bottom

<i>bl</i>	Boundary layer
<i>bwc</i>	Blackwater core
<i>c</i>	Critical
<i>d</i>	Deflector / Drawdown
<i>D</i>	Design
<i>i</i>	Inception point
<i>I</i>	Inner spread
<i>jb</i>	Jetbox
<i>l</i>	Lower surface
<i>last</i>	Most downstream profile measured
<i>o</i>	Approach flow
<i>O</i>	Outer spread
<i>s</i>	Step
<i>t</i>	Takeoff
<i>u</i>	Quasi-uniform flow / Upper surface
<i>w</i>	Equivalent blackwater
<i>W</i>	Water

Acronyms

APS	Automatic positioning system
PIV	Particle image velocimetry
PMF	Probable maximum flood
RCC	Roller compacted concrete
RMS	Root mean square

Chapter 1

Introduction

1.1 Problem outline

Spillways are hydraulic structures that allow a controlled release of floods downstream of dams. With the development of dams during the 20th century, spillways were designed for increasingly large height and large unit discharges. With time, damages resulting from cavitation were observed on structures with high velocity flows (Figure 1.1). Research demonstrated that a small air concentration in the flow could prevent damages and affected spillways were from thereon equipped with aerators.



Figure 1.1 – Cavitation damages on the Karun dam spillway 1987 (photo: Prof. Hans-Erwin Minor)

Roller compacted concrete (RCC) dams emerged in the 1980s. They, under certain circumstances,

offer time and cost advantages over conventional gravity dams, and their typical stepped face prompted the rapid development of stepped spillways. Used since antiquity (Chanson 2002), *stepped* spillways have the benefit of a higher kinetic energy dissipation than *smooth* spillways, and therefore require theoretically smaller dissipation structures at their toe. Steep ($\varphi \approx 50^\circ$) step spillways are found on the downstream face of RCC or gravity dams, while moderate slope ($\varphi \leq 30^\circ$) stepped spillways are found on embankment dams. A larger range of slopes are used for spillways integrated on the topography surrounding dams.

The steps increase flow turbulence which causes the self-aeration or inception point to be higher upstream than that of smooth spillways. Downstream of this point, the air entrained naturally protects the spillway from cavitation damages. However, upstream of the inception point, stepped spillways are potentially more exposed to cavitation than smooth spillways due to flow separation combined with low pressures on each step. Until studies in the past decade, the conditions leading to cavitation inception were unknown for stepped spillways. Cavitation damages were observed on the Danjiangkou dam (China) stepped spillway for a unit discharge of $q = 120 \text{ m}^2/\text{s}$ (Lin and Han 2001; Wang et al. 2012). This lack of knowledge led to conservative unit discharges up to some $q = 30 \text{ m}^2/\text{s}$ compared to $q = 280 \text{ m}^2/\text{s}$ for smooth spillways (Volkart 1984).

1.2 Stepped spillway aerators

To overcome the uncertainties regarding the cavitation risk on stepped spillways, i.e. avoid cavitation damages and use relatively high unit discharges, project engineers are using different designs to force flow aeration. Four different designs to aerate stepped spillways have been found:

- The 111 m high Dachaoshan dam (China) was built during 1997–2003 with a step height of 1 m (Figure 1.2a). The spillway is equipped with flaring gate piers (vertical deflectors on the downstream side of each piers) that contract the flow on only 30 % of the spillway width (Lin and Han 2001). The spillway bottom surface is smooth until the end of the piers. An angle difference between this smooth surface and the stepped chute (Figure 1.2b) combined with a 2 m high first step creates an air cavity under the flow along the first six steps and entrains air close to the bottom (Deng et al. 2003). The unit discharge is $q = 193.6 \text{ m}^2/\text{s}$ for the safety flood. Prototype pressures, velocities and air concentrations were measured on four steps for $q = 165 \text{ m}^2/\text{s}$ in 2002, and the bottom air concentration C_b was found to be higher than $C > 0.30$ (Guo et al. 2003). Other Chinese dams such as Shuidong and Baise use a similar design. The flaring gate piers design was also used for the 146 m high Murum dam (Malaysia) with a maximum unit discharge $q = 39.2 \text{ m}^2/\text{s}$ and was tested on a 1:40 physical model (Wang et al. 2012). Damages due to fluctuating hydrodynamic pressures in concrete fissures were observed on several stepped spillways combined with flaring gate piers (Li and Yin 2016).
- The 75 m high Wadi Dayqah dam (Oman) was built during 2006–2009 with a step height of 1.2 m (Figure 1.3a). The spillway is 201 m wide and fusegates on the dam crest are used

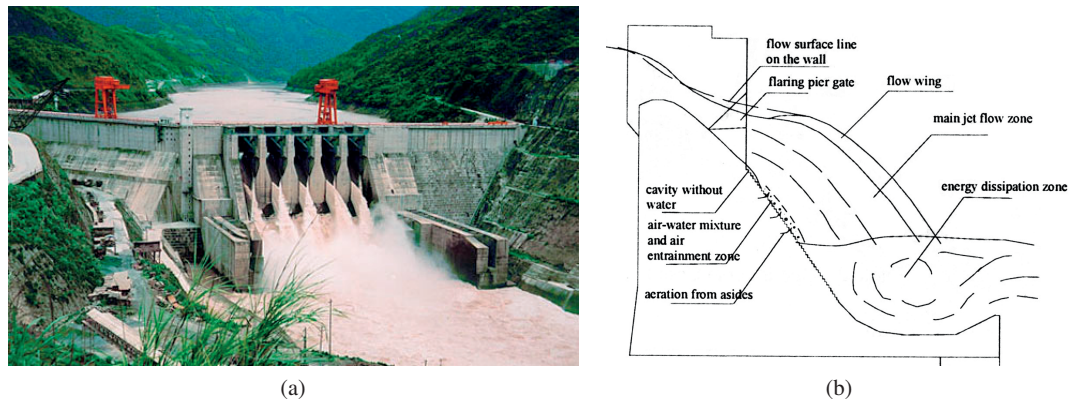


Figure 1.2 – Dachaoshan dam (a) photo of the spillway in operation (photo: Yunnan Adventure Travel), (b) spillway section (Deng et al. 2003)

for discharges larger than the 10000-year flood (Prisk et al. 2009; Al Harthy et al. 2010; Strobl 2013). Splitter teeth (Mason 1983) extending 4 m horizontally are located at a vertical elevation of 11.5 m below the spillway crest, have a width of 3 m and are spaced of 3 m (Figure 1.3b). A continuous lip extending 4 m horizontally is located 4 m below the splitter teeth. Both the splitter teeth and the lip are aerated. The spillway bottom surface is smooth upstream of the lip and stepped downstream. The flow is mostly lifted above the steps for high discharges. The 1000-year flood leads to a unit discharge of $q = 49.8 \text{ m}^2/\text{s}$, the 10000-year flood $q = 67.1 \text{ m}^2/\text{s}$ and the PMF $q = 84.1 \text{ m}^2/\text{s}$. A 1:65 physical model was used to verify the design.

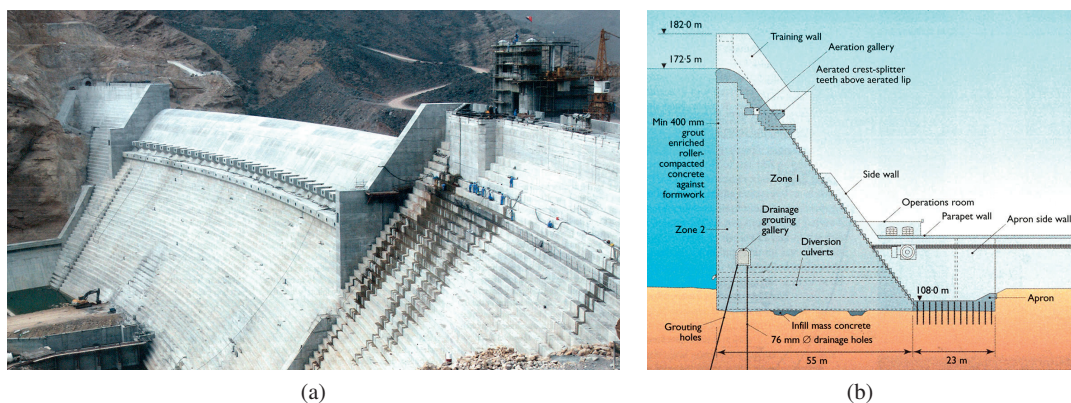


Figure 1.3 – Wadi Dayqah dam (a) construction photo (Prisk et al. 2009), (b) spillway section (Prisk et al. 2009)

- The 79 m high Boguchany dam (Russia) was built during 1974–2012. Although it is a combination of a rock-fill and conventional concrete gravity dam, a stepped spillway with a step height of 1.5 m is part of the gravity dam to raise energy dissipation (Figure 1.4). A first aerator is located at the transition of the smooth ogee and the seven 0.5 m high transition steps. It consists of a 1 m step combined with a recess of 1.5 m of the piers to aerated the flow.

A second aerator is made of a 3.6 m high step at the end of the piers. Both aerators are groove type aerators (Figure 2.12). The maximum unit discharge is $q = 45 \text{ m}^2/\text{s}$. A 1:30 physical model of the spillway was built and a negligible amount of air entrainment was observed at the first aerator, while the second performs adequately (Toloshinov et al. 2009). A bottom air concentration of $C_b = 0.20$ was measured after the aerator, and $C_b = 0.10\text{--}0.15$ along the chute.

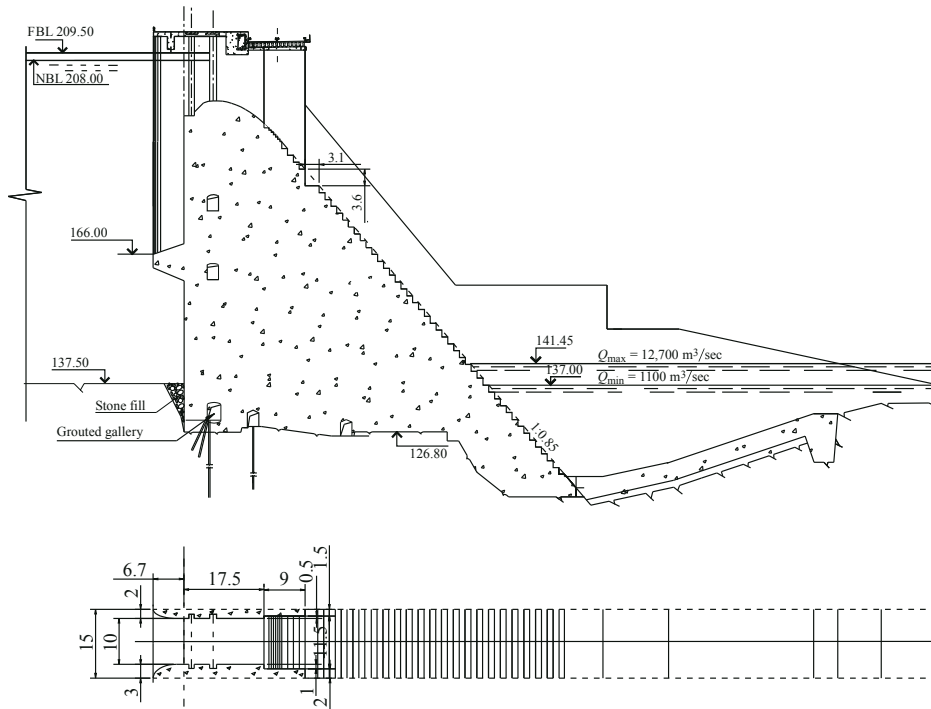


Figure 1.4 – Section and plan of one span of the stepped spillway of Boguchany dam (Toloshinov et al. 2009)

- The 87 m high enlarged Cotter RCC dam (Australia) was built during 2009–2013 with a step height of 1.2 m (Figure 1.5a). It has a 70 m wide primary spillway on the center of the downstream face with secondary spillways on its side (Willey et al. 2010). The 1000-year flood leads to a unit discharge of $q = 8 \text{ m}^2/\text{s}$ on the primary spillway, and the PMF to $q = 48 \text{ m}^2/\text{s}$. The aerator was designed according to Ozturk et al. (2008) and is placed 25 m vertically below the crest. The criteria for the aerator location was a flow velocity of 15 m/s based on Amador et al. (2009), which is reached for $q = 19.3 \text{ m}^2/\text{s}$. Two steps are filled upstream of the deflector to obtain a smooth bottom (Figure 1.5b). A numerical model and a 1:45 physical model were used to verify and optimize the general performance of the spillways and the stilling basin. Regarding the aerator, the model led to a modification of the air intake tower shape to produce less flow disturbance on the secondary spillway.

The first two examples are unconventional stepped spillways. With flaring gate piers, the flow is three dimensional and has little contact with the steps. In the second example the flow is lifted above the steps along most of the chute by the lip. The third and fourth example are conventional

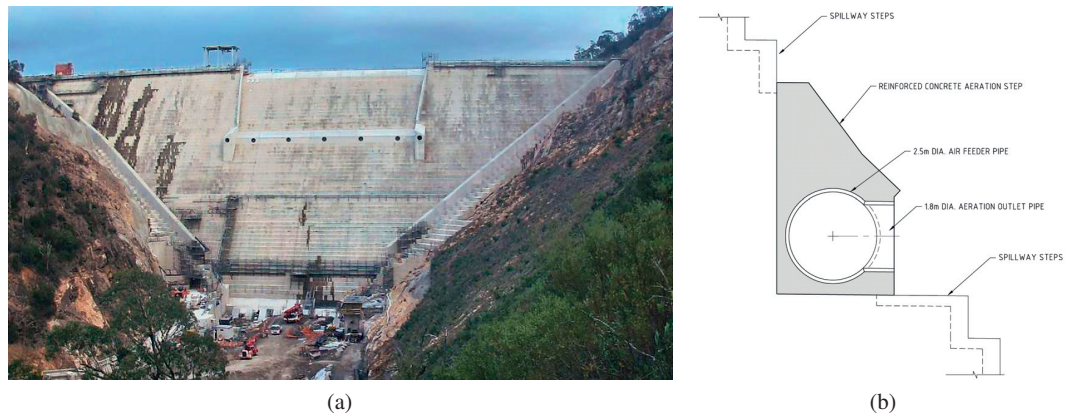


Figure 1.5 – Enlarged Cotter dam (a) construction photo (ACTEW, 2013), (b) aerator geometry (Willey et al. 2010)

stepped spillway, with minimal flow perturbations by the aerator. However, for the Boguchany dam spillway there might be a risk of choking as observed with groove aerators on smooth chutes. For the enlarged Cotter dam primary spillway, the aerator was designed with smooth chute guidelines without knowing the effect of the step induced turbulence upstream and without knowing the resulting air concentrations downstream.

Physical models were built for all the projects presented, but their scale was likely too small to accurately reproduce air entrainment processes without scale effects. This variety of aerator designs results from the lack of knowledge on how to efficiently aerate stepped spillway flows.

1.3 Objectives

Several research projects in the past decades investigated stepped spillways, but none have systematically studied forced aeration. Despite this gap of knowledge, stepped spillways are built with increasing specific discharges such that cavitation damages could theoretically occur without aerators.

The objective of this research is to investigate the aeration of stepped spillways by applying the well documented smooth chute deflector aerator to stepped chutes, study its performance, investigate the influence of relevant parameters and assess its effect on the downstream flow.

To achieve this goal, physical experiments are performed to measure the aerator air entrainment and the local air concentration development downstream. The analysis of the results allow to complete the following objectives:

- Describe the effect of the aerator on the flow
- Investigate the effect of each parameter
- Define an aerator geometry that minimizes flow perturbation

- Define the conditions that maximize the bottom air concentration
- Define the influence length of the aerator

1.4 Structure of the report

This report is divided in ten chapters. Chapter 1 introduced the general problematic of cavitation on stepped spillways. In Chapter 2, a review of literature on stepped spillways, cavitation and aerators is presented. The physical model setup and the test performed are detailed in Chapter 3. Reference tests without aerator are presented first in Chapter 4. General results of aerator tests such as the flow zones and air entrainment coefficient are given in Chapter 5. The characteristics of the jet generated by the jet as well as an approach to determine the lower and upper jet surface are presented in Chapter 6. The development of the average and bottom air concentrations is discussed in Chapter 7. The effect of an increased approach bottom roughness and a pre-aerated approach flow is introduced in Chapter 8. Chapter 9 gives a practical design example of a stepped spillway aerator. Finally, Chapter 10 summarizes the limits of the study and the results achieved.

Chapter 2

Literature Review

This literature review is divided according to its three main topics. The properties of *stepped spillway* flows are presented first with a focus on the characteristics relevant for cavitation inception or protection. In the second part, the *cavitation* process, the measures that can be taken to prevent cavitation damages and the cavitation potential on stepped spillways are introduced. The third topic discusses the characteristics of *smooth spillways aerators*, including the aerator air entrainment, the jet generated by the aerator and the development of the flow downstream of the aerator. Finally, the three topics are combined in the fourth part where preliminary stepped spillways aerator studies are presented.

Throughout this report, two-phase flows are described with various characteristics and definitions of the main ones are given here:

- The mixture flow depth h_{90} is commonly adopted and defines the depth from the bottom until a virtual surface where the local air concentration C is $C = 0.90$.
- The average air concentration C_a is defined by the integration of the local air concentration C from the bottom to h_{90} divided by the flow depth h_{90} (Straub and Anderson 1958)

$$C_a = \frac{1}{h_{90}} \int_0^{h_{90}} C \cdot dz \quad (2.1)$$

- The average air concentration C_a allows to easily calculate the equivalent blackwater flow depth h_w

$$h_w = \int_0^{h_{90}} (1 - C) \cdot dz = (1 - C_a)h_{90} \quad (2.2)$$

- The bottom air concentration C_b is defined as the lowest, i.e. closest to the bottom, air concentration point measured in an air concentration profile.

2.1 Stepped spillways

General features of stepped spillways are first introduced in the overview. Then characteristics important for this study, such as the different flow regions, air concentration profiles and the flow pressure on the steps, are presented. Finally, other researches on stepped spillways are presented last.

2.1.1 Overview

Stepped spillways have been used since Antiquity (Chanson 2002), but were hardly used during the 20th century as smooth spillways were preferred for their higher discharge capacity and their ease of construction. As a consequence, only a few researches were performed on stepped spillway (Hager and Pfister 2013). The development of RCC dams in the 1980s provoked a regain of interest in stepped spillways. Since then, stepped spillways are commonly used and have been intensively investigated in the past decades. A review of the topics studied is given in Matos and Meireles (2014).

Steep step spillways are found on the downstream face of a RCC or gravity dam with a chute angle of $\varphi = 50\text{--}53^\circ$. Besides, step spillways are increasingly built on embankment dams to increase the overtopping protection and have a flat to moderate angle of $\varphi \leq 30^\circ$. Most studies are either focusing on steep stepped spillways or embankment stepped spillways.

Figure 2.1 shows a steep stepped spillway built on a RCC dam. The crest generally has a smooth standard ogee, and the steps starts at the tangency between the standard ogee profile and the downstream face of the dams. Sometimes, steps of variables height are used to make the ogee so that the step edges follow the ogee profile (Sorensen 1985). Transitions steps with half the standard step height s can be used at the transition between the smooth bottom and the stepped chute. The surface that links the step edges is the *pseudo-bottom*. As on smooth spillways, a turbulent boundary layer develops from the crest along the chute bottom. The flow is non-aerated in this region and its surface is smooth. When the boundary layer reaches the surface, air is entrained from the surface into the flow. This point is called the *inception point* of self-aeration. Downstream of the inception point, a gradually varied aerated flow occurs and has a rough surface. Finally the flow is near equilibrium in the quasi-uniform flow region.

The flow on stepped spillways can be characterized in three different regimes. The *nappe flow* regime occurs for low discharges, and the flow plunges from one step to the next, impacting each step. A small pool and hydraulic jump form on each step. The *skimming flow* regime occurs at high discharges. In this regime, the flow forms a coherent stream parallel and above the pseudo-bottom. Below the pseudo-bottom, recirculating vortices form in the step cavities. An intermediate *transition flow* regime occurs between the two previous regimes with significant longitudinal variations (Ohtsu and Yasuda 1997). This instable flow regime is chaotic, produces splashing and should be avoided for design purposes. The type of regime depends on the chute angle φ and the unit discharge represented by the ratio of critical depth h_c over the step height s . The regime limits suggested

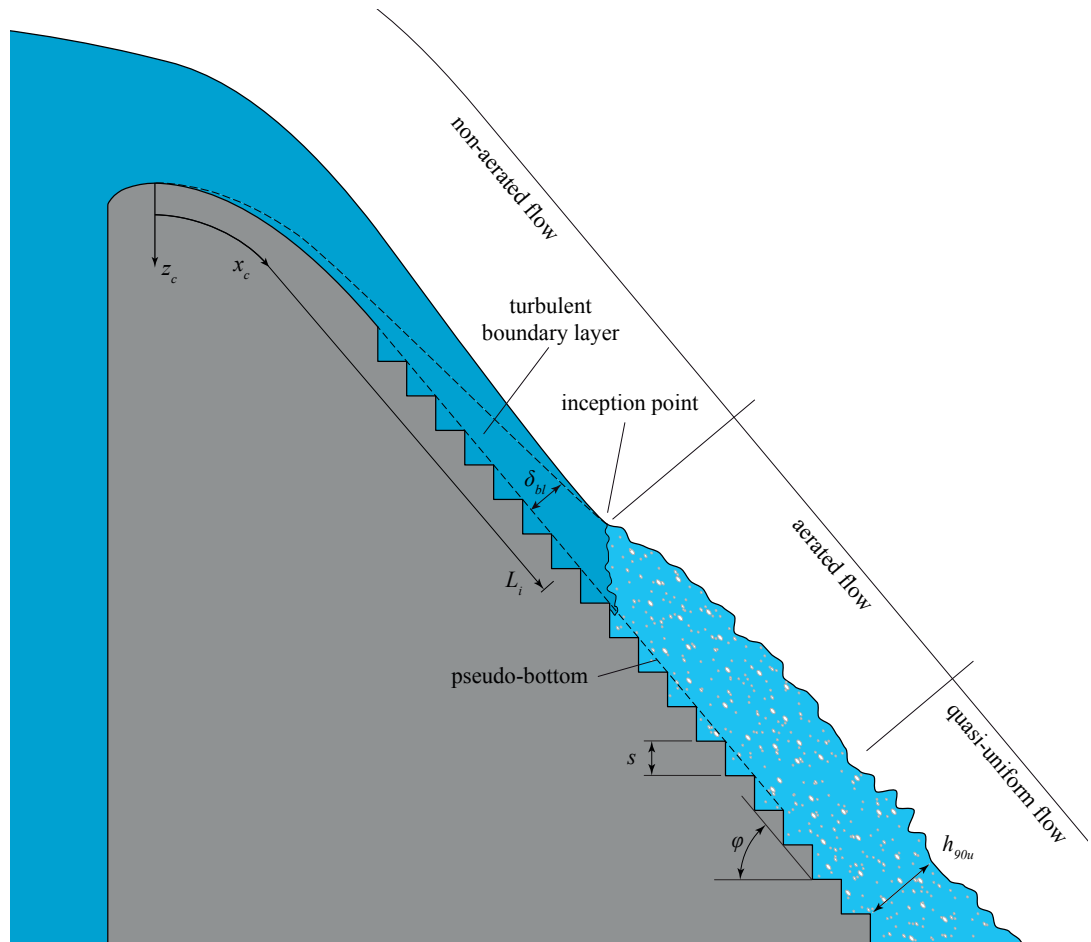
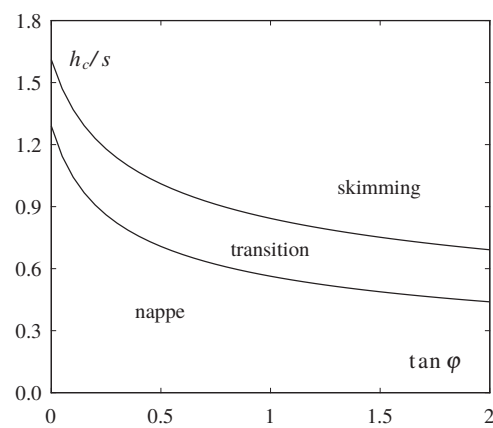


Figure 2.1 – Definition scheme of a stepped spillway and the related flow

Figure 2.2 – Limits of flow regimes as a function of the chute angle ϕ and the relative critical depth h_c/s (Chanson et al. 2015)

by Chanson et al. (2015) are shown in Figure 2.2. As large unit discharges are of interest for the present study, only skimming flow characteristics are introduced thereafter.

Stepped spillway design guidelines have been presented among others by Matos (2000b), Chanson (2002), Boes and Hager (2003a), Gonzalez and Chanson (2007), Bung (2011), Hunt et al. (2014) and Felder and Chanson (2016). These guidelines allow to determine the inception point characteristics, the flow depth development, the air concentration characteristics, the friction factor and the residual energy.

2.1.2 Non-aerated flow

The non-aerated flow is located upstream of the inception point (Figure 2.1). From the crest of the spillway, a turbulent boundary layer develops, and its thickness δ_{bl} can be expressed with the general equation (Bauer 1953)

$$\frac{\delta_{bl}}{x_c} = a \left(\frac{x_c}{k_s} \right)^{-b} \quad (2.3)$$

with x_c as the streamwise coordinate from the spillway crest, a and b as coefficients, and k_s as the surface roughness.

Amador et al. (2006) used particle image velocimetry (PIV) measurements to determine the growth of the turbulent boundary layer and obtained $a = 0.112$ and $b = 0.309$ for a chute angle of $\varphi = 51.3^\circ$ and using the step roughness $k = s \cos \varphi$ instead of the equivalent sand surface roughness k_s . Meireles et al. (2012) used a conductivity probe as well as a back-flushing pitot tube to measure the flow velocity. They observed fluctuations in the turbulent boundary layer thickness, and the average boundary thickness is obtained with $a = 0.114$ and $b = 0.311$. Both studies obtained a practically identical result, and shows that the turbulent boundary layer grows between two to three times faster on stepped chutes than on smooth chutes with $a = 0.03$ and $b = 0.14$ (Wood 1991).

For steep stepped spillways, the equivalent blackwater flow depth h_w upstream of the inception point can be obtained for $0.1 \leq x_c/L_i \leq 1$, $0.4 \leq h_c/s \leq 19.3$, and $\varphi = 53^\circ$ by (Meireles et al. 2012)

$$\frac{h_w}{h_{wi}} = 1.17 - 0.25 \frac{x_c}{L_i} + \frac{0.084}{x_c/L_i} \quad (2.4)$$

with h_{wi} as the equivalent blackwater flow depth at the inception point, and L_i the coordinate of the inception point (§2.1.3).

For embankment stepped spillways, a similar relation is given in Meireles and Matos (2009), and Hunt and Kadavy (2014) suggest a relation based on the chute angle φ , the critical depth h_c , and the relative unit discharge h_c/s .

The air concentration C_a is practically constant for $x_c/L_i \leq 0.8$, and can be expressed for $0.3 \leq$

$x_c/L_i \leq 1$ and $\phi = 53^\circ$ by (Meireles et al. 2012)

$$C_a = 0.14 - 0.063 \left(\frac{x_c}{L_i} \right)^{10.8} \quad (2.5)$$

Pfister and Boes (2014) suggest that C_a should be smaller ($C \rightarrow 0$) near the crest. This difference comes from surface oscillation and entrapped air (Meireles et al. 2014).

The head H at a point x_c can be obtained for $\phi = 53^\circ$ by (Meireles et al. 2012)

$$\frac{H}{H_{max}} = 1 - 0.315 \frac{x_c}{L_i} \quad (2.6)$$

with H_{max} as the upstream reservoir head with the elevation of x_c as the reference elevation. It indicates that $\sim 30\%$ of the energy has been dissipated at the inception point. A similar equation for embankment stepped spillways is given in Meireles and Matos (2009).

The PIV measurements of Amador et al. (2006) revealed that shear strain and vorticity is stronger close to the pseudo-bottom, with peaks directly behind the step edge. A turbulence intensity $T_u = 0.04$ was measured at the transition between the turbulence boundary layer and the irrotational flow, and $T_u = 0.40\text{--}0.65$ near the pseudo-bottom.

2.1.3 Inception point of free-surface aeration

The inception point is the location where natural air entrainment starts (Figure 2.1). It occurs when the edge of the turbulent boundary layer reaches the free surface (Wood et al. 1983). The surface flow turbulence becomes large enough to break the surface tension and droplets are ejected from the flow. The droplets then entrain air in their wakes as they fall back into the flow with gravity. In addition, collapsing waves entrain large amounts of air. The position of air entrainment fluctuates in time as both the boundary layer and free surface are unsteady due to turbulence (Wood 1991; Pfister and Hager 2011).

For the design of a stepped spillway, the inception point is important regarding cavitation and energy dissipation (Pfister and Hager 2011). It is the most exposed location to cavitation on the chute. Upstream, the cavitation risk is lower due to slower flow velocities, whereas downstream, the chute is protected by self-aeration.

Compared to smooth chutes, the inception point is located higher upstream on the chute due to the enhanced growth of the boundary layer caused by the steps. The steps size influences the location and this effect is generally taken into account with the step roughness Froude number F_k

$$F_k = \frac{q}{\sqrt{g \sin \phi k^3}} \quad (2.7)$$

with $k = s \cos \varphi$ the step roughness.

Other similar definitions include the inception Froude number F_i and the step height Froude number F_s . Further, these definitions are adapted as functions of F_k to allow a direct comparison

$$F_i = \frac{q}{\sqrt{g \tan \varphi k^3}} = \cos^{0.5} \varphi \cdot F_k \quad (2.8)$$

$$F_s = \frac{q}{\sqrt{g \tan \varphi s^3}} = \cos^{1.5} \varphi \cdot F_k \quad (2.9)$$

Various methods and definitions are used to define the inception point. They include visual observation, PIV (particle image velocimetry), air concentration and velocity profiles, an average air concentration ($C_a = 0.20$) and a bottom air concentration ($C_b = 0.01$). Meireles et al. (2012) discussed the differences and showed that due to the inability to observe small air concentrations, the visual observations method overestimate the position of the inception point.

Relations for the streamwise position L_i , the mixture flow depth h_i , the equivalent blackwater depth h_{wi} and the average air concentration C_{ai} of the inception point for mild and steep chutes are given below and compared in Figures 2.3 and 2.4. In addition, Chanson and Toombes (2002b), Gonzalez and Chanson (2007), Felder and Chanson (2009b), Hunt and Kadavy (2011) and Hunt and Kadavy (2013) presented equations to obtain L_i for embankment dams ($\varphi \leq 26.6^\circ$).

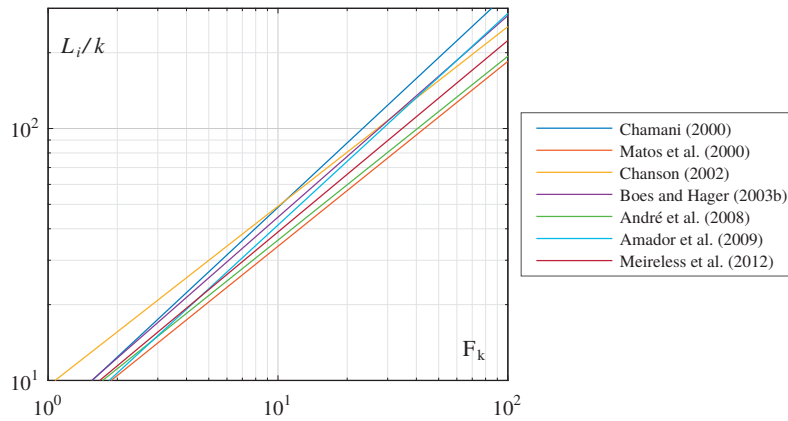


Figure 2.3 – Empirical equations for the streamwise position of the inception point L_i as a function of the step roughness Froude number F_k

Chamani (2000) with visual observation, for $51.3^\circ \leq \varphi \leq 59^\circ$

$$\frac{L_i}{k} = 8.29 \cos^{0.425} \alpha \cdot F_k^{0.85} \quad (2.10)$$

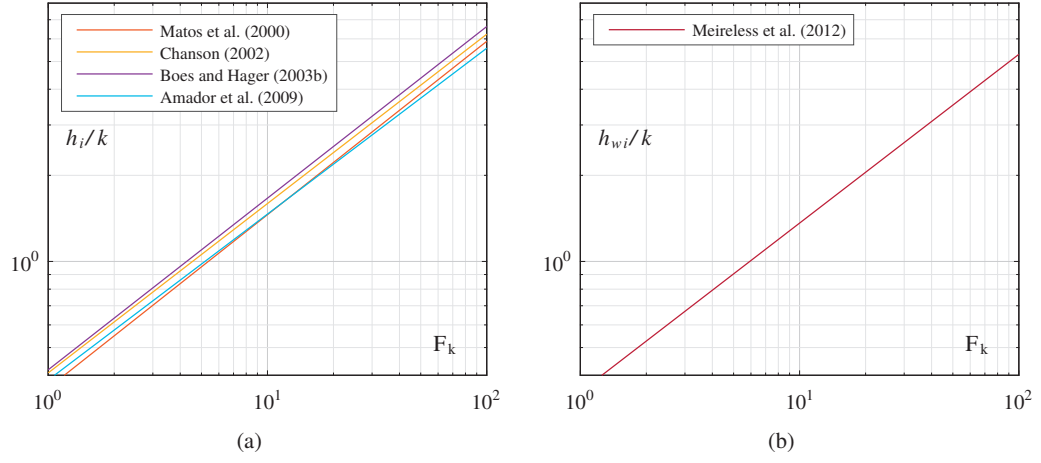


Figure 2.4 – Empirical equations for (a) the mixture flow depth at the inception point h_i , (b) the equivalent blackwater depth at the inception point h_{wi} as a function of the step roughness Froude number F_k

Matos et al. (2000) with air concentration and velocity profiles, for $\varphi = 53.1^\circ$

$$\frac{L_i}{k} = 6.289 \cdot F_k^{0.734} \quad (2.11)$$

$$\frac{h_i}{k} = 0.361 \cdot F_k^{0.606} \quad (2.12)$$

$$C_{ai} = 0.163 \cdot F_k^{0.154} \quad (2.13)$$

Chanson (2002) with visual observation, for $27^\circ \leq \varphi \leq 52^\circ$

$$\frac{L_i}{k} = 9.719 \sin^{0.0796} \alpha \cdot F_k^{0.713} \quad (2.14)$$

$$\frac{h_i}{k} = \frac{0.4034}{\sin^{0.04} \varphi} \cdot F_k^{0.592} \quad (2.15)$$

Boes and Hager (2003b) with $C_b = 0.01$, for $26^\circ \leq \varphi \leq 55^\circ$

$$\frac{L_i}{k} = 5.90 \frac{\cos^{0.2} \varphi}{\sin \varphi} \cdot F_k^{0.80} \quad (2.16)$$

$$\frac{h_i}{k} = \frac{0.40}{\cos^{0.1} \varphi} \cdot F_k^{0.60} \quad (2.17)$$

$$C_{ai} = 0.0012 \cdot (240 - \varphi) \quad (\varphi \text{ in degrees}) \quad (2.18)$$

André et al. (2008a) with visual observation, for $18.6^\circ \leq \varphi \leq 30^\circ$

$$\frac{L_i}{k} = \frac{8}{\tan \varphi} \cdot F_k^{0.73} \quad (2.19)$$

Amador et al. (2009) with PIV, for $\varphi = 51.3^\circ$

$$\frac{L_i}{k} = 5.982 \cdot F_k^{0.84} \quad (2.20)$$

$$\frac{h_i}{k} = 0.385 \cdot F_k^{0.580} \quad (2.21)$$

Meireles et al. (2012) with air concentration and velocity profiles, for $\varphi = 53.1^\circ$

$$\frac{L_i}{k} = 6.75 \cdot F_k^{0.76} \quad (2.22)$$

$$\frac{h_{wi}}{k} = 0.35 \cdot F_k^{0.59} \quad (2.23)$$

$$C_{ai} \approx 0.20 \quad (2.24)$$

Surprisingly, increasing the roughness of the step surfaces moves the inception point further downstream compared to a standard stepped chute (Takahashi et al. 2006; Gonzalez et al. 2008).

2.1.4 Aerated flow

From the inception point, air is rapidly entrained into the flow, which leads to an increase of the mixture flow depth h_{90} , the average air concentration C_a and the bottom air concentration C_b . The average flow velocity also increases due to a reduction of friction with increasing air concentration (Matos and Meireles 2014).

To calculate the flow depth for $\varphi = 55^\circ$, Takahashi and Ohtsu (2014) suggest an analytical model based on the air concentration development model of Chanson (1993). Bung (2011) gives relation to obtain the mixture flow depth h_{90}/s , equivalent blackwater depth h_w/s and the average air concentration C_a for embankment spillways. These relation are function of the step roughness Froude number F_k and the relative vertical drop z_c/z_{cu} , with z_{cu} is the vertical drop where quasi-uniform flow is reached.

For the average air concentration development C_a , Matos (2000b) suggests a relation function of $(x - L_i)/h_i$, while Pfister and Hager (2011) suggest that C_a/C_{au} is a function of x_c/L_i , with C_{au} as the quasi-uniform average air concentration. Both relations are for steep stepped chutes ($\varphi \approx 50^\circ$).

For the bottom air concentration development C_b , Boes and Hager (2003b) suggest for $26^\circ \leq \varphi \leq 55^\circ$

$$C_b(x) = 0.015 \left(\frac{x - L_i}{h_i} \right)^{\sqrt{\tan \varphi}/2} \quad (2.25)$$

And for a chute of $\varphi = 53^\circ$, Matos et al. (2000) suggest

$$C_b(x) = \frac{0.324}{1 + \left(\frac{(x - L_i)/h_i}{10.195} \right)^{-1.79}} \quad (2.26)$$

2.1.5 Quasi-uniform flow

Quasi-uniform conditions are reached after a certain elevation drop z_{cu} below the ogee crest. The drop is function of the unit discharge expressed by the critical depth h_c and the chute angle φ (Boes and Hager 2003a; Bung 2011). In addition, Ohtsu et al. (2004) suggest an influence of the relative step height s/h_c . Pfister and Hager (2011) showed that the uniform average air concentration C_{au} is attained after $x_c \approx 2L_i$.

The quasi-uniform flow is characterized by its flow depth h_{90u} and equivalent blackwater depth h_{wu} . Boes and Hager (2003a) obtained for $30^\circ \leq \varphi \leq 50^\circ$

$$\frac{h_{90u}}{s} = 0.50 \cdot F_s^{0.1 \tan \varphi + 0.5} \quad (2.27)$$

$$\frac{h_{wu}}{s} = 0.23 \cdot F_s^{0.65} \quad (2.28)$$

with F_s given by equation (2.9).

Equation (2.28) can be approximated by

$$\frac{h_{wu}}{h_c} = 0.215 \cdot \sin^{-1/3} \varphi \quad (2.29)$$

It indicates that only the chute angle φ has an influence on the uniform flow depth besides the discharge. In addition, Takahashi and Ohtsu (2012) presented a procedure based on the friction coefficient f to obtain h_{wu} , and the mixture flow depth h_{90u} can then be calculated from the average air concentration.

Another important quasi-uniform flow characteristic is the uniform average air concentration C_{au} .

Boes (2000c) obtained

$$C_{au} = 0.43 - 0.00234 \cdot F_s \quad \text{for } \varphi = 30^\circ \quad (2.30a)$$

$$C_{au} = 0.60 - 0.00611 \cdot F_s \quad \text{for } \varphi = 50^\circ \quad (2.30b)$$

As suggested by Matos (2005), the uniform average air concentration can be deduced from equations (2.27) and (2.28) giving

$$C_{au} = 1 - \frac{h_{wu}}{h_{90u}} = 1 - 0.46 \cdot F_s^{0.15 - 0.1 \tan \varphi} \quad (2.31)$$

The equations are compared in Figure 2.5a. There is fairly good agreement for $\varphi = 30^\circ$, but an important difference for $\varphi = 50^\circ$ with large F_s . In addition, Ohtsu et al. (2004) presented a relation with low values of C_{au} for small relative step height s/h_c , and Takahashi and Ohtsu (2012) suggest an equation adapted from Wilhelms and Gulliver (2005)

$$C_{au} = 0.073 + \left(\frac{6.9}{\varphi} - 0.12 \right) \frac{s}{h_c} + 0.656 \left(1 - e^{-0.0356(\varphi - 10.9)} \right) \quad (\varphi \text{ in degrees}) \quad (2.32)$$

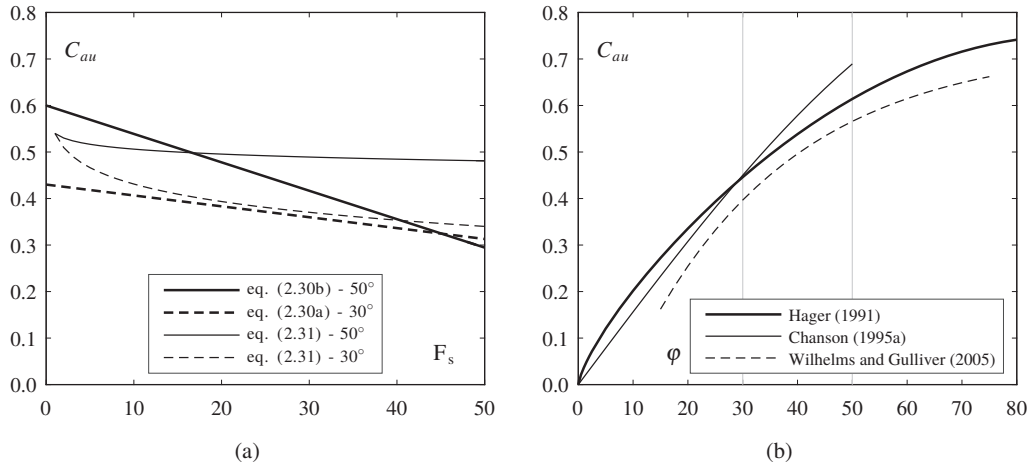


Figure 2.5 – Comparison of the uniform average air concentration C_{au} (a) for stepped chutes as a function of F_s , for (b) smooth chutes as a function of the chute angle φ

According to Chanson (1995b), Matos (2000a) and Boes and Hager (2003b), the uniform average air concentration C_{au} is similar for smooth and stepped spillways, as the roughness is not a relevant parameter. Three common empirical relations for smooth chutes are presented below and compared in Figure 2.5b

Hager (1991) based on the data of Wood (1983)

$$C_{au} = 0.75 \sin^{0.75} \varphi \quad (2.33)$$

Chanson (1993) for $\varphi \leq 50$

$$C_{au} = 0.9 \sin \varphi \quad (2.34)$$

Wilhelms and Gulliver (2005)

$$C_{au} = 0.073 + 0.656 \left(1 - e^{-0.0356(\varphi - 10.9)} \right) \quad (\varphi \text{ in degrees}) \quad (2.35)$$

When the step height s converges towards zero (giving large F_s), the relations for stepped chutes (Figure 2.5a) should give similar results to that for smooth chutes (Figure 2.5b). Equation (2.31) produces better results than equation (2.30) in that regard. By design, equation (2.32) gives the same results as equation (2.35).

Finally the quasi-uniform bottom air concentration C_{bu} was studied by Boes (2000c) and he found

$$C_{bu} = 0.068 - 6.21 \cdot 10^{-4} \cdot F_s \quad \text{for } \varphi = 30^\circ \quad (2.36a)$$

$$C_{bu} = 0.268 - 5.69 \cdot 10^{-4} \cdot F_s \quad \text{for } \varphi = 50^\circ \quad (2.36b)$$

These relations give significantly lower C_{bu} than the relation of Hager (1991) for smooth chutes (with φ in degrees)

$$C_{bu} = 1.25 \left(\frac{\pi}{180} \varphi \right) \quad 0^\circ \leq \varphi \leq 40^\circ \quad (2.37a)$$

$$C_{bu} = 0.65 \sin \varphi \quad 40^\circ \leq \varphi \leq 80^\circ \quad (2.37b)$$

2.1.6 Air concentration profiles

The air concentration profiles on an aerated stepped chute are similar to the profiles of an aerated smooth chute (Matos et al. 2000; Chanson 2002). A theoretical diffusion model developed by Chanson (1995a) for smooth chutes and gives favorable results for stepped chutes (Chanson et al. 2002)

$$C = 1 - \tanh^2 \left(K' - \frac{Z}{2D'} \right) \quad (2.38)$$

with D' as the dimensionless turbulent diffusivity which is assumed to be constant across the flow, K' as an integration constant and $Z = z/z_{90}$ as the relative depth. The diffusivity and integration constant can be estimated with the following equations for $C_a \leq 0.7$ (Chanson et al. 2002)

$$D' = \frac{0.848C_a - 0.00302}{1 + 1.1375C_a - 2.2925C_a^2} \quad (2.39)$$

$$K' = \operatorname{atanh}(\sqrt{0.1}) + \frac{0.5}{D'} \quad (2.40)$$

An adapted model was suggested by Chanson and Toombes (2002a) with a dimensionless turbulent diffusivity D' function of the average air concentration C_a defined by

$$D' = \frac{D_o}{1 - 2(Z - 1/3)^2} \quad (2.41)$$

with D_o as a function of the average air concentration C_a .

The air concentration profile is then obtained by

$$C = 1 - \tanh^2 \left(K'' - \frac{Z}{2D_o} + \frac{(Z - 1/3)^3}{3D_o} \right) \quad (2.42)$$

with K'' as an integration constant.

The values of D_o and K'' can be obtained from Carosi and Chanson (2008)

$$C_a = 0.7622 (1.0434 - e^{-3.614D_o}) \quad (2.43)$$

$$K' = 0.32745015 + \frac{1}{2D_o} - \frac{8}{81D_o} \quad (2.44)$$

These profiles are valid at the step edges. Chanson and Toombes (2002a) observed higher air concentrations when measuring the profile between the steps. A model for the rapidly varied flow directly downstream of the inception point is presented by Zhang and Chanson (2016).

2.1.7 Pressure on the steps

The recirculating cells that form in the step cavities under the flow in the skimming flow regime induce hydrodynamic pressures. On the horizontal face of steps, there is a maximum of pressure close to the edge of the step due to the impact of the overlying flow (Figure 2.6), and a minimum at about a third of the step length away from the step corner (Sánchez-Juny et al. 2007; Amador et al. 2009; André et al. 2008b; André and Schleiss 2008). On the vertical face, the maximum occurs at

the corner of steps, and a negative pressure occurs on the upper part due to flow separation.

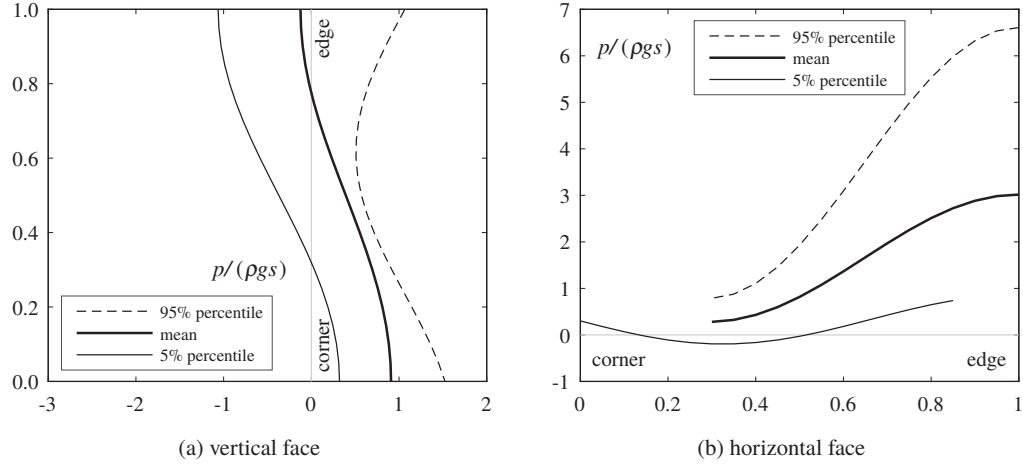


Figure 2.6 – Dimensionless pressure $p/(\rho g s)$ on the step faces in a fully developed aerated flow according to the model of Sánchez-Juny et al. (2008) for $h_c/s = 2.25$ and the maximum of the wavy pattern

By measuring the pressure at the center of the horizontal face of steps, Sánchez-Juny and Dolz (2005) observed a streamwise wavy pattern in the pressure. This seems to indicate that the separation of the main flow and the recirculating cells is not exactly defined by the pseudo-bottom. The flow can hit the step edge or on the contrary separate from the step. A model (Figure 2.6) taking into account the minimum and maximum of this pattern was developed to obtain the 5 % percentile, the mean and the 95 % percentile (Sánchez-Juny et al. 2007, 2008) of the pressure in a fully developed aerated flow.

Both the mean pressure and the pressure fluctuations in the non-aerated flow upstream of the inception point are higher than in the aerated flow downstream due to a cushion effect induced by the presence of air (Amador et al. 2005, 2009; Sánchez-Juny and Dolz 2005). The maximum of the pressure fluctuations occurs around the inception point (Amador et al. 2009). The consequences of the negative mean pressure and the pressure fluctuations on the cavitation potential are discussed further in §2.2.3.

2.1.8 Control section and transition steps

A standard ogee is usually built for steep spillways as a non-regulated control section, whereas as broad crested weir is more common for embankment dams. For $\varphi = 50^\circ$, Pfister (2009) studied the effect of a broad crested weir or a flap-gate instead of the standard ogee. The broad crested weir generates subpressures in the first steps and an air supply should be provided to create a jet. Spray then occurs at the jet impact on the steps. The flap-gate design is not recommended as it creates a fluctuating flow, long jets and intense spray.

Experiments on a broad crested weir were also performed by Zhang and Chanson (2015) on a

$\varphi = 45^\circ$ chute. Adding a small rounding at the top of the first vertical step face was found to be an efficient measure to control the jet deflection.

The influence of the relative step height s/h_c , as well as different transition step heights on the pressure in the inner step corners was presented by Yasuda et al. (2006). Large steps lead to larger pressures and are therefore recommended to avoid cavitation potential.

2.1.9 Flow velocity profile

According to Cain and Wood (1981), the velocity profile can be approximated by a power law

$$\frac{u}{u_{90}} = \left(\frac{z}{z_{90}} \right)^{1/N} \quad (2.45)$$

with u as the velocity, u_{90} as the velocity at the surface ($C = 0.90$) and N as the velocity power law exponent.

The exponent N has been studied by multiple authors and is depending on the chute angle φ (Bung 2011; Takahashi and Ohtsu 2012) and on the relative step height s/h_c (Takahashi and Ohtsu 2012). The exponent N decreases with an increasing chute angle φ . Typical values of $3 \leq N \leq 6.5$ are obtained for steep stepped spillways (Boes 2000a; Amador et al. 2006; Meireles et al. 2012), and $4 \leq N \leq 11$ for moderately sloped stepped spillways (Gonzalez and Chanson 2004; Meireles and Matos 2009; Bung 2011). Boes and Hager (2003b) and André et al. (2005) presented a slight variation of equation (2.45) where the power law is used only for a fraction of the flow depth and a multiplicative coefficient is used.

2.1.10 Friction factor and energy dissipation

The main advantage of stepped spillways in the increased energy dissipation compared to smooth chutes. The Darcy-Weisbach friction factor f has therefore been investigated in multiple studies (Tozzi 1994; Chamani and Rajaratnam 1999; Matos 1999; Chanson and Toombes 2002b; Chanson et al. 2002; Boes and Hager 2003a; Ohtsu et al. 2004; Amador et al. 2006; Chanson 2006; Felder and Chanson 2009a; Takahashi and Ohtsu 2012). Unlike smooth spillways where energy is dissipated by skin friction, form drag is dominant for stepped spillways and might have a few modes of excitation (Chanson 2015). In quasi-uniform flow f can be obtained by

$$f = \frac{2g \cdot \sin \varphi \cdot d_h}{u^2} \quad (2.46)$$

with d_h as the hydraulic diameter.

The equivalent blackwater flow depth h_w has to be used to obtain the flow velocity u and hydraulic

diameter d_h . Matos (1997, 2005) and Boes and Hager (2003a) showed that using the mixture flow depth increasingly overestimates the friction factor for large average air concentrations C_a , and it was the source of many disagreements on f in early studies. The friction factor f depends on the chute angle φ (Tozzi 1994; Boes and Hager 2003a; Takahashi and Ohtsu 2012), and a small effect of the relative step height s/h_c or s/d_h (Boes and Hager 2003a; Matos 2005; Takahashi and Ohtsu 2012). Chanson (2006) argues that the inflow conditions (standard ogee, broad crested weir, jetbox) have an effect on f . Boes and Hager (2003a) presented a method to correct the friction factor to obtain the effect of the steps without the sidewalls, and slightly larger f are obtained.

A wide range of f is still reported by Chanson et al. (2015). A reason to explain high values obtained might be that quasi-uniform flow conditions are not reached in all studies. Matos (2005) and Matos and Meireles (2014) showed that f decreases due to flow aeration along the spillway and stabilizes for quasi-uniform flow. Since free-surface aeration occurs rapidly, it is difficult to measure f without the effect of aeration. To eliminate the effect of aeration, Tozzi (1994) studied the friction factor in a closed conduit and obtained $f = 0.06\text{--}0.16$ for $\varphi = 53^\circ$. Amador et al. (2006) found $f \approx 0.12$ with PIV measurements in the non-aerated flow.

The head H along the spillway can be calculated with

$$H = h_w \cos \varphi + \alpha_k \frac{u^2}{2g} \quad (2.47)$$

with α_k as a kinetic energy correction coefficient to take into account the difference between the flow velocity profile and the mean flow velocity u . Values or relations to obtain α_k have been given by Matos (2000b), Boes and Hager (2003a), Meireles and Matos (2009), Meireles et al. (2012), Takahashi and Ohtsu (2012) and Hunt et al. (2014). Typical values are around $\alpha_k = 1.05\text{--}1.20$. Takahashi and Ohtsu (2012) showed that α_k increases with an increasing chute angle φ .

Relations to obtain the residual energy as a function of the equivalent blackwater depth or in quasi-uniform conditions have been presented by Matos (2000b), Boes and Hager (2003a), Takahashi and Ohtsu (2012) and Chanson et al. (2015). The residual energy can be measured by the tailwater depth downstream of the hydraulic jump at the toe of the spillway (Pegram et al. 1999). The plunging flow of a stepped chute in a channel downstream has been investigated by Yasuda and Ohtsu (2000).

2.1.11 Step surface roughness and macro-roughness elements

Various investigations were performed on the step surface roughness, the placement of macro roughnesses or elements in the steps, and the step shape.

The influence of the step surface roughness was investigated by Takahashi et al. (2006) and Gonzalez et al. (2008). Counter intuitively, a rough surface leads to a lower location of the inception point and lower energy dissipation compared to a smooth step surface. It is explained by lower turbulence levels in the flow. Less air was found in the rough step cavities.

André (2004) studied different layouts of macro-roughness elements paced on the edge of horizontal step faces on an embankment stepped spillway. The layout of one channel width element on every step hardly changes the flow, whereas layouts with multiple narrow elements on each step lead to a higher location of the inception point and lower flow velocities (André et al. 2008a). The drag is increased by the macro-roughness elements and thus more energy is dissipated (André et al. 2008b). The two-phase flow properties of two layouts were presented by Kökpınar (2004).

A non-uniform steps configuration was investigated by Felder and Chanson (2014) on an embankment stepped spillway. On a uniform standard stepped chute with a step height s , inserts with a height of $0.5s$ were placed every two steps to form the non-uniform step configuration. Compared to a uniform stepped spillway, the differences in two-phase flow properties are small, with more variations and flow instabilities for the non-uniform configuration.

Gonzalez and Chanson (2008) studied the influence of longitudinal triangular vanes placed in the steps and leveled with the pseudo-bottom. The recirculating cells in the steps is strongly influenced by the vanes, and the momentum exchange between the recirculating flow and the overlaying skimming flow is increased. The vanes also increase the flow resistance, particularly for a zigzag pattern.

Zare and Doering (2012) studied flow characteristics on a $\phi = 45^\circ$ stepped spillway with rounded step edges. The inception point was found to be further downstream for low discharges with rounded steps, and further upstream for high discharges with rounded edges. A slightly larger energy dissipation was also observed.

2.1.12 Air-water flow properties

Multiple studies (e.g. Chanson and Toombes 2002a,b; Gonzalez and Chanson 2004; Kökpınar 2004; Carosi and Chanson 2008; Felder and Chanson 2009b; Bung 2011; Pfister and Hager 2011; Felder and Chanson 2011; Zhang and Chanson 2016) investigated the air-water flow properties of skimming flow, such as the air concentration, the flow velocity, the bubble frequency, the bubble chord length, the bubble clustering and the flow turbulence intensity.

Chanson and Toombes (2002a) showed that turbulence levels are high on the whole depth, and that turbulence is related to the bubble frequency. Gonzalez and Chanson (2004) observed a well defined mixing layer directly downstream of each step edge with a greater expansion rate than that of mono-phase flow. The step cavities were further investigated by Felder and Chanson (2011) where a local maximum of air concentration was observed below the pseudo-bottom, highlighting a trapping of bubbles in the cavities. Pfister and Hager (2011), based on visual observations and measurements, showed that air is entrained at the bottom and in the niches by a combination of air troughs and air-water flow protruding in the steps.

2.1.13 Lateral constriction

Spillways have to be integrated on the downstream face of dams or in the surrounding topography, and valleys restrict the available width at the bottom. Hunt et al. (2012) investigated the effect of converging sidewalls for a non-aerated flow on a $\phi = 18.4^\circ$ chute. On the contrary, Estrella et al. (2015) studied an unconstrained stepped spillway without sidewalls

2.2 Cavitation

2.2.1 Overview

Cavitation is the formation of vapor cavities in water as a consequence of a reduction of the local pressure below the vapor pressure. It occurs mostly in hydraulic machines and structures. A nuclei such as impurities or microscopic gas bubbles is required for cavitation inception. The low pressure necessary results from flow separation of a high velocity flow along the boundary and of the related local pressure fluctuations (Figure 2.7). It appears on the boundary for streamlined surfaces, and within the shear layer of the flow for rough surfaces (Falvey 1990). Shear flows generate streamwise vortices that collect bubble in their core where they can coalesce into long bubbles.

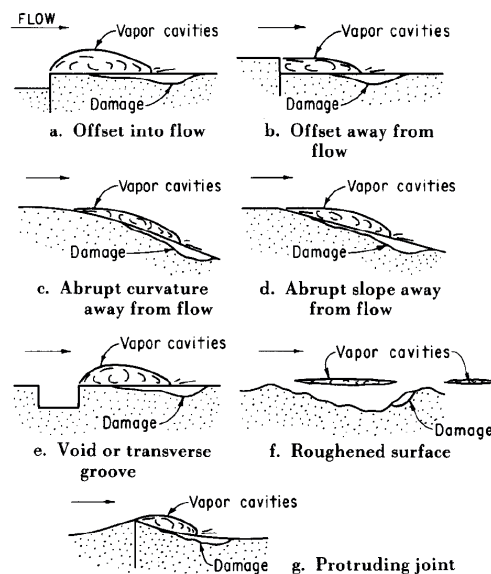


Figure 2.7 – Typical cases of flow separation and location of the resulting cavitation damage (Falvey 1990)

Vapor bubbles are swept downstream until they reach a zone with pressures high enough for their collapse. During the collapse, a shock wave is formed as the bubble size rebounds. The shock wave of a bubble propagates at the sonic speed of the fluid and triggers the implosion of the surrounding swarm of bubbles which creates a higher intensity shock wave. Resulting pressures of 1500 MPa have been measured (Lesleighter 1988). When the collapse occurs close to a boundary or in a

hydraulic gradient, it is asymmetrical as one side collapses faster (Figure 2.8) and creates a microjet in the center of the bubble. This microjet can have a velocity in excess of 100 m/s (Brujan et al. 2002). Pitting on the boundary occurs as a consequence of these processes and an intense noise can be heard when cavitation occurs.

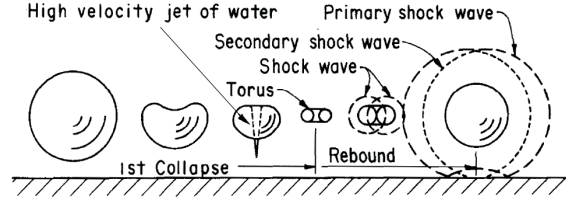


Figure 2.8 – Collapse of a bubble near a boundary (Falvey 1990)

The inception of cavitation can be determined with the cavitation index σ derived from Bernoulli's equation

$$\sigma = \frac{p + p_a - p_v}{\rho u^2 / 2} \quad (2.48)$$

with p as the local pressure, p_a as the atmospheric pressure, p_v as the vapor pressure and u as the average flow velocity.

Due to local velocities and pressure fluctuations, cavitation inception starts at a critical cavitation index σ_c depending on the geometric configuration. Multiple studies presented in (Falvey 1990) determined σ_c of various geometric singularities. For smooth chutes within strict tolerances (§2.2.2), the critical cavitation index is $\sigma_c \approx 0.2$ (Hamilton 1983; Pugh and Rhone 1988; Falvey 1990). Measures are required to avoid cavitation damages on the structure if the cavitation index σ is smaller than $\sigma < \sigma_c$.

2.2.2 Cavitation damages and prevention

While the cavitation index allows to know when cavitation presumably occurs, it does not predict damages. The damages depend from (i) where the cavitation occurs, (ii) the cavitation intensity, (iii) the time of exposure, (iv) the surface material resistance and (v) the air concentration in the flow (Falvey 1983, 1990). Figure 2.9 illustrates that a cavitation index $\sigma = 0.2$ is critical for long operation durations, whereas σ is by trend slightly higher for shorter operation durations. Examples of cavitation damages are given in Falvey (1983) and Minor (2000).

Cavitation damages can be prevented in different ways (Falvey 1990; Kells and Smith 1991):

- *Cavitation prevention*: eliminating cavitation can be achieved with two methods: (i) Reducing the flow velocity or increasing the flow pressure. Flow velocity can be reduced by a uniformly rough bottom surface, by limiting the chute angle and length or replacing the lower part of the spillway by a ski jump. Similarly, pressure can be increased by reducing the slope or a concave bottom curvature. These methods are often not practical due to topographical

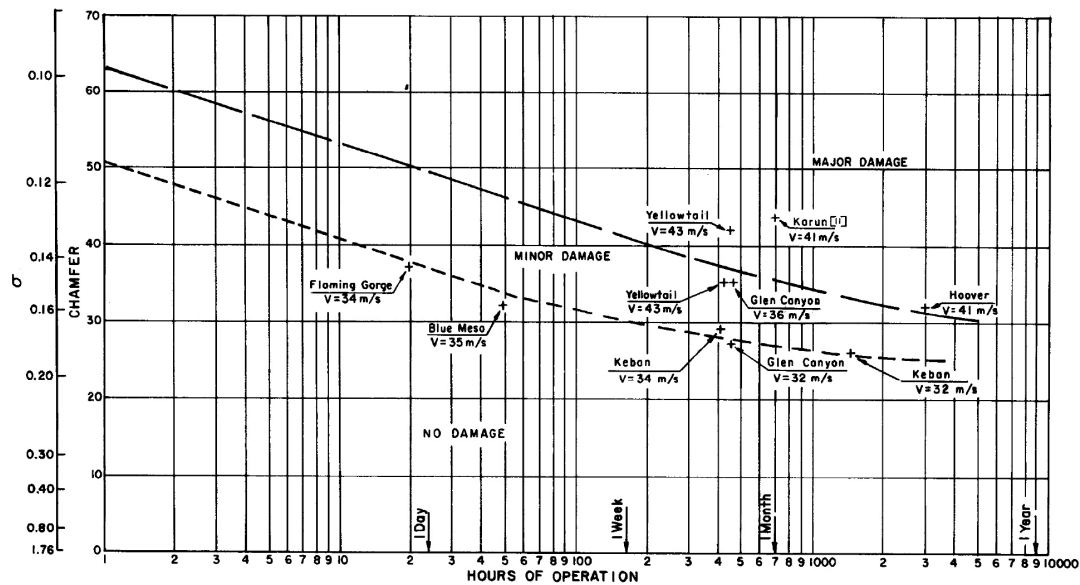


Figure 2.9 – Report of cavitation damages on spillways as a function of hours of operations and cavitation index σ (Falvey 1990)

constraints. (ii) Avoiding flow separation by adopting fine constructions tolerances (Ball 1976; Drewes 1988; Falvey 1990). Surfaces have to be exempt of irregularities, construction joints require offsets smaller than 3 mm, and higher offset need to be grinded with very low slopes (typically 1:50). These measures are costly, and may be compromised by the aging and weathering of the structure.

- *Collapse control*: if the cavitation bubbles collapse in the flow and away from the boundary, cavitation damages are avoided. This method is however difficult to apply for spillways.
- *Cavitation resistant materials*: the concrete used to build spillways can have a wide range of compressive and tensile strength which influences the resistance to cavitation damages (Russell and Sheehan 1974; Colgate 1977). The resistance to damages can be increased by adding steel fibers, or coating the surface with epoxies or polymers (Schrader 1983). Furthermore, steel or other metals can be used for small surfaces such as gates and outlets, but the cost is prohibitive for spillways.
- *Flow aeration*: studies show that a small air concentration in the flow can prevent damages. Peterka (1953) measured the weight loss of two concrete test blocks placed in the ceiling of an expanding section directly downstream of a constriction in a pressurized system. Various concentrations of air were injected upstream of the constriction to investigate the reduction of cavitation damages. For an average air concentration (in standard pressure conditions) $C_a = 0.02$, the damages are greatly reduced, while $C_a = 0.074$ is required to stop the damages. Measurements showed that the cavitation index increases linearly with the volume of air added due to the increased pressure in the low-pressure areas where cavitation forms. Rasmussen (1956) performed two experiments to measure the weight loss of samples due to cavitation.

In the first, a disk with two holes close to the perimeter is rotating in a tank. Erosion was measured on aluminum samples placed behind the holes. The results showed the influence of aluminum hardness on the erosion rate, and an air concentration of 1 % was sufficient to stop damages. In the second experiment, a cylindrical sample was placed in the center of a rectangular constriction in a pressurized flow. An air concentration of 0.8–1 % was enough to almost stop cavitation erosion for aluminum, brass, iron and ebonite. Russell and Sheehan (1974) performed experiments with various compressive strength concrete samples placed in the ceiling of a pressurized rectangular section. Bolts were used to trigger cavitation. An average air concentration of $C_a = 0.055$ injected in the ceiling upstream of the samples eliminated damages.

Flow aeration is often the most practical and economical measure avoid cavitation damages. Literature shows that a small concentration of air can stop cavitation damages. However, these investigations were performed in pressurized flow as it is difficult to use high velocity flows on a model (Russell and Sheehan 1974) and only an average air concentration was measured. The local air concentration close to the sample are unknown. As a consequence, the bottom air concentration necessary to protect spillways is not well defined.

2.2.3 Cavitation potential on stepped chutes

Due to the steps protruding into the flow, stepped chutes are more prone to cavitation than smooth chutes. However, a stepped chute is not a singular asperity and is rather a uniformly rough surface which reduces the velocities close to boundary. The increased roughness also shift the inception point of self-aeration further upstream and therefore naturally protects the chute downstream against cavitation damages. Another favorable aspect is that the flow moves away from the vertical faces of steps and therefore cavitation does not occur on the boundary (Frizell and Mefford 1991). The inception point has been identified as the most critical zone for cavitation as it has the highest flow velocities, but is not yet protected by self-aeration. Studies suggesting limits of terms of flow velocities u , unit discharge q or cavitation index σ to avoid cavitation in stepped chutes are presented herein.

To assess the cavitation potential on stepped chutes, a method is to use hydrodynamic pressure measurements. Amador et al. (2005) first suggested a limit unit discharge q of 13.9, 11.5 and 8.4 m²/s for a prototype step height s of respectively 1.2, 0.9 and 0.6 m and a chute angle of $\varphi = 51.3^\circ$. The 0.1 % percentile of the pressure measured suggested by Lopardo (2002) at the inception point was used to define these limits. This research was further developed in Amador et al. (2009). A streamwise maximum of mean pressure p and of the root mean square of the pressure fluctuations p' was found at the inception point, and p as well as p' decrease in the aerated flow downstream due to a cushion effect. The pressure was normalized using the pressure coefficient C_p

$$C_p = \frac{p}{\rho u^2/2} \quad (2.49)$$

The extreme negative pressure was defined by the 0.1 % pressure percentile, and its corresponding coefficient $C_{p0.1\%}$. Considering a measured $C_{p0.1\%} = 0.8$ and the vapor pressure p_v , a critical flow velocity of $u = 15.7 \text{ m/s}$ can be obtained from equation (2.49). Using the observed flow depth at the inception point, it corresponds to a limit unit discharge q of 16.3, 14.9 and $13.12 \text{ m}^2/\text{s}$ for a prototype step height s of respectively 1.2, 0.9 and 0.6 m. According to Pfister and Boes (2014), $q = 15 \text{ m}^2/\text{s}$ leads to a critical cavitation index of $\sigma_c \approx 0.5$ for $s = 0.3 \text{ m}$ and $\sigma_c \approx 0.7$ for $s = 1.2 \text{ m}$. at the inception point

Gomes et al. (2007) performed a similar study, and suggest that a minimum $C_{p0.1\%}$ occurs at $x_c = 1.2 \cdot L_i$. An empirical model of $C_{p0.1\%}$ is given for $0.3 \leq x_c/L_i \leq 2$ (Figure 2.1) and allows to calculate the limit discharge for cavitation inception. A higher $C_{p0.1\%}$ than that of Amador et al. (2009) at the inception point gives a limit unit discharge q of $18\text{--}22 \text{ m}^2/\text{s}$, and at $x_c = 1.2 \cdot L_i$ the limit unit discharge q is $13\text{--}16 \text{ m}^2/\text{s}$.

Another method was used by Frizell et al. (2013) to assess the cavitation potential. A reduced ambient pressure chamber was used with steps on the invert. Two step angles $\varphi = 21.8^\circ$ and $\varphi = 68.2^\circ$ were tested with two step height s each. For each configuration and various discharges, piezometers on the lid allowed to calculate the friction factor f , and the cavitation activity was acoustically measured. A critical cavitation index σ_c of $\sigma_c = 0.60\text{--}0.65$ was obtained for $\varphi = 68.2^\circ$ and $\sigma_c = 0.30\text{--}0.40$ for $\varphi = 21.8^\circ$. These σ_c values do not indicate the onset of cavitation but the point from which a large increase in cavitation activity is observed. The data obtained follows the relation $\sigma_c = 4f$ suggested by Arndt and Ippen (1968). PIV measurements show a high intensity shear layer along the pseudo-bottom, and show that this layer impacts the edge of horizontal step faces for $\varphi = 21.8^\circ$ (Figure 2.10). Secondary streamwise vortices form in the shear layer, and the low pressure in the core of these vortices is a likely location for cavitation formation. Observations seems to confirm it, and show that cavitation bubbles can impact the horizontal face of steps for $\varphi = 21.8^\circ$ (Figure 2.10b). For $\varphi = 21.8^\circ$, despite a lower critical cavitation index σ_c , this shear layer impact on the step suggests that milder slope stepped chutes might be more prone to cavitation damages than steeper slopes where the shear layer is mostly above the pseudo-bottom.

Although it has been proven that cavitation is physically probable to occur on stepped spillways, no cavitation damages have yet been reported on stepped spillways, even for large unit discharges (Chanson 2015). However, the Dachaoshan and Shuidong dams (Chapter 1) are unconventional stepped spillways with their flaring gate piers that create a three dimensional flow covering only 30 % of the spillway width (Lin and Han 2001). The limit unit discharge for which damages could occurs remains therefore unclear (Frizell et al. 2015).

Frizell et al. (2015) performed additional experiments on a different facility to have higher flow velocities and observed pitting on the outer third of the horizontal face for all steps for $\varphi = 21.8^\circ$ and $\sigma = 0.3$. Lesser damages were observed for $\varphi = 68.2^\circ$.

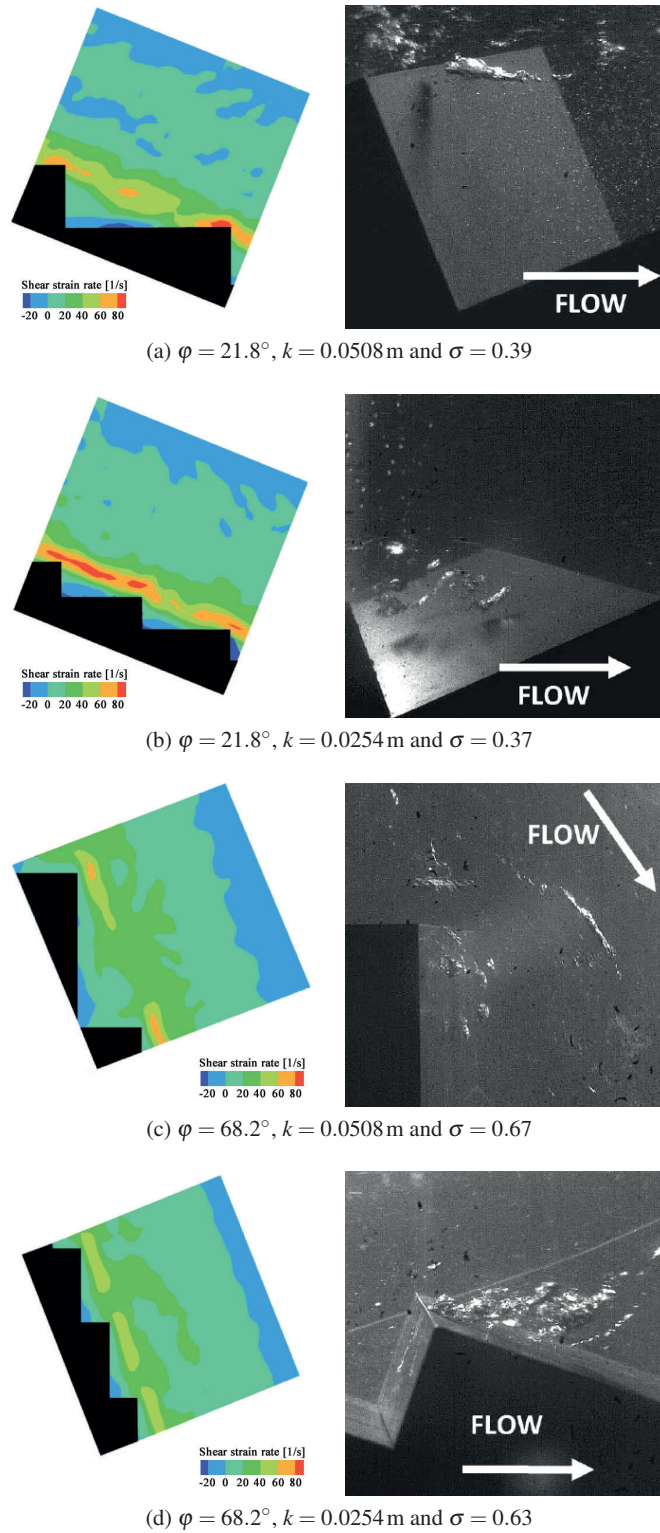


Figure 2.10 – PIV measurement of the shear strain rate (left) and photo of cavitation taken at the cavitation index σ (right) for four configurations (Frizell et al. 2013)

2.3 Smooth chute aerators

2.3.1 Overview

A chute aerator is the most efficient technical solution to control cavitation damages on high-velocity flow spillways. A historical development of chute aerators and the main contributing authors was presented by Hager and Pfister (2009).

With increasing head and unit discharges at the beginning of the 20th century, scour-like damages were observed on spillways. An example is the damages to the Arizona spillway tunnel of Hoover Dam. During an inspection, a 35 m long, 10 m wide and 15 m deep hole was discovered. Misalignment of the invert directly upstream of the damaged area, where velocities reached 45 m/s, led to flow separation and cavitation. Bradley (1945) was charged to investigate various devices (Figure 2.11) to introduce air into the flow hoping that air would act as a cushion between the flow and the tunnel invert, and that it would reduce the subpressure caused by flow separation. He found that a limited amount of air could be injected, that air did not remain close to the invert and that a deflector (sometimes named ramp, ③ in Figure 2.11) produced the best results. Other damages were reported in later decades (Falvey 1990).

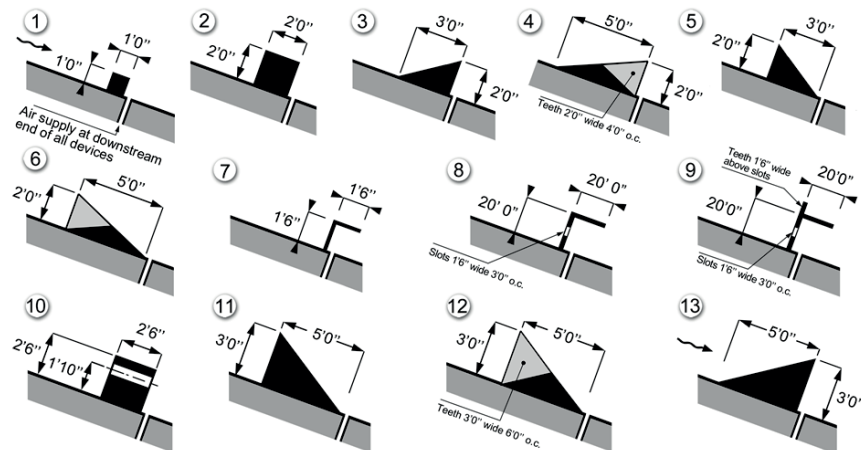


Figure 2.11 – Aerator devices tested by Bradley (1945)

In the Soviet Union, Galperin et al. (1971) presented a research to identify the critical cavitation index σ_c of various elements. Successful results of a chute aerator at prototype scale were obtained by Semenov and Lentyaev (1973) on Bratsk dam. They tested the implementation of one and two aerators on a spillway that previously showed cavitation damages. No damages were observed after the aerators were built. The air concentration measurements showed that most of the aeration occurs at the first aerator, and that there was a streamwise decrease in the air concentration of 0.4–0.8 % per meter. One of the first book on cavitation and hydraulic structures was later published by Galperin et al. (1977).

Multiple aerators studies were performed for specific spillways. Pinto et al. (1982a,b) discussed the models and prototype spillway aerators of Foz do Areia dam (Brasil). To asses the amount of air

entrained, the air entrainment coefficient β of an aerator describing the ratio of air discharge over water discharge $\beta = q_A/q$ was found to be related to the relative jet length L/h_o (Figure 2.13). The subpressure Δp in the air cavity under the jet controls the amount of air that can be supplied through the air inlet, and the throttling effect of large subpressures was investigated. The spacing of aerators was questioned, leading to the conclusion that more research is required to assess the streamwise air concentration downstream of aerators. The authors correctly identified that unknown scale effects would occur on the 1:50 model and a study on four different model scales was later presented in Pinto (1984). The 1:8 model showed a very good agreement with prototype measurements. Similar conclusions about the model scale were found by Zagustin et al. (1982), and about the subpressure by Marcano and Castillejo (1984) for the spillways of Guri dam (Venezuela). Damages on one of the latter due to cavity subpressure were reported by Marcano and Patiño (1989). Tan (1984), besides studying the effect of the jet length and cavity subpressure for the Clyde dam spillway (New Zealand), did preliminary measurements of the air concentration downstream of the aerator which showed a continuous air detrainment along the bottom. The same model was further investigated by Low (1986) and the influence of the Froude number F_o on β was highlighted. Successful implementation of aerators on the spillways of Alicura dam (Argentina) and Restitucion dam (Peru) was reported by Minor (1987).

In parallel, researches were performed in the 1980s at the Laboratory of Hydraulics, Hydrology and Glaciology (VAW) of ETH Zurich and led to preliminary design recommendations for chute aerators (Vischer et al. 1982; Volkart 1984; Volkart and Rutschmann 1986). The strong effect of the cavity subpressure Δp on the air entrainment coefficient β was also identified. The scaling of aerated flow was studied by Vischer et al. (1982) and Volkart and Rutschmann (1984) and an underestimation of prototype air entrainment was found for model scales smaller than 1:10 to 1:15. Different aerators geometries were studied including a deflector, an offset and a groove (Figure 2.12), and the best performances were obtained with a deflector or a deflector combined with an offset (Volkart and Chervet 1983). The local air concentration was measured in the flow, and the bottom air concentration was used to estimate the required aerator spacing (Vischer et al. 1982). As an alternative to using the relative jet length L/h_o to characterize β , Volkart and Rutschmann (1986) suggested a definition of β as a function of the Froude number F_o and the cavity subpressure Δp .

The preceding studies were generally for specific spillways or for a limited set of parameters. Simultaneous PhD theses by Koschitzky (1987), Chanson (1988) and Rutschmann (1988) systematically varied the relevant parameters of chute aerators to provide general design guidelines in term of air entrainment. These studies were later complemented by Rutschmann and Hager (1990), and by supplementary researches of Chanson (1989a,b, 1991, 1994a,b, 1995c) who used air concentration measurements to assess the aerator spacing, the air entrainment and detrainment characteristics, the reduction of friction in aerated flows and the filling of the air cavity. Additional investigations were later presented by Balaguer (1992) and Skripalle (1994) on the effect of turbulence, and Kökpınar and Göğüş (2002).

Wood (1991) published a monograph on air entrainment in free-surface flows. It summarizes all the knowledge about flow aeration in different hydraulics structures such as chute aerators, self-aerated

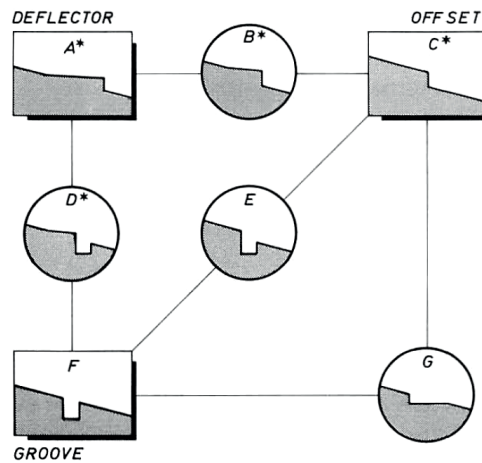


Figure 2.12 – Aerator geometries tested by Volkart and Chervet (1983)

spillways, plunging jets or hydraulics jumps. The same year, Kells and Smith (1991) presented a state of the art article of chute aerator design.

Indirectly related to aerators, Ervine and Falvey (1987) studied the behavior of jets in air and the effect of turbulence in the transversal spread of a jet. Later, Falvey and Ervine (1988) presented the mechanisms influencing the air entrainment and highlighted the differences in jets, chutes, plunge pools and hydraulics jumps aeration. Continuing the jet aeration studies, Ervine et al. (1995) made turbulence measurement in the vicinity on a deflector aerator. The results show that a deflector acts as a turbulence generator, and that the turbulence decays in the jet. They suggest taking into account the turbulence to calculate the air entrainment of the aerator with the inclusion of a scale effect factor.

To protect a surface against damages, a certain concentration of air is required close to the location where cavitation occurs. Knowing the bottom air concentration and its streamwise detrainment is therefore important, especially to determine the spacing required between aerators. All the studies mentioned earlier focused mainly on the air entrainment coefficient which indicates the air supplied below the flow at the aerator and not the air concentration downstream. Kramer (2004) systematically studied the development of the average and bottom air concentration and the air detrainment process downstream of a deflector aerator or a pre-aerated flow, focusing on the far-field of chute aerators. Later, Pfister (2008) completed the study by investigating the near-field of chute aerators so that the design of optimal aerators is now possible in terms of aerator air entrainment and air concentrations downstream.

More details about selected topics relevant for the present study – namely the air entrainment coefficient, jets characteristics, and the air transport downstream of the aerator – are presented hereafter.

2.3.2 Air entrainment coefficient

The performance of an aerator is commonly assessed with the air entrainment coefficient $\beta = q_A/q$ which describes the relative discharge of air supplied by the aerator. It is important to properly design the air supply system, but it does not indicate how much air is present in the flow downstream of the aerator. It is the air concentration along the chute bottom that is crucial to prevent cavitation damages. A selection of the main findings on the air entrainment coefficient β are summarized herein.

A typical deflector generated jet is presented in Figure 2.13 with the parameters used to describe it. The following parameters have been identified to influence β :

- the chute angle φ
- the approach flow Froude number F_o
- the approach flow depth h_o
- the deflector angle α
- the deflector height t
- the offset height o
- the approach flow turbulence intensity T_u

An additional parameter takes into account the air supply characteristics: the cavity subpressure Δp which is the difference of pressure between the atmosphere and air cavity below the jet. All these parameters have an influence on the jet length L , and L/h_o can be used to express β .

Koschitzky (1987) studied deflector aerators with chute angles of $\varphi = 1.7^\circ$ and $\varphi = 20.3^\circ$, deflectors with $5.2^\circ \leq \alpha \leq 7.9^\circ$ and $0.023 \text{ m} \leq t \leq 0.050 \text{ m}$. With data from previous studies, he found that β mainly depends on the Froude number F_o and the cavity subpressure Δp

$$\beta = K_1 \cdot (F_o - F_c)^{K_3} \cdot \left(1 - K_2 \frac{\Delta p}{\rho g h_o} \right) \quad (2.50)$$

with K_1, K_2, K_3 as factors depending on the aerator geometry, and F_c as the critical Froude number for which the aerator starts entraining air.

Rutschmann (1988) studied a combination of deflector and offset aerators. He found that steeper deflectors performed well in all conditions. For a zero subpressure ($\Delta p = 0$; the losses were compensated by a blower), he obtained a relation only depending on the relative jet length

$$\beta = 0.0372 \left(\frac{L}{h_o} \right) - 0.266 \quad (2.51)$$

valid for a large parameters ranges $0^\circ \leq \varphi \leq 68^\circ$, $2.8^\circ \leq \alpha \leq 5.7^\circ$, $o \leq 4t$ and $L/h_o \leq 50$.

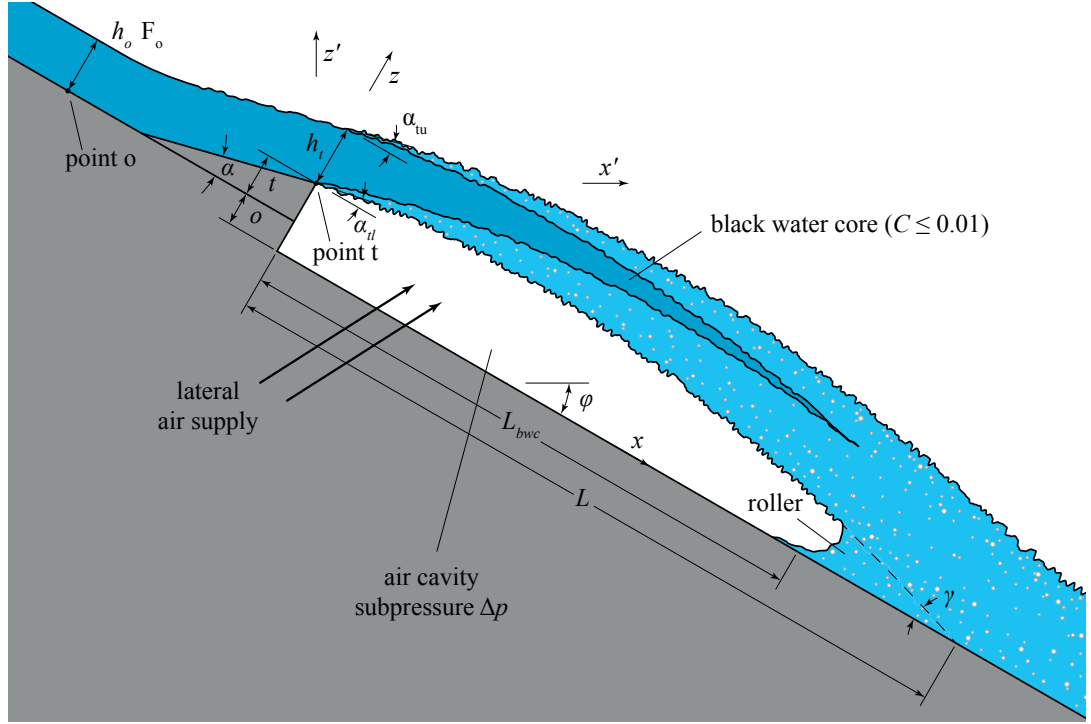


Figure 2.13 – Definition scheme of an aerator (deflector with offset) with notation

Note that he measured the jet length until the impact of the center axis of the jet, and not until the impact of the lower jet surface as shown in Figure 2.13. The relation can also be used for a non-zero subpressure by adapting the jet length to the cavity subpressure and the results are within $\pm 20\%$. The tests with subpressure led to

$$\beta = 0.0493 \left(\frac{L}{h_o} \right) - 0.061 F_o^2 - 0.0859 \quad (2.52)$$

valid for a narrower range of $14^\circ \leq \phi \leq 51^\circ$, $4.0^\circ \leq \alpha \leq 7.4^\circ$, $o \leq 4t$ and $L/h_o \leq 50$.

Chanson (1988) studied two aerators geometries on a $\phi = 52.3^\circ$ chute. The first was a $\alpha = 5.7^\circ$ deflector combined with an $o = 0.030$ m offset, and the second is an $o = 0.030$ m offset. He obtained for $3 \leq F_o \leq 25$ and $0.023 \text{ m} \leq h_o \leq 0.120 \text{ m}$

$$\beta = K \cdot \left[F_o + 8.17 - 5.77 \frac{h_o}{o} + 0.605 \left(\frac{h_o}{o} \right)^2 - 23.51 \left(\frac{h_o}{o} \right)^{-1.5} \sqrt{\frac{\Delta p}{\rho g h_o}} \right] \quad (2.53)$$

with $K = 0.2$ for the deflector or $K = 0.04$ for the offset aerator.

Rutschmann and Hager (1990) analyzed the data of Rutschmann (1988) and found that the cavity

subpressure Δp can be taken into account with the Euler number $E = \rho u^2 / \Delta p$

$$\frac{\beta}{\beta_{max}} = \left[\frac{2}{\pi} \arctan(0.003 \cdot \Delta E) \right]^{0.7} \quad (2.54)$$

with β_{max} as the air entrainment coefficient without subpressure, $\Delta E = E - E_{min}$, and E_{min} as the Euler number for which $\beta = 0$.

Further analysis led to

$$\beta_{max} = \tan^{1.15} \varphi \cdot \exp \left[(1.15 \tan \alpha)^2 \right] \cdot (F_o - 5.4)^{0.35} \quad (2.55)$$

$$0.003 \cdot E_{min} = \frac{1}{2.3} \tan^{1.15} \varphi \cdot \exp [1.15 \tan^2 \alpha] + \frac{t}{3h_o} \quad (2.56)$$

Skripalle (1994) studied an offset aerator with a chute angle of $\varphi = 0^\circ$. In addition to a regular smooth bottom, two rougher surfaces were used to increase the flow turbulence. The thickness of the boundary layer δ_{bl} was also varied. Without subpressure, he obtained

$$\beta = 0.9 \frac{L}{h_o} \frac{\delta_{bl}}{h_o} \frac{u^*}{u_\infty} \quad (2.57)$$

with $u^* = \sqrt{gh_o J}$ as the shear velocity, u_∞ as the flow velocity outside of the boundary layer and J as the energy line gradient.

With a subpressure, the relation is adapted to

$$\beta = 0.9 \frac{1}{h_o^2} \frac{u^*}{u_\infty} [L \delta_{bl} - o (L_{max} - L)] \quad (2.58)$$

with L_{max} as the jet length without subpressure.

Kökpınar and Göğüş (2002) studied an offset $o = 0.050\text{m}$ aerator with and without $\alpha = 5.7^\circ$ deflectors. With the addition of results from previous studies, they obtained for $0^\circ \leq \varphi \leq 51.3^\circ$, $5.5 \leq F_o \leq 10$, $0^\circ \leq \alpha \leq 9.45^\circ$, $0.06 \leq (o + t)/h_o \leq 2.1$, $0 \leq t/o \leq 0.8$, $0 \leq t/h_o \leq 0.4$ and $0.02 \leq A_A/bh_o \leq 1$

$$\beta = 0.0189 \left(\frac{L}{h_o} \right)^{0.83} \left[\frac{A_A}{bh_o} (1 + \tan \varphi) \right]^{0.24} \quad (2.59)$$

with A_A as the air supply area and b as the channel width.

Finally, Pfister (2008) studied deflector and offset aerators on three slopes with $\Delta p / (\rho gh_o) \approx 0$. He

obtained for $0 \leq \beta \leq 0.8$

$$\beta = 0.0028 \cdot F_o^2 \cdot (1 + F_o^2 \tan \alpha) - 0.1 \quad (2.60)$$

It agrees well with the data of Koschitzky (1987), Rutschmann (1988), Skripalle (1994) and prototype measurements. The relation limits could thus be extended to $0^\circ \leq \varphi \leq 50^\circ$, $5.8 \leq F_o \leq 16$, $0^\circ \leq \alpha \leq 11.3^\circ$ and $0.06 \leq (o+t)/h_o \leq 2.1$. Steeper deflectors were later analyzed and this relation can also be applied for $\alpha \leq 18.4^\circ$, but it is overestimating β for $18.4^\circ \leq \alpha \leq 26.6^\circ$ (Pfister 2011). With a cavity subpressure, β can be obtained for $0.5 \leq \beta/\beta_{max} \leq 1$

$$\frac{\beta}{\beta_{max}} = 6 \sqrt{\frac{\Delta p}{\rho g h_o F_o}} + 1.3 \quad (2.61)$$

with β_{max} as the air entrainment coefficient without subpressure.

In addition, Ervine et al. (1995) suggest a procedure to obtain the air discharge q_A with the turbulent velocity fluctuations u' . Based on their measurements for three deflector angles α , it is possible to obtain the ratio u'/u^* . The air discharge q_A can then be calculated from the relative jet length L/h_o as illustrated in Figure 2.14. It shows that less air is entrained after $L/h > 10$ since turbulence decays in the jet, and a correction factor for the turbulent velocity u' is necessary since jet aeration only occurs when $u' > 0.25$ m/s.

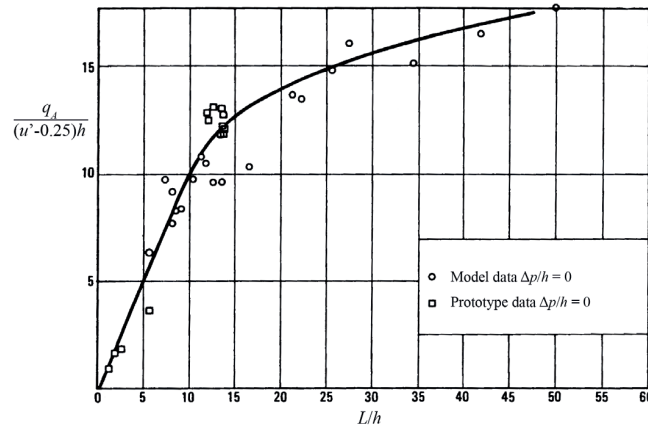


Figure 2.14 – Variation of air entrainment with the relative jet length L/h without cavity subpressure (adapted from Ervine et al. 1995)

2.3.3 Aerator jets

A jet is created by a chute aerator to provide an air cavity below the flow. Jet characteristics relevant for aerators are presented herein, particularly about jets generated by a deflector since deflectors are the most effective aerator type. Air entrainment is strongly influenced by the jet length.

Cavity subpressure

A subpressure Δp compared to the atmospheric pressure occurs in the cavity below an aerator jet to allow the supply of air into the cavity. It results from the equilibrium between the characteristics of the supply system and the characteristics of the aerator air demand (Figure 2.15). The characteristic of the supply system depends on the head losses which are related to the air supply area and to the air discharge $\Delta p \propto u_A^2 \propto q_A^2$. The aerator air demand depends on multiple parameters as presented in §2.3.2, with more air entrained for low Δp .

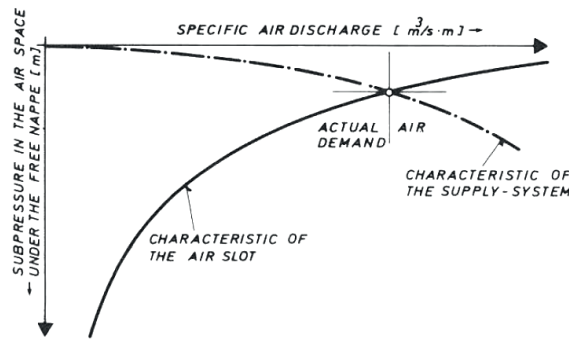


Figure 2.15 – Determination of the cavity subpressure Δp in function of the specific air discharge q_A (Volkart and Chervet 1983)

The subpressure has to be taken into account in the design of an aerator as it reduces the jet length and the air entrainment. In severe cases that were analyzed by Chanson (1995c), the subpressure can lead to the filling of an aerator groove. Pfister (2011) observed a collapse of the air cavity and choking of deflector and offset aerators for $\Delta p / (\rho g h_o) \geq 1$. The effect of the cavity subpressure on the flow is small for $\Delta p / (\rho g h_o) \leq 0.1$. Kökpınar and Göğüş (2002) presented a relation to obtain the cavity subpressure on a specific physical model based on the air supply area. But the application to prototypes showed scale effects and differences of one order of magnitude.

Jet trajectories

The jet trajectory follows a ballistic parabola, but is affected by the subpressure in the cavity under the jet and energy losses. Schwartz and Nutt (1963) presented an analytical solution of the jet trajectory taking into account a subpressure. Falvey (1990) presented an approach based on Glazov (1984) and Pan et al. (1980) taking into account the subpressure. Wei and Defazio (1982) presented an approach based on a finite element method.

For engineering purposes, Tan (1984) suggested neglecting the subpressure component parallel to the chute to have an explicit equation. For a low angle deflector ($\alpha = 4^\circ$) almost identical results were obtained compared with Schwartz and Nutt (1963), but greater differences are expected for steeper deflectors.

Another practical approach is used by Heller et al. (2005), Steiner et al. (2008) and Pfister and

Hager (2009) for a well ventilated cavity with negligible subpressure. In this case, the upper and lower jet surfaces follow the ballistic parabola

$$z'(x') = z'_t + \tan \alpha'_t x' - \frac{gx'^2}{2u_t^2 \cos^2 \alpha'_t} \quad (2.62)$$

with x' and z' as respectively the horizontal and vertical coordinates originating from the deflector crest (Figure 2.13), z'_o as the takeoff elevation, α'_t as the takeoff angle (measured from axis x') and u_t as the average takeoff velocity (Figure 2.13).

In coordinates x and z respectively parallel and perpendicular to the chute, the parametric equation is

$$\begin{cases} x(T) = u_t \cos \alpha_t T + 0.5g \sin \varphi T^2 \\ z(T) = z_t + u_t \sin \alpha_t T - 0.5g \cos \varphi T^2 \end{cases} \quad (2.63)$$

with T as the time from takeoff, α_t as the takeoff angle (measured from the chute axis x) and z_t as the elevation at takeoff. For the lower jet trajectory (subscript l) $z_{tl} = o + t$ and for the upper jet trajectory (subscript u) $z_{tu} = o + t + h_t$, with the offset height o , the deflector height t , and h_t the flow depth at takeoff.

The trajectories can be normalized with the coordinates of the maximum elevation of the jet z_{max} and its location x_{max}

$$X_j = \frac{x}{x_{max}} \quad (2.64a)$$

$$Z_j = \frac{z - z_t}{z_{max} - z_t} \quad (2.64b)$$

The trajectory can then be expressed as

$$Z_j = 2X_j - X_j^2 \quad (2.65)$$

The location of the maximum elevation of the jet can be obtained analytically or empirically. Based on their own data and the data obtained by Steiner et al. (2008), Pfister and Hager (2009) found the following regression functions to obtain respectively x_{max} and z_{max}

$$\Psi_x = F_0^2 \cdot \tan^{0.6} \alpha \cdot (t/h_o)^{0.2} \cdot (1 + \sin \varphi)^{0.5} \quad (2.66a)$$

$$\Psi_z = F_0^2 \cdot \tan^{1.5} \alpha \cdot (t/h_o)^{0.5} \quad (2.66b)$$

The upper jet is then for $0 < x_{maxu}/h_o < 26$ and $0 < (z_{maxu} - z_{ou})/h_o < 7$

$$\frac{x_{maxu}}{h_o} = 0.58 \cdot \Psi_x \quad (2.67a)$$

$$\frac{z_{maxu} - z_{ou}}{h_o} = 0.25 \cdot \Psi_z \cdot (1 + \sin \varphi)^{0.5} \quad (2.67b)$$

And the lower jet for $0 < x_{maxl}/h_o < 22$ and $0 < (z_{maxl} - z_{ol})/h_o < 6$

$$\frac{x_{maxl}}{h_o} = 0.45 \cdot \Psi_x \quad (2.68a)$$

$$\frac{z_{maxl} - z_{ol}}{h_o} = 0.18 \cdot \Psi_z \quad (2.68b)$$

The relations presented consider a blackwater approach flow. For a pre-aerated approach flow, the upper trajectory is lifted, whereas the lower trajectory is slightly decreased resulting in a shorter jet length (Pfister and Hager 2012).

Jet takeoff angle

The effective jet takeoff angle α_t differs from the deflector angle α due to the inability of the streamlines to follow the abrupt change of slope of the deflector, to the pressure gradient relaxation and to the jet spread caused by the internal turbulence. It is essential to know the takeoff angle to estimate the jet trajectory and the jet length. In addition of Falvey (1990) giving an abacus to obtain α_t/α in function of α and the relative deflector height t/h_o , the following empirical relations have been suggested.

Pan et al. (1980) for $\alpha \leq 15^\circ$ and $t/h_o \leq 0.3$

$$\frac{\alpha_t}{\alpha} = \sqrt{\tanh\left(\frac{t}{h_o \alpha}\right)} \quad (2.69)$$

Wu and Ruan (2007), based on Pan et al. (1980) and Glazov (1984) for $0^\circ \leq \varphi \leq 48^\circ$, $1^\circ \leq \alpha \leq 21.7^\circ$, $0.03 \leq t/h_o \leq 0.57$, $2.1 \leq F_o \leq 11.4$ and $1.75 \text{ m/s} \leq u_o \leq 36.2 \text{ m/s}$

$$\frac{\alpha_t}{\alpha} = 0.48 \cdot \sqrt{\tanh\left(\frac{t}{h_o \alpha}\right)} + 0.52 \cdot (\alpha - \arctan(T_u)) \quad (2.70)$$

Steiner et al. (2008) for $\varphi = 0^\circ$ and $0.01 \leq t/(h_o F_o) \cdot \tan \alpha \leq 0.30$

$$\frac{\alpha_t}{\alpha} = c \left(1.05 - \frac{t}{h_o F_o} \tan \alpha \right) \quad (2.71)$$

with $c = 1.0$ for the upper takeoff angle α_{tu} and $c = 0.89$ for the lower takeoff angle α_{tl} .

Pfister (2012) for $0^\circ \leq \varphi \leq 15^\circ$, $0^\circ \leq \alpha \leq 33.2^\circ$, $t/h_o \leq 1.7$ and $3.0 \leq F_o \leq 10.4$

$$\tan \alpha_t = 0.17 \left[\sqrt{1 + \frac{t}{h_o}} \cdot (1 + \tan \alpha)^{1.5} \cdot (1 + \sin \varphi)^{-0.5} \cdot F_o^{0.2} \right] - 0.26 \quad (2.72)$$

Jet length

The jet length L is an important parameter to characterize zones and air transport downstream of the aerator. It can be obtained from the various analytical trajectory equations mentioned before.

Another approach to obtain L is based on empirical relations depending on the aerator geometry and the flow conditions. Rutschmann and Hager (1990) presented an explicit solution for the equation of Schwartz and Nutt (1963) valid for a small subpressure $\Delta p/(\rho g h_o)$ and small takeoff angle α'_t measured from axis x' . Kökpınar and Göğüş (2002) found for $5.56 \leq F_o \leq 10.0$, $0.198 \leq (o+t)/h_o \leq 1.985$, $0^\circ \leq \alpha \leq 9.45^\circ$, $0^\circ \leq \varphi \leq 51.3^\circ$ and $0.00684 \leq A_A/(b h_o) \leq 1$

$$\frac{L}{h_o} = 0.28 \cdot F_o^{1.75} \cdot \left((1 + \tan \varphi) \frac{A_A}{b h_o} \right)^{-0.087} \cdot \left(\frac{o+t}{h_o} \right)^{0.44} \cdot (1 + \sin \alpha)^{0.22} \quad (2.73)$$

with A_A as the area of the aerator slot under the deflector.

Pfister and Hager (2010a) suggest for $0 < L/h_o < 50$, $12^\circ \leq \varphi \leq 50^\circ$, $5.8 \leq F_o \leq 10.4$, $0^\circ \leq \alpha \leq 11.3^\circ$, $0.1 \leq (o+t)/h_o \leq 2.1$ and $\Delta p/(\rho g h_o) \approx 0$

$$\frac{L}{h_o} = 0.77 \cdot F_o \cdot (1 + \sin \varphi)^{1.5} \cdot \left(\sqrt{\frac{o+t}{h_o}} + F_o \sin \alpha \right) \quad (2.74)$$

It can be applied as well for deflectors with an angle up to $\alpha \leq 18.4^\circ$, but higher α lead to an overestimation of the jet length (Pfister 2011). It agrees with data from Chanson (1988), Rutschmann (1988) and prototype measurements. Pfister et al. (2011) found no influence of a pre-aerated flow on the jet length. The reduction of the jet length L by a relative subpressure $\Delta p/(\rho g h_o)$ follows (Pfister 2011)

$$\frac{L_{\Delta p}}{L_{max}} = \exp \left(-0.85 \frac{\Delta p}{\rho g h_o} \right) \quad (2.75)$$

with $L_{\Delta p}$ as the jet length with subpressure and L_{max} as the jet length without subpressure.

Jet impact angle

The air detrainment at the jet impact is related to the jet impact angle γ on the chute bottom (§2.3.4). Chanson (1994a) presented the analytical solution of γ for the method of Tan (1984)

$$\tan(\gamma) = \tan \alpha_t \cdot \sqrt{1 + 2g \frac{(o+t)(\cos \varphi + \Delta p / (\rho g h_o))}{u_t^2 \sin^2 \alpha_t}} \quad (2.76)$$

Pfister (2012) obtained the following empirical relation for $12^\circ \leq \varphi \leq 50^\circ$, $5.8 \leq F_o \leq 10.4$, $0^\circ \leq \alpha \leq 26.6^\circ$, $0.1 \leq (o+t)/h_o \leq 2.1$ and $\Delta p / (\rho g h_o) \approx 0$

$$\tan(\gamma) = 0.15 \cdot \sqrt{\frac{o+t}{h_o}} \cdot (1 + \tan \alpha)^2 \cdot (1 + \sin \varphi)^{-1} \quad (2.77)$$

Deflector induced bottom pressure

The increase of the bottom pressure p_d caused by deflectors results from the force required to deviate the streamlines. Steiner et al. (2008) investigated the pressure (to be added to the hydrostatic pressure) in a flat channel ($\varphi = 0^\circ$). The maximum pressure $p_{d,max}$ is located where the deflector starts at $x = -L_d$, and depends on the approach flow Froude number F_o and the deflector angle α

$$\frac{p_{d,max}}{\rho g h_o} = 0.3(F_o \sin \alpha^{0.2})^2 \quad (2.78)$$

The transition from the hydrostatic pressure upstream to the maximum $p_{d,max}$, as well as the transition downstream to the atmospheric pressure at the takeoff was also described by Steiner et al. (2008).

Jet spread and blackwater core

According to Ervine and Falvey (1987), the turbulent kinetic energy is the source of the spread of a jet by creating surface disturbances. However, the turbulent kinetic energy must be sufficient to overcome the surface tension. They found that for a circular jet, the outer spread δ_O/x (Figure 2.16) is related to the turbulence intensity $T_u = u'/u$

$$\frac{\delta_O}{x} = 0.38 \cdot T_u \quad (2.79)$$

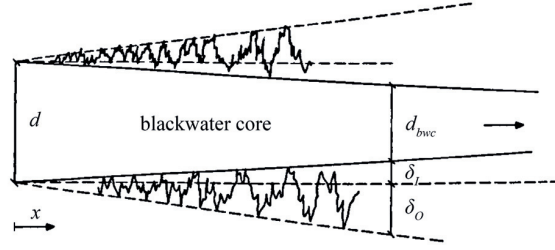


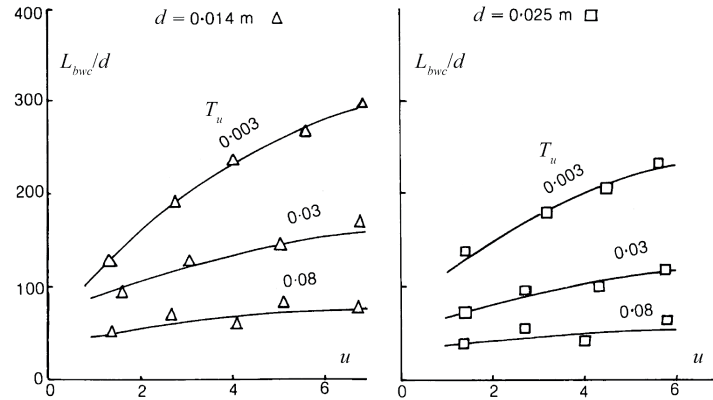
Figure 2.16 – Definition of the jet spread (adapted from Ervine and Falvey 1987)

For a circular jet, the inner spread δ_I/x is given by continuity

$$\frac{\delta_O}{\delta_I} = \frac{C_{aI}}{1 - C_{aO}} \quad (2.80)$$

with C_{aI} and C_{aO} as respectively the average air concentration in the inner and outer spread.

Due to this internal spread, the thickness of the blackwater core decreases with an angle of a few degrees. For turbulence intensity values $T_u = 5 - 6\%$, they obtained $\delta_O = 3 - 4\%$ and $\delta_I = 0.5 - 1\%$. The relative blackwater core length is then $L_{bwc}/d = 50 - 100$ (Figure 2.13). This is in agreement with previous results from Ervine et al. (1980) (Figure 2.17).

Figure 2.17 – Influence of the jet velocity u and the turbulence intensity T_u on the relative blackwater core length L_{bwc}/d (adapted from Ervine et al. 1980)

Using the definition of $C \leq 0.01$ for the blackwater core, Pfister and Hager (2009) obtained the following blackwater core length for a jet created by a deflector and $7 < L_{bwc}/h_o < 20$

$$\frac{L_{bwc}}{h_o} = 74 \cdot F_o^{-1} \cdot (1 + \tan \alpha)^{-0.5} \cdot (1 + \sin \varphi) \quad (2.81)$$

With a pre-aerated approach flow average air concentration C_{a0} and a chute angle $\varphi = 12^\circ$, the

equation can be adapted according to Pfister and Hager (2012)

$$\frac{L_{bwc}}{h_o} = 74 \cdot (F_o^{-1} \cdot (1 + \tan \alpha)^{-0.5} \cdot (1 + \sin \varphi) - 6C_{ao}^3) \quad (2.82)$$

An extended definition for other core air concentrations as well as equations describing the decrease of the core are presented in Pfister and Schwindt (2014).

2.3.4 Air transport

The air transport in the flow downstream of an aerator can be separated in three zones defined by the normalized streamwise coordinate x/L (Pfister and Hager 2010a):

- the jet zone : $0 \leq x/L \leq 1$
- the spray and reattachment zone : $1 \leq x/L \leq 3$
- the far-field zone : $x/L \geq 3$

The development of the air concentration in each of these zones is presented in this part.

Jet zone

The air entrained by the jet and its disintegration is influenced by the jet turbulence, the relaxation of the pressure and velocity gradients at takeoff, and the interaction with the air. Air entrainment starts on both the lower and upper surfaces of a deflector jet even if the boundary layer has not reached the surface. Ervine et al. (1995) made an important contribution to deflector jets by measuring the turbulence upstream of a deflector, on the deflector and in the jet. They showed that the deflector acts as a turbulence generator, typically increasing it of 20 % to 30 %. In the jet, turbulence decays with the relative length x/h_o . They suggest that air entrainment is directly linked to the jet turbulence. Air entrainment is high at the start of the jet, and progressively decreases along the jet with the decay of turbulence. A minimal turbulent velocity $u' = 0.25$ m/s seems to be required for the process to start.

The development of the average air concentration C_a in deflector jets was measured by Pfister and Hager (2009). They found that C_a is related to the blackwater core length L_{bwc} , and obtained for $0 < x/L_{bwc} < 4$

$$C_a = \tanh \left(0.4 \left(\frac{x}{L_{bwc}} \right)^{0.6} \right) \quad (2.83)$$

This relation shows a high air entrainment immediately after takeoff, reaching a value of $C_a = 0.38$ at $x = L_{bwc}$, and a diminishing air entrainment with the distance, in agreement with Ervine et al. (1995). The relation is also valid for a pre-aerated flow with a chute angle $\varphi = 12^\circ$ (Pfister et al.

2011). Similarly, the minimum air concentration C_{min} starts increasing after reaching the end of the blackwater core ($x = L_{bwc}$). The following relation is obtained for $1 < x/L_{bwc} < 4$ (Pfister and Hager 2009)

$$C_{min} = 0.01 + 0.1 \left(\frac{x}{L_{bwc}} + 1 \right)^{1.5} \quad (2.84)$$

The minimum air concentration is located at a relative depth of $Z = 0.6$ to 0.8 in the first portion of the jet, and then tends to $Z = 0.6$ to 0.7 . It implies a larger spread in the lower jet which can be explained by gravity. The water particles ejected from the lower surface leave the jet while those ejected from the upper surface return in the jet. An adapted relation for pre-aerated flow is given in Pfister and Hager (2012).

Jet impact detrainment

The impact of the jet on the chute bottom compresses the air in the flow and air is rapidly detrained. The detrainment D defined by Chanson (1994a) is

$$D = \frac{Q_{A,jet,max} - Q_{A,impact}}{Q_{A,jet,max}} \quad (2.85)$$

with $Q_{A,jet,max}$ as the maximum air discharge in the jet and $Q_{A,impact}$ as the air discharge just after the jet impact.

The air discharge Q_A can be obtained from

$$Q_A = Q \frac{C_a}{1 - C_a} \quad (2.86)$$

with Q as the water discharge

Chanson (1994a) obtained the following relation for $3^\circ < \gamma < 9^\circ$, with γ in degrees

$$D = 0.0762\gamma \quad (2.87)$$

Pfister (2012) defined $Q_{A,jet,max} = Q_A(x/L = 0.75)$ and $Q_{A,impact} = Q_A(x/L = 1.25)$, and obtained for $1.3^\circ < \gamma < 15.6^\circ$

$$D = 0.8 \tanh(8 \tan \gamma) \quad (2.88)$$

This relation tends to an asymptotic value of 80 %, and D is larger than 70 % for $\gamma > 10^\circ$.

Spray and reattachment zone

Gaskin et al. (2003) presented results of average air concentration C_a at a single point located 4 m downstream of a deflector aerator on a 1:15 model with a chute slope of $10^\circ \leq \varphi \leq 20.6^\circ$. They found an influence of the Froude number F_o , the chute angle φ and the deflector angle α .

The air concentration in the spray and reattachment zone was systematically studied by Pfister (2008). For the average air concentration C_a , a minimum is reached at $x/L \approx 1.25$, rapidly followed by a maximum along $1.5 \leq x/L \leq 2$. A quantification of C_a is difficult in this zone. The following relation is suggested at $x/L = 3$ and for $5 \leq L/h_o \leq 40$ (Pfister and Hager 2010b)

$$C_a(x/L = 3) = 0.008 \frac{L}{h_o} + 0.1 \quad (2.89)$$

The average air concentration C_a is increased if the approach flow is pre-aerated, and the adapted relation is given in Pfister et al. (2011).

The bottom air concentration C_b rapidly and continuously decreases after the jet impact (Figure 2.18). For deflector aerators, the development of C_b can be described for $1 \leq x/L \leq 3$, $12^\circ \leq \varphi \leq 50^\circ$, $5.8 \leq F_o \leq 10.4$, $0^\circ \leq \alpha \leq 11.3^\circ$, $0.1 \leq (o+t)/h_o \leq 2.1$ and $\Delta p \approx 0$ by (Pfister and Hager 2010b)

$$C_b = 1 - \tanh \left(4.8 \left(\frac{x}{L} - 1 \right)^{0.25} \cdot F_o^{0.25n} \cdot \tan^{0.25m} \alpha \cdot \left(\frac{h_o}{o+h_o} \right)^{-0.05} \right) \quad (2.90a)$$

$$m = 0.5 - (1.5 \sin \varphi)^3 \quad (2.90b)$$

$$n = -1 - (1.5 \sin \varphi)^3 \quad (2.90c)$$

An adapted equation must be used for offset aerators (Pfister and Hager 2010b). For deflectors with $\alpha \geq 11.3^\circ$, there is marginally more bottom air concentration than for $\alpha = 11.3^\circ$ (Pfister 2011). For a pre-aerated approach flow, C_b is increased, whereas a cavity subpressure decreases C_b . The adapted equations can respectively be found in Pfister et al. (2011) and Pfister (2011).

Far-field zone

The far-field was studied in detail by Kramer (2004) downstream of an aerator or a pre-aerated flow. Air is continuously detrained from the bottom until a minimum is reached at the inception point. For a chute slope $\varphi \leq 26.6$ and $5 \leq F_o \leq 12$, C_b is defined in the air detrainment region by (Kramer et al. 2006)

$$C_b = C_{bo} \cdot \exp \left(- (7.2 \cdot 0.006^{\tan \varphi} + 6.6) F_o^{-2.5} \cdot \frac{x}{h_{90u}} \right) \quad (2.91)$$

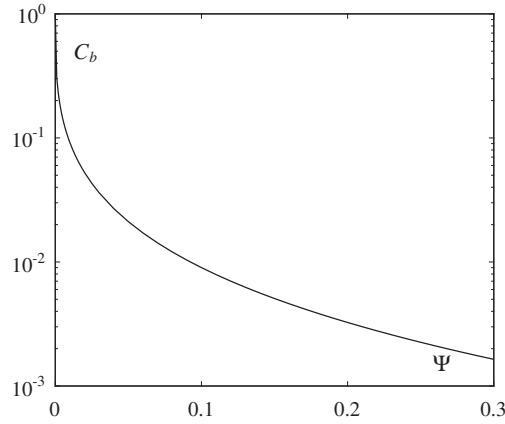


Figure 2.18 – Continuous decrease of the bottom air concentration C_b with $\Psi = (x/L - 1) \cdot F_o^{-1 - (1.5 \sin \varphi)^3} \cdot (\tan \alpha)^{0.5 - (1.5 \sin \varphi)^3} \cdot (h_o / (o + h_o))^{-0.2}$ (Pfister and Hager 2010b)

with C_{bo} as the bottom air concentration at the transition between the near and far-field (equation (2.90)) can be used to obtain C_{bo} .

A relation for the minimum C_b reached at the inception point was also obtained. The bubble rise velocity that controls the air detrainment was found to depend on the local air concentration and the Froude number (Kramer and Hager 2005). The beginning of the far-field zone was also included in the study of Pfister (2008). For the average air concentration C_a , Pfister and Hager (2010b) suggest for $3 \leq L/h_o \leq 9$

$$C_a = C_a(x/L = 3) + 0.02 \left(\frac{x}{L} - 3 \right) \sin(\varphi - 30^\circ) \quad (2.92)$$

with $C_a(x/L = 3)$ obtained from equation (2.89).

For the bottom air concentration C_b they suggest for $3 \leq L/h_o \leq 9$

$$C_b = C_b(x/L = 3) \cdot \exp \left(-8.5 \left(\frac{x}{L} - 3 \right) F_o^{-1.5} \right) \quad (2.93)$$

with $C_b(x/L = 3)$ obtained from equation (2.90)

2.4 Stepped chute aerators

Despite the potential cavitation damage on stepped spillways, only limited studies were performed on stepped chute aerators. These are presented hereafter.

2.4.1 Deflector aerator

Pfister et al. (2006a) investigated the effect of a deflector located at the first step after a standard smooth crest (design discharge $q_D = 0.863 \text{ m}^2/\text{s}$). The discharge was varied between $0.11 < q < 0.86 \text{ m}^2/\text{s}$ for a chute angle $\varphi = 50^\circ$, a step height of $s = 0.093 \text{ m}$, a deflector angle $\alpha = 8.13^\circ$ (1:7) and a deflector height $t = 0.008 \text{ m}$. Two positions of the deflector were considered: upstream of or in the first step (Figure 2.19).

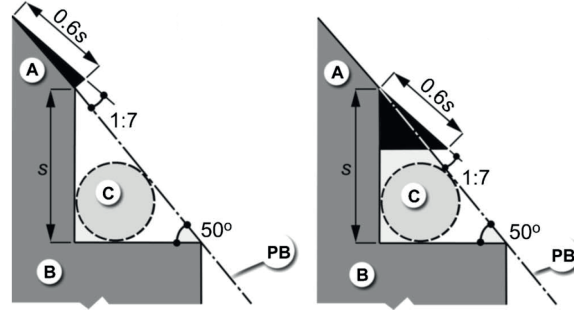


Figure 2.19 – Position of the deflectors with (A) aerator, (B) first step, (C) air supply, (PB) pseudo-bottom (adapted from Pfister et al. 2006a)

The study was focused on the bottom air concentration C_b and four regions were defined (Figure 2.20):

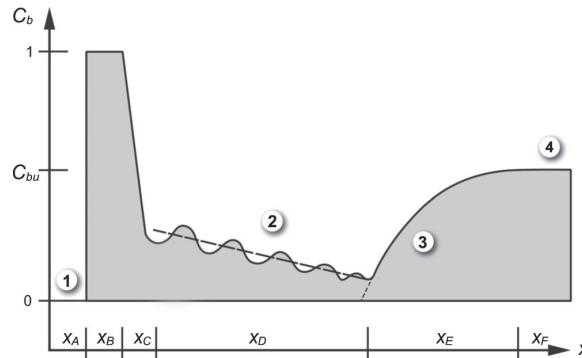


Figure 2.20 – Typical bottom air concentration C_b showing the four regions (adapted from Pfister et al. 2006a)

1. Blackwater and jet region: there is blackwater with no air present up to the deflector's edge (x_A). Then the flow is lifted from the bottom and an air cavity is formed until the jet reaches the pseudo-bottom (x_B)
2. Transition region: a rapid air detrainment occurs at the jet impact (x_C), followed by a slow decrease of the bottom air concentration (x_D). A bottom air layer forms with a blackwater core still present above. Its growth, similarly to a turbulent boundary layer, explains the decrease in the bottom air concentration while no air is detrained
3. Developing flow region: the inception point is reached and air from the surface is gradually entrained to the bottom (x_E)

4. Uniform flow region: the uniform bottom air concentration C_{bu} is attained (x_F)

For small discharges, the inception point is located somewhat downstream compared to a stepped chute without aerator, whereas it was slightly upstream for large discharges, including the design discharge. The aerator has a local effect in region 1 and 2, and a very limited effect beyond.

2.4.2 Step aerator

To avoid spray produced by the jet impact on steps with a deflector at low discharges and in order to increase the bottom air concentration, Pfister et al. (2006b) first proposed a so-called "step" aerator located in the first step downstream of the ogee (Figure 2.21a). It exploits the negative pressure observed on the upper part of vertical steps (§2.1.7) to entrain air at the bottom of the flow. A separation element was necessary to isolate the subpressure in the upper step face to entrain air. The study was limited to three discharges on the same model as Pfister et al. (2006a) for the deflector aerator.

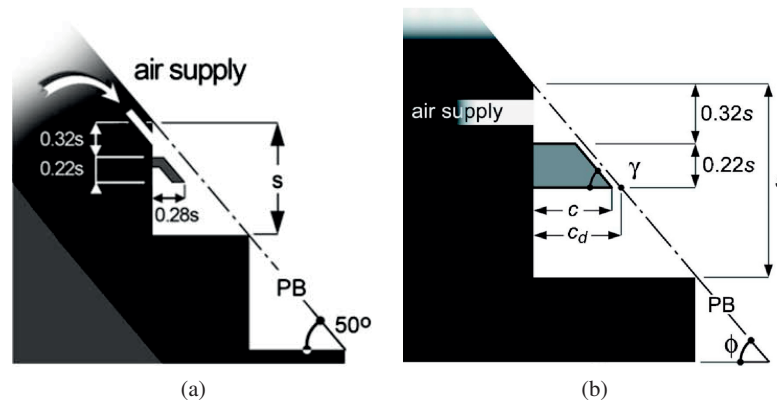


Figure 2.21 – Step aerator geometries (Pfister et al. 2006b; Schiess Zamora et al. 2008)

Schiess Zamora et al. (2008) continued this research and investigated the geometry of the separation element (Figure 2.21b). A maximal discharge beyond which no air is entrained was found as a function of the length of the separation element c/c_d . With a length of $c/c_d = 0.93$ and an angle of $\gamma = 50^\circ$, no limit was found for the tested discharges. This configuration was used for the step aerator study.

Five discharges were used to investigate the aerator performance. Similarly to the deflector aerator, a bottom air layer forms with a black water core above it, until the inception point is reached. The development of the bottom air layer was characterized in terms of maximum air concentration, air layer thickness and bottom air concentration C_b in the streamwise direction. The bottom air concentration attained is relatively small and has no significant effect of the energy dissipation and the location of the inception point. In addition to the aerator, the use of steps insets was studied to reduce spray formation.

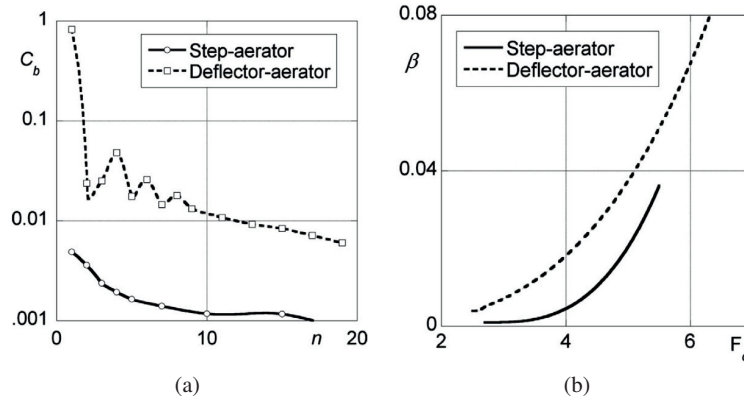


Figure 2.22 – Effect of deflector and step aerators (a) on the bottom air concentration C_b versus step number n and (b) on the air entrainment coefficient β versus approach Froude number F_o (Schiess Zamora et al. 2009)

2.4.3 Comparison of stepped chute aerators

A comparison of the two stepped chute aerators types is presented in Schiess Zamora et al. (2009). It shows that the bottom air concentration is significantly larger with a deflector aerator (Figure 2.22). As more air is present in the flow with a deflector, the air entrainment coefficient is larger. The latter is greatly influenced by the Froude number. The minimum Froude number to entrain air on stepped chutes ($F_o \approx 2$ for deflector and $F_o \approx 2.7$ for step aerator) is lower than for smooth chutes with $F_o \approx 6$ for offsets and $F_o \approx 4 - 5$ for deflectors Pfister and Hager (2010b). While presenting an inferior protection against cavitation, the step aerator has the advantage of reducing spray.

Chapter 3

Experimental setup

3.1 Channel description

The experiments are carried out in the steep channel of the Laboratory of Hydraulic Constructions (LCH) of EPFL previously used by André (2004) (Figure 3.1). The channel is made of four 2 m long modules and the elevation difference between its upstream and downstream ends can be adjusted up to a total of 4.8 m. For angles below $\varphi \leq 36^\circ$, four modules are used giving a total length of 8 m. Otherwise only 3 modules can be used for a total length of 6 m. The width of the prismatic rectangular channel is $b = 0.5$ m and the depth perpendicular to the channel bottom 0.6 m. One sidewall is made of acrylic to allow flow observation.

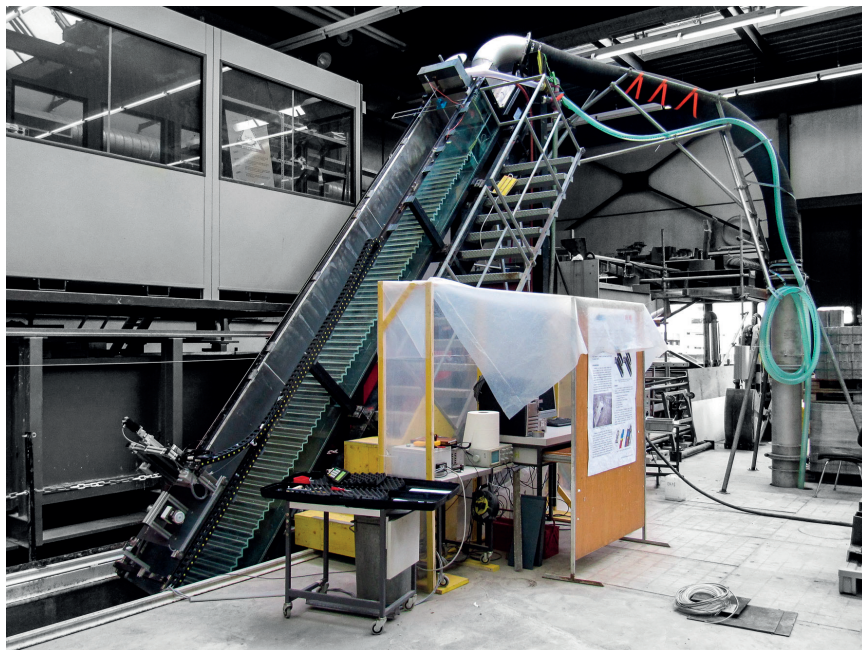


Figure 3.1 – Overview of the experimental facility with an angle of $\varphi = 50^\circ$

3.1.1 Jetbox

Water is supplied to the channel via a jetbox (Schwalt and Hager 1992). It generates the transition between pressurized to free surface flow. Unlike an uncontrolled ogee, it allows to set independently the approach flow depth h_o and Froude number F_o . Five guiding walls inside the jetbox and twenty-two at the exit (Figure 3.2a) ensure a homogeneous flow distribution.

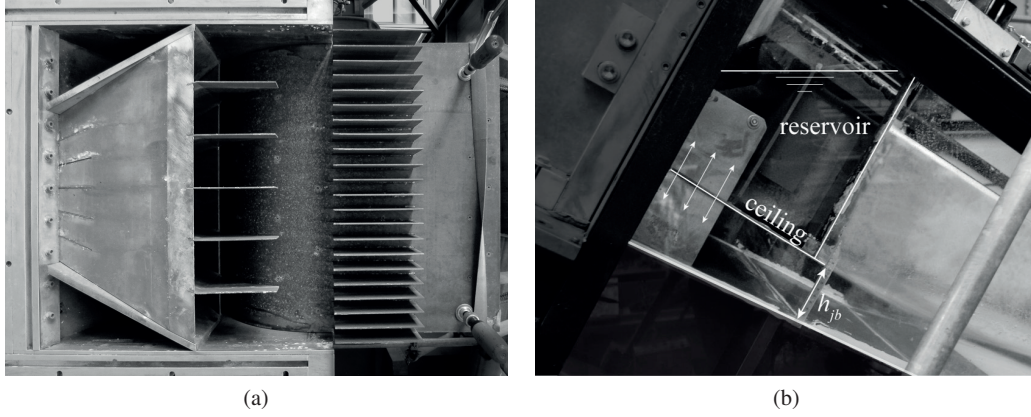


Figure 3.2 – (a) Bottom view of the guiding walls in the jetbox with water flowing from left to right (bottom removed), (b) side view of the reservoir above the jetbox ceiling

The jetbox height h_{jb} can be varied in the range $0.015 \leq h_{jb} \leq 0.113$ m. The maximum discharge provided by the pump if the jetbox is fully opened is $Q = 0.245 \text{ m}^3/\text{s}$, corresponding to a unit discharge of $q = 0.490 \text{ m}^2/\text{s}$. This discharge decreases when the opening of the jetbox is reduced as a result of higher head losses. No permanent water sealing of the jetbox is possible and a small reservoir is established above the ceiling (Figure 3.2b). For low Froude numbers, water has to be supplied to this reservoir to ensure a sufficient depth and avoid air entrainment into the jetbox. For high Froude numbers, too much water accumulates in the reservoir and the excess has to be evacuated. The discharge supplied or evacuated is measured and respectively added or subtracted from the main supply to obtain the total discharge, and is typically in the order of $\pm 0.002 \text{ m}^3/\text{s}$.

The blackwater drawdown curve upstream of the jetbox can be computed to obtain a fictitious crest location. Based on the method of Chow (1959), Hager and Blaser (1998) presented an approximated dimensionless drawdown equation for smooth chutes

$$Z_d(X_d) = \left[1 - \left(1 - Z_{dp}^{-1} \right) \exp\left(-\frac{30}{3} X_d\right) \right]^{-1} \quad (3.1)$$

with $X_d = x/x_s$ as dimensionless streamwise coordinate originating from a point p, $Z_d = h/h_{wu}$ as dimensionless flow depth, $Z_{dp} = h_p/h_{wu}$ as dimensionless flow depth at point p, $x_s = h_c^3/(h_{wu}^2 \sin \varphi)$, h as flow depth, h_c as critical flow depth, h_d as flow depth at point p, and h_{wu} as the equivalent blackwater quasi-uniform flow depth.

This method was applied by Hager and Boes (2000) and Boes and Hager (2003b) on stepped spillways using the equivalent blackwater depth h_w since self-aeration occurs much closer to the crest than for smooth chutes. They made the hypothesis that the fictitious crest is located at $h = h_c \cos \varphi$. The dimensionless streamwise coordinate of the jetbox from the fictitious crest $X_{c,jb} = x_{c,jb}/x_s$ relative to the jetbox can be obtained with

$$Z_d(X_{c,jb}) = \frac{h_c \cos \varphi}{h_{wu}} = \left[1 - \left(1 - \frac{h_{wu}}{h_{jb}} \right) \exp\left(-\frac{30}{3} X_{c,jb}\right) \right]^{-1} \quad (3.2)$$

with h_{jb} as the jetbox opening.

The uniform equivalent blackwater flow depth can either be calculated (§2.1.5) or measured if the channel is long enough. Equivalent blackwater depths measured along the channel are used to confirm the correct fit (Figure 3.3).

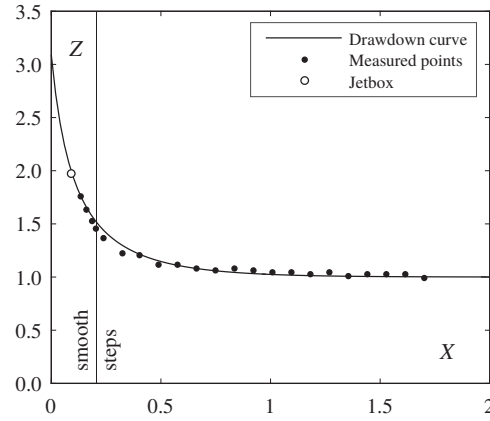


Figure 3.3 – Example of drawdown curve for test 56, with a Froude number $F = 2.67$ at the jetbox

However, the development of the turbulent boundary layer with a jetbox is different from that of an uncontrolled chute (Chanson 2005, 2006). On one hand the flow is thinner and faster which makes the turbulent boundary layer reach the surface faster. On the other hand, the turbulent boundary layer has a shorter length to develop. For a jetbox Froude number, with h_{jb} as a reference length, $F_{jb} \leq 4$ necessary to obtain an accurate drawdown curve, Boes and Hager (2005) found an excellent agreement with uncontrolled ogee data for the length from the crest to the inception point.

3.1.2 Steps

The steps are made of folded aluminum sheets with a step height $s = 0.06$ m. The fold radius is 5.5 mm for $\varphi = 50^\circ$ and 6 mm for $\varphi = 30^\circ$. The pseudo-bottom of the steps is located 0.2 m above the bottom of the channel in order to have enough space for the air supply of the aerator. Rectangular wood inserts with a 1 mm chamfer are placed in each aluminum step to have a step height $s = 0.03$ m (Figure 3.4). There are 67 steps of $s = 0.06$ m for $\varphi = 50^\circ$ and 60 steps for $\varphi = 30^\circ$. For $s = 0.03$ m,

134 steps are provided for $\varphi = 50^\circ$ and 120 steps for $\varphi = 30^\circ$. The steps begin 0.047 m downstream of the jetbox at $x = 0$ (Figure 3.9).

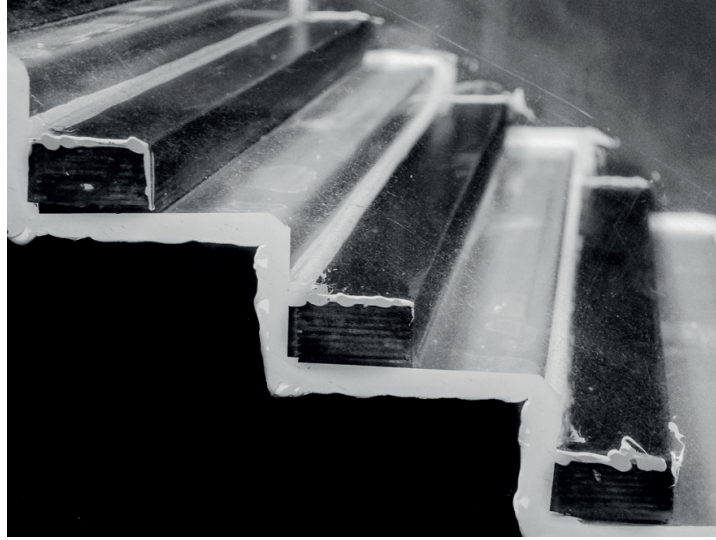


Figure 3.4 – Side view of the steps for $\varphi = 30^\circ$ and $s = 0.03$ m with the wooden inserts (dark steps)

3.2 Aerator design

A smooth bottom is used upstream of the aerator, characterizing the final part of a standard ogee. Figure 3.5 shows the cavitation index σ (§2.2) at the tangency point between an ogee and a constant angle chute considering the measured pressure on the bottom of a standard ogee (U.S. Army Corps of Engineers 1987). If the steps start at this location, the cavitation index is even lower in the upper

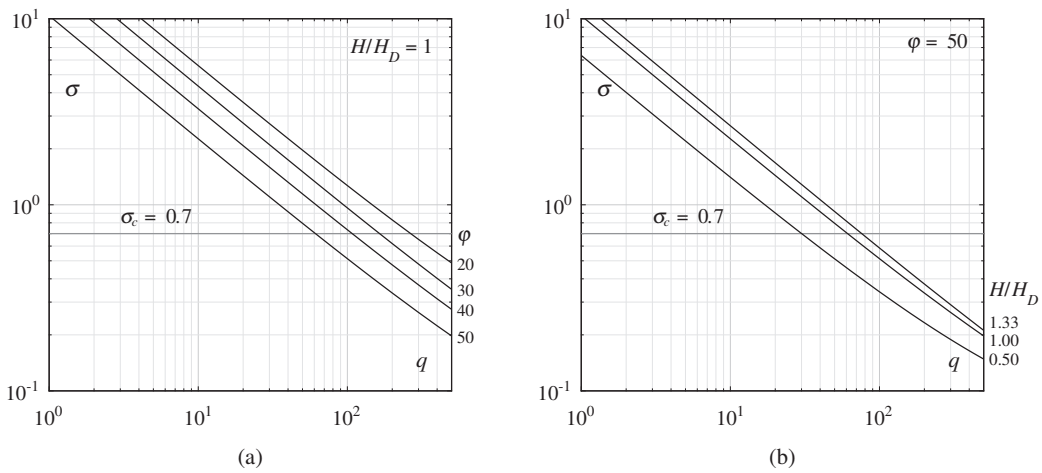


Figure 3.5 – Cavitation index σ at the tangency point between a standard ogee in function of specific discharge q with (a) different chute angles φ , (b) various ogee head ratios H/H_D

part of the vertical face of steps because of negative pressures (§2.1.7). For a chute of $\varphi = 50^\circ$ and a critical cavitation index of $\sigma_c = 0.7$ (§2.2.3), the maximum admissible specific discharge is $q = 60 \text{ m}^2/\text{s}$. This limit decreases if the unit discharge q is lower than the ogee design unit discharge q_D as the tangency point is located lower for small H/H_D ($q = 30 \text{ m}^2/\text{s}$ for $H/H_D = 0.5$ and $\varphi = 50^\circ$). This demonstrates the necessity of an aerator located at the beginning of a stepped spillway for large design unit discharges. For smaller design discharges, the aerator can be placed lower downstream as the critical cavitation index appears further downstream. In this case, a smooth bottom should be used between the ogee and the aerator for constructive reasons. Building the aerator requires the use of conventional concrete instead of roller compacted concrete and it is therefore easier to use a smooth conventional concrete for the spillway surface between the ogee and the aerator.

The consequence of an aerator located far upstream on the chute is that the local Froude number is rather small ($F = 2.9$ for $\varphi = 50^\circ$), and below the common values required for smooth chute aerators (Figure 3.6). In the latter, air entrainment starts at an approach flow Froude number $F_o \approx 4$ for steep deflectors and $F_o \approx 5$ for flat deflectors (Pfister and Hager 2010b). Tests with a low F are therefore investigated, and the aerator is placed near the jetbox to avoid the rapid increase of the Froude number on steep chutes.

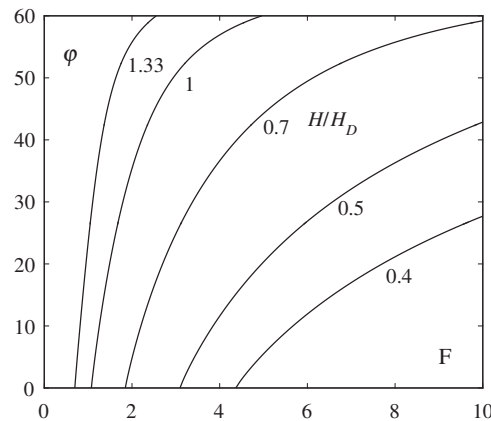


Figure 3.6 – Froude number F at the tangency point between a standard ogee and a chute with an angle φ for various ogee head ratios H/H_D

The aerator air supply is designed to provide air below the deflector. It is located at the beginning of the channel and under the jetbox (Figure 3.7). It has a wide section of 0.050 m^2 in order to limit the air head losses and thus the subpressure in the cavity under the jet. The air enters the aerator air supply through a PVC air duct used to measure the air discharge. Depending on how much air is entrained (namely on the air Reynolds number R_A), a 1 m long duct of 0.103 m internal diameter (mainly for the tests with $F_o = 3.2$) or a larger 1.8 m duct of 0.152 m internal diameter (for the remaining tests) is used.

The deflector is mounted to the aerator air supply with two screws to be easily exchanged between experiments. The horizontal air slot with a width of 0.48 m and height of 0.02 m ($A_A = 0.0096 \text{ m}^2$)

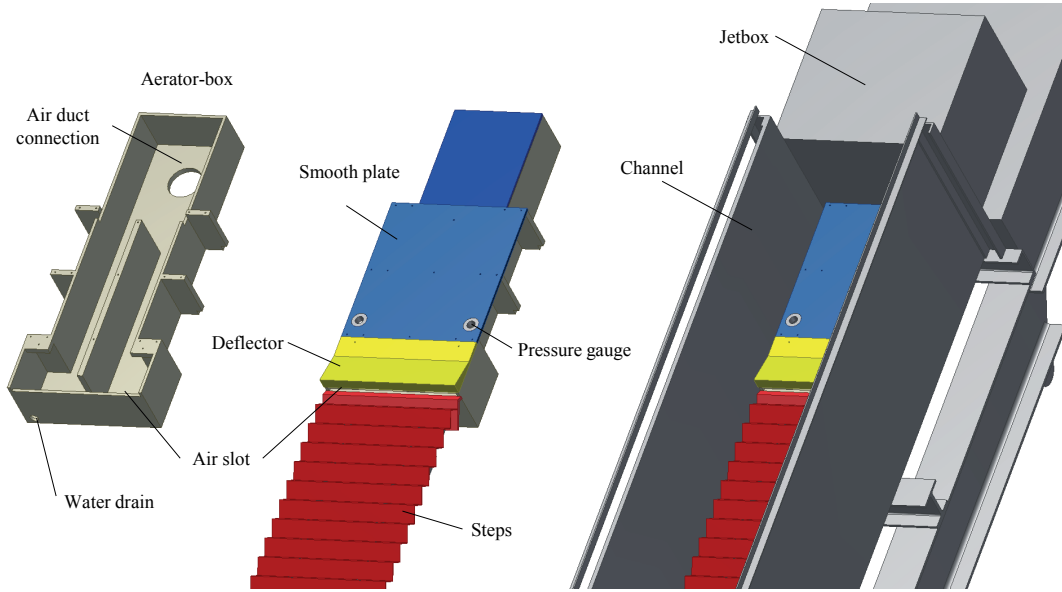


Figure 3.7 – Aerator air supply and its location in the channel

is located in the top part of the vertical face of the first step (Figure 3.8). A water drain evacuates any water in the aerator air supply. It remains closed during the experiments as no water enters the aerator air supply for the discharges tested.

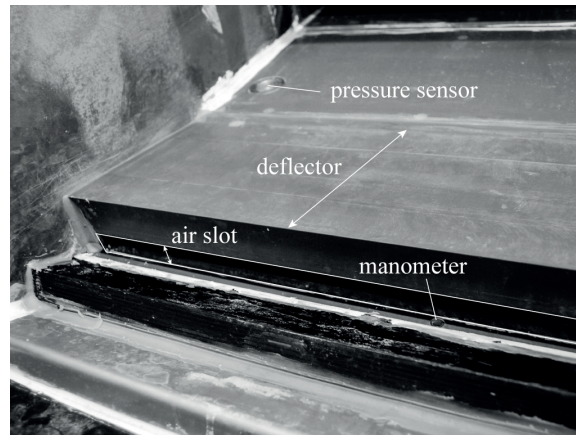


Figure 3.8 – Position of the 0.02 m high horizontal air slot and the manometer at its exit

3.3 Dimensional analysis

According to literature, the characteristic independent parameters governing the performance of aerators for the present study are:

- Fluid properties: ρ , ν , σ_w
- Flow properties: u_o , h_o

- Geometry: φ, s, α, t
- Gravity: g
- Cavity property: Δp

And the dependent parameters are:

- Jet length L
- Air entrainment coefficient β
- Air concentration C

The relation between the dependent and independent parameters can be expressed as

$$L, \beta, C = f(\rho, v, \sigma_w, u_o, h_o, \varphi, s, \alpha, t, g, \Delta p)$$

The π theorem (Buckingham 1914) states that if n dimensional parameters using k fundamental dimensions are necessary to describe a property, then the property can be described with $(n - k)$ dimensionless parameters. For this study, there are 11 parameters and 3 fundamental dimensions: length, time and mass. Using ρ , g and h_o as the basic parameters, the resulting 8 dimensionless parameters are:

$$\Pi_1 = \frac{u}{\sqrt{gh_o}} = F_o$$

$$\Pi_2 = \frac{v}{\sqrt{gh_o^3}}$$

$$\Pi_3 = \frac{\sigma_w}{\rho gh_o^2}$$

$$\Pi_4 = \varphi$$

$$\Pi_5 = \frac{s}{h_o}$$

$$\Pi_6 = \alpha$$

$$\Pi_7 = \frac{t}{h_o}$$

$$\Pi_8 = \frac{\Delta p}{\rho gh_o}$$

These are the common parameters of relations found in literature and typical of a Froude similitude. Another set of basic parameters are required for a Reynolds or Weber similitude. By respecting the scaling limits presented in §3.7, Π_2 and Π_3 can be neglected. And with the large areas in the air supply system to obtain an optimal aerator performance, the subpressure is small and Π_8 can also

be neglected. The dependent parameters can finally be expressed as

$$\frac{L}{h_o}, \beta, C = f(F_o, \varphi, \frac{s}{h_o}, \alpha, \frac{t}{h_o})$$

3.4 Parameters and test program

The six dimensional parameters obtained in the dimensional analysis are systematically varied during the experiments to investigate their effect on the aerator performance. The parameters are illustrated in Figure 3.9 and their range presented in Table 3.1.

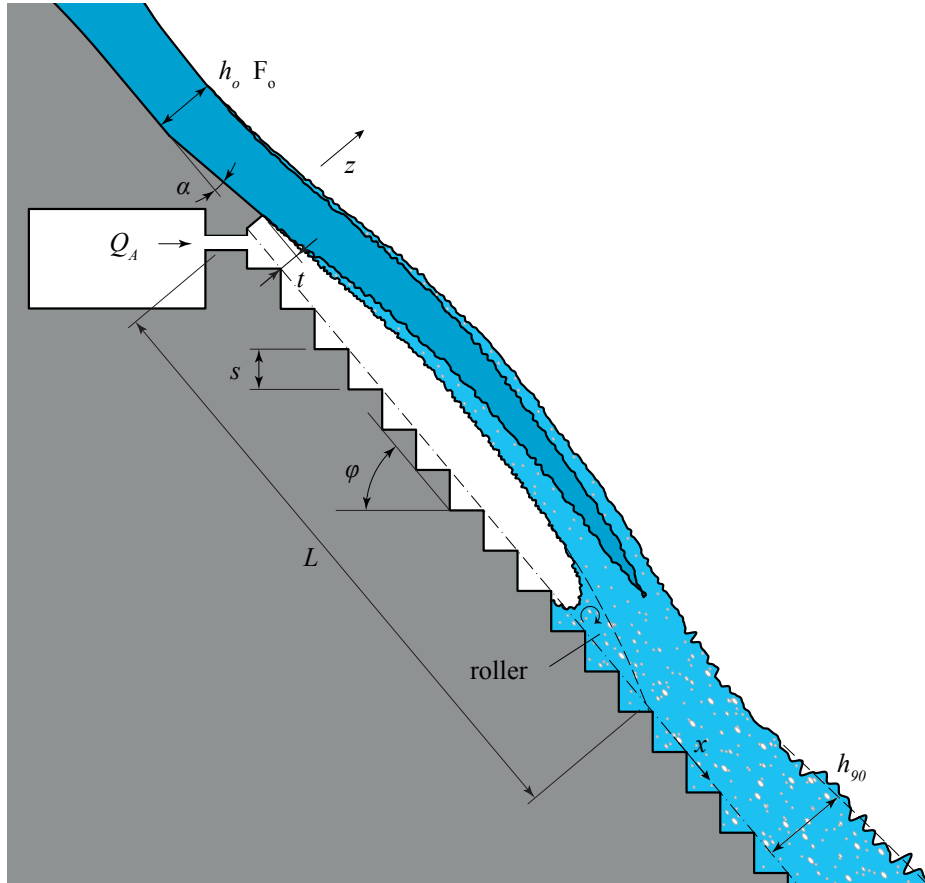


Figure 3.9 – Definition scheme of stepped spillways aerator with notation

An pseudo-bottom angle of $\varphi = 50^\circ$ is typical for spillways on RCC dams as the downstream face of gravity dams requires a slope lower than 1.28 (1V:0.78H) i.e. an angle lower than $\varphi = 52^\circ$ (Schleiss and Pougatsch 2011). A second angle of $\varphi = 30^\circ$ (1V:1.73H) was tested to have conditions closer to embankment dams.

RCC dams are often built with 0.3 m thick layers. The spillway step height is consequently a multiple of this thickness. The scale factor for the standard step height $s = 0.06\text{ m}$ would be 1:5 for

Table 3.1 – Tested parameters range

Parameter	Symbol	Unit	Tested values
Pseudo-bottom angle	φ	[°]	30, 50
Step height	s	[m]	0.03, 0.06
Approach Froude number	F_o	[-]	3.2, 5.5, 7.5
Approach flow depth	h_o	[m]	0.052, 0.075, 0.092
Deflector angle	α	[°]	5.71, 9.46, 14.04
Deflector height	t	[m]	0.015, 0.030, 0.045

a prototype with a step height of $s = 0.3$ m or 1:10 for prototype steps of $s = 0.6$ m.

Flow parameters were defined after testing the jetbox capacity (Figure 3.10). The unit water discharge was limited to $q \geq 0.2 \text{ m}^2/\text{s}$ to avoid scale effects (§3.7). Five combinations of h_o and $F_o = q/(gh_o^3)^{0.5}$ were chosen to allow the independent testing of each parameter with three values. As explained in §3.2, one combination includes a low Froude number of $F_o = 3.2$. All flow conditions are clearly in the skimming flow regime with $2.7 \leq h_c/s \leq 9.6$.

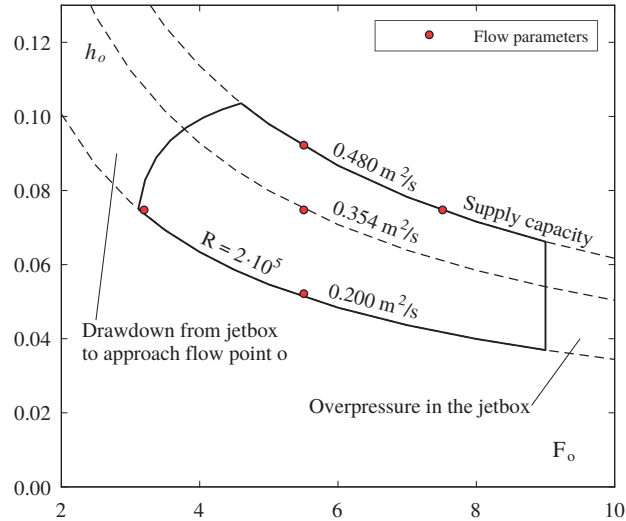


Figure 3.10 – Limits of approach flow depth h_o and Froude number F_o generated by the jetbox, and the selected flow parameters

The deflector angles correspond to slopes (V:H) of 1:10, 1:6 and 1:4 respectively. The deflector height was chosen to be a factor of the step height. Only the deflectors shorter than $L_d = t / \tan \alpha = 0.20$ m are tested, giving a total of six deflectors.

In addition to the aerator tests, reference tests without aerator are performed. A smooth bottom is placed instead of the deflector, and the air slot is closed and made air-tight. The reference tests allow to precisely assess the effect of the aerator and compare the present model data with other studies. A corresponding reference test is carried out for every equivalent aerator test. The tested combinations with their parameter values are given in Table 3.2. There are 18 reference tests and 44 aerator tests.

Table 3.2 – Test numbers and their parameters, with h_o , s and t in [m]

			F _o = 3.2	F _o = 5.5				F _o = 7.5
			<i>h</i> _o = 0.075	<i>h</i> _o = 0.052	<i>h</i> _o = 0.075	<i>h</i> _o = 0.092	<i>h</i> _o = 0.075	
Reference	<i>φ</i> = 50°	<i>s</i> = 0.06	17	15	13	14	16	
		<i>s</i> = 0.03	10	9	8	7	6	
	<i>φ</i> = 30°	<i>s</i> = 0.06	41	40	38	39	42	
		<i>s</i> = 0.03	56		54		55	
<i>α</i> = 5.71° <i>t</i> = 0.015	<i>φ</i> = 50°	<i>s</i> = 0.06	29	33	32	30	31	
		<i>s</i> = 0.03						
	<i>φ</i> = 30°	<i>s</i> = 0.06						
		<i>s</i> = 0.03						
<i>α</i> = 9.46° <i>t</i> = 0.015	<i>φ</i> = 50°	<i>s</i> = 0.06	27	25	24	26	23	
		<i>s</i> = 0.03			12			
	<i>φ</i> = 30°	<i>s</i> = 0.06			47			
		<i>s</i> = 0.03			58			
<i>α</i> = 9.46° <i>t</i> = 0.030	<i>φ</i> = 50°	<i>s</i> = 0.06	18	21	20	19	22	
		<i>s</i> = 0.03	3	2	1	4	5	
	<i>φ</i> = 30°	<i>s</i> = 0.06	52	46	44	45	43	
		<i>s</i> = 0.03	62		57		58	
<i>α</i> = 14.04° <i>t</i> = 0.015	<i>φ</i> = 50°	<i>s</i> = 0.06						
		<i>s</i> = 0.03						
	<i>φ</i> = 30°	<i>s</i> = 0.06			48			
		<i>s</i> = 0.03						
<i>α</i> = 14.04° <i>t</i> = 0.030	<i>φ</i> = 50°	<i>s</i> = 0.06	28	34	35	36	37	
		<i>s</i> = 0.03			11			
	<i>φ</i> = 30°	<i>s</i> = 0.06			49			
		<i>s</i> = 0.03			60			
<i>α</i> = 14.04° <i>t</i> = 0.045	<i>φ</i> = 50°	<i>s</i> = 0.06						
		<i>s</i> = 0.03						
	<i>φ</i> = 30°	<i>s</i> = 0.06	53		50		51	
		<i>s</i> = 0.03			61			

Table 3.3 – Additional tests for $\varphi = 30^\circ$ and $s = 0.03$ m, with h_o and t in [m]

		$h_o = 0.075$	
		$F_o = 5.5$	$F_o = 7.5$
Reference	standard	54	55
	grid	63	66
$\alpha = 9.46^\circ$ $t = 0.030$	standard	57	58
	grid	64	65
	pre-aerated	67	68

Preliminary tests to investigate two additional parameters were performed as well (Table 3.3):

- A metal *grid* is attached to the bottom to increase the bottom roughness and the flow turbulence (Figure 3.11). A study of offset aerator on a flat chute ($\varphi = 0^\circ$) with different bottom roughness was presented by Skripalle (1994). The grid is 1.5 mm thick with square holes of 8 mm spaced by 2 mm. It is placed from $x = -0.48$ m to $x = -0.19$ m. Holes in the grid are cut around the pressure transducers.
- The effect of a *pre-aeration* of the approach flow. Pressurized air is injected in the water supply pipe 15 m upstream of the jetbox.

These six additional preliminary tests are discussed in Chapter 8, and were not considered for the principal data analysis.

A testsheet summarizing the parameters and results of each aerator, grid and pre-aerated test is given in Appendix F.

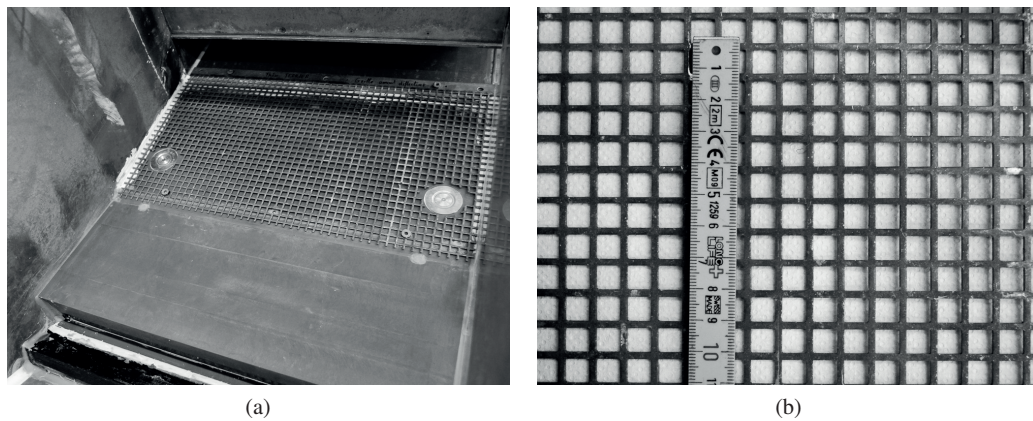


Figure 3.11 – Location and dimension of the grid for the preliminary tests (measuring tape in [cm])

3.5 Instrumentation

3.5.1 Fiber optical probe

Most results of this research rely on the local air concentration C measured by a *RBI Instrumentation* (France) fiber optical probe. This system was previously documented, tested and used by Boes (2000c), André (2004), Kramer (2004) and Pfister (2008). It includes three elements plus the data treating software:

1. The *probe* itself is made of two optical fibers each with a $80\mu\text{m}$ sapphire prism at the tip (Figure 3.12). The physical principle behind the air-water phase detection is the difference in the refraction indexes of air (1.0), water (1.33) and sapphire (1.62). All the light is reflected back into the optical fiber when the probe tip is in the air, while only a very small fraction of

the light is reflected when the probe tip is in the water. Having a second tip directly behind the first tip allows to calculate the flow velocity by cross-correlation between the two signals. Only the air concentration of the first tip is considered herein as the second is partially influenced by the first, typically resulting in a higher air concentration and more bubbles detected. A few different probes were used for the experiments and the spacing between the tips varied between 1.5 and 2 mm.

2. The *opto-electronic module* emits light pulses in the optical fibers and receives back the reflections of the sapphire prism. The received optic signal is converted to an electric signal. The resulting tension is visualized on an oscilloscope and adjusted on the opto-electronic module according to the manual in order to have the highest tension at 5 V (air), and the lowest at 0 V (water).
3. The *acquisition module* connects the opto-electronic module and a computer. it allows the acquisition of the signals of the opto-electronic module at a frequency of 1 MHz.
4. The software *Interface Software for Optical probe (ISO)* allows to define the settings of the acquisition module and start the acquisition. Each point's measurements are saved in a proprietary *.rbi* file on the computer. The signals recorded can be visualized with the software, as well as analyzed to obtain the air concentration, the bubble frequency, the flow velocity and the Sauter mean diameter. A batch function allows the analysis of multiple files and summarizes the results in a spreadsheet with one line per *.rbi* file. Version 2.09 of the software was used.



Figure 3.12 – The tips of the fiber optical probe. The optical fibers are protected in thin metallic tubes until the last few millimeters. The sapphire prisms are the light tips at the end of the metallic tubes. The probe is oriented for a flow from left to right. The measuring tape is in centimeters

Based on the findings of Kramer (2004), an acquisition time of 20 s was selected for all the tests. The flow depths along the channel are defined based on the air concentration profiles.

3.5.2 Automatic positioning system

To measure the spatial distribution of air concentration $C(x, z)$, the fiber optical probe is mounted on an automatic positioning system (APS). It is motorized on the streamwise (x) and depth (z , perpendicular to x) axes. The lateral position is set at 0.03 m from the center of the channel. Whenever the chute angle φ or the step height s is modified, the steps geometry is measured with a laser mounted on the APS. For all the configurations, the steps edges were within ± 2 mm. The fiber optical probe is mounted so that its tips are 0.002–0.003 m away from the highest protruding step.

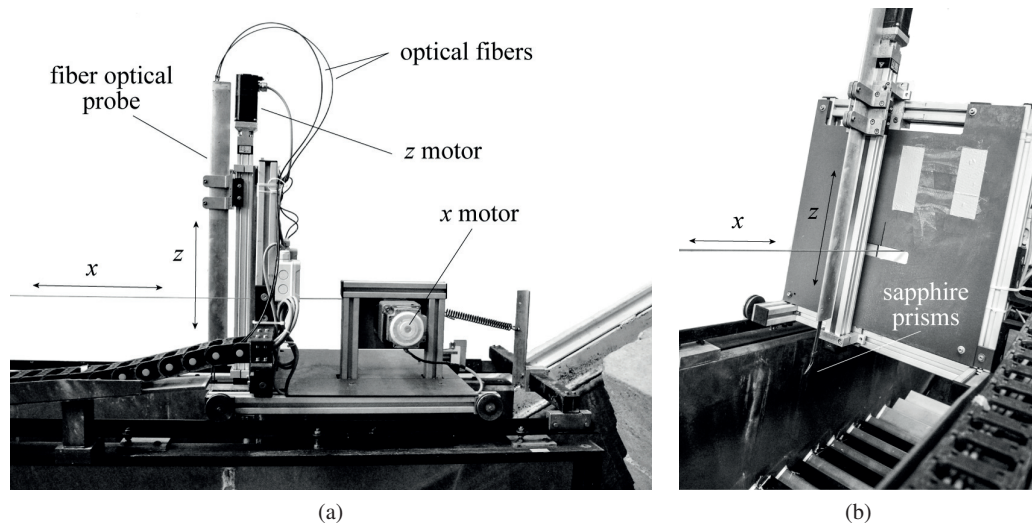


Figure 3.13 – The automatic positioning system

The APS can measure in the range of $0 \leq x \leq 4.35$ m (for $\varphi = 50^\circ$) or $0 \leq x \leq 6.35$ m (for $\varphi = 30^\circ$), and $0 \leq z \leq 0.42$ m (cf. Figure 3.9 for axis definition). The depth profiles are measured at the same streamwise position for each chute angle φ . The first profile is located at the edge of step 1, and then every three steps (4, 7, 10...). The same coordinate x is kept for the smaller steps $s = 0.03$ m (profiles at steps 2, 8, 14, 20...). A total of 19 profiles are measured for $\varphi = 50^\circ$ and 18 for $\varphi = 30^\circ$. The measurements start from the most downstream profile.

A G-code script containing the commands for the APS is generated before a test. After starting the script, the APS moves to each coordinates specified in the script. When the APS reaches a point, it triggers a signal to the RBI acquisition module to start the point measurement. The APS pauses until the measurement is finished and then moves to the next point. At the end of the script, the APS remains at the last point measured. Its vertical position is measured to verify the accuracy.

3.5.3 Flowmeter

The water discharge Q is measured by an electromagnetic flowmeter *ABB FXE400 (COPA-XE)* (Switzerland) on the DN 300 supply pipe. The flowmeter can measure discharges up to $Q = 0.667$ m³/s with an accuracy of $\pm 0.05Q$ for discharges $Q \geq 0.047$ m³/s. For the maximum discharge

tested ($0.242 \text{ m}^3/\text{s}$), the maximum error is $0.00121 \text{ m}^3/\text{s}$. The flowmeter was calibrated before the first test for five discharges from 0.050 to $0.245 \text{ m}^3/\text{s}$. The acquisition is made through the pumps command system at a frequency of $1/3 \text{ Hz}$.

The auxiliary discharge supplied to (for $F_o = 3.2$) or siphoned from (for $F_o = 7.5$) the jetbox reservoir (§3.1.1) was measured by the time required to fill a 0.050 m^3 volume. The discharge measured by the flowmeter was corrected accordingly.

3.5.4 Anemometer

A thermoelectric anemometer *Schiltknecht ThermoAir64* (Switzerland) with a measuring range of 0.015 to 5 m/s is used to measure the air velocity in the air duct. The accuracy is $\pm 0.5\%$ of full scale plus $\pm 1.5\%$ of the value measured. The maximum error is then $\pm 0.1 \text{ m/s}$ for 5 m/s . The anemometer is placed in the center of the air supply duct, at $3/5$ of the length from the intake (Figure 3.14). The acquisition is made with LabVIEW at 10 Hz for the duration of the fiber optical probe measurements.

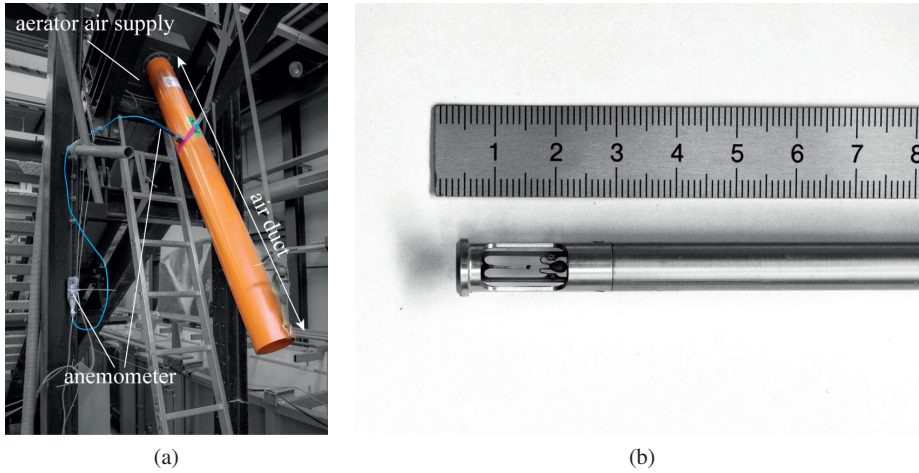


Figure 3.14 – (a) location of the anemometer in the air duct connected to the aerator air supply, and (b) detail of anemometer (measuring tape in centimeters)

When the fiber optical probe measures the jet downstream of the deflector, the air entrainment of the aerator is influenced with both lower and higher air entrainments depending on the probe position. Only the unaffected part on the lower part of the channel is considered for the analysis of the air discharge.

The velocity measured in the center of the air duct is the maximum velocity $u_{A,max}$. However, the average velocity u_A is required to obtain the air discharge Q_A . The following iterative procedure based on the logarithmic velocity profile is used to calculate u_A :

1. The air Reynolds number R_A is calculated

$$R_A = \frac{u_A \cdot d}{\nu_A} \quad (3.3)$$

with d the duct diameter and ν_A the kinematic viscosity of air ($\nu_A = 1.45 \cdot 10^{-5} \text{ m}^2/\text{s}$). For the first iteration, the maximum velocity $u_{A,max}$ is used instead of u_A .

2. The friction coefficient f is iteratively obtained from

$$\frac{1}{\sqrt{f}} = -2 \cdot \log \left(\frac{\varepsilon}{3.71} + \frac{2.51}{R_A \sqrt{f}} \right) \quad (3.4)$$

with $\varepsilon = k_s/d$ the relative roughness and k_s the duct wall roughness ($k_s = 1 \cdot 10^{-5} \text{ m}$).

3. The velocity profile is given by

$$\frac{u(y)}{u_{A,max}} = 1 + \frac{0.884\sqrt{f}}{1 + 1.326\sqrt{f}} \cdot \ln \left(1 - \frac{y}{d/2} \right) \quad (3.5)$$

with y the coordinate originating from the center of the duct. The average velocity u_A occurs at a distance $y = 0.777 \cdot d/2$. The value of u_A obtained is used for a new iteration.

This procedure rapidly converges and is only valid for a turbulent flow ($R_A \geq 2300$). In order to have turbulent flow in the air duct and remain in the measuring range of the anemometer, two air ducts were necessary (§3.2).

3.5.5 Pressure transducers

Two pressure transducers *Baumer ED701 J20.633* (Switzerland) are located at $x_p = -0.27 \text{ m}$ (i.e. upstream of the deflector) on the left and right side of the channel, each at a distance of 0.045 m from the sidewall. Their accuracy is $\pm 0.1 \%$ of the full scale of measurement (1 m), so $\pm 0.001 \text{ m}$. The pressure is measured for 65.5 s at 1000 Hz with LabVIEW at the beginning of each test.

The time-averaged pressure p as well as the root mean square of the pressure fluctuations p' are obtained from the measurements. The values of p and p' are the average of the values obtained for each of the two sensors.

3.5.6 Point gauge

A manual point gauge is used to measure the water depth on and upstream of the deflector at coordinates $x = 0, -0.1, -0.2$ and -0.3 m (Figure 3.9). The depth at $x = -0.2 \text{ m}$ is the approach flow depth $h_o = h(x = -0.2)$. In addition, the opening of the jetbox is measured at $x = -0.47 \text{ m}$.

3.5.7 Manometer

The subpressure $\Delta p/(\rho g)$ in the air cavity below the jet is measured with a U-shaped water manometer. It is located on the surface at the exit of the air slot, in the center of the channel (Figure 3.8). The value is read optically with an accuracy of ± 0.001 m. The subpressure was not varied as a parameter and results only from the characteristics of the air supply system.

3.5.8 Observed jet length

The observed jet length L_{obs} is measured visually. It is defined at the impact of the lower jet surface on the pseudo-bottom. The lower jet surface is difficult to define as the jet becomes aerated and the sidewall decelerates the jet. As a consequence, the jet length is often underestimated. It is rounded to the closest step, giving an "accuracy" of one step length L_s .

3.6 Test procedure

To perform the tests, a testsheet including all the test parameters, space for manual measurements and a checklist is prepared. The following procedure is followed for each test:

1. The model is prepared with the required test conditions until permanent conditions are reached.
2. The settings of the fiber optical probe are verified and adjusted if necessary.
3. The maximum flow depth is optically measured (highest point of the jet for aerator tests) and the APS script is adapted accordingly.
4. The flow depths are measured with the point gauge.
5. The dynamic bottom pressure upstream of the deflector is measured and recorded in a file *Pressure*.
6. The acquisition of the discharge is started and recorded in a file *Discharge*.
7. The acquisition of the air velocity is started and recorded in a file *AirVelocity*.
8. The APS script is launched.
9. Immediately afterwards, the acquisition of the fiber optical probe is started, producing one *.rbi* file for each point.
10. The jet length is measured visually.
11. The cavity subpressure is measured.
12. Photos are taken.
13. During the acquisition of the test, the model is regularly observed.

14. When the APS is finished, its position is verified.
15. If required, the auxiliary water discharge is measured.
16. The model is turned off.

After the test, the following procedure is followed to process and verify the data:

1. The test parameters and manual measurements are entered in a spreadsheet *Input*.
2. The *.rbi* files are processed with ISO (fiber optical probe software) which summarizes the results in a spreadsheet *RBI*.
3. A first MATLAB code using the files *Input* and *RBI* creates the matrices of the air concentration, the average bubble velocity, the bubble frequency and the Sauter mean diameter, and then saves them in a spreadsheet *Distribution* with their coordinates.
4. The matrices are manually checked for errors. Water drops can remain attached to the probe tips when they are in the air, especially in the air cavity below the jet. In this case, the value is manually set to 1 (air). In the rare cases of an error in the multi-phase flow, the value is replaced by the average of the point below and the point above in the same profile.
5. A second MATLAB code using the files *Input*, *AirVelocity*, *Discharge*, *Pressure* and *Distribution* does all the calculations necessary for the test. All the parameters and the results are written in a column specific to the test in a spreadsheet *Summary*. Graphs of the air concentration, the air velocity, the discharge and the pressure are produced. Automatic and manual controls based on the graphs are performed in the script to check the reliability and quality of the measurements.
6. The results of *Summary* can directly be used for further analysis.

3.7 Scale effects

The Froude similitude is adopted to drive free surface models flow by gravity. It conserves the ratio of the two dominant forces, gravity and inertia, described by the Froude number F

$$F(L_{ref}) = \frac{u}{\sqrt{gL_{ref}}} \quad (3.6)$$

where L_{ref} is a reference length and u a characteristic velocity.

For two-phase flows, turbulence and surface tension generate additional forces, respectively de-

scribed by the Reynolds R and Weber W numbers

$$R(L_{ref}) = \frac{uL_{ref}}{\nu} \quad (3.7)$$

$$W^2(L_{ref}) = \frac{\rho u^2 L_{ref}}{\sigma_w} \quad (3.8)$$

where ν is the kinematic viscosity, ρ the water density and σ_w the surface tension between air and water.

To have a full dynamic similarity between model and prototype, the Froude, Reynolds and Weber similarity laws would have to be fulfilled simultaneously. Applying the dynamic similarity and using the same fluids (air and water), turbulent air-water flow cannot be modeled without scale effects. The Froude similarity leads to air bubbles being too large in the model, which results in a higher detrainment rate and lower transport capacity compared to a prototype (Kobus 1984a). For jets disintegration, the water drops are too large in the model, although the jet dispersion is identical (Pfister and Hager 2010a).

Besides theoretical considerations, model families are used to study scales effects. They allow giving recommendations of minimal values of Reynolds and Weber numbers required to limit scale effects. Multiple researches about scale effects on the air entrainment coefficient β of spillway aerators are presented in Kobus (1984b). For stepped spillways, Boes and Hager (2003b) studied air concentration and velocity profiles. They observed a decrease of air concentration close to the bottom and an increase close to the surface when the scale factor λ increases.

Table 3.4 summarizes relevant scale effects researches related to stepped spillways aeration. It shows that multiple reference lengths are used to define the Reynolds and Weber numbers. Besides, there are differences in the limits depending on the characteristics investigated. A study by Chanson (2008) reveals for example that bubble properties are much more affected by scale effects than the air concentrations or velocities.

In addition to limitations of Reynolds and Weber numbers, Pinto (1984), Volkart and Rutschmann (1984), Pan and Shao (1984) and Boes (2000b) suggested limiting the scale factor to approximately 1:15 to 1:20 for aerator or two-phase flows investigations. Ervine et al. (1995) highlighted that a turbulent velocity of 0.25 to 0.3 m/s is required to break the surface tension and to initiate the aeration process. They also indicated that the inability to properly scale the bottom roughness can lead to slower velocities on a model.

Using the water depth h as the reference length L_{ref} , the Reynolds number becomes $R(h) = q/\nu$ and stays constant in a channel. If the same reference length L_{ref} is used, the three numbers described previously are linked by the Morton number M describing the fluids physical properties

$$M = \frac{g\mu^4}{\rho\sigma_w^3} = \frac{W^6}{F^2R^4} \quad (3.9)$$

Table 3.4 – Recommended limitations to avoid scale effects in two-phase flows

Reference	Application	Characteristic	Limit
Kobus (1984a)	General	Air entrainment	$R(h) \geq 10^5$
Pinto (1984)	Aerators	β	$W(L) \geq 500$
Koschitzky (1987)	Aerators	β	$R(h) \geq 10^5$
Rutschmann (1988)	Aerators	β	$W(h_o) \geq 110$
Skipalle (1994)	Aerators	β	$W(h_o) \geq 170$
Wahrheit-Lensing (1996)	Stepped spillways	Air entrainment	$R(h) \geq 7.5 \cdot 10^5$
Boes (2000b)	Stepped spillways	C and u profiles	$W(L_s) \geq 100$ $R(h) \geq 10^5$
Chanson et al. (2004)	Plunging jets	C	$W(d) \geq 32$
Takahashi et al. (2005)	Stepped spillways	C profiles	$R(h) \geq 4 \cdot 10^4$
Chanson (2009)	Hydraulic structures	Air bubble properties	$R(h) \geq 5 \cdot 10^5$
Pfister and Hager (2010a)	Aerators	C_b	$W(h_o) \geq 140$

with μ as the dynamic water viscosity.

The same fluids are generally used in the model and prototype, giving a constant Morton number. It gives a direct relation between the Reynolds and Weber numbers for a Froude similitude. Respecting $R \geq 2 \cdot 10^5$ to $3 \cdot 10^5$ is sufficient to minimize scale effects for $F \geq 5$ as the Weber number limit is implicitly respected, whereas selecting a Weber number limit is more relevant for $F \leq 5$ (Pfister and Hager 2014; Pfister and Chanson 2014).

The five flow conditions selected (§3.4) for the tests have a Reynolds number within $202000 \leq R \leq 486000$ and an approach flow Weber number within $87 \leq W_o \leq 209$ (Figure 3.15). The average air concentration C_a and bottom air concentration C_b are adequately represented, except the two flow conditions at $R \approx 2 \cdot 10^5$ which might show minor scale effects for C_b based on Pfister and Hager (2010a). All other secondary two-phase flow properties, such as bubble size and bubble count rate, are not correctly represented. However, the present study is exclusively based on air concentration measurements.

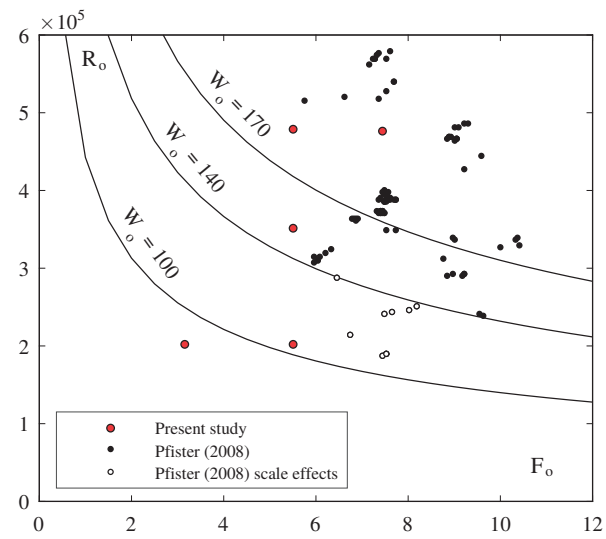


Figure 3.15 – Scale effects with h_o as the reference length

Chapter 4

Reference tests

4.1 Overview

Reference tests are performed without aerator in order to have reference values which are used to compare and assess the effect of the aerator. The deflector is removed and replaced by a flat smooth bottom, and the air slot is obstructed so that no air can be entrained from the bottom. The data derived from the 18 reference tests are presented in this chapter.

The example of test 13 with a chute angle $\varphi = 50^\circ$, a step height $s = 0.06$ m, an approach Froude number $F_o = 5.5$ and an approach flow depth $h_o = 0.075$ m is used in this overview to describe typical characteristics and results of a reference test. The relevant hydraulic values of all tests are analyzed further in this chapter.

The air concentration measurements are presented in Figure 4.1a. The steps are strongly distorted due to the different scale used for axes x and z . The drawdown curve on the smooth bottom ($x \leq 0$) is measured with the point gauge, and the first point at $x = -0.47$ m is the jetbox opening h_{jb} . The decrease in the flow depth indicates an acceleration of the flow. The air concentration is measured by depth-profiles starting from step 1 until step 55 (step 52 for tests with $\varphi = 30^\circ$) with a spacing Δx of three steps, giving a total of 19 profiles (18 for $\varphi = 30^\circ$). A depth-profile consists of 25 air concentration points measured with a vertical spacing Δz constant for each test. The vertical spacing varied in the range $4.2 \leq \Delta z \leq 8.3$ mm for reference tests. The 475 points (450 for $\varphi = 30^\circ$) per test are used to create the contour plot shown. A cubic interpolation is used to obtain the contours, and artifacts are sometimes visible (particularly for aerator tests).

The contour plot is only used to have an overview of the spatial distribution of the air concentration. The highest contour visible is the surface z_{90} which includes by definition $C = 0.90$, and is also the depth h_{90} . The areas between the contours are shaded according to the measured air concentration. The darkest shade is used for an air concentration $0 \leq C \leq 0.05$ (blackwater), and white is used for $C \geq 0.90$. The flow is formed of blackwater until step 10. In this section, the surface shows a streamwise decrease in the air concentration gradient (the contours start to diverge) indicating that

the surface progressively becomes rougher. After step 10, there is a very rapid increase in the air concentration at the surface. The inception, defined by $C_b = 0.01$, is reached at $x_i = 0.90$ m. Due to the sudden high air entrainment, the surface z_{90} rapidly increases and a maximum is reached at $x = 2.21$ m with $z_{90} = 0.131$ m, which is close to twice the approach flow depth $h_o = 0.075$ m. The aerated developing flow continues until $x = 3$ m where quasi-uniform conditions seem to be attained since the contours remain at a constant depth.

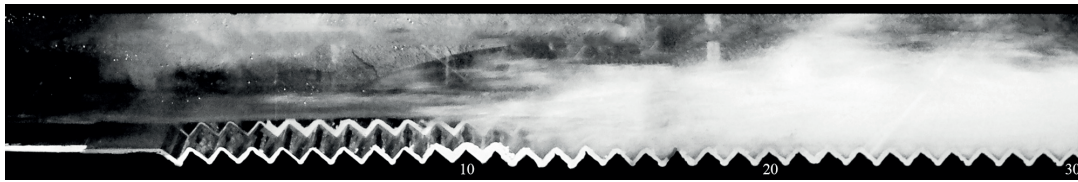
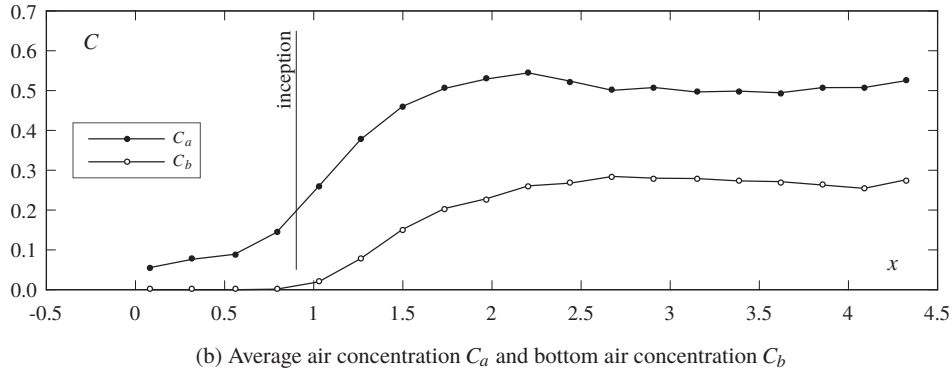
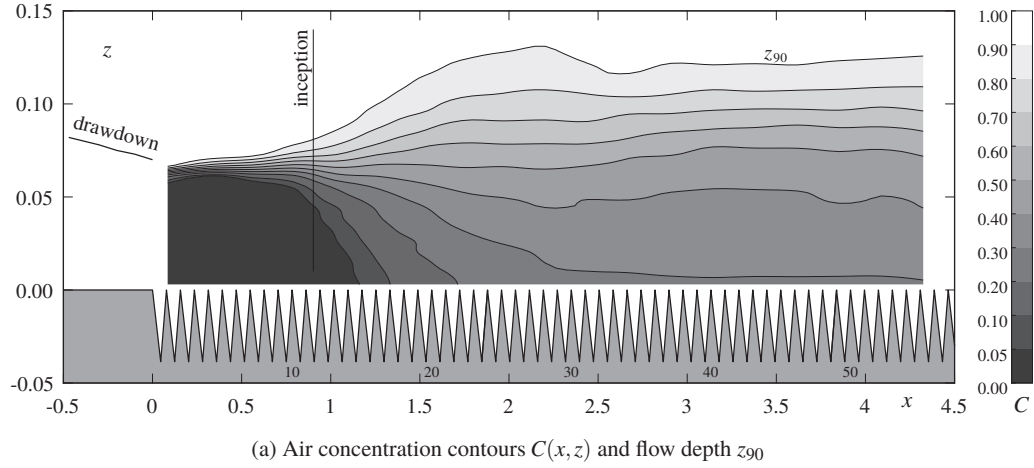


Figure 4.1 – Typical result of a reference test (test 13)

The average air concentration C_a (Figure 4.1b) does not precisely start at $C_a = 0$. The depth z_{90} is linearly interpolated between the points neighboring $C = 0.90$. This method overestimates the air entrained just under the surface when the air concentration gradient is high (like it is at the beginning of the channel). For example, for 10 points measured in a pure water flow ($C = 0$) and an 11th point in pure air ($C = 1$), the calculated average air concentration is $C_a = 0.078$. The vertical

spacing of $\Delta z = 4\text{--}8\text{ mm}$ results in 9 to 15 points in the flow for the first profile, and an initial air concentration of $C_a \approx 0.05\text{--}0.10$.

The average air concentration rapidly rises after $x = 0.57\text{ m}$ (step 7), and achieves $C_a = 0.20$ at the inception point. A maximum of $C_a = 0.54$ is reached at $x \approx 2\text{ m}$ before a stabilization at $C_a \approx 0.50$. The bottom air concentration C_b is zero for the first four profiles. The value of $C_b = 0.01$ defining the inception point is attained at $x_i = 0.90\text{ m}$ using a linear interpolation between the profiles at $x = 0.79\text{ m}$ (step 10) and $x = 1.03\text{ m}$ (step 13). It then rapidly increases before stabilizing at $C_b \approx 0.27$.

The photo shows (Figure 4.1c) a transparent flow resulting from the absence of air until step 8. The steps and back wall of the channel are thus visible through the flow. The water surface is well defined along this reach, with some local air entrainment (lighter color) starting downstream of step 3 on the back wall. In the middle of the channel, air entrainment on the surface starts after step 8 on a small transversal width. The reduction of the flow transparency close to the surface indicates that air starts to be entrained in the flow. The aeration on the full depth occurs rapidly (white flow) with the inception point reached between steps 11 and 12. Around the inception point, the flow depth increases (flow bulking) and the surface becomes irregular. Spray (water lumps projected in the air) is visible, particularly above steps 22 and 27 where it almost reaches the top of the channel. This spray is the cause of the maximum depth and air concentration previously described at $x \approx 2\text{ m}$.

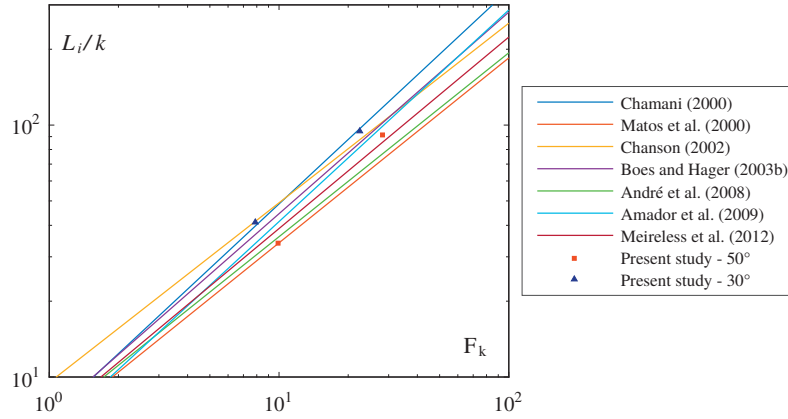
4.2 Inception point of self-aeration characteristics

The definition $C_b = 0.01$ is used to locate the inception point. Its position x_i , mixture depth h_i , equivalent blackwater flow depth h_{wi} and average air concentration C_{ai} are linearly interpolated between the two profiles adjacent to $C_b = 0.01$.

For the 4 tests with $F_0 = 3.2$, the procedure detailed in §3.1.1 was applied to calculate L_i . All tests respect the relations from literature (Figure 4.2). However, there is a difference between the two chutes angles φ , probably related to the estimation of the distance from between the jetbox and the fictitious ogee crest. The drawdown method cannot be applied to tests with $F_0 \geq 4$.

The mixture flow depth h_i at the inception point x_i is identical with the local mixture flow depth h_{90} . It shows a good agreement with relations from literature (Figure 4.3a), with no difference between the two chute angles φ . The two tests slightly below the general trend are the tests with $F_0 = 7.5$ and $s = 0.06\text{ m}$. At this Froude number, the flow is decelerating when it reaches the steps (h_w is increasing). With the step height $s = 0.06\text{ m}$, the inception point occurs during the deceleration, while it occurs after the deceleration phase for $s = 0.03\text{ m}$. These two tests are unusual cases for stepped spillway and are not considered for the inception point flow depth analysis. The following relation is obtained for $30^\circ \leq \varphi \leq 50^\circ$ ($r^2 = 0.993$)

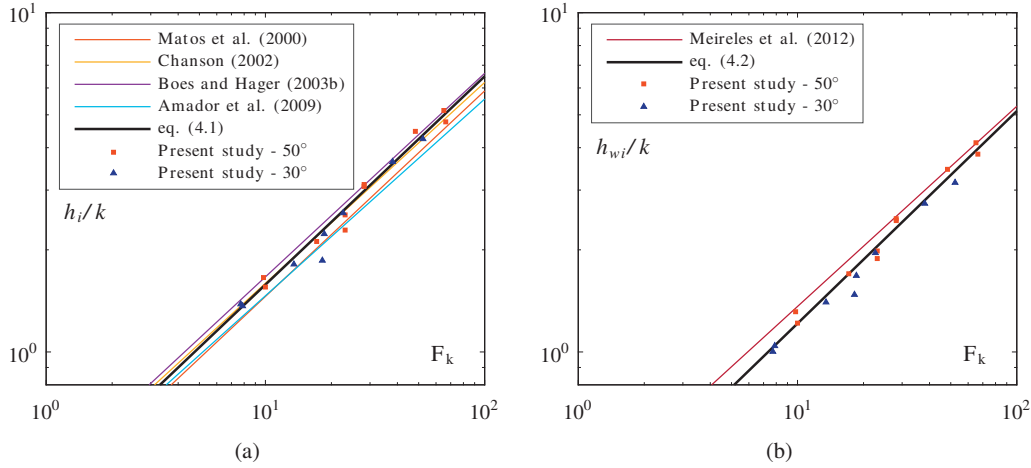
$$\frac{h_i}{k} = 0.384 \cdot F_k^{0.614} \quad (4.1)$$

Figure 4.2 – Streamwise position of the inception point L_i

with k as the step roughness, and F_k as the step roughness Froude number given by equation (2.7).

The equivalent blackwater flow depth at the inception point h_{wi} gives smaller depths than Meireles et al. (2012) which might be explained by a different method to locate the inception point. The following relation is obtained for $30^\circ \leq \varphi \leq 50^\circ$ ($r^2 = 0.988$)

$$\frac{h_{wi}}{k} = 0.287 \cdot F_k^{0.626} \quad (4.2)$$

Figure 4.3 – Inception point (a) mixture flow depth h_i , and (b) equivalent blackwater flow depth h_{wi}

The relation between the mixture depth h_i and the equivalent blackwater flow depth h_{wi} (Figure 4.4a) is ($r^2 = 0.975$)

$$h_i = 1.285 h_{wi} \quad (4.3)$$

which gives an average air concentration at the inception point of $C_{ai} = 1 - h_{wi}/h_i = 0.222$.

Figure 4.4b shows that C_{ai} decreases with the chute angle, as previously found by Boes and Hager (2003b). Lower values are obtained for $\varphi = 50^\circ$ compared to Boes and Hager (2003b). The average value is $C_{ai} = 0.241$ for $\varphi = 30^\circ$, and $C_{ai} = 0.201$ for $\varphi = 50^\circ$. It agrees very well with $C_{ai} = 0.20$ found by Matos et al. (2000) and Meireles et al. (2012) for 53.1° .

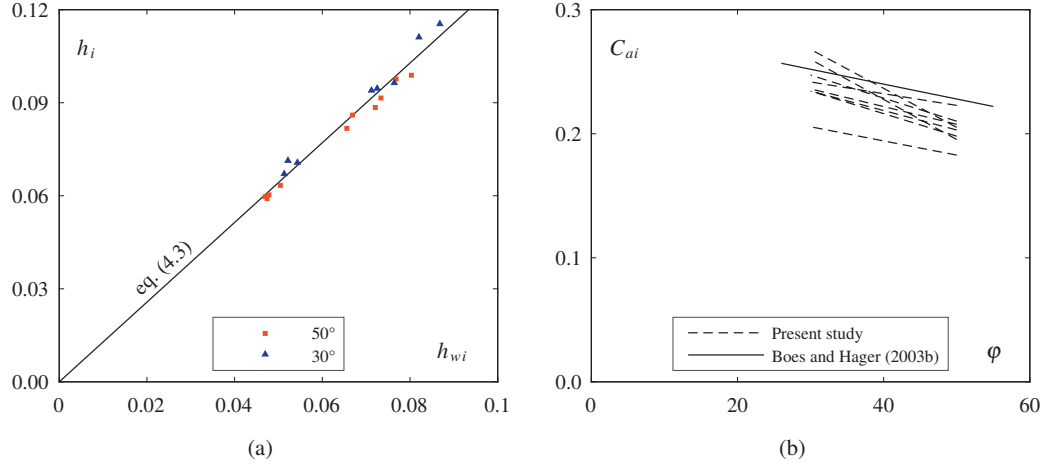


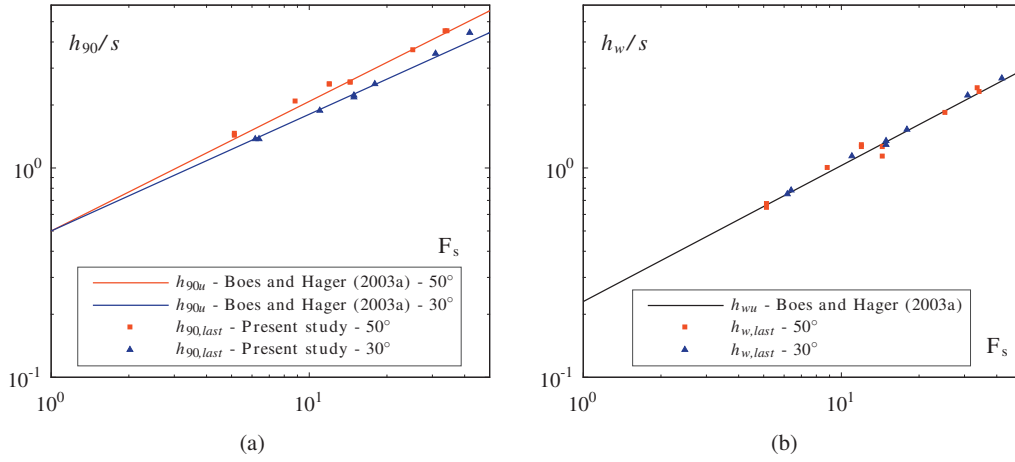
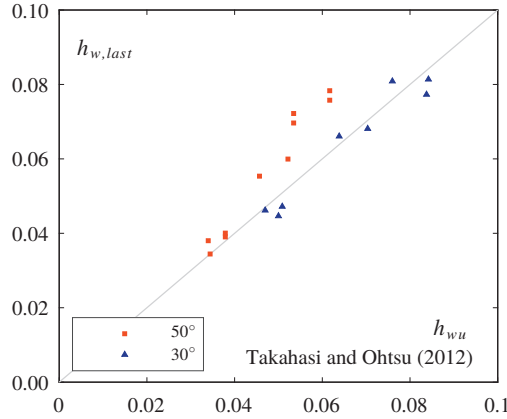
Figure 4.4 – (a) Relation at the inception point between the mixture flow depth h_i and the equivalent blackwater flow depth h_{wi} , (b) Influence of the chute angle φ on the average air concentration at the inception point C_{ai} , with each line giving pairs of tests where only φ was varied

4.3 Flow depth development

The mixture flow depth $h_{90,last}$ and equivalent blackwater flow depth $h_{w,last}$ of the most downstream measured profile are first compared to literature for quasi-uniform flow. An excellent agreement is observed with Boes and Hager (2003a) for both flow depths (Figure 4.5). For $h_{w,last}$ and the tests with $\varphi = 50^\circ$, the lowest discharge ($F_s = 5.1$ and 14.1) gives slightly lower depths than the quasi-uniform equivalent blackwater depth h_{wu} , whereas the highest discharge ($F_s = 11.9$ and 33.9) gives higher depths. The procedure of Takahashi and Ohtsu (2012) using the friction factor to calculate the quasi-uniform equivalent blackwater flow depth gives good results for $\varphi = 30^\circ$ (Figure 4.6). For $\varphi = 50^\circ$, there are more differences for large flow depths (larger discharges). This can be explained by a flow still accelerating for large discharges, or an underestimation of the friction factor for small values of s/h_c . Considering the good agreement of results with Boes and Hager (2003a), the latter hypothesis is more likely.

The quasi-uniform flow depths h_{90u} and h_{wu} of Boes and Hager (2003a) are used to present the dimensionless flow depth development (Figure 4.7). The streamwise coordinate from the inception point ($x - x_i$) is normalized with the critical flow depth h_c .

For the mixture depth h_{90} , four tests begin with $h_{90} \geq 0.8h_{90u}$. These are the tests with $F_0 = 3.2$. There is first an acceleration of the flow on the smooth bottom (drawdown curve) followed by a

Figure 4.5 – Uniform (a) mixture flow depth h_{90u} and (b) equivalent blackwater flow depth h_{wu} Figure 4.6 – Comparison of the measured quasi-uniform equivalent blackwater flow depth h_{wu} for reference tests with the calculated value from Takahashi and Ohtsu (2012)

stabilization when the steps are reached. Shortly before the inception point located at $(x - x_i)/h_c = 0$, the mixture flow depth rapidly increases towards $h_{90}/h_{90u} = 1$. At the inception point, the $\varphi = 30^\circ$ tests show a higher h_{90}/h_{90u} than the $\varphi = 50^\circ$ tests. The exception is the test with $F_o = 7.5$ and $s = 0.06\text{ m}$ that was excluded during the inception point analysis (§4.2). The other excluded test is the $\varphi = 50^\circ$ test with the lowest h_{90}/h_{90u} value at the inception point. The tests with $\varphi = 50^\circ$ show a maximum at $(x - x_i)/h_c \approx 5$ associated with spray, while the tests with $\varphi = 30^\circ$ almost immediately converge to $h_{90}/h_{90u} = 1$. The tests with the lowest discharges, and thus the lowest h_c , extend the furthest. The tests with $\varphi = 30^\circ$ go further than the tests with $\varphi = 50^\circ$ due to the longer channel. No common characteristics were found for the tests ending above $h_{90}/h_{90u} = 1$.

The equivalent blackwater flow depth h_w shows similar trends as h_{90} , with the four tests at $F_o = 3.2$ starting above $h_w/h_{wu} = 1.5$. The four tests at $F_o = 7.5$, with $h_w/h_{wu} \leq 1$ before the inception point, show a short decrease in the equivalent blackwater flow depth (acceleration) on the smooth bottom followed by an increase in the depth (deceleration) when the steps are reached. The tests with

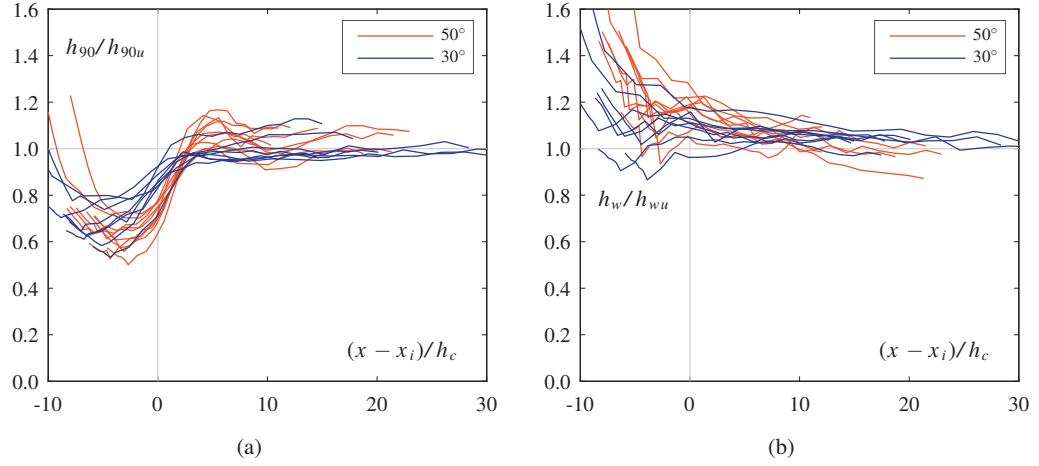


Figure 4.7 – Development of (a) the mixture depth h_{90} and (b) the equivalent blackwater flow depth h_w normalized with the quasi-uniform flow values from Boes and Hager (2003a)

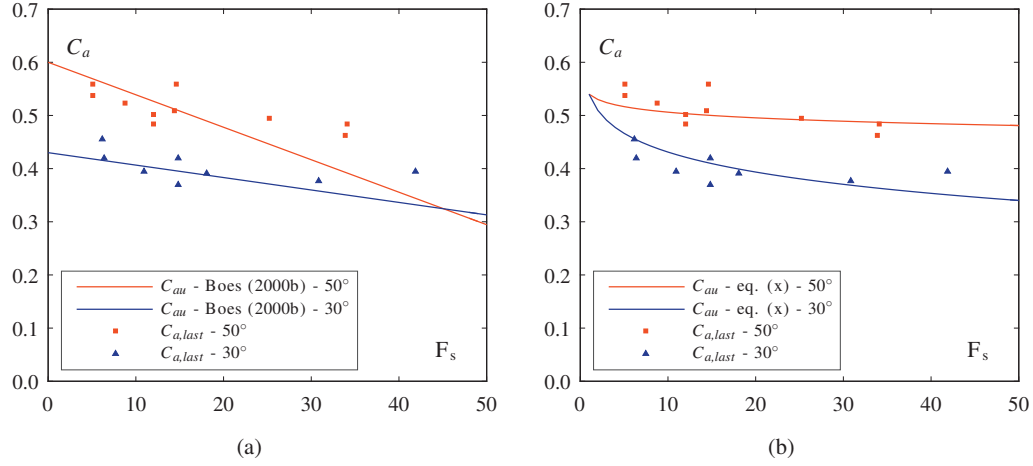
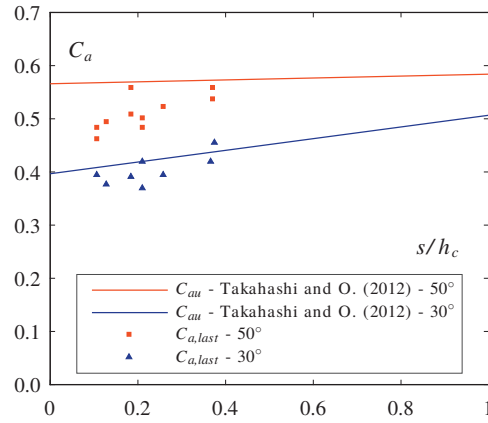
$\varphi = 30^\circ$ converge more rapidly towards $h_w/h_{wu} = 1$ than the tests with $\varphi = 50^\circ$.

In conclusion, the present study agrees well with the quasi-uniform flow depths h_{90u} and h_{wu} given by Boes and Hager (2003a). Quasi-uniform flow condition are reached after $20h_c$ for $\varphi = 30^\circ$ and $\varphi = 50^\circ$.

4.4 Average air concentration development

The average air concentration $C_{a,last}$ of the most downstream measured profile is first compared values derived from literature for quasi-uniform flow. The tests agree with Boes (2000c) for $F_s \leq 20$ (Figure 4.8a). For tests with $F_s \geq 20$ (with a step height $s = 0.03$ m), slightly higher average air concentrations are measured in the present study. Using equation (2.31) gives better results (Figure 4.8b). The "vertical pairs" visible are tests with the same discharge and the same step height, but with a different approach flow Froude number F_0 . The test with the highest F_0 has always a higher C_a than the other test of the pair, which suggests that the average air concentration is still increasing for the test with the lower F_0 . The tests compare well with Takahashi and Ohtsu (2012) for $\varphi = 30^\circ$ (Figure 4.9).

The development of the average air concentration C_a shows (Figure 4.10a) that all tests start in the range of $0.05 \leq C_a \leq 0.10$ for the reason explained in §4.1. As seen in §4.2, the average air concentration is $C_{ai} \approx 0.22$ at the inception point. For the $\varphi = 30^\circ$ tests, the average air concentration rapidly stabilizes to a slow growth after reaching $C_a \approx 0.35$. For the $\varphi = 50^\circ$ tests, the average air concentration grows until reaching a maximum caused by spray. It is followed by a minimum due to the fall of the spray back into the flow which causes a compression of the air entrained in the flow. For tests with discharges $q \geq 0.350 \text{ m}^2/\text{s}$, the end of the channel is reached here at $(x - x_i)/h_c \approx 10$. For the tests with the lowest discharge ($q \approx 0.200 \text{ m}^2/\text{s}$), the average air concentration increases

Figure 4.8 – Comparison of the quasi-uniform average air concentration C_{au} Figure 4.9 – Comparison of the quasi-uniform average air concentration C_{au}

again along $10 \leq (x - x_i)/h_c \leq 15$, and a stable value seems to be reached after $(x - x_i)/h_c \geq 15$. With the same discharge, the two tests with $F_0 = 5.5$ and $h_o = 0.052$ m (each with a different step height) end at higher C_a values than the two tests with $F_0 = 3.2$ and $h_o = 0.075$ m. This suggests that the tests with $F_0 = 3.2$ have not reached equilibrium at the end of the channel.

To further analyze the development of the average air concentration, C_a is normalized with the quasi-uniform average air concentration C_{au} on smooth chutes according to Wilhelms and Gulliver (2005) as these values are used by Takahashi and Ohtsu (2012) for $s/h_c = 0$ (Figure 4.10b). For $\varphi = 30^\circ$, the quasi-uniform average air concentration is $C_{au} = 0.40$ according to Wilhelms and Gulliver (2005), and most corresponding tests end within 10 %. The two tests that end with values $C_a/C_{au} \geq 1$ at $(x - x_i)/h_c = 30$ might indicate that C_{au} is underestimated at $\varphi = 30^\circ$. Hager (1991) gives $C_{au} = 0.42$ – 0.45 for that chute angle, and Chanson (1995b) gives $C_{au} = 0.45$. Many of the $\varphi = 50^\circ$ tests end at $C_a/C_{au} \approx 0.9$ and are still rising. The two tests mentioned previously with the lower discharge, $F_0 = 5.5$ and $h_o = 0.052$ m end at $C_a/C_{au} \approx 1.0$.

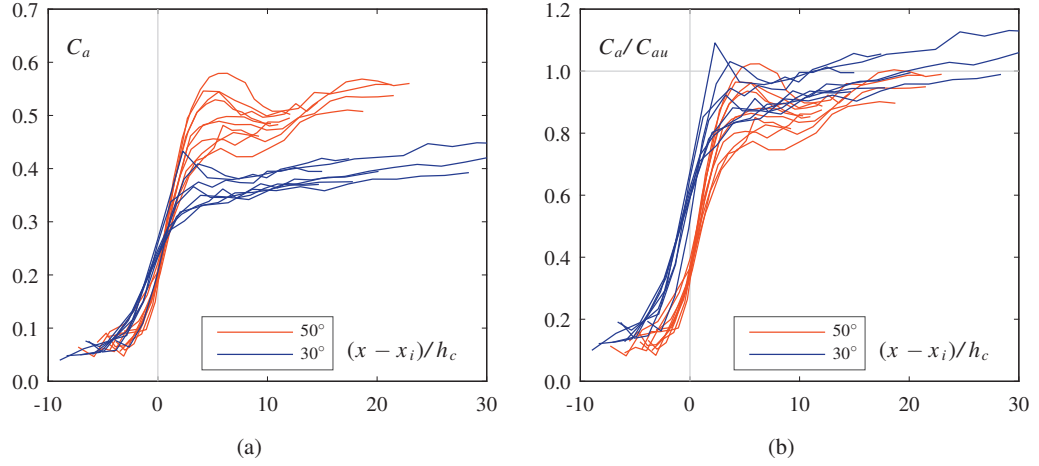


Figure 4.10 – Development of (a) the average air concentration C_a , (b) the average air concentration normalized with the quasi-uniform average air concentration C_{au} according to Wilhelms and Gulliver (2005)

Pfister and Hager (2011) used $(x - x_i)/L_i$ for the normalized position, which gives similar results. The normalization $(x - x_i)/h_c$, also used by Pfister et al. (2006b), was kept as h_c is easier to obtain. Pfister and Hager (2011) suggest that the quasi-uniform flow starts at a distance of $\sim L_i$ downstream of the inception point ($(x - x_i)/L_i \approx 1$). For the present study, $L_i \approx 10h_c$ with L_i calculated according to Meireles et al. (2012), which gives a quasi-uniform flow limit at $(x - x_i)/h_c \approx 10$. Alternately, Figure 4.10b shows that quasi-uniform flow is reached rather at $(x - x_i)/h_c \approx 20$.

The trend to observe higher C_{au} values for a decreasing F_s or increasing s/h_c respectively described by Boes (2000c) and Takahashi and Ohtsu (2012) is also observed for the present study. In other words, small discharges or large steps produce higher C_{au} . It is suggested that this effect is mostly due to a longer relative distance $(x - x_i)/h_c$ allowing a longer flow development for small discharges, and not an effect of the steps. This signifies that C_a only depends on the chute angle ϕ and that smooth and stepped chutes have the same uniform average air concentration C_{au} as suggested by Chanson (1995b), Matos (2000a) and Boes and Hager (2003b).

4.5 Bottom air concentration development

The minimum air concentration C_{min} is typically located at the pseudo-bottom, at the lowest point of a depth-profile. Rarely, this was not the case and the minimum was located a few points higher (cf. Appendix F for the position of C_{min}). To be conservative, the minimum air concentration C_{min} of each profile is considered to analyze the bottom air concentration C_b .

The minimum air concentration $C_{min,last}$ of the most downstream measured profile are compared to the quasi-uniform bottom air concentration C_{bu} suggested by Boes (2000c) in Figure 4.11. The values of the present study are distinctly above the relations of Boes (2000c) for both chute angles.

They also do not show a clear decrease of C_{bu} with F_s . Similarly to what was observed for C_{au} , some tests probably do not reach equilibrium and the corresponding C_{bu} values are underestimated.

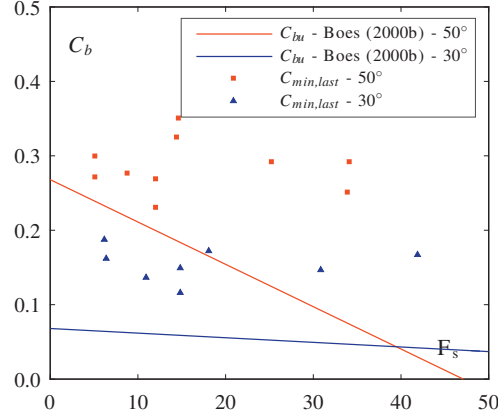


Figure 4.11 – Comparison of the quasi-uniform bottom air concentration C_{bu} with Boes (2000c)

Boes and Hager (2003b) presented equation (2.25), and Matos et al. (2000) equation (2.26) for the development of the bottom air concentration C_b starting from the inception point. For both, the streamwise position is normalized with $(x - x_i)/h_i$. Equation (2.17) is used to normalize the tests of the present study with h_i in Figure 4.12a. The $\varphi = 30^\circ$ tests are clearly apart from the $\varphi = 50^\circ$ tests. Some tests show a wavy pattern that was previously observed by Sánchez-Juny and Dolz (2005) for pressures, and by Pfister et al. (2006a) for the bottom air concentration. For $\varphi = 50^\circ$, the tests with a step height $s = 0.03$ m all end with a certain increase of C_b , whereas the tests with $s = 0.06$ m end lower, with a decreasing or almost stable trend.

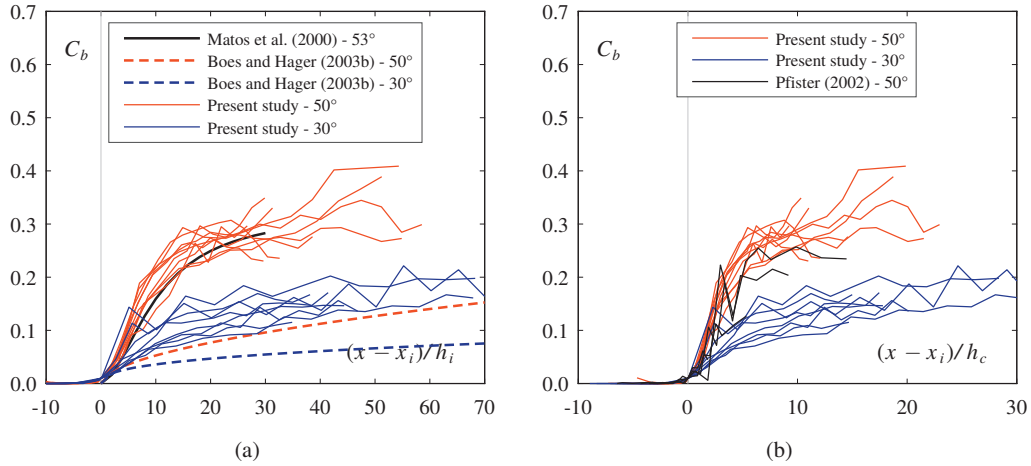


Figure 4.12 – Development of the bottom air concentration C_b

The $\varphi = 50^\circ$ tests agree well with Matos et al. (2000). There is however a different trend between the present study and the development of C_b observed by Boes and Hager (2003b). It could be explained by scale effects. Pfister and Hager (2010a) suggest a limit $W_o \geq 140$ for the bottom air

concentration on smooth chute aerators. For the present study, $\phi = 50^\circ$ tests with $(x - x_i)/h_i \geq 40$ and $\phi = 30^\circ$ tests with $(x - x_i)/h_i \geq 50$ are under this limit ($88 \leq W_o \leq 107$), but do not show a different trend compared to the other tests. Results $(x - x_i)/h_i \geq 100$ are presented by Boes and Hager (2003b) for a similar channel length, indicating much lower discharges compared to the present study and thus even lower W_o .

The streamwise normalization previously used for the flow depth and the average concentration is shown in Figure 4.12b. The tests of Pfister (2002) (performed on the same model as Pfister et al. (2006a) but without aerator) with a relatively short channel are added. They confirm the trend observed by Matos et al. (2000) and the present study. The conservative value of $C_b = 0.08$ to protect against cavitation damages (§2.2) is exceeded after $(x - x_i)/h_c \approx 2$ for $\phi = 50^\circ$ and $(x - x_i)/h_c \approx 7$ for $\phi = 30^\circ$. The quasi-uniform flow limit at $(x - x_i)/h_c \approx 20$ suggested for the flow depth and the average air concentration seems also valid for the bottom air concentration.

Considering Figure 4.11 and Figure 4.12, a constant quasi-uniform bottom air concentration $C_{bu} = 0.17$ is suggested for $\phi = 30^\circ$, and $C_{bu} = 0.32$ for $\phi = 50^\circ$. For $\phi = 30^\circ$, it is close to $C_{bu} = 0.18$ for smooth chutes (Hager 1991), but there is an important difference for $\phi = 50^\circ$ with $C_{bu} = 0.50$. The bottom air concentration normalized with the quasi-uniform bottom air concentration C_{bu} suggested is presented in Figure 4.13.

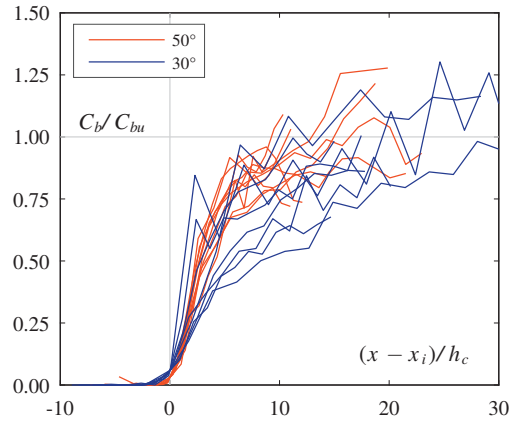


Figure 4.13 – Development of the bottom air concentration C_b

4.6 Air concentration profiles

Air concentration profiles are shown in Figure 4.14 at three different relative locations $(x - x_i)/h_c$ using the relative depth $Z = z/z_{90}$. They are linearly interpolated between the two neighboring profiles to allow a better comparison between the tests. They are compared to the two diffusion models presented in §2.1.6.

At the inception point $(x - x_i)/h_c = 0$, the tests of each chute angle ϕ show a practically identical profile (Figure 4.14a,b). Only test 42 for $\phi = 30^\circ$ is slightly different with a lower air concentration.

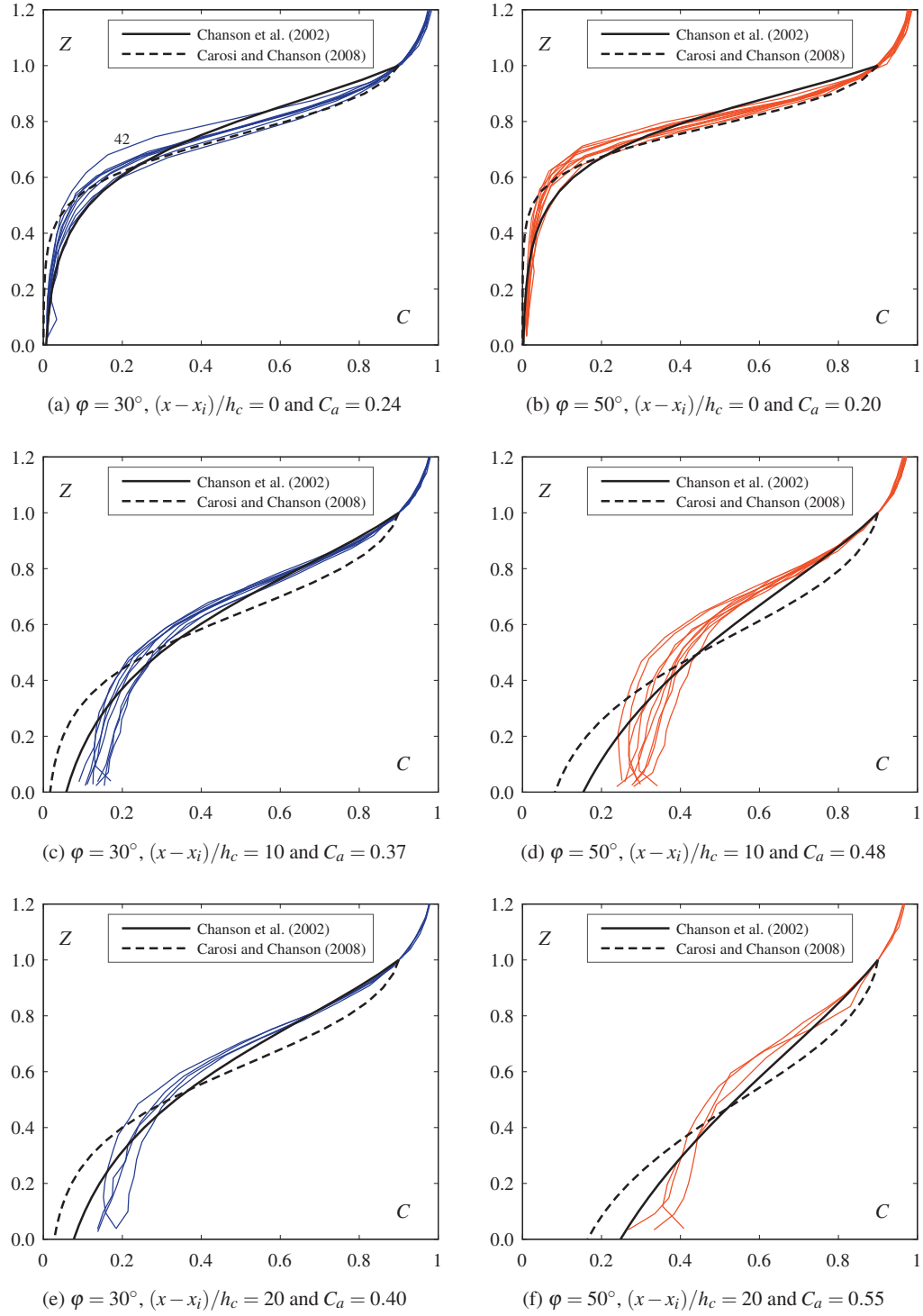


Figure 4.14 – Air concentration profiles for both chute angles φ and at three positions $(x - x_i)/h_c$. The average air concentration C_a indicates the value used for the profiles of Chanson et al. (2002) and Carosi and Chanson (2008)

By definition, all tests converge to an air concentration $C = 0.01$ at the lowest point measured. The difference in average air concentration between the two chute angles φ is mostly visible at $Z \approx 0.6$. The two models give good estimations even though conditions are far from equilibrium.

At a relative distance of $(x - x_i)/h_c = 10$ corresponding to the end of spray (Figure 4.14c,d), test 7 is already beyond the channel length and is therefore missing. For $\varphi = 50^\circ$, the four remaining tests with $s = 0.03$ m show an increase in the air concentration at the bottom, while on the contrary, tests with $s = 0.06$ m show a decrease. This trend was previously observed in §4.5. For $\varphi = 30^\circ$, only one test with $s = 0.03$ m shows this increase. Tests with $\varphi = 50^\circ$ show a greater variability which is likely due to the variation of the spray amplitude. The model of Chanson et al. (2002) with a constant diffusion shows a better concordance with the measured data, particularly for $\varphi = 30^\circ$. Both models overestimate the air concentration in the upper half of the profile and underestimate it in the lower half.

At a relative distance of $(x - x_i)/h_c = 20$ (Figure 4.14e,f), only the tests with the lowest discharge are remaining except one with the intermediate discharge. The increase of air concentration compared to the profile at $(x - x_i)/h_c \approx 10$ is visible close to the bottom. Both models show a better agreement with the measurements compared to the previous profile and it is likely due to reaching quasi-uniform flow conditions.

Overall, for the present study, the air concentration profile model of Chanson et al. (2002) to obtain the air concentration profile gives a better estimation than the model of Carosi and Chanson (2008). For all tests, both models underestimate the bottom air concentration.

4.7 Summary

The reference tests performed are in good agreement with literature. At the inception point, equation (4.1) was obtained for the mixture depth h_i , as well as equation (4.2) for the equivalent blackwater flow depth h_{wi} . The results show that quasi-uniform flow conditions are reached at a distance of $\sim 20h_c$ after the inception point defined by $C_b = 0.01$. The quasi-uniform average air concentration C_{au} is likely independent from step height, and equivalent to that of smooth chutes. Table 4.1 summarizes the quasi-uniform flow values that will be used further to analyze aerator tests. The limitations of the present study are summarized in §10.2. Again, the goal of the herein presented reference tests is mainly to evaluate the aerator performance. The latter data are compared with the aerator tests and the differences indicate the influence of the aerator.

Table 4.1 – Summary of the quasi-uniform flow characteristic

Parameter	$\varphi = 30^\circ$	$\varphi = 50^\circ$
Mixture flow depth h_{90u}	equation (2.27)	
Equivalent blackwater flow depth h_{wu}	equation (2.28)	
Average air concentration C_{au}	equation (2.35)	
Bottom air concentration C_{bu}	0.17	0.32

Chapter 5

Aerator tests

Similarly to the reference tests presented in Chapter 4, general issues of the aerator tests are discussed herein. The characteristics of the jet generated by the deflector and particularly the methodology to obtain jet length L are presented in Chapter 6, and the details regarding air concentration and air transport follow in Chapter 7.

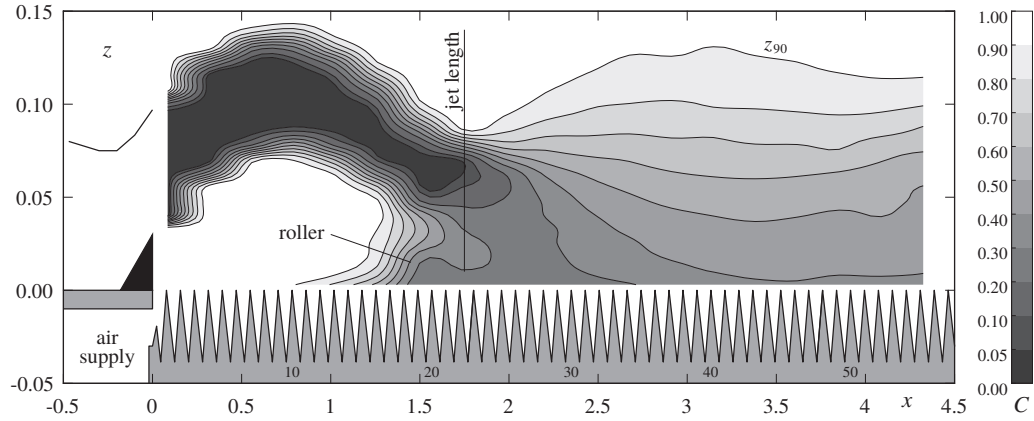
5.1 Overview

A total of 44 aerator tests were performed with six different deflectors geometries. The example of test 20 with a chute angle $\varphi = 50^\circ$ and a step height $s = 0.06$ m is used in this overview to describe typical characteristics and results of an aerator test. It has the same chute and flow characteristics as the reference test 13 presented in §4.1, with the addition of a $\alpha = 9.46^\circ$ and $t = 0.030$ m deflector. The profiles are measured at the same location as in the reference tests, with a vertical spacing in the range of $5 \leq \Delta z \leq 11.7$ mm. The data and graphs of all aerator tests can be found in Appendix F.

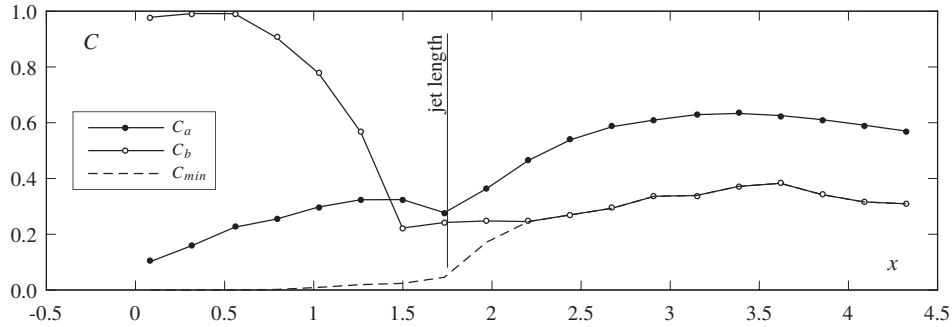
In Figure 5.1a, the triangular deflector is indicated in black. The aerator air supply with a large section is located below the bottom. The horizontal air slot with a height of 0.02 m is located at $x = 0$ in the figure. The lower half of the first vertical step face appears to limit the air section more than the air slot, but this is exclusively a consequence from the distortion between axes x and z , and an open section height of 0.02 m is always guaranteed.

The flow surface starts to be affected by the deflector shortly before the latter begins at $x \approx -L_d$. The combination of the deflector and the free atmospheric pressure below it allows the generation of a jet. The wavy pattern of the jet surfaces particularly visible for $0 \leq x \leq 0.5$ m results only from interpolation artifacts. The jet is formed of a blackwater core with a decreasing thickness in the streamwise direction as both jet surfaces become aerated. For long and thin jets, the blackwater core ends in the jet, whereas for short and thick jets, the blackwater core ends at and due to the jet impact. An air cavity is formed under the jet and allows the aeration on the lower jet surface. The jet length L is defined by the impact of the lower jet surface trajectory on the pseudo-bottom

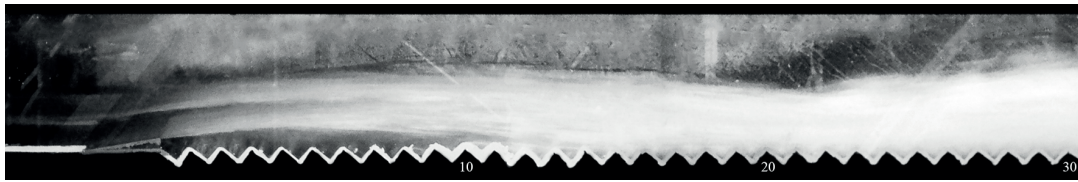
(cf. Chapter 6). A *roller* is located directly upstream of the jet impact. It is multiple step high, and higher than that observed on smooth chutes (Chanson 1995c; Wu et al. 2013). The definition of roller used here includes the water projected out of the jet by flow turbulence and the resulting nappe flow on the steps. There is generally a bottom air concentration minimum in the roller. After the jet impact, spray is formed which increases the water surface z_{90} . A maximum is reached at $x = 3.15$ m. Spray returns to the flow close to the channel end.



(a) Air concentration C distribution and flow depth z_{90}



(b) Average air concentration C_a , bottom air concentration C_b and minimum air concentration C_{min}



(c) Photo of the upper part of the channel (from $x = -0.5$ m until $x = 2.35$ m)

Figure 5.1 – Typical result of an aerator test (test 20)

The average air concentration C_a (Figure 5.1b) steadily increases along the jet, and a maximum is attained at $x \approx 1.4$ m. The following decrease in C_a is due to the inclusion of the roller in the profile and to the jet impact where air is compressed and detrained. A second maximum at $x = 3.15$ m linked to spray occurs before C_a converges towards the quasi-uniform average air concentration C_{au} . For this test, the air concentration has not reached an equilibrium and C_a is still decreasing

at the end of the channel. The bottom air concentration is by definition $C_b = 1$ in the air cavity. However, there is generally a small number of water drops below the jet that slightly decrease C_b . The roller decreases C_b before the jet impact and a minimum often occurs in the roller, here at $x = 1.50$ m. After the jet impact, there are various trends that will be described in Chapter 7 with differences between $\varphi = 30^\circ$ and $\varphi = 50^\circ$. Unlike what is observed for smooth chute aerators, C_b does not rapidly decrease towards values below a few percents. The minimum air concentration C_{min} is located in the center of the jet (blackwater core) at the beginning, and it remains at the pseudo-bottom after the jet impact as indicated by the overlap of C_b and C_{min} .

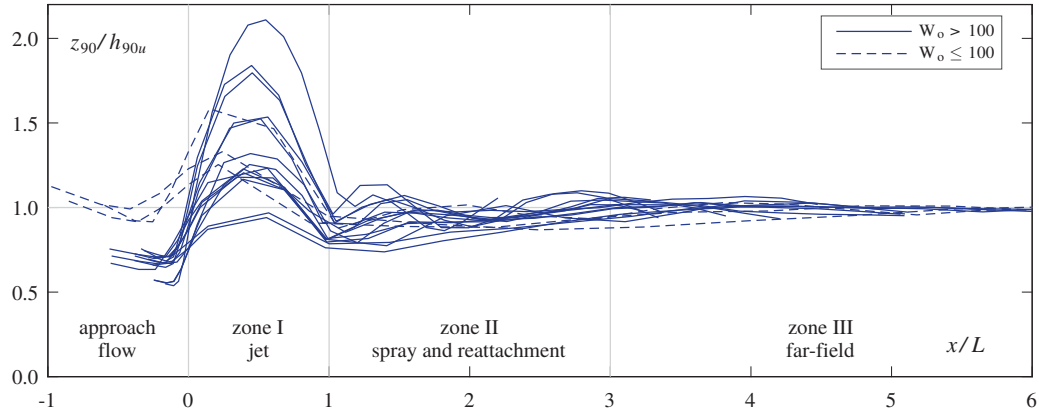
The photo (Figure 5.1c) shows the undistorted jet. At takeoff ($x = 0$), both the upper and lower jet surface become white, indicating the onset of aeration. The blackwater core can be seen until step 8. The sidewall locally slows down the jet and affects the local aeration. The consequence is that the blackwater core extends further than it is visible (as shown by Figure 5.1a), and that the visually observed jet length $L_{obs} = 1.17$ m is shorter than the measured jet length $L = 1.75$ m (between step 22 and 23). After the jet impact, a rough surface indicates the beginning of spray.

5.2 Flow zones and general results

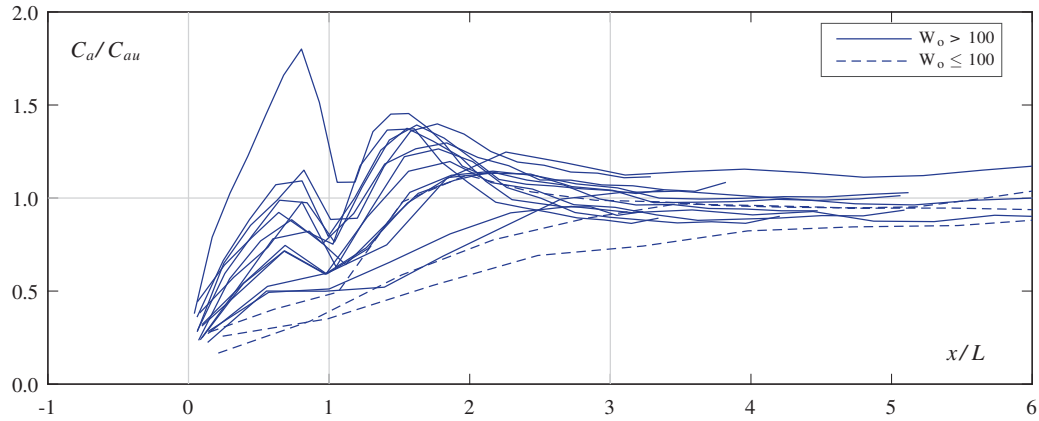
A normalization is applied to identify the main flow zones observed. The normalization of the streamwise coordinate x with the jet length L as used by Pfister and Hager (2010a) for smooth chute aerators is appropriate as well for stepped chutes. Quasi-uniform flow values (Table 4.1) are used to normalize the ordinate. An alternate normalization of the abscissa with the critical depth h_c as well as a normalization of the ordinate with the measured values of the last measured profile ($h_{90,last}$, $C_{a,last}$, $C_{b,last}$) of the corresponding reference test can be found in Appendix D.

Aerator tests are shown in Figure 5.2 for $\varphi = 30^\circ$ and in Figure 5.3 for $\varphi = 50^\circ$. In the approach flow ($x \leq 0$), three distinct normalized flow depths can be distinguished according to the three Froude numbers F_o investigated. Tests with $F_o = 3.2$ start at $z_{90}/h_{90u} \approx 1$. Downstream of the deflector ($x \geq 0$), the three zones observed by Pfister and Hager (2010a) apply as well for stepped chutes. The zones are:

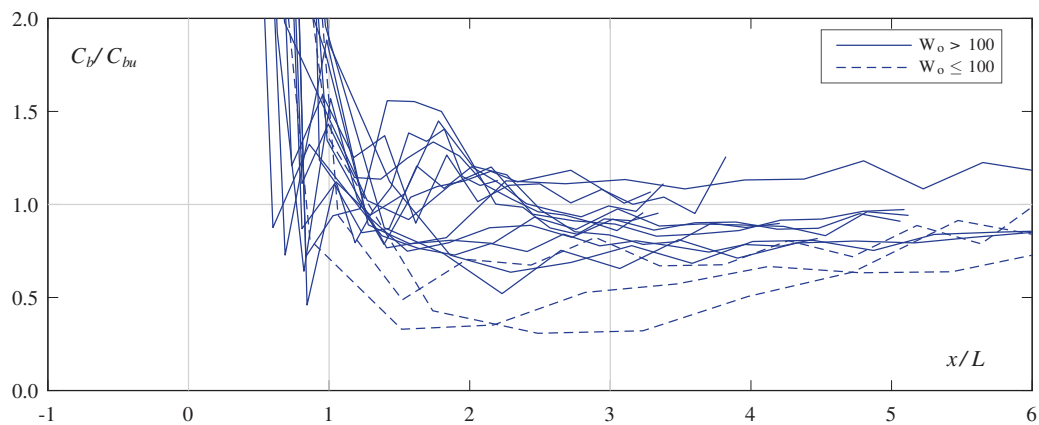
- **zone I: jet zone** for $0 \leq x/L \leq 1$. The surface elevation z_{90} is highly affected by the deflector geometry (Figure 5.4). The maximum jet elevation increases with increasing α or t . For the flat deflector ($\alpha = 5.71^\circ$), the elevation z_{90} remains under $z_{90}/h_{90u} < 1$, whereas $z_{90}/h_{90u} > 2$ for the steep deflector ($\alpha = 14.0^\circ$) combined with a high $F_o = 7.5$ (test 51 for $\varphi = 30^\circ$ and test 37 for $\varphi = 50^\circ$). The average air concentration C_a increases in the jet zone until a maximum at $x/L \approx 0.8$. Although air entrainment continues on the upper surface, the inclusion of the roller if the profile decreases C_a . A minimum in C_a appears at the jet impact ($x/L \approx 1$) due to flow compression and air detrainment around the jet impact. The bottom air concentration is $C_b \approx 1$ in the jet zone for $x/L \leq 0.6$. The roller is then encountered which very rapidly decreases C_b to $C_b/C_{bu} \approx 1$. A minimum in C_b can be reached in the roller. This minimum is more pronounced for $\varphi = 30^\circ$ than for $\varphi = 50^\circ$. At the jet impact ($x/L = 1$), C_b is around



(a) Surface elevation

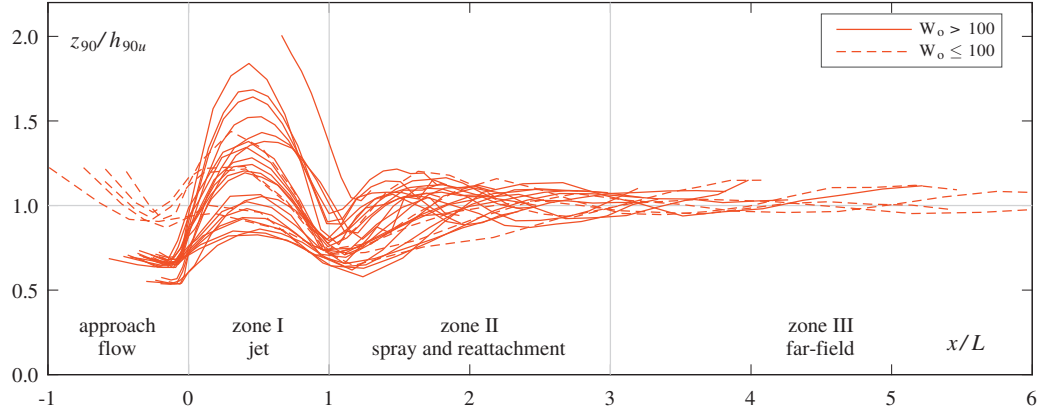


(b) Average air concentration

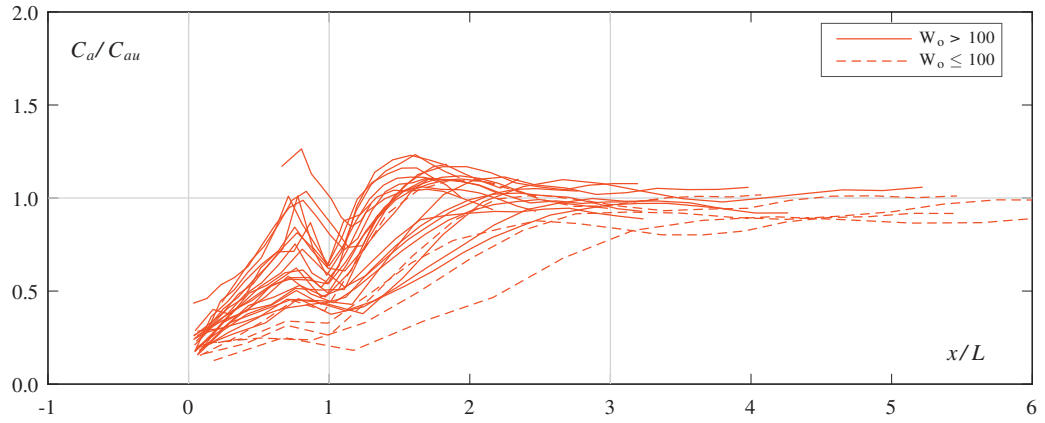


(c) Bottom air concentration

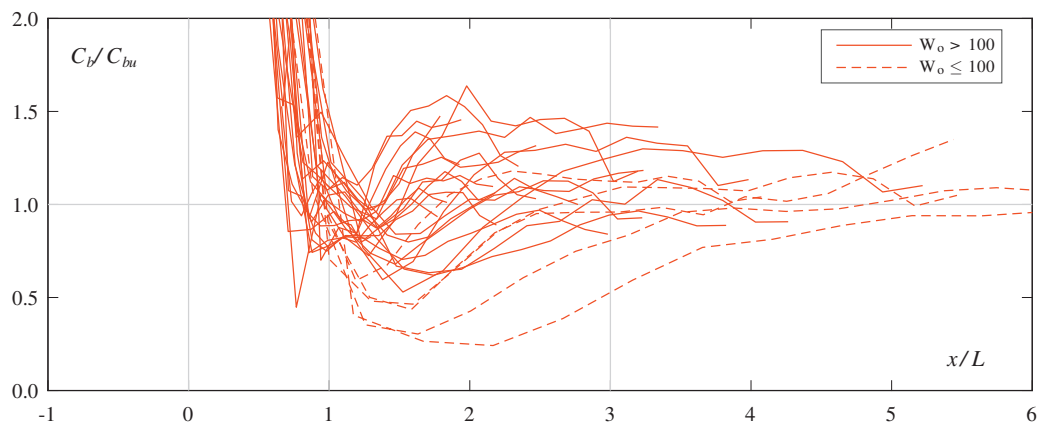
Figure 5.2 – Normalization and flow zones of aerator tests for $\varphi = 30^\circ$



(a) Surface elevation



(b) Average air concentration



(c) Bottom air concentration

Figure 5.3 – Normalization and flow zones of aerator tests for $\varphi = 50^\circ$

the quasi-uniform bottom air concentration C_{bu} .

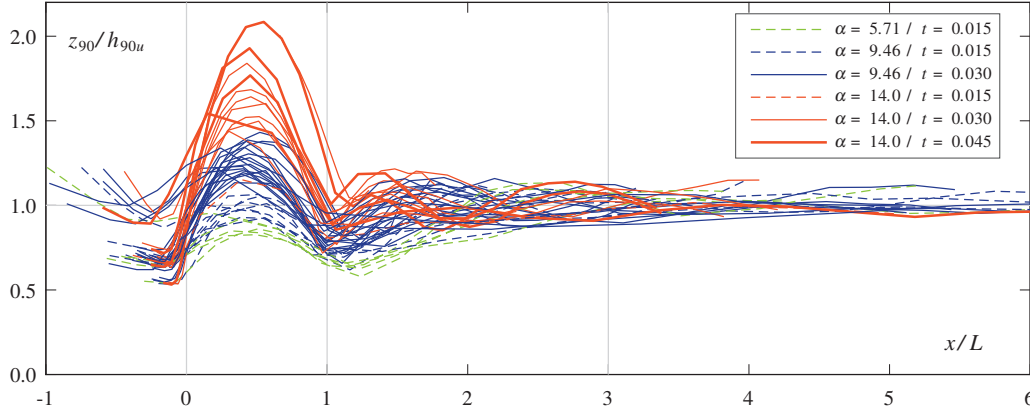


Figure 5.4 – Effect of the deflector geometry on the flow elevation z_{90}

- **zone II:** *spray and reattachment zone* for $1 \leq x/L \leq 3$. The surface elevation z_{90} shows fluctuations due to the jet impact and spray. There are less fluctuations for $\varphi = 30^\circ$ than $\varphi = 50^\circ$, since the surface elevation is almost at the quasi-uniform elevation at the jet impact for $\varphi = 30^\circ$ and the effect of gravity is stronger for a moderate φ . Figure 5.4 shows that the surface fluctuations depend on the deflector geometry. The average air concentration C_a rapidly increases directly after the jet impact. A majority of tests reach a second maximum in this zone. The remaining tests show a slower increase of C_a . Following the jet impact, a decrease of the bottom air concentration C_b below C_{bu} is observed. Comparing the two chute angles φ , there are more differences in C_b , than C_a or z_{90} . Some tests show a minimum and a maximum while others directly stabilize around C_{bu} . Tests with $F_o = 3.2$ have a Weber number $F_o \approx 88$ and show a different trend likely due to scale effects. The development of average and bottom air concentrations is analyzed in detail in Chapter 7.
- **zone III:** *far-field zone* for $x \geq 3$. The flow characteristics h_{90} , C_a and C_b stabilize and tend towards quasi-uniform values.

5.3 Air entrainment coefficient

Literature for smooth chute aerators shows two approaches to estimate the air entrainment coefficient β (without cavity subpressure). The first gives β as a function of the relative jet length L/h_o , while the second is mostly a function of the approach Froude number F_o , with additional parameters related to the deflector and offset. The present data are analyzed with the two approaches. Only tests with a cavity subpressure $\Delta p/(\rho g h_o) \leq 0.1$ are considered (5 tests are ignored).

5.3.1 Relative jet length approach

Several authors (Pinto et al. 1982a; Rutschmann 1988; Skripalle 1994; Ervine et al. 1995; Kökpinar and Göğüş 2002) showed that the air entrainment coefficient β can be expressed as a linear function of the relative jet length L/h_o . Beyond a certain limit, progressively less air is entrained. A linear trend is observed for the present study (Figure 5.5) with $r^2 = 0.864$

$$\beta = 0.0077 \cdot \frac{L}{h_o} \quad (5.1)$$

The relation is valid for all Froude numbers tested. The slope of equation (5.1) is lower than that obtained by Pinto et al. (1982a) and Rutschmann and Hager (1990). Different measurement techniques as well as another definition of L might explain the discrepancy. Tests with a flow depth $h_o = 0.092$ m show a larger air entrainment coefficient, while two tests with $h_o = 0.052$ m show a smaller β . This might be a model effect due to more turbulence for larger flow depths. An approach to include the turbulence intensity, although incomplete due to physical restriction, is presented in Appendix A.1. Additional tests with a rougher bottom surface to increase the flow turbulence show a major effect on the air entrainment coefficient β (Chapter 8).

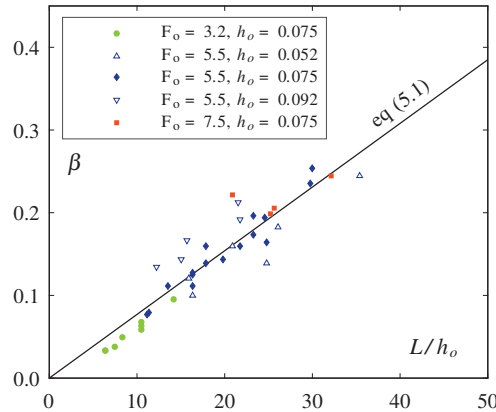


Figure 5.5 – Air entrainment coefficient β as a function of the relative jet length L/h_o

5.3.2 Froude number approach

Pfister and Hager (2010b) presented equation (2.60) to obtain the air entrainment coefficient β as a function of the Froude number F_o and the deflector angle α . It agrees well with other physical model studies and prototype values. The present study shows a similar trend (Figure 5.6a), with a higher air entrainment coefficient β for low $\Psi_1 = F_o^2(1 + F_o \tan \alpha)$ values which indicates a better performance for lower Froude numbers. There is however a large scatter of β for a single value of Ψ .

Studying the influence of each parameter reveals a different effect of the Froude number F_o and

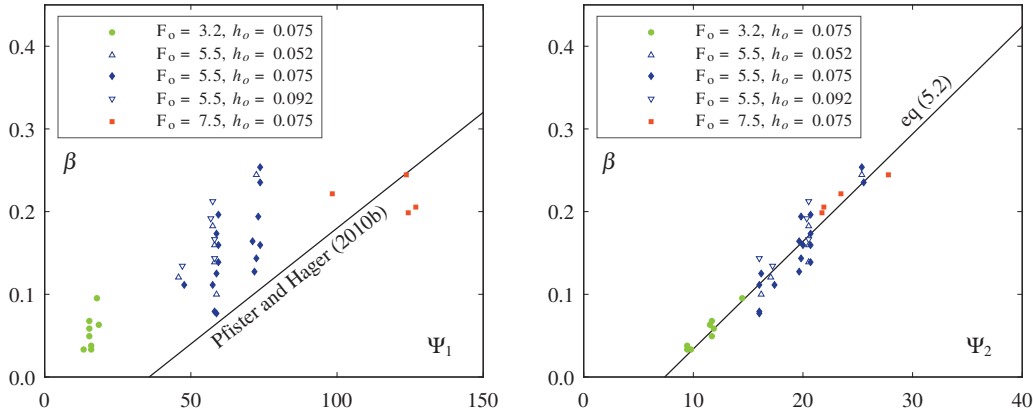


Figure 5.6 – Air entrainment coefficient β as a function of (a) $\Psi_1 = F_o^2(1 + F_o \tan \alpha)$ (Pfister and Hager 2010b), (b) $\Psi_2 = F_o \cdot (1 + \sin \varphi)^{1.5} \cdot (1 + \tan \alpha)^3$

the chute angle φ than proposed by Pfister (2008) (Appendix E.1). The following relation best describes the air entrainment coefficient ($r^2 = 0.906$)(Figure 5.6b)

$$\beta = 0.013 \cdot F_o \cdot (1 + \sin \varphi)^{1.5} \cdot (1 + \tan \alpha)^3 - 0.096 \quad (5.2)$$

The limitations of the relation are summarized in §10.2. It indicates that air entrainment starts at a Froude number of $F_o = 2.0$ for $\varphi = 50^\circ$ and $\alpha = 10^\circ$, and at $F_o = 2.5$ for $\varphi = 30^\circ$ and $\alpha = 10^\circ$. These values have not been tested on the model. The term $(1 + \sin \varphi)^{1.5}$ might indicate that the process of air detrainment at the jet impact and recirculation in the air cavity depends on the chute angle φ . The relative deflector height t/h_o has only a marginal an effect on β (Appendix A.2.1). The relative step height s/h_o has an even smaller effect, with larger steps slightly increasing β (Appendix A.2.2).

A smooth chute is a particular case of a stepped chute with a relative step height tending towards zero. However, equation (5.2) cannot be applied to smooth chutes as s/h_o is not included. The investigation of a common equation was not successful. The best relation obtained for stepped and smooth chutes does not include s/h_o (Appendix A.2.3). The distance from the jetbox to the takeoff point is (0.47 m for present study and 2 m for Pfister, which gives a different development of the turbulent boundary layer. Otherwise, the jet and the flow upstream are practically identical in both cases. The main difference is thus likely at the jet impact. Pfister (2012) showed that air detrainment is related to the jet impact angle γ on the chute bottom. On stepped chutes, the jet impacts the horizontal face of the steps. A different process of air detrainment and air recirculation in the cavity might occur, especially since the roller between the jet and the chute bottom upstream of the jet impact seems to extend further upstream on the stepped chute.

5.4 Summary

The key characteristics of aerated flow are given. The three flow zones described by Pfister and Hager (2010a) for smooth chutes, i.e. (i) the jet zone, (ii) the spray zone and (iii) the far-field zone, are applicable as well for stepped chutes. The measurements show that the mixture flow depth h_{90} , the average air concentration C_a and the bottom air concentration C_b rapidly tend towards quasi-uniform values after the jet impact. Unlike smooth chutes, no continuous detrainment is observed for C_b . For tests with $W_o \geq 100$, the bottom air concentration measured remains $C_b \geq 0.09$ which is sufficient for cavitation protection. Tests with $W_o \leq 100$ might have scale effects on C_b which will be further investigated in Chapter 7.

The air entrainment coefficient β correlates with the relative jet length L/h_o . An equation of β including the Froude number F_o , the chute angle φ and deflector angle α was suggested. The stepped chute aerator shows higher entrainment for low Froude numbers F_o than that on smooth chutes.

Chapter 6

Deflector jet characteristics

Comparing the visually observed jet length L_{obs} (through the model sidewall) with the trajectory of the lower jet surface obtained from the air concentration measurements shows a difference for all tests (Figure 6.1). The difference comes from the channel sidewall (model effect) which slows down the jet and thus gives a shorter length compared to the center of the channel where air concentrations are measured.

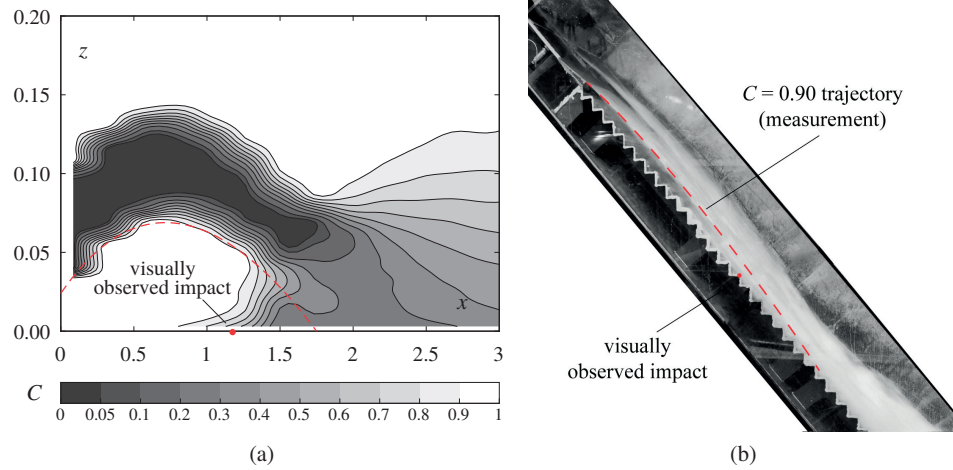


Figure 6.1 – Visually observed point of impact and lower jet trajectory of $C = 0.90$ for test 20

The jet length L is an important parameter to describe flow features and air concentrations downstream of chute aerators (§2.3.4). An accurate length is required to normalize the streamwise air development. It was therefore decided to define the jet length based on the trajectory of the lower jet surface.

This chapter presents how the jet length as well as other jet characteristics are obtained. It provides an approach to obtain the jet length based on the jet takeoff velocity and jet takeoff angle.

6.1 Jet trajectories

The approach of normalized jet trajectories found in literature is applied first. Another approach based on the takeoff angle and takeoff velocity is then presented with three possible methods.

6.1.1 Normalized jet trajectories

The approach used by Pfister and Hager (2009) and previous authors (§2.3.3) to normalize the lower and upper jet trajectories with coordinates X_j and Z_j is applied. Note that h_t was used in the definition of z_t in equation (2.64b) instead of h_o to take into account the flow acceleration between the approach flow point and the takeoff point. Only the tests with at least four points measured before the jet impact were considered to have a decent estimation of the maximum elevation.

The maximum elevation of the lower jet surface z_{maxl} is significantly higher than the relation of Pfister and Hager (2009) (equation 2.68b), with $z_{maxl}/h_o = 0.37 \cdot \Psi_z$ ($r^2 = 0.859$) for the present study (Figure 6.2a). There is less difference for the maximum elevation of the upper jet surface z_{maxu} with $(z_{maxu} - h_o)/h_o = 0.33 \cdot \Psi_z \cdot (1 + \sin \varphi)^{0.5}$ ($r^2 = 0.948$) compared to equation (2.67b), and the upper jet surface is also higher (Figure 6.2b).

The streamwise position of the maximum elevation x_{max} evidently reflects the differences observed in z_{max} (Figure 6.3). The relation $x_{maxl}/h_o = 0.72 \cdot \Psi_x$ ($r^2 = 0.614$) is obtained for the lower jet surface compared to equation (2.68a), and $x_{maxu}/h_o = 0.77 \cdot \Psi_x$ ($r^2 = 0.810$) for the upper jet surface compared to equation (2.67a). The important scatter is due to the large spacing between the measurement profiles $\Delta x = 0.235\text{--}0.360\text{ m}$. The jet being flat relatively, the streamwise position of the maximum elevation is sensitive.

There is a good agreement between the measurements and the normalized jet trajectory for $X_j \leq 1$, whereas there is a scatter for $X_j > 1$, especially for the upper jet surface (Figure 6.4). The important streamwise profile spacing Δx does not allow to precisely determine the position of the maximum elevation, resulting in the scatter observed. The points with $X_j = 3.2$ for the upper jet are tests 28 and 32, with five profiles before the jet impact. In both cases, the maximum elevation is located between the second and third profile, with the second profile giving a slightly higher elevation than the third. Had the maximum been measured at the third profile, X_j would have been nearly halved but still off the normalized jet trajectory.

It is difficult to accurately measure the location of the trajectory maximum elevation x_{max} used in this approach. Likewise, the relations to obtain the coordinates of the maximum elevation z_{max} show moderate accuracy for design purposes. Therefore this approach is not used further on.

6.1.2 Takeoff defined jet trajectories

The lower and upper jet trajectories defined by the air concentration measurements are fitted with a ballistic parabola to the jet surfaces. The equation (2.63) for a cavity subpressure equal to zero is

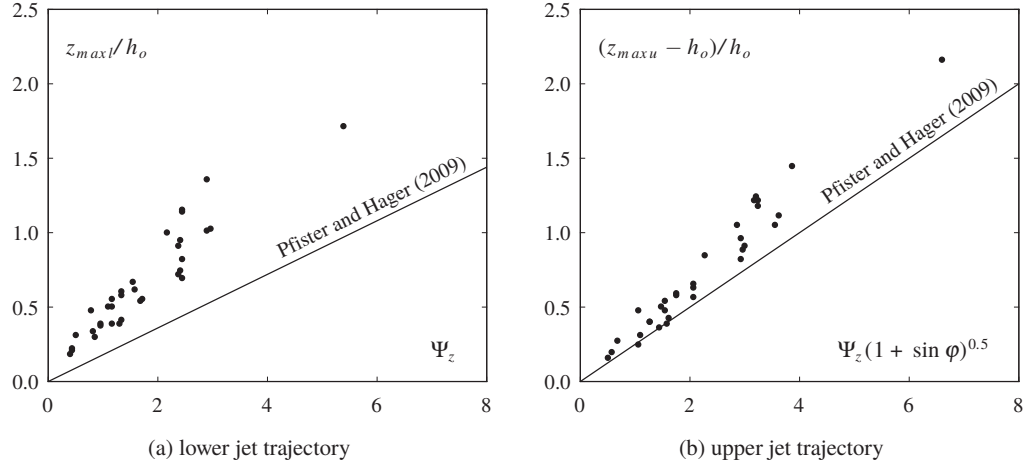
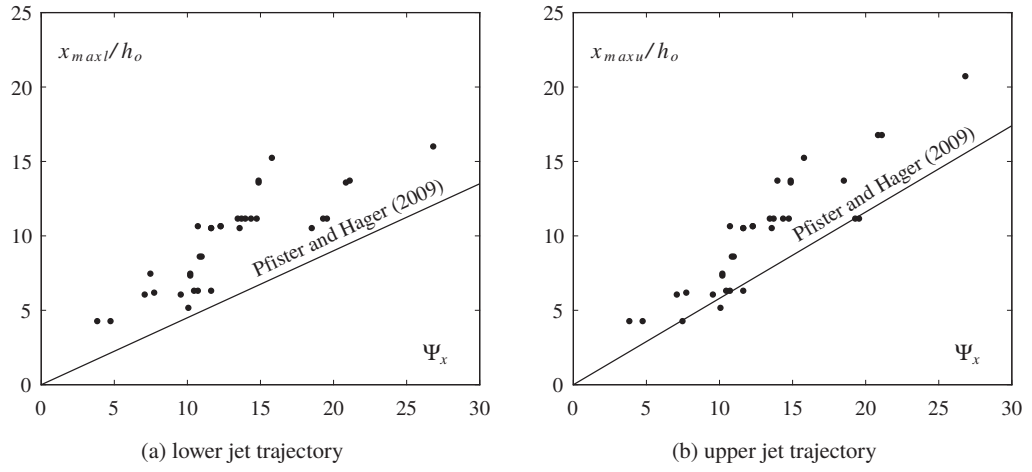
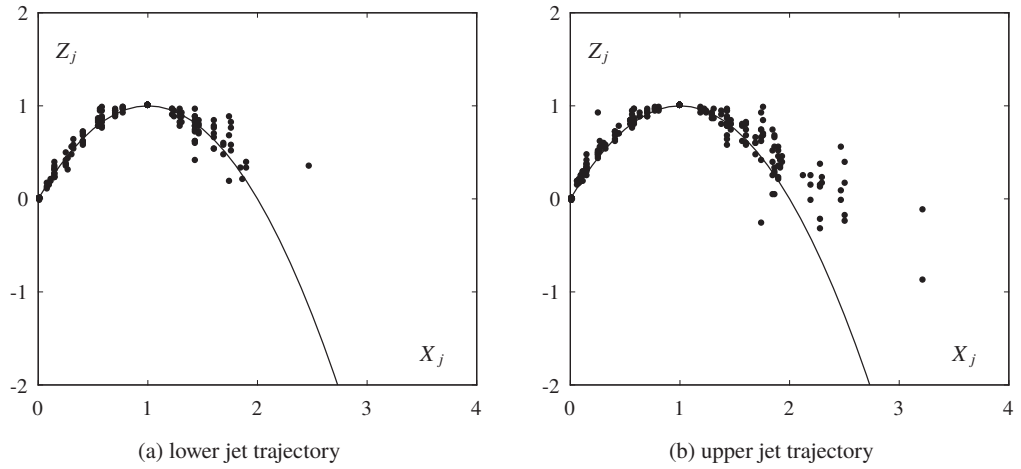
Figure 6.2 – Normalized maximum jet height in function of Ψ_z given by eq. (2.66b)Figure 6.3 – Normalized position of the maximum height in function of Ψ_x given by eq. (2.66a)

Figure 6.4 – Normalized trajectories according to equation (2.64)

used. The takeoff elevation z_t (subscript t for takeoff) is known, while two unknown parameters, the takeoff angle α_t and velocity u_t , are required to describe a trajectory. A numerical solver is used to minimize the root-mean-square error e between the calculated jet trajectory and the measured jet surface to obtain the best fitting trajectory and its parameters. For the lower jet surface, the measured points z_{90l} are used with $z_t = o + t$ to obtain the lower jet trajectory. For the upper jet surface, the points z_{90} are used with $z_t = o + t + h_t$ to obtain the upper jet trajectory.

Three different methods are considered:

- **Method M1:** the takeoff velocity is approximated by using the depth-average velocity $u_{t\phi}$ considering the takeoff flow depth h_t measured perpendicularly to the chute

$$u_{t\phi} = q/h_t \quad (6.1)$$

and the takeoff angle $\alpha_{t\phi}$ is thereafter optimized. The relation is likely appropriate for streamlines hardly affected by the deflector (small relative deflector height t/h_o).

- **Method M2:** the takeoff velocity is approximated by using the depth-average velocity $u_{t\alpha}$ considering the takeoff flow depth measured perpendicularly to the deflector being $h_t \cos \alpha$

$$u_{t\alpha} = q/h_t \cos \alpha \quad (6.2)$$

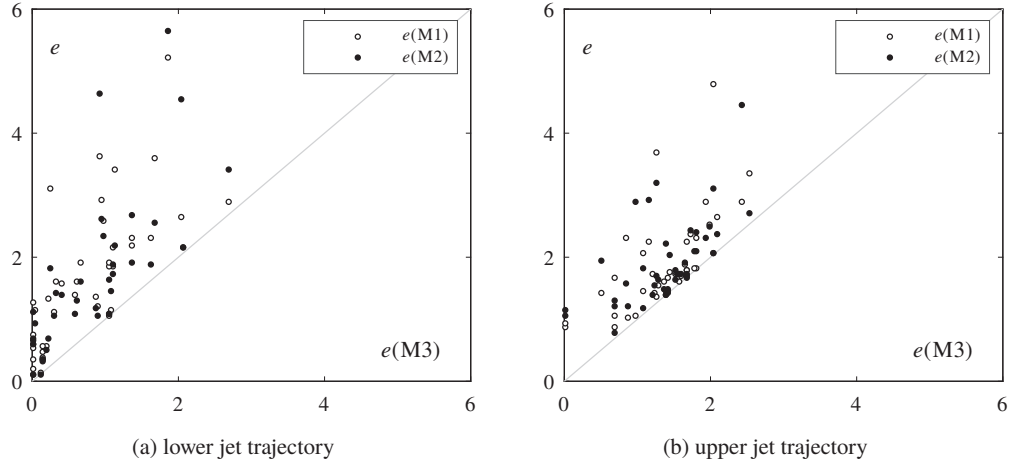
and the takeoff angle $\alpha_{t\alpha}$ is thereafter optimized. The relation is likely appropriate for streamlines that have enough time to reorient at the deflector (large relative deflector height t/h_o).

- **Method M3:** the velocity can also be included in the optimization of the root mean square error e , giving the optimum takeoff velocity $u_{t\text{opt}}$ and takeoff angle $\alpha_{t\text{opt}}$. While this method gives the lowest error e , it could however lead to physically unrealistic results.

The first two methods have the advantage that the takeoff velocity can be calculated, and only the takeoff angle needs to be determined. The last method might give better results, but two parameters need to be determined which might be more difficult to apply for design purposes. A preliminary analysis compares the error e , the takeoff velocities u_t and takeoff angles α_t of the methods to assess the differences. The selection of the method based on the accuracy of the results and its relevance for design purposes is explained further during the analysis of each jet characteristics.

The errors e (given in millimeters) obtained with the three different methods are within a few millimeters, indicating an excellent accuracy of the jet trajectories (Figure 6.5). For most tests, using method M2 gives lower e than method M1 for the lower jet trajectory. For the upper jet trajectory, there is no indication than M2 gives better results than method M1.

The highests e are obtained for tests with a cavity subpressure $\Delta p/(\rho g h_o) > 0.1$. The errors of method M2 are shown as a function of the relative subpressure $\Delta p/(\rho g h_o)$ in Figure 6.6a. The

Figure 6.5 – Comparison of error values e obtained for the three methods considered

subpressure influences the jet by creating a force towards the pseudo-bottom that reduces the jet length, and is not considered in equation (2.63) used to define the jet trajectories. The consequences are analyzed in Appendix B and the conclusions are given here. With a subpressure, the jet trajectory is better described with a slower velocity than the effective takeoff velocity, the takeoff angle is slightly increased to compensate, and the jet length is hardly affected. This methodology can be applied to calculate the jet length L with a subpressure $\Delta p/(\rho g h_o) \leq 0.3$, but the subpressure should be limited to $\Delta p/(\rho g h_o) \leq 0.1$ for the takeoff angle α_t .

The lower jet trajectory of test 51 with $\Delta p/(\rho g h_o) = 0.107$ is taken as an example (Table 6.1). In order to fit the furthest points and take into account the subpressure, method M3 leads to a reduced takeoff velocity and an increased takeoff angle compared to the two other methods. The jet trajectories are shown in Figure 6.6b. The jet length is slightly overestimated by using method M2 (0.09 m between method M2 and M3), but the difference remains smaller than the accuracy for the visually observed jet length (the distance between step edges $L_s = 0.12$ m) for $\varphi = 50^\circ$.

Table 6.1 – Lower jet trajectories parameters for test 51

Method	Velocity [$^\circ$]	Angle [$^\circ$]	e [mm]	Jet length L [m]
M1	$u_{t\varphi} = 7.00$	$\alpha_{t\varphi} = 12.0$	2.64	2.87
M2	$u_{t\alpha} = 7.22$	$\alpha_{t\alpha} = 11.5$	4.55	2.92
M3	$u_{t\text{opt}} = 6.86$	$\alpha_{t\text{opt}} = 12.3$	0.98	2.83

The difference between $u_{t\varphi}$ (method M1) and $u_{t\alpha}$ (method M2) remains within 3 % for the deflectors tested (Figure 6.7). Five groups of points with the same velocity $u_{t\varphi}$ or $u_{t\alpha}$ can be observed, corresponding to the five flow conditions tested (§3.4). The spread in $u_{t\text{opt}}$ of each group for the lower jet trajectory depends on the deflector geometry and the chute angle φ . However, no clear trend regarding α , t/h_o or φ could be recognized to improve the definition of the takeoff velocity (Appendix E.2). For the upper jet surface, the grouped points show that the optimum takeoff velocity is much less influenced by the deflector or the chute slope. Only the slowest flow with $F_o = 3.2$ and

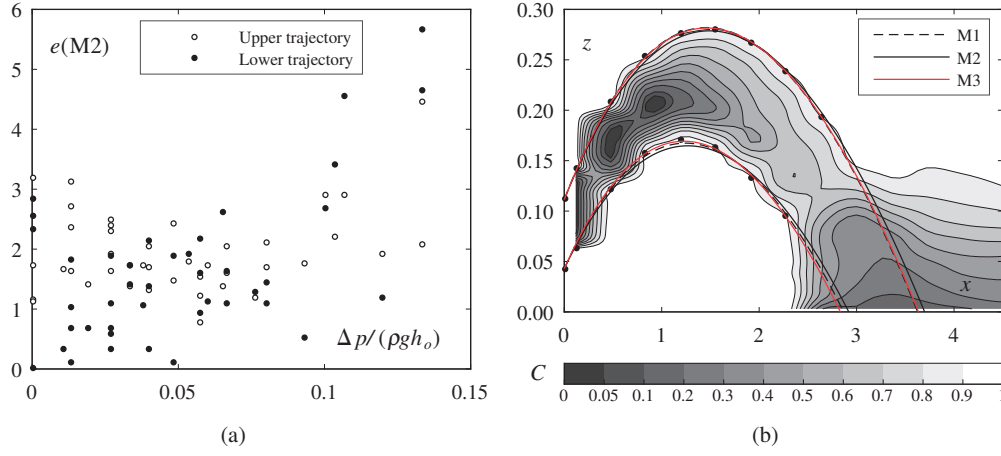


Figure 6.6 – (a) Error e in function of the cavity subpressure $\Delta p/(\rho g h_o)$ for method M2, (b) Jet trajectories for test 51 with a cavity subpressure of $\Delta p/(\rho g h_o) = 0.107$

$u_t = 3.3 \text{ m/s}$ shows an influence of other parameters.

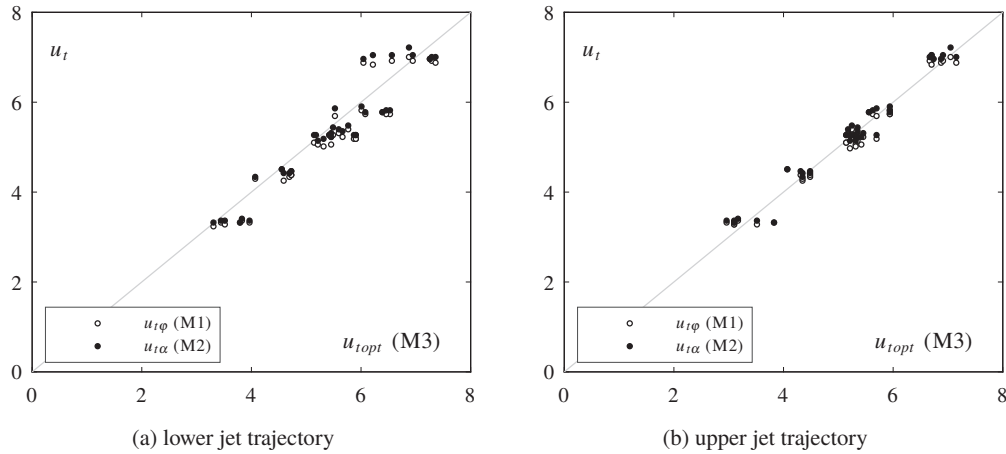


Figure 6.7 – Comparison of takeoff velocities u_t of method M1, M2 and M3

Using $u_{t\alpha}$ gives better results than $u_{t\phi}$ for the lower jet trajectory (Figure 6.8a). This is particularly visible for tests with $\alpha = 14.04^\circ$, with takeoff angles between 10° and 13.1° , where $\alpha_{t\alpha}$ is closer from $\alpha_{t,opt}$. As explained previously, tests with cavity subpressure results in higher takeoff angles $\alpha_{t,opt}$ which is clearly visible. Similarly to the observations made for errors e , neither $u_{t\alpha}$ nor $u_{t\phi}$ gives better results than the other for the takeoff angle (Figure 6.8b).

6.2 Jet takeoff flow depth

The takeoff flow depth h_t is an essential parameter to estimate the jet takeoff velocity u_t related to the jet trajectories of methods M1 and M2. Using the approach flow depth h_o instead leads

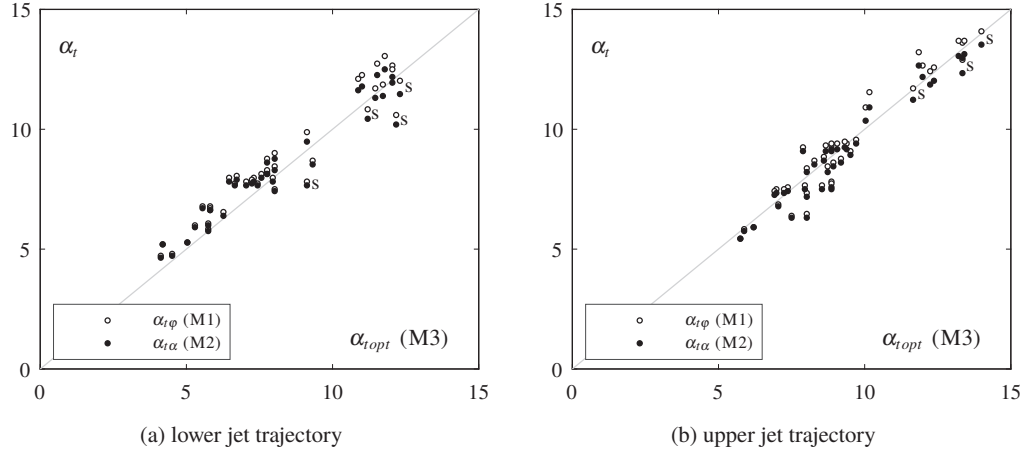


Figure 6.8 – Comparison of takeoff angles α_t of method M1, M2 and M3, with letter s indicating tests affected by cavity subpressure

to overestimating h_t for low Froude numbers as the flow is still accelerating (Figure 6.9a). The jet trajectory is sensitive to the takeoff velocity and an accurate value of the takeoff flow depth is required. An estimation can be obtained using Bernoulli's principle between the approach flow and the takeoff point considering atmospheric pressure at the takeoff point

$$h_t = \sqrt{\frac{q^2}{2g \cos^2(\alpha)} \cdot \frac{1}{\Delta z' + h_o \cos \varphi + u_o^2/2g}} \quad (6.3)$$

with $\Delta z'$ as the vertical bottom elevation difference between h_o and h_t . The term $\cos \alpha$ is used to calculate the velocity perpendicularly to the deflector as h_t is perpendicular to the pseudo-bottom.

The measured bottom pressure p was used instead of the hydrostatic pressure $h_o \cos \varphi$ as the approach flow was still influenced by the jetbox ($p > \rho g h_o \cos(\varphi)$, Appendix C.1.1). An excellent agreement is found with $r^2 = 0.994$ (Figure 6.9b).

6.3 Jet takeoff angles

To investigate the lower and upper takeoff angles, two additional datasets are used to extend the parameter ranges. The jet trajectory method is selected considering the three datasets and equations are introduced to obtain the lower and upper takeoff angles.

6.3.1 Datasets used for the analysis

To obtain a relation valid for a wider range of parameter values, two other datasets are used in addition to the present study (Table 6.2).

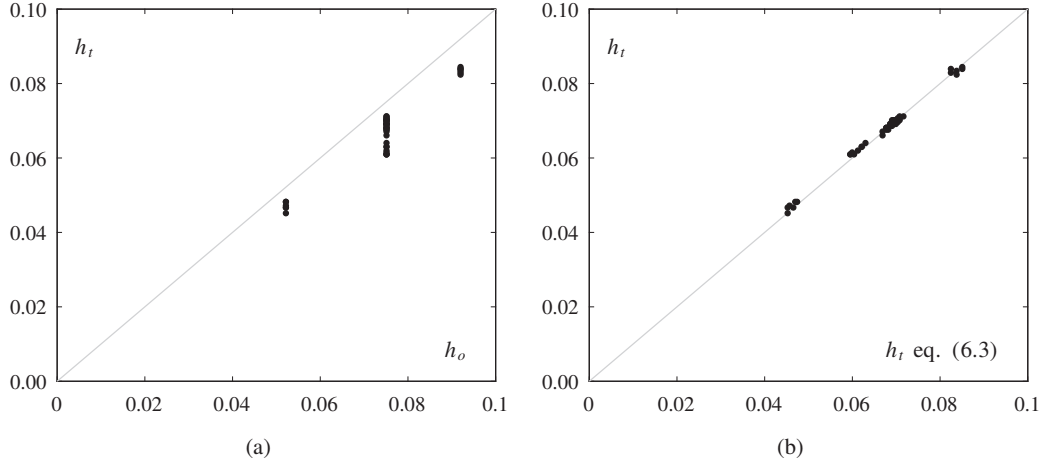


Figure 6.9 – (a) Difference between the takeoff flow depth h_t and the approach flow depth h_o , (b) Agreement between the measured takeoff flow depth h_t and the estimation of the takeoff flow depth obtained with equation (6.3)

Table 6.2 – Range of parameters of the datasets used for the effective takeoff angle relation

Dataset	φ [°]	F [-]	h_o [m]	t/h_o [-]	α [°]
Present study	30, 50	3.2 – 7.5	0.052 – 0.092	0.16 – 0.60	5.7 – 14.0
Pfister (2008)	12, 30, 50	5.7 – 10.4	0.040 – 0.094	0.10 – 0.42	5.7 – 26.6
Steiner et al. (2008)	0	3.0 – 8.0	0.030 – 0.070	0.19 – 1.65	8.2 – 33.2

Pfister (2008) studied smooth chute aerators with a similar experimental setup. The air concentrations were also measured with a fiber optical probe, allowing the same definition $C = 0.90$ for the jet surfaces. However, the flow depth at takeoff h_t was not measured. Two different approaches were tested to estimate it. The first uses Bernoulli's principle (§6.2) from the measured approach flow point. The second is a linear interpolation of the water depth obtained from the two first air concentration profiles. It was found that the second method overestimates the water depth, and thus the first approach was retained. The tests without a deflector, i.e. just an offset, are not considered. The additional tests 127–141 with steep deflectors of Pfister (2011) are included in this dataset.

Steiner et al. (2008) studied deflector ski jumps on a flat chute ($\varphi = 0^\circ$). The jet surfaces were measured with a hook point gauge, giving a different jet surface definition and precision compared to the other datasets. The flow depth at takeoff h_t was measured. With a flat slope, using h_o instead of h_t would underestimate the takeoff flow depth. The agreement between measured takeoff flow depth h_t and calculated h_t with equation (6.3) is $r^2 = 0.964$.

6.3.2 Selection of jet trajectory method

The methods presented in §6.1 are applied to find the upper and lower takeoff angles. To guarantee the quality of the datasets, only tests with at least three measured points and without cavity

subpressure ($\Delta p/(\rho g h_o) \leq 0.1$) are considered.

The takeoff angle $\alpha_{t\text{opt}}$ of method M3 is typically lower than the geometrical deflector angle, meaning that the deflector never fully deflects the flow (Figure 6.10). The tests of Pfister (2008) display smaller takeoff angles than the two other datasets. Tests with $\alpha = 26.6^\circ$ are especially low. This can be explained by a smaller relative deflector height ($0.16 < t/h_o < 0.21$), while the tests of Steiner et al. (2008) for the same α have higher relative deflector heights ($1.07 < t/h_o < 1.67$). Similar conclusions are obtained for methods M1 and M2.

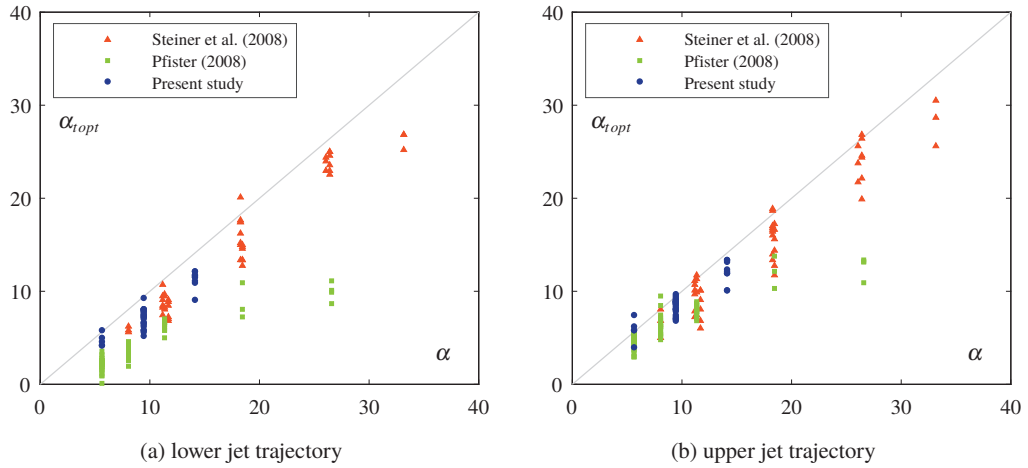


Figure 6.10 – Influence of the deflector angle α on the takeoff angle $\alpha_{t\text{opt}}$ of method M3

The takeoff angle $\alpha_{t\phi}$ of method M1 shows significant differences with the optimal angle $\alpha_{t\text{opt}}$ for steep deflectors (Figure 6.11), showing the necessity of using the flow depth perpendicular to the deflector. As a consequence, **method M1 is not considered anymore further on**. The takeoff angles $\alpha_{t\alpha}$ of method M2 coincide well with $\alpha_{t\text{opt}}$ of method M3, especially for the lower jet surface (Figure 6.12).

The takeoff velocities $u_{t\alpha}$ of method M2 and $u_{t\text{opt}}$ of method M3 are also in good agreement (Figure 6.13). The tests of Pfister (2008) have higher $u_{t\text{opt}}$ than $u_{t\alpha}$, particularly for the lower jet surface. This is physically unlikely and could indicate that the takeoff flow depth is overestimated. No substantial parameter influence can be observed for $u_{t\text{opt}}/u_{t\alpha}$ (Appendix E.2), and thus no relation could be found for $u_{t\text{opt}}$. Therefore, and as both $\alpha_{t\alpha}$ and $\alpha_{t\text{opt}}$ are similar and $\alpha_{t\alpha}$ can be easily obtained, only $\alpha_{t\alpha}$ of **method M2** is considered for the following takeoff angle investigation. It will be distinguished as α_{tl} for the lower jet surface and α_{tu} for the upper jet trajectory.

6.3.3 Comparison with the takeoff angle relations of Steiner et al. (2008)

Steiner et al. (2008) suggested a relation (§2.3.3) in function of $\Psi = (t/h_o) \tan(\alpha)/F_o$ for the lower and upper takeoff angle valid for $0.01 < \Psi < 0.3$. Figure 6.14 shows the takeoff angles in function of Ψ . Note that the method to obtain the takeoff angles is different and thus gives slightly different

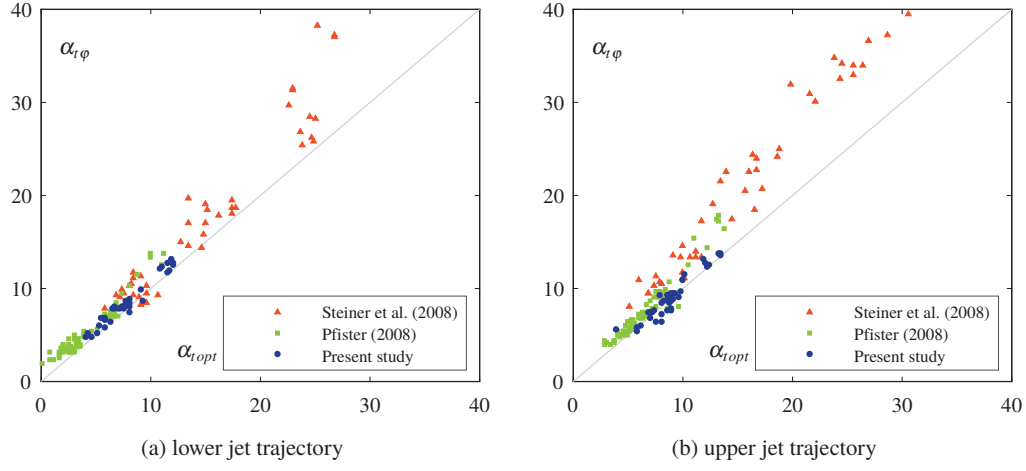


Figure 6.11 – Comparison of the takeoff angles $\alpha_{t\phi}$ (method M1) and $\alpha_{t\text{opt}}$ (method M3)

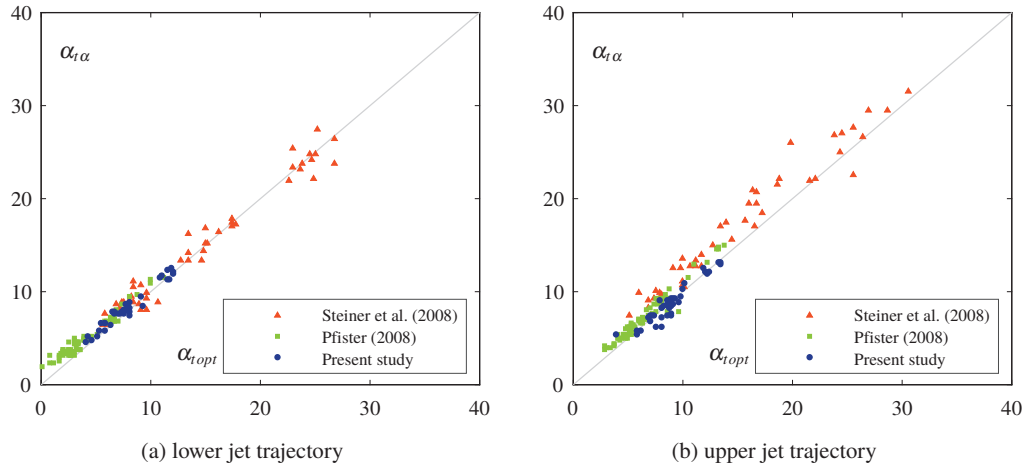


Figure 6.12 – Comparison of the takeoff angles $\alpha_{t\alpha}$ (method M2) and $\alpha_{t\text{opt}}$ (method M3)

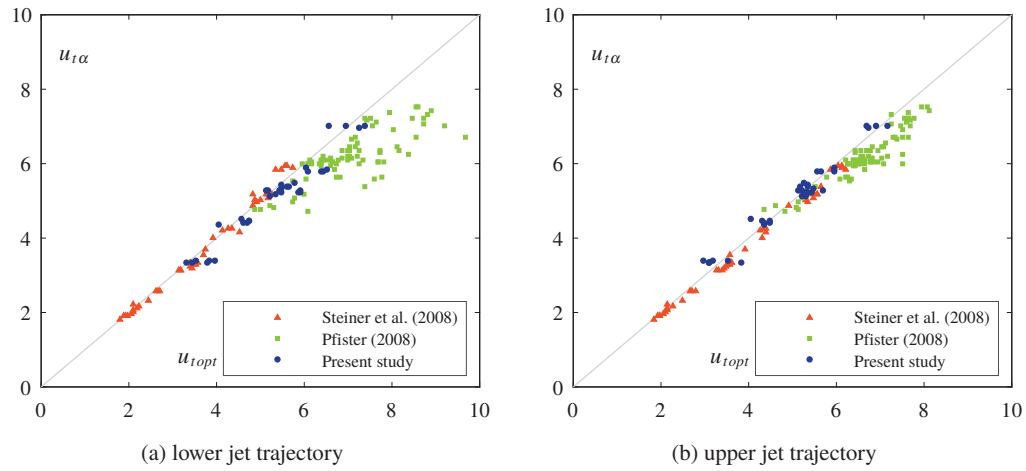


Figure 6.13 – Comparison of takeoff velocities $u_{t\alpha}$ (method M2) and $u_{t\text{opt}}$ (method M3)

results than the original study of Steiner et al. (2008). The criteria $0.01 < \Psi$ is only respected for 55 % of the present study tests and 6 % of Pfister (2008) tests due to lower t/h_o . The relation of Steiner et al. (2008) underestimates the takeoff angle for low values of Ψ , especially for the lower jet surface. This is likely an effect of the small relative deflector height t/h_o .

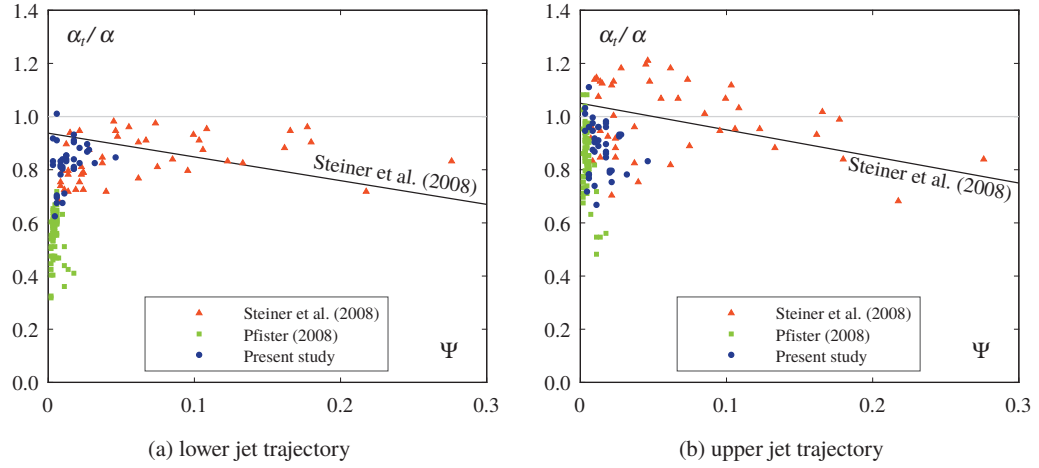


Figure 6.14 – Takeoff angle α_t relation (black line) obtained by Steiner et al. (2008) with $\Psi = (t/h_o) \tan(\alpha)/F_o$

6.3.4 Jet spread difference compared to Pfister (2008)

The dataset of Pfister (2008) systematically gives smaller α_t/α values than the present study (Figure 6.14a). This is surprising as the experimental conditions are similar. Comparing an almost identical test of each dataset (Figure 6.15) indicates that the jet spread of both the upper and lower jet surfaces is different. A general comparison of these two tests is presented in Terrier et al. (2015).

The presumed difference is an effect of turbulence conditions. Ervine and Falvey (1987) showed that jet spread is related to the jet velocity and turbulence intensity. Later, Ervine et al. (1995) suggested that the amount of air entrained by a jet is proportional to the turbulence. In addition, Skripalle (1994) studied the air entrainment of offset aerators and demonstrated that more air is entrained as the turbulent boundary layer develops.

For the present study, the deflector's crest was located 0.47 m downstream of the jetbox, whereas this distance was 2.0 m for Pfister (2008). The turbulent boundary layer has thus less time to develop in the present study, which can explain the smaller jet spread of the lower jet surface. For the upper jet surface, the spread is higher for the present study as more turbulence might remain from the jetbox. To conclude, the flow turbulence has an effect on the jet spread and takeoff angle, but this effect could not be included as it was not measured.

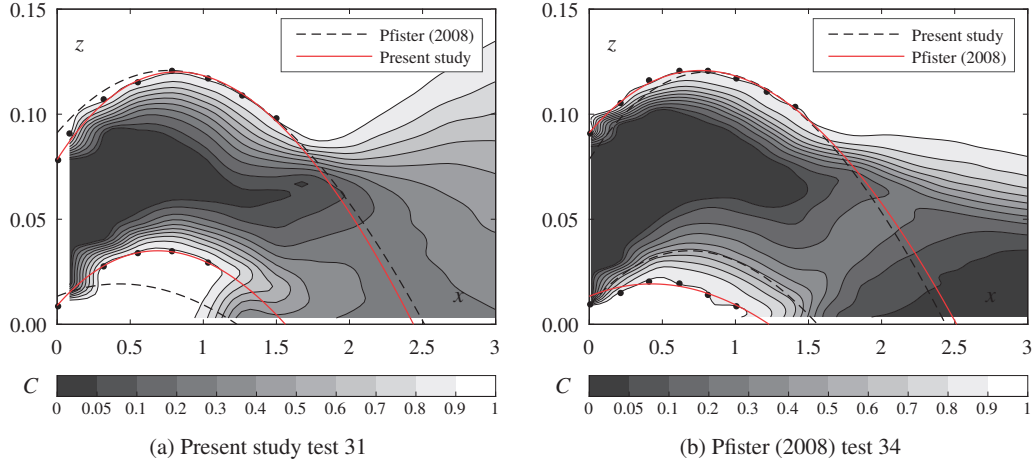


Figure 6.15 – Jet trajectories with nearly identical parameters ($\varphi = 50^\circ$, $F_o = 7.5/7.4$, $h_o = 0.075/0.080$ m, $\alpha = 5.71^\circ$ and $t = 0.015/0.013$ m respectively for the present study / Pfister (2008)). The lower takeoff angle is 4.7° for the present study and 3.1° for Pfister (2008)

6.3.5 Lower takeoff angle relation

The analysis of each parameter's influence (Appendix E.3) on the lower takeoff angle α_{tl} for the present study generally confirms the parameters used by Steiner et al. (2008) in equation (2.71). It shows a strong influence of α and t/h_o , but no clear trend is visible for F_o . The following relation is suggested for the lower takeoff angle

$$\frac{\alpha_{tl}}{\alpha} = \cos \alpha \cdot \tanh \left(2 \cdot \sqrt{\frac{t}{h_o}} \right) \quad (6.4)$$

The limitations of the relation are summarized in §10.2. The term $\cos(\alpha)$ is a correction factor that was found necessary for steep deflectors. With large angles, it is more difficult to completely deflect the flow streamlines. The hyperbolic tangent allows having simultaneously a small α_{tl}/α for a very low relative deflector height t/h_o , and α_{tl} close to α for a large relative deflector height (Figure 6.16a). In the first case, the deflector is too small to influence the flow streamlines, whereas the streamlines have enough time to change direction in the second case. An adapted approach of Pfister et al. (2014) considering a term $(1 - t/h_o)$ was less successful for deflectors.

For the present study, a coefficient of determination $r^2 = 0.960$ was obtained (Figure 6.16b). A group of points with $\alpha_{tl} \simeq 5^\circ$ have a slightly underestimated takeoff angle. They were all obtained with the flattest deflector ($\alpha \simeq 5.7^\circ$ and $t = 0.015$ m). The dataset of Steiner et al. (2008) also shows an excellent agreement ($r^2 = 0.968$). The dataset of Pfister (2008) shows a systematic overestimation of the effective takeoff angle ($r^2 = 0.446$) for the reasons explained in §6.3.4.

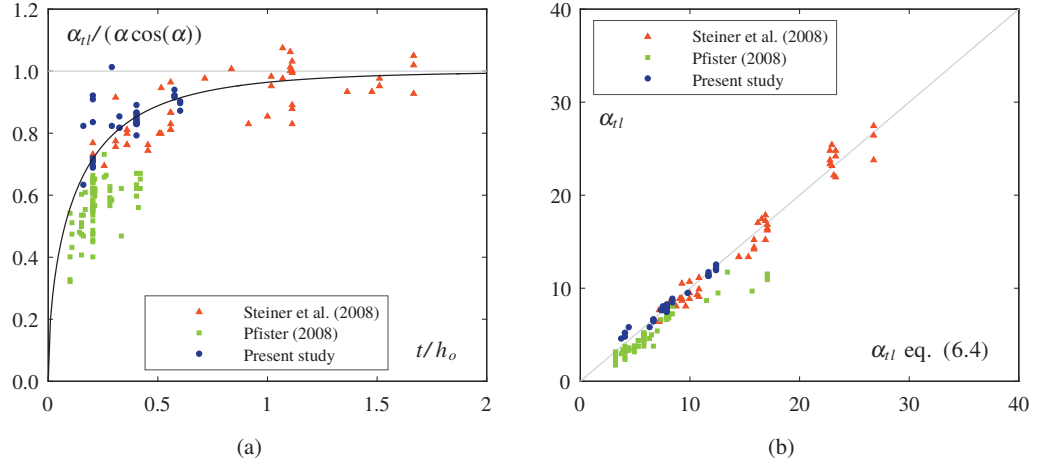


Figure 6.16 – (a) Hyperbolic tangent to take into account the effect of the deflector relative height t/h_o , (b) Comparison of the takeoff angle $\alpha_{tl,calc}$ with eq. (6.4)

6.3.6 Upper takeoff angle relation

Similarly to the lower takeoff angle, the upper takeoff angle α_{tu} shows an influence of α , t/h_o , and also F_o as found by Steiner et al. (2008) (Appendix E.4). The following relation is suggested

$$\frac{\alpha_{tu}}{\alpha} = 0.83 \cdot F_o^{0.2} \cdot (1 + \sin \alpha)^{-0.5} \cdot \tanh \left(2 \cdot \sqrt{\frac{t}{h_o}} \right) \quad (6.5)$$

The limitations of the relation are summarized in §10.2. The same hyperbolic tangent function used in equation (6.4) was obtained to describe the effect of t/h_o . The takeoff angle increases with the Froude number, indicating that a high velocity flow is more affected by the deflector than a slower flow. The decrease of α_{tu}/α for large values of α is best defined by $(1 + \sin \alpha)^{-0.5}$.

For the present study, a coefficient of determination $r^2 = 0.945$ was obtained (Figure 6.17b). The dataset of Steiner et al. (2008) also shows a good agreement ($r^2 = 0.939$). The dataset of Pfister (2008) is notably better estimated compared to the lower jet surface ($r^2 = 0.799$). This improvement is related to a more similar jet spread among the datasets.

6.4 Jet spread angle

The jet spread angle at takeoff δ_s is the difference between the upper α_{tu} and lower α_{tl} takeoff angles

$$\delta_s = \alpha_{tu} - \alpha_{tl} \quad (6.6)$$

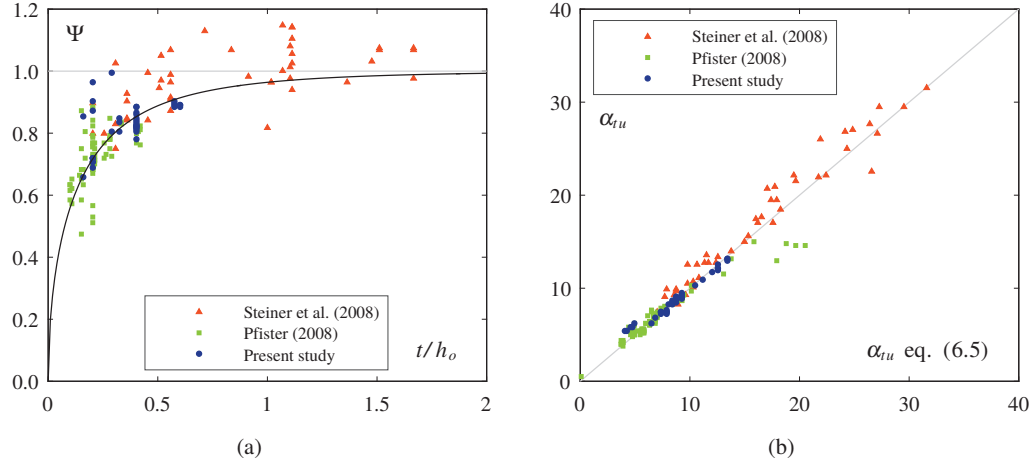


Figure 6.17 – (a) Hyperbolic tangent to take into account the effect of the deflector relative height t/h_o with $\Psi = \alpha_{tu}/(\alpha \cdot 0.83 \cdot F_o^{0.2} \cdot (1 + \sin\alpha)^{-0.5})$, (b) Comparison of the takeoff angle α_{tu} with eq. (6.5)

The jet trajectory **method M3** is used as it produces a better estimation of the jet trajectories for Steiner et al. (2008). There is little difference between method M2 and M3 for the other datasets. The jet spread angle is relatively small (Figure 6.18), with a median of 1.35° for present study, 2.26° for Pfister (2008) and 0.70° for Steiner et al. (2008). The negative values for Steiner et al. (2008) might be explained by a different definition of the jet surface (measured with a point gauge) compared to the other datasets. For the present study, the negative values are tests with $F_o = 3.2$ where the jet thickness is decreasing due to flow acceleration. The only parameters clearly influencing δ_s is the Froude number F_o (Appendix E.5). The spread angle δ_s increases with an increasing F_o . The tests of Pfister (2008) have high Froude numbers which can explain the higher spread angle δ_s . The difference between equations (6.5) and (6.4) does not provide an accurate estimation of the jet spread angle.

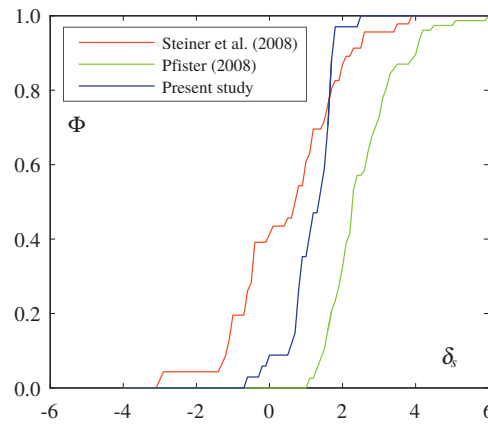


Figure 6.18 – Cumulative distribution function Φ of the jet spread angle δ_s

6.5 Jet length

Two approaches are reported to calculate the jet length. First, the physically based approach including trajectory computation is presented. Then, a more limited empirical approach to obtain the jet length with the basic parameters varied in this study is given. This second approach is less laborious for application in practice.

6.5.1 Jet trajectory approach

The jet length L is obtained from equation (2.63) with the takeoff velocity u_t and the takeoff angle α_t given by methods M2 and M3. Solving $z(T_{jet}) = 0$ for the lower jet surface gives the flight time T_{jet} from takeoff to impact on the pseudo-bottom. The jet length is then calculated by

$$L = x(T_{jet}) \quad (6.7)$$

For the tests of Steiner et al. (2008), a virtual offset $o = 0.1$ m is considered to define the bottom and calculate L . The jet length calculated with methods M2 (L_α) and M3 (L_{opt}) shows little difference (Figure 6.19a). The length obtained with **method M3** is kept further on as the jet length $L = L_{opt}$ since better results are obtained for a few long jets.

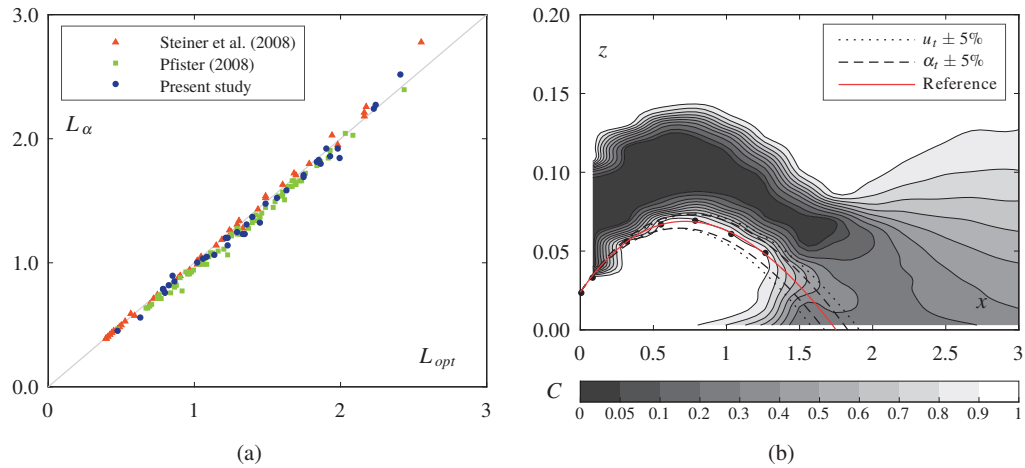


Figure 6.19 – (a) Comparison of the jet length obtained with methods M2 (L_α) and M3 (L_{opt}), (b) Sensitivity of the lower jet trajectory for a change of $\pm 5\%$ of the takeoff velocity u_{tl} and takeoff angle α_{tl} for test 20

Figure 6.19b shows the sensitivity of the jet trajectory to the takeoff velocity and angle. A change of the takeoff velocity u_{tl} of $\pm 5\%$ modifies the jet length L of $\pm 9\%$, while a change of takeoff angle α_{tl} of $\pm 5\%$ modifies L of $\pm 4.5\%$. The jet length and jet trajectory is thus in general more sensitive to a change of u_t than α_t .

The visually observed jet length L_{obs} for the present study is in average a third shorter than the jet length L obtained with the lower jet surface jet trajectory $L_{obs} = 0.68L$ ($r^2 = 0.939$) (Figure 6.20a). For Pfister (2008) there is an good agreement with the observed jet length ($r^2 = 0.936$). No data is shown for Steiner et al. (2008) as the jet length was not observed.

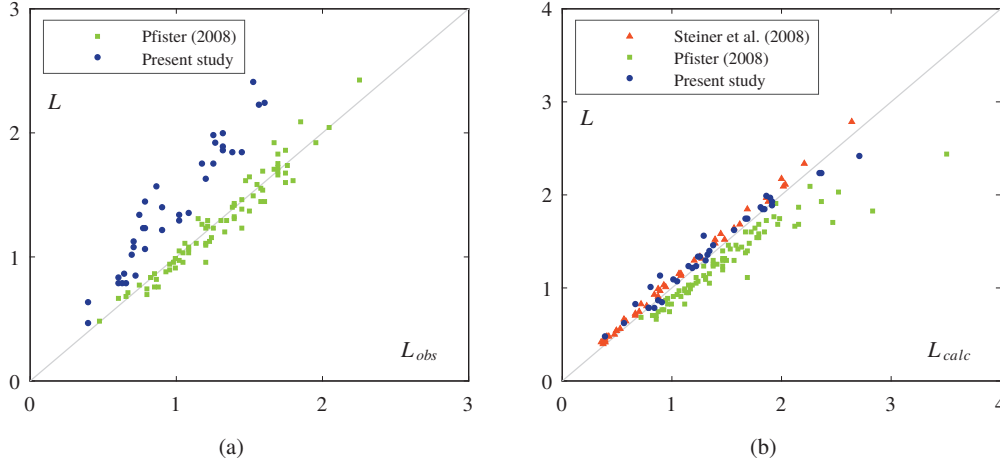


Figure 6.20 – Comparison of the jet length L with (a) the observed jet length L_{obs} and (b) the calculated jet length L_{calc}

With the jet trajectory approach and method M2, the jet length can be calculated by solving equation (6.7) when inserting equation (6.2), obtained with equation (6.3), and (6.4) in (2.63). Figure 6.20b compares the jet length L_{calc} obtained. There is an excellent agreement for the present study ($r^2 = 0.952$) and for Steiner et al. (2008) ($r^2 = 0.977$). For Pfister (2008), there is a systematic overestimation which is directly linked to the overestimation of the takeoff angle ($r^2 = 0.485$). The overestimation is less than 20 % for 75 % of the tests, and less than 25 % for deflector angles $\alpha \leq 18.4^\circ$. Using a factor of 0.84 for the calculated value of Pfister (2008) improves the results to $r^2 = 0.874$.

This approach to obtain L_{calc} is only valid for a small subpressure ($\Delta p / (\rho g h_o) \leq 0.1$). Figure 6.21a shows that L_{calc} is gradually overestimated as $\Delta p / (\rho g h_o)$ increases. The observed jet length L_{obs} is used for Pfister (2008) as the trajectory method presented herein cannot be applied for large $\Delta p / (\rho g h_o)$. Pfister (2011) suggests equation (2.75) to take into account the subpressure. This correction is applied with $L_{max} = L_{calc}$ for tests with $\Delta p / (\rho g h_o) \geq 0.1$ and the corrected jet length $L_{\Delta p}$ is shown in Figure 6.21b. It shows a good agreement with the observed jet length L_{obs} for Pfister (2008). There are more differences for $\Delta p / (\rho g h_o) \geq 1.5$, but such a subpressure should not be used for the design of an aerator.

6.5.2 Empirical approach

Pfister and Hager (2010a) suggest equation (2.74) to estimate the jet length. The jet length is compared to $\Psi_1 = F_o \cdot (1 + \sin \varphi)^{1.5} \cdot (\sqrt{(o+t)/h_o} + F_o \tan \alpha)$ in Figure 6.22a. For Pfister (2008),

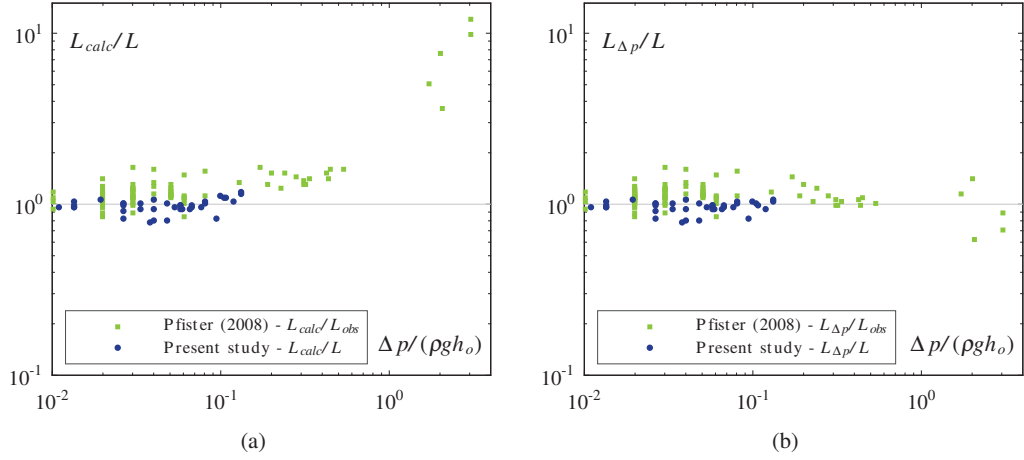


Figure 6.21 – Ratio of the calculated jet length L_{calc} and measured jet length L as a function of the cavity subpressure $\Delta p/(\rho gh_o)$ (a) without subpressure correction, and (b) with subpressure correction from Pfister (2011) for $\Delta p/(\rho gh_o) \geq 0.1$

the best fit is $L/h_o = 0.74 \cdot \Psi_1$ ($r^2 = 0.850$). The slightly lower multiplicative coefficient is a consequence of the inclusion of the additional steep deflectors tests of Pfister (2011). Good agreements are obtained for the present study with $L/h_o = 1.12 \cdot \Psi_1$ ($r^2 = 0.910$), and with $L/h_o = 1.08 \cdot \Psi_1$ ($r^2 = 0.982$) for Steiner et al. (2008). The notable increase of the relation slope can be explained by different turbulence conditions in the approach flow, as previously discussed (§6.3.4).

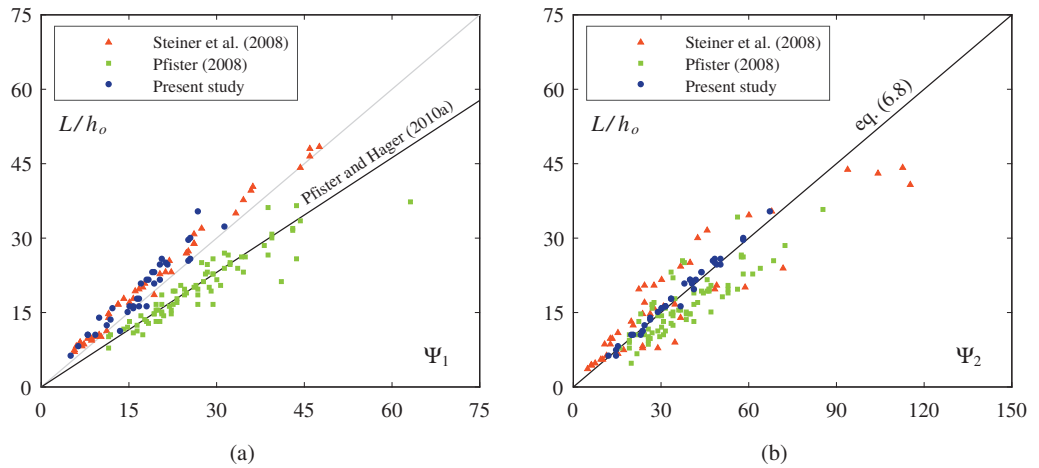


Figure 6.22 – Relative jet length L/h_o as a function of (a) $\Psi_1 = (1 + \sin \varphi)^{1.5} \cdot F_o \cdot (\sqrt{(o+t)/h_o} + F_o \tan \alpha)$ from Pfister and Hager (2010a), and (b) $\Psi_2 = (1 + \sin \varphi)^2 \cdot (1 + \tan \alpha)^4 \cdot F_o^{1.4} \cdot (t/h_o)^{0.4}$

In addition of the physical approach based on the trajectories, an empirical relation for the relative jet length L/h_o based on the basic parameters was investigated in the present study. The following relation valid only **without offset**, for the limits of the present study described in 10.2 and without

cavity subpressure is obtained (Figure 6.22b)

$$\frac{L}{h_o} = 0.5 \cdot (1 + \sin \varphi)^2 \cdot (1 + \tan \alpha)^4 \cdot F_o^{1.4} \cdot \left(\frac{t}{h_o} \right)^{0.4} \quad (6.8)$$

The trajectories developed earlier were used to obtain the relative jet length L/h_o without offset for the tests of Pfister (2008) and Steiner et al. (2008). It agrees well with the present study ($r^2 = 0.979$). As with the previous trajectory approach, L/h_o is overestimated for Pfister (2008) ($r^2 = 0.468$). For Steiner et al. (2008) ($r^2 = 0.748$), the points are underestimated for low α and underestimated for high α and equation (6.8) should only be used for $\alpha \leq 20^\circ$.

6.6 Jet impact angle on pseudo-bottom

The jet impact angle on the pseudo-bottom γ can be obtained by differentiating equation (2.63)

$$\frac{dz}{dx} = -\tan(\gamma) = \frac{u_t \sin(\alpha_t) - g \cos(\varphi) T_{jet}}{u_t \cos(\alpha_t) + g \sin(\varphi) T_{jet}} \quad (6.9)$$

Figure 6.23 compares the impact angle γ obtained with **method M3** and the calculated impact angle γ_{calc} obtained with equations (6.2), (6.4) and (6.9). Similarly to the jet length, there is an excellent agreement for the present study ($r^2 = 0.961$) and Steiner et al. (2008) ($r^2 = 0.975$), while δ is overestimated for Pfister (2008) ($r^2 = 0.495$). Using a factor of 0.83 (similar to the one obtained for the calculated jet length in §6.5) for the calculated value of Pfister (2008) improves the results to $r^2 = 0.894$. The tests of Steiner et al. (2008) have a larger impact angle owing to steep deflectors combined with $\varphi = 0^\circ$.

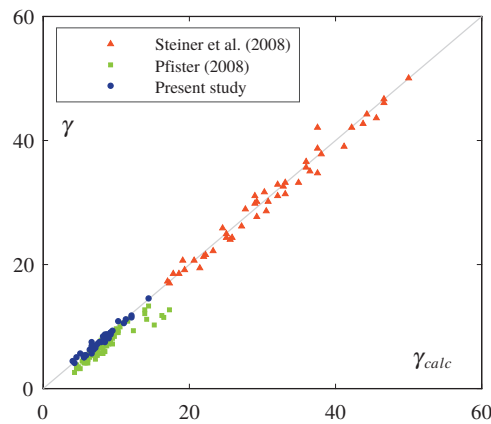


Figure 6.23 – Comparison of the measured jet impact angle γ with the calculated jet impact angle γ_{calc}

6.7 Maximum jet elevation

The maximum elevation of the upper jet trajectory z_{max} can be obtained by differentiating $z(T)$ of equation (2.63). Solving $dz(T)/dT = 0$ gives the flight time T_{max} from takeoff to the maximum elevation

$$T_{max} = \frac{u_t \sin \alpha}{g \cos \varphi} \quad (6.10)$$

The maximum elevation of the upper jet trajectory z_{max} is then calculated by

$$z_{max} = z(T_{max}) \quad (6.11)$$

6.8 Cavity subpressure

The cavity subpressure Δp results from an equilibrium between the air entrained by the flow and the head losses of the air supply system. The head losses in the supply can be estimated by

$$\frac{\Delta p}{\rho g} = \xi \cdot \frac{u_A^2}{2g} = \xi \cdot \frac{Q_A^2}{2gA_A^2} \quad (6.12)$$

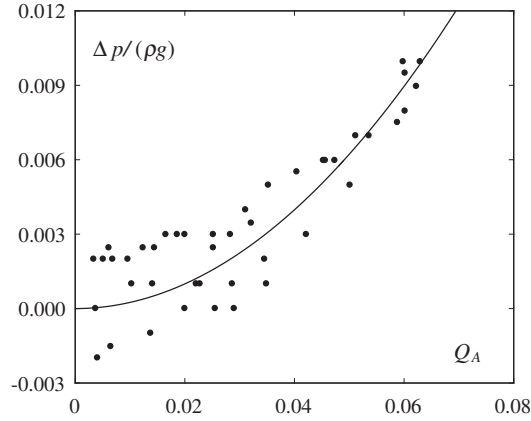
with ξ as the head loss coefficient (sum of linear and singular head losses), u_A as the air velocity, Q_A as the air discharge and A_A as the air duct section.

The cavity subpressure Δp is plotted against the air discharge Q_A to validate the measurements (Figure 6.24). Considering the air velocity through the slot under the deflector with $A_s = 0.02 \cdot 0.48 \text{ m} = 0.0096 \text{ m}^2$ (the smallest section of the air supply system), the head loss coefficient was found to be $\xi = 0.045$. Some scatter is visible for low discharges, but it decreases for higher discharges.

6.9 Jet blackwater core length

The length of the blackwater core L_{bwc} defined with $C = 0.01$ (Figure 2.13) is obtained by linear interpolation between the two profiles around $C_{min} = 0.01$. The accuracy of this measurement is moderate due to the relatively large streamwise spacing $\Delta x = 0.235\text{--}0.360 \text{ m}$ and depth wise spacing $\Delta z = 0.005\text{--}0.012 \text{ m}$. Depending on approach flow and deflector parameters, the blackwater core can extend up to the jet impact or even beyond. In this case, the end of the blackwater core is not due to the jet spread, but to the jet impact. Therefore, only the cases with $L_{bwc} \leq 0.9L$ are considered.

The blackwater core decreases by an angle of a few degrees on each jet surfaces, and thus L_{bwc} is a function of h_o . The angle depends on the turbulence intensity according to Ervine and Falvey

Figure 6.24 – Cavity subpressure $\Delta p/(\rho g)$ in function of the air discharge Q_A

(1987). Pfister and Hager (2009) suggest equation (2.81) to obtain L_{bwc}/h_o from the flow conditions, the deflector and chute angles. A similar influence of parameters is observed for the present study for F_o , α and t/h_o , while a lesser effect is observed for φ (Appendix E.6). However, despite being used for the normalization of L_{bwc} , the approach flow depth h_o still has strong influence.

Figure 6.25 shows that the length of the blackwater core is shorter than the estimation obtained from Pfister and Hager (2009). There are no points with $F_o = 3.2$ as the blackwater core is still existing at $x = 0.9L$. A small difference is observed between $h_o = 0.075$ m and $h_o = 0.092$ m. The only test with $h_o = 0.052$ m that respects $L_{bwc} \leq 0.9L$ is test 34 with the steepest deflector and $L_{bwc}/h_o = 28.1$. It is significantly higher than the other points. For the approach flow with $h_o = 0.075$ m, the slope of equation (2.81) can be adapted with satisfactory results ($r^2 = 0.798$) to

$$\frac{L_{bwc}}{h_o} = 49 \cdot \Psi = 49 \cdot F_o^{-1} \cdot (1 + \tan \alpha)^{-0.5} \cdot (1 + \sin \varphi) \quad (6.13)$$

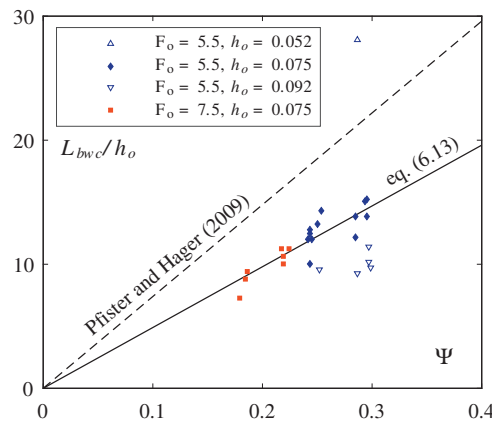
Figure 6.25 – Length of blackwater core L_{bwc} as a function of $\Psi = F_o^{-1} \cdot (1 + \tan \alpha)^{-0.5} \cdot (1 + \sin \varphi)$

Figure 6.26 shows that the influence of the approach flow depth h_o on the relative blackwater core

length L_{bwc}/h_o is linked to the spread of the upper jet surface which occurs with a larger angle for $h_o = 0.092$ m. A difference in the spread of both jet surfaces between the present study and Pfister (2008) was previously observed in §6.3.4. This indicates that the approach flow turbulence is an important additional parameter to determine the length of the blackwater core. The influence of a rougher bottom upstream of the deflector is discussed in Chapter 8.

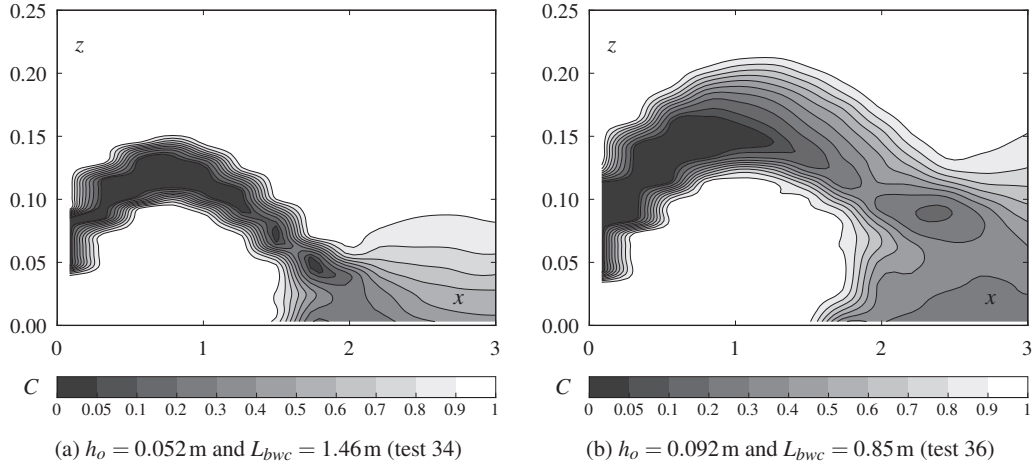


Figure 6.26 – Aeration of the jet for two different approach flow depths h_o with other parameters kept constant. The interruption of the contour $C = 0.05$ between the profiles $x = 1.26$ m and $x = 1.50$ m, as well as between $x = 1.50$ m and $x = 1.73$ m for test 34 is only due to the interpolation artifacts

6.10 Design example

To summarize the relation obtained in this chapter, the parameters of one test are used as a design example. Test 20 is chosen as it is considered a typical case for a steep stepped spillway. The parameters are:

F_o	=	5.55	[-]
h_o	=	0.075	[m]
φ	=	50	[°]
s	=	0.06	[m]
α	=	9.46	[°]
t	=	0.03	[m]

To allow the comparison with the measurements on the model, two additional parameters are required: the streamwise coordinate of the approach flow point $x_o = -0.27$ m and the approach flow pressure $p/(\rho g) = 0.141$ m as the pressure was not hydrostatic due to the proximity of the jetbox.

The takeoff flow depth h_t is obtained with equation (6.3). The specific discharge is calculated with $q = F_o \cdot \sqrt{g} \cdot h_o^{3/2} = 0.357$ m²/s and the depth-average approach flow velocity with $u_o = q/h_o = 4.76$ m/s. The bottom elevation difference between h_o and h_t is given by $\Delta z' = -x_o \sin \varphi - t \cos \varphi = 0.188$ m.

The takeoff flow depth is then

$$h_t = 0.067 \text{ m}$$

The takeoff velocity u_t is given by equation (6.2)

$$u_t = 5.40 \text{ m/s}$$

The lower takeoff angle α_{tl} is given by equation (6.4) and the upper takeoff angle α_{tu} by equation (6.5)

$$\alpha_{tl} = 7.95^\circ$$

$$\alpha_{tu} = 8.74^\circ$$

The jet length is obtained from equation (2.63). Solving $z(T) = 0$ for the lower jet with $z_t = t$ gives the flight time from takeoff to impact $T_{jet} = 0.272 \text{ s}$. The jet length is then given by equation (6.7)

$$L_{calc} = 1.73 \text{ m}$$

The maximum jet elevation is given by equation (6.11)

$$z_{max} = 0.150 \text{ m}$$

The jet impact angle on the pseudo-bottom γ is given by equation (6.9)

$$\gamma = 7.46^\circ$$

The calculated values agree well with the measured values, with little differences (Table 6.3). For tests without cavity subpressure $\Delta p / (\rho g h_o) \leq 0.1$, the jet length difference is always $|L - L_{calc}| / L \leq 0.1$, except for the smallest deflector with $\alpha = 5.71^\circ$ and $t = 0.015 \text{ m}$ where $|L - L_{calc}| / L \leq 0.2$.

6.11 Summary

A simple approach based on ballistic trajectories is presented to determine the lower and upper jet surfaces. Three datasets were used to derive the equations of this approach: the present study, Pfister (2008) and Steiner et al. (2008). Three parameters are required to describe a trajectory:

Table 6.3 – Comparison of measured and calculated values for test 20

Parameter	Unit	Measured	Calculated	Difference
h_t	m	0.067	0.067	0 %
u_t	m	5.40	5.40	0 %
α_{tl}	°	8.10	7.95	−1.8 %
α_{tu}	°	8.63	8.74	1.2 %
L	m	1.75	1.73	−1.1 %
z_{max}	m	0.145	0.150	3.7 %
γ	°	7.03	7.46	6.1 %

- The takeoff elevation z_t with respect to the pseudo-bottom. For the lower jet trajectory it is given by the offset o and the deflector height t . For the upper jet trajectory the takeoff flow depth h_t has to be added to o and t . The takeoff flow depth h_t can be obtained by applying Bernoulli's principle given in equation (6.9) between the approach flow point and the takeoff point.
- The takeoff velocity u_t , which can be estimated from equation (6.2) for the lower and upper trajectories.
- The effective takeoff angle α_t which is different from the deflector angle α . It can be obtained from equation (6.4) for the lower jet trajectory, and from equation (6.5) for the upper jet trajectory.

The trajectories are then given by equation (2.63). The trajectories allow to determine the maximum elevation of the jet z_{max} , the jet length L , and the jet impact angle on the pseudo-bottom γ . The approach is only valid for small cavity subpressure ($\Delta p / (\rho g h_o) \leq 0.1$). As an example, this approach is applied to one test and a good agreement is found with the measured values.

A direct equation function of the basic parameters is also given for the jet length. In addition the jet spread angle as well as the blackwater core length of the jet are presented.

Chapter 7

Air transport characteristics

The characteristics of air transport downstream of a stepped chute aerator in terms of average and bottom air concentration are presented herein. The results are discussed to assess the influence of the basic parameters on the bottom air concentration, and they are compared to the preliminary study performed by Pfister et al. (2006a).

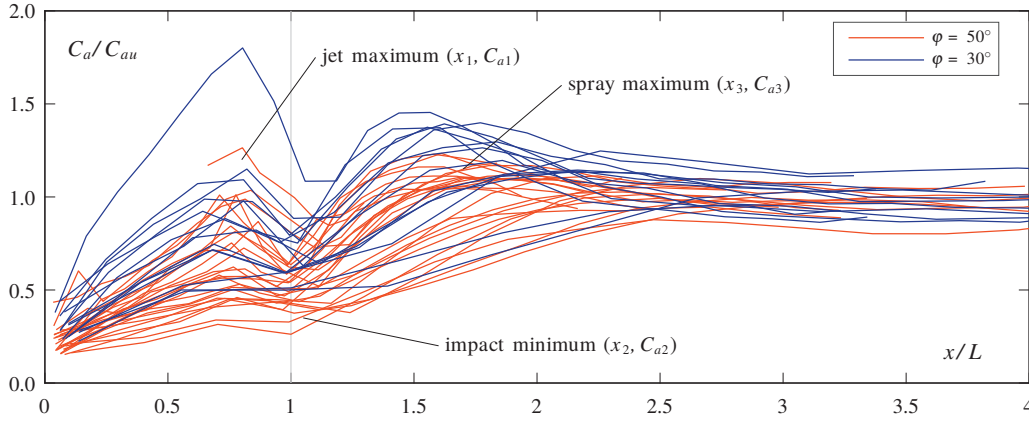
7.1 Average air concentration development

The development of the average air concentration downstream of the aerator shows common characteristics for most tests with three distinct extrema (Figure 7.1). The first extrema is a maximum shortly before the jet impact. This point will be referred further as the *jet maximum* with its streamwise coordinate x_1 and average air concentration C_{a1} . It is quickly followed by a *impact minimum* close to the jet impact (x_2 and C_{a2}). The average air concentration increases again in the spray zone to a second maximum, the *spray maximum* (x_3 and C_{a3}). Finally the average air concentration tends towards the quasi-uniform average air concentration C_{au} . Most tests with $F_o = 3.2$ show no extrema, with a slow increase of C_a that tends directly towards the uniform average air concentration C_{au} . The few tests without extrema were not considered for the analysis. The development of C_a for each individual test can be found in Appendix F.

Equations defining the extrema are given herein, and their limitations are summarized in §10.2. The impact minimum and spray maximum are related with the relative jet length L/h_o . This correlation is presented, but relations are generally better expressed with the basic set of parameters ϕ , s/h_o , F_o , α and t/h_o .

7.1.1 Jet maximum and jet air entrainment

The streamwise coordinate of the jet maximum x_1 is presented first. Figure 7.1 shows that it is located at $x_1/L \approx 0.8$ for all tests. There are in average only 5.5 profiles measured between the jet takeoff and impact, which limits the precision of the x_1 measurement to half the air concentration

Figure 7.1 – Definition of the extrema of the average air concentration C_a

profiles spacing Δx . To take into account this uncertainty, a probability density plot is used. If x_1 is the actual location of the maximum for all tests, and $x_{1,meas}$ the measured location of the maximum of each test, $P_1(x_{1,meas} - 0.5\Delta x \leq x_1 \leq x_{1,meas} + 0.5\Delta x)$ shows the probability that x_1 is less than a distance of $\pm 0.5\Delta x$ away from $x_{1,meas}$ (Figure 7.2a). The probability P_1 is higher than 80 % for $0.74 \leq x_1/L \leq 0.82$, and therefore the streamwise coordinate of the jet maximum is located at

$$x_1/L = 0.78 \quad (7.1)$$

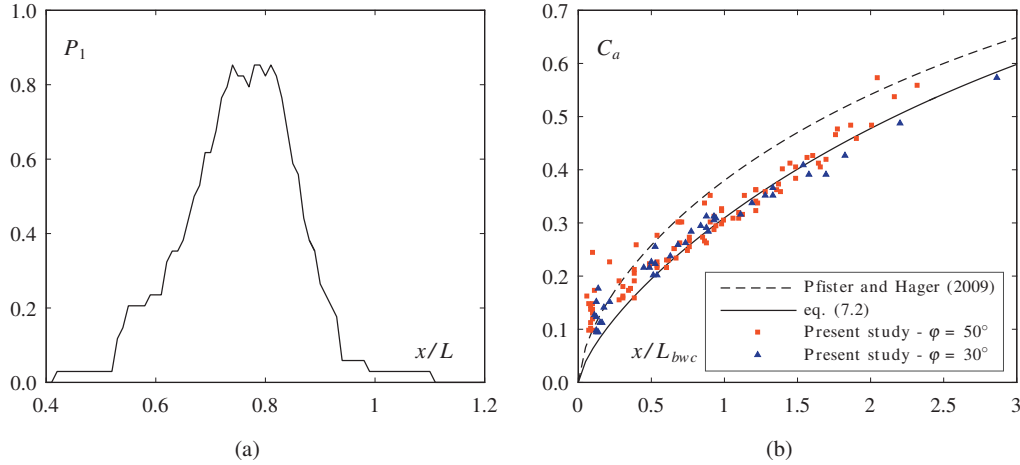


Figure 7.2 – (a) Probability P_1 of the jet maximum coordinate x_1/L to be less than a distance of $0.5\Delta x/L$ away from the location of the measured maximum of each test, and (b) development of the average air concentration C_a in the jet

Pfister and Hager (2009) presented equation (2.83) to describe the increase of the average air concentration C_a in a jet as a function of the blackwater core length L_{bwc} . The present study data is compared to this relation in Figure 7.2b. Only the points until the jet maximum ($x \leq x_1$) are

used. As previously explained in §4.1, C_a is not $C_a \approx 0$ at $x = 0$ due the integration of discrete air concentrations points. For aerator tests which have two air-water interfaces (lower and upper surfaces of the jet), there are between 5 and 15 points in the jet for the first profile, respectively giving a C_a of 15 % and 5 % in perfect conditions (pure water or pure air). The data agree with Pfister and Hager (2009) with slightly lower values. An adapted relation is suggested for $x/L_{bwc} \leq 3$

$$C_a = \tanh \left(0.32 \left(\frac{x}{L_{bwc}} \right)^{0.7} \right) \quad (7.2)$$

This relation can be used to determine C_{a1} in the jet at $x_1/L = 0.78$.

7.1.2 Jet impact minimum

The streamwise coordinate of the impact minimum x_2/L is assessed similarly as x_1/L . If x_2 is the actual location of the minimum for all tests, and $x_{2,meas}$ the measured location of the minimum of each test, shows the probability $P_2(x_{2,meas} - 0.5\Delta x \leq x_2 \leq x_{2,meas} + 0.5\Delta x)$ shows the probability that x_2 is less than a distance of $0.5\Delta x$ away from $x_{2,meas}$ (Figure 7.3a). The probability P_2 is higher than 80 % for $1.01 \leq x_1/L \leq 1.05$, and therefore the streamwise coordinate of the impact minimum is located at

$$x_2/L = 1.03 \quad (7.3)$$

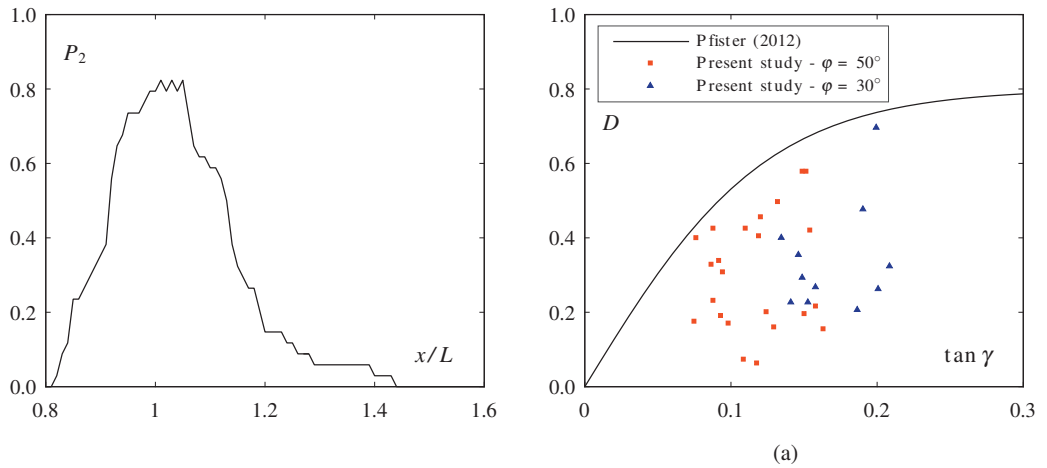


Figure 7.3 – (a) Probability P_2 of the impact minimum coordinate x_2/L to be less than a distance of $0.5\Delta x/L$ away from the location of the measured minimum of each test, (b) air detrainment D as a function of the jet impact angle γ

The minimum in average air concentration C_{a2} is due to flow compression and air detrainment at the jet impact. Chanson (1994a) and Pfister (2012) showed that the air detrainment D defined by

equation (2.85) is related to the jet impact angle γ for smooth chutes. Air detrainment is different on a stepped chute as there is no correlation between the two parameters (Figure 7.3b).

No equation was derived for the air detrainment D , and other approaches were attempted to describe the decrease of C_a at the jet impact. For example, the ratio C_{a2}/C_{a1} was found to be within $0.6 \leq C_{a2}/C_{a1} \leq 1$ but seems unrelated to other parameters. The minimum average air concentration C_{a2} was then analyzed directly and a correlation was obtained with the relative jet length L/h_o (Figure 7.4a). A relation for C_{a2} is obtained with ($r^2 = 0.863$)(Figure 7.4b)

$$C_{a2} = 0.0182 \cdot (1 + \sin \varphi)^{1.1} \cdot (1 + \tan \alpha)^{2.5} \cdot F_o^{1.1} \cdot \left(\frac{t}{h_o} \right)^{0.15} \quad (7.4)$$

All four terms directly influence and increase the jet length, and better results are obtained with this relation compared to a relation based on L/h_o with additional parameters. The presence of steps on the chute bottom clearly has an effect as the air detrainment is different from smooth chutes, but no influence of the relative step height s/h_o on C_{a2} is quantified.

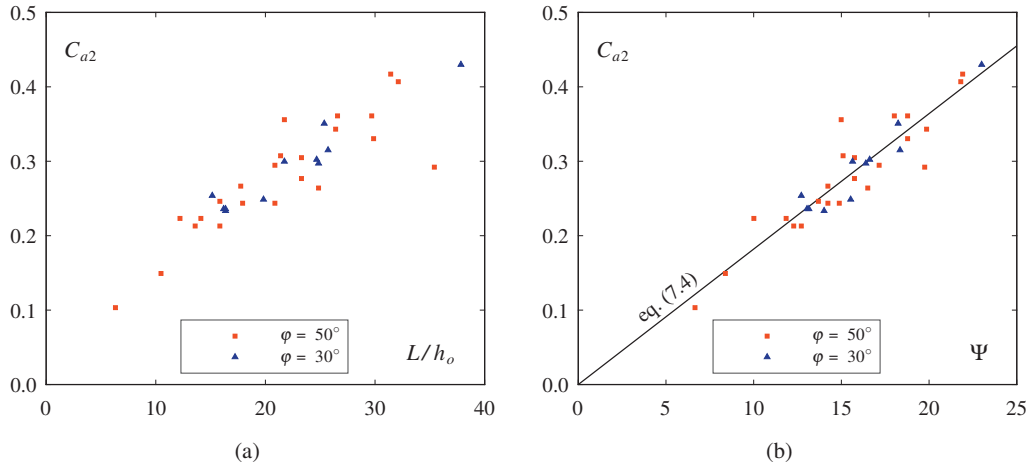


Figure 7.4 – Average air concentration C_{a2} of the minimum as a function of (a) the relative jet length L/h_o , and (b) $\Psi = (1 + \sin \varphi)^{1.1} \cdot (1 + \tan \alpha)^{2.5} \cdot F_o^{1.1} \cdot (t/h_o)^{0.15}$

7.1.3 Spray maximum

Unlike the two previous extrema, the streamwise coordinate of the spray maximum varies for each test. A few tests are excluded of the analysis because the jet was too long and the spray maximum was not reached before the end of the channel, or the spray maximum was not well defined (mostly tests with $F_o = 3.2$).

The streamwise coordinate of the spray maximum x_3/L is somewhat correlated with relative jet length L/h_o , with x_3/L decreasing for long L/h_o (Figure 7.5a). The following relation is obtained

for $1.5 \leq x_3/L \leq 3$ with $r^2 = 0.958$ (Figure 7.5b)

$$\frac{x_3}{L} = 1 + 8.26 \cdot (1 + \sin \varphi)^{-1} \cdot (1 + \tan \alpha)^{-5} \cdot F_o^{-0.75} \cdot \left(\frac{t}{h_o}\right)^{-0.55} \cdot \left(\frac{s}{h_o}\right)^{0.3} \quad (7.5)$$

The relation starts at $x_3/L = 1$ which is the jet impact point. An increase of any of the four first terms increases the jet length, and the negative exponents make x_3/L decrease with the jet length. A larger relative step height s/h_o increases x_3/L which suggests a dampening of the jet deflection by large steps.

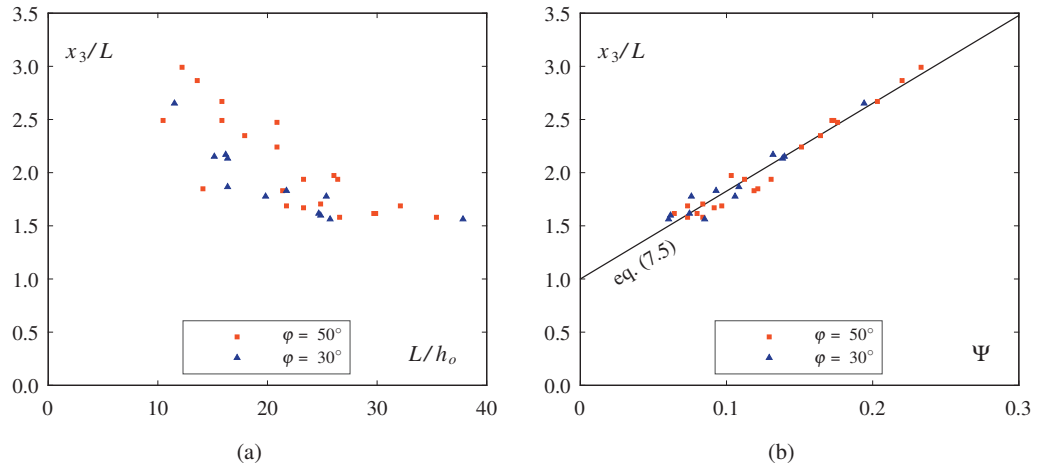


Figure 7.5 – Streamwise coordinate of the spray maximum x_3/L as a function of (a) the relative jet length L/h_o , (b) $\Psi = (1 + \sin \varphi)^{-1} \cdot (1 + \tan \alpha)^{-5} \cdot F_o^{-0.75} \cdot (t/h_o)^{-0.55} \cdot (s/h_o)^{0.3}$

The average air concentration C_{a3} of the spray maximum is strongly influenced by the chute angle φ (Figure 7.6a). It was therefore successfully attempted to normalize it with the uniform average air concentration C_{au} from Wilhelms and Gulliver (2005). Better results were then obtained with C_{au} from Hager (1991), and finally a slight variation from the latter was retained with only the term $\sin^{0.7} \varphi$. The following relation is obtained ($r^2 = 0.876$) (Figure 7.6b)

$$C_{a3} = 0.491 \cdot \sin^{0.7} \varphi \cdot (1 + \tan \alpha) \cdot F_o^{0.25} \cdot \left(\frac{t}{h_o}\right)^{0.15} \quad (7.6)$$

Similarly to the minimum C_{a2} , better results are obtained by using the parameters influencing L/h_o , instead of L/h_o with corrections. Additionally, the relative step height s/h_o has a small influence, with a slightly larger C_{a3} for an increasing s/h_o , but it only marginally improves equation (7.6).

Finally, stable values of C_a close to the quasi-uniform average air concentration C_{au} are reached after $x/L \geq 3$ (Figure 7.1). This limit can also be expressed as $(x - L) \geq 15h_c$ (Appendix D).

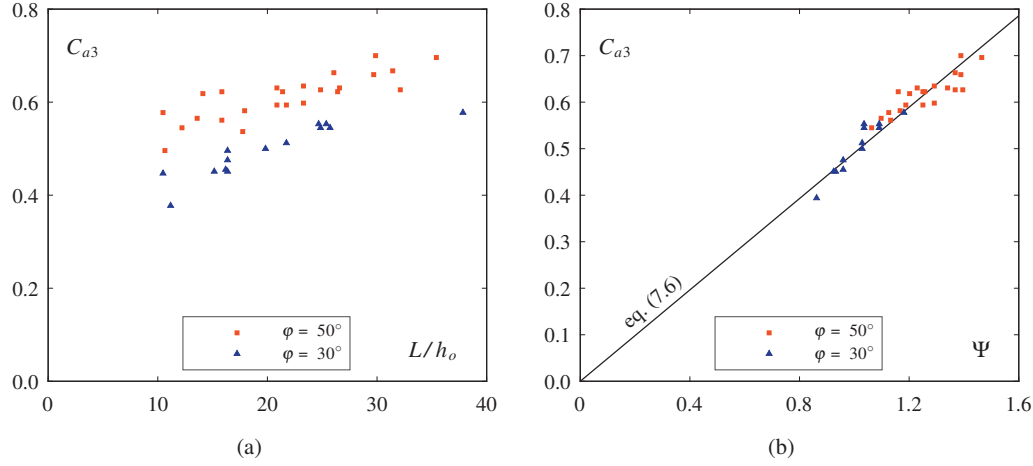


Figure 7.6 – Average air concentration C_{a3} of the spray maximum as a function of (a) the relative jet length L/h_o , and (b) $\Psi = \sin^{0.7} \varphi \cdot (1 + \tan \alpha) \cdot F_o^{0.25} \cdot (t/h_o)^{0.15}$

7.2 Bottom air concentration development

Trends in the bottom air concentration C_b are less distinct than for the average air concentration C_a (Figure 5.2c and 5.3c). For clarity reasons, only two tests are shown in Figure 7.7, both performed with the same flow conditions ($F_o = 5.5$ and $h_o = 0.075$ m) and the same deflector ($\alpha = 9.46^\circ$ and $t = 0.030$ m) but with a different chute angle φ . The bottom air concentration decreases rapidly along $0.5 \leq x/L \leq 1$ due to the roller. Some tests show a *roller minimum*. This location is not considered critical for cavitation since $C_b > 0.1$ and the velocities are small. After the jet impact at $x/L = 1$, C_b shows a rapid but continuous decrease similar to observations on smooth chute aerators, until a *minimum* is reached (x_4 and C_{b4} ; continuing the numbering of the average air concentration extrema to avoid confusion). It is difficult to observe this decrease for a single test since it occurs on a short distance and only a few points are available. It is better highlighted in Figure 7.8 where C_b is shown along $0.75 \leq x/L \leq x_4/L$ for all tests and with the roller minimum removed.

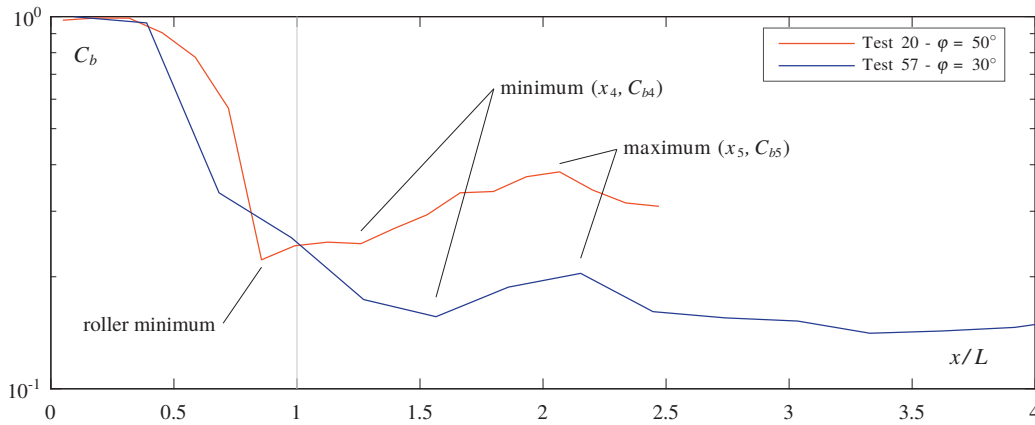


Figure 7.7 – Definition of the extrema of the bottom air concentration C_b

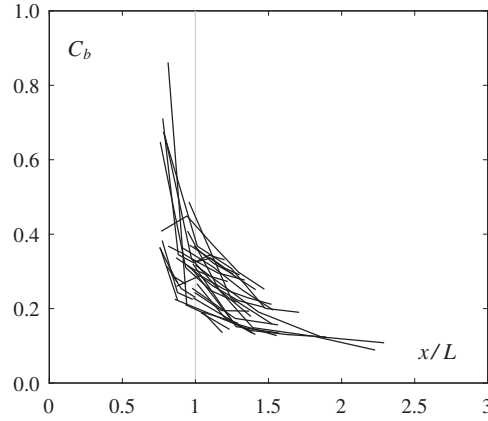


Figure 7.8 – Decrease of C_b along $0.75 \leq x/L \leq x_4/L$ with the roller minimum removed

From the minimum, C_b increases to a *maximum* (x_5 and C_{b5}) which is more pronounced for $\varphi = 50^\circ$. The maximum is not always distinct, especially for $\varphi = 30^\circ$. Without the maximum, or after the maximum, C_b tends towards the quasi-uniform bottom air concentration C_{bu} .

Tests with $W_o = 88$ (the tests with $F_o = 3.2$) show potential scale effects, particularly for C_{b4} (Figure 5.2c and 5.3c). Therefore, all the test with $W_o = 88$ were excluded from the analysis. They are however shown in the figures to illustrate the differences.

Similarly to the previous section on the C_a extrema, relations to obtain the C_b extrema are presented herein and their limitations are summarized in §10.2. The extrema are again related with the relative jet length L/h_o . The scale effects are discussed afterwards, and a connection between C_a and C_b is investigated at the end.

7.2.1 Minimum bottom air concentration

The streamwise coordinate of the minimum x_4/L is close to the jet impact for long relative jet length L/h_o , and further away for shorter relative jet length (Figure 7.9a). Tests with $W_o < 100$ are away from the general trend. A relation for x_4 is obtained with the four parameters characterizing the jet length ($r^2 = 0.841$)(Figure 7.9b)

$$\frac{x_4}{L} = 3.22 \cdot (1 + \sin \varphi)^{-1} \cdot (1 + \tan \alpha)^{-1.75} \cdot F_o^{-0.17} \cdot \left(\frac{t}{h_o} \right)^{-0.23} \quad (7.7)$$

Tests with $W_o < 100$ are well defined by this relation and suggests that the streamwise coordinate x_4/L is not affected by scale effects. It also indicates that the Froude number has an effect when x_4/L is expressed as a function of L/h_o . For the same L/h_o , x_4/L is closer from the jet impact for $F_o = 3.2$, than for higher Froude numbers. This influence is not visible in equation (7.7) as it is combined with the influence of F_o on the jet length L .

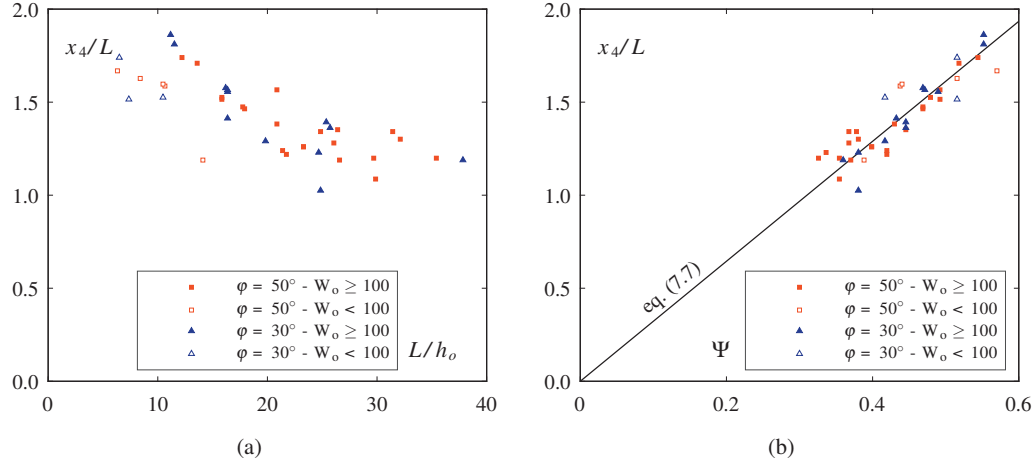


Figure 7.9 – Streamwise coordinate of the minimum x_4/L as a function of (a) the relative jet length L/h_o , (b) $\Psi = (1 + \sin \varphi)^{-1} \cdot (1 + \tan \alpha)^{-1.75} \cdot F_o^{-0.17} \cdot (t/h_o)^{-0.23}$

For the minimum bottom air concentration C_{b4} , there is an important influence of the chute angle φ and C_{b4} is higher for longer relative jet lengths L/h_o (Figure 7.10a). The tests with $W_o < 100$ do not show any major difference. However they are below the general trend that seem to converge at $C_{b4} \approx 0.1$ for $L/h_o = 0$. A good agreement for C_{b4} is found for $1 \leq x_4/L \leq 2$ with ($r^2 = 0.924$)(Figure 7.10b)

$$C_{b4} = 0.184 \cdot \sin^{1.4} \varphi \cdot (1 + \tan \alpha) \cdot F_o^{0.3} \cdot \left(\frac{t}{h_o} \right)^{0.15} \cdot \left(\frac{s}{h_o} \right)^{-0.3} \quad (7.8)$$

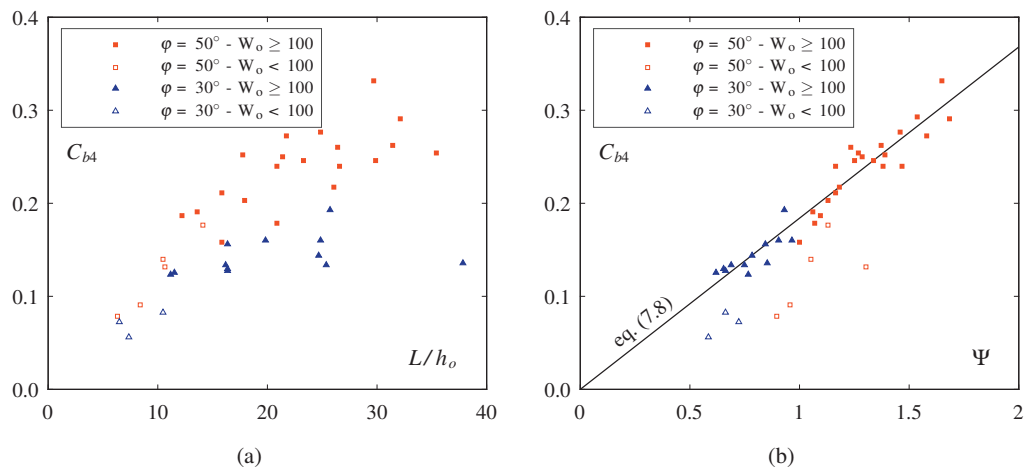


Figure 7.10 – Minimum bottom air concentration C_{b4} as a function of (a) the relative jet length L/h_o , and (b) $\Psi = \sin^{1.4} \varphi \cdot (1 + \tan \alpha) \cdot F_o^{0.3} \cdot (t/h_o)^{0.15} \cdot (s/h_o)^{-0.3}$

Values as low as half the estimation of equation (7.8) are obtained for with $W_o < 100$ clearly

indicating scale effects.

7.2.2 Maximum bottom air concentration

Many $\varphi = 30^\circ$ tests do not show a distinct maximum and were therefore excluded, including all tests with $W_o < 100$. The streamwise coordinate of the maximum x_5/L shows a similar trend compared to x_4/L (Figure 7.11a). A relation for x_5/L is obtained for $1.4 \leq x_5/L \leq 3.5$ with ($r^2 = 0.845$)(Figure 7.11b)

$$\frac{x_5}{L} = 53.8 \cdot (1 + \sin \varphi)^{-2} \cdot (1 + \tan \alpha)^{-4} \cdot F_o^{-1} \cdot \left(\frac{s}{t}\right)^{0.3} \quad (7.9)$$

The relative deflector height t/h_o and relative step height s/h_o had opposite powers and were therefore combined. The three tests with $W_o < 100$ have slightly lower x_5/L compared to equation (7.9).

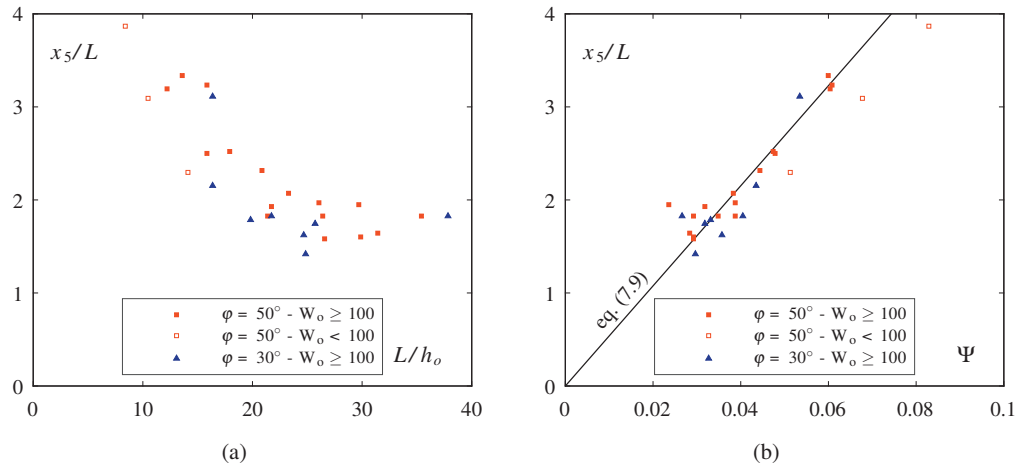


Figure 7.11 – Streamwise coordinate of the minimum x_5/L as a function of (a) the relative jet length L/h_o , (b) $\Psi = (1 + \sin \varphi)^{-2} \cdot (1 + \tan \alpha)^{-4} \cdot F_o^{-1} \cdot (s/t)^{0.3}$

As with previous air concentrations, the maximum bottom air concentration C_{b5} is highly influenced by the chute angle φ (Figure 7.12a). A relation for C_{b4} is obtained with $r^2 = 0.782$ (Figure 7.12b)

$$C_{b5} = 0.502 \cdot \sin^{1.5} \varphi \cdot F_o^{0.2} \cdot \left(\frac{t}{h_o}\right)^{0.25} \cdot \left(\frac{s}{h_o}\right)^{-0.1} \quad (7.10)$$

The three tests with $W_o < 100$ have similar C_{b5} compared to the others tests. Five other tests with $W_o < 100$ do not show a maximum.

Finally, stable values of C_b close to the quasi-uniform average air concentration C_{bu} are reached after $x/L \geq 4$ (Figures 5.2c and 5.3c).

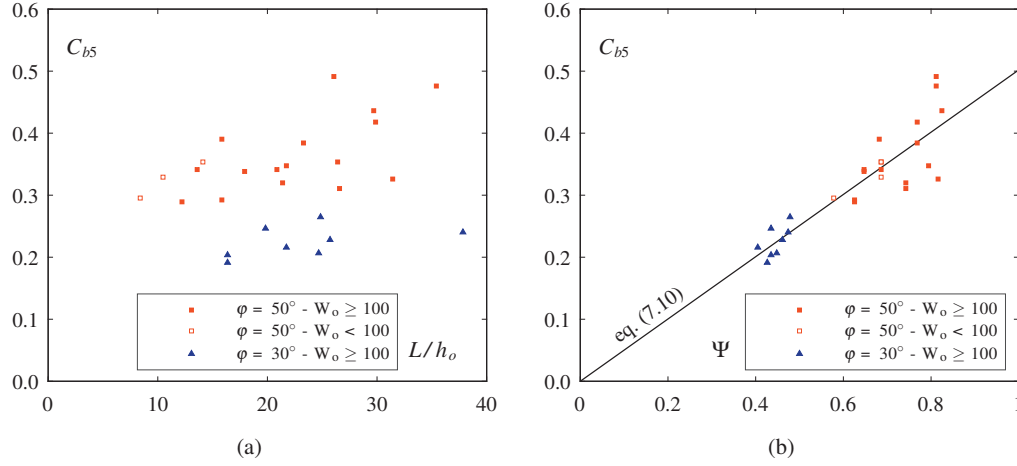


Figure 7.12 – Maximum bottom air concentration C_{b5} as a function of (a) the relative jet length L/h_o , and (b) $\Psi = \sin^{1.5} \varphi \cdot F_o^{0.2} \cdot (t/h_o)^{0.3} \cdot (s/h_o)^{-0.1}$

7.2.3 Scale effects on bottom air concentration

On a smooth chute aerator, Pfister and Hager (2010a) observed scale effects on the development of the bottom air concentration C_b for $W_o < 140$. The present study shows clear scale effects on C_{b4} for the $W_o = 88$ tests with an underestimation of the air concentration. Lower downstream, the scale effects are minimal for the maximum of air concentration C_{b5} with $\varphi = 50^\circ$, and the measured coordinate x_5/L seems to be reached further down than the estimation with equation (7.9). This difference in scale effects between the minimum C_{b4} and the maximum C_{b5} can be explained by flow acceleration between the two points which increases the local Weber number. No $\varphi = 30^\circ$ tests have a maximum and potential scale effects cannot be assessed for C_{b5} .

The tests with $F_o = 5.5$ and $h_o = 0.052$ m have the same discharge as the tests with $F_o = 3.2$, and thus the same Reynolds number $R_o = 205000$. With the increased approach flow velocity, the Weber number is $W_o = 106$ and these tests do not show scale effects. This highlights that scale effects limits have to be chosen carefully and a Reynolds number limit is not enough for $F_o \leq 5$ as suggested by Pfister and Chanson (2014).

7.2.4 Correlation of extrema

Various correlations between the three extrema of the average air concentration and the two extrema of the bottom air concentration were investigated since they are somewhat related. The only conclusive result is between the average air concentration spray maximum (x_3, C_{a3}) and the bottom air concentration maximum (x_5, C_{b5}). In average, x_5 is located slightly downstream of x_3 with $x_5 = 1.06 \cdot x_3$ ($r^2 = 0.882$) which suggests that air from the surface is rapidly entrained to the pseudo-bottom by flow turbulence (Figure 7.13a). The maximum bottom air concentration C_{b5} agrees well with a typical air concentration profile downstream of the inception point calculated

with C_{a3} (Chanson et al. 2002)(Figure 7.13b). Air concentration profiles are further investigated in §7.4.

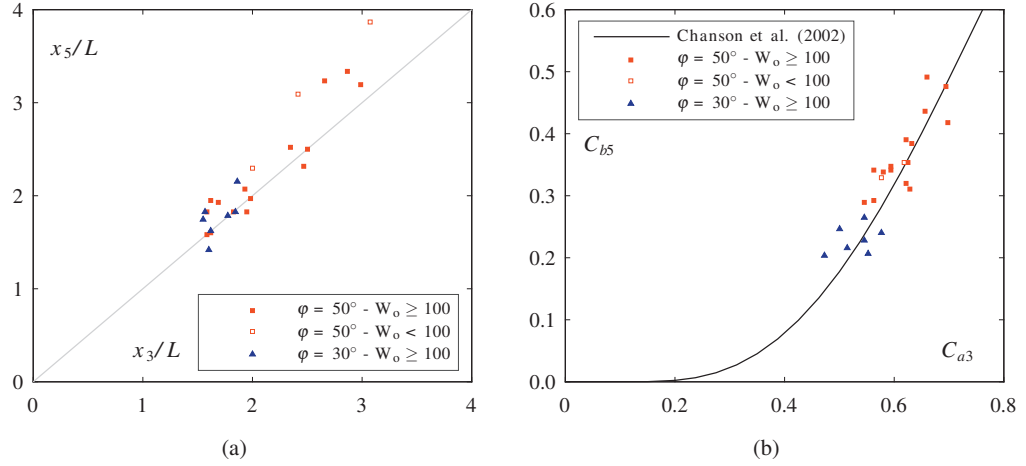


Figure 7.13 – Relation between (a) the coordinate x_3/L and x_5/L , (b) the air concentration C_{a3} and C_{b5} compared with the relation $C_b(C_a)$ of a typical air concentration profile (Chanson et al. 2002)

7.2.5 Effect of Froude number

Figure 7.14 presents a series of tests for both chute angles ϕ where only the Froude number F_o was varied to analyze its effect on the bottom air concentration C_b . On the left graphs, the streamwise coordinate is normalized with the jet length, and points show the extrema calculated with equations (7.7) to (7.10). On the right graphs, the dimensional streamwise coordinate is shown. The tests with $F_o = 3.2$ are shown despite their scale effects.

For a high Froude number F_o , the minimum bottom air concentration C_{b4} is higher and the normalized coordinate x_4/L is closer from the jet impact (Figure 7.14a,c). However, the dimensional coordinate x_4 is further away from the aerator for high F_o due to a longer jet (Figure 7.14b,d). Similarly, the maximum bottom air concentration C_{b5} is higher for a high Froude number F_o , its normalized coordinate x_5/L is closer from the jet impact, and the dimensional coordinate x_5 is further away.

The estimation of the minimum and maximum bottom air concentrations with equations (7.7) to (7.10) (points) are in good agreement with the measurements (lines), especially if the accuracy and resolution of the measurements is taken into account. The minimum is slightly underestimated for $F_o = 7.5$. For $F_o = 3.2$, the measured bottom air concentration C_b is underestimated due to scale effects. Nonetheless, the test for $\phi = 50^\circ$ shows a good agreement between the measurement and the estimation in the far-field zone ($x/L \geq 3$), which suggest that scale effects are limited on the lower part of the channel due to flow acceleration. For the lower chute angle $\phi = 30^\circ$ there are still scale effects for C_{b5} due to a slower flow acceleration.

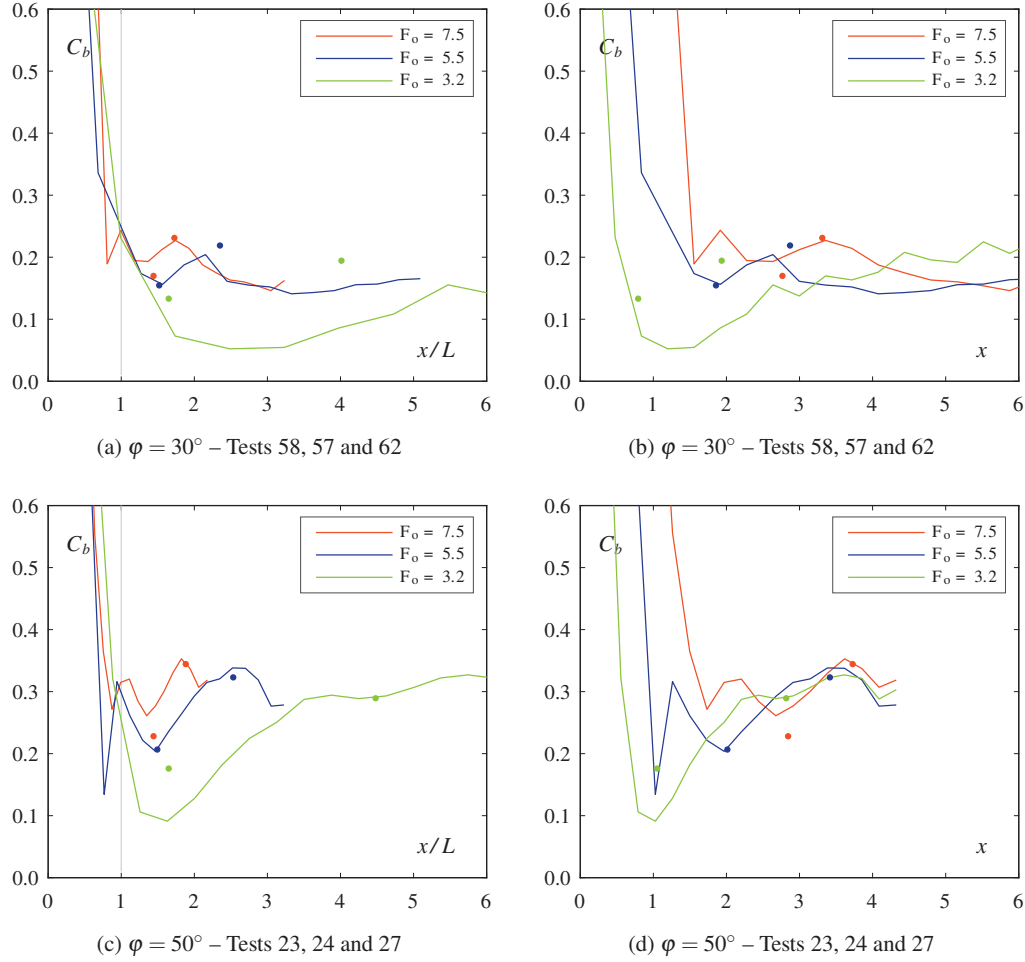


Figure 7.14 – Effect of the Froude number F_o on the bottom air concentration C_b . The points indicate the estimation calculated with equations (7.7) to (7.10)

7.2.6 Effect of chute geometry

The effect of the chute angle φ and relative step height s/h_o are presented in Figure 7.15. The large differences of air concentration with φ are related to the quasi-uniform bottom air concentration C_{bu} . The tests with $\varphi = 50^\circ$ show a greater increase between C_{b4} and C_{b5} than the tests with $\varphi = 30^\circ$. The small relative step height s/h_o leads to slightly larger C_b , and the minimum air concentration C_{b4} is systematically larger for $s/h_o = 0.4$. The relative coordinate x_4/L is practically unaffected by the step height, while the relative coordinate x_5/L is closer from the jet impact with a small s/h_o .

There is a good agreement of equations (7.7) to (7.10) (points) with the measurements (lines), especially for the minimum. The maximum C_{b5} is slightly overestimated for the two $\varphi = 30^\circ$ tests, but this is not the case for all $\varphi = 30^\circ$ tests.

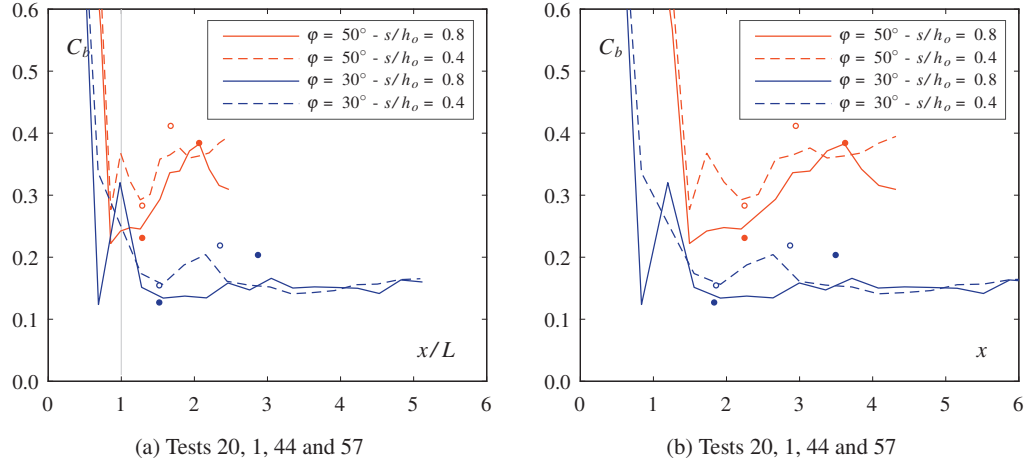


Figure 7.15 – Effect of the chute angle φ and relative step height s/h_o on the bottom air concentration C_b . The points indicate the estimation calculated with equations (7.7) to (7.10)

7.2.7 Effect of deflector

The effect of the deflector angle α and relative deflector height t/h_o are presented in Figure 7.16. A high α or t/h_o increases the jet length and in consequence increases the minimum bottom air concentration C_{b4} , decreases the normalized coordinate x_4/L and increases the dimensional coordinate x_4 . The same respective observation can be made for C_{b5} and x_5/L . The dimensional coordinate x_5 is however almost independent of the deflector geometry. Inserting equation (6.8) in equation (7.9), the coordinate x_5 can be expressed as $x_5 = 26.9 \cdot h_o \cdot F_o^{0.4} \cdot (t/h_o)^{0.1} \cdot (s/h_o)^{0.3}$. The flow depth has a major influence on x_5 , followed by F_o and s , and lastly t with a small exponent.

The estimation of equations (7.7) to (7.10) (points) agree well with the measurements (lines). The estimations for x_5 are not aligned for the same t/h_o since the measured jet length was used and not equation (6.8).

7.3 Comparison with the preliminary research of Pfister et al. (2006a)

The present study is compared to the preliminary investigation performed by Pfister et al. (2006a) on a similar stepped chute aerator configuration (§2.4.1). The constant geometrical parameters of the latter were $\varphi = 50^\circ$, $s = 0.093$ m, $\alpha = 8.13^\circ$ and $t = 0.008$ m with a standard ogee upstream of the aerator. Five discharge were tested and the main characteristics of each test are presented in Table 7.1.

The development of the average air concentration C_a and the bottom air concentration C_b downstream of the aerator are presented in Figure 7.17. An air concentration profile was measured at every step corner along $0.1 \leq x \leq 2.3$, but due to the large step height ($s = 0.093$ m) and the short jet length there is a smaller data resolution compared to the present study. The bottom air concentration

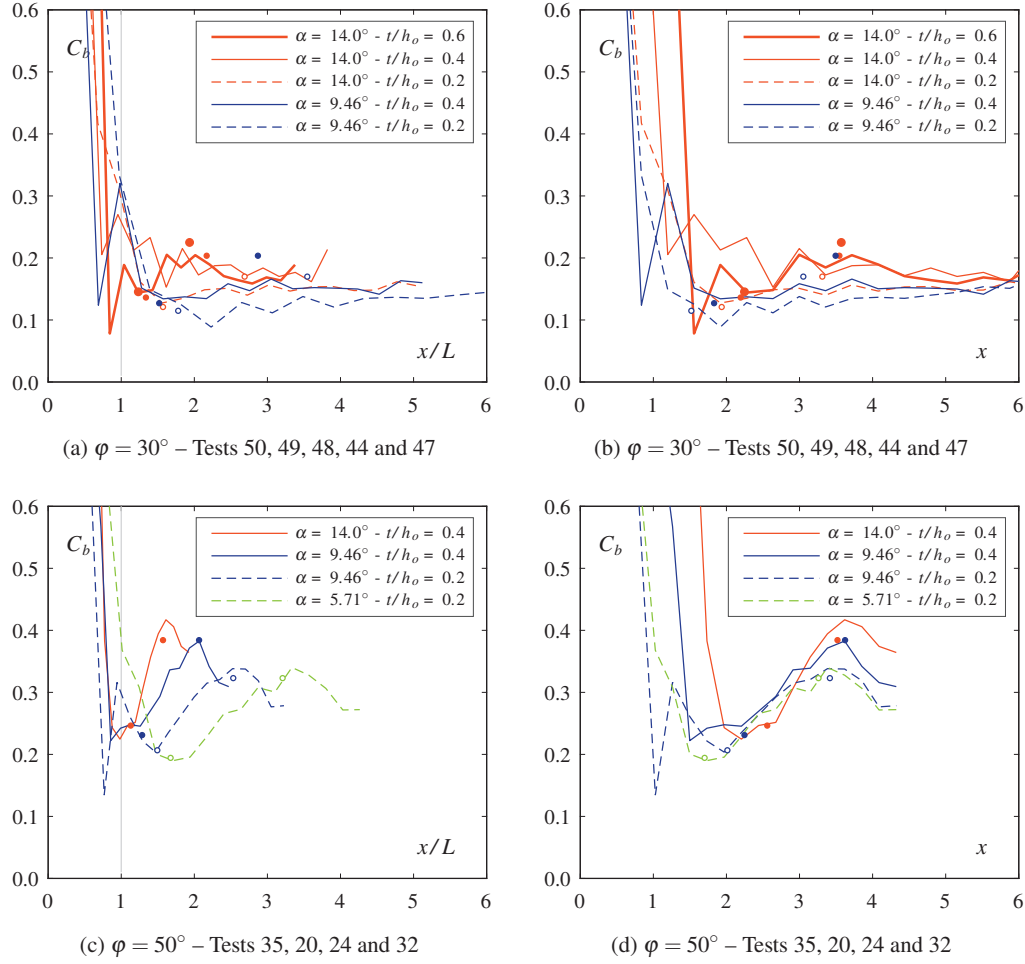


Figure 7.16 – Effect of the deflector angle α and relative deflector height t/h_o on the bottom air concentration C_b . The points indicate the estimation calculated with equations (7.7) to (7.10)

Table 7.1 – Tests of Pfister et al. (2006a) with their parameters

Test	q [m ² /s]	F_o	W_o	t/h_o	L/h_o
P1	0.109	5.8	70	0.24	10.3
P2	0.216	4.7	104	0.13	5.2
P3	0.431	3.6	151	0.07	1.7
P4	0.647	3.0	187	0.05	0.9
P5	0.859	2.7	216	0.04	0.5

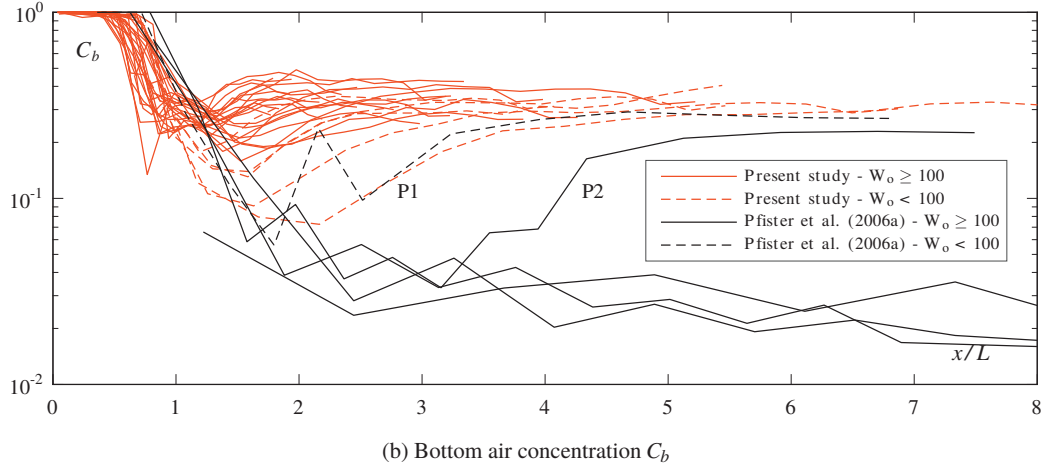
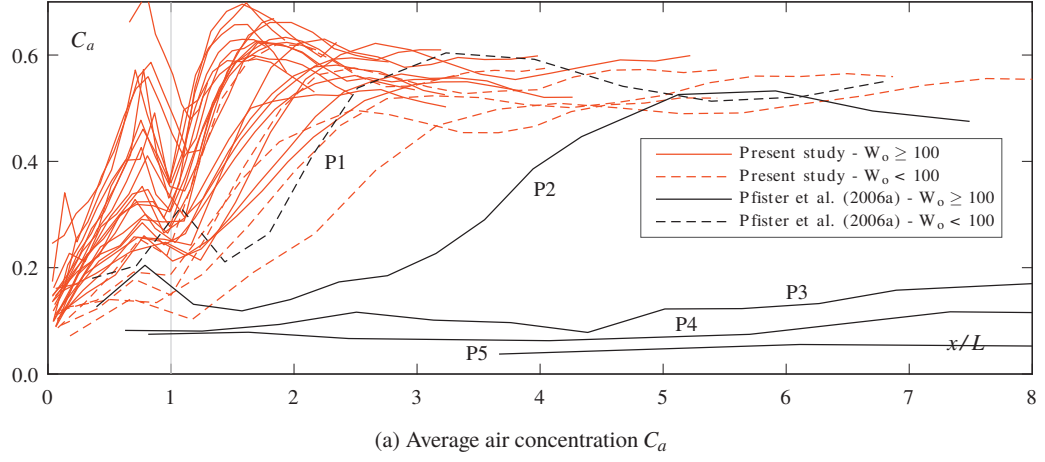


Figure 7.17 – Comparison of present study $\phi = 50^\circ$ tests with Pfister et al. (2006a)

C_b shows substantial differences, with the tests of Pfister et al. (2006a) reaching C_b values one order of magnitude lower than that of the present study. Test P1 is the most similar to the present study. However, it has a Weber number of $W_o = 70$ and scale effects are probable. Test P2 shows a decrease of C_b since only the bottom part of the profile is affected by the aeration (low C_a). A minimum is reached at $x/L \approx 3$, where a kind of inception occurs and the entire flow depth becomes aerated. Tests P3, P4 and P5 are only aerated with small air concentrations close to the bottom, and C_b continuously decreases due to the diffusion in the flow of air present at the bottom. Values of $C_b \leq 0.02$ are reached at the end of the channel without any increase in C_b .

Why are there such differences for a similar spillway and aerator geometry? Three causes have been identified:

- The relative deflector height $0.04 \leq t/h_o \leq 0.24$ of Pfister et al. (2006a) is small compared to $0.16 \leq t/h_o \leq 0.6$ for the present study. Ervine et al. (1995) showed that a deflector generates turbulence in the flow. A small deflector likely create less turbulence than a high one, and therefore less air is entrained.

- The relative jet length $0.5 \leq L/h_o \leq 10.3$ of Pfister et al. (2006a) is small compared to $6.3 \leq L/h_o \leq 44$ for the present study. Shorter jets entrain less air. Figure 7.9a shows that small L/h_o lead to a minimum bottom air concentration C_{b4} far from the jet impact, and according to Figure 7.10a with small C_{b4} .
- The subpressure Δp in the air cavity was not measured by Pfister et al. (2006a). If the subpressure was higher than $\Delta p/(\rho g h_o) \geq 0.1$, both the air entrainment and the jet length would have been reduced.

These three factors result in a partial aeration of the flow depth and consequently a low C_b which continuously decreases. The bottom air concentration C_b starts increasing only when the entire depth becomes aerated, which occurs after a point analogous to the inception point has been reached. It can therefore be concluded that minimum values of t/h_o and L/h_o are required for the aeration of the entire depth and to obtain the relatively high C_b observed for the present study.

7.4 Air concentration profiles

Typical air concentration profiles for $\varphi = 30^\circ$ are shown in Figure 7.18 for three relative jet length L/h_o . The chute and flow parameters are constant, and only the deflector geometry is varied. Profiles upstream of the jet impact are on the left, and downstream profiles on the right. On the latter, the diffusion model of Chanson et al. (2002), calculated with the average air concentration of the most downstream profile $C_{a,last}$, is shown.

The first profile in the jet shows a high air concentration gradient (almost horizontal line) on both the upper and lower surfaces. This gradient reduces in the following profiles as the jet starts entraining air. The most downstream profile in the jet shows the roller at the bottom, with $C < 0.9$. There is a larger aeration on the lower surface than on the upper surface of the shortest L/h_o (Figure 7.18a), and the minimum air concentration is found at $Z \approx 0.7$ for profile 3. Similar observations are made for the intermediate L/h_o (Figure 7.18c), with a minimum air concentration at $Z \approx 0.6$ for profile 3. The longest L/h_o shows a symmetrical aeration of both surfaces (Figure 7.18e), with a minimum air concentration at $Z \approx 0.5$ for profile 4.

Downstream of the jet impact, the core of the jet rapidly becomes aerated, particularly for the intermediate and long L/h_o . The shortest L/h_o (Figure 7.18b) shows a direct convergence to a stable air concentration profile that has identical characteristics as the quasi-uniform profile from reference tests (Figure 4.14e). A higher air entrainment than quasi-uniform condition occurs just after the impact for the intermediate L/h_o (profiles 7 and 8 in (Figure 7.18d). It corresponds to the spray maximum of the average air concentration (§7.1.3) and is even more apparent for the longest L/h_o (Figure 7.18f). The bottom air concentration ($Z \approx 0$) is hardly affected compared to the center of the profile ($Z \approx 0.5$). The three L/h_o end with the same average air concentration.

Most of these observations also apply for $\varphi = 50^\circ$ (Figure 7.19). There are more profiles in the jet since the spacing between the profiles Δx is shorter. The minimum air concentration in the jet is at

a smaller elevation than for $\varphi = 30^\circ$ and indicates a higher aeration from the upper surface. For the longest L/h_o (Figure 7.19d), the center of the jet shows an increase of air concentration between profiles 6 to 8. It then remains stable between profiles 8 to 10 where the jet becomes influenced by the roller and the flow downstream.

Downstream of the impact, the shortest L/h_o (Figure 7.19b) shows a decrease in the bottom air concentration between profiles 5 to 7 (minimum bottom air concentration C_{b4}), followed by an increase. For tests 20 and 35 (Figure 7.19d,f), the minimum is reached directly at the first profile after the impact, and the jet core becomes aerated faster. The three tests end with different average air concentrations $C_{a,last}$ close to the quasi-uniform average air concentration $C_{au} = 0.57$ according to Wilhelms and Gulliver (2005). Given that tests 32 and 20 show an air detrainment at $Z \approx 0.6$ at the end of the channel, it is likely that it would also occur on test 35 further downstream than the last profile measured.

7.5 Summary

Three extrema were observed for the average air concentration C_a (Figure 7.1):

- A *jet maximum* is observed at the location $x_1/L = 0.78$. The corresponding average air concentration C_{a1} can be obtained from equation (7.2) adapted from Pfister and Hager (2009).
- An *impact minimum* is observed just after the impact of the lower jet surface at the location $x_2/L = 1.03$. The corresponding average air concentration C_{a2} can be obtained from equation (7.4) expressed with the basic parameters of the study and no correlation was found for the air detrainment from the jet maximum average air concentration C_{a1} .
- A *spray maximum* is observed at a location x_3/L given by equation (7.5). The corresponding average air concentration C_{a3} can be obtained from equation (7.6). This maximum is more pronounced for a large deflector angle α or a large relative deflector height t/h_o . Further downstream, C_a tends towards the quasi-uniform average air concentration C_{au} .

The bottom air concentration C_b is characterized by $C_b = 1$ in the air cavity until the roller is encountered at $x/L \approx 0.8$. A local minimum is sometimes measured in the roller. From the jet impact, two extrema were observed (Figure 7.7):

- Similarly to smooth chute aerators, C_b rapidly decreases after the jet impact. However, a *minimum* is rapidly reached at x_4/L defined by equation (7.7) with a value C_{b4} defined by equation (7.8).
- A *maximum* occurs at x_5/L defined by equation (7.9) with a value C_{b5} defined by equation (7.10). This maximum is more pronounced for the chute angle $\varphi = 50^\circ$ than for $\varphi = 30^\circ$ where it is not always observed. A correlation was found with the spray maximum of the average air concentration (x_3, C_{a3}). Further downstream, C_b tends towards the quasi-uniform bottom air concentration C_{bu} .

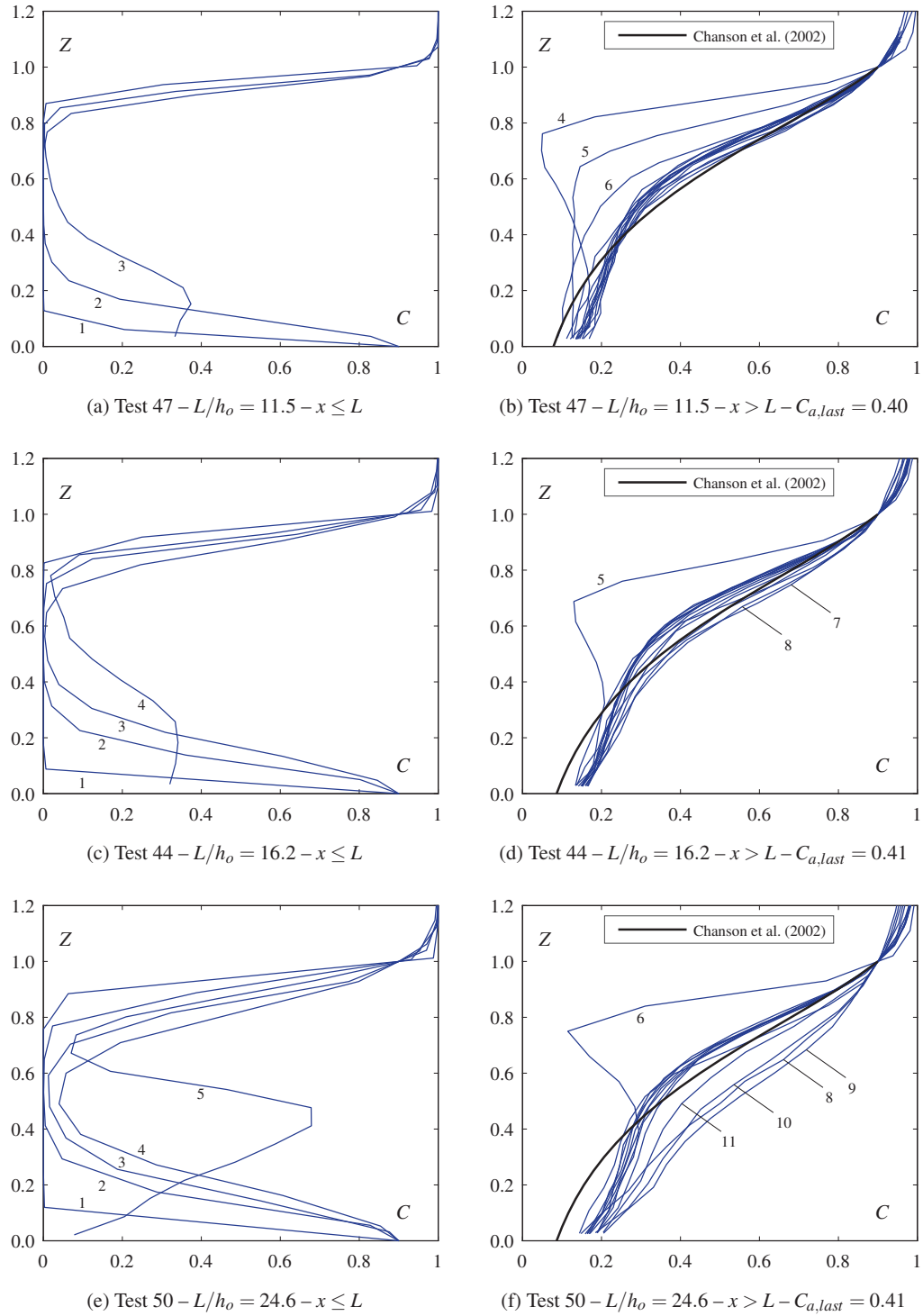


Figure 7.18 – Typical air concentration profiles (a, c, e) in the jet, and (b, d, f) downstream of the jet impact for three increasing relative jet lengths L/h_o . The chute and flow parameters are constant for the three tests ($\phi = 30^\circ$, $s = 0.06$ m, $F_o = 5.5$ and $h_o = 0.075$ m) and only the deflector geometry was changed. The profile order is indicated from 1 (upstream) to 18 (downstream), and $C_{a,last}$ indicates the value used for the profile of Chanson et al. (2002)

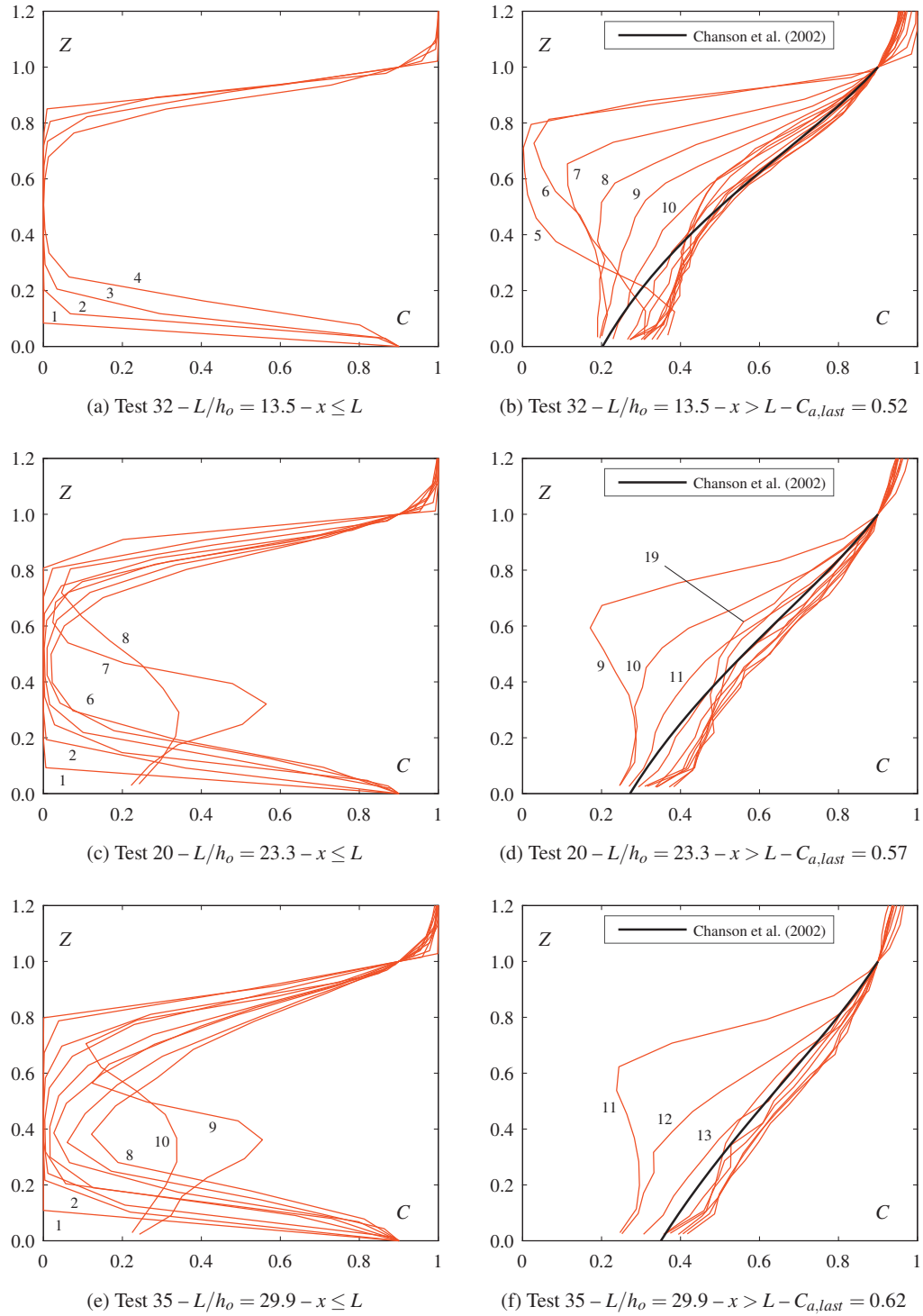


Figure 7.19 – Typical air concentration profiles (a, c, e) in the jet, and (b, d, f) downstream of the jet impact for three increasing relative jet lengths L/h_o . The chute and flow parameters are constant for the three tests ($\varphi = 50^\circ$, $s = 0.06$ m, $F_o = 5.5$ and $h_o = 0.075$ m) and only the deflector geometry was changed. The profile order is indicated from 1 (upstream) to 19 (downstream), and $C_{a,last}$ indicates the value used for the profile of Chanson et al. (2002)

The limitations of the present study associated with these relations are summarized in §10.2. In addition to the relations presented, the extrema of both C_a and C_b are related to the relative jet length L/h_o . Scale effects were observed for the minimum air concentration C_{b4} for the tests with $F_o = 3.2$ and Weber number $W_o = 88$. A scale effect limit is suggested at $W_o = 100$.

Excluding tests with scale effects, a minimum bottom air concentration $C_b = 0.09$ is observed for $\varphi = 30^\circ$ (test 47) and $C_b = 0.16$ (test 33) for $\varphi = 50^\circ$. These bottom air concentrations C_b are higher than the average air concentrations C_a observed by Peterka (1953), Rasmussen (1956) and Russell and Sheehan (1974) to stop cavitation damages. For the configurations tested, a stepped spillway is therefore fully protected against cavitation damages downstream of a single aerator.

The present study was compared to the preliminary study of Pfister et al. (2006a). The latter observed only a partial aeration of the flow depth after the jet impact and a continuous decrease of C_b until an inception point is reached far downstream. It contrasts with the present study where the entire depth was aerated for all tests. The differences originate in smaller relative deflector heights t/h_o and smaller relative jet lengths L/h_o for Pfister et al. (2006a). As a consequence and based on the results of the present study, a relative deflector height of $t/h_o > 0.16$ and a relative jet length $L/h_o > 8$ are recommended to aerate the entire depth and obtain comparable C_b to that of the present study.

Finally, air concentration profiles were presented for different relative jet lengths L/h_o . After the jet impact, the profiles measured rapidly tend towards typical profiles observed in self-aerated stepped chutes. High air concentrations are observed at mid-depth in the spray zone, especially for longer L/h_o .

Chapter 8

Effect of turbulence and pre-aeration

Literature shows that turbulence has an influence on the air entrainment in addition to the six basic parameters varied in this present study (Skrupalle 1994; Ervine et al. 1995). Having steps upstream of the aerator instead of the smooth bottom used on the model would increase turbulence. A grid is thus attached to the bottom to increase the bottom roughness, and to investigate the effect of the resulting turbulence.

Furthermore, the present study includes tests with a non-aerated approach flow. In special circumstances, for example if another aerator upstream is present or for small discharges, the approach flow can be partially aerated. Two tests are performed to evaluate the resulting aerator performance.

Qualitative characteristics of *grid* and *pre-aerated* tests are presented herein and compared to the *standard* tests previously described (tests 1–62). Table 3.3 shows the parameters of the grid and pre-aerated tests, and their corresponding standard test.

8.1 Tests characteristics

8.1.1 Grid tests

The addition of a grid (described in §3.4) increases the bottom roughness which generates a more turbulent boundary layer. This results in a larger jet spread and a higher air entrainment. Four tests were performed with the grid. Two are reference tests and the other two are the corresponding aerator tests. Flows with Froude numbers $F_o = 5.5$ and $F_o = 7.5$ were investigated, whereas the other parameters remained approximately constant with $\varphi = 30^\circ$, $s = 0.03$ m, $\alpha = 9.46^\circ$, $t = 0.03$ m and $h_o = 0.075$ m (Table 3.3).

With the grid, the mean pressure p measured at $x_p = -0.27$ m is decreased compared to the corresponding standard test. This is a model effect as the grid facilitates the dissipation of the pressure induced by the jetbox in the approach flow (Appendix C.1.1). The root mean square of the

pressure fluctuations p' shows an increase of 40–60 % compared to the standard tests. More details about pressure measurements are given in Appendix C.

8.1.2 Pre-aerated tests

For the pre-aerated tests, pressurized air is injected 15 m upstream of the jetbox to ensure an homogeneous distribution within the flow.

In order to compare the pre-aerated tests with the standard tests, the equivalent blackwater approach flow depth h_{wo} and equivalent blackwater approach Froude number F_{wo} are used. Two tests with aerator are investigated for Froude numbers $F_{wo} = 5.5$ and $F_{wo} = 7.5$ and the other parameters remained constant with $\varphi = 30^\circ$, $s = 0.03$ m, $\alpha = 9.46^\circ$, $t = 0.03$ m and $h_{wo} = 0.075$ m (Table 3.3).

To obtain the blackwater equivalent values, a reference air concentration profile is first measured at $x = 0$ without the aerator to avoid any effect of the deflector (§2.3.3). The jetbox opening is adjusted in order achieve the required h_{wo} . The deflector is then inserted and the air concentration profiled is measured again at $x = 0$. Figure 8.1 shows minimal differences between the air concentration profile without and with the aerator. The air concentration C is slightly smaller for $z \leq 0.07$ m as air is compressed by the deflector induced overpressure. The surface air concentration gradient is larger with the deflector. There is a distinct depth difference compared to the standard reference test measured slightly downstream at $x = 0.117$ m.

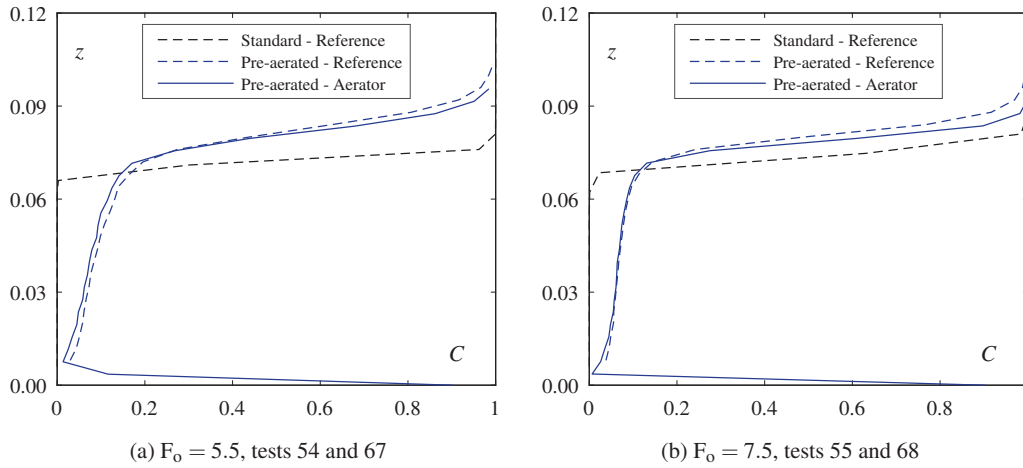


Figure 8.1 – Air concentration C profiles at $x = 0$ for the pre-aerated tests and $x = 0.117$ m for the standard tests. The elevation z is adjusted for the aerator test in order to have the lower jet surface z_{90l} at $z = 0$

Table 8.1 shows the approach flow characteristics derived from the air concentration profiles presented in Figure 8.1. As the profiles of standard tests are measured slightly downstream compared to pre-aerated tests, they have higher F_{wo} and smaller h_{wo} due to flow acceleration. The equivalent blackwater approach flow depth h_{wo} and equivalent blackwater approach Froude number F_{wo} of the pre-aerated reference tests are at the typical values h_o and F_o tested in standard tests. The approach

flow air discharge q_{Ao} is practically the same for tests 67 and 68 as the maximum capacity of the air supply was used.

Table 8.1 – Approach flow characteristics for the standard (measured at $x = 0.117$ m) and pre-aerated (measured at $x = 0$ m) tests

Test	Type	Configuration	h_{90o} [m]	h_{wo} [m]	F_{wo}	C_{ao}	q_{Ao} [m ² /s]
54	standard	reference	0.073	0.069	6.25	0.048	0.018
67	pre-aerated	reference	0.091	0.075	5.54	0.180	0.078
67	pre-aerated	aerator	0.089	0.073	5.75	0.181	0.079
55	standard	reference	0.077	0.071	8.18	0.075	0.039
68	pre-aerated	reference	0.088	0.075	7.47	0.144	0.081
68	pre-aerated	aerator	0.084	0.072	7.93	0.140	0.078

8.2 Reference tests with a grid

Two new grid reference tests (63 and 66) were performed under the same conditions as their corresponding standard reference test (respectively 54 and 66)(Table 8.2). They are compared in Figure 8.2. The most apparent difference is an upstream shift of ~ 0.3 m of the inception point (Table 8.2) which is clearly visible in the development of C_a and C_b . This was expected as the inception point is located higher for large steps (§2.1.3).

The flow depth h_{90} with the grid decreases upstream of the inception point. With a larger average air concentration C_a in that reach, it indicates a faster flow velocity with the grid. Table 8.2 shows the inception mixture flow depth h_i and the inception equivalent blackwater depth h_{wi} are reduced by the grid. The average air concentration at the inception point C_{ai} is increased for $F_o = 5.5$ whereas it is reduced for $F_o = 7.5$. There are minor differences downstream of the inception point.

Table 8.2 – Inception point characteristics for the standard and grid reference tests

Test	Type	F_o	x_i [m]	h_i [m]	h_{wi} [m]	C_{ai}
54	standard	5.52	2.07	0.094	0.071	0.24
63	grid	5.55	1.79	0.090	0.068	0.25
55	standard	7.49	1.93	0.111	0.082	0.26
66	grid	7.46	1.59	0.097	0.075	0.23

8.3 Aerator tests with a grid or pre-aerated approach flow

8.3.1 Visual comparison

Photos of standard, grid and pre-aerated tests are shown in Figure 8.3 for $F_o = 7.3$ – 7.5 and otherwise similar conditions. Compared to the standard test, the grid test shows a shorter jet due to the slightly

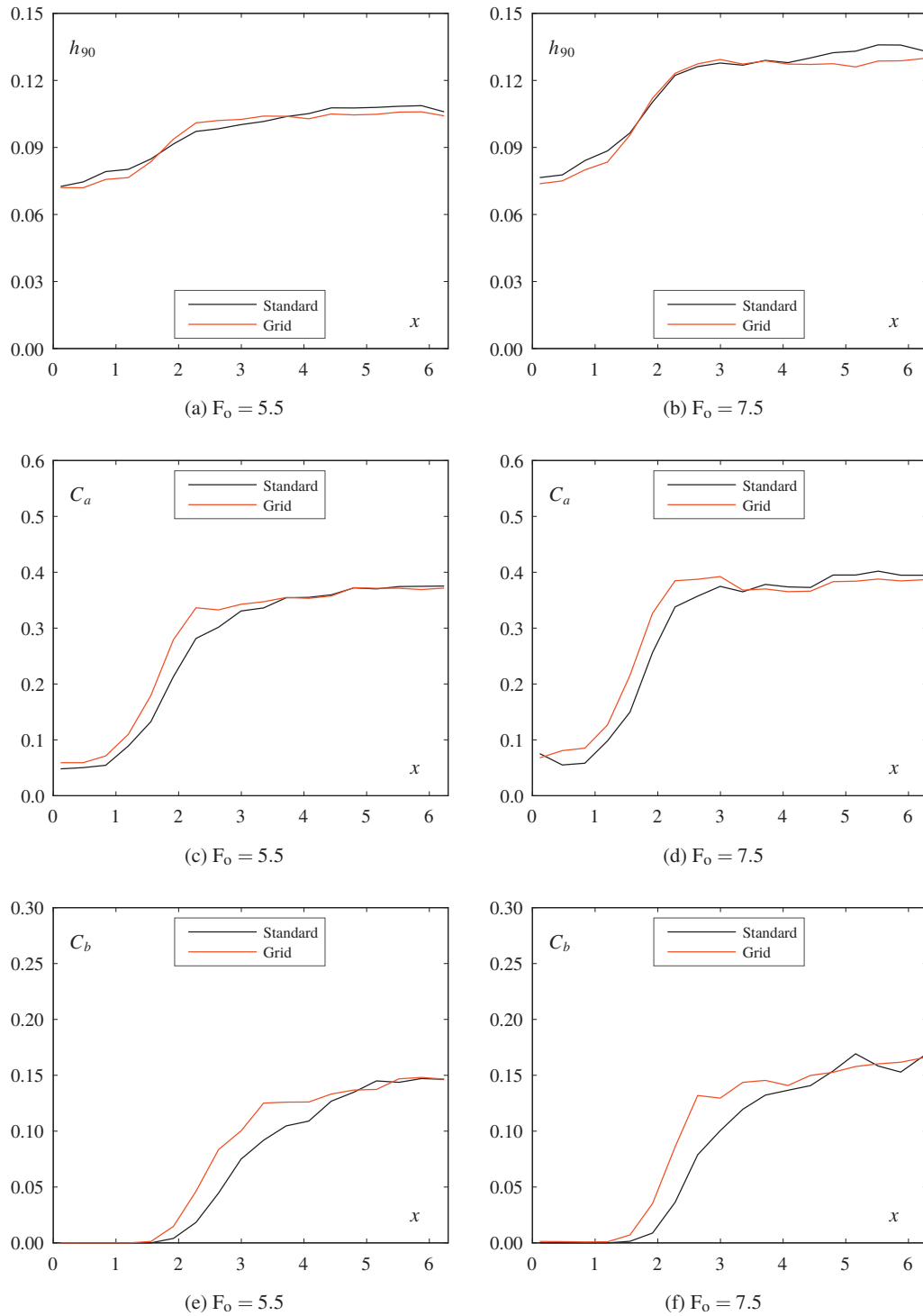


Figure 8.2 – Comparison of the streamwise development of the flow depth h_{90} , the average air concentration C_a and the bottom air concentration C_b for the standard reference and the grid reference tests, and the two Froude numbers F_0 investigated

lower Froude number F_o . The increase in jet spread is revealed by a shorter blackwater core and an impact of the lower jet surface on the pseudo-bottom closer to the aerator. Less spray is observed for the grid test downstream of the jet impact. The pre-aerated test shows exclusively whitewater. No distinct difference can be observed on the upper jet surface, while a slightly larger spread is visible for the lower jet surface. This spread is lower than that of the grid test. Similarly to the grid test, less spray is observed downstream of the jet impact compared to the standard test.

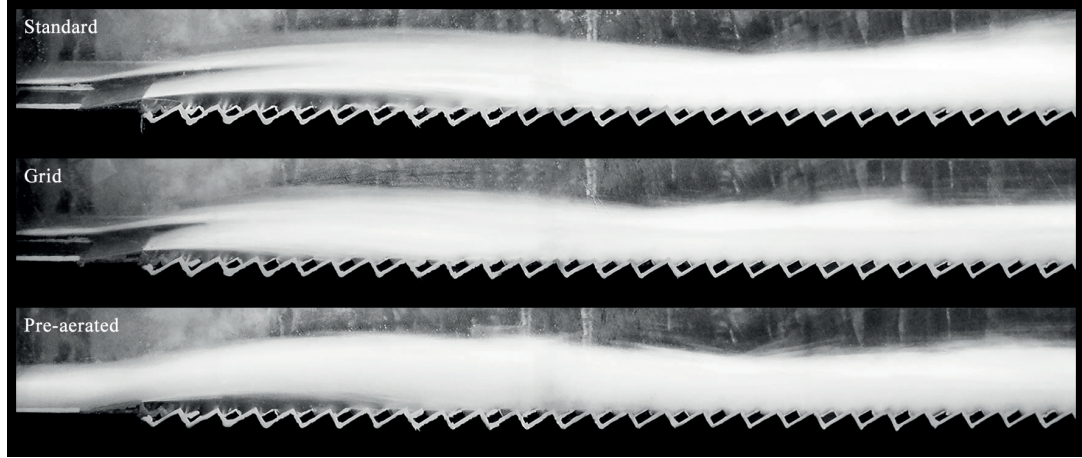


Figure 8.3 – Visual comparison of the standard, grid and pre-aerated tests (respectively tests 58, 65 and 68) for $F_o = 7.3\text{--}7.5$

8.3.2 Jet length and air entrainment coefficient

Both the grid and pre-aerated tests show a decrease in the jet length L (Figure 8.4). The decrease is due to a higher turbulence that enhances the jet spread. For the grid test 65, there is also a larger subpressure than any of the standard tests (Table 8.3) which contributes reducing the jet length. No effect of a pre-aerated approach flow on L was observed by Pfister et al. (2011) on a smooth chute aerator, and the difference is likely due to a lower bottom flow turbulence in standard tests of the present study (§6.3.4). The lower takeoff angle α_{tl} is decreased for the grid and pre-aerated tests compared to the standard tests. The upper takeoff angle α_{tu} is decreased for the grid tests, and slightly increased for pre-aerated tests compared to standard tests.

Table 8.3 – Jet characteristics of standard, grid and pre-aerated aerator tests

Test	Type	F_o	L [m]	α_{tl} [°]	α_{tu} [°]	L_{bwc} [m]	β	$\Delta p/(\rho gh_o)$
57	standard	5.49	1.22	7.91	9.06	1.08	0.112	0.00
64	grid	5.52	1.00	5.90	8.01	0.54	0.216	0.04
67	pre-aerated	5.54	0.95	7.20	10.35	-	0.149	0.01
58	standard	7.51	1.93	7.73	9.20	0.66	0.207	0.07
65	grid	7.29	1.56	5.65	7.99	0.47	0.297	0.16
68	pre-aerated	7.47	1.66	7.19	9.45	-	0.244	0.09

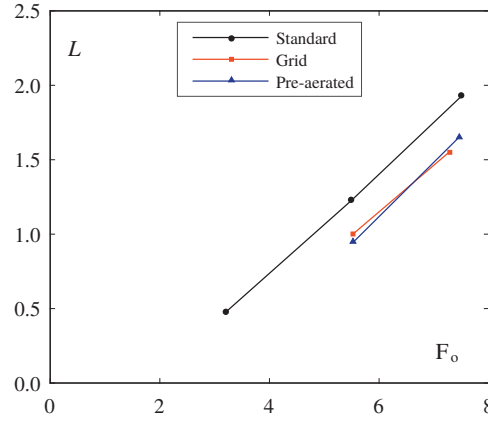


Figure 8.4 – Comparison of the jet length L as a function of the Froude number F_o for the standard, grid and pre-aerated tests

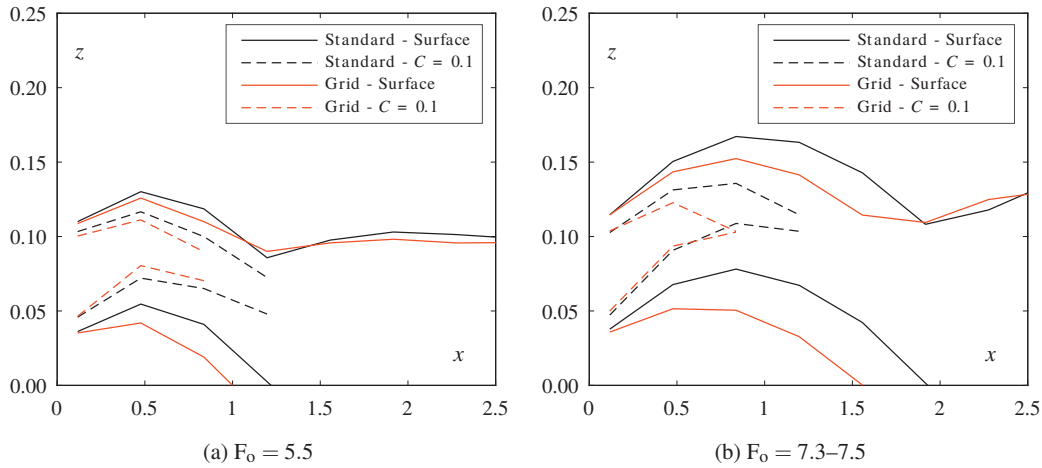


Figure 8.5 – Comparison of the reduction of the core defined by $C = 0.1$ in the jet for the standard and grid tests

Figure 8.5 compares the decrease of the core defined by the contour $C = 0.10$ for the standard and grid tests. For the lower Froude number ($F_o = 5.5$), there is a significant increase of the lower jet surface spread with the grid, compared to the standard test. In contrast, there are minimal differences on the upper jet surface. For the higher Froude number $F_o \approx 7.5$, the general trajectory of the jet is different due to variation in the Froude numbers (Table 8.3). Nevertheless, there is again an important increase of the lower jet surface spread with the grid. The spread on the upper surface for $F_o \approx 7.5$ is more important than that of $F_o = 5.5$. As a consequence of the increased spread on both jet surfaces, the length of the blackwater core length L_{bwc} ($C \leq 0.01$) is reduced (Table 8.3).

The addition of the grid increases the air entrainment coefficient β (Figure 8.6). The grid test with $F_o \approx 7.3$ has a small cavity subpressure Δp , so that β would be even higher without the subpressure.

Expressing β as a function of the relative jet length L/h_o gives for the grid tests (Figure 8.6b)

$$\beta \approx 0.0151 \cdot \frac{L}{h_o} \quad (8.1)$$

The air entrainment coefficient β for the grid tests is consequently twice that of standard tests given by equation (5.1). There is only a moderate increase with a pre-aerated approach flow compared to standard tests. Only a small effect of the pre-aerated approach flow on β was observed by Pfister et al. (2011) on a smooth chute aerator. For the present study, the increase of β with the pre-aerated approach flow is due to an increase of bottom flow turbulence.

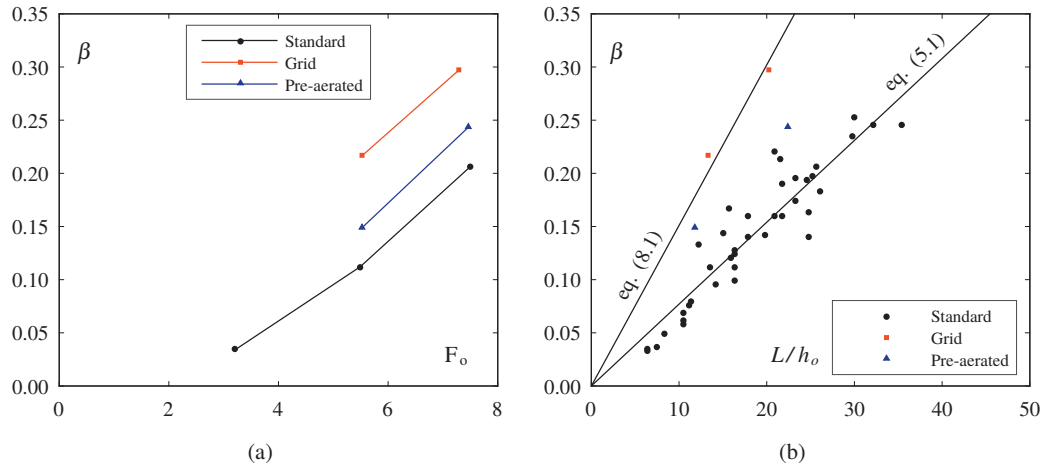


Figure 8.6 – Comparison of the air entrainment coefficient β as a function of (a) the Froude number F_o and (b) the relative jet length L/h_o for the standard ($\Delta p/(\rho g h_o) \leq 0.1$), grid and pre-aerated tests

8.3.3 Flow development

The two flow conditions investigated for the grid tests (64 and 65) and pre-aerated tests (67 and 68) are compared to the corresponding standard test (57 and 58) in Figure 8.7. The definitions of the air concentration extrema defined in Chapter 7 are used further to describe the results.

For $F_o = 5.5$, the surface elevation z_{90} is higher in the jet zone for the pre-aerated test since the approach flow depth h_{90o} includes an air discharge (Figure 8.7a). For the grid test, z_{90} is slightly decreased. Downstream of the jet impact, the three tests are similar. For $F_o = 7.3$ – 7.5 , there is less differences in the jet for the pre-aerated test compared to the standard test, and pre-aeration seems to dampen the jet impact as there is less spray (Figure 8.7b). The decrease in z_{90} observed for the grid test is partially due to a lower Froude number compared to the standard test. All three tests are remarkably similar at the end of the channel.

The average air concentration C_a is greatly increased in the jet for the grid and pre-aerated tests compared to the standard tests (Figure 8.7c,d). The impact minimum C_{a2} is however not proportion-

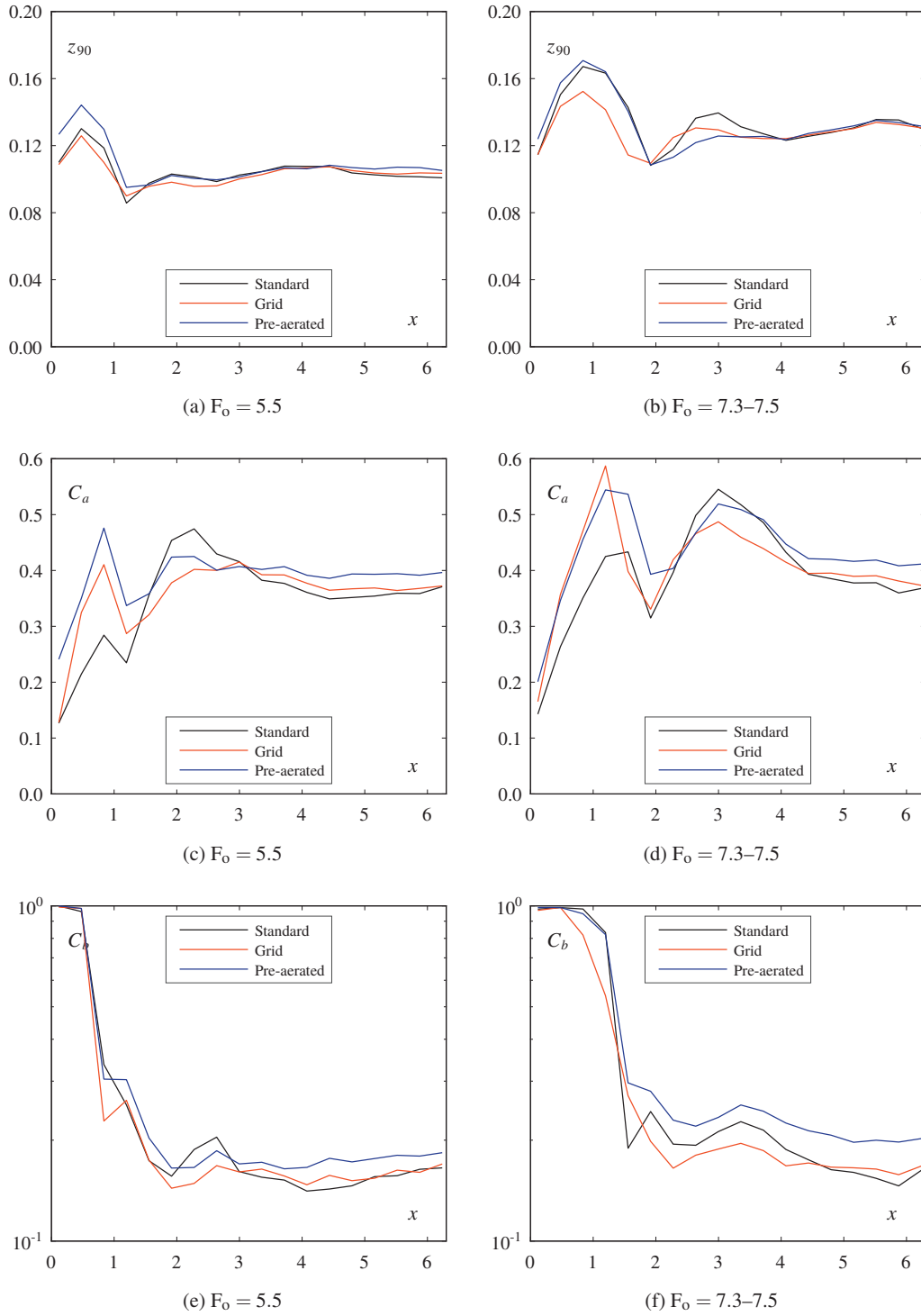


Figure 8.7 – Comparison of the streamwise development of the flow depth h_{90} , the average air concentration C_a and the bottom air concentration C_b for the standard, the grid and the pre-aerated tests

ally increased, and for the grid with $F_o = 7.3$ it is similar to the standard test. The spray maximum C_{a3} is reduced for the pre-aerated tests and the grid tests, suggesting a dampening of the jet impact and the resulting spray by a higher air concentration in the jet. In the far-field zone, the grid tests are similar to the standard tests, whereas the pre-aerated flow have a higher C_a . An increase of C_a was also observed downstream of pre-aerated smooth chute aerators (Pfister et al. 2011). The uniform average air concentration for $\varphi = 30^\circ$ is $C_{au} = 0.40$ according to Wilhelms and Gulliver (2005) and the pre-aerated tests seem to converge towards this value. It would suggest that quasi-uniform conditions are reached faster with a pre-aerated approach flow.

A semi-logarithmic plot is used to better assess the differences in the bottom air concentration C_b (Figure 8.7e,f). The grid tests show a lower minimum C_{b4} and maximum C_{b5} than that of standard tests. The differences are small in the far-field zone for the grid tests. The pre-aerated tests have a higher minimum C_{b4} than the standard tests. For $F_o = 5.5$, the maximum bottom air concentration C_{b5} is smaller than that of the standard test, whereas it is higher for the high Froude number. The higher C_b for pre-aerated tests of the present study contrasts with the smooth chute aerator tests of Pfister et al. (2011), where a minimal decrease of C_b was observed with pre-aeration. Similarly to C_a , C_b seems to converge faster to quasi-uniform flow conditions in the far-field zone for pre-aerated tests.

8.4 Summary

Adding a grid on the chute bottom upstream of the aerator to increase the flow turbulence leads to a larger spread of the lower jet surface. This spread reduces the relative jet length L/h_o and increases the air entrainment coefficient β . Despite the higher air entrainment in the jet, the average air concentration C_a after the jet impact is similar to that of tests without grid. The higher air concentration in the jet seems to dampen the jet impact as less spray is observed. Surprisingly, a slightly lower minimum bottom air concentration C_{b4} is observed. The flow is hardly affected in the far-field zone. While interesting, these results have little practical application as the flow turbulence is defined by the concrete roughness and can hardly be influenced on a prototype spillway.

A pre-aerated approach flow with $C_{ao} = 0.14$ to 0.18 increases the flow turbulence, yet not as much as the grid. It reduces the jet length L and increases the air entrainment coefficient β . A higher average air concentration than for the grid or the standard tests is observed at the jet impact. Similarly to grid tests, the spray is reduced compared to standard tests. The bottom air concentration C_b is increased, except for the maximum with $F_o = 5.5$. Pre-aerated tests have higher air concentrations C_a and C_b in the far-field zone and seem to convergence faster to the quasi-uniform flow air concentrations C_{au} and C_{bu} . These results somewhat differ from the pre-aerated smooth chute aerator tests of Pfister et al. (2011) which might be explained by distinct approach flow turbulence conditions.

Chapter 9

Design example

An example is given to demonstrate the results obtained. An aerator is designed for a design unit discharge $q_D = 60 \text{ m}^2/\text{s}$ on a stepped spillway with a chute angle $\varphi = 50^\circ$ and a step height $s = 1.5 \text{ m}$ (Example E1). The spillway is made of a standard ogee crest, with steps starting from the tangency point (Figure 9.1). The flow characteristics on the same spillway are also shown for a lower discharge with a ratio of ogee head to ogee design head of $H/H_D = 0.5$ (Example E2).

9.1 Spillway drawdown curve and cavitation index

To begin, the spillway characteristics such as the design head H_D , the flow depth h , the Froude number F and the cavitation index are calculated until the inception point. The streamwise coordinate x_c starting from the ogee crest is used (Figure 9.1), and the numerical values obtained are summarized in Table 9.1.

Considering a standard ogee (U.S. Army Corps of Engineers 1987) designed for the unit discharge q_D , the design head H_D can be obtained from

$$H_D = \left(\frac{q_D}{C_{dD} \cdot \sqrt{2g}} \right)^{2/3}$$

with $C_{dD} = 0.494$ as the discharge coefficient for the design head.

The unit discharge q of example E2 with $H/H_D = 0.5$ can be obtained from

$$q = C_d \cdot \sqrt{2g} \cdot H^{3/2}$$

with $C_d = C_{dD} \cdot (H/H_D)^{0.12}$ as the discharge coefficient.

The step roughness k is given by $k = s \cdot \cos \varphi$, and the step roughness Froude number F_k by

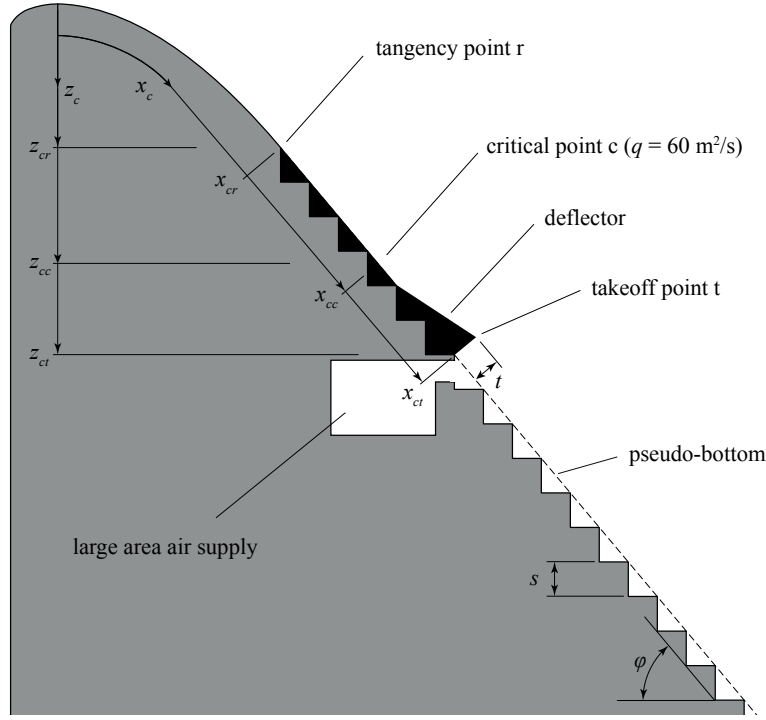


Figure 9.1 – General definition scheme of the design example

equation (2.7). The location of the inception point L_i can then be estimated with equation (2.22) from Meireles et al. (2012).

The flow depth h_r and bottom pressure p_r at tangency point r (Figure 9.1) between the smooth ogee and the pseudo-bottom of the stepped chute are obtained from the charts of U.S. Army Corps of Engineers (1987). The mean flow velocity u_r is obtained from $u_r = q/h_r$ and the cavitation index σ_r from equation (2.48) with $p_a = 101$ kPa and $p_v = 1.23$ kPa. To calculate the head H_r relative to the crest elevation, the kinetic energy correction coefficient α_k from Meireles et al. (2012) is used

$$\alpha_k = 1 + 0.19 \left(\frac{x_c}{L_i} \right)^{1.28}$$

For example E1, the cavitation index at the tangency point $\sigma = 0.71$ is already close to the critical value for cavitation inception.

From the tangency point, the drawdown curve is calculated until the inception point considering a stepped chute. Various studies presented a large range of friction factors f (§2.1.10), and generally for self-aerated quasi-uniform flow. Matos and Meireles (2014) show that f is larger on the upper part than on the lower part of a chute. For $\phi = 50^\circ$ in quasi-uniform flow, Boes and Hager (2003a) gives $f \approx 0.06$, and Takahashi and Ohtsu (2012) gives $f = 0.06$ with $s/h_c = 0.2$. In a closed conduit, Tozzi (1994) suggests $f = 0.12$ for $\phi = 53^\circ$ and $h/k = 4$. A conservative friction factor of $f = 0.1$ is chosen. A low friction factor reduces the friction, increases the flow velocities and

Table 9.1 – Spillway and flow characteristics for examples E1 and E2

General characteristics	E1	E2	Unit
Unit discharge q	60	19.52	[m ² /s]
Critical depth h_c	7.16	3.39	[m]
Ogee head H	9.09	4.55	[m]
Step height s	1.5	1.5	[m]
Step chord length L_s	1.96	1.96	[m]
Step roughness k	0.96	0.96	[m]
Step roughness Froude number F_k	23.1	7.5	[-]
Location of inception point L_i	70.8	30.2	[m]
Tangency point r			
Streamwise coordinate x_{cr}	14.97	14.97	[m]
Relative coordinate x_{cr}/L_i	0.21	0.50	[-]
Vertical coordinate z_{cr}	7.89	7.89	[m]
Flow depth h_r	3.49	1.29	[m]
Flow velocity u_r	17.19	15.15	[m/s]
Froude number F_r	2.94	4.26	[-]
Bottom pressure $p_r/(\rho g)$	0.50	0.56	[m]
Cavitation index σ_r	0.71	0.92	[-]
Head H_r	8.07	5.28	[m]
Critical cavitation point c ($\sigma = 0.7$)			
Streamwise coordinate x_{cc}	21.7	26.8	[m]
Relative coordinate x_{cc}/L_i	0.31	0.89	[-]
Vertical coordinate z_{cc}	13.02	16.97	[m]
Step # $(z_{cc} - z_{cr})/s$	3.4	6.1	[-]
Flow depth h_c	3.24	1.12	[m]
Flow velocity u_c	18.54	17.48	[m/s]
Froude number F_c	3.29	5.28	[-]
Bottom pressure $p_c/(\rho g)$	2.08	0.72	[m]

thus decreases the cavitation index. The drawdown curve obtained is compared in Figure 9.2 to equation (2.4) of Meireles et al. (2012). The agreement confirms the friction factor selected. The offset at $x_c/L_i = 0.21$ and $x_c/L_i = 0.50$ respectively for example E1 and E2 is due to the change in bottom pressure at the tangency point. Upstream of this point the bottom pressure is reduced by the convex ogee profile, while downstream the hydrostatic pressure is used. In reality, there is a gradual transition.

The critical cavitation index $\sigma_c = 0.7$ (§2.2.3) is reached at the point c (Figure 9.1). The regions $x_c/L_i \geq 0.31$ for example E1 and $x_c/L_i \geq 0.89$ for example E2 are exposed to cavitation and require aeration. In number of steps from the tangency point, the exposed region begins after $(z_{cc} - z_{cr})/s = 3.4$ steps and $(z_{cc} - z_{cr})/s = 6.1$ steps respectively. The flow characteristics of the critical cavitation point c are given in Table 9.1.

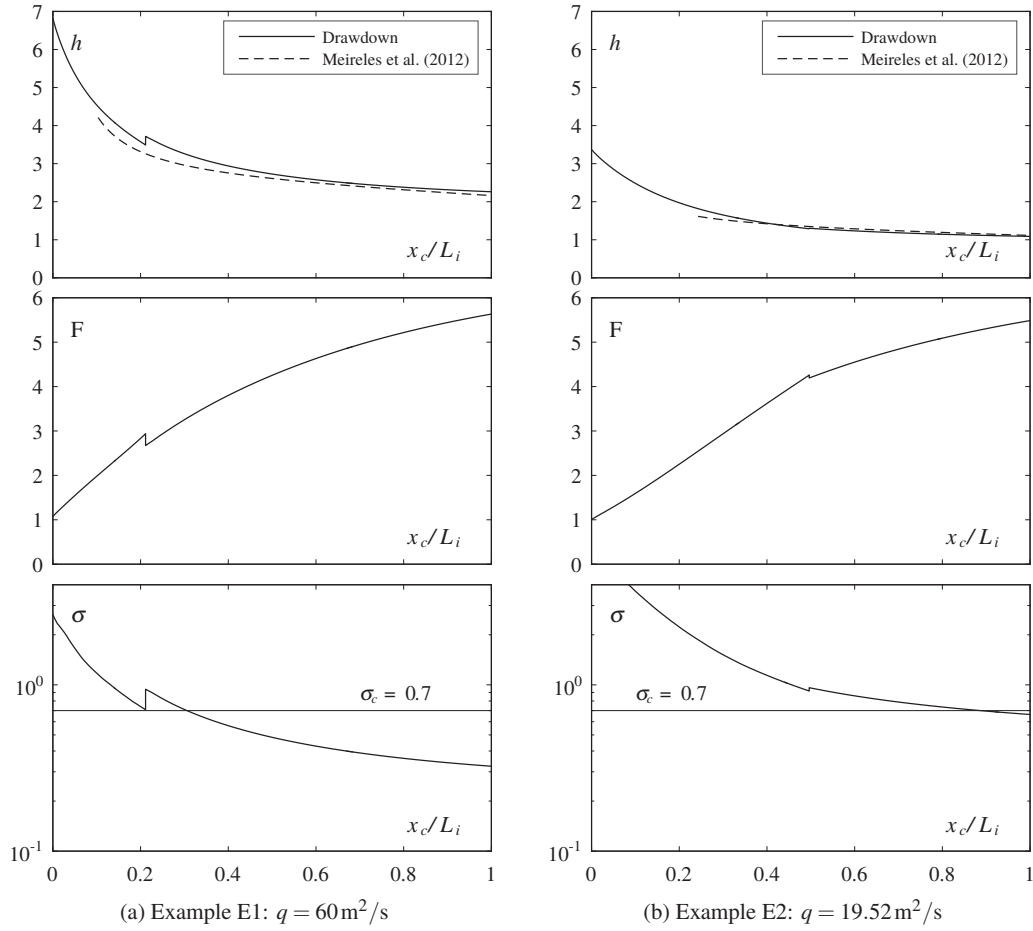


Figure 9.2 – Flow depth h , Froude number F and cavitation index σ from the crest of the spillway until the inception point

9.2 Aerator and jet characteristics

The flow properties at the location of the critical cavitation point c for $q = 60 \text{ m}^2/\text{s}$ are chosen as the approach flow of the aerator for both examples. The deflector geometry is defined first, and the jet characteristics are calculated afterwards. The two examples are compared to the measured values of a similar model test scaled to prototype dimensions (Table 9.2). For example E1 it is test T27 with a scale factor $\lambda = 45$, and for E2 it is test T21 with $\lambda = 21$.

A deflector angle $\alpha = 9.46^\circ$ (slope of 1:6) is chosen as it produces more turbulence than $\alpha = 5.71^\circ$ (slope of 1:10) and a lower jet than $\alpha = 14.0^\circ$ (slope of 1:4). A relative deflector height of $t/h_o = 0.2$ is chosen and rounded to the closest multiple of 0.05 m (Table 9.2), resulting in a deflector length L_d about two times the step chord length L_s .

The step where $\sigma = 0.7$ occurs as well as the steps upstream are filled to the pseudo-bottom to obtain a smooth bottom. The two steps downstream are also filled to place the deflector. The latter is positioned so that its crest is aligned in the streamwise direction with a step edge (Figure 9.1).

Table 9.2 – Deflector and jet characteristics for examples E1 and E2, and their closest corresponding scaled model tests T27 and T21

General characteristics	E1	T27	E2	T21	Unit
Scale factor λ	-	45	-	21	[-]
Unit discharge q	60	61.3	19.52	19.62	[m ² /s]
Approach flow Froude number F_o	3.29	3.16	4.89	5.49	[-]
Approach flow depth h_o	3.24	3.38	1.18	1.09	[m]
Relative step height s/h_o	0.46	0.80	1.28	1.15	[-]
Deflector characteristics					
Deflector angle α	9.46	9.46	9.46	9.46	[°]
Deflector height t	0.65	0.68	0.65	0.63	[m]
Relative deflector height t/h_o	0.20	0.20	0.55	0.58	[-]
Deflector length L_d	3.90	4.05	3.90	3.78	[m]
Deflector relative length L_d/Ls	1.99	1.15	1.99	2.30	[-]
Streamwise coordinate of takeoff x_{ct}	26.72	-	26.72	-	[m]
Vertical coordinate of takeoff z_{ct}	16.9	-	16.9	-	[m]
Jet characteristics					
Air entrainment coefficient β	0.063	0.050	0.141	0.182	[-]
Air entrainment unit discharge q_A	3.80	3.06	2.75	3.58	[m ² /s]
Takeoff flow depth h_t	2.86	2.75	1.05	0.98	[m]
Takeoff velocity u_t	21.26	22.66	18.93	20.37	[m/s]
Lower takeoff angle α_{tl}	6.67	6.71	8.43	8.80	[°]
Upper takeoff angle α_{tu}	6.60	6.30	9.03	9.20	[°]
Maximum jet elevation z_{90max}	3.98	3.76	2.39	2.31	[m]
Jet length L	24.6	28.3	24.4	28.4	[m]
Relative jet length L/h_o	7.6	8.4	20.8	26.0	[-]
Jet impact angle γ	7.5	5.8	8.5	7.5	[°]
Blackwater core length L_{bwc}	78.8	-	19.3	-	[m]

The deflector could be placed higher upstream, but the lower Froude number would reduce its performance.

The coordinate of the deflector crest from the ogee crest is x_{ct} in the streamwise direction and z_{ct} in vertical elevation (Table 9.2). Thereafter the coordinate x and z are used (Figure 3.9) to describe the jet and the flow development. The streamwise coordinate x_c is given by $x_c = x_{ct} + x$, and the vertical elevation of the bottom $z_c = z_{ct} - x \sin \phi$.

The lower and upper jet trajectories determination was presented in the example of §6.10. To summarize the procedure, the air entrainment coefficient β is calculated with equation (5.2), takeoff flow depth h_t with equation (6.3), the flow takeoff velocity u_t with equation (6.2), the lower takeoff angle α_{tl} with equation (6.4), the upper takeoff angle α_{tu} with equation (6.5), the maximum jet elevation z_{max} with equations (6.11) and (2.63), the jet length L with $z(T) = 0$ in equation (2.63), the jet impact angle on the pseudo-bottom γ with equation (6.9), and finally the blackwater core length L_{bwc} with equation (6.13).

The trajectories of example E1 and E2 obtained are compared respectively to the scaled measured trajectories of test T27 and T21 in Figure 9.3. The examples have slightly larger flow depths h_t than the scaled model tests, which reduces the takeoff velocities u_t and the jet lengths L compared to the model tests.

The results obtained are only valid for a small cavity subpressure $\Delta p/(\rho g h_o) \leq 0.1$, and the air supply needs to be designed accordingly.

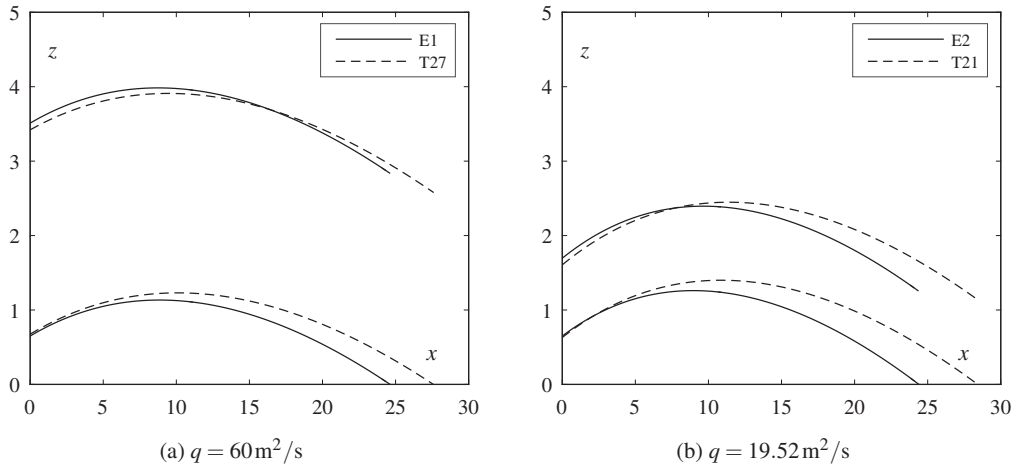


Figure 9.3 – Jet trajectories of examples E1 and E2 compared to their closest upscaled model test, respectively test T27 and T21

9.3 Air concentration development

To determine the development of the average air concentration C_a downstream of the aerator, the three extrema are calculated (§7.1). The jet maximum is obtained with $x_1/L = 0.78$ and C_{a1} with equation (7.2). The impact minimum is obtained with $x_2/L = 1.03$ and C_{a2} with equation (7.4). The jet maximum (x_3, C_{a3}) is calculated with equations (7.5) and (7.6). The quasi-uniform average air concentration C_{au} is calculated with Wilhelms and Gulliver (2005). The values obtained are given in Table 9.3. Test T27 has no values as it shows a nearly continuous growth and therefore no extrema. The result is shown as well in Figure 9.4. An arbitrary $C_a = 0.05$ is chosen for $x = 0$, and it is considered that quasi-uniform flow is reached at $x/L = 4$. The dotted segments between the points for the examples E1 and E2 are only indicative. Although examples and tests have slightly different initial conditions and a different jet length, a good agreement is obtained.

The two extrema of the bottom air concentration C_b downstream of the aerator are calculated similarly. The minimum (x_4, C_{b4}) is calculated with equations (7.7) and (7.8), whereas the maximum (x_5, C_{b5}) is calculated with equations (7.9) and (7.10). The quasi-uniform bottom air concentration C_{bu} is taken from Table 4.1. The values obtained are given in Table 9.3 and shown in Figure 9.4. The roller is neglected and C_b starts decreasing at $x/L = 0.8$. The large difference in the minimum

Table 9.3 – Deflector and jet characteristics for examples E1 and E2, and their closest corresponding upscaled model tests T27 and T21. No values are given for tests T21 and T27 when the extrema are undefined or when there are scale effects for the bottom air concentration

Average air concentration	E1	T27	E2	T21	Unit
Coordinate jet maximum x_1	19.2	-	19.0	-	[m]
Jet maximum average air concentration C_{a1}	0.12	-	0.31	-	[-]
Coordinate impact minimum x_2	25.4	-	25.1	-	[m]
Impact minimum average air concentration C_{a2}	0.15	-	0.24	-	[-]
Coordinate spray maximum x_3	66.5	-	48.3	56.2	[m]
Spray maximum average air concentration C_{a3}	0.50	-	0.65	0.66	[-]
Bottom air concentration					
Coordinate minimum x_4	40.5	-	29.7	36.4	[m]
Minimum bottom air concentration C_{b4}	0.21	-	0.20	0.22	[-]
Coordinate maximum x_5	89.6	-	59.7	56.2	[m]
Maximum bottom air concentration C_{b5}	0.31	-	0.39	0.49	[-]
Vertical coordinate below crest $z_c(x_5)$	85.1	-	62.2	-	[m]
Quasi-uniform flow characteristics					
Start of quasi-uniform flow x_u ($x_u/L = 4$)	98.5	-	97.6	-	[m]
Quasi-uniform average air concentration C_{au}	0.57	-	0.57	-	[-]
Quasi-uniform bottom air concentration C_{bu}	0.32	-	0.32	-	[-]

between example E1 and test T27 is due to scale effects for test T27. Example E2 and test T21 agree well considering the approach flow differences. The maximum C_{b5} is reached $z_c = 85.1$ m or $z_c = 62.2$ m vertically below the crest, respectively for test E1 and E2. As with stepped spillways without aerator, large dams are required to reach a quasi-uniform flow conditions

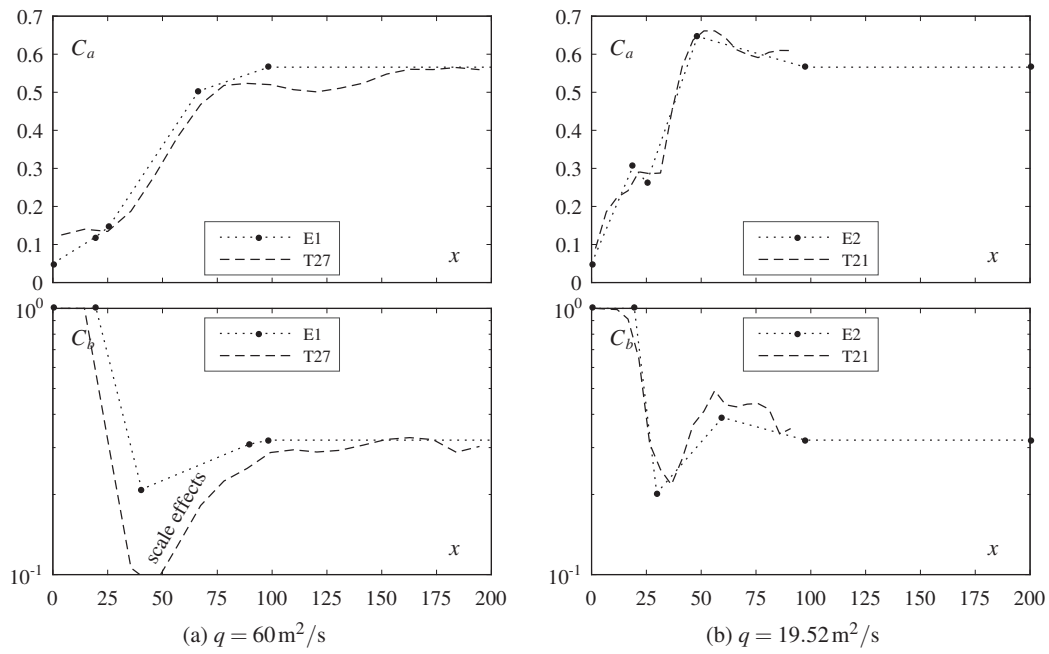


Figure 9.4 – Average C_a and bottom C_b air concentration development downstream of the deflector.
Note: test T27 showed scale effects for C_b

Chapter 10

Conclusions

Aerators protect spillways against cavitation damages by entraining air at the flow bottom. The performance of an aerator on a stepped spillway was systematically investigated herein on a physical model. The latter allowed to measure the air entrained by the aerator as well as the resulting average and bottom air concentration development downstream of it. The main findings and limitations of the research are summarized herein.

10.1 Results

Reference tests without the aerator were performed to have reference values in order to assess the effect of the aerator, and to compare the model data to literature. The following conclusions were obtained:

- The inception point was defined with $C_b = 0.01$. Equation (4.1) was suggested for the mixture flow depth h_i at the inception point, and equation (4.2) for the equivalent blackwater flow depth h_{wi} at the inception point.
- Quasi-uniform conditions are reached at a distance of $\sim 20h_c$ after the inception point. The quasi-uniform mixture flow depth h_{90u} and equivalent blackwater depth h_{wu} compare well with literature. The quasi-uniform average air concentration C_{au} is likely independent from step height s , and equivalent to that of smooth chutes. Similarly, the results show that C_{bu} is mainly influenced by the chute angle ϕ , and values for a chute angle $\phi = 50^\circ$ and $\phi = 30^\circ$ are suggested in Table 4.1.

For the *aerator tests*, the main conclusions are:

- The flow downstream of the aerator was divided in the same three zones as observed on smooth chutes (Pfister and Hager 2010a) being a function of the normalized coordinate x/L : (i) The jet zone for $0 \leq x/L \leq 1$ where the flow elevation is highly influenced by the deflector geometry; (ii) The spray and reattachment zone for $1 \leq x/L \leq 3$ where spray is created due to the jet deflection and where there is a rapid development of the air concentration; (iii) The

far-field zone for $x/L \geq 3$ where the flow stabilizes and gradually tends towards quasi-uniform values.

- Similarly to smooth chutes, the air entrainment coefficient β is correlated with the relative jet length L/h_o . Equation (5.2) is suggested to obtain β as a function of the studied parameters. For a deflector angle of $\alpha \approx 10^\circ$, a minimum Froude number is required to start the air entrainment, being $F_o = 2.0$ for a chute angle $\varphi = 50^\circ$ and $F_o = 2.5$ for $\varphi = 30^\circ$. A higher F_o is necessary for a smaller α . At the jet impact, the chute angle φ likely has an effect on the air detrainment and recirculation in the air cavity.
- The upper and lower surfaces of the jet generated by the deflector were fitted with ballistic trajectories. The datasets of Pfister (2008) and Steiner et al. (2008) were used to broaden the parameter range (Table 6.2). The analysis indicates how to define the upper and lower trajectories of a deflector jet, as well as the jet length. It includes four parts: (i) Determination of the takeoff flow depth with equation (6.3) (Bernoulli); (ii) Calculation of the takeoff velocity with equation (6.2); (iii) Estimation of the lower takeoff angle with equation (6.4) or the upper take off angle with equation (6.5); (iv) The trajectory is then given by equation (2.63) from which the maximum elevation, the jet length and the jet impact angle can be obtained. A good agreement was found for the present study and Steiner et al. (2008), while the jet length is slightly overestimated for Pfister (2008) probably due to different approach flow turbulence. Alternately, the jet length can be obtained directly as a function of the studied parameters with equation (6.8).
- The average air concentration C_a was defined with three extrema (Figure 7.1): (i) A jet maximum occurs in the jet shortly before the jet impact; (ii) A minimum appears at the jet impact; (iii) A spray maximum occurs in the spray zone. A correlation with the relative jet length L/h_o was observed. Equations (7.1) to (7.6) were presented for the streamwise position and average air concentration of the three extrema. After the spray maximum, C_a tends towards the quasi-uniform average air concentration C_{au} .
- The bottom air concentration C_b was defined with two extrema (Figure 7.1): (i) After the jet impact, C_b rapidly decreases to a local minimum; (ii) A maximum, related to the average air concentration spray maximum, occurs for some tests in the spray zone. Equations (7.7) to (7.10) for the streamwise position and bottom air concentration of the two extrema were presented. After the spray maximum, C_b tends towards the quasi-uniform bottom air concentration C_{bu} . There is no continuous detrainment as observed on smooth chutes, and therefore one single aerator is supposed to be sufficient. To increase the minimum of C_b , the Froude number F_o , the chute angle φ , the deflector angle α and the relative deflector height t/h_o should be increased, whereas the relative step height s/h_o should be decreased. Practically, mainly α and t can be adapted, i.e. the deflector geometry.
- The minimum bottom air concentration observed for all aerator tests was $C_b = 0.09$. It is higher than the generally recommended average air concentration found in literature (Peterka 1953; Rasmussen 1956; Russell and Sheehan 1974).

- The present study was compared to the preliminary study of Pfister et al. (2006a). The latter observed only a partial aeration of the flow depth after the jet impact and a continuous decrease of C_b until an inception point is reached far downstream. It contrasts with the present study, where the entire depth was aerated for all tests. The differences originate in smaller relative deflector heights t/h_o ($0.04 \leq t/h_o \leq 0.24$) and smaller relative jet lengths L/h_o ($0.5 \leq s/h_o \leq 10.3$) for Pfister et al. (2006a).
- As a consequence and based on the results of the present study, a relative deflector height of $t/h_o > 0.16$ and a relative jet length $L/h_o > 8$ are recommended for the relevant discharge to aerate the entire depth and obtain comparable results to that of the present study.
- The influence of an increased approach flow turbulence was investigated. It increases the spread of the jet and the air entrainment coefficient β . Less spray was observed downstream of the jet impact as the increased air concentration in the jet dampens the jet deflection. There are however little differences in the average air concentration C_a downstream of the jet impact, and slightly lower bottom air concentrations C_b are observed.
- A pre-aerated approach flow upstream of the deflector was tested. An increased turbulence was observed, and therefore a higher entrainment coefficient β . Downstream of the aerator, higher C_a and C_b were measured compared to standard tests with a non-aerated approach flow.
- A practical design example was given to illustrate the results obtained and was compared to the results of a test scaled to prototype dimensions.
- Except the sparsely documented spillway of Danjiangkou (Lin and Han 2001), no cavitation damages were observed so far on stepped spillways up to the knowledge of the author. Two explanations are possible: (i) Although cavitation can occur on stepped spillways, steps are not sensitive to damages due to most of the cavitation occurring away from the boundary (Frizell et al. 2015); (ii) The absence of reported damages is a consequence of low unit discharges used in the past decades leading to high inception points. Future will show how high unit discharges perform on stepped spillways.

10.2 Limitations of the study

The study is limited by the following considerations:

- Six dimensional parameters were investigated (Figure 3.9), resulting in five dimensionless parameters. The range of the latter are: chute angle $30^\circ \leq \varphi \leq 50^\circ$, relative step height $0.32 \leq s/h_o \leq 1.16$, deflector angle $5.7^\circ \leq \alpha \leq 14^\circ$, relative deflector height $0.16 \leq t/h_o \leq 0.60$ and approach flow Froude number $3.2 \leq F_o \leq 7.5$.
- For the jet trajectories, the addition of the datasets of Pfister (2008) and Steiner et al. (2008) allowed to extend the range of the parameters to: chute angle $0^\circ \leq \varphi \leq 50^\circ$, deflector angle

$5.7^\circ \leq \alpha \leq 33.2^\circ$, relative deflector height $0.10 \leq t/h_o \leq 1.65$ and approach flow Froude number $3.2 \leq F_o \leq 10.4$.

- The relative cavity subpressure $\Delta p/(\rho g h_o)$ was measured but not varied. By choosing large areas in the air supply, the experiments had negligible cavity subpressures. The few tests that did not fulfill the criteria $\Delta p/(\rho g h_o) \leq 0.1$ were excluded for the analysis of the air entrainment coefficient β and the jet length L . The maximum subpressure measured of all tests was $\Delta p/(\rho g h_o) = 0.16$.
- The chute bottom upstream of the deflector was smooth, and a jetbox was used to set the approach flow conditions.
- Regarding the scaling of the experiments, the Reynolds number range was $202\,000 \leq R \leq 486\,000$ and the approach flow Weber number range $87 \leq W_o \leq 209$, following most of the recommendations to minimize scale effects related to air concentrations. As anticipated, tests with $F_o = 3.2$ and $W_o \approx 88$ showed some scale effects on the bottom air concentration C_b . No distinct scale effects were observed for the tests with $F_o = 5.5$ and $W_o \approx 106$, and a limit of $W_o \geq 100$ is therefore suggested herein to limit scale effects.

10.3 Outlook

The following topics could be investigated in the future to expand the knowledge on stepped spillway aerators:

- The jet impact on the steps modifies the pressure distribution on the steps. The pressures should be systematically measured in all the steps close to the jet impact to assess if negative fluctuating pressure peaks occur.
- The bottom surface roughness and the turbulent boundary layer thickness influence the air discharge entrained into the flow by the aerator. It was investigated by Skripalle (1994) on offset aerators and should be pursued on deflector aerators. Although turbulence can hardly be influenced on prototype-scaled aerators given that the surface is made of concrete, it would be of interest to broaden the scientific knowledge on air entrainment.
- As described in §7.2.3, tests with a Froude number $F_o = 3.2$ were by trend affected by scale effects for the bottom air concentration C_b . Similar tests could be performed at a larger scale to assess the aerator effect and the development of C_b with low F_o .

Appendix A

Air entrainment coefficient

The air entrainment coefficient β as a function of the relative jet length L/h_o is further analyzed in an attempt to include the effect of turbulence. Then additional relations for β as a function of the basic parameters are given.

A.1 Relations based on the jet length

An excellent correlation is obtained between the unit discharge of air q_A and the product of the jet length and the pressure fluctuations $L \cdot p' / (\rho g)$ (Figure A.1a), although the dimensions are incorrect. The normal fluctuating velocity u' should be used instead of pressure fluctuations p' . It was hypothesized that p' is proportional to u' .

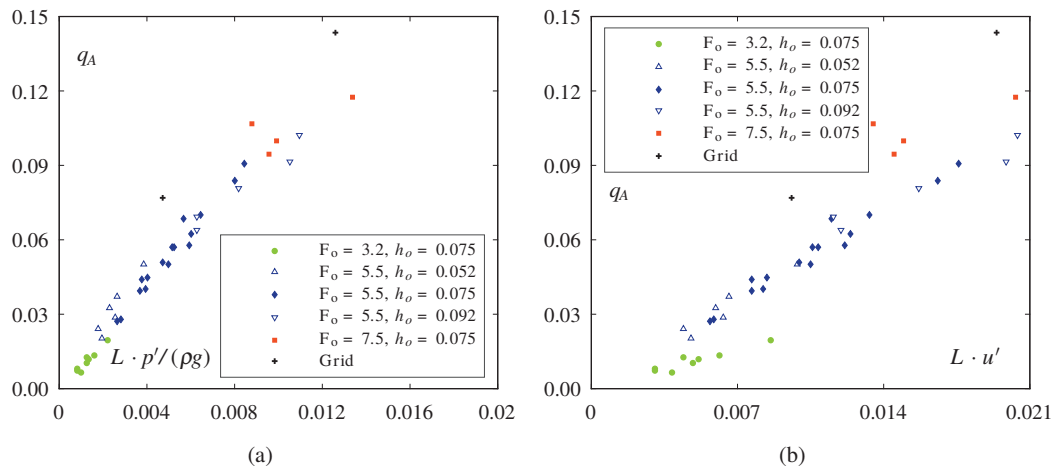


Figure A.1 – Relations for the specific air discharge q_A as a function of the relative jet length L

The normal fluctuating velocity u' was therefore estimated in Appendix C.3. The values obtained are **physically inaccurate and too low** due to the large size of the pressure transducers used, but they **might still be representative of general trends**. The unit air discharge q_A is plotted in Figure A.1b

as a function of $L \cdot u'$ to observe the trend. The results show different slopes of $\beta(L \cdot u')$ depending on the Froude number F_o , with a low slope of $F_o = 3.2$. Ervine et al. (1995) suggested that aeration only starts for $u' \geq 0.25$ m/s, and $(u' - 0.25)$ should be used instead of u' . This can lead to scale effects on models. It is not possible to apply this here due to the error in the estimation of u' . As the tests with $F_o = 3.2$ have the lowest u' , this might explain the lower slope observed. Tests with $F_o = 5.5$ might also be affected. The test with $F_o = 7.5$ are aligned with the grid.

Normalizing both axes by the discharge q , the air entrainment coefficient β is obtained on the ordinate as a function of the relative jet length L/h_o and the turbulence intensity T_u on the abscissa (Figure A.2). Without the tests with the lower discharge ($F_o = 3.2 / h_o = 0.075$ m and $F_o = 5.5 / h_o = 0.052$ m), a good trend is observed. It would be interesting to confirm the trend with accurate normal fluctuating velocities, and to use a modified definition of T_u to take into account the minimal fluctuating velocity suggested by Ervine et al. (1995).

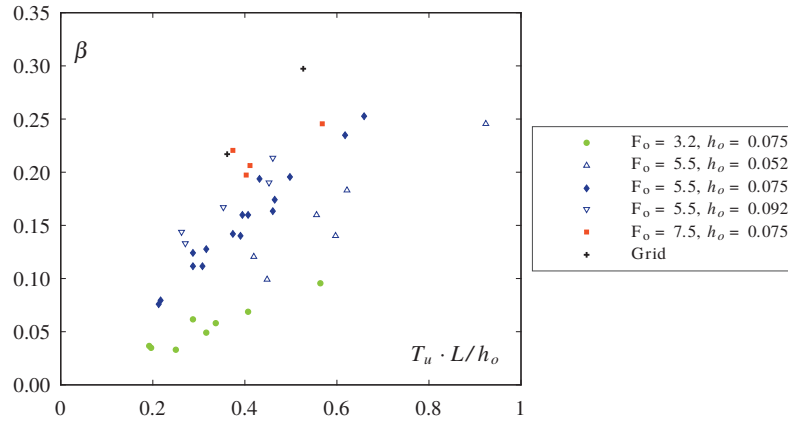


Figure A.2 – Air entrainment coefficient β as a function of the relative jet length L/h_o and the turbulence intensity T_u

A.2 Relations based on the Froude number

Additional relations obtained for the air entrainment coefficient β are given herein.

A.2.1 Inclusion of the relative deflector height

Taking into account the relative deflector height t/h_o slightly improves equation (5.2) to ($r^2 = 0.921$, Figure A.3a)

$$\beta = 0.017 \cdot F_o^{0.95} \cdot (1 + \sin \varphi)^{1.5} \cdot (1 + \tan \alpha)^{2.6} \cdot \left(\frac{t}{h_o} \right)^{0.08} - 0.104 \quad (\text{A.1})$$

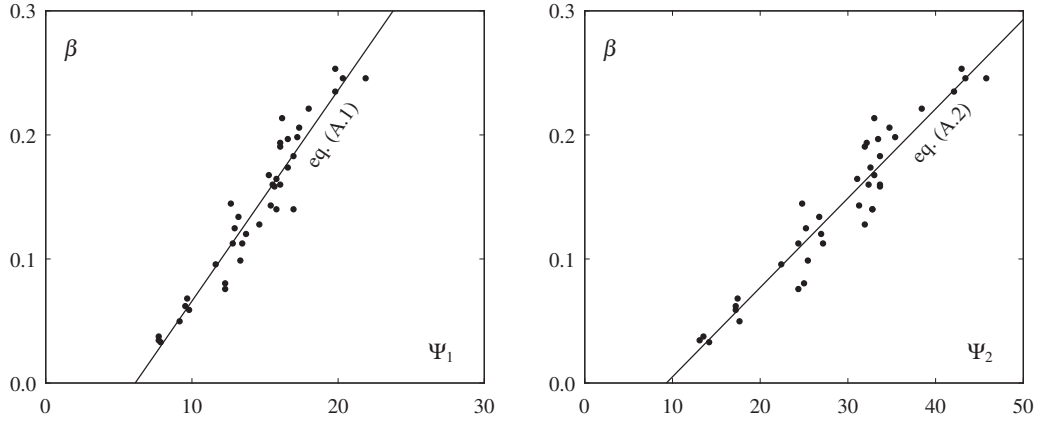


Figure A.3 – Air entrainment coefficient β as a function of (a) $\Psi_1 = F_o^{0.95} \cdot (1 + \sin \varphi)^{1.5} \cdot (1 + \tan \alpha)^{2.6} \cdot (t/h_o)^{0.08}$, and (b) $\Psi_2 = F_o^{1.15} \cdot (1 + \sin \varphi)^{1.75} \cdot (1 + \tan \alpha)^{3.6} \cdot (s/h_o)^{0.035}$

A.2.2 Inclusion of the relative step height

Taking into account the relative step height s/h_o slightly improves equation (5.2) to ($r^2 = 0.910$, Figure A.3b)

$$\beta = 0.0072 \cdot F_o^{1.15} \cdot (1 + \sin \varphi)^{1.75} \cdot (1 + \tan \alpha)^{3.6} \cdot \left(\frac{s}{h_o} \right)^{0.035} - 0.067 \quad (\text{A.2})$$

A.2.3 Smooth and stepped chute common relation

A common equation for both smooth and stepped chutes was investigated. Compromises were required to include the different effect of the Froude number F_o and chute angle φ giving (Figure A.4)

$$\beta = 0.019 \cdot F_o \cdot (1 + F_o \tan \alpha) \cdot (1 + \sin \varphi)^{0.5} - 0.11 \quad (\text{A.3})$$

The relation is not very conclusive with $r^2 = 0.594$ for stepped chutes (present study) and $r^2 = 0.769$ for smooth chutes (Pfister 2008). There still remains a different slope of β for smooth and stepped chutes.

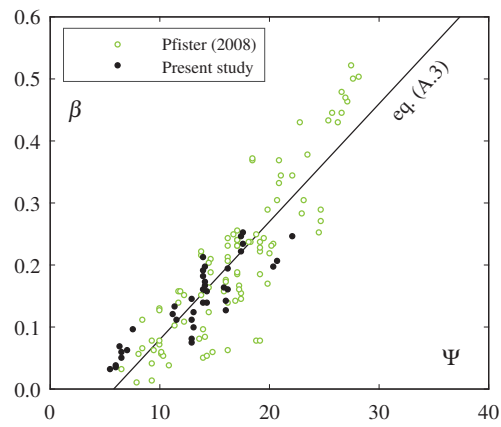


Figure A.4 – Air entrainment coefficient β as a function of $\Psi = F_o \cdot (1 + F_o \tan \alpha) \cdot (1 + \sin \varphi)^{0.5}$

Appendix B

Subpressure effect on jet trajectories

The jet trajectory regression method (§6.1.2) neglects cavity subpressure. To assess the effects, it is compared to the analytical solution presented by Schwartz and Nutt (1963) taking into account cavity subpressure :

$$\begin{cases} x'(T) = x'_t + h_t \left[-\frac{u_t T}{ah_t} + \frac{F_t^2 \sin \alpha'_t}{a \sin \theta} \left(\sin \left(\frac{u_t a T}{ch_t} + \theta \right) - \sin \theta \right) \right] \\ z'(T) = z'_t + h_t \left[\frac{F_t^2 \sin \alpha'_t}{a \sin \theta} \left(\cos \theta - \cos \left(\frac{u_t a T}{ch_t} + \theta \right) \right) \right] \end{cases} \quad (\text{B.1})$$

where x' and z' are respectively the horizontal and vertical coordinates, x'_t and z'_t the coordinates at the takeoff point, T the time, h_t the flow depth at takeoff, F_t the Froude number at takeoff, u_t the flow velocity at takeoff, α'_t the takeoff angle measured from horizontal (positive if the jet is pointing downwards), $a = \Delta p / (\rho g h_o)$ the cavity subpressure, and $\theta = \arctan(a \sin \alpha'_t / (a \cos \alpha'_t + 1))$.

Four main parameters influence the jet trajectory: a , F_t , h_t and α'_t . The influence of each parameter on the trajectory regression is studied considering the following standard values of the physical model experiments: $\alpha_t = 9.46^\circ$, $F_t = 5.5$, $h_t = 0.075$ m and $t = 0.045$ m. Although the standard value of the deflector height is $t = 0.030$ m, the highest value $t = 0.045$ m is chosen to have longer jet lengths. For the effect of α'_t , the two chute angles φ are considered separately, giving $\alpha'_t = \varphi - \alpha_t = 40.54^\circ$ for $\varphi = 50^\circ$, and $\alpha'_t = \varphi - \alpha_t = 20.54^\circ$ for $\varphi = 30^\circ$.

A total of 30 points describing a trajectory from takeoff to impact are calculated with equation (B.1). The jet trajectory regression method M3 (§6.1.2) is then applied to the 30 points to obtain the ratios u_{tM3}/u_t , α_{tM3}/α_t and L_{tM3}/L_t , as well as the RMS error e . This procedure is followed for 5 subpressures $a = \Delta p / (\rho g h_o)$ and multiple values of: the takeoff Froude number F_t (Figure B.1), the takeoff flow depth h_t (Figure B.2), the takeoff angle α_t for $\varphi = 30^\circ$ (Figure B.3) and the takeoff angle α_t for $\varphi = 50^\circ$ (Figure B.4).

The main trends valid for standard values of the physical model are:

- The takeoff velocity u_{tM3} obtained is reduced to compensate the subpressure ($u_{tM3} = 0.89u_t$ for $a = 0.10$ and the conditions defined above)
- The takeoff angle α_{tM3} is slightly increased ($\alpha_{tM3} = 1.04\alpha_t$ for $a = 0.10$ and the conditions defined above)
- The jet length L is practically identical
- A steeper chute angle φ produces higher RMS error e as well as higher u_{tM3}/u_t and α_{tM3}/α_t differences, due to the increase of the horizontal component of the subpressure. A flat chute ($\varphi = 0^\circ$) has only a difference in the takeoff velocity, and not in the takeoff angle.
- The differences in takeoff velocity and takeoff angle decrease when F_t and h_t increase, and when α_t decreases

Neglecting the subpressure influences the takeoff angle and velocity, but the trajectory is well described. The takeoff angle deviations are considered acceptable as long as $a = \Delta p / (\rho g h_o) \leq 0.1$, $F_t \geq 3$, $h_t \geq 0.04$ m, $\alpha_t \leq 30^\circ$ and $\varphi \leq 50^\circ$, and the jet length deviations are acceptable for $a = \Delta p / (\rho g h_o) \leq 0.3$.

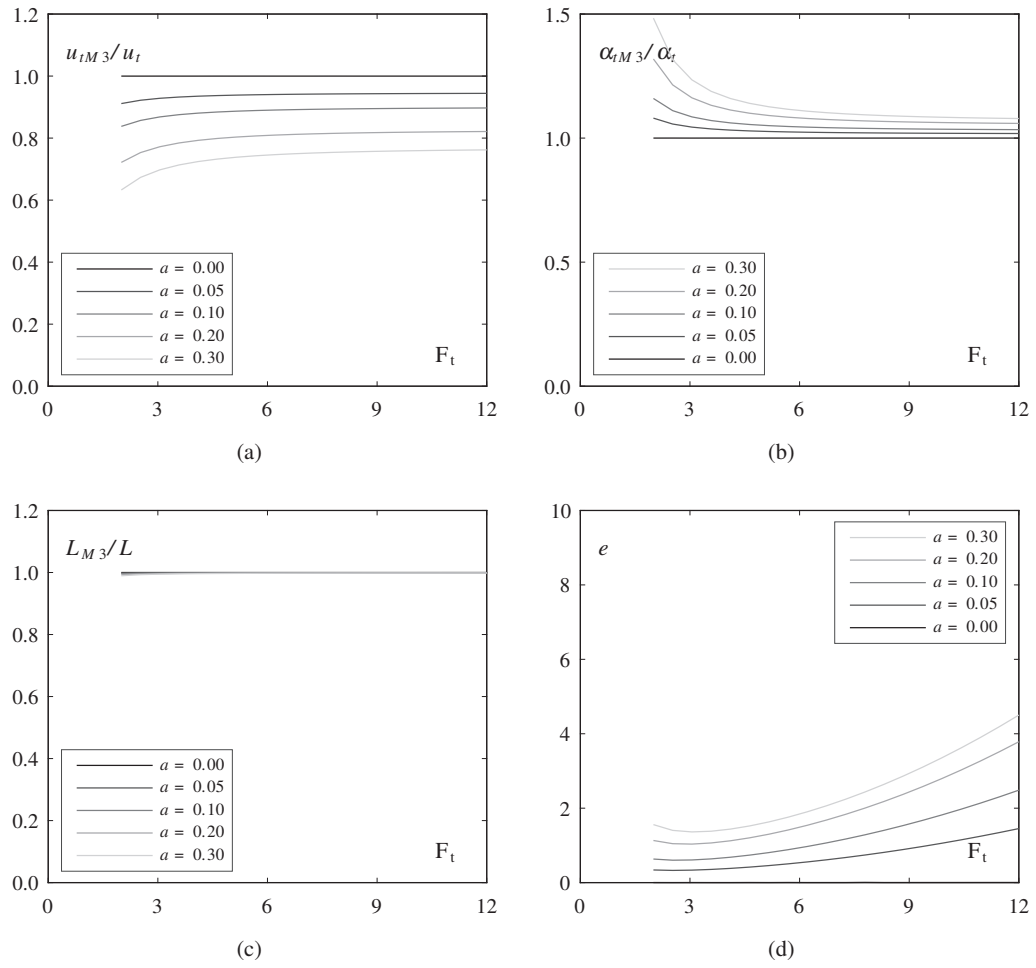


Figure B.1 – Effect of the subpressure $a = \Delta p / (\rho g h_o)$ with method M3 on (a) the takeoff velocity, (b) the takeoff angle, (c) the jet angle, and (d) the trajectory error as a function of the takeoff Froude number F_t

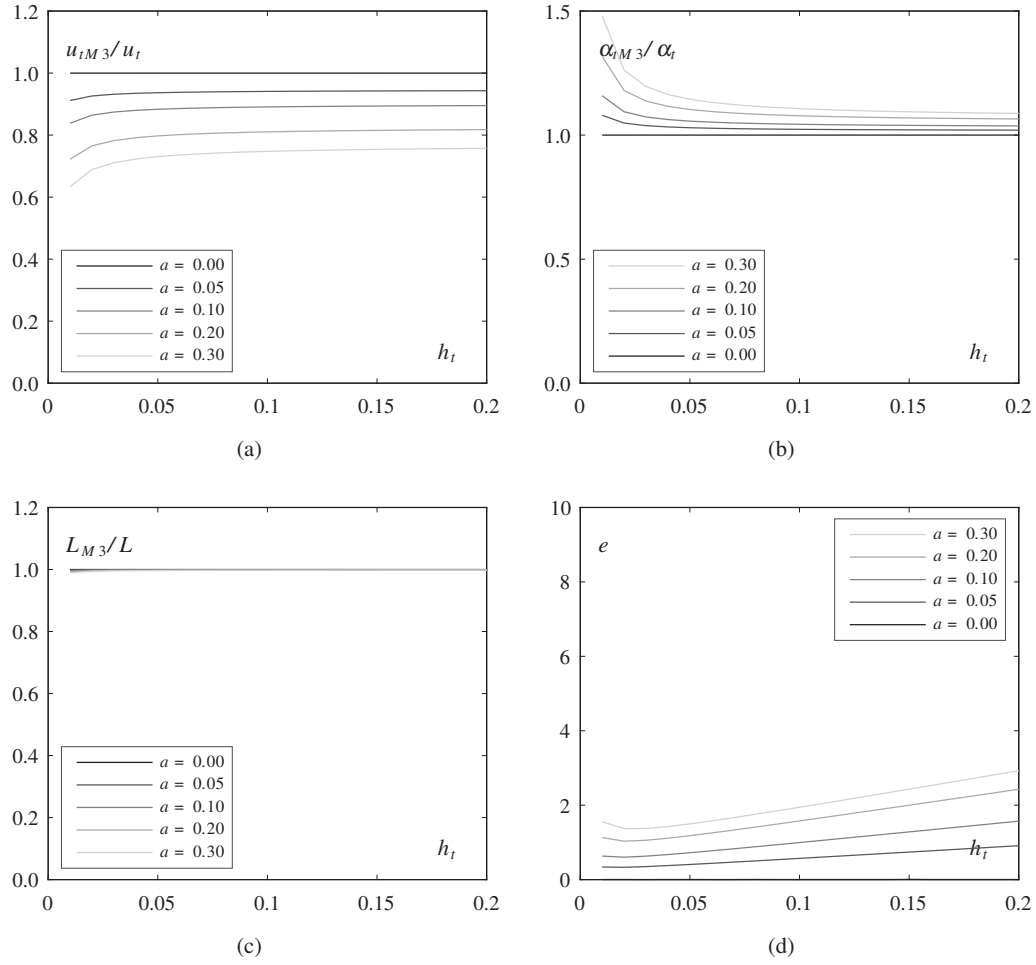


Figure B.2 – Effect of the subpressure $a = \Delta p / (\rho g h_o)$ with method M3 on (a) the takeoff velocity, (b) the takeoff angle, (c) the jet angle, and (d) the trajectory error as a function of the takeoff flow depth h_t

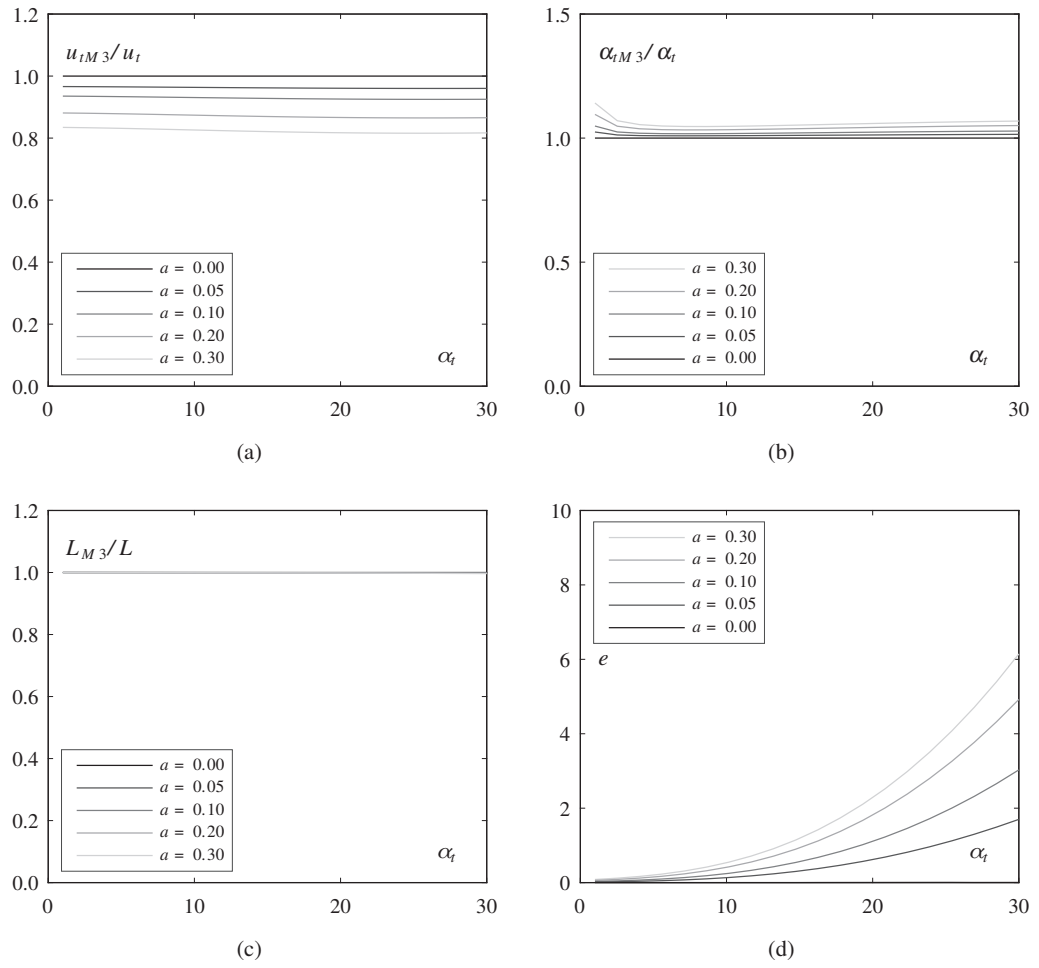


Figure B.3 – Effect of the subpressure $a = \Delta p / (\rho g h_o)$ with method M3 on (a) the takeoff velocity, (b) the takeoff angle, (c) the jet angle, and (d) the trajectory error as a function of the deflector angle α_t for $\varphi = 30^\circ$

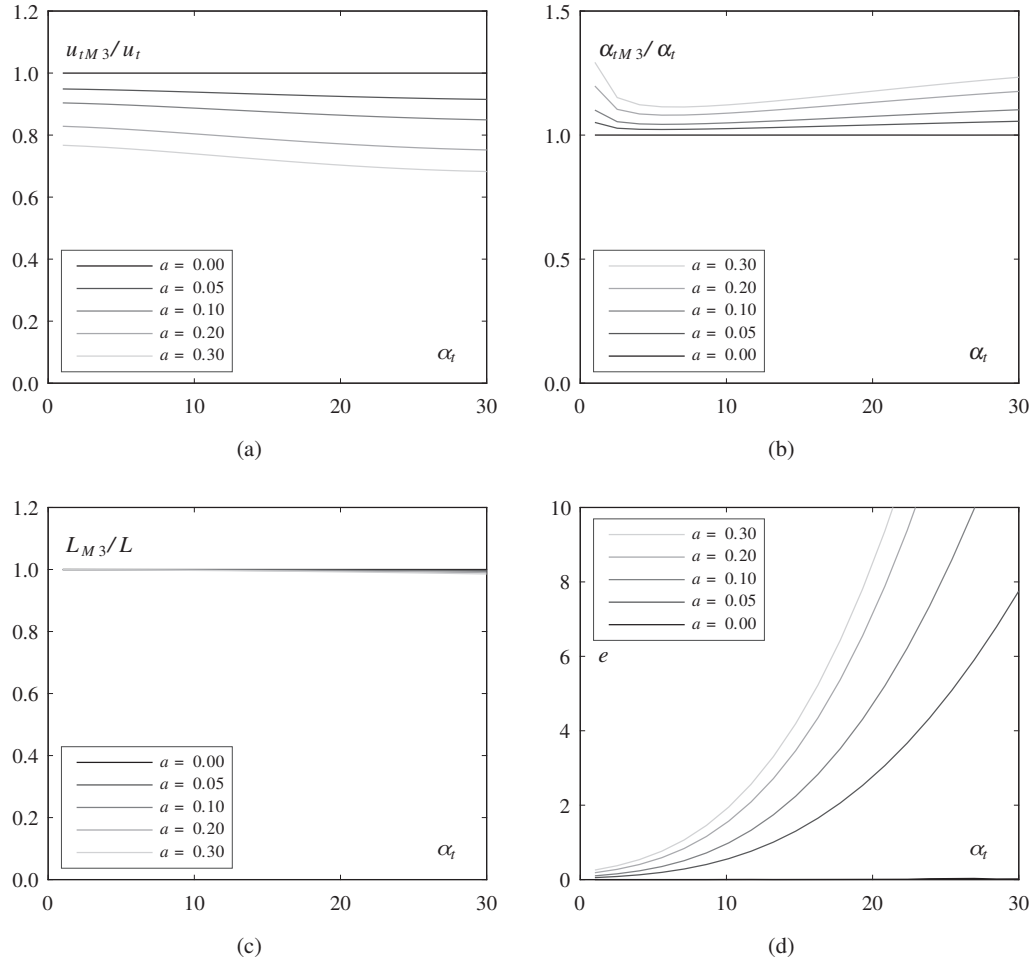


Figure B.4 – Effect of the subpressure $a = \Delta p / (\rho g h_o)$ with method M3 on (a) the takeoff velocity, (b) the takeoff angle, (c) the jet angle, and (d) the trajectory error as a function of the deflector angle α_t for $\varphi = 50^\circ$

Appendix C

Pressure measurements

The bottom pressure measured at $x_p = -0.27$ m (0.2 m downstream of the jetbox) is documented here. This location is 0.07 m apart from the approach flow depth h_o and Froude number F_o at $x_o = -0.20$ m. The flow depth $h_p = h(x_p)$ is linearly interpolated between the measurements of $x = -0.20$ m and $x = -0.30$ m. The corresponding Froude number is F_p .

C.1 Average pressure

C.1.1 Influence of jetbox

The approach flow pressure $p/(\rho g)$ measured is consistently higher than the theoretical piezometric head of $h \cos \varphi$, indicating an effect of the jetbox. The difference $p/(\rho g) - h_p \cos \varphi$ is investigated for the reference tests. The Froude number F_p shows the following power trend with $r^2 = 0.992$ (Figure C.1a)

$$p/(\rho g) - h_p \cos \varphi = 0.0263 \cdot F_p^{1.81} \quad (\text{C.1})$$

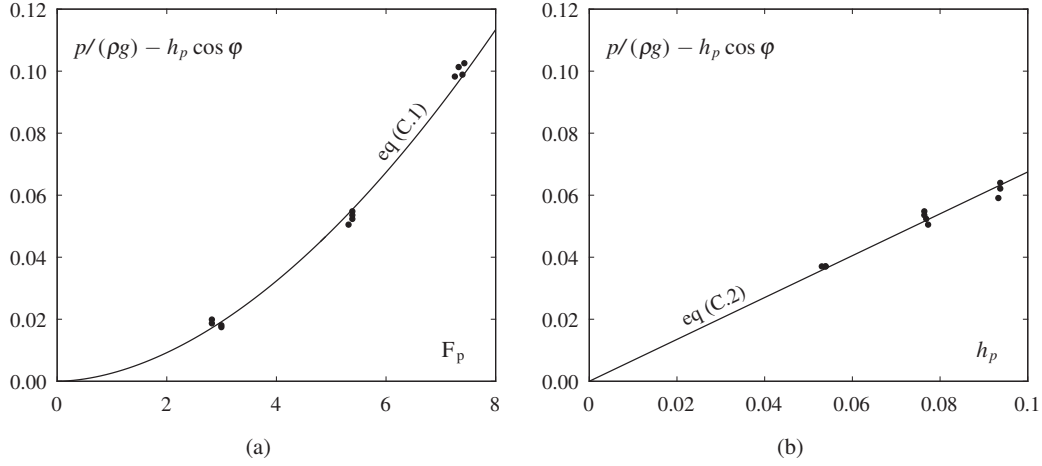
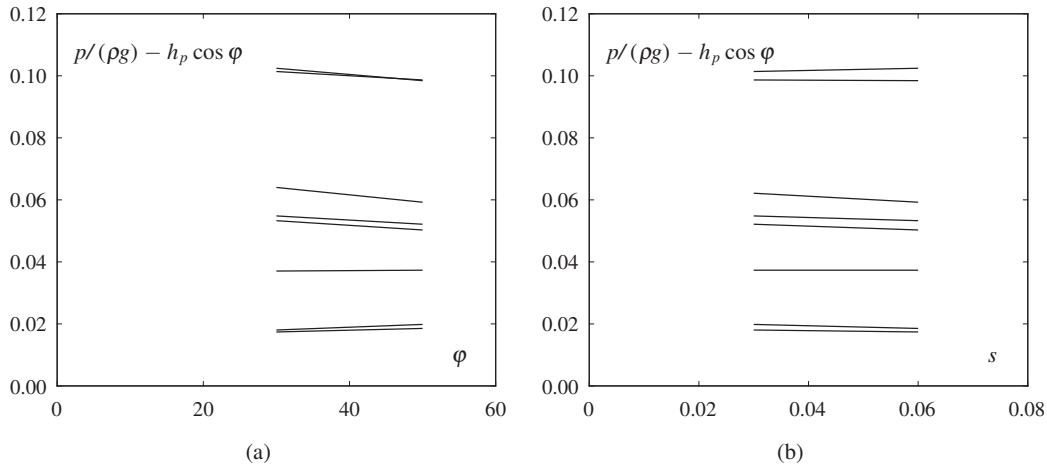
The flow depth h_p shows a linear trend with $r^2 = 0.962$ (Figure C.1b)

$$p/(\rho g) - h_p \cos \varphi = 0.675 \cdot h_p \quad (\text{C.2})$$

There is no significant trend with the chute slope φ (Figure C.2a). And evidently there is no difference with the step height s as the steps only begin downstream at $x = 0$ (Figure C.2b).

In conclusion, the bottom pressure with the influence of the jetbox can be estimated by (Figure C.3).

$$p/(\rho g) = h_p \cos \varphi + 0.0345 \cdot h_p \cdot F_p^{1.81} \quad (\text{C.3})$$


 Figure C.1 – Influence of the flow parameters on the jetbox overpressure $p/(\rho g) - h_p \cos \varphi$

 Figure C.2 – Influence of the chute parameters on the jetbox overpressure $p/(\rho g) - h_p \cos \varphi$

C.1.2 Influence of deflector

A deflector has an influence on the pressure in the adjacent flow upstream of the deflector and creates an overpressure p_d (Steiner et al. 2008). The pressure sensor is measured at $x_p = -0.27$ m and the deflector starts at $x_d = -L_d$. Because only one location is measured and the distance $x_d - x_p$ changes with each deflector tested, no relation can be obtained for p_d . However, the influence of each parameter is commented (Figure E.9).

The increase of p_d with the Froude number is consistent with the influence F_o^2 obtained in equation (2.78). There is an increase of p_d with the flow depth h_p since the hydrostatic pressure increases and the relative distance $(x_d - x_p)/h_o$ becomes smaller. The deflector angle α and height t changes the distance $x_d - x_p$. Therefore, the influence of the deflector geometry on the pressure p_d cannot be assessed independently from $x_d - x_p$. The decrease of p_d with α is due to the increase of the

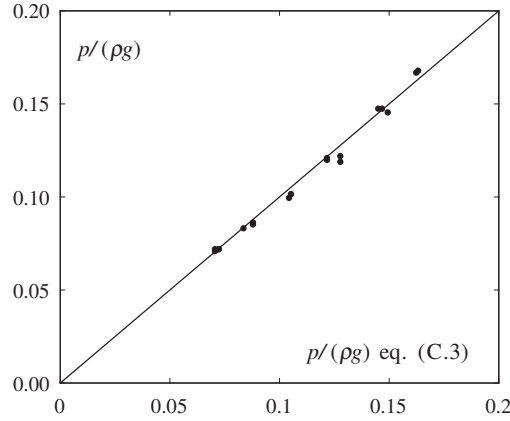


Figure C.3 – Comparison of the measured pressure p' with p from equation (C.3)

distance $x_d - x_p$ when the deflector becomes steeper and not due to α . Similarly, the distance $x_d - x_p$ becomes smaller when the deflector height t increases, which explains the increase of p_d with t . There is no effect of the chute angle ϕ and evidently none from the step height s .

C.2 Pressure fluctuations

The RMS of the pressure fluctuations p' is strongly correlated with the flow parameters F_p and h_p (Figure E.8). The two flow conditions pairs $F_p = 3.2 / h_p = 0.075$ m and $F_p = 5.5 / h_p = 0.052$ m, as well as $F_p = 7.5 / h_p = 0.075$ m and $F_p = 5.5 / h_p = 0.092$ m have about the same pressure fluctuations. This can be explained by the same unit discharge for each pair (respectively $q = 202 \text{ m}^2/\text{s}$ and $q = 480 \text{ m}^2/\text{s}$). The pressure fluctuations p' is thus correlated with the Reynolds number R . With the flow depth h_p , there are two distinct trends for $\phi = 30^\circ$ (the two lower curves) and for $\phi = 50^\circ$ (the seven upper curves). This increase p' with ϕ is visible for higher p' (higher discharges). And while the pressure p is influenced by the deflector, the fluctuations p' are not as indicated by the overlap of reference and aerator tests.

C.3 Normal fluctuating velocity

According to Arndt and Ippen (1970), the pressure fluctuations p' can be converted to a normal fluctuating velocity u' with the following relation

$$u' = \frac{p'}{\rho u_o} \quad (\text{C.4})$$

The higher terms are neglected during the conversion, and an error of 5 % is estimated for a turbulence intensity of $T_u = 10\%$. The size of the pressure transducer should be smaller than

micro-scale of the turbulence.

This is **not** the case for the present study as the pressure transducer membrane has a diameter $d = 0.0255$ m which is thought to be larger than the turbulence scale. The pressure transducer can only measure turbulence with a larger scale than its membrane, and smaller turbulences are averaged. The guiding walls of the jetbox limit the turbulence scale to a maximum of 0.021 m. In comparison, the tubes originally used by Arndt and Ippen (1970) had a diameter $d = 0.0024$ m. **The estimation of u' is thus physically inaccurate but might still be representative of general trends.**

According to Falvey and Ervine (1988), u' is related to the shear velocity u^* with $u' \approx u^* = u\sqrt{f/8}$. The normal fluctuating velocity u' is calculated with equation (C.4) and compared with the shear velocity u^* (considering $f = 0.015$) in Figure C.4. The normal fluctuating velocity u' is an order of magnitude lower than the shear velocity u^* .

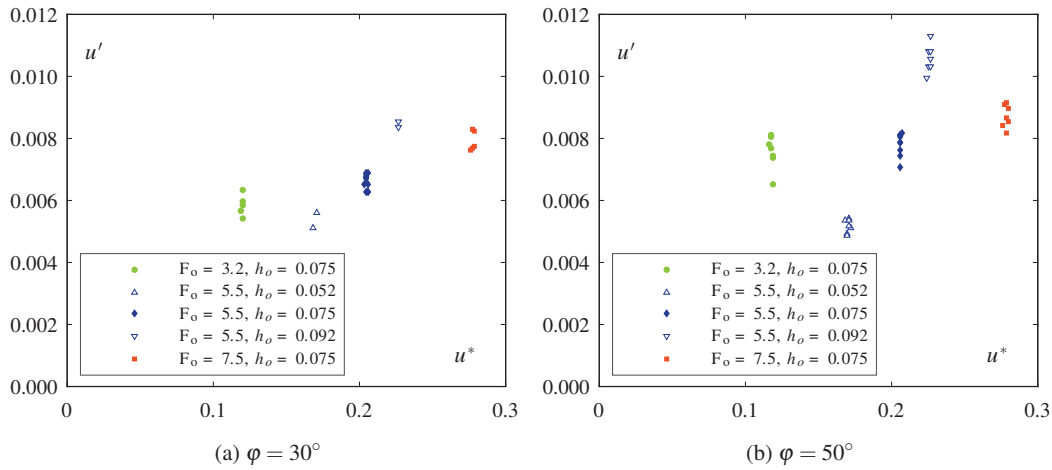


Figure C.4 – Comparison of the estimated normal fluctuating velocity u' with the shear velocity u^*

The normal fluctuating velocity u' obtained is strongly correlated to the approach flow depth h_o , and somewhat to the approach flow Froude number F_o and the chute angle ϕ (Figure E.10).

C.4 Turbulence intensity

As a reference, the influence of the parameters on the estimated turbulence intensity $T_u = u'/u_o$ is shown in E.11. Tests with a low Froude number have the highest turbulence intensity.

C.5 Influence of grid and pre-aerated approach flow

The addition of the grid in the approach flow reduces the pressure p in both the reference and aerator tests (Figure C.5a). This effect is induced by the reduction of the influence of the jetbox on p . A pre-aerated approach flow slightly reduces p .

As expected, the grid increases the turbulence and therefore the pressure fluctuations p' (Figure C.5b). The pre-aerated approach flow greatly increases p' . The scale of the turbulence is probably larger with a mixture flow and thus better measured by the large diameter pressure transducer. The higher discharge of $F_o = 7.5$ ensures a better temporal distribution of air which likely explains the reduction of p' with increasing F_o .

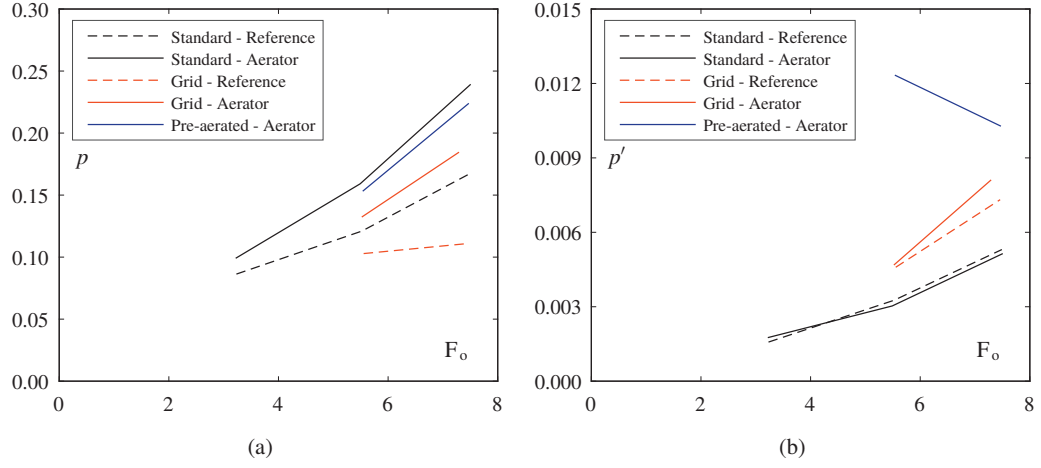


Figure C.5 – Influence of grid and pre-aerated approach flow on the mean pressure $p/(\rho g)$ and the pressure fluctuations $p'/(\rho g)$ compared to the standard tests for different approach Froude numbers F_o

Appendix D

Flow development of aerator tests

Alternate normalizations to the one showed in §5.2 to describe the flow zones are given here. The normalizations are:

- Normalization of the abscissa with the critical flow depth h_c (as used in Chapter 4 for the reference tests), and the ordinate with the quasi-uniform flow value
- Normalization of the abscissa with the jet length L , and the ordinate with the value of the last measured profile from the corresponding reference test ($h_{90,last}$, $C_{a,last}$ and $C_{b,last}$)
- Normalization of the abscissa with the jet length L , and no ordinate normalization
- Normalization of the abscissa with the critical flow depth h_c , and no ordinate normalization

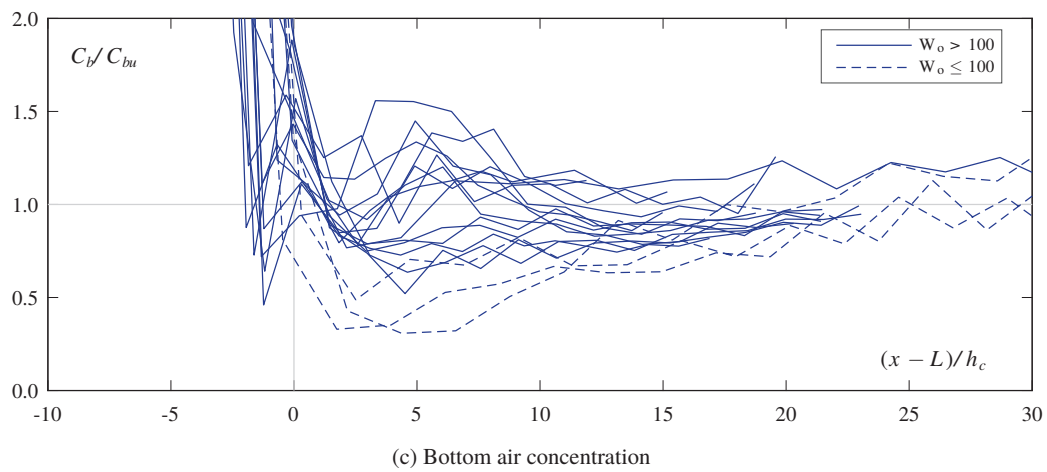
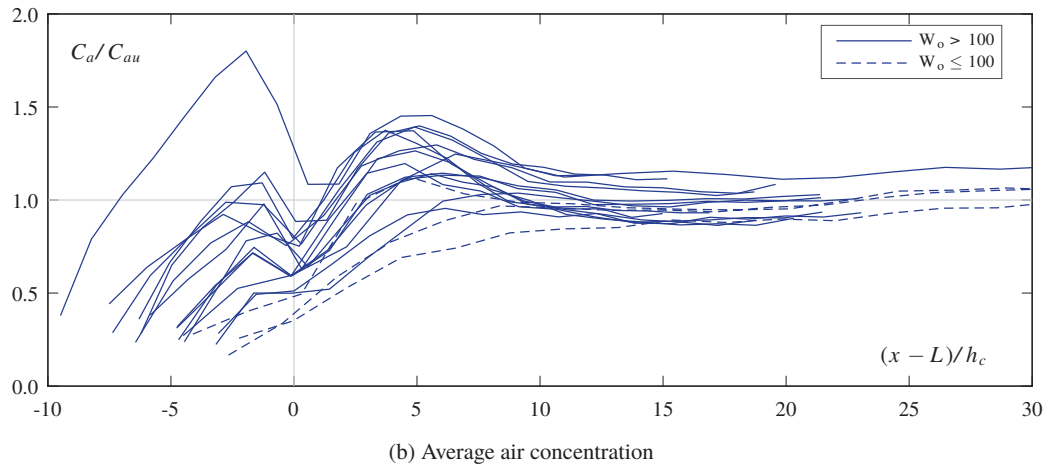
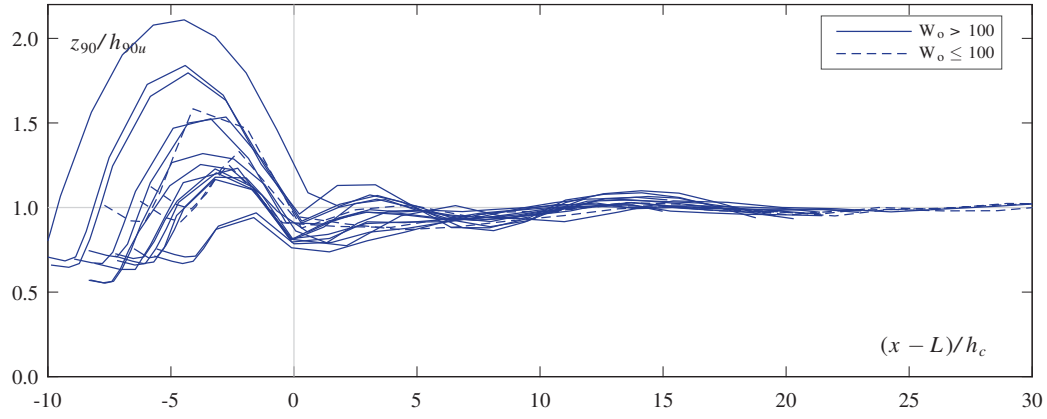
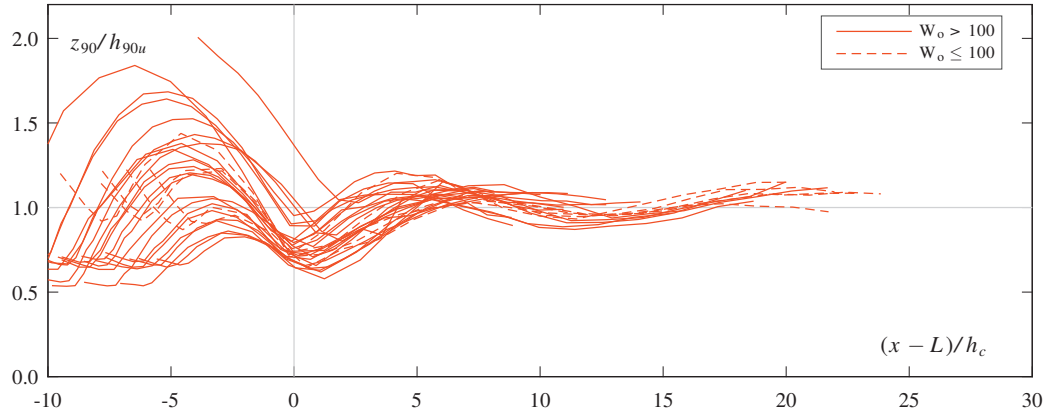
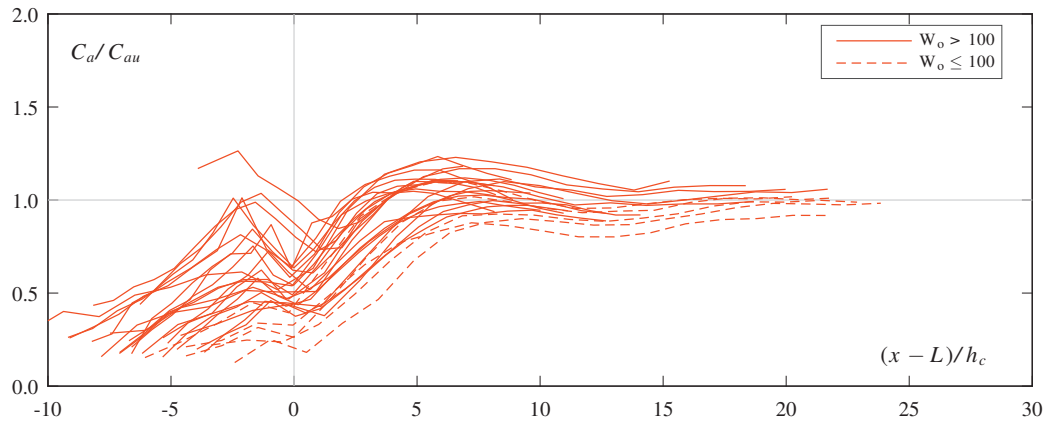


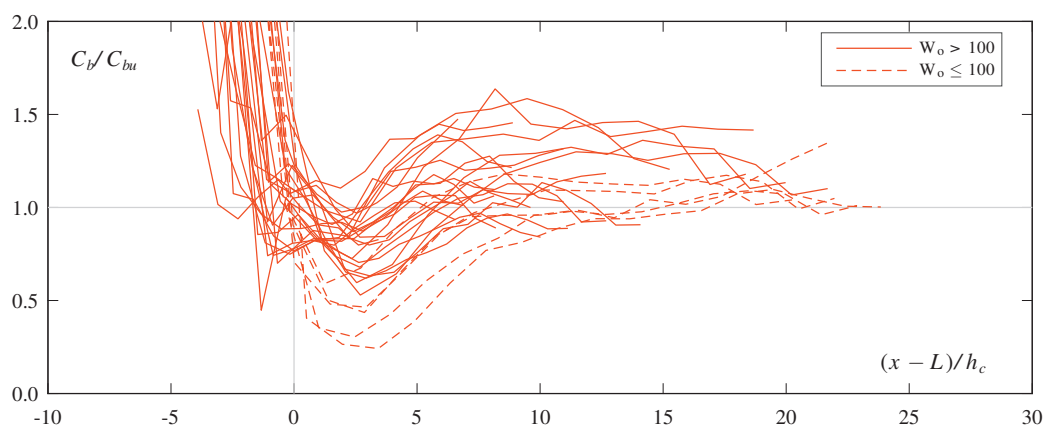
Figure D.1 – Normalization with the critical depth h_c and the quasi-uniform flow values for $\varphi = 30^\circ$



(a) Surface elevation

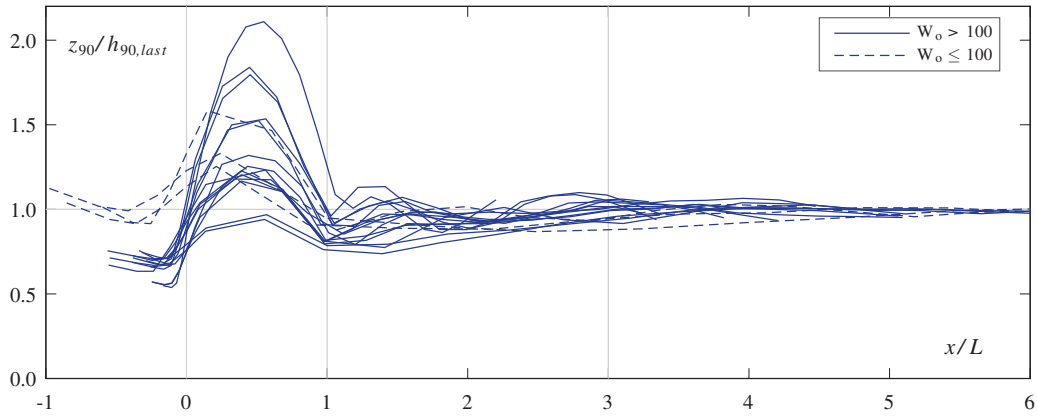


(b) Average air concentration

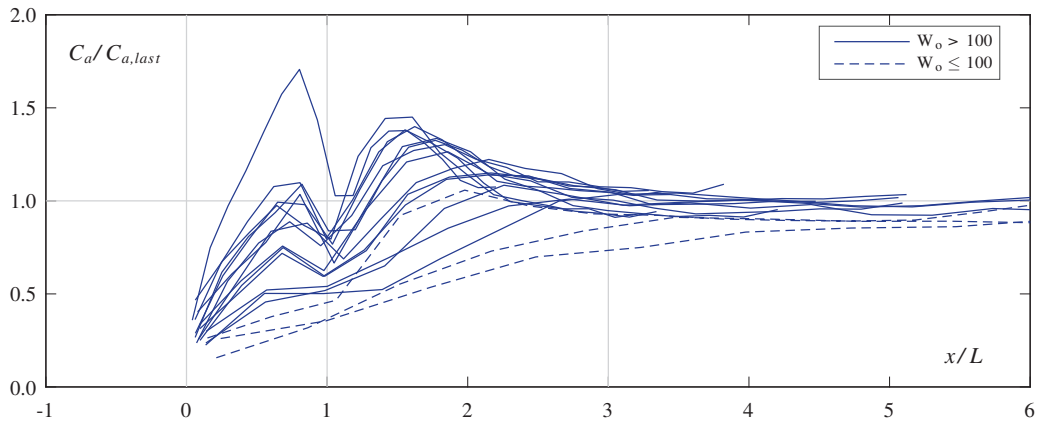


(c) Bottom air concentration

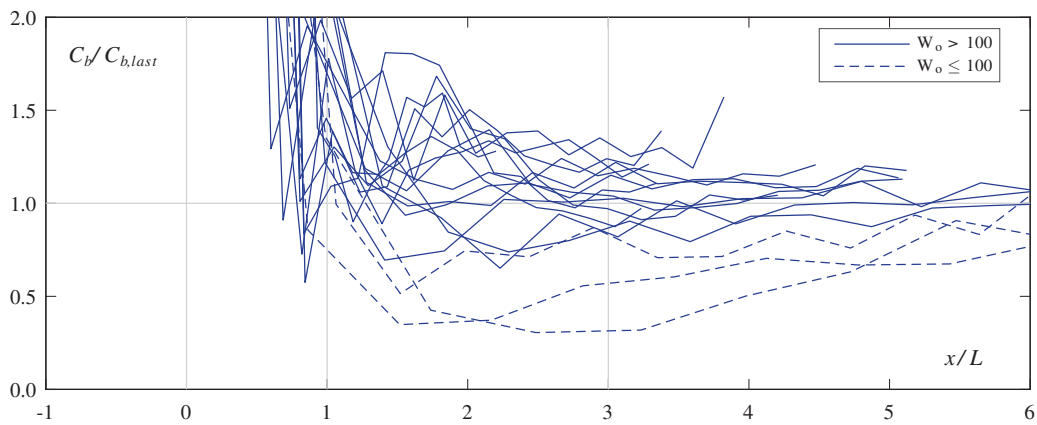
Figure D.2 – Normalization with the critical depth h_c and the quasi-uniform flow values for $\varphi = 50^\circ$



(a) Surface elevation

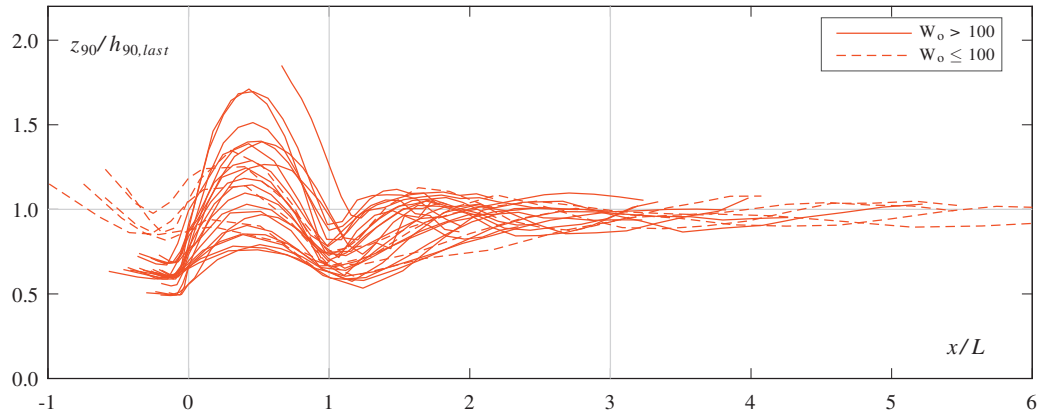


(b) Average air concentration

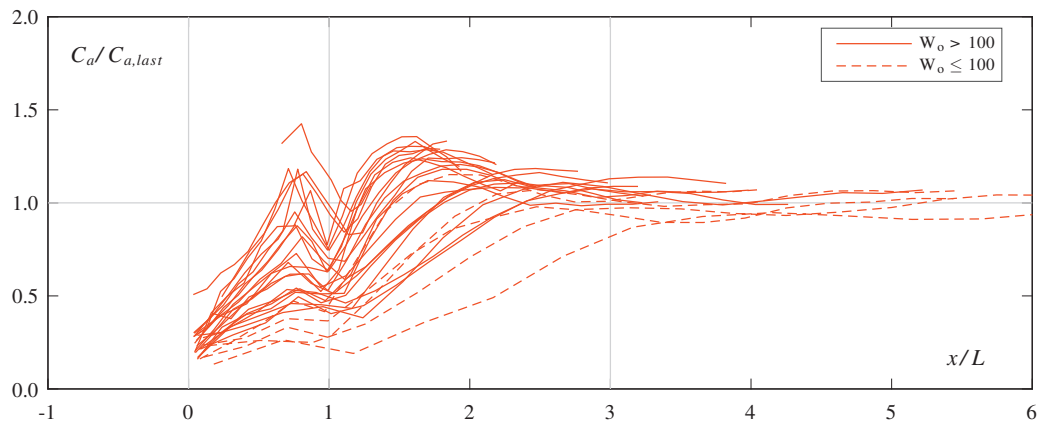


(c) Bottom air concentration

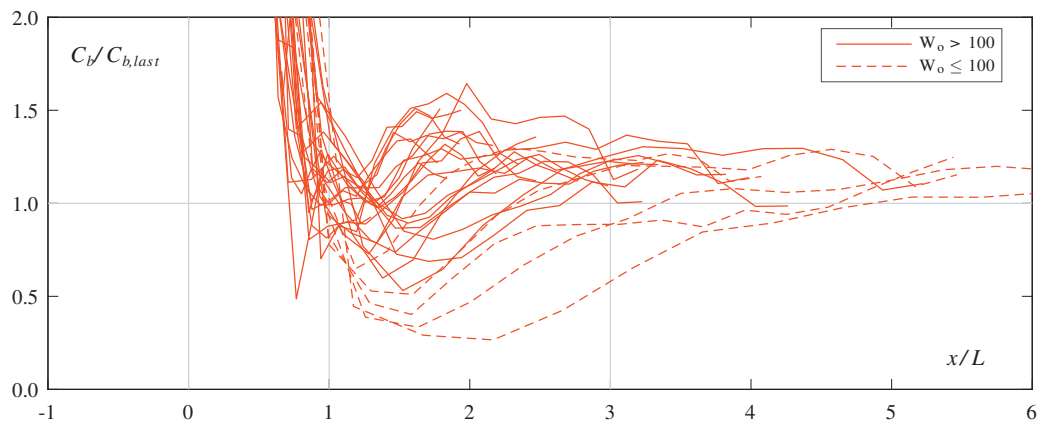
Figure D.3 – Normalization with the jet length L and the value of the last measured profile from the corresponding reference test for $\varphi = 30^\circ$



(a) Surface elevation

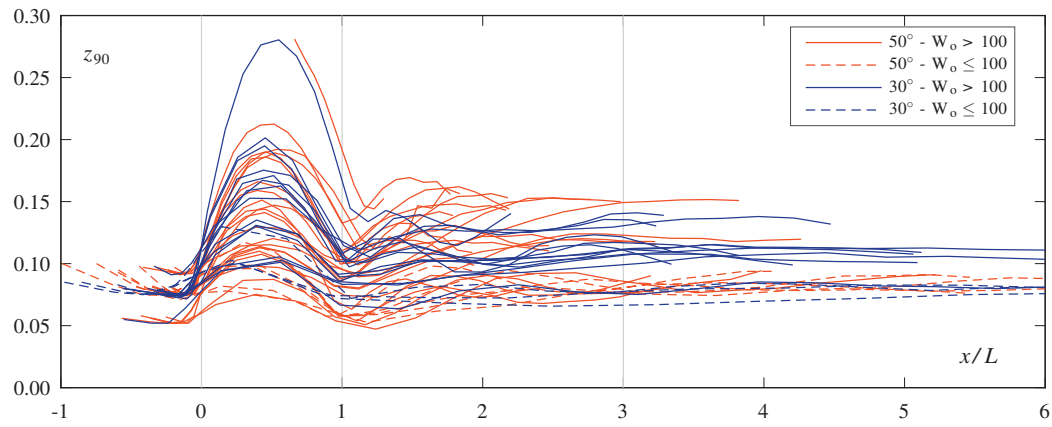


(b) Average air concentration

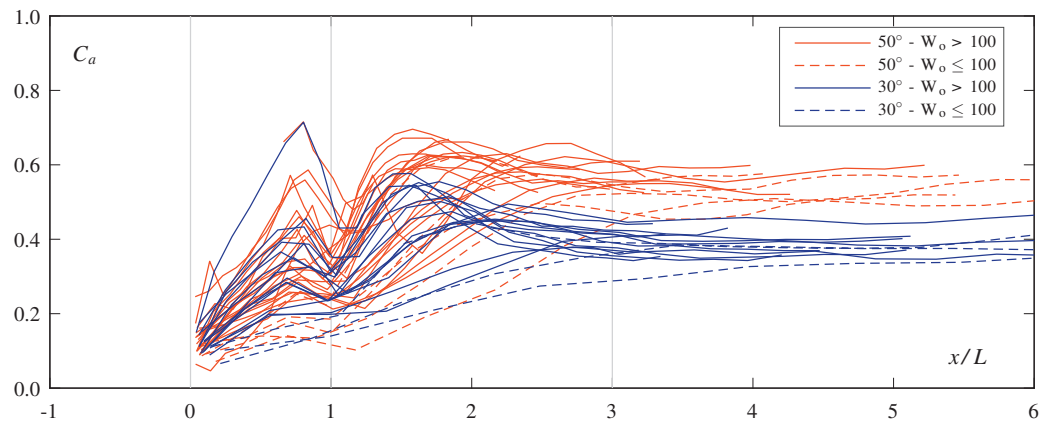


(c) Bottom air concentration

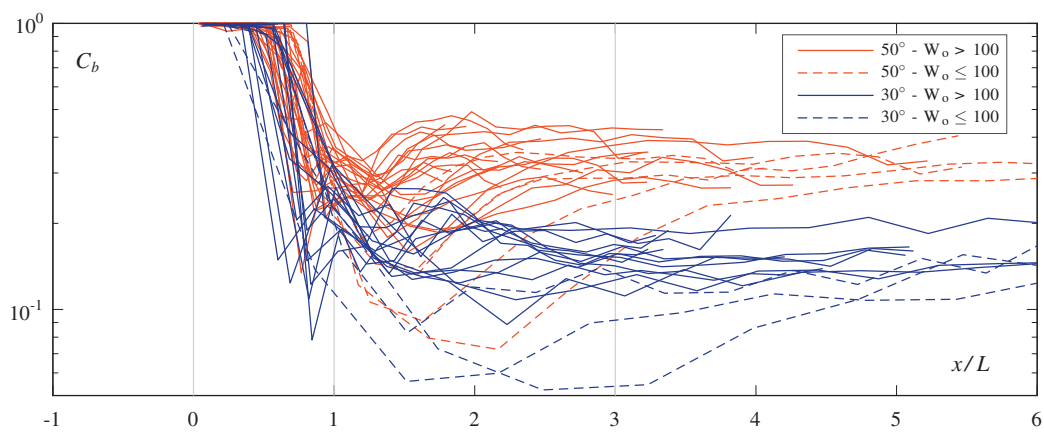
Figure D.4 – Normalization with the jet length L and the value of the last measured profile from the corresponding reference test for $\varphi = 50^\circ$



(a) Surface elevation

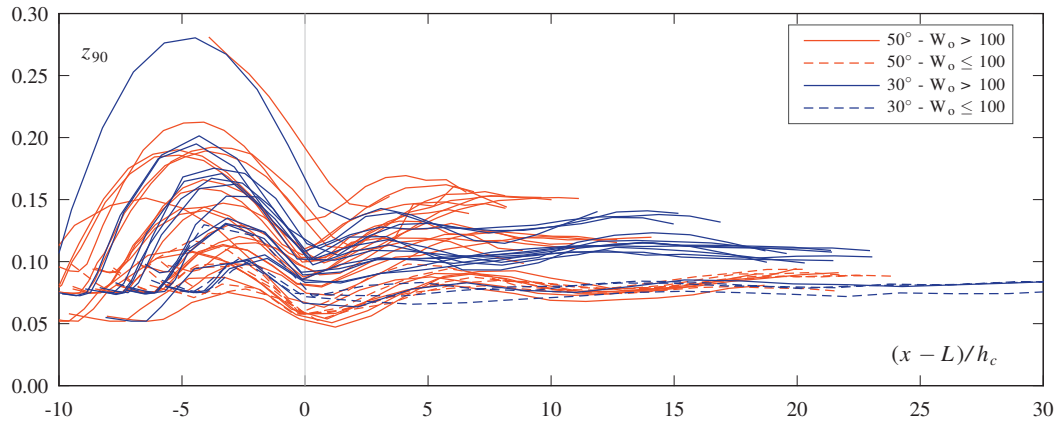


(b) Average air concentration

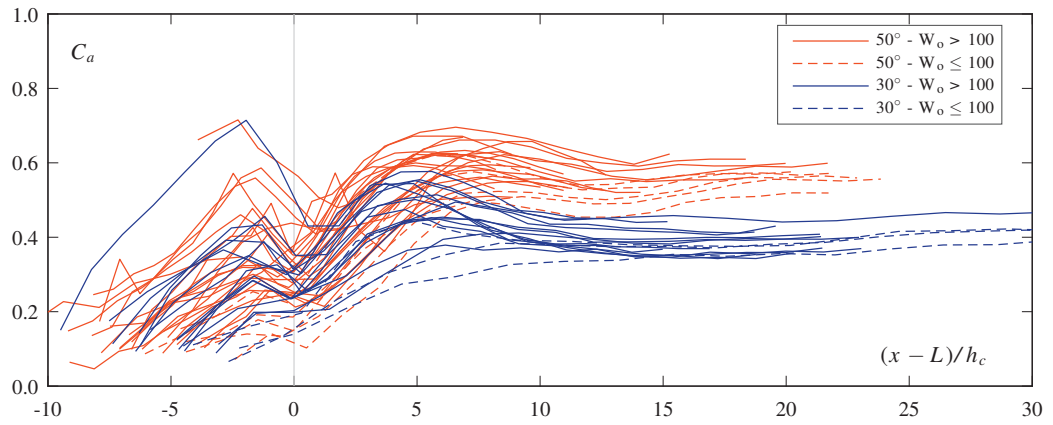


(c) Bottom air concentration

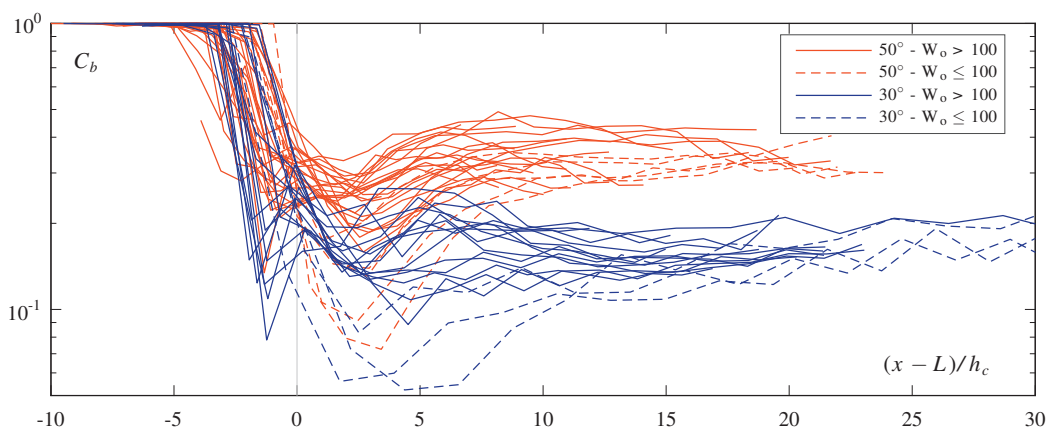
Figure D.5 – Normalization with the jet length L



(a) Surface elevation



(b) Average air concentration



(c) Bottom air concentration

Figure D.6 – Normalization with the critical depth h_c

Appendix E

Parameter influence

The influence of the basic parameters on different variables is presented in this Appendix. For each line in the graphs, only the parameter in abscissa (approach flow Froude number F_o , approach flow depth h_o , deflector angle α , deflector height t or relative deflector height t/h_o , chute angle φ and step height s or relative step height s/h_o) is varied and all the other parameters remain constant. The variables presented are :

- Air entrainment coefficient β
- Ratio of the lower takeoff velocity $u_{t\text{opt}}/u_{t\alpha}$ (respectively method M3/M2)
- Relative lower takeoff angle α_{tl}/α
- Relative upper takeoff angle α_{tu}/α
- Jet spread angle δ_s
- Relative blackwater core length L_{bwc}/h_o
- Approach flow bottom pressure $p/(\rho g)$
- Approach flow bottom pressure RMS fluctuations $p'/(\rho g)$
- Deflector overpressure $p_d/(\rho g)$
- Approach flow normal fluctuating velocity u'
- Approach flow turbulence intensity $T_u = u'/u_o$

E.1 Air entrainment coefficient

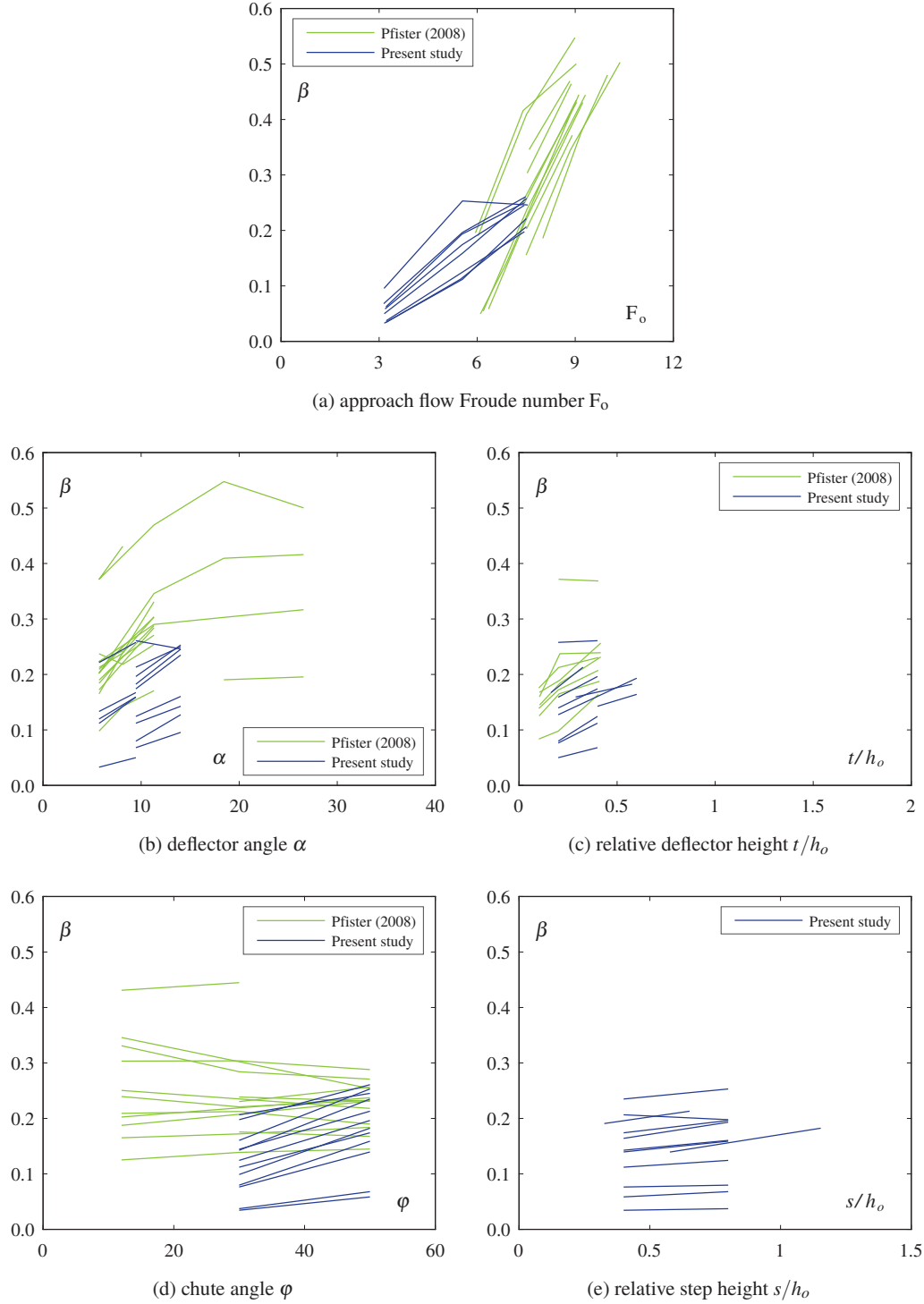


Figure E.1 – Influence of the parameters on the air entrainment coefficient β

E.2 Lower takeoff velocity

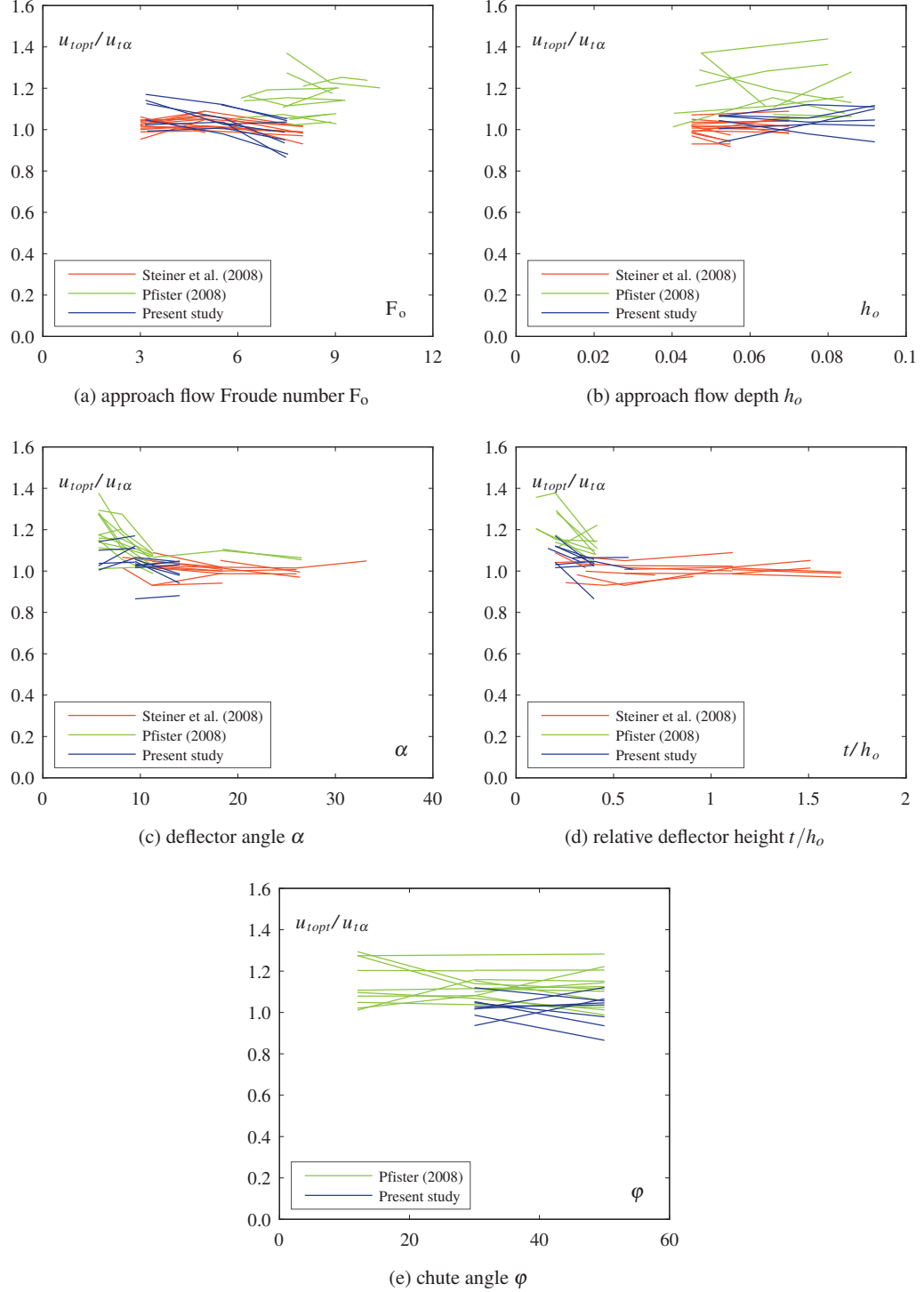


Figure E.2 – Influence of the parameters on the ratio lower takeoff velocity $u_{topt}/u_{t\alpha}$ (method M3/M2)

E.3 Lower takeoff angle

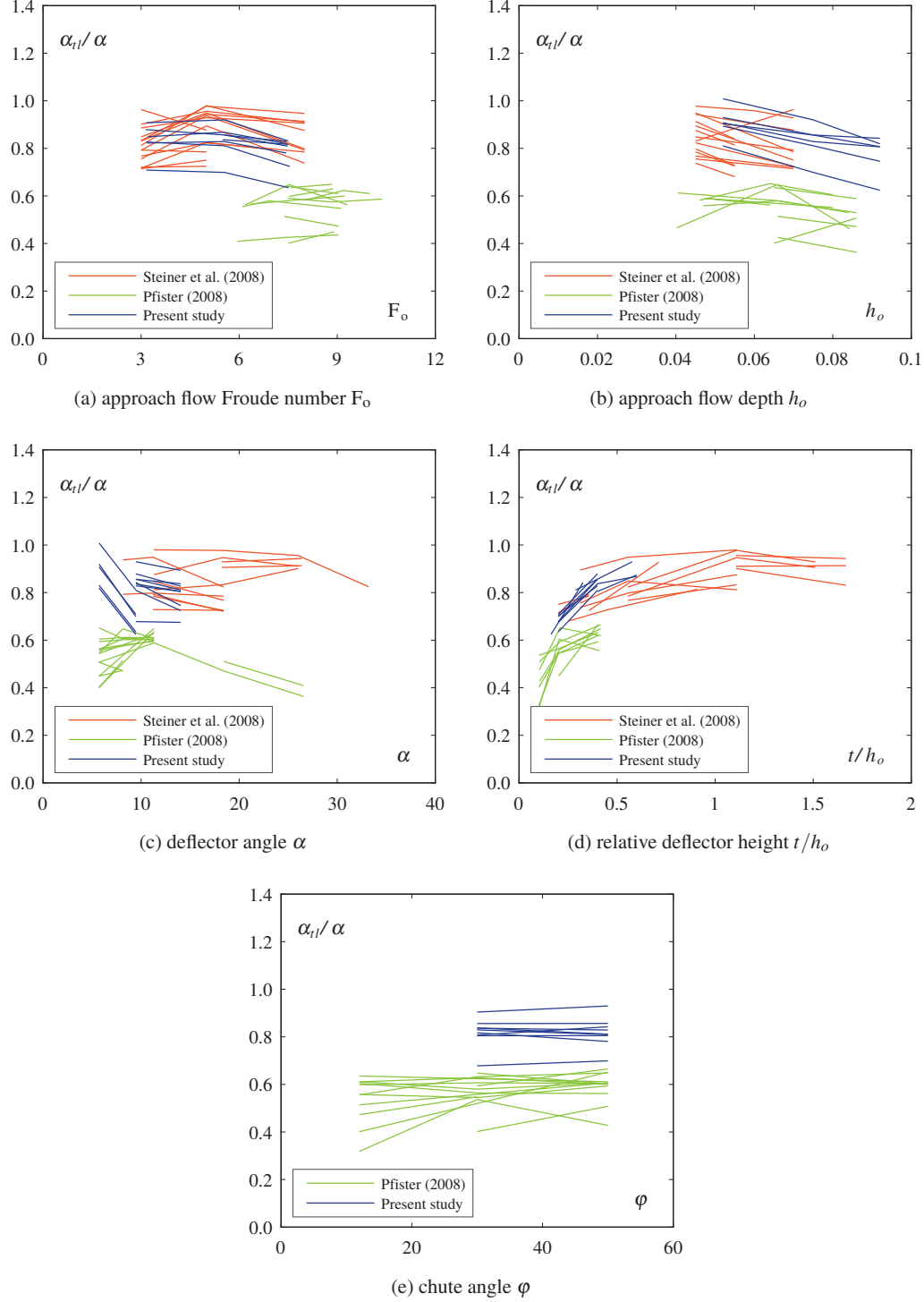


Figure E.3 – Influence of the parameters on the relative lower takeoff angle α_{tl}/α

E.4 Upper takeoff angle

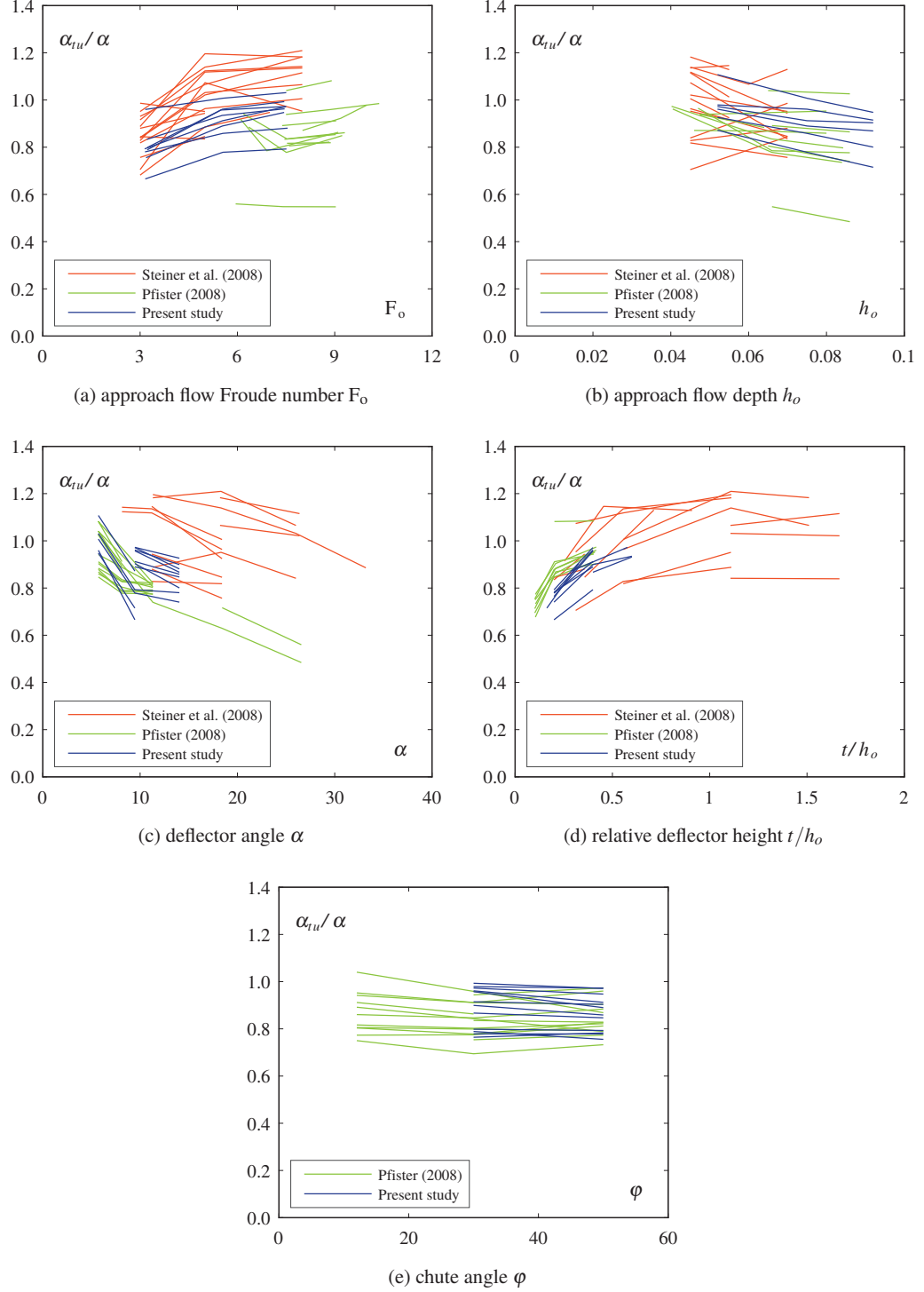


Figure E.4 – Influence of the parameters on the relative upper takeoff angle α_{tu}/α

E.5 Jet spread angle

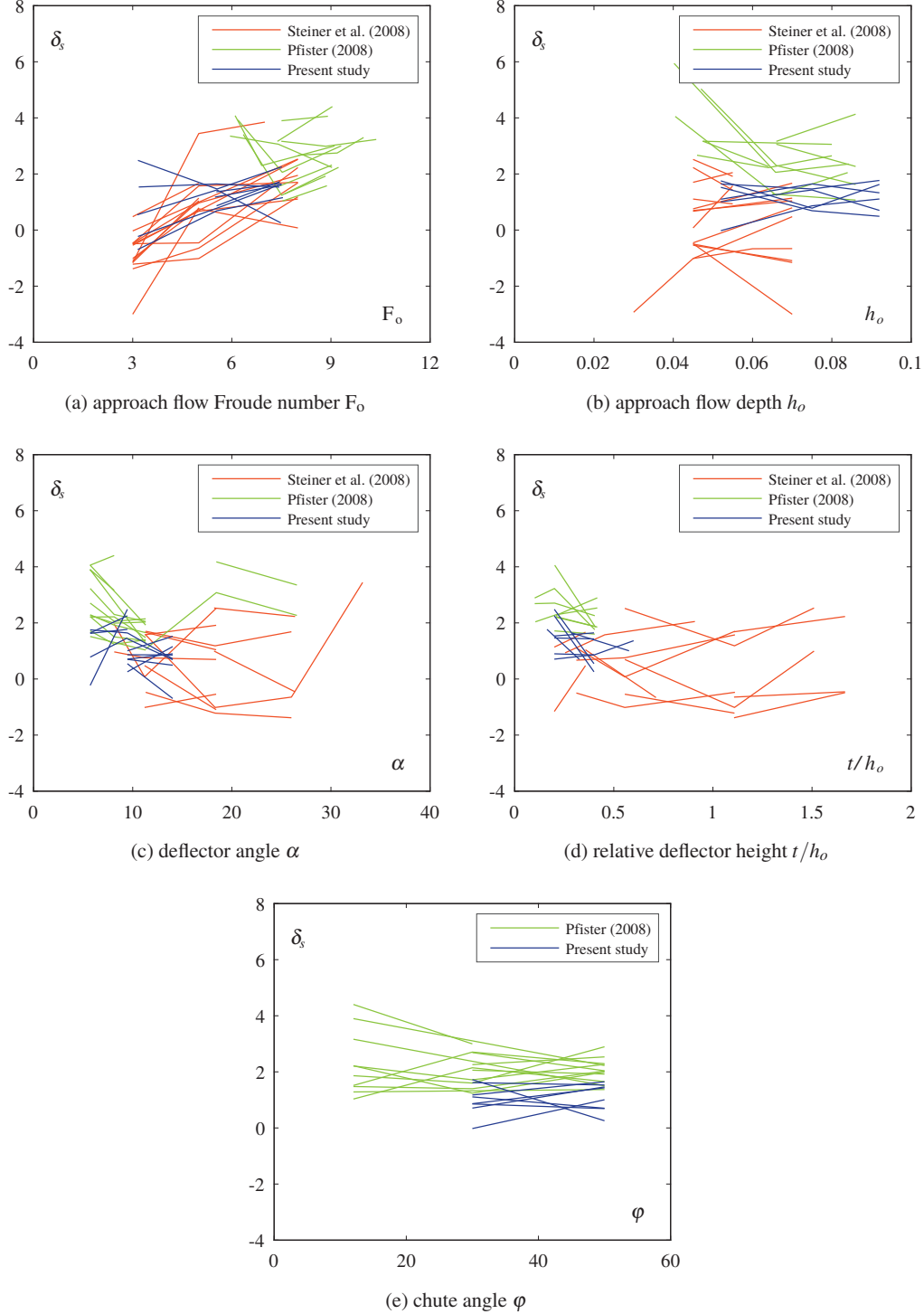


Figure E.5 – Influence of the parameters on the jet spread angle δ_s

E.6 Blackwater core length

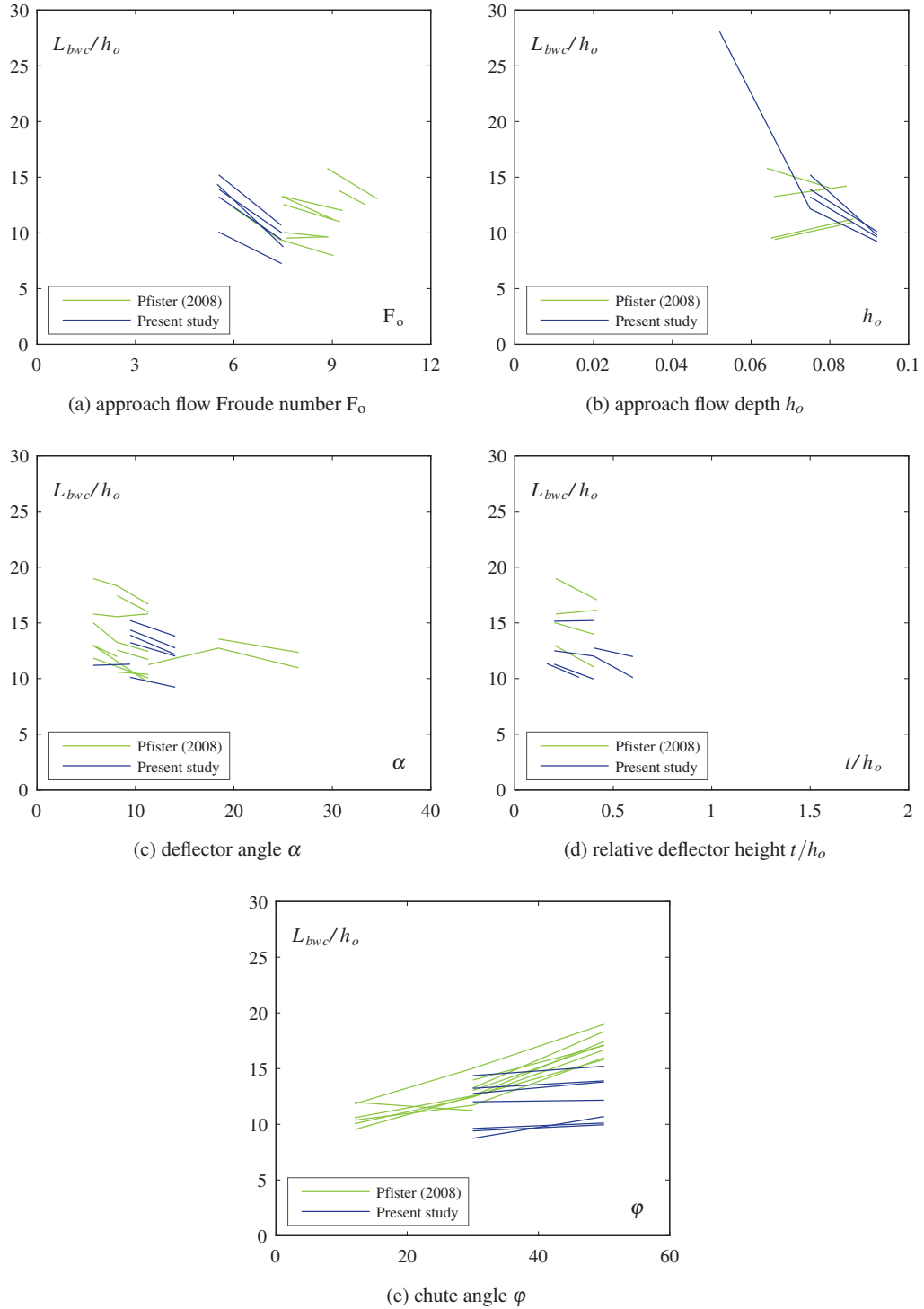


Figure E.6 – Influence of the parameters on the relative blackwater core length L_{bwc}/h_o

E.7 Approach flow bottom pressure

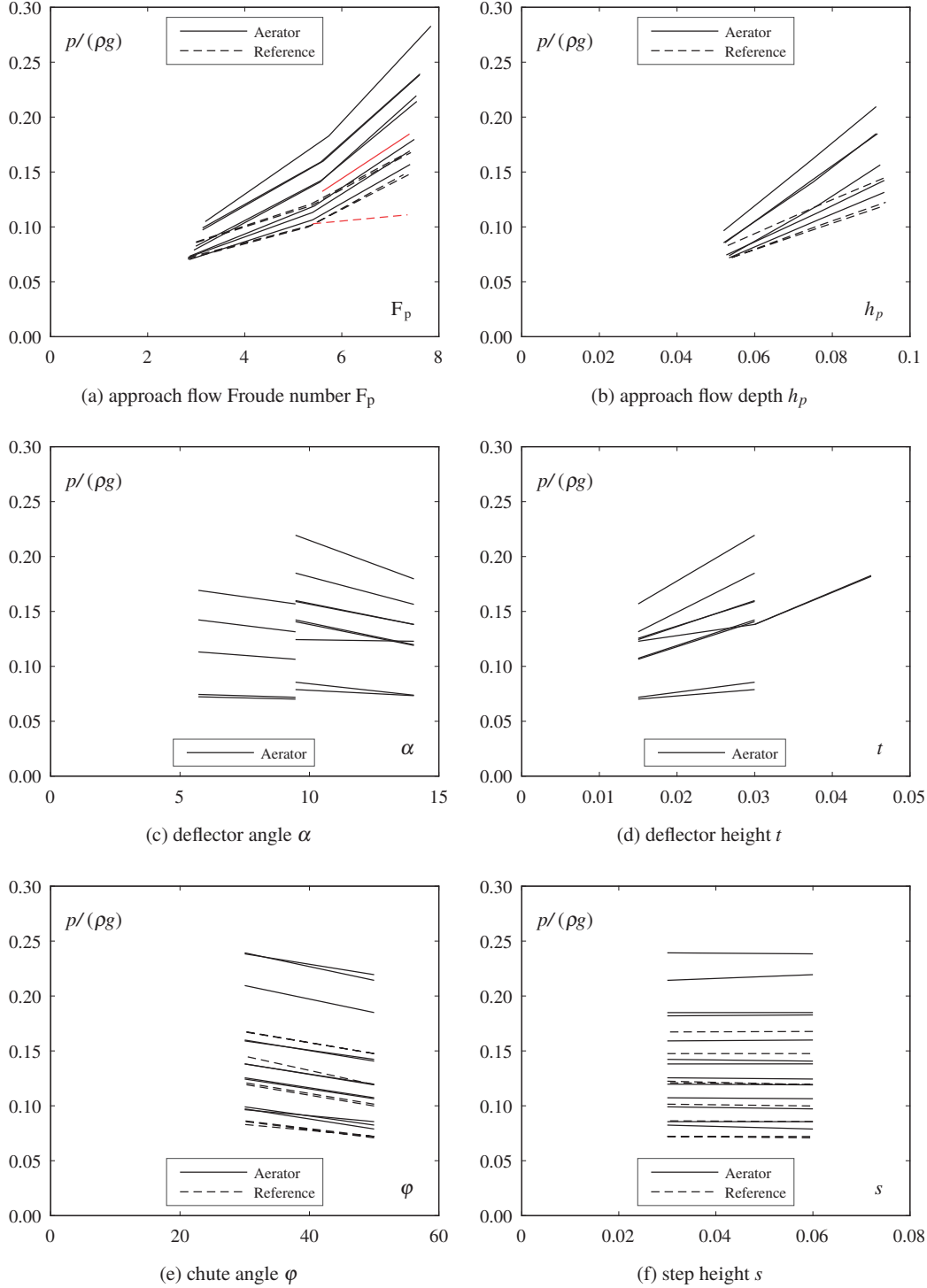


Figure E.7 – Influence of the parameters on the approach flow bottom pressure $p/(\rho g)$ (red indicates tests with the grid)

E.8 Approach flow bottom pressure fluctuations

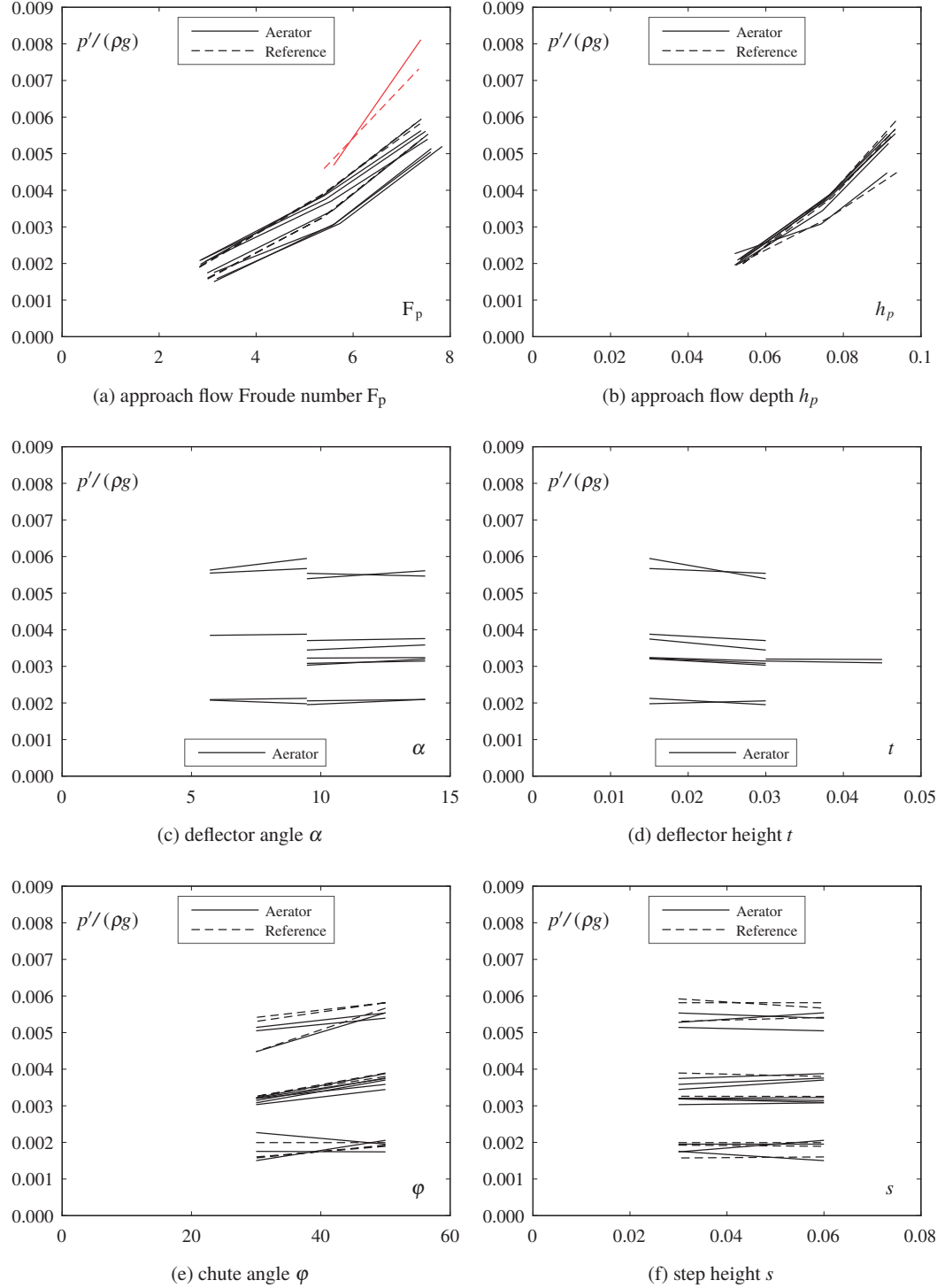


Figure E.8 – Influence of the parameters on the approach flow bottom pressure RMS fluctuations $p'/(ρg)$ (red indicates tests with the grid)

E.9 Deflector overpressure

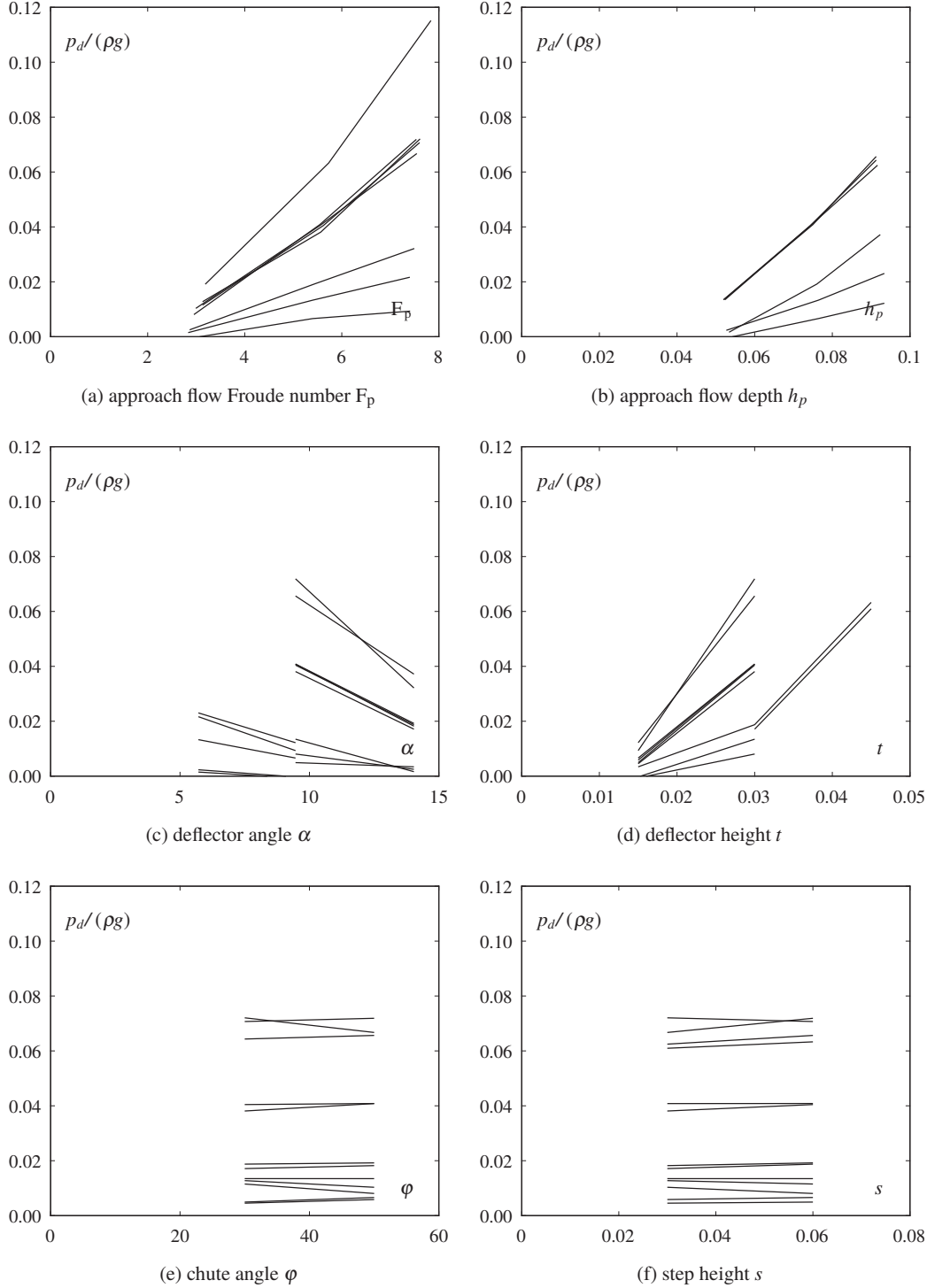


Figure E.9 – Influence of the parameters on the deflector overpressure $p_d' / (\rho g)$

E.10 Approach flow normal fluctuating velocity

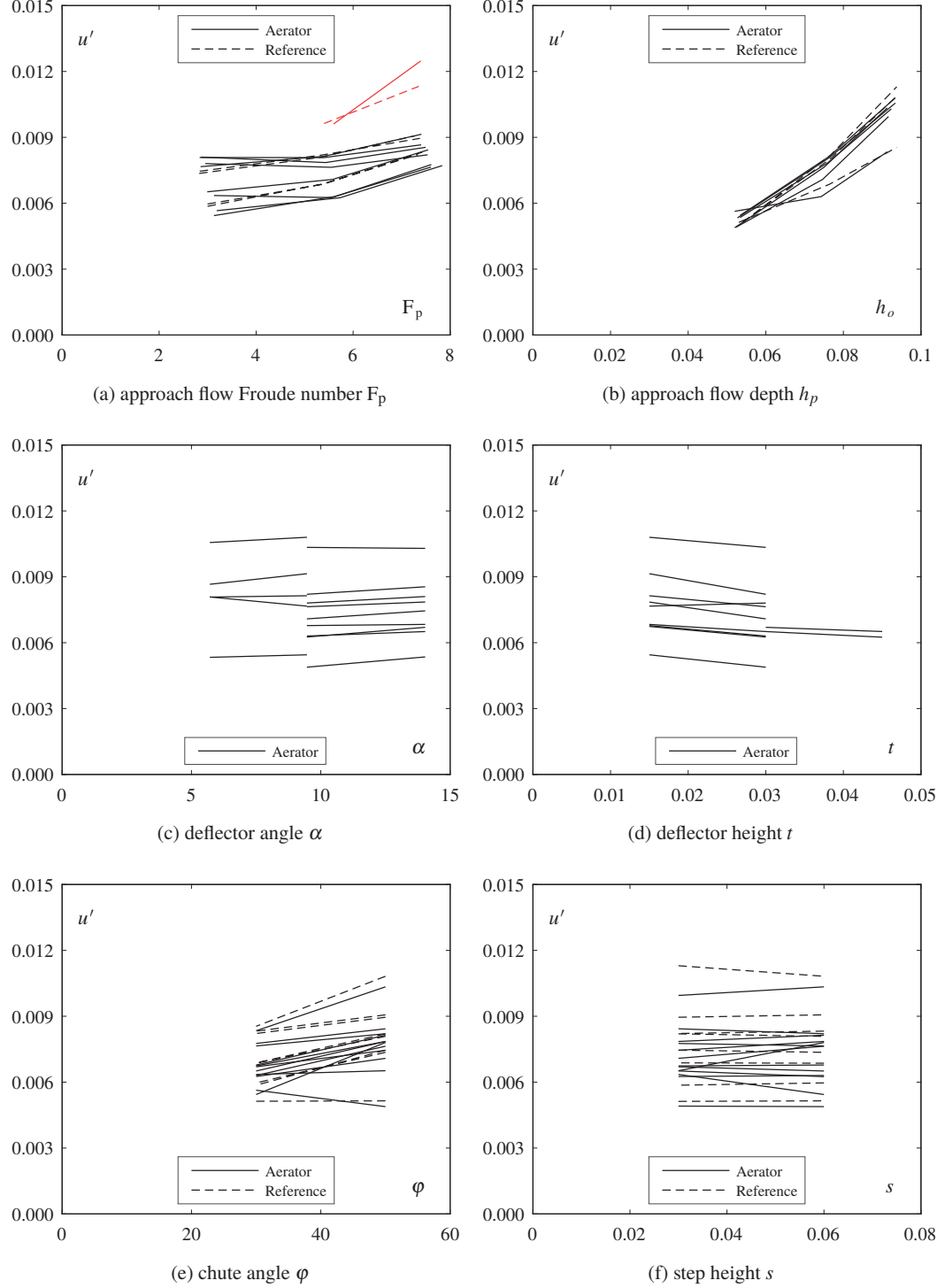


Figure E.10 – Influence of the parameters on the normal fluctuating velocity u' deduced from p' (cf. Appendix C)(red indicates tests with the grid)

E.11 Approach flow turbulence intensity

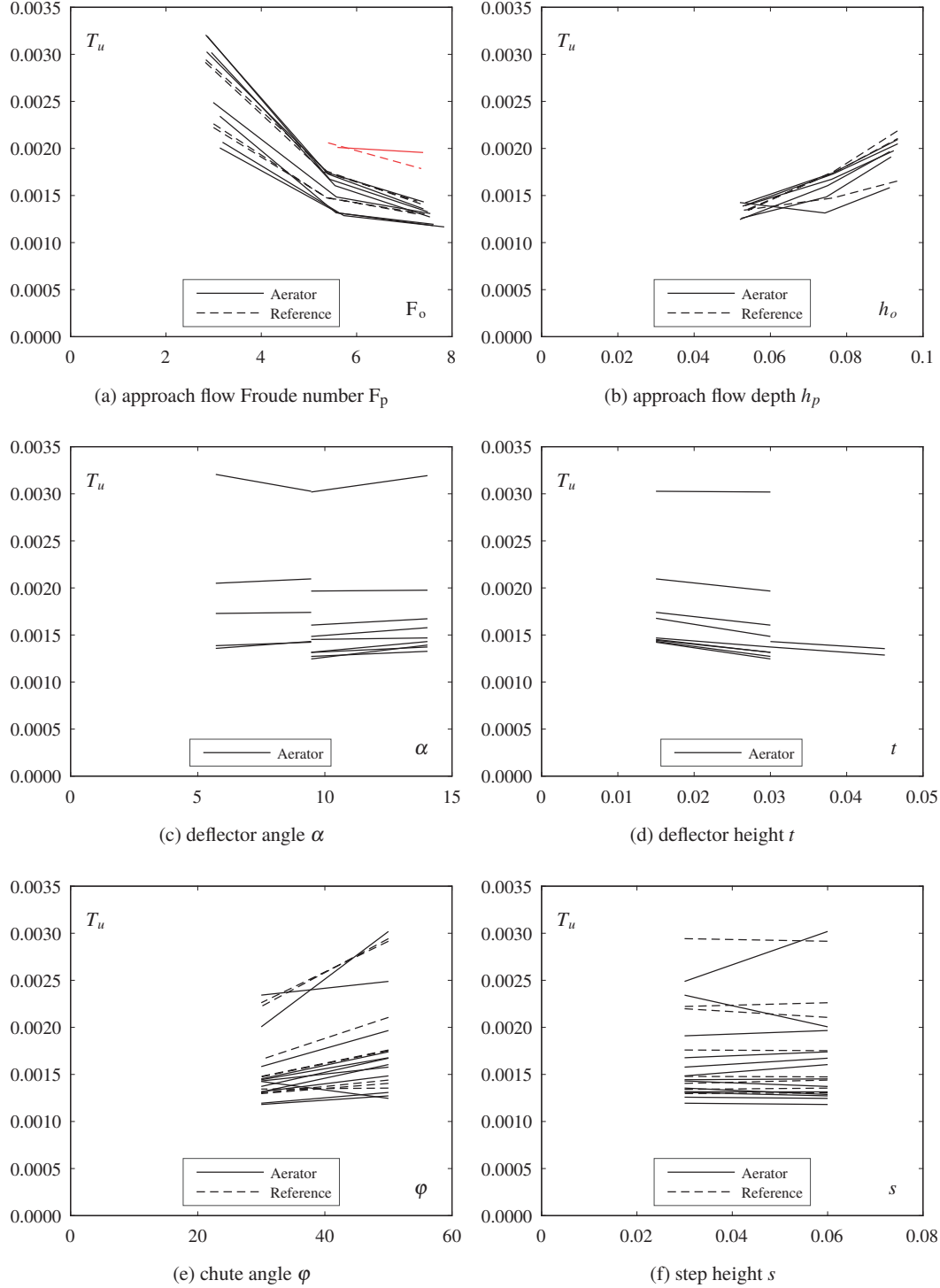


Figure E.11 – Influence of the parameters on the turbulence intensity $T_u = u'/u_o$ (red indicates tests with the grid)

Appendix F

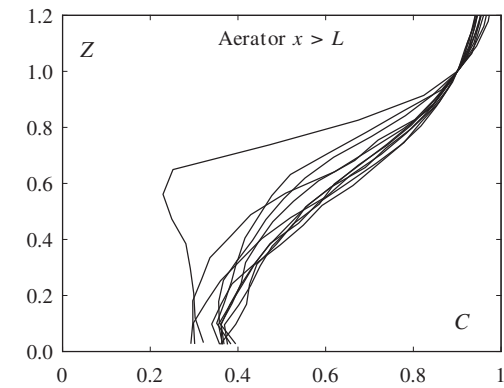
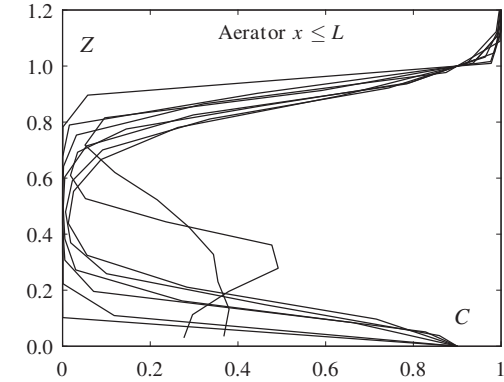
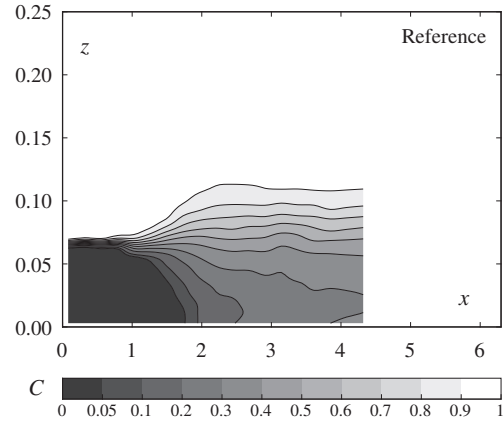
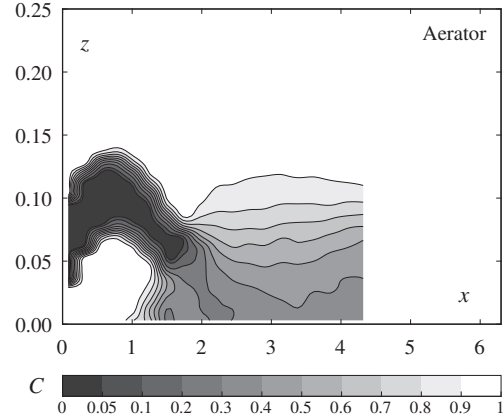
Testsheets

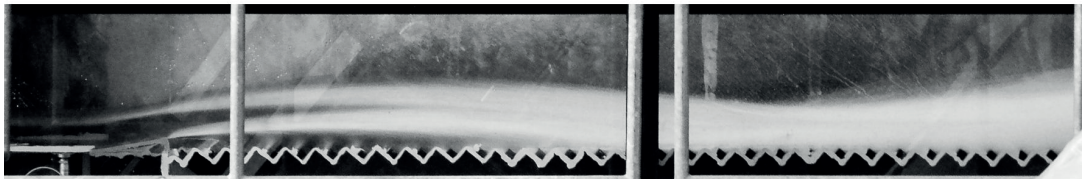
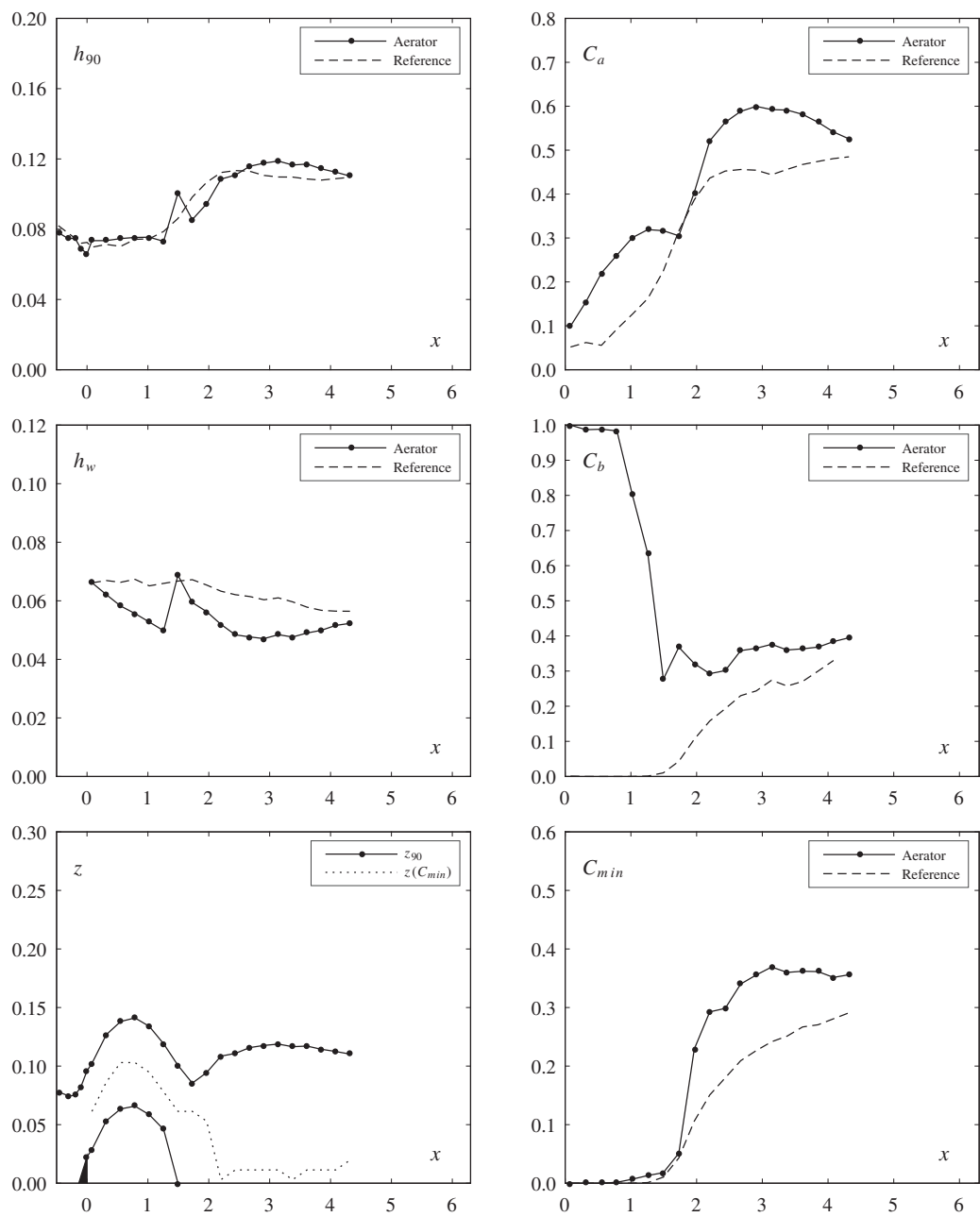
Testsheets summarizing the main results of each test are presented in this Appendix. An aerator testsheet includes the data from the corresponding reference test, and therefore no testsheets are given for reference tests. Photos of the reference tests are given at the end.

A few remarks on the testsheets:

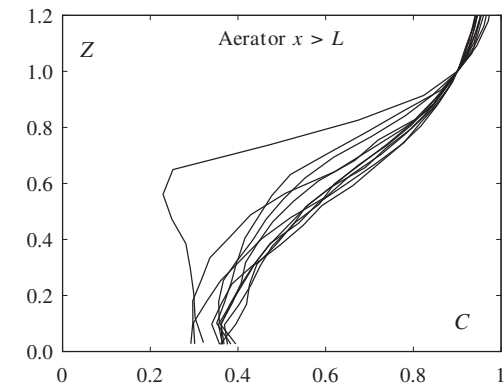
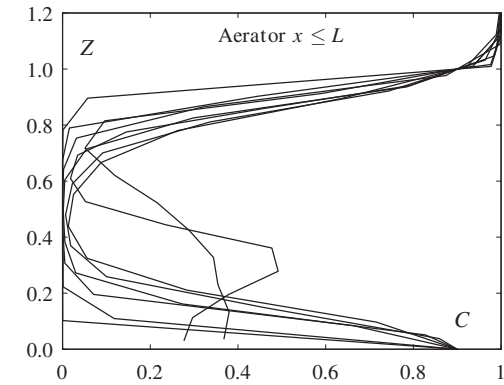
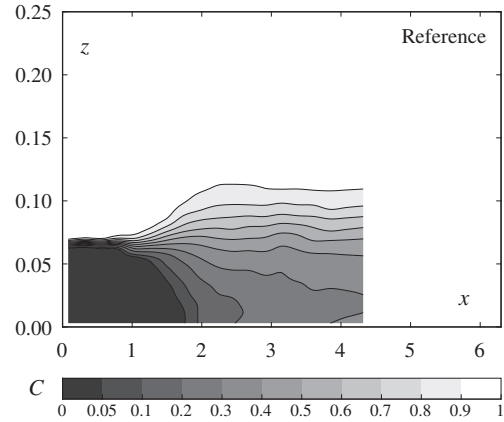
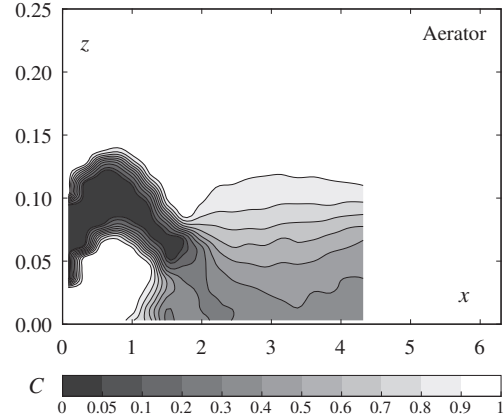
- The discontinuity in h_{90} at $x = 0$ is due to the change of measurement technique (point gauge for $x \leq 0$, fiber optical probe for $x > 0$).
- The discontinuity in h_{90} , h_w and sometimes C_b shortly before $x \approx L$ is due to the roller.
- The elevation of the minimum air concentration $z(C_{min})$ is not accurate at the beginning in the jet blackwater core as multiple points have a concentration $C \approx 0$.
- The vertical bars across the photos are the handrails of the stairs next to the channel. They were digitally removed in the photos presented in the report.

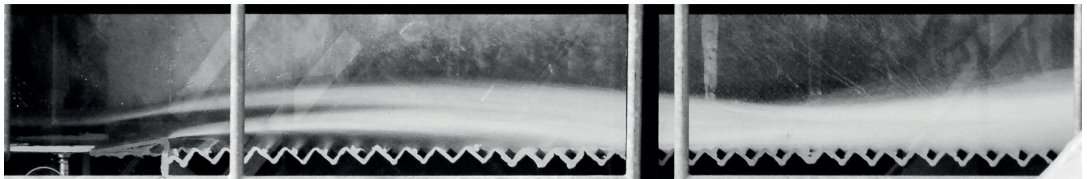
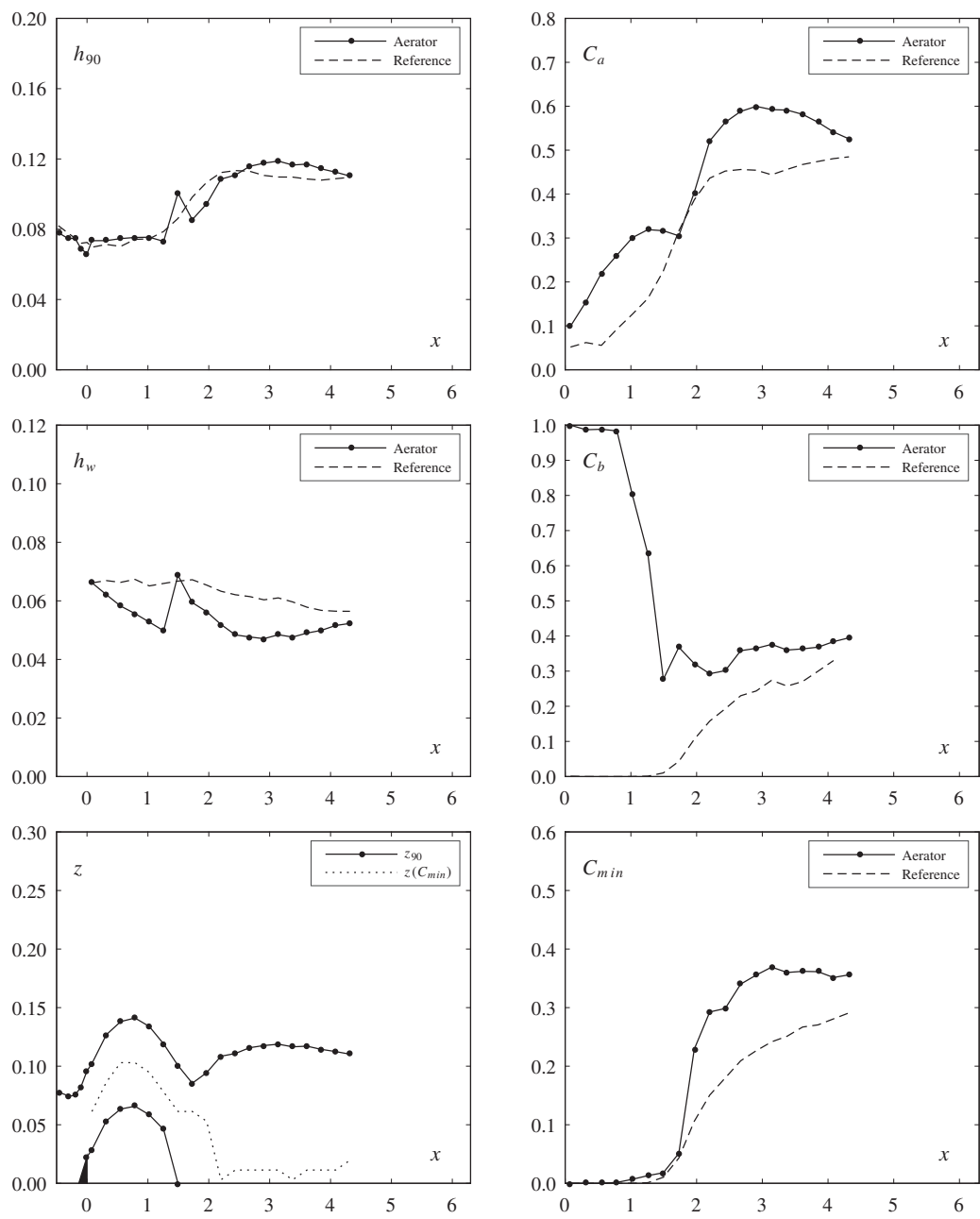
	Aerator	Reference	
Test	1	8	
Parameters			
φ	50	50	[°]
s	0.030	0.030	[m]
F_o	5.54	5.56	[-]
h_o	0.075	0.075	[m]
α	9.46	-	[°]
t	0.030	-	[m]
Flow			
q	0.356	0.358	[m ² /s]
h_c	0.235	0.235	[m]
h_c/s	7.82	7.85	[-]
u_o	4.75	4.77	[m/s]
Pressure			
$p/(\rho g)$	0.142	0.101	[m]
$p'/(\rho g)$	0.0034	0.0039	[m]
Dimensionless numbers			
R	356218	357723	[-]
W_o	153	154	[-]
F_k	48.5	48.7	[-]
F_s	25.0	25.1	[-]
Inception point			
x_i	-	1.49	[m]
h_i	-	0.086	[m]
h_{wi}	-	0.067	[m]
Air entrainment			
β	0.174	-	[-]
q_A	0.062	-	[m ² /s]
$u_{A,max}$	2.08	-	[m/s]
u_A	1.71	-	[m/s]
Jet			
L	1.75	-	[m]
L/h_o	23.3	-	[-]
L_{obs}	1.25	-	[m]
$\Delta p/h$	0.05	-	[-]
h_t	0.066	-	[m]
α_{tu}	8.42	-	[°]
α_{tl}	7.84	-	[°]
γ	6.73	-	[°]
Observation			
-			



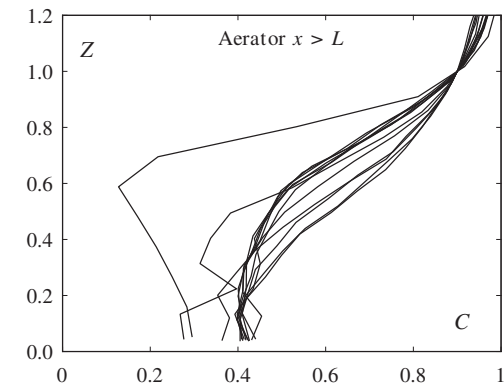
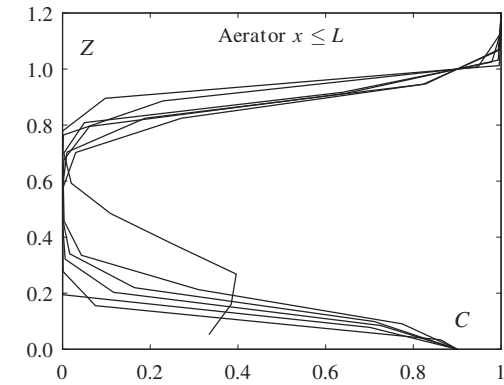
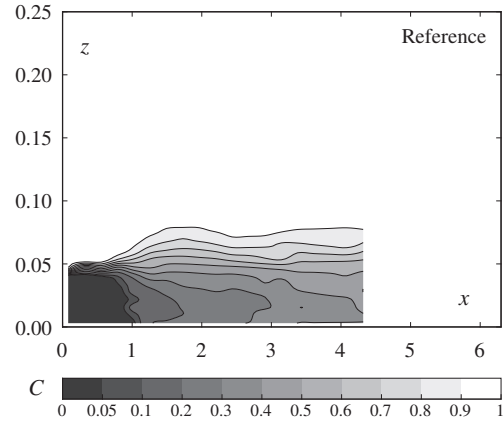
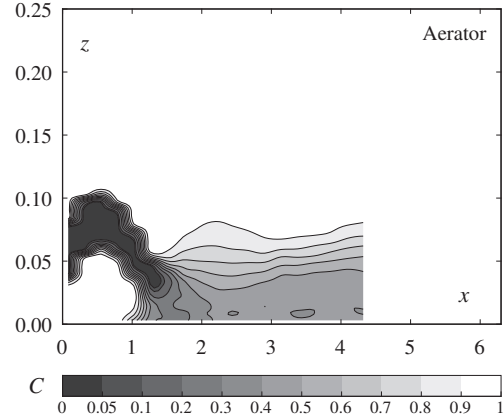


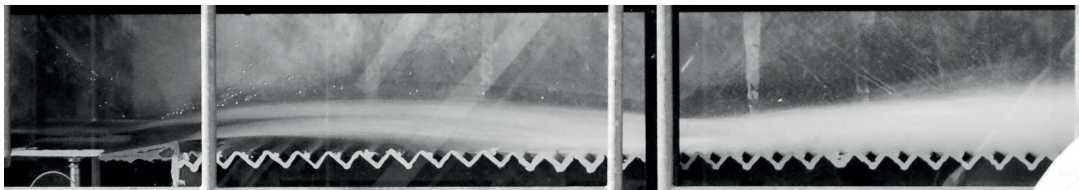
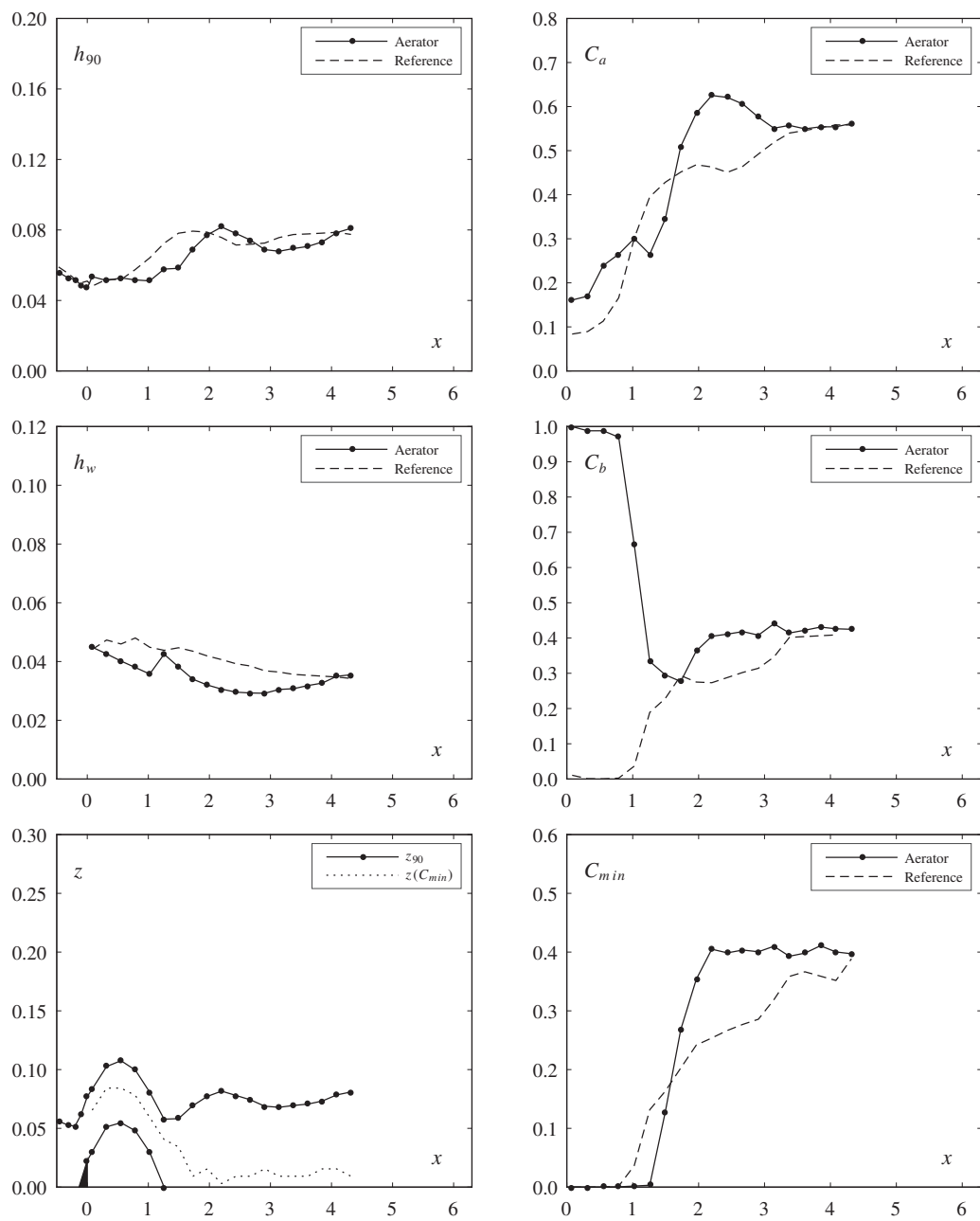
	Aerator	Reference	
Test	1	8	
Parameters			
φ	50	50	[°]
s	0.030	0.030	[m]
F_o	5.54	5.56	[-]
h_o	0.075	0.075	[m]
α	9.46	-	[°]
t	0.030	-	[m]
Flow			
q	0.356	0.358	[m ² /s]
h_c	0.235	0.235	[m]
h_c/s	7.82	7.85	[-]
u_o	4.75	4.77	[m/s]
Pressure			
$p/(\rho g)$	0.142	0.101	[m]
$p'/(\rho g)$	0.0034	0.0039	[m]
Dimensionless numbers			
R	356218	357723	[-]
W_o	153	154	[-]
F_k	48.5	48.7	[-]
F_s	25.0	25.1	[-]
Inception point			
x_i	-	1.49	[m]
h_i	-	0.086	[m]
h_{wi}	-	0.067	[m]
Air entrainment			
β	0.174	-	[-]
q_A	0.062	-	[m ² /s]
$u_{A,max}$	2.08	-	[m/s]
u_A	1.71	-	[m/s]
Jet			
L	1.75	-	[m]
L/h_o	23.3	-	[-]
L_{obs}	1.25	-	[m]
$\Delta p/h$	0.05	-	[-]
h_t	0.066	-	[m]
α_{tu}	8.42	-	[°]
α_{tl}	7.84	-	[°]
γ	6.73	-	[°]
Observation			
-			



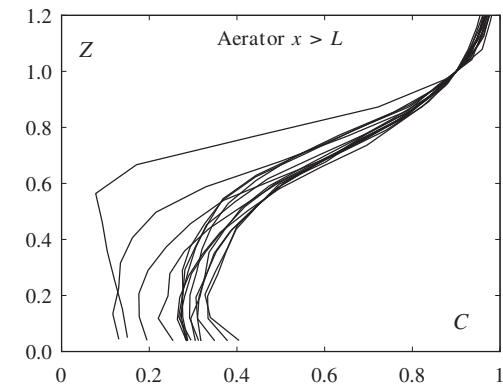
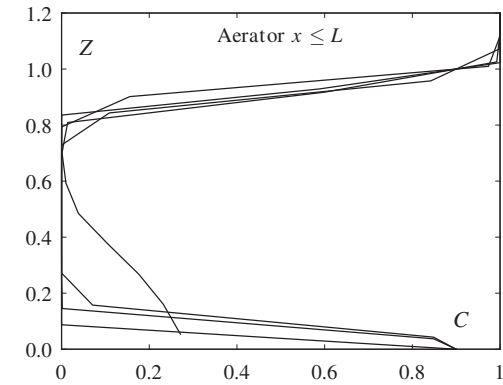
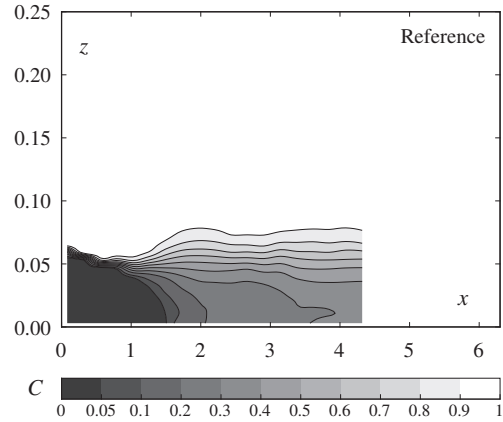
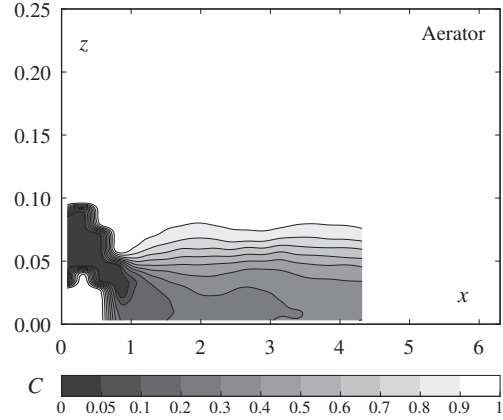


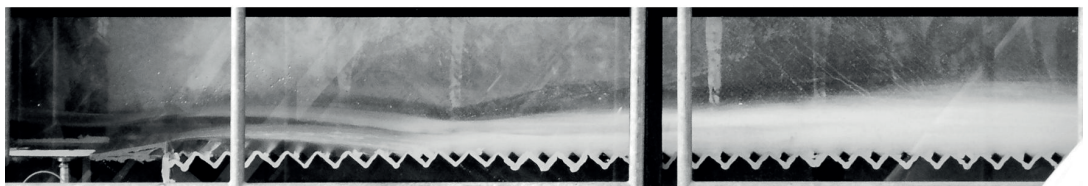
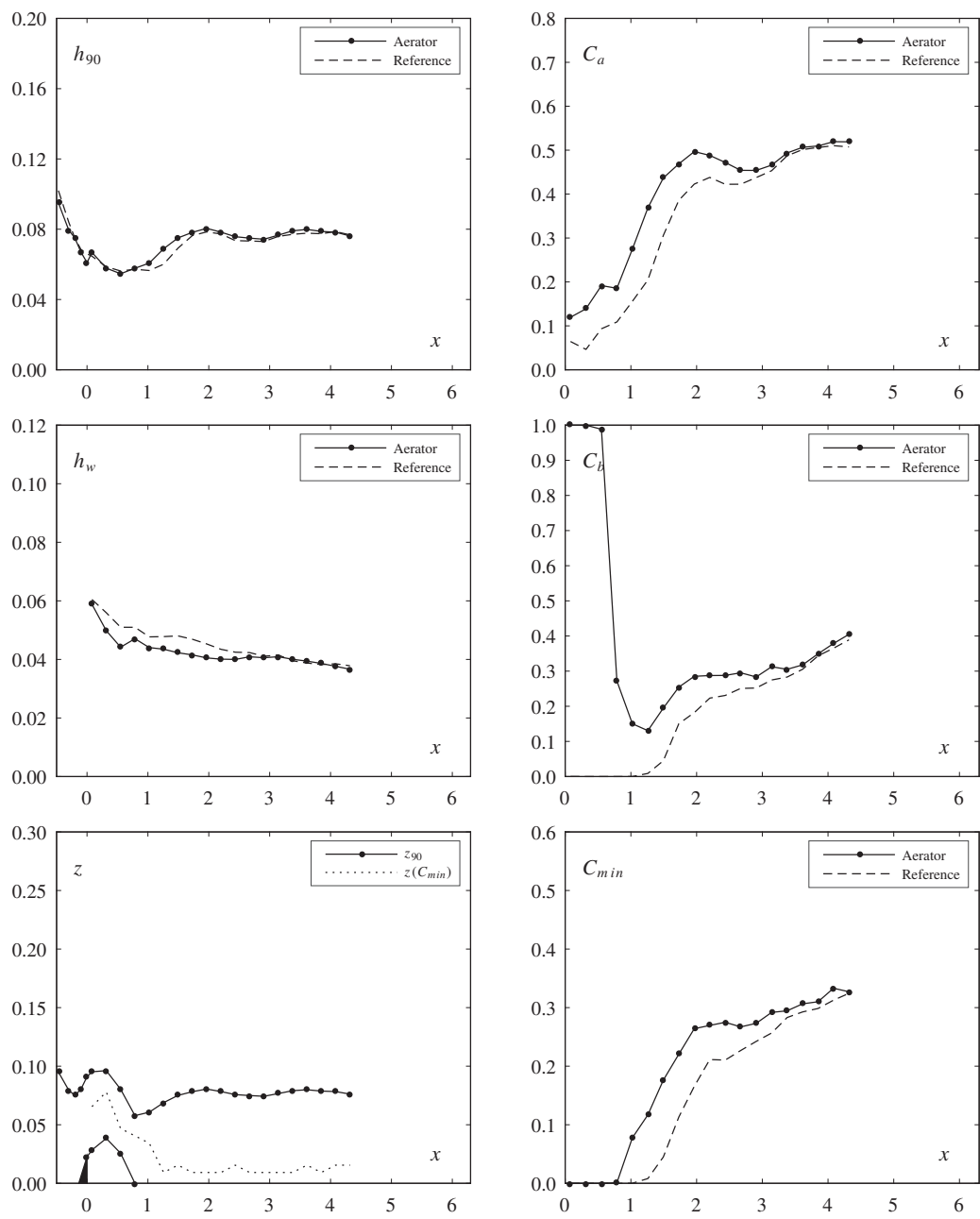
	Aerator	Reference	
Test	2	9	
Parameters			
φ	50	50	[°]
s	0.030	0.030	[m]
F_o	5.50	5.56	[-]
h_o	0.052	0.052	[m]
α	9.46	-	[°]
t	0.030	-	[m]
Flow			
q	0.204	0.207	[m ² /s]
h_c	0.162	0.163	[m]
h_c/s	5.40	5.44	[-]
u_o	3.93	3.97	[m/s]
Pressure			
$p/(\rho g)$	0.086	0.072	[m]
$p'/(\rho g)$	0.0020	0.0020	[m]
Dimensionless numbers			
R	204256	206621	[-]
W_o	106	107	[-]
F_k	27.8	28.1	[-]
F_s	14.3	14.5	[-]
Inception point			
x_i	-	0.84	[m]
h_i	-	0.059	[m]
h_{wi}	-	0.047	[m]
Air entrainment			
β	0.139	-	[-]
q_A	0.028	-	[m ² /s]
$u_{A,max}$	2.10	-	[m/s]
u_A	1.71	-	[m/s]
Jet			
L	1.29	-	[m]
L/h_o	24.9	-	[-]
L_{obs}	1.02	-	[m]
$\Delta p/h$	0.05	-	[-]
h_t	0.047	-	[m]
α_{tu}	9.10	-	[°]
α_{tl}	8.59	-	[°]
γ	7.39	-	[°]
Observation			
-			



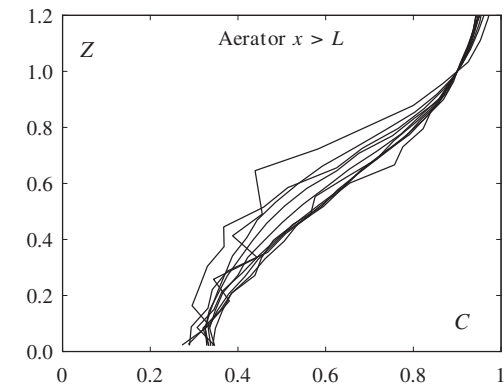
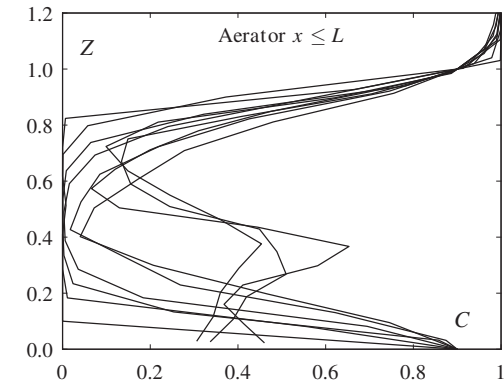
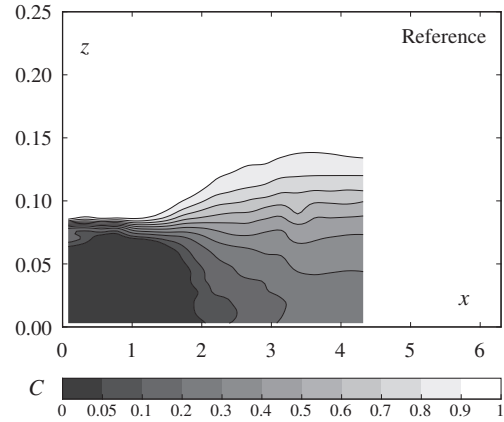
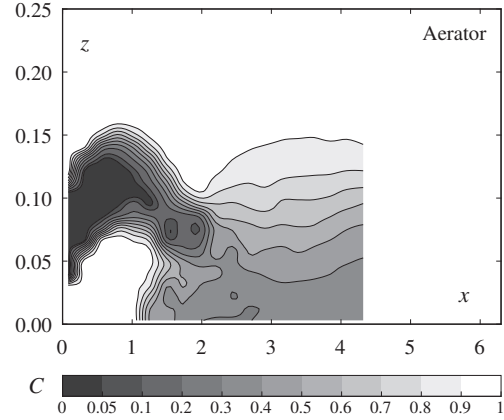


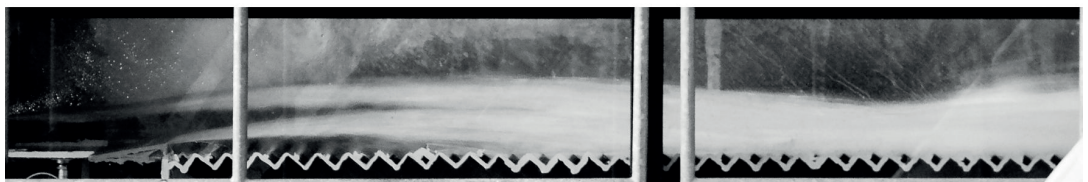
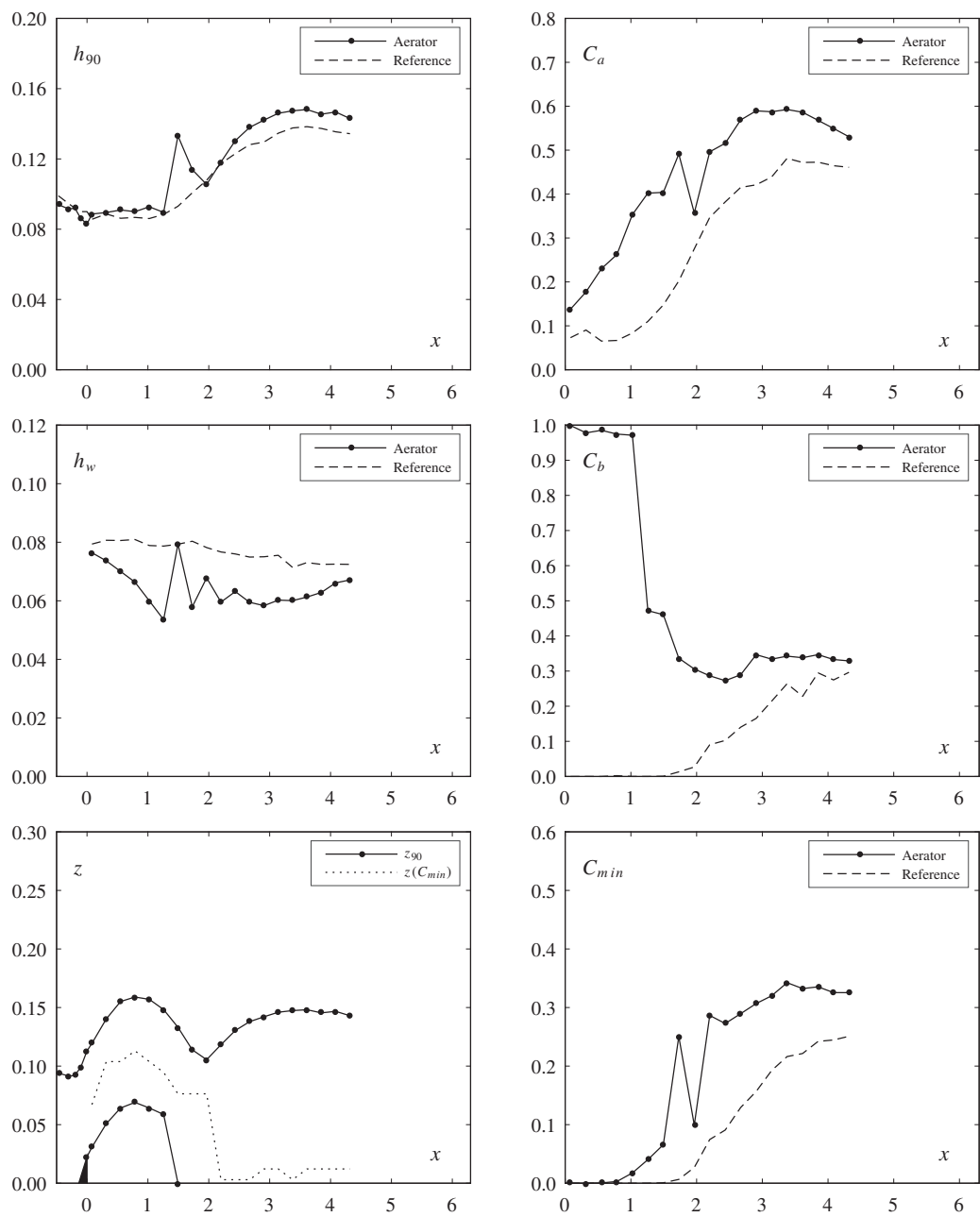
	Aerator	Reference	
Test	3	10	
Parameters			
φ	50	50	[°]
s	0.030	0.030	[m]
F_o	3.18	3.20	[-]
h_o	0.075	0.075	[m]
α	9.46	-	[°]
t	0.030	-	[m]
Flow			
q	0.205	0.206	[m ² /s]
h_c	0.162	0.163	[m]
h_c/s	5.41	5.43	[-]
u_o	2.73	2.75	[m/s]
Pressure			
$p/(\rho g)$	0.082	0.072	[m]
$p'/(\rho g)$	0.0017	0.0019	[m]
Dimensionless numbers			
R	204759	206022	[-]
W_o	88	89	[-]
F_k	27.9	28.1	[-]
F_s	14.4	14.5	[-]
Inception point			
x_i	-	1.27	[m]
h_i	-	0.060	[m]
h_{wi}	-	0.048	[m]
Air entrainment			
β	0.059	-	[-]
q_A	0.012	-	[m ² /s]
$u_{A,max}$	0.42	-	[m/s]
u_A	0.33	-	[m/s]
Jet			
L	0.79	-	[m]
L/h_o	10.6	-	[-]
L_{obs}	0.61	-	[m]
$\Delta p/h$	0.03	-	[-]
h_t	0.061	-	[m]
α_{tu}	7.15	-	[°]
α_{tl}	7.78	-	[°]
γ	7.61	-	[°]
Observation			
-			



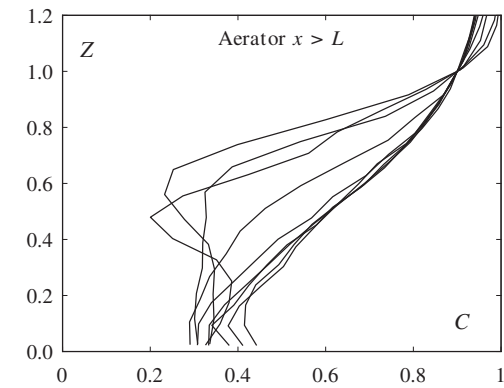
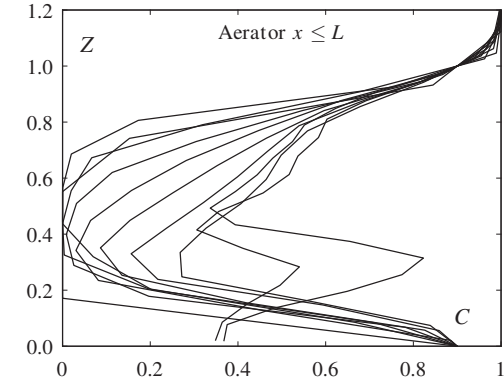
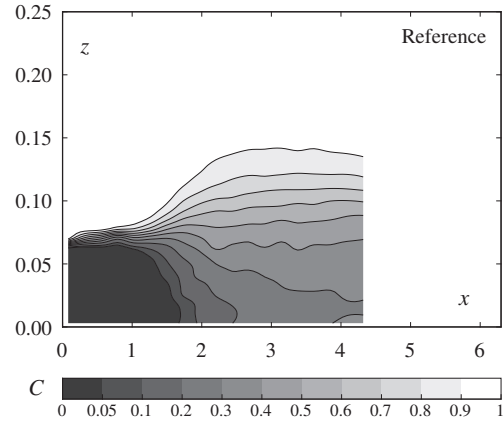
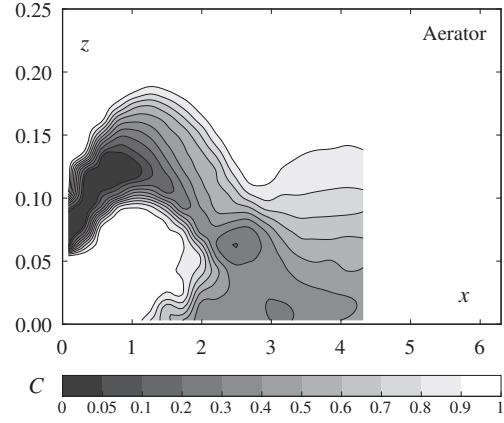


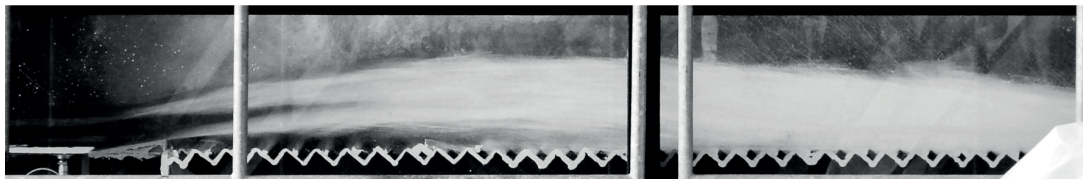
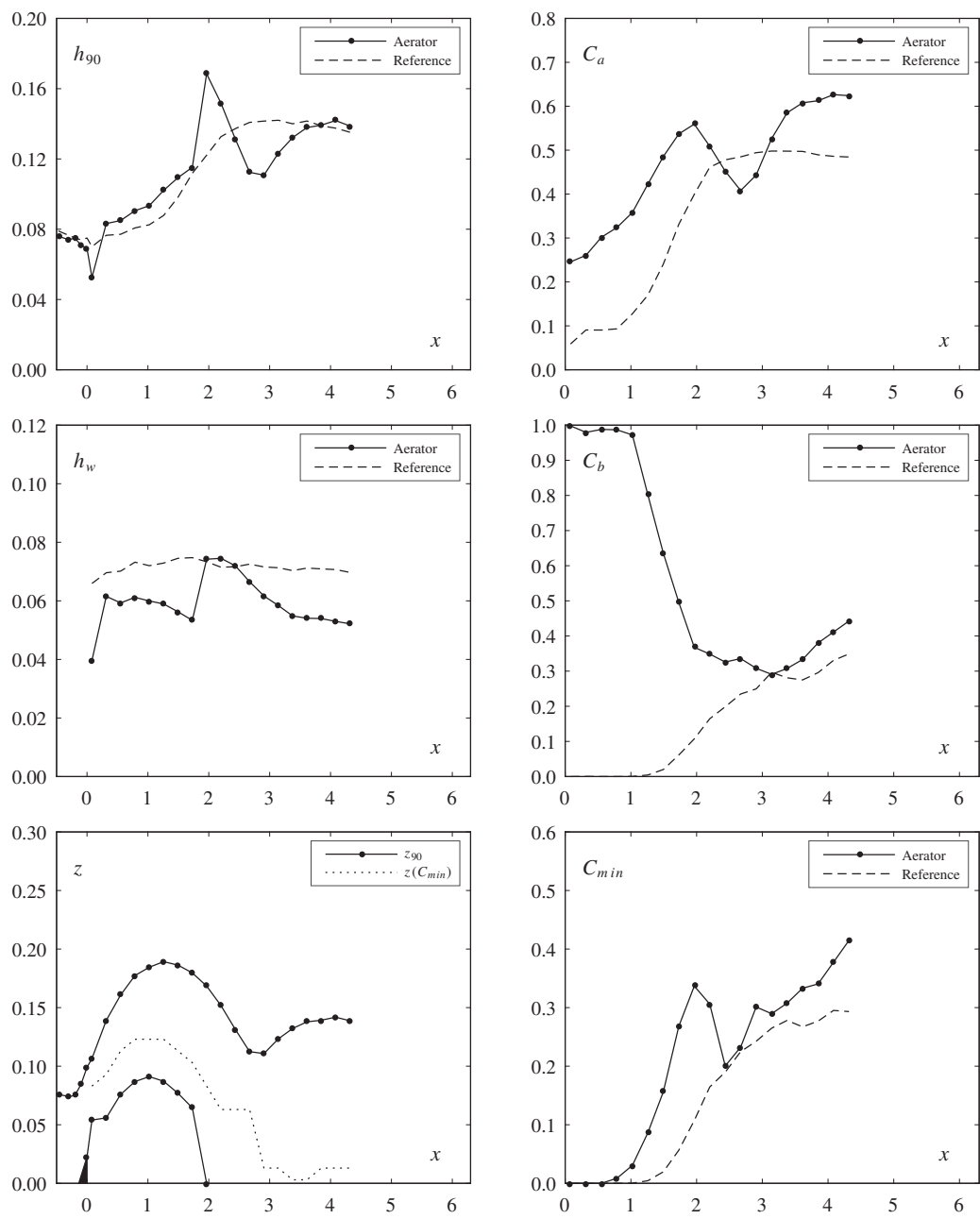
	Aerator	Reference	
Test	4	7	
Parameters			
φ	50	50	[°]
s	0.030	0.030	[m]
F_o	5.46	5.51	[-]
h_o	0.092	0.092	[m]
α	9.46	-	[°]
t	0.030	-	[m]
Flow			
q	0.477	0.482	[m ² /s]
h_c	0.285	0.287	[m]
h_c/s	9.51	9.57	[-]
u_o	5.19	5.24	[m/s]
Pressure			
$p/(\rho g)$	0.185	0.122	[m]
$p'/(\rho g)$	0.0053	0.0059	[m]
Dimensionless numbers			
R	477252	481989	[-]
W_o	185	187	[-]
F_k	65.0	65.7	[-]
F_s	33.5	33.8	[-]
Inception point			
x_i	-	1.67	[m]
h_i	-	0.099	[m]
h_{wi}	-	0.080	[m]
Air entrainment			
β	0.191	-	[-]
q_A	0.091	-	[m ² /s]
$u_{A,max}$	3.03	-	[m/s]
u_A	2.51	-	[m/s]
Jet			
L	1.99	-	[m]
L/h_o	21.7	-	[-]
L_{obs}	1.32	-	[m]
$\Delta p/h$	0.07	-	[-]
h_t	0.083	-	[m]
α_{tu}	8.22	-	[°]
α_{tl}	7.63	-	[°]
γ	6.24	-	[°]
Observation			
-			



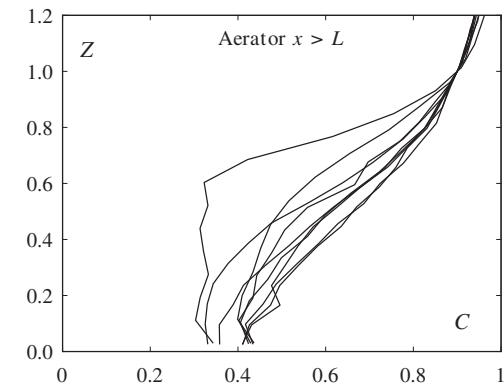
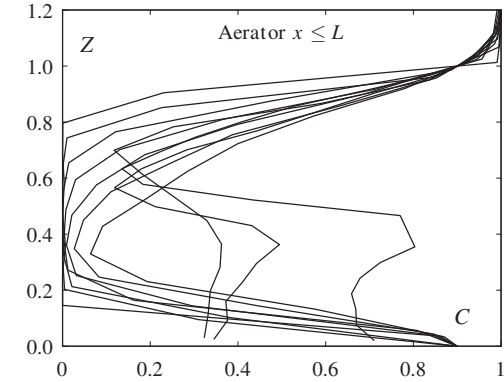
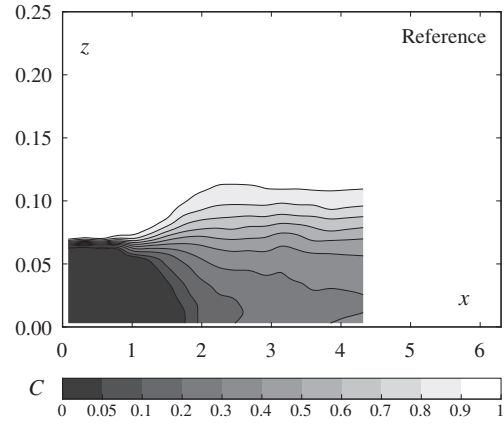
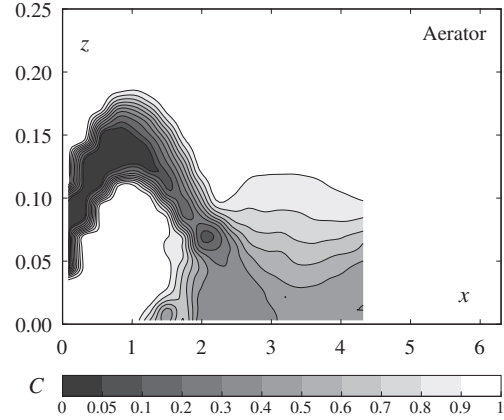


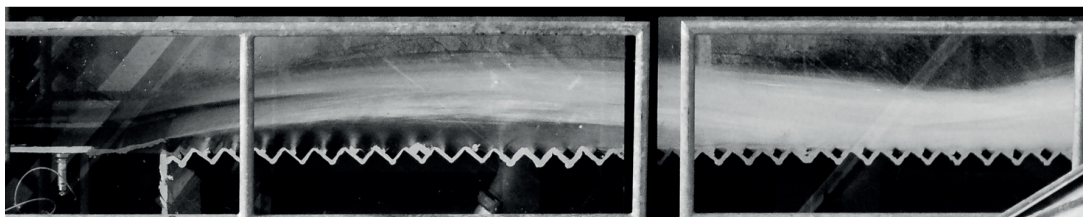
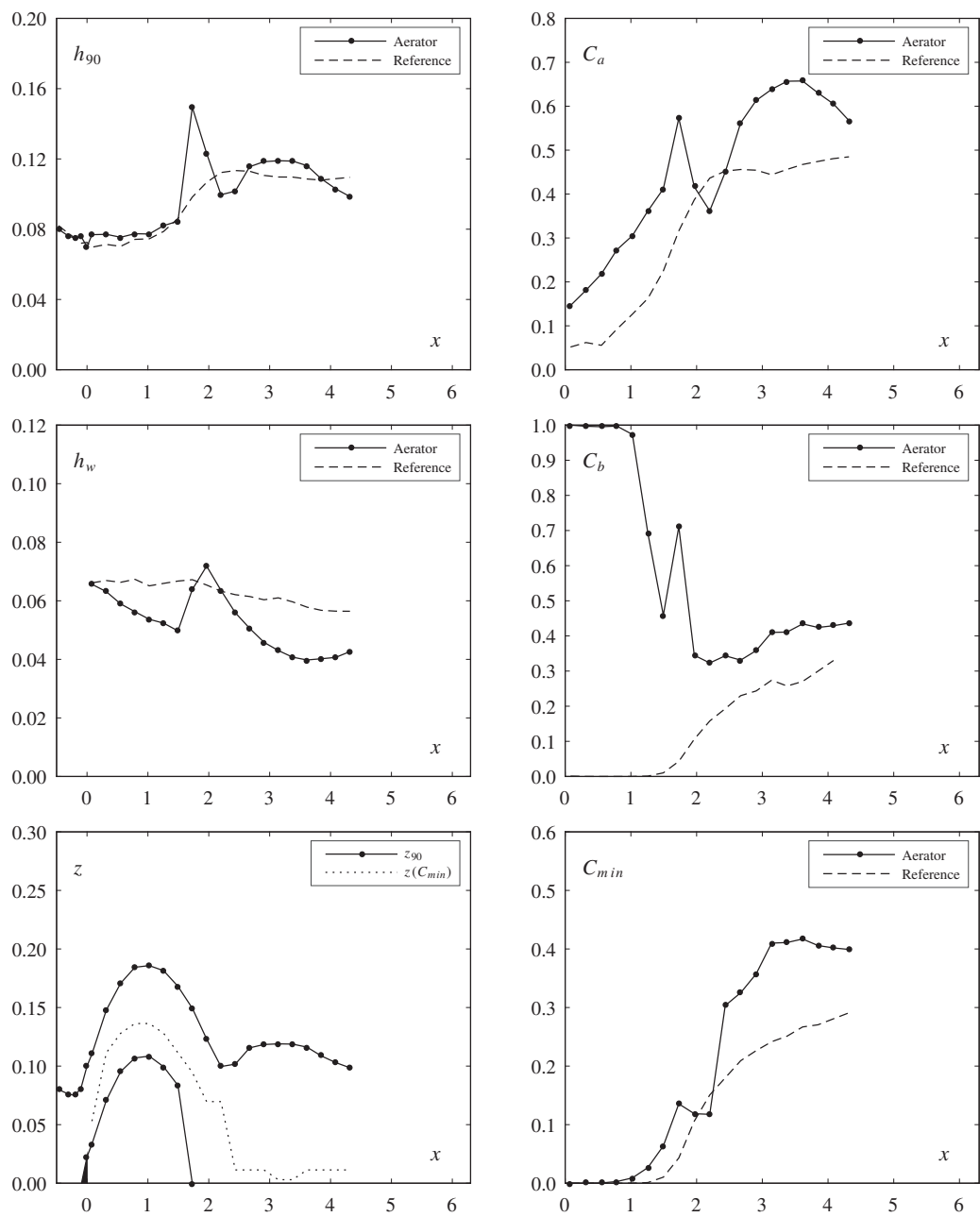
	Aerator	Reference	
Test	5	6	
Parameters			
φ	50	50	[°]
s	0.030	0.030	[m]
F_o	7.44	7.53	[-]
h_o	0.075	0.075	[m]
α	9.46	-	[°]
t	0.030	-	[m]
Flow			
q	0.479	0.485	[m ² /s]
h_c	0.286	0.288	[m]
h_c/s	9.53	9.61	[-]
u_o	6.38	6.46	[m/s]
Pressure			
$p/(\rho g)$	0.214	0.148	[m]
$p'/(\rho g)$	0.0055	0.0058	[m]
Dimensionless numbers			
R	478662	484628	[-]
W_o	206	209	[-]
F_k	65.2	66.0	[-]
F_s	33.6	34.0	[-]
Inception point			
x_i	-	1.34	[m]
h_i	-	0.092	[m]
h_{wi}	-	0.073	[m]
Air entrainment			
β	0.245	-	[-]
q_A	0.117	-	[m ² /s]
$u_{A,max}$	3.88	-	[m/s]
u_A	3.23	-	[m/s]
Jet			
L	2.41	-	[m]
L/h_o	32.2	-	[-]
L_{obs}	1.52	-	[m]
$\Delta p/h$	0.10	-	[-]
h_t	0.069	-	[m]
α_{tu}	8.96	-	[°]
α_{tl}	7.39	-	[°]
γ	6.82	-	[°]
Observation			
-			



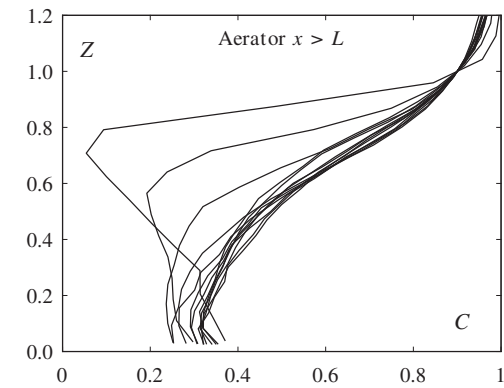
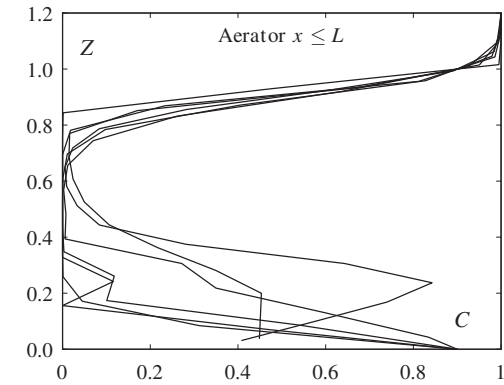
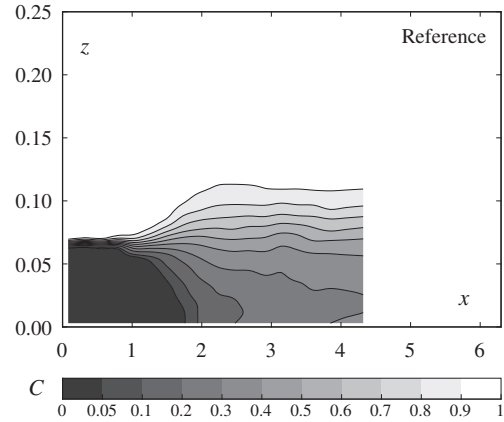
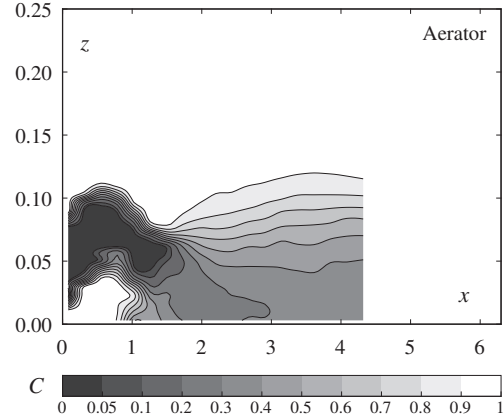


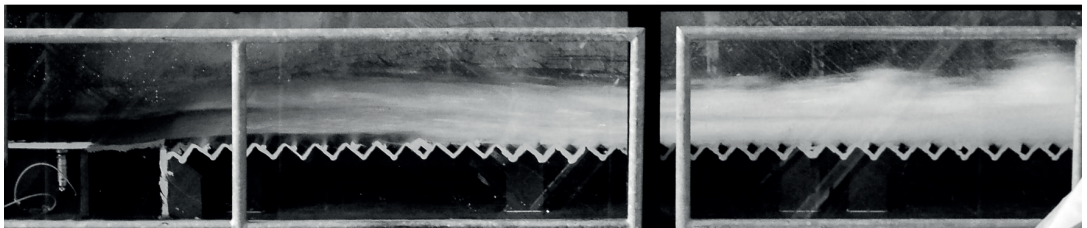
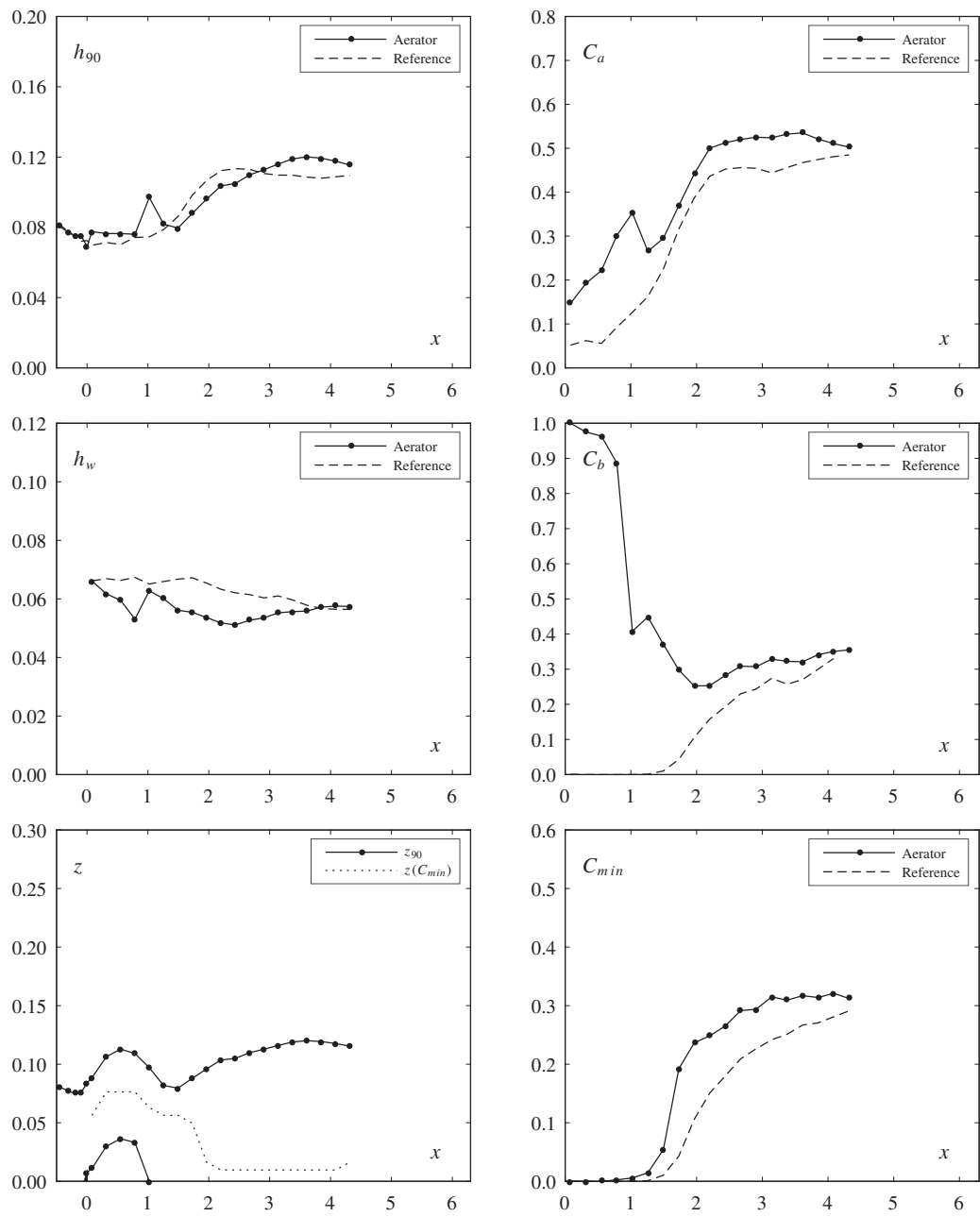
	Aerator	Reference	
Test	11	8	
Parameters			
φ	50	50	[°]
s	0.030	0.030	[m]
F_o	5.56	5.56	[-]
h_o	0.075	0.075	[m]
α	14.04	-	[°]
t	0.030	-	[m]
Flow			
q	0.357	0.358	[m ² /s]
h_c	0.235	0.235	[m]
h_c/s	7.84	7.85	[-]
u_o	4.77	4.77	[m/s]
Pressure			
$p/(\rho g)$	0.120	0.101	[m]
$p'/(\rho g)$	0.0036	0.0039	[m]
Dimensionless numbers			
R	357437	357723	[-]
W_o	154	154	[-]
F_k	48.7	48.7	[-]
F_s	25.1	25.1	[-]
Inception point			
x_i	-	1.49	[m]
h_i	-	0.086	[m]
h_{wi}	-	0.067	[m]
Air entrainment			
β	0.235	-	[-]
q_A	0.084	-	[m ² /s]
$u_{A,max}$	2.80	-	[m/s]
u_A	2.31	-	[m/s]
Jet			
L	2.23	-	[m]
L/h_o	29.7	-	[-]
L_{obs}	1.57	-	[m]
$\Delta p/h$	0.04	-	[-]
h_t	0.070	-	[m]
α_{tu}	11.89	-	[°]
α_{tl}	11.30	-	[°]
γ	8.59	-	[°]
Observation			
-			



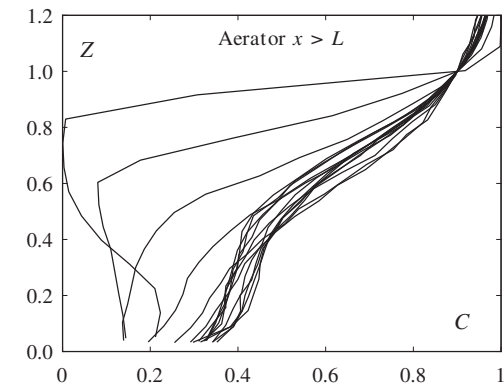
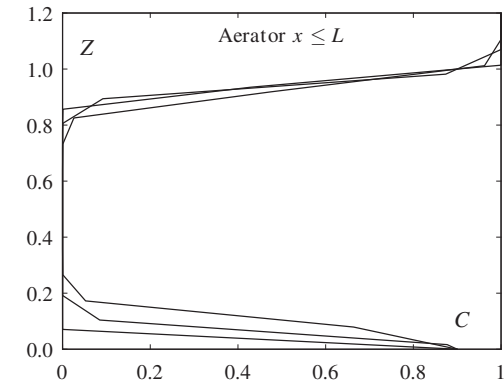
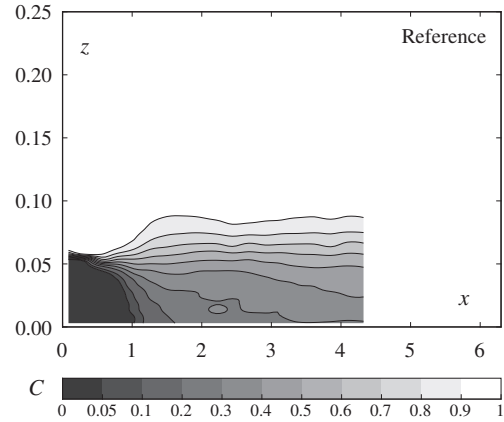
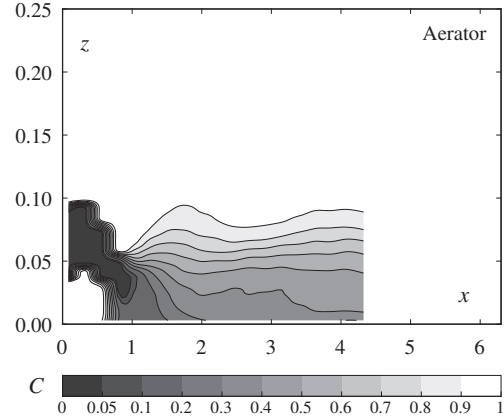


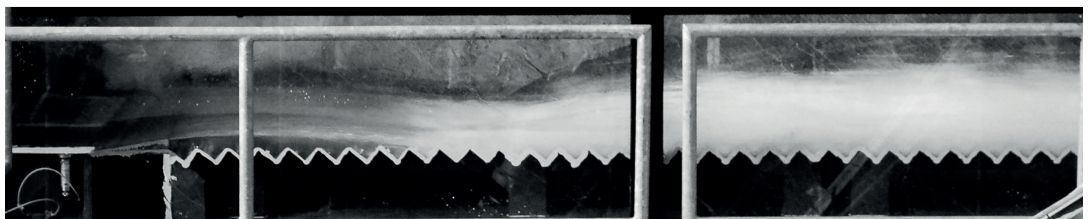
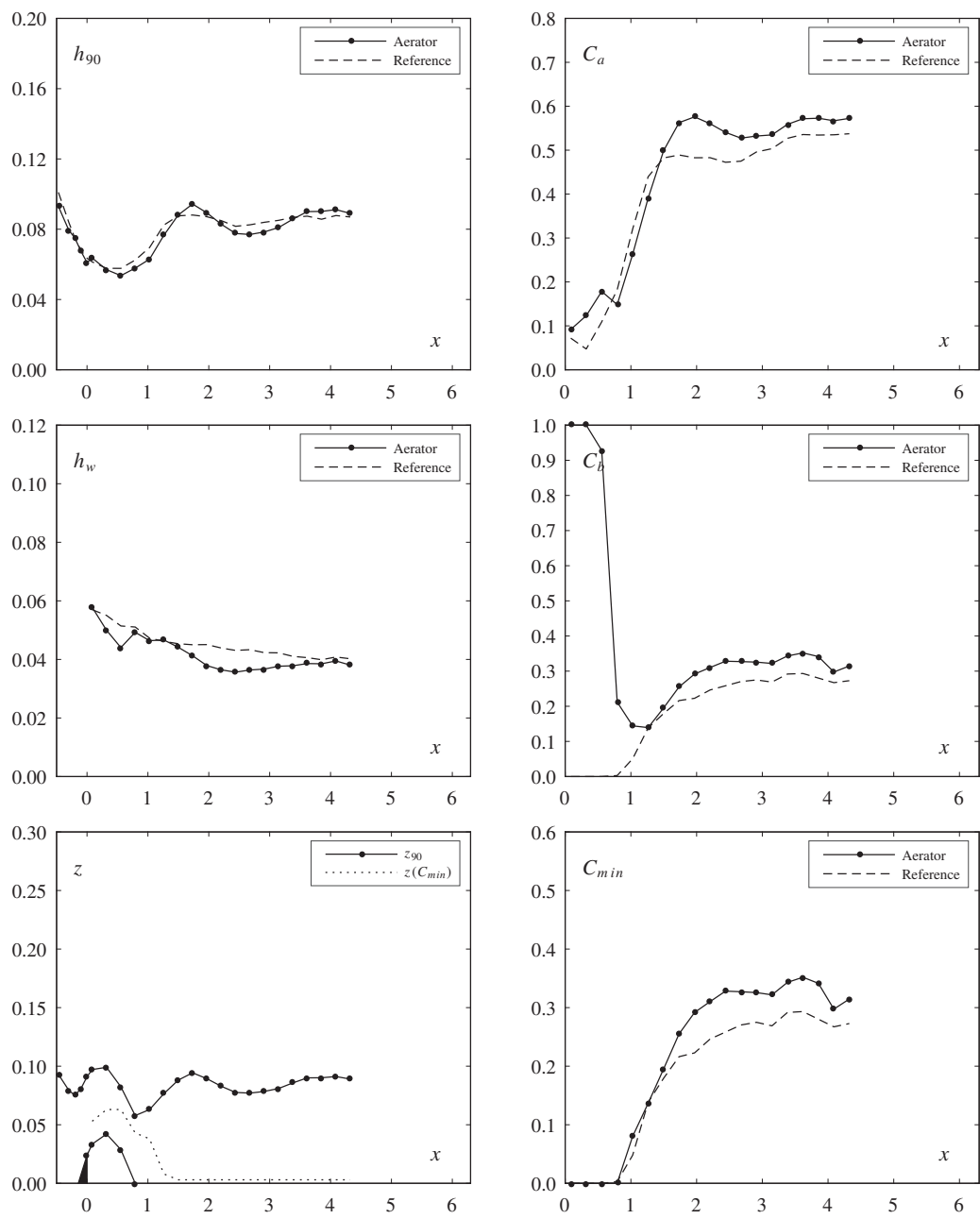
	Aerator	Reference	
Test	12	8	
Parameters			
φ	50	50	[°]
s	0.030	0.030	[m]
F_o	5.56	5.56	[-]
h_o	0.075	0.075	[m]
α	9.46	-	[°]
t	0.015	-	[m]
Flow			
q	0.358	0.358	[m ² /s]
h_c	0.235	0.235	[m]
h_c/s	7.85	7.85	[-]
u_o	4.77	4.77	[m/s]
Pressure			
$p/(\rho g)$	0.107	0.101	[m]
$p'/(\rho g)$	0.0037	0.0039	[m]
Dimensionless numbers			
R	357633	357723	[-]
W_o	154	154	[-]
F_k	48.7	48.7	[-]
F_s	25.1	25.1	[-]
Inception point			
x_i	-	1.49	[m]
h_i	-	0.086	[m]
h_{wi}	-	0.067	[m]
Air entrainment			
β	0.140	-	[-]
q_A	0.050	-	[m ² /s]
$u_{A,max}$	1.68	-	[m/s]
u_A	1.38	-	[m/s]
Jet			
L	1.33	-	[m]
L/h_o	17.8	-	[-]
L_{obs}	1.02	-	[m]
$\Delta p/h$	0.03	-	[-]
h_t	0.069	-	[m]
α_{tu}	7.41	-	[°]
α_{tl}	6.64	-	[°]
γ	5.22	-	[°]
Observation			
-			



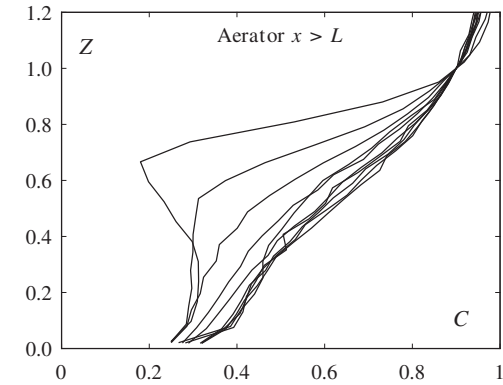
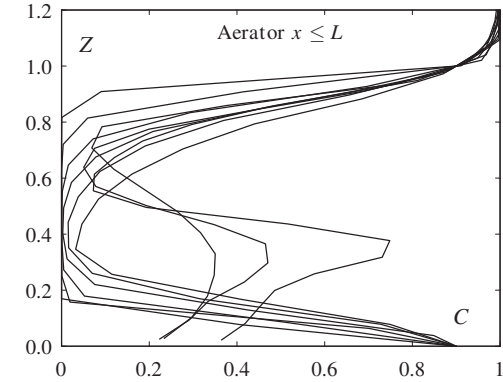
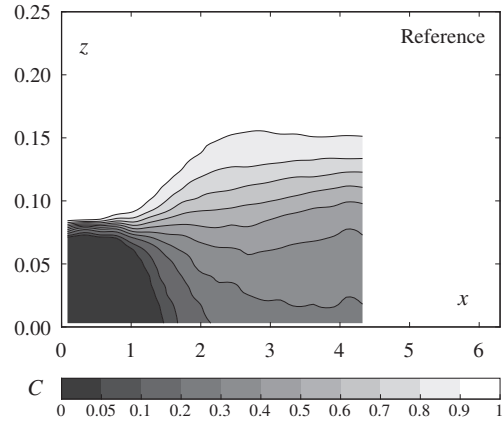
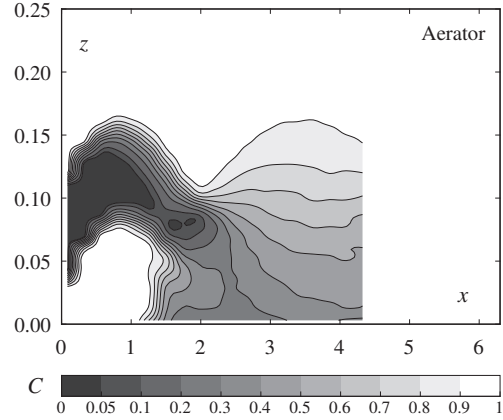


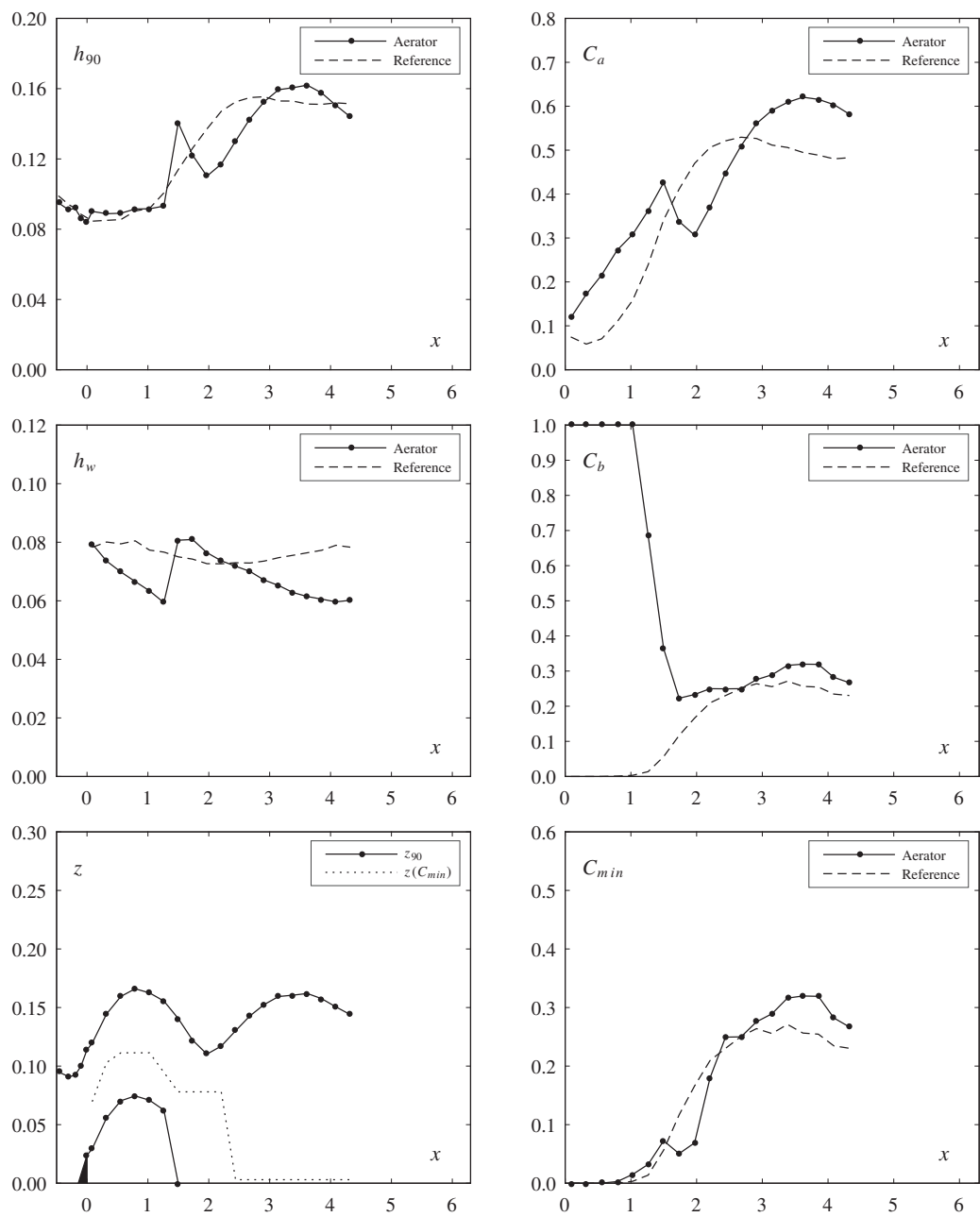
	Aerator	Reference	
Test	18	17	
Parameters			
φ	50	50	[°]
s	0.060	0.060	[m]
F_o	3.14	3.19	[-]
h_o	0.075	0.075	[m]
α	9.46	-	[°]
t	0.030	-	[m]
Flow			
q	0.202	0.205	[m ² /s]
h_c	0.161	0.163	[m]
h_c/s	2.68	2.71	[-]
u_o	2.69	2.74	[m/s]
Pressure			
$p/(\rho g)$	0.079	0.071	[m]
$p'/(\rho g)$	0.0021	0.0019	[m]
Dimensionless numbers			
R	202060	205205	[-]
W_o	87	88	[-]
F_k	9.7	9.9	[-]
F_s	5.0	5.1	[-]
Inception point			
x_i	-	0.83	[m]
h_i	-	0.064	[m]
h_{wi}	-	0.050	[m]
Air entrainment			
β	0.068	-	[-]
q_A	0.014	-	[m ² /s]
$u_{A,max}$	1.03	-	[m/s]
u_A	0.82	-	[m/s]
Jet			
L	0.79	-	[m]
L/h_o	10.6	-	[-]
L_{obs}	0.63	-	[m]
$\Delta p/h$	0.03	-	[-]
h_t	0.061	-	[m]
α_{tu}	7.50	-	[°]
α_{tl}	8.31	-	[°]
γ	8.56	-	[°]
Observation			
-			



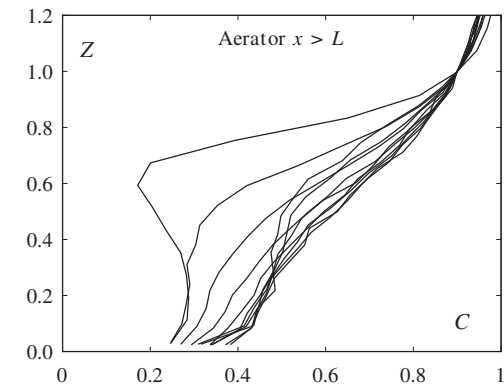
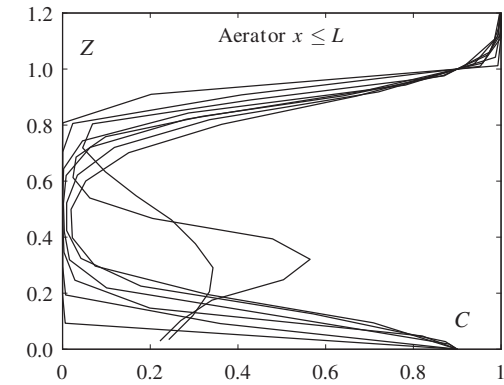
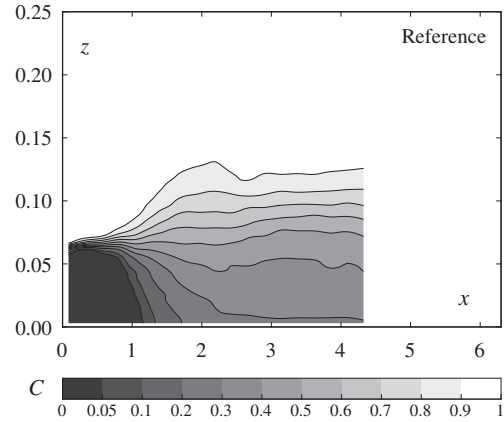
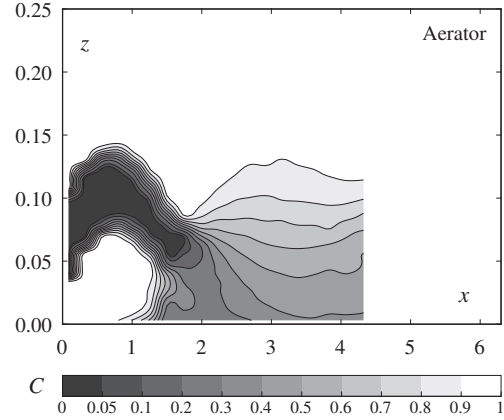


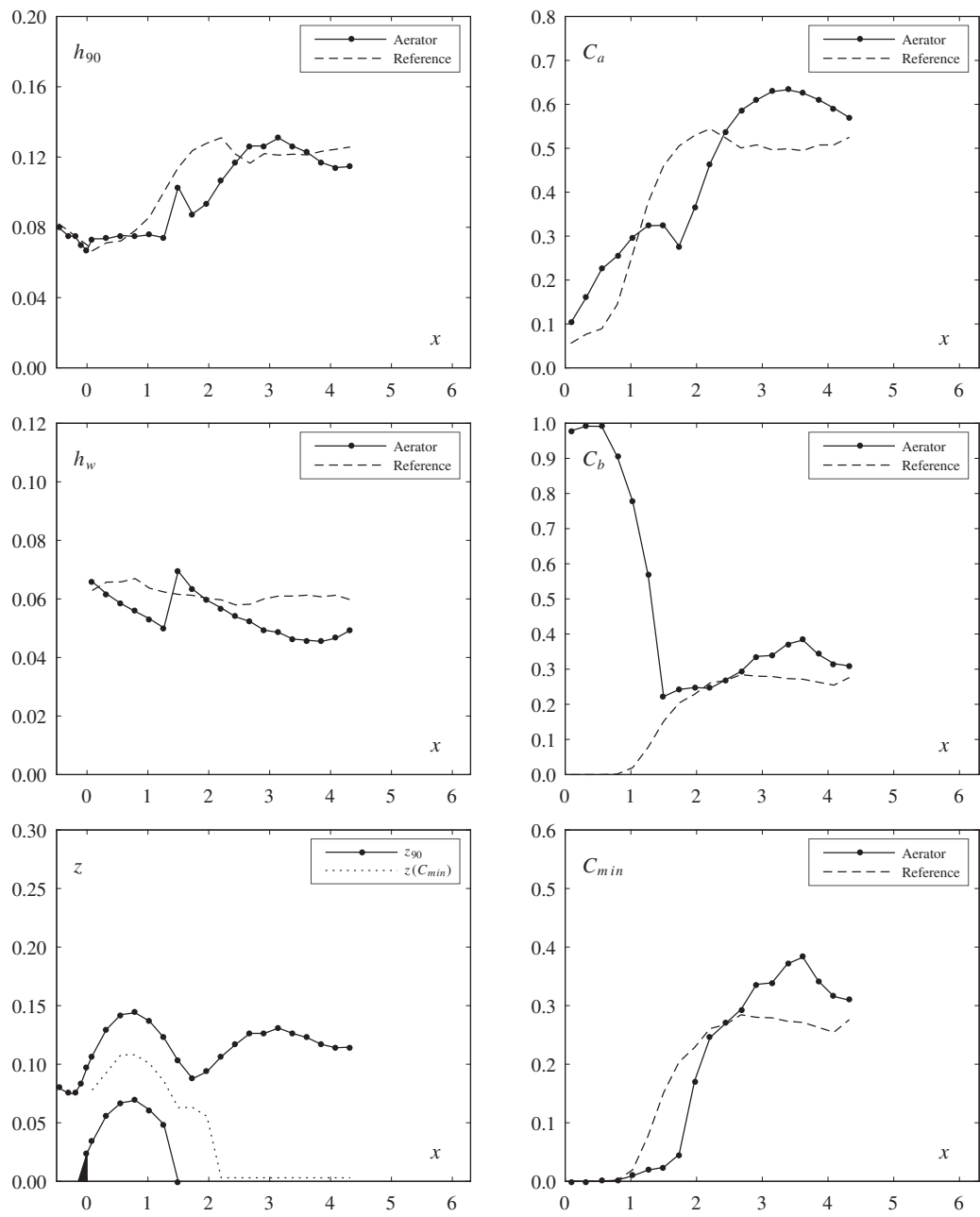
	Aerator	Reference	
Test	19	14	
Parameters			
φ	50	50	[°]
s	0.060	0.060	[m]
F_o	5.49	5.49	[-]
h_o	0.092	0.092	[m]
α	9.46	-	[°]
t	0.030	-	[m]
Flow			
q	0.480	0.480	[m ² /s]
h_c	0.286	0.286	[m]
h_c/s	4.77	4.77	[-]
u_o	5.22	5.22	[m/s]
Pressure			
$p/(\rho g)$	0.185	0.119	[m]
$p'/(\rho g)$	0.0055	0.0057	[m]
Dimensionless numbers			
R	480017	479863	[-]
W_o	187	186	[-]
F_k	23.1	23.1	[-]
F_s	11.9	11.9	[-]
Inception point			
x_i	-	1.18	[m]
h_i	-	0.098	[m]
h_{wi}	-	0.077	[m]
Air entrainment			
β	0.213	-	[-]
q_A	0.102	-	[m ² /s]
$u_{A,max}$	3.39	-	[m/s]
u_A	2.82	-	[m/s]
Jet			
L	1.98	-	[m]
L/h_o	21.5	-	[-]
L_{obs}	1.25	-	[m]
$\Delta p/h$	0.08	-	[-]
h_t	0.084	-	[m]
α_{tu}	8.55	-	[°]
α_{tl}	7.97	-	[°]
γ	6.80	-	[°]
Observation			
-			



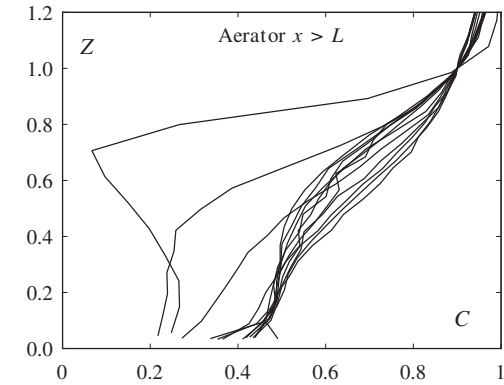
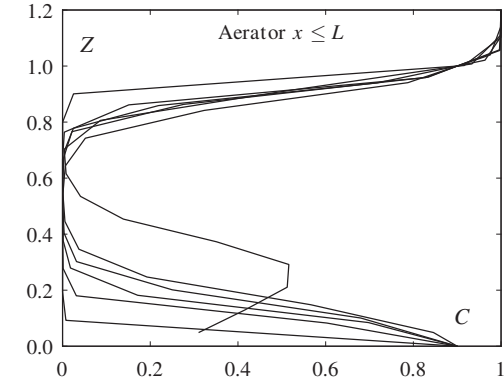
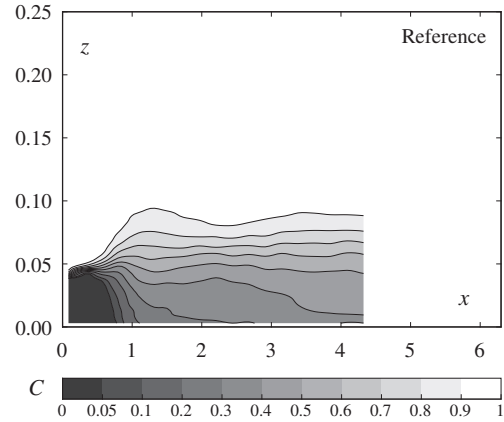
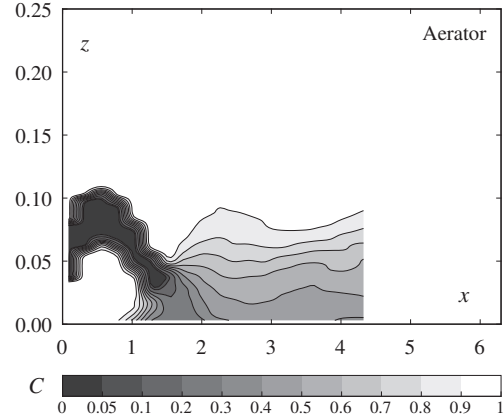


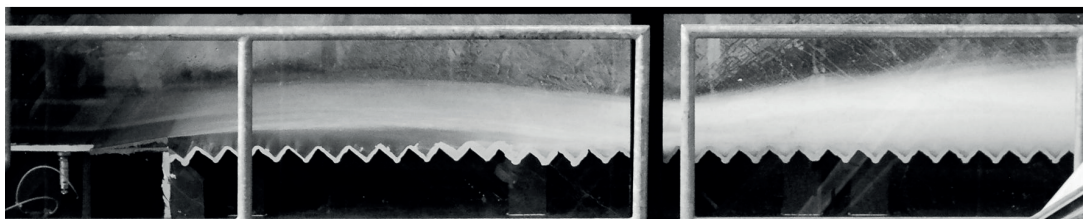
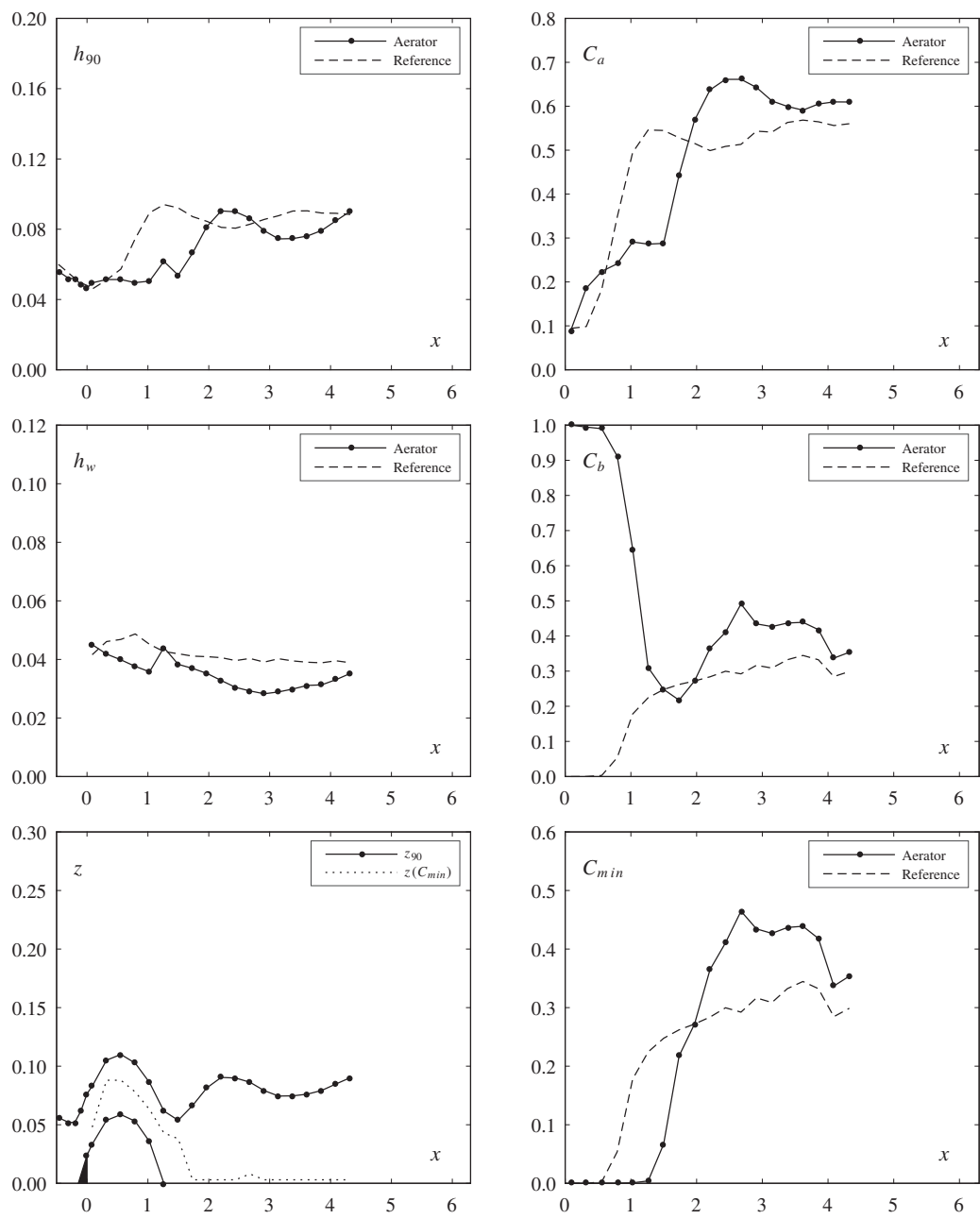
	Aerator	Reference	
Test	20	13	
Parameters			
φ	50	50	[°]
s	0.060	0.060	[m]
F_o	5.55	5.53	[-]
h_o	0.075	0.075	[m]
α	9.46	-	[°]
t	0.030	-	[m]
Flow			
q	0.357	0.356	[m ² /s]
h_c	0.235	0.234	[m]
h_c/s	3.92	3.91	[-]
u_o	4.76	4.74	[m/s]
Pressure			
$p/(\rho g)$	0.141	0.100	[m]
$p'/(\rho g)$	0.0037	0.0038	[m]
Dimensionless numbers			
R	356890	355670	[-]
W_o	154	153	[-]
F_k	17.2	17.1	[-]
F_s	8.9	8.8	[-]
Inception point			
x_i	-	0.90	[m]
h_i	-	0.082	[m]
h_{wi}	-	0.065	[m]
Air entrainment			
β	0.196	-	[-]
q_A	0.070	-	[m ² /s]
$u_{A,max}$	2.34	-	[m/s]
u_A	1.93	-	[m/s]
Jet			
L	1.75	-	[m]
L/h_o	23.3	-	[-]
L_{obs}	1.17	-	[m]
$\Delta p/h$	0.07	-	[-]
h_t	0.067	-	[m]
α_{tu}	8.63	-	[°]
α_{tl}	8.10	-	[°]
γ	7.03	-	[°]
Observation			
-			



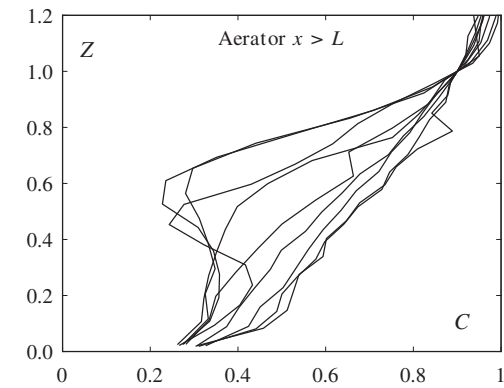
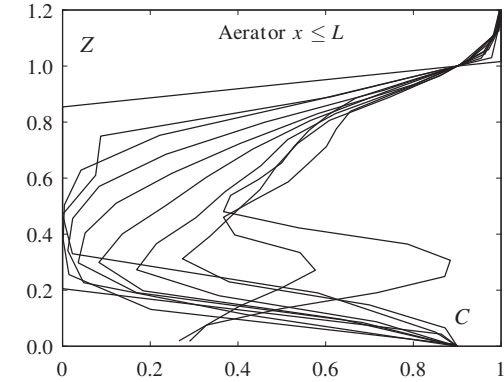
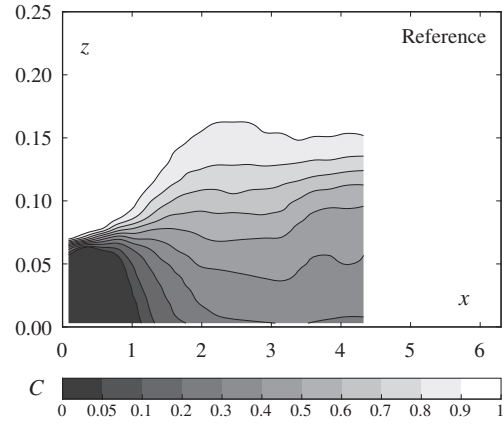
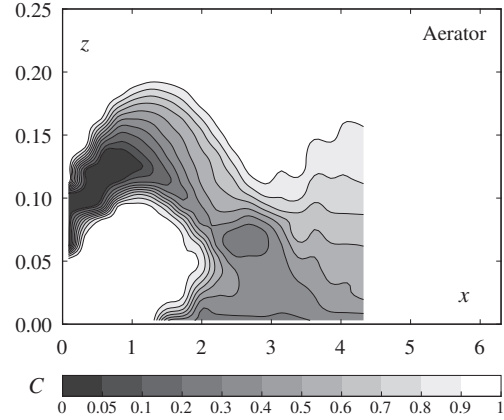


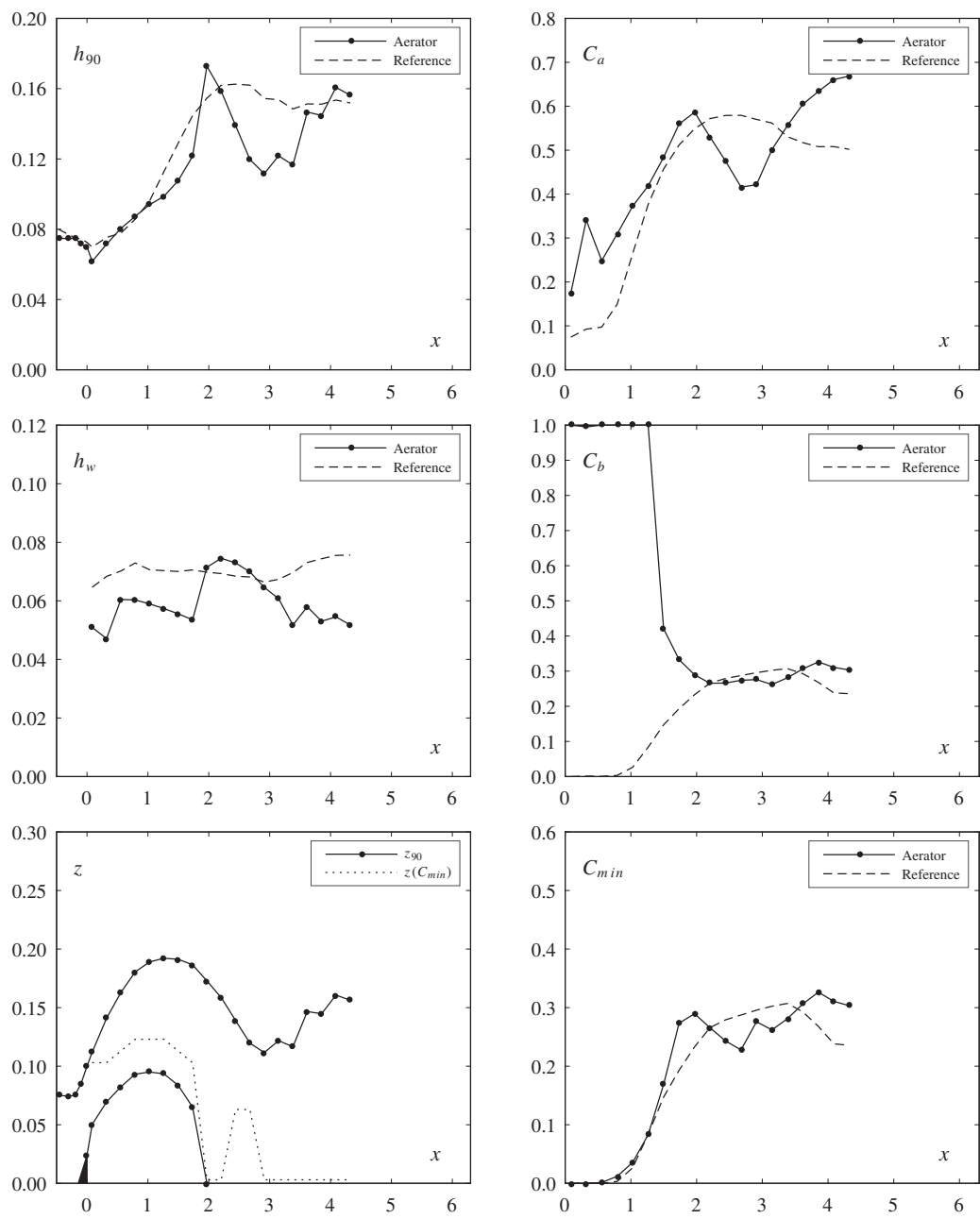
	Aerator	Reference	
Test	21	15	
Parameters			
φ	50	50	[°]
s	0.060	0.060	[m]
F_o	5.49	5.54	[-]
h_o	0.052	0.052	[m]
α	9.46	-	[°]
t	0.030	-	[m]
Flow			
q	0.204	0.206	[m ² /s]
h_c	0.162	0.163	[m]
h_c/s	2.70	2.71	[-]
u_o	3.92	3.95	[m/s]
Pressure			
$p/(\rho g)$	0.086	0.072	[m]
$p'/(\rho g)$	0.0020	0.0020	[m]
Dimensionless numbers			
R	203917	205611	[-]
W_o	105	106	[-]
F_k	9.8	9.9	[-]
F_s	5.1	5.1	[-]
Inception point			
x_i	-	0.59	[m]
h_i	-	0.060	[m]
h_{wi}	-	0.047	[m]
Air entrainment			
β	0.182	-	[-]
q_A	0.037	-	[m ² /s]
$u_{A,max}$	1.26	-	[m/s]
u_A	1.02	-	[m/s]
Jet			
L	1.35	-	[m]
L/h_o	26.0	-	[-]
L_{obs}	1.09	-	[m]
$\Delta p/h$	0.06	-	[-]
h_t	0.046	-	[m]
α_{tu}	9.20	-	[°]
α_{tl}	8.80	-	[°]
γ	7.53	-	[°]
Observation			
-			



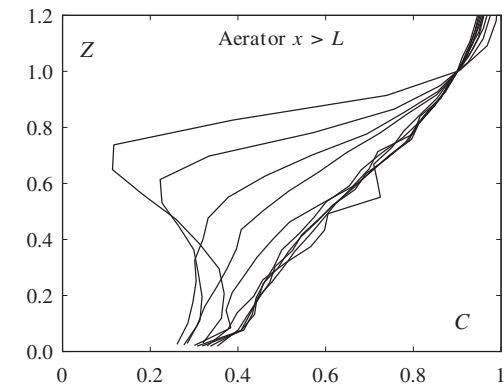
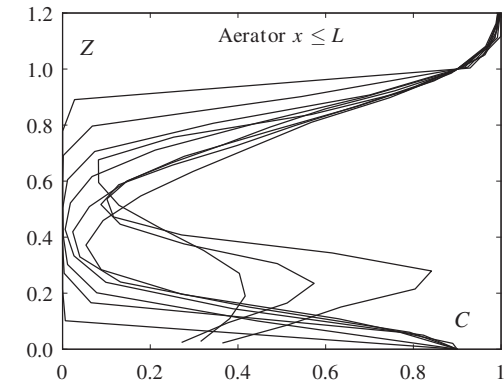
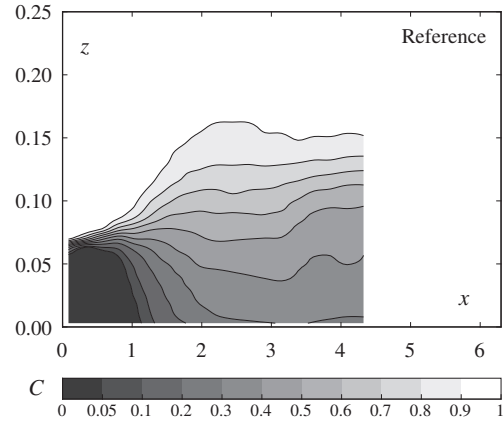
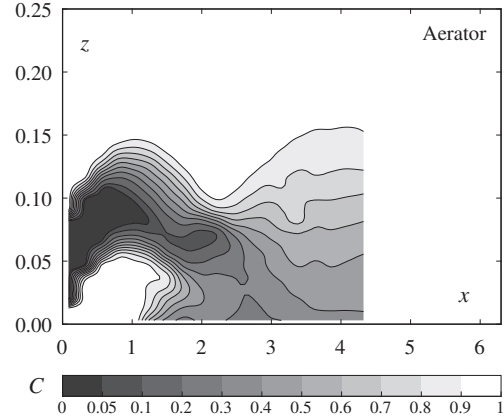


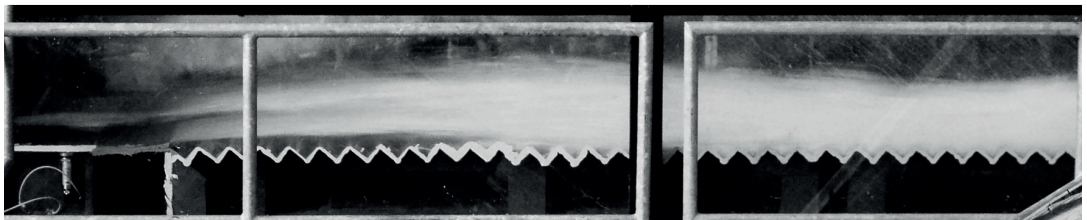
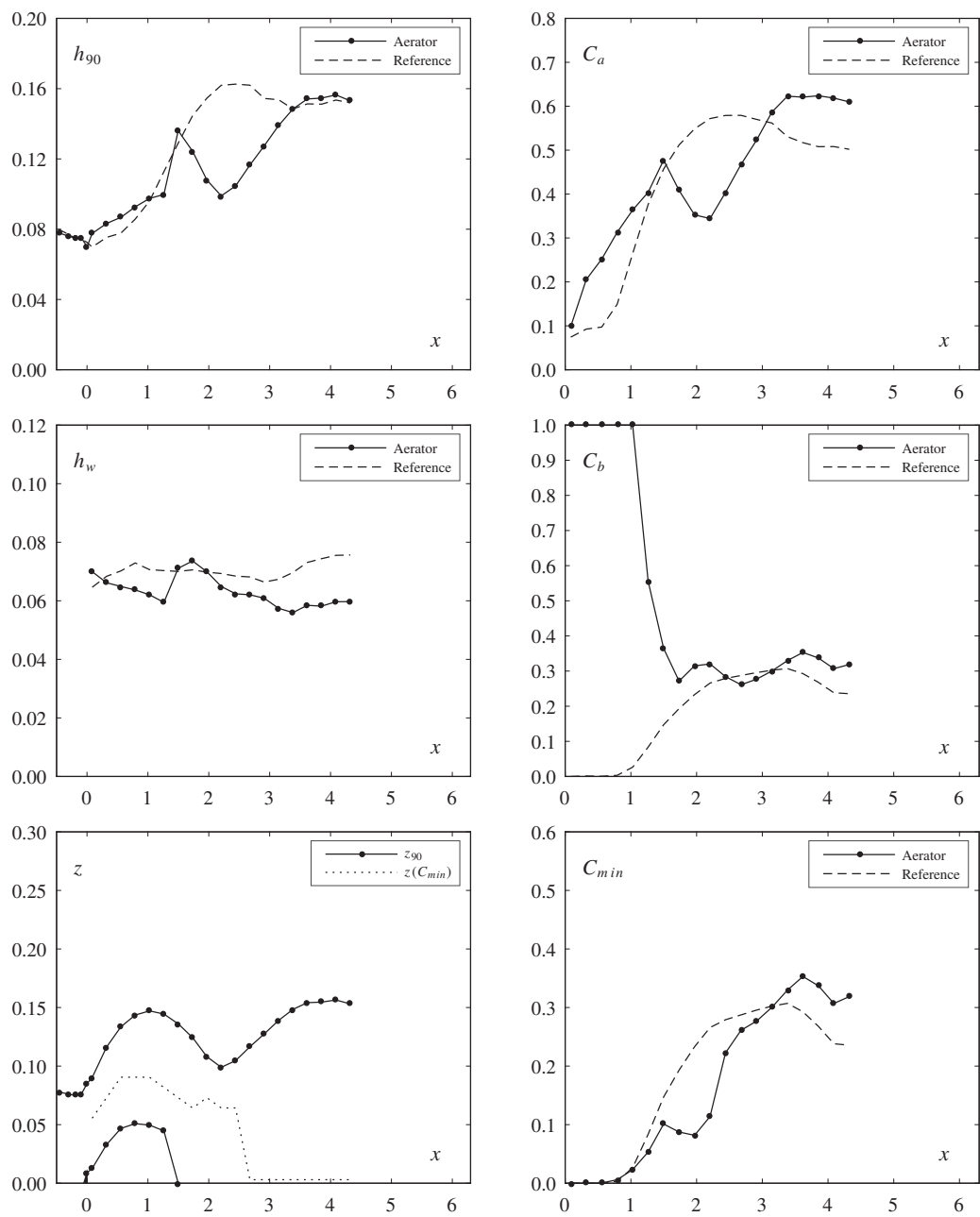
	Aerator	Reference	
Test	22	16	
Parameters			
φ	50	50	[°]
s	0.060	0.060	[m]
F_o	7.48	7.48	[-]
h_o	0.075	0.075	[m]
α	9.46	-	[°]
t	0.030	-	[m]
Flow			
q	0.481	0.481	[m ² /s]
h_c	0.287	0.287	[m]
h_c/s	4.78	4.78	[-]
u_o	6.42	6.41	[m/s]
Pressure			
$p/(\rho g)$	0.219	0.148	[m]
$p'/(\rho g)$	0.0054	0.0058	[m]
Dimensionless numbers			
R	481467	480936	[-]
W_o	207	207	[-]
F_k	23.2	23.2	[-]
F_s	12.0	11.9	[-]
Inception point			
x_i	-	0.86	[m]
h_i	-	0.089	[m]
h_{wi}	-	0.072	[m]
Air entrainment			
β	0.261	-	[-]
q_A	0.126	-	[m ² /s]
$u_{A,max}$	4.15	-	[m/s]
u_A	3.46	-	[m/s]
Jet			
L	2.35	-	[m]
L/h_o	31.4	-	[-]
L_{obs}	1.64	-	[m]
$\Delta p/h$	0.13	-	[-]
h_t	0.070	-	[m]
α_{tu}	9.19	-	[°]
α_{tl}	7.66	-	[°]
γ	7.48	-	[°]
Observation			
-			



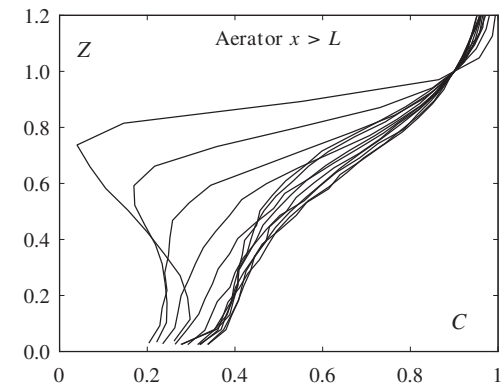
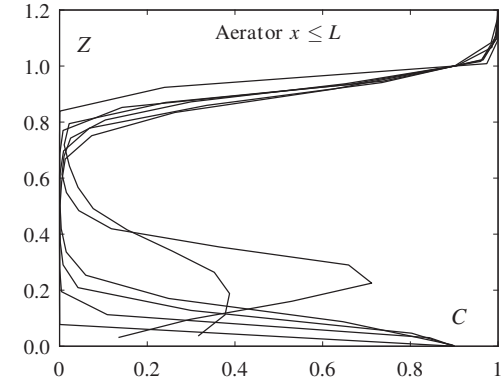
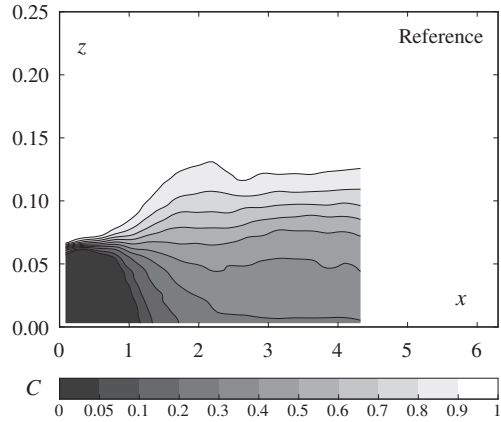
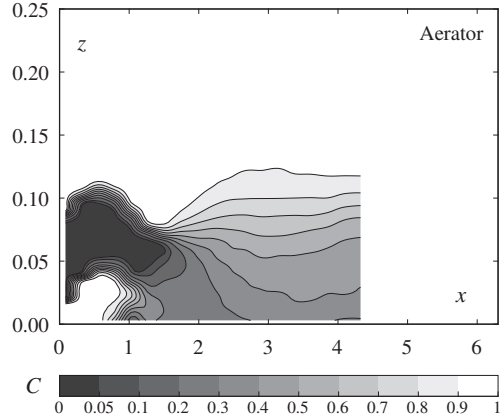


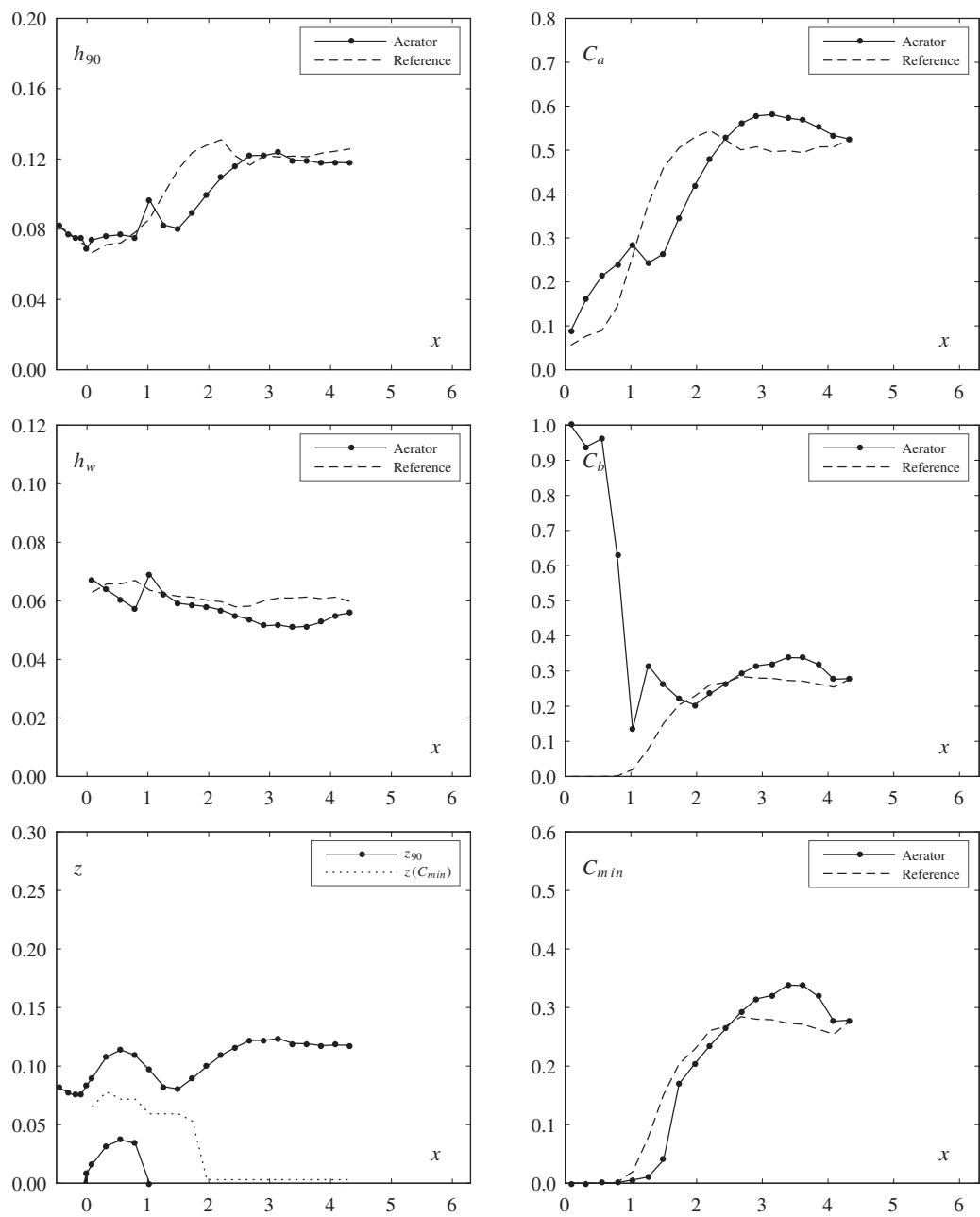
	Aerator	Reference	
Test	23	16	
Parameters			
φ	50	50	[°]
s	0.060	0.060	[m]
F_o	7.51	7.48	[-]
h_o	0.075	0.075	[m]
α	9.46	-	[°]
t	0.015	-	[m]
Flow			
q	0.483	0.481	[m ² /s]
h_c	0.288	0.287	[m]
h_c/s	4.79	4.78	[-]
u_o	6.44	6.41	[m/s]
Pressure			
$p/(\rho g)$	0.157	0.148	[m]
$p'/(\rho g)$	0.0059	0.0058	[m]
Dimensionless numbers			
R	483276	480936	[-]
W_o	208	207	[-]
F_k	23.3	23.2	[-]
F_s	12.0	11.9	[-]
Inception point			
x_i	-	0.86	[m]
h_i	-	0.089	[m]
h_{wi}	-	0.072	[m]
Air entrainment			
β	0.258	-	[-]
q_A	0.125	-	[m ² /s]
$u_{A,max}$	4.12	-	[m/s]
u_A	3.43	-	[m/s]
Jet			
L	1.98	-	[m]
L/h_o	26.5	-	[-]
L_{obs}	1.09	-	[m]
$\Delta p/h$	0.12	-	[-]
h_t	0.070	-	[m]
α_{tu}	7.50	-	[°]
α_{tl}	6.01	-	[°]
γ	5.04	-	[°]
Observation			
-			



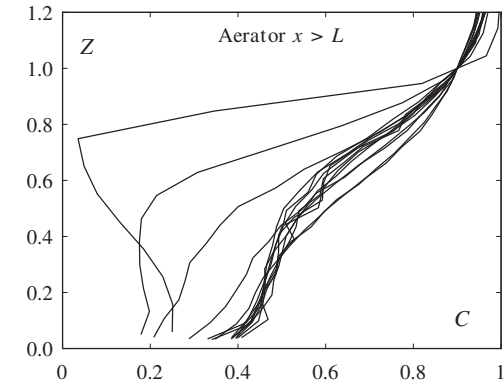
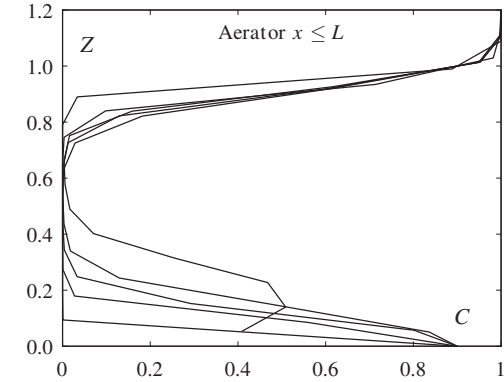
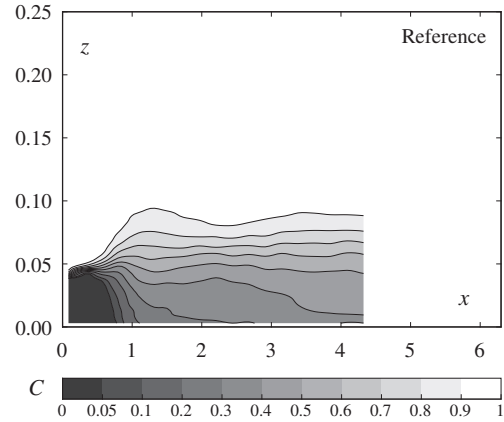
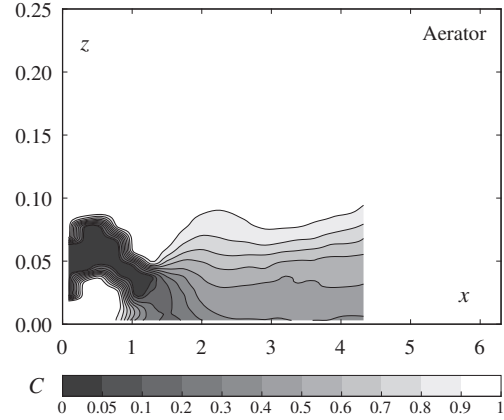


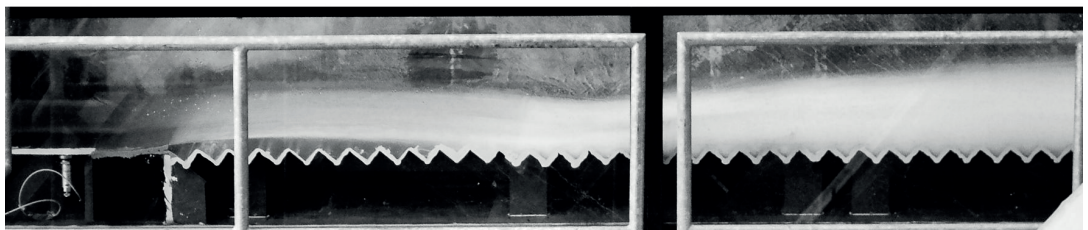
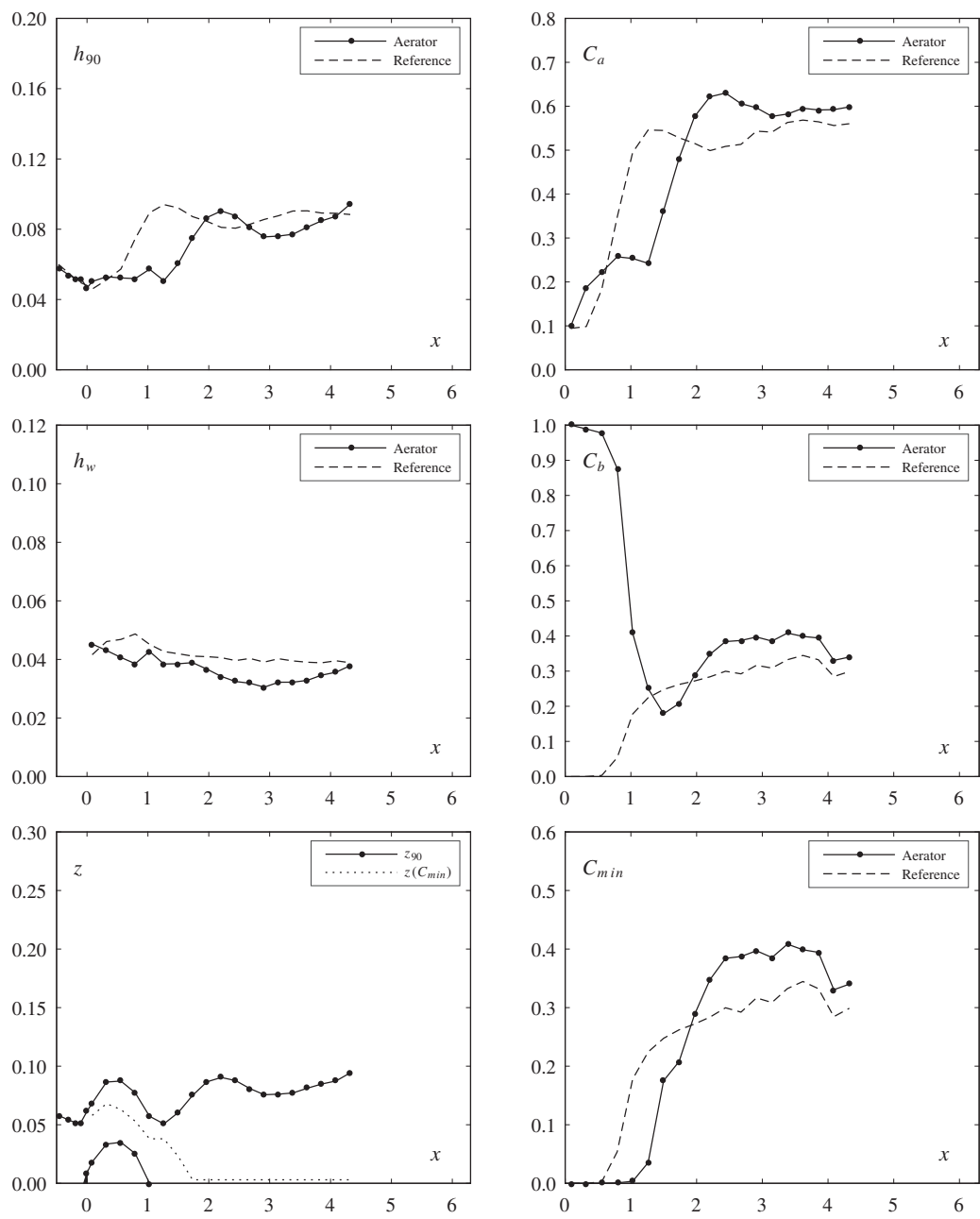
	Aerator	Reference	
Test	24	13	
Parameters			
φ	50	50	[°]
s	0.060	0.060	[m]
F_o	5.55	5.53	[-]
h_o	0.075	0.075	[m]
α	9.46	-	[°]
t	0.015	-	[m]
Flow			
q	0.357	0.356	[m ² /s]
h_c	0.235	0.234	[m]
h_c/s	3.92	3.91	[-]
u_o	4.76	4.74	[m/s]
Pressure			
$p/(\rho g)$	0.106	0.100	[m]
$p'/(\rho g)$	0.0039	0.0038	[m]
Dimensionless numbers			
R	357252	355670	[-]
W_o	154	153	[-]
F_k	17.2	17.1	[-]
F_s	8.9	8.8	[-]
Inception point			
x_i	-	0.90	[m]
h_i	-	0.082	[m]
h_{wi}	-	0.065	[m]
Air entrainment			
β	0.159	-	[-]
q_A	0.057	-	[m ² /s]
$u_{A,max}$	1.91	-	[m/s]
u_A	1.56	-	[m/s]
Jet			
L	1.34	-	[m]
L/h_o	17.9	-	[-]
L_{obs}	0.75	-	[m]
$\Delta p/h$	0.04	-	[-]
h_t	0.069	-	[m]
α_{tu}	7.37	-	[°]
α_{tl}	6.61	-	[°]
γ	5.29	-	[°]
Observation			
-			



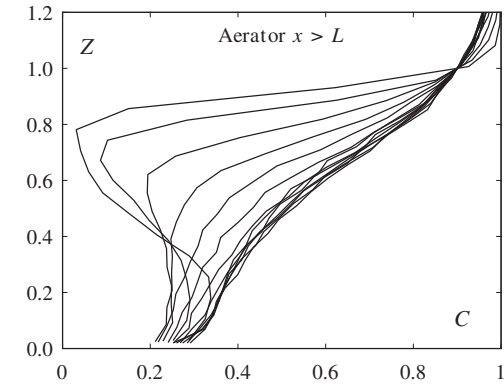
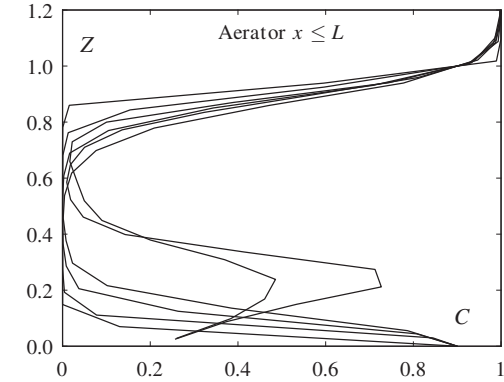
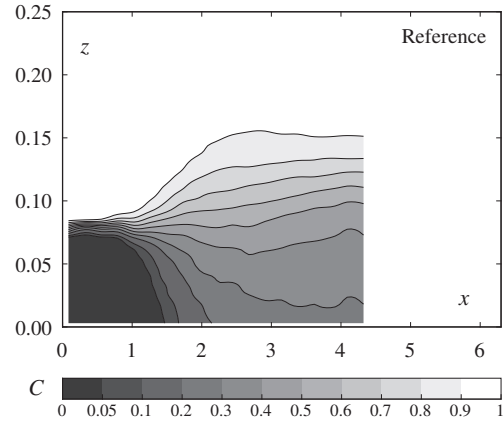
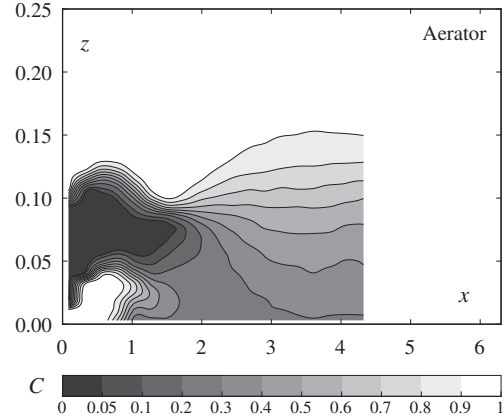


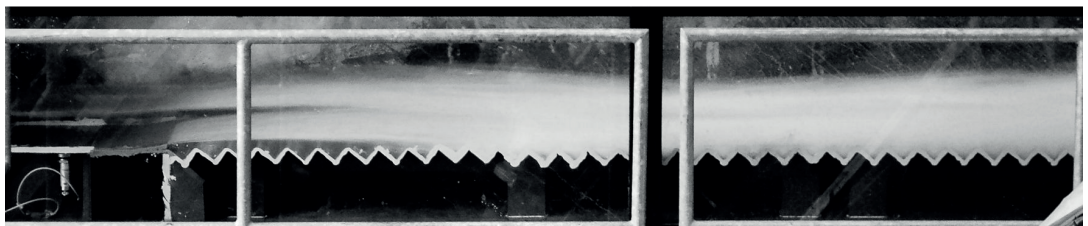
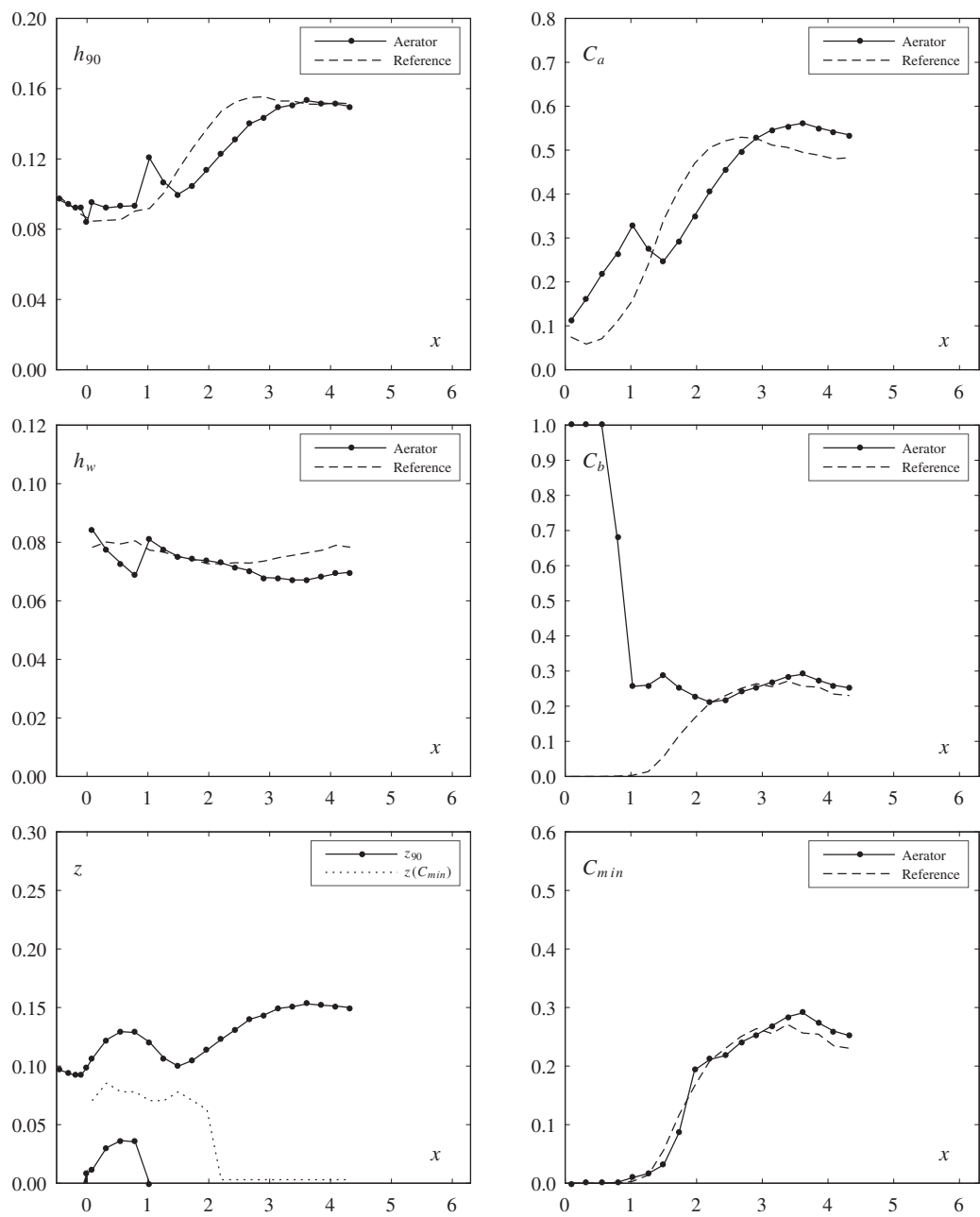
	Aerator	Reference	
Test	25	15	
Parameters			
φ	50	50	[°]
s	0.060	0.060	[m]
F_o	5.50	5.54	[-]
h_o	0.052	0.052	[m]
α	9.46	-	[°]
t	0.015	-	[m]
Flow			
q	0.204	0.206	[m ² /s]
h_c	0.162	0.163	[m]
h_c/s	2.70	2.71	[-]
u_o	3.93	3.95	[m/s]
Pressure			
$p/(\rho g)$	0.072	0.072	[m]
$p'/(\rho g)$	0.0021	0.0020	[m]
Dimensionless numbers			
R	204411	205611	[-]
W_o	106	106	[-]
F_k	9.8	9.9	[-]
F_s	5.1	5.1	[-]
Inception point			
x_i	-	0.59	[m]
h_i	-	0.060	[m]
h_{wi}	-	0.047	[m]
Air entrainment			
β	0.159	-	[-]
q_A	0.033	-	[m ² /s]
$u_{A,max}$	1.11	-	[m/s]
u_A	0.90	-	[m/s]
Jet			
L	1.09	-	[m]
L/h_o	20.9	-	[-]
L_{obs}	0.71	-	[m]
$\Delta p/h$	0.06	-	[-]
h_t	0.046	-	[m]
α_{tu}	8.25	-	[°]
α_{tl}	7.67	-	[°]
γ	6.19	-	[°]
Observation			
-			



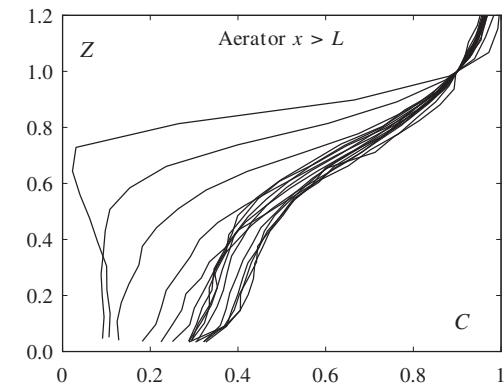
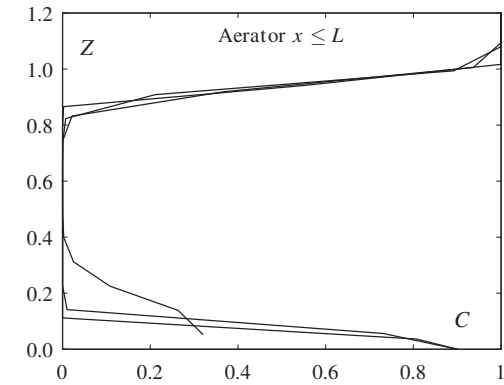
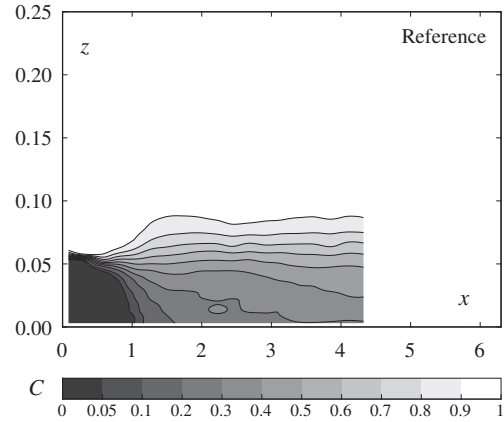
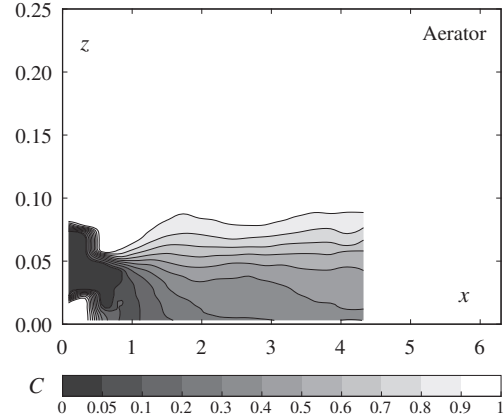


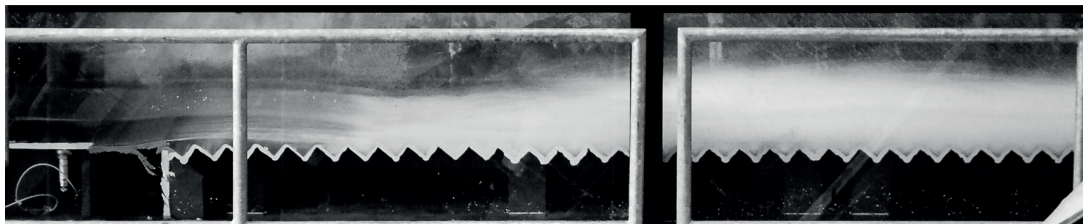
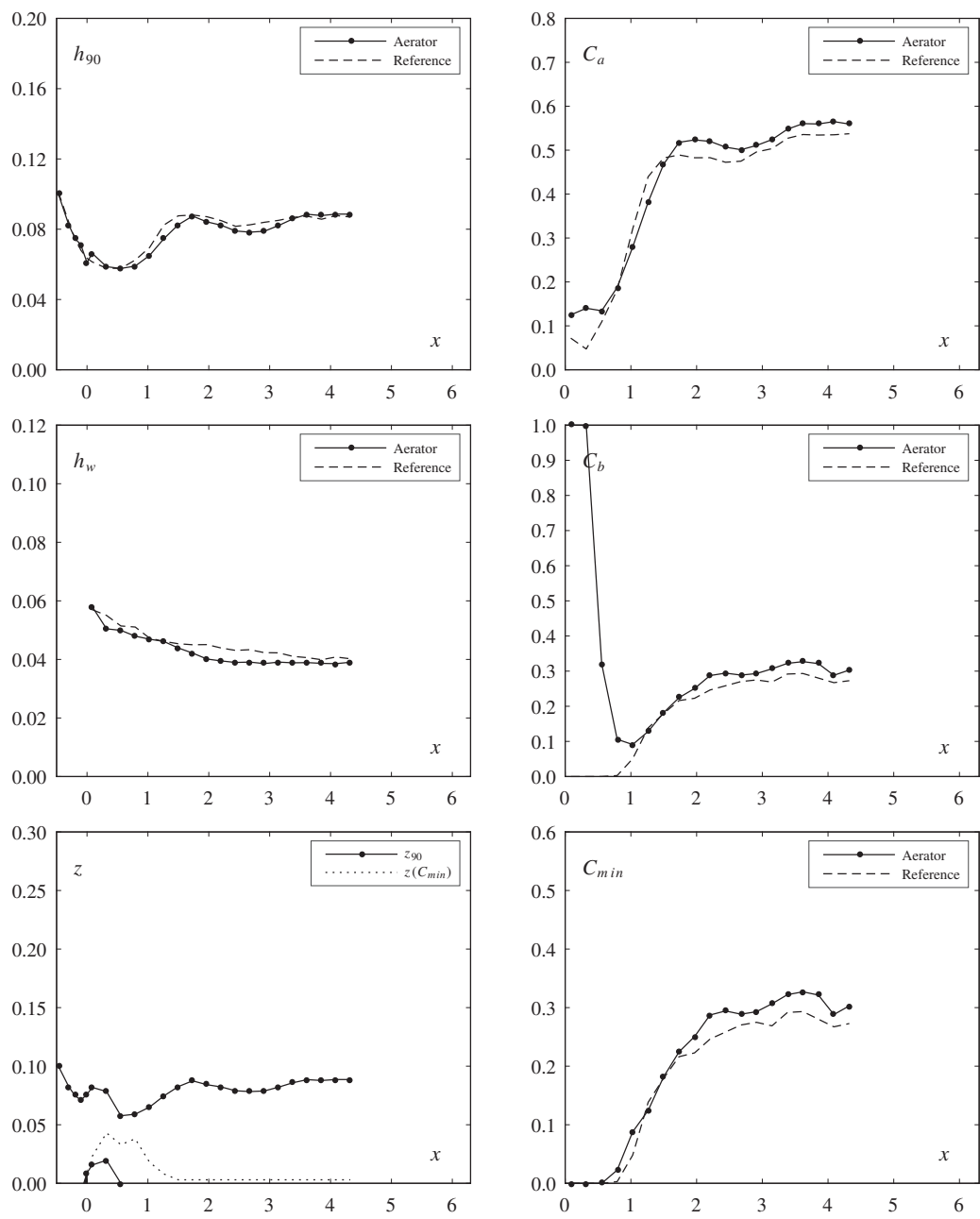
	Aerator	Reference	
Test	26	14	
Parameters			
φ	50	50	[°]
s	0.060	0.060	[m]
F_o	5.51	5.49	[-]
h_o	0.092	0.092	[m]
α	9.46	-	[°]
t	0.015	-	[m]
Flow			
q	0.481	0.480	[m ² /s]
h_c	0.287	0.286	[m]
h_c/s	4.78	4.77	[-]
u_o	5.23	5.22	[m/s]
Pressure			
$p/(\rho g)$	0.131	0.119	[m]
$p'/(\rho g)$	0.0057	0.0057	[m]
Dimensionless numbers			
R	481256	479863	[-]
W_o	187	186	[-]
F_k	23.2	23.1	[-]
F_s	11.9	11.9	[-]
Inception point			
x_i	-	1.18	[m]
h_i	-	0.098	[m]
h_{wi}	-	0.077	[m]
Air entrainment			
β	0.167	-	[-]
q_A	0.081	-	[m ² /s]
$u_{A,max}$	2.69	-	[m/s]
u_A	2.22	-	[m/s]
Jet			
L	1.45	-	[m]
L/h_o	15.8	-	[-]
L_{obs}	0.79	-	[m]
$\Delta p/h$	0.06	-	[-]
h_t	0.084	-	[m]
α_{tu}	6.77	-	[°]
α_{tl}	5.90	-	[°]
γ	4.90	-	[°]
Observation			
-			



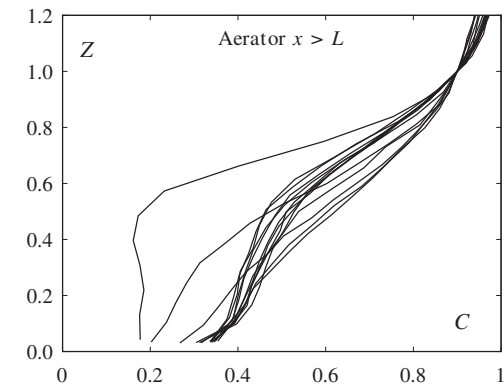
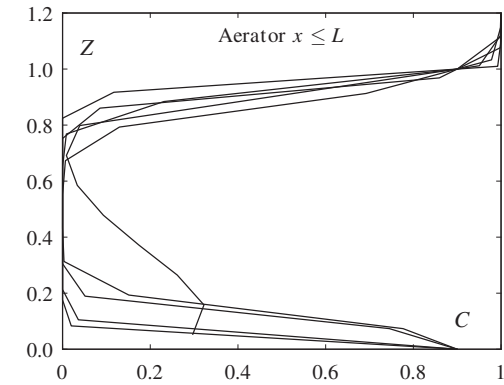
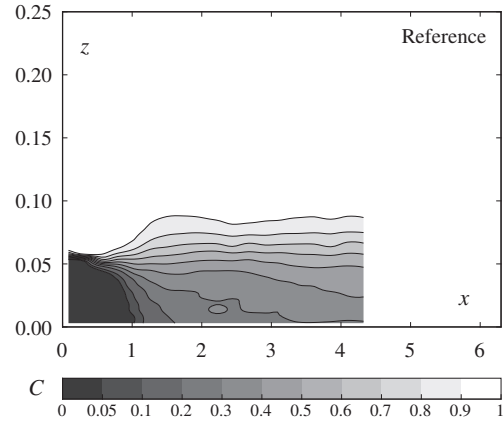
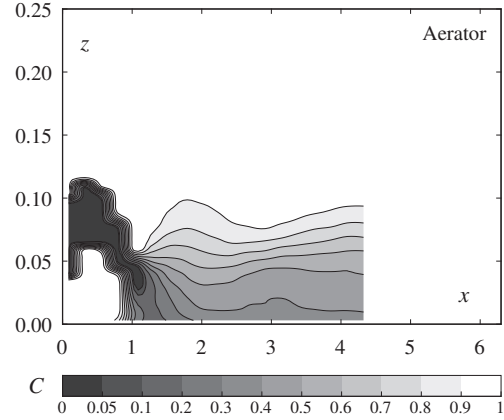


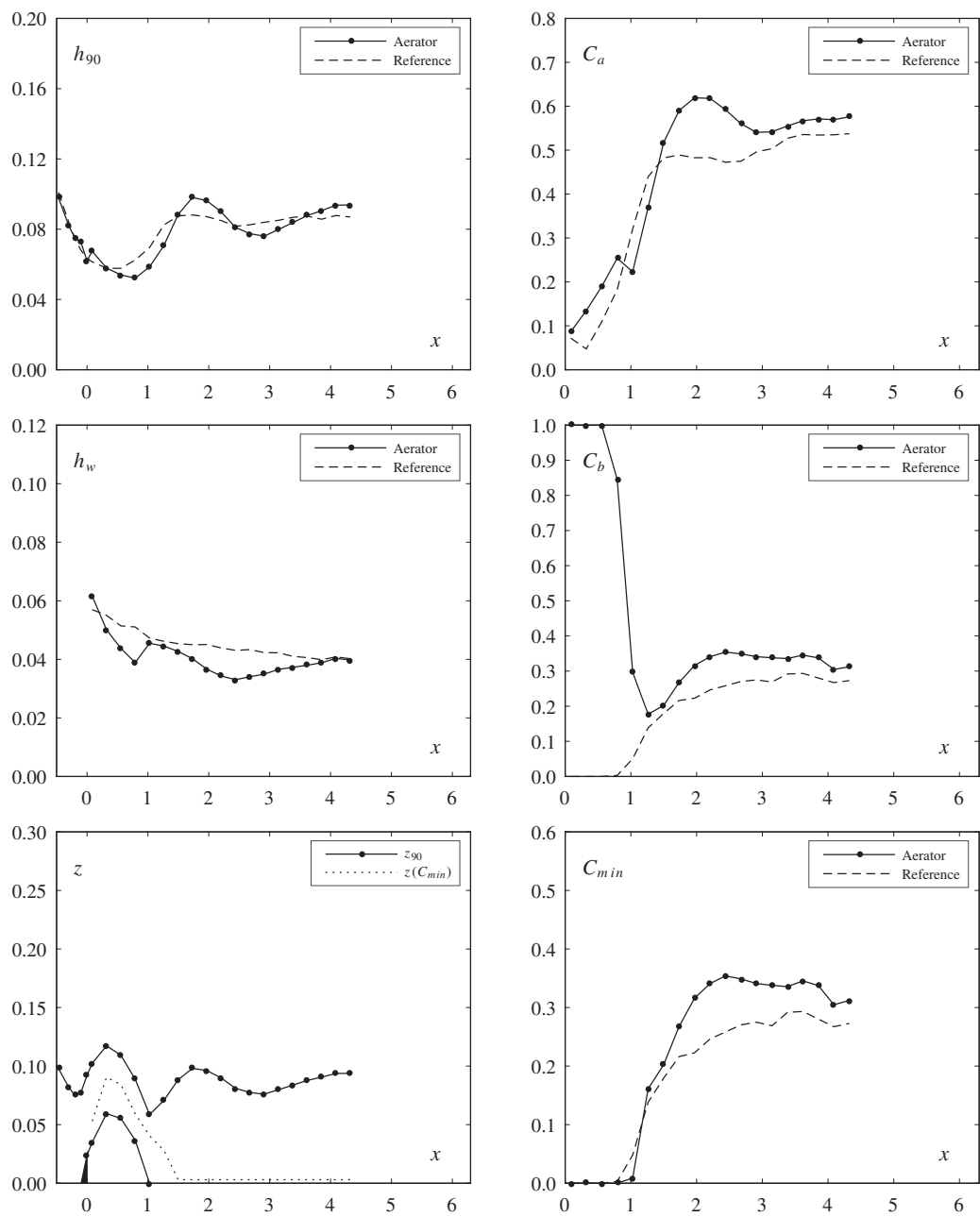
	Aerator	Reference	
Test	27	17	
Parameters			
φ	50	50	[°]
s	0.060	0.060	[m]
F_o	3.16	3.19	[-]
h_o	0.075	0.075	[m]
α	9.46	-	[°]
t	0.015	-	[m]
Flow			
q	0.203	0.205	[m ² /s]
h_c	0.161	0.163	[m]
h_c/s	2.69	2.71	[-]
u_o	2.71	2.74	[m/s]
Pressure			
$p/(\rho g)$	0.070	0.071	[m]
$p'/(\rho g)$	0.0020	0.0019	[m]
Dimensionless numbers			
R	203208	205205	[-]
W_o	87	88	[-]
F_k	9.8	9.9	[-]
F_s	5.0	5.1	[-]
Inception point			
x_i	-	0.83	[m]
h_i	-	0.064	[m]
h_{wi}	-	0.050	[m]
Air entrainment			
β	0.050	-	[-]
q_A	0.010	-	[m ² /s]
$u_{A,max}$	0.77	-	[m/s]
u_A	0.61	-	[m/s]
Jet			
L	0.63	-	[m]
L/h_o	8.4	-	[-]
L_{obs}	0.40	-	[m]
$\Delta p/h$	0.03	-	[-]
h_t	0.061	-	[m]
α_{tu}	6.30	-	[°]
α_{tl}	6.71	-	[°]
γ	5.81	-	[°]
Observation			
-			



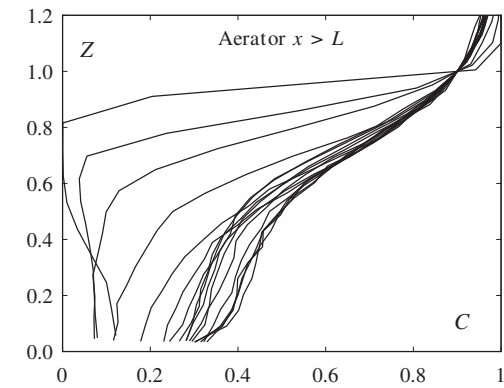
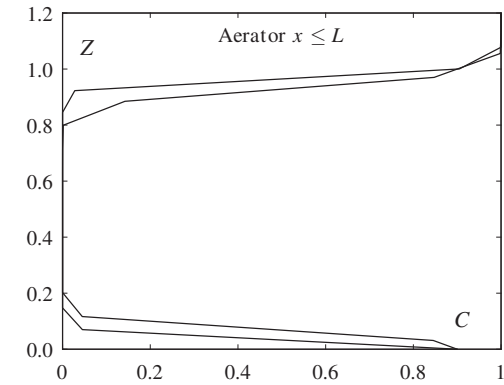
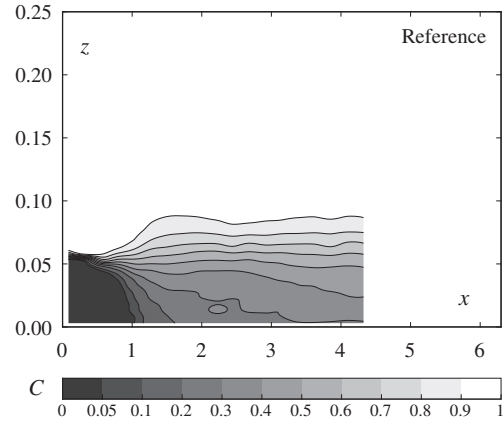
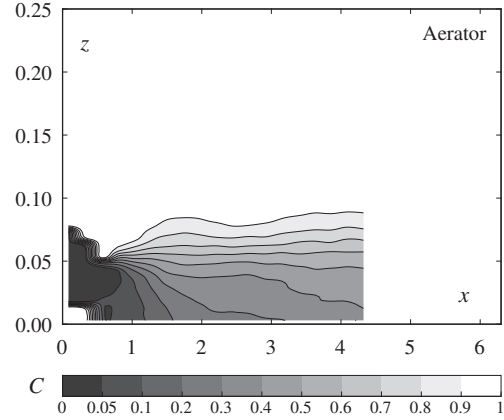


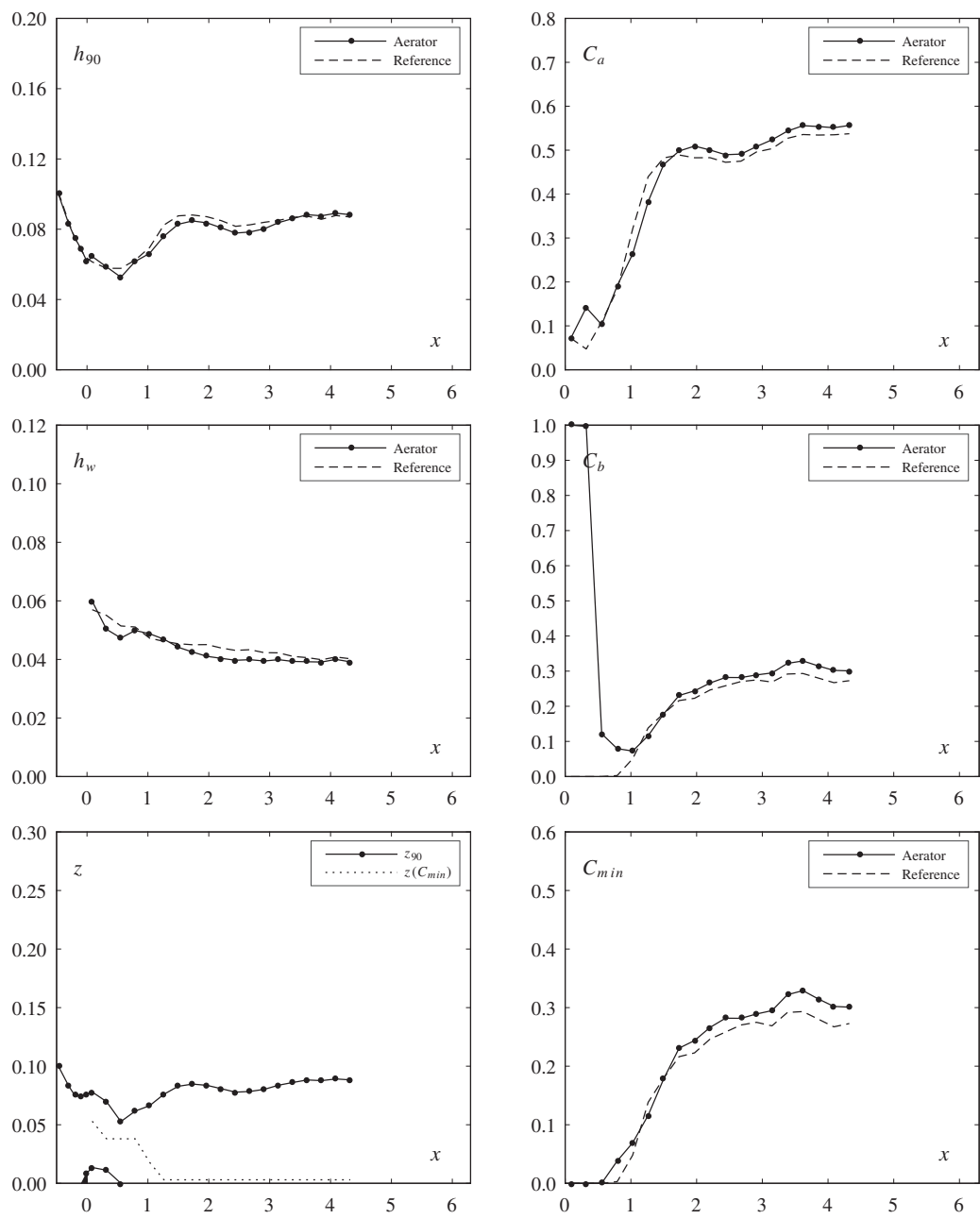
	Aerator	Reference	
Test	28	17	
Parameters			
φ	50	50	[°]
s	0.060	0.060	[m]
F_o	3.15	3.19	[-]
h_o	0.075	0.075	[m]
α	14.04	-	[°]
t	0.030	-	[m]
Flow			
q	0.203	0.205	[m ² /s]
h_c	0.161	0.163	[m]
h_c/s	2.69	2.71	[-]
u_o	2.70	2.74	[m/s]
Pressure			
$p/(\rho g)$	0.073	0.071	[m]
$p'/(\rho g)$	0.0021	0.0019	[m]
Dimensionless numbers			
R	202717	205205	[-]
W_o	87	88	[-]
F_k	9.8	9.9	[-]
F_s	5.0	5.1	[-]
Inception point			
x_i	-	0.83	[m]
h_i	-	0.064	[m]
h_{wi}	-	0.050	[m]
Air entrainment			
β	0.096	-	[-]
q_A	0.019	-	[m ² /s]
$u_{A,max}$	1.44	-	[m/s]
u_A	1.16	-	[m/s]
Jet			
L	1.06	-	[m]
L/h_o	14.2	-	[-]
L_{obs}	0.79	-	[m]
$\Delta p/h$	0.03	-	[-]
h_t	0.062	-	[m]
α_{tu}	10.95	-	[°]
α_{tl}	11.60	-	[°]
γ	9.27	-	[°]
Observation			
-			



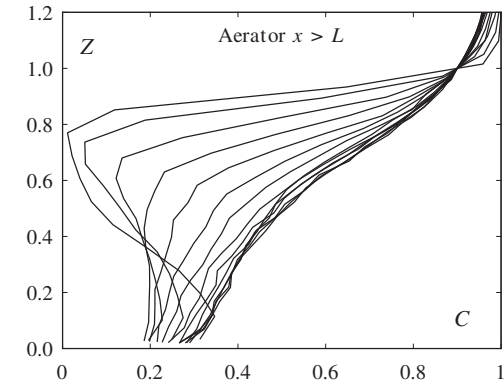
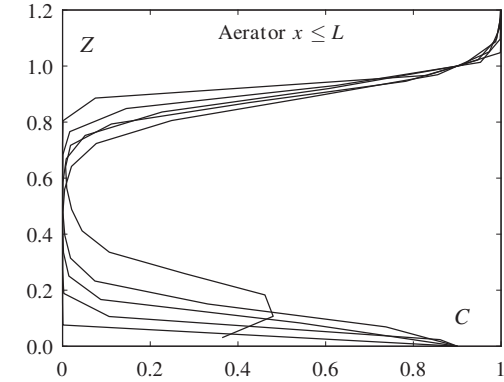
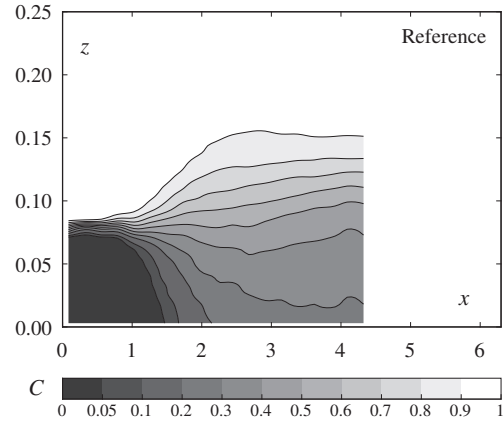
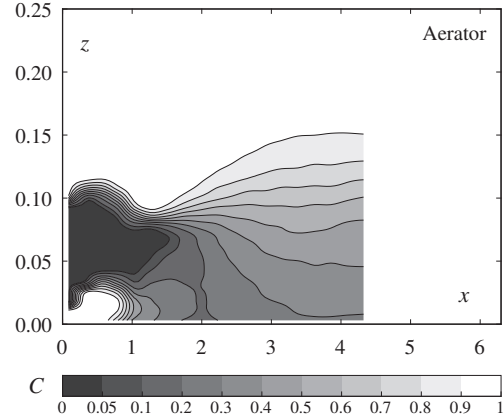


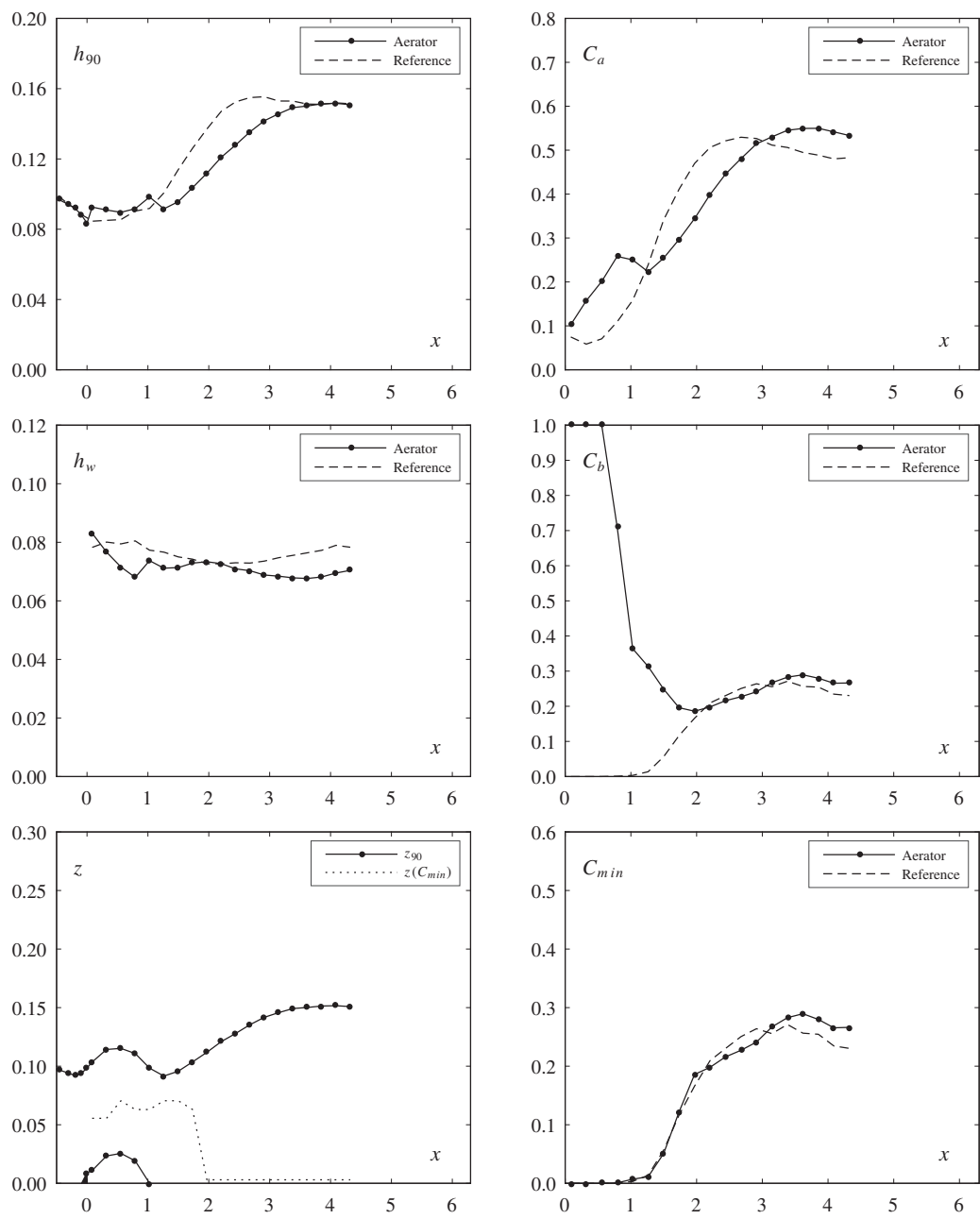
	Aerator	Reference	
Test	29	17	
Parameters			
φ	50	50	[°]
s	0.060	0.060	[m]
F_o	3.16	3.19	[-]
h_o	0.075	0.075	[m]
α	5.71	-	[°]
t	0.015	-	[m]
Flow			
q	0.203	0.205	[m ² /s]
h_c	0.161	0.163	[m]
h_c/s	2.69	2.71	[-]
u_o	2.71	2.74	[m/s]
Pressure			
$p/(\rho g)$	0.072	0.071	[m]
$p'/(\rho g)$	0.0021	0.0019	[m]
Dimensionless numbers			
R	203175	205205	[-]
W_o	87	88	[-]
F_k	9.8	9.9	[-]
F_s	5.0	5.1	[-]
Inception point			
x_i	-	0.83	[m]
h_i	-	0.064	[m]
h_{wi}	-	0.050	[m]
Air entrainment			
β	0.033	-	[-]
q_A	0.007	-	[m ² /s]
$u_{A,max}$	0.51	-	[m/s]
u_A	0.40	-	[m/s]
Jet			
L	0.47	-	[m]
L/h_o	6.3	-	[-]
L_{obs}	0.40	-	[m]
$\Delta p/h$	0.03	-	[-]
h_t	0.062	-	[m]
α_{tu}	5.48	-	[°]
α_{tl}	5.18	-	[°]
γ	5.37	-	[°]
Observation			
-			



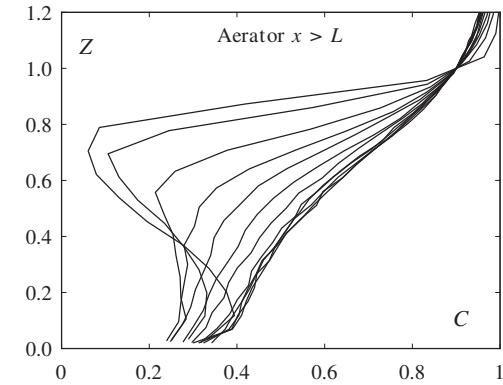
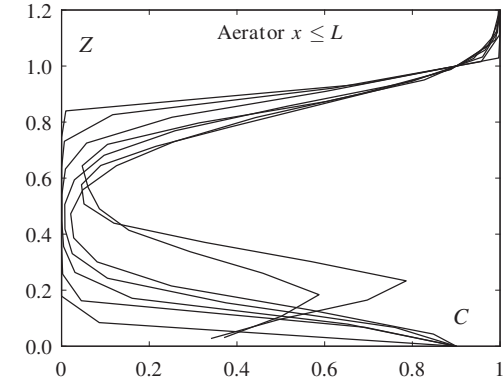
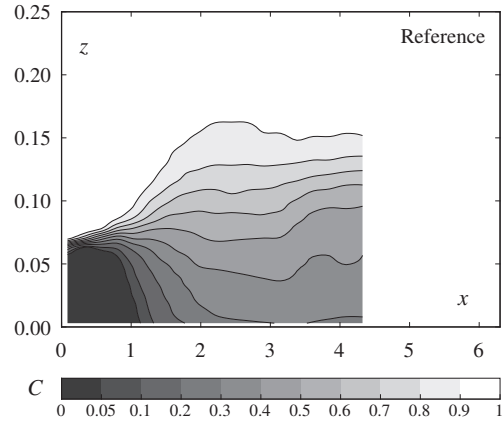
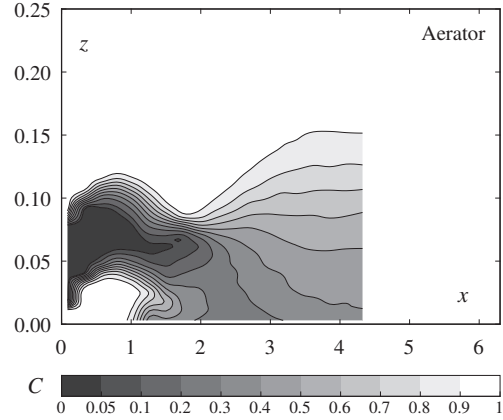


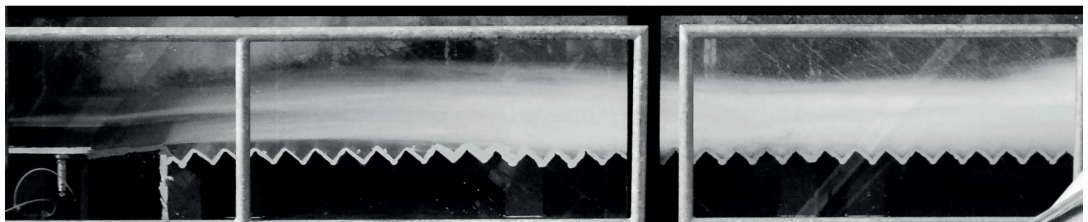
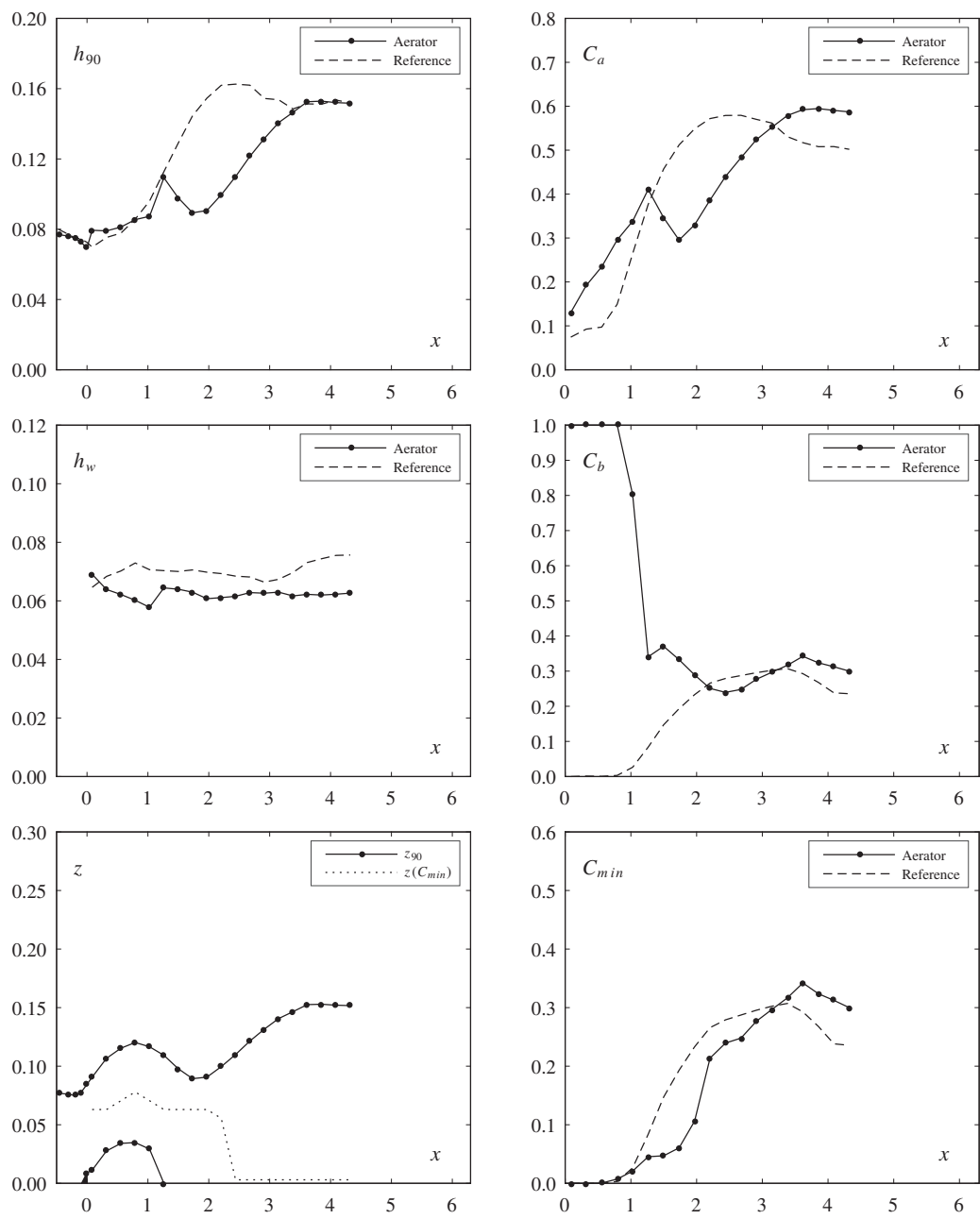
	Aerator	Reference	
Test	30	14	
Parameters			
φ	50	50	[°]
s	0.060	0.060	[m]
F_o	5.51	5.49	[-]
h_o	0.092	0.092	[m]
α	5.71	-	[°]
t	0.015	-	[m]
Flow			
q	0.481	0.480	[m ² /s]
h_c	0.287	0.286	[m]
h_c/s	4.78	4.77	[-]
u_o	5.23	5.22	[m/s]
Pressure			
$p/(\rho g)$	0.142	0.119	[m]
$p'/(\rho g)$	0.0055	0.0057	[m]
Dimensionless numbers			
R	481315	479863	[-]
W_o	187	186	[-]
F_k	23.2	23.1	[-]
F_s	11.9	11.9	[-]
Inception point			
x_i	-	1.18	[m]
h_i	-	0.098	[m]
h_{wi}	-	0.077	[m]
Air entrainment			
β	0.133	-	[-]
q_A	0.064	-	[m ² /s]
$u_{A,max}$	2.15	-	[m/s]
u_A	1.77	-	[m/s]
Jet			
L	1.13	-	[m]
L/h_o	12.3	-	[-]
L_{obs}	0.71	-	[m]
$\Delta p/h$	0.04	-	[-]
h_t	0.083	-	[m]
α_{tu}	5.41	-	[°]
α_{tl}	4.68	-	[°]
γ	4.28	-	[°]
Observation			
-			



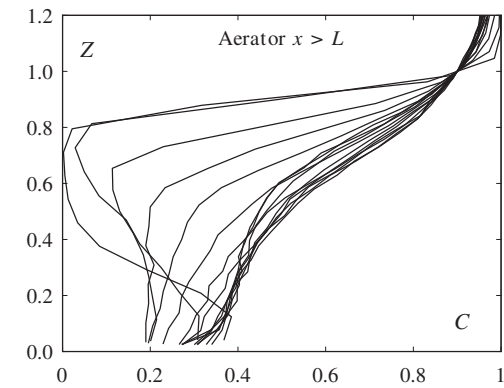
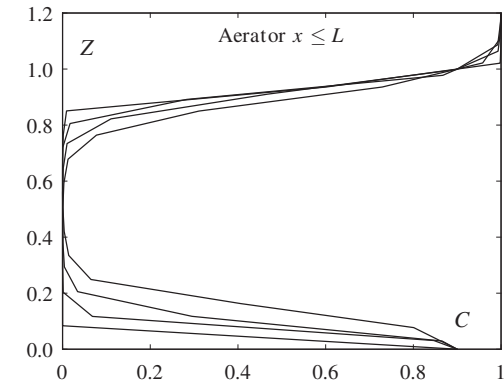
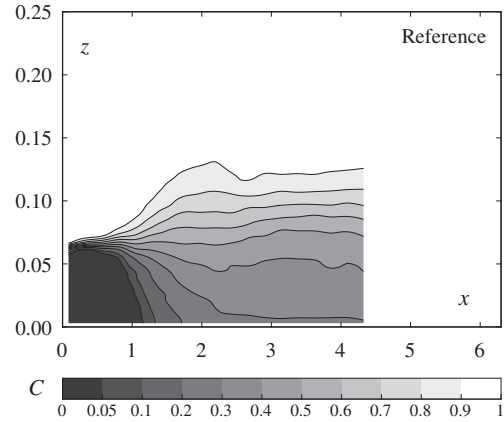
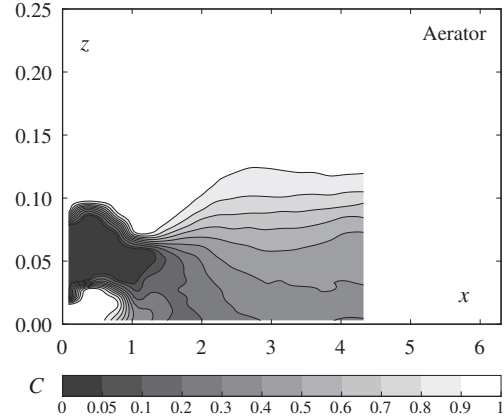


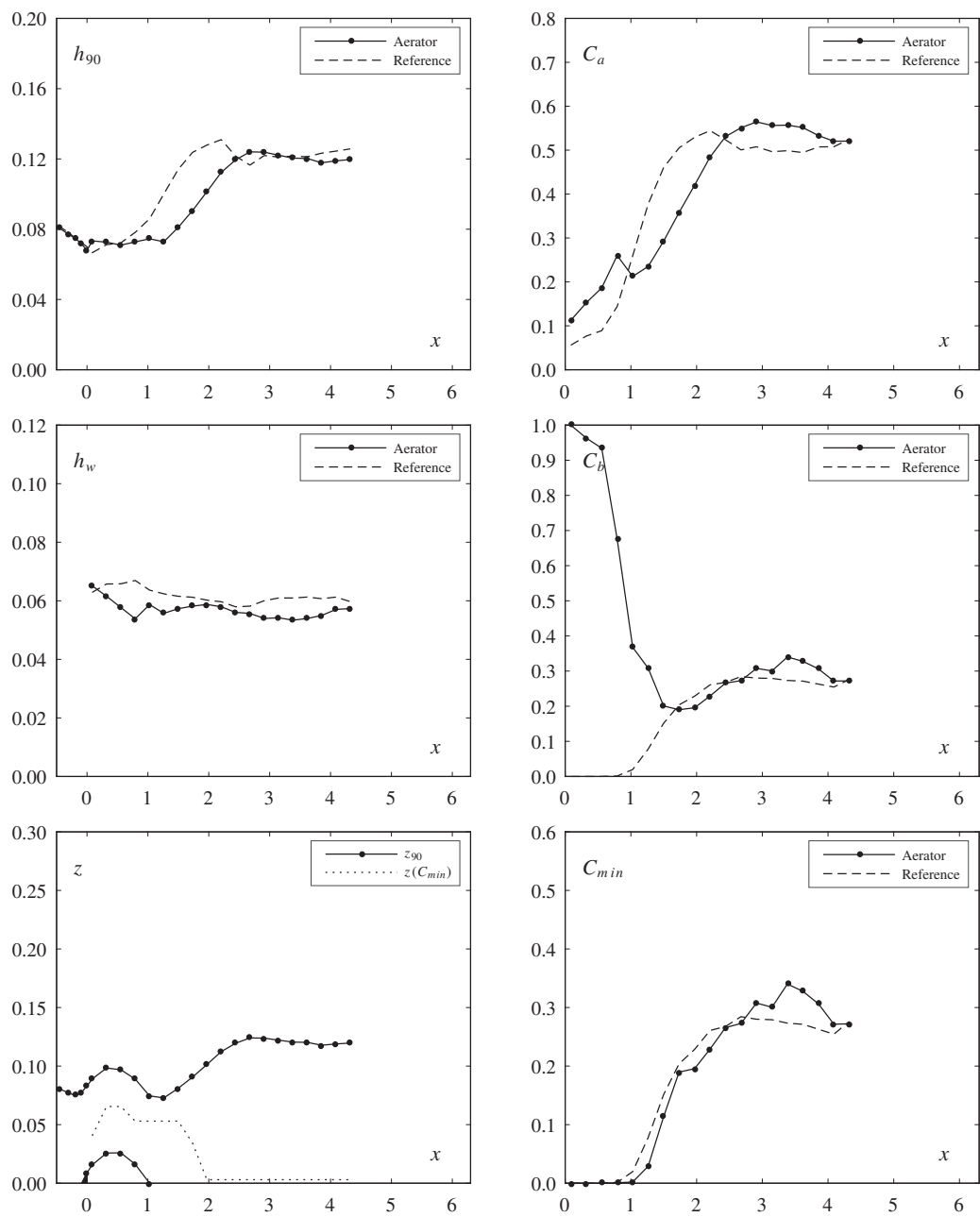
	Aerator	Reference	
Test	31	16	
Parameters			
φ	50	50	[°]
s	0.060	0.060	[m]
F_o	7.51	7.48	[-]
h_o	0.075	0.075	[m]
α	5.71	-	[°]
t	0.015	-	[m]
Flow			
q	0.483	0.481	[m ² /s]
h_c	0.288	0.287	[m]
h_c/s	4.79	4.78	[-]
u_o	6.44	6.41	[m/s]
Pressure			
$p/(\rho g)$	0.169	0.148	[m]
$p'/(\rho g)$	0.0056	0.0058	[m]
Dimensionless numbers			
R	482860	480936	[-]
W_o	208	207	[-]
F_k	23.3	23.2	[-]
F_s	12.0	11.9	[-]
Inception point			
x_i	-	0.86	[m]
h_i	-	0.089	[m]
h_{wi}	-	0.072	[m]
Air entrainment			
β	0.221	-	[-]
q_A	0.107	-	[m ² /s]
$u_{A,max}$	3.54	-	[m/s]
u_A	2.95	-	[m/s]
Jet			
L	1.56	-	[m]
L/h_o	20.8	-	[-]
L_{obs}	0.86	-	[m]
$\Delta p/h$	0.09	-	[-]
h_t	0.069	-	[m]
α_{tu}	5.89	-	[°]
α_{tl}	4.74	-	[°]
γ	4.37	-	[°]
Observation			
-			



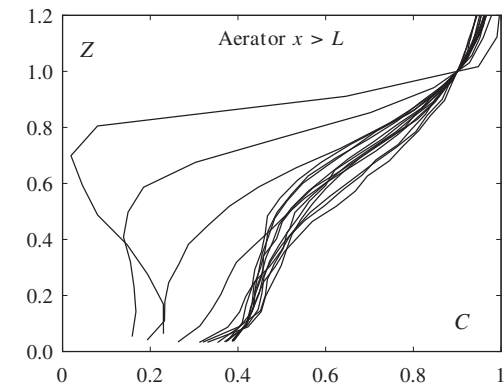
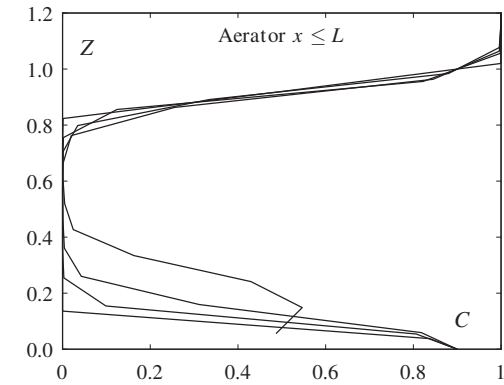
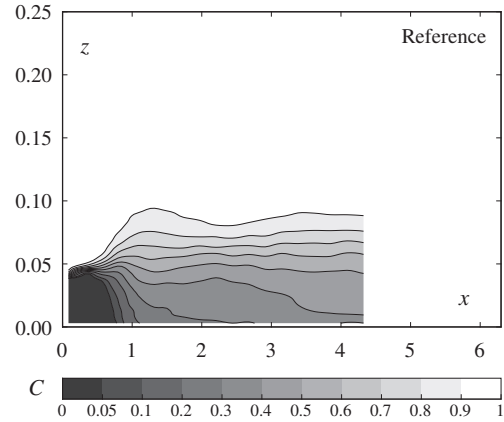
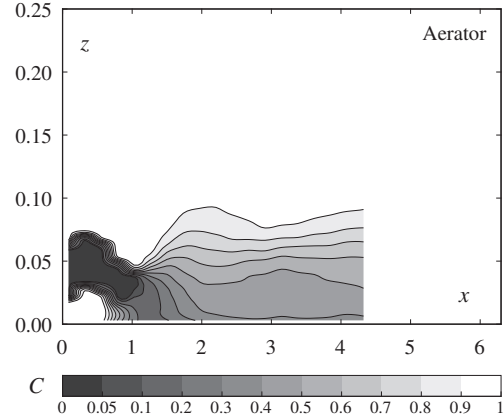


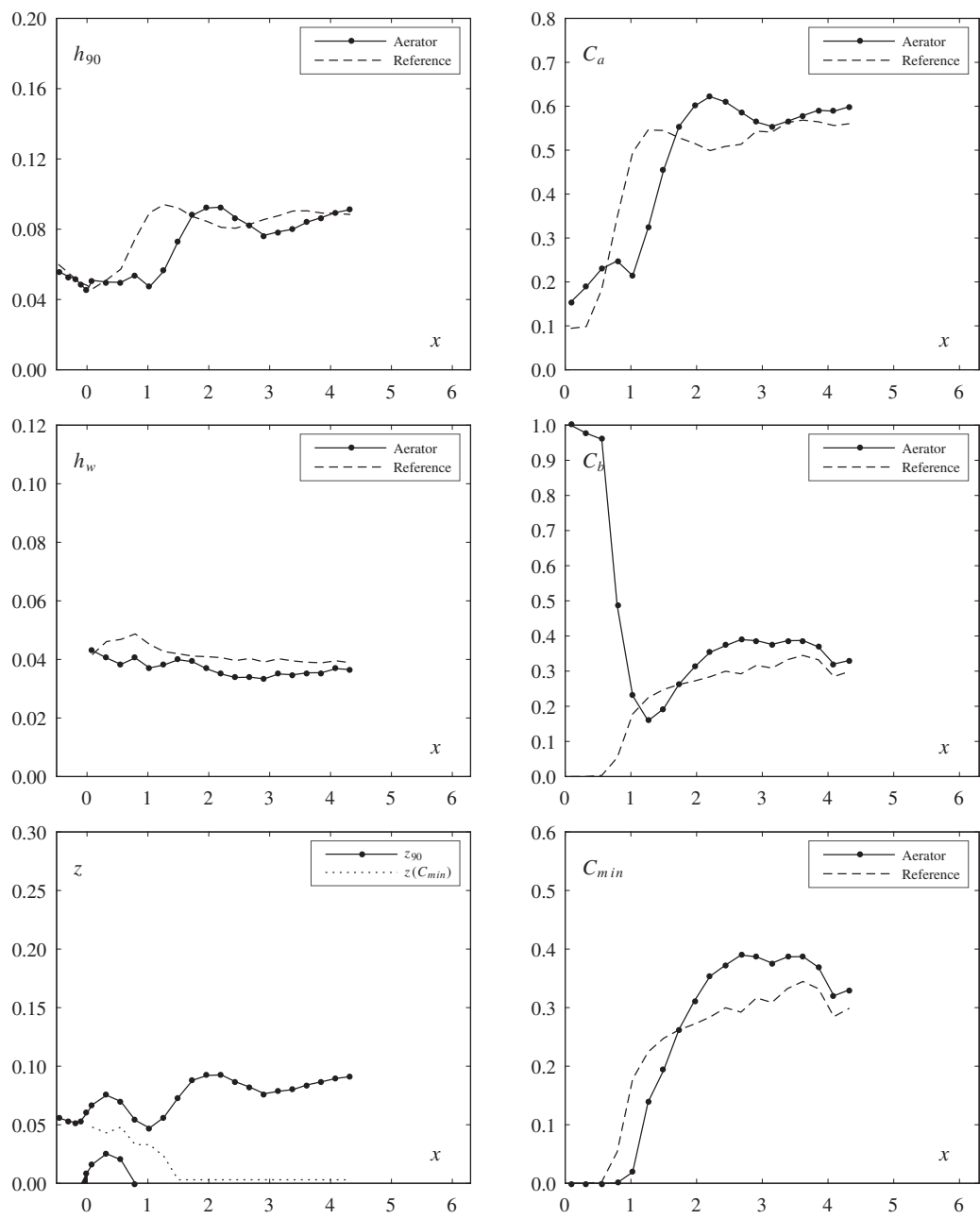
	Aerator	Reference	
Test	32	13	
Parameters			
φ	50	50	[°]
s	0.060	0.060	[m]
F_o	5.55	5.53	[-]
h_o	0.075	0.075	[m]
α	5.71	-	[°]
t	0.015	-	[m]
Flow			
q	0.357	0.356	[m ² /s]
h_c	0.235	0.234	[m]
h_c/s	3.92	3.91	[-]
u_o	4.76	4.74	[m/s]
Pressure			
$p/(\rho g)$	0.113	0.100	[m]
$p'/(\rho g)$	0.0038	0.0038	[m]
Dimensionless numbers			
R	356998	355670	[-]
W_o	154	153	[-]
F_k	17.2	17.1	[-]
F_s	8.9	8.8	[-]
Inception point			
x_i	-	0.90	[m]
h_i	-	0.082	[m]
h_{wi}	-	0.065	[m]
Air entrainment			
β	0.112	-	[-]
q_A	0.040	-	[m ² /s]
$u_{A,max}$	1.35	-	[m/s]
u_A	1.10	-	[m/s]
Jet			
L	1.01	-	[m]
L/h_o	13.5	-	[-]
L_{obs}	0.69	-	[m]
$\Delta p/h$	0.04	-	[-]
h_t	0.068	-	[m]
α_{tu}	5.75	-	[°]
α_{tl}	5.25	-	[°]
γ	5.01	-	[°]
Observation			
-			



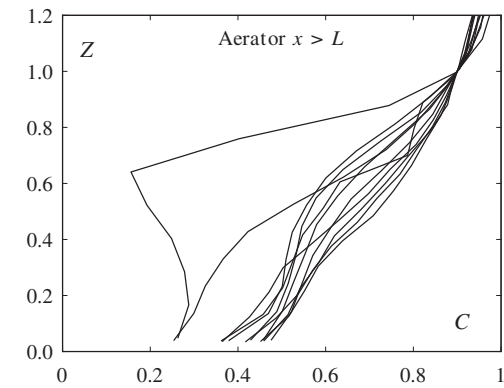
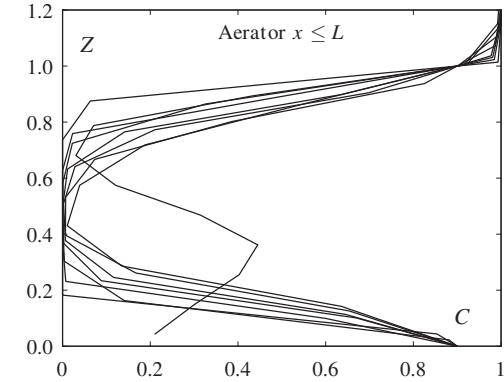
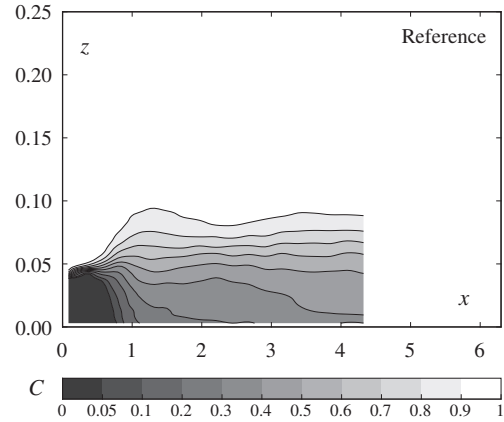
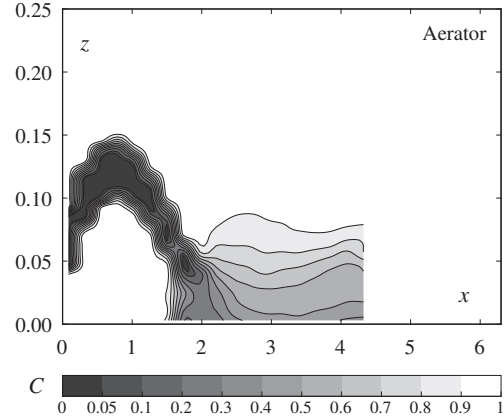


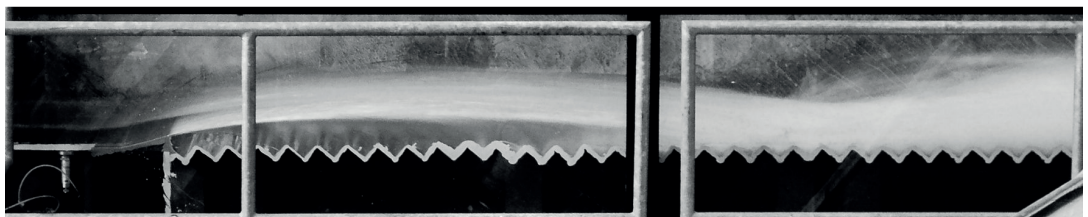
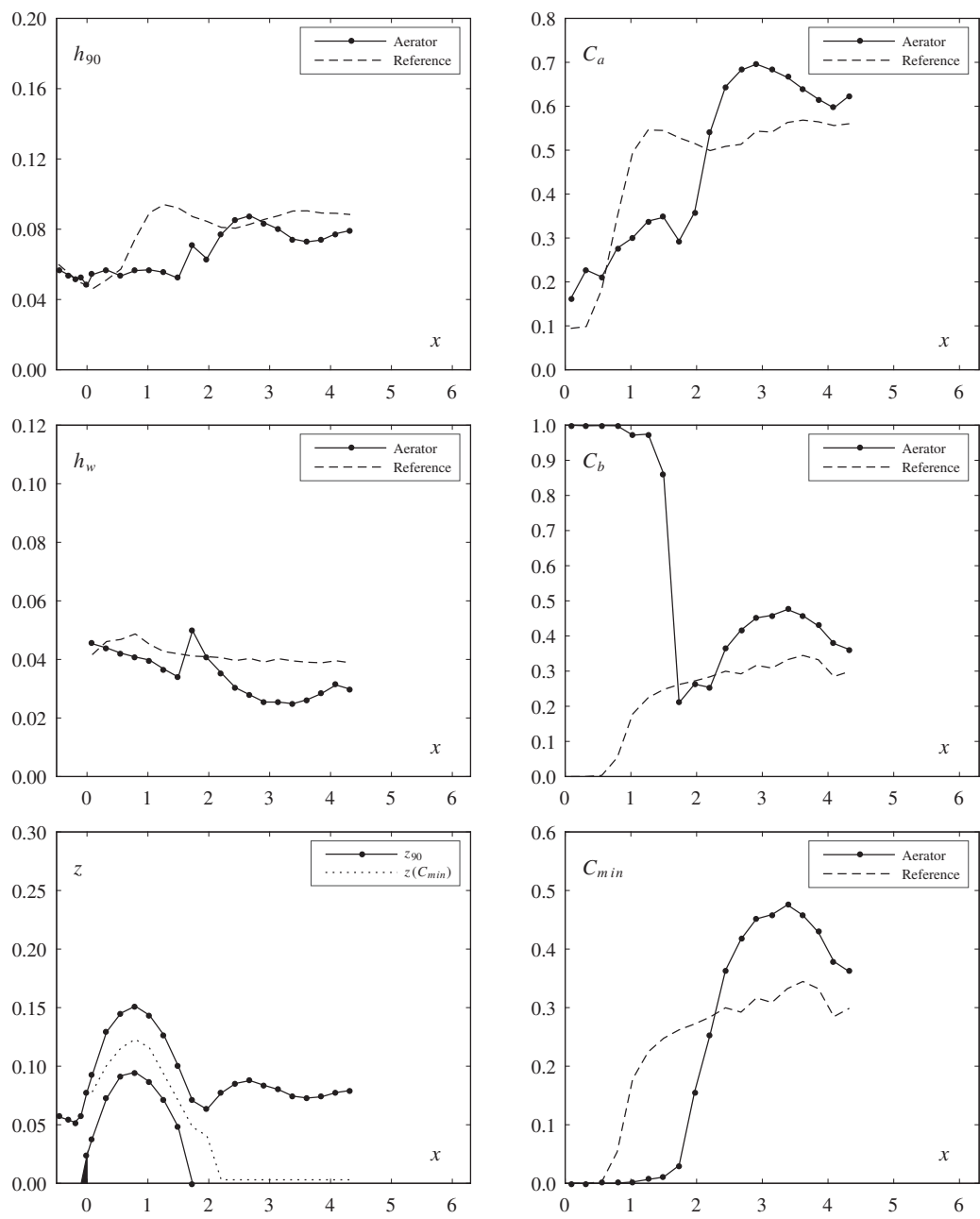
	Aerator	Reference	
Test	33	15	
Parameters			
φ	50	50	[°]
s	0.060	0.060	[m]
F_o	5.46	5.54	[-]
h_o	0.052	0.052	[m]
α	5.71	-	[°]
t	0.015	-	[m]
Flow			
q	0.203	0.206	[m ² /s]
h_c	0.161	0.163	[m]
h_c/s	2.69	2.71	[-]
u_o	3.90	3.95	[m/s]
Pressure			
$p/(\rho g)$	0.074	0.072	[m]
$p'/(\rho g)$	0.0021	0.0020	[m]
Dimensionless numbers			
R	202700	205611	[-]
W_o	105	106	[-]
F_k	9.8	9.9	[-]
F_s	5.0	5.1	[-]
Inception point			
x_i	-	0.59	[m]
h_i	-	0.060	[m]
h_{wi}	-	0.047	[m]
Air entrainment			
β	0.120	-	[-]
q_A	0.024	-	[m ² /s]
$u_{A,max}$	0.83	-	[m/s]
u_A	0.67	-	[m/s]
Jet			
L	0.83	-	[m]
L/h_o	15.9	-	[-]
L_{obs}	0.61	-	[m]
$\Delta p/h$	0.05	-	[-]
h_t	0.045	-	[m]
α_{tu}	6.32	-	[°]
α_{tl}	5.76	-	[°]
γ	5.62	-	[°]
Observation			
-			



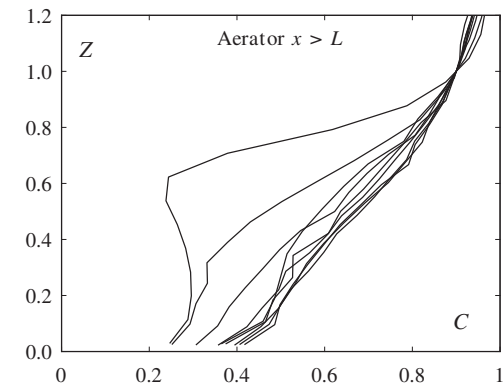
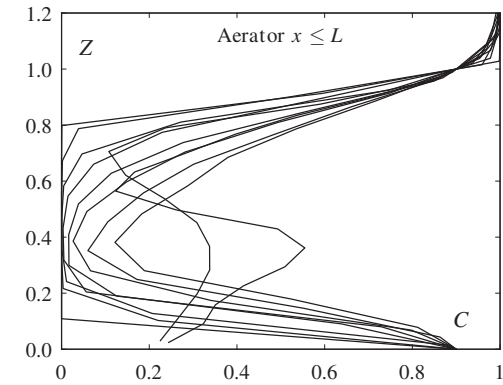
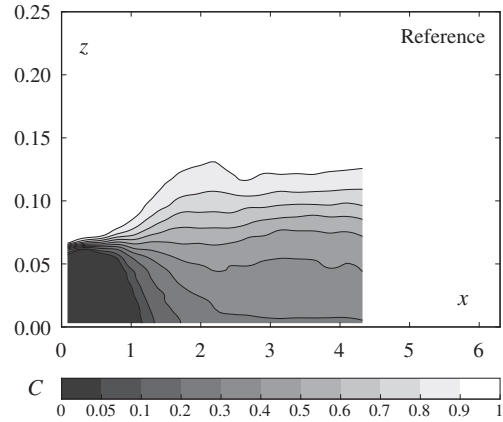
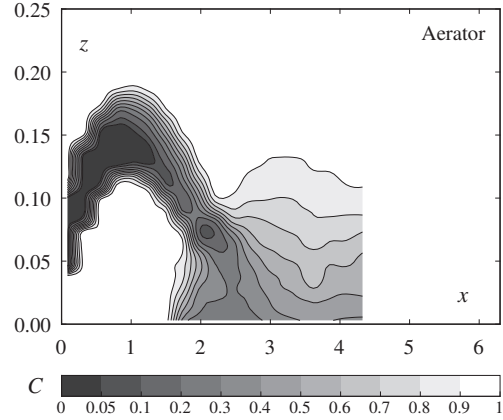


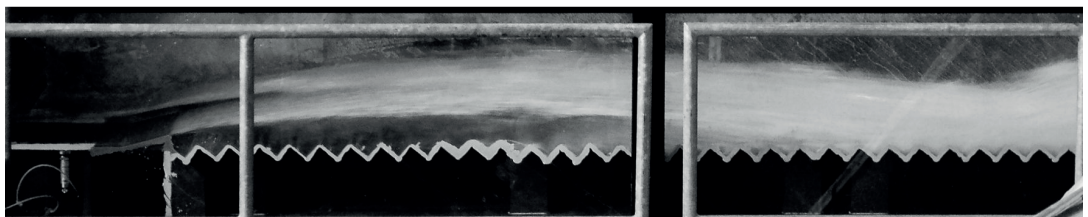
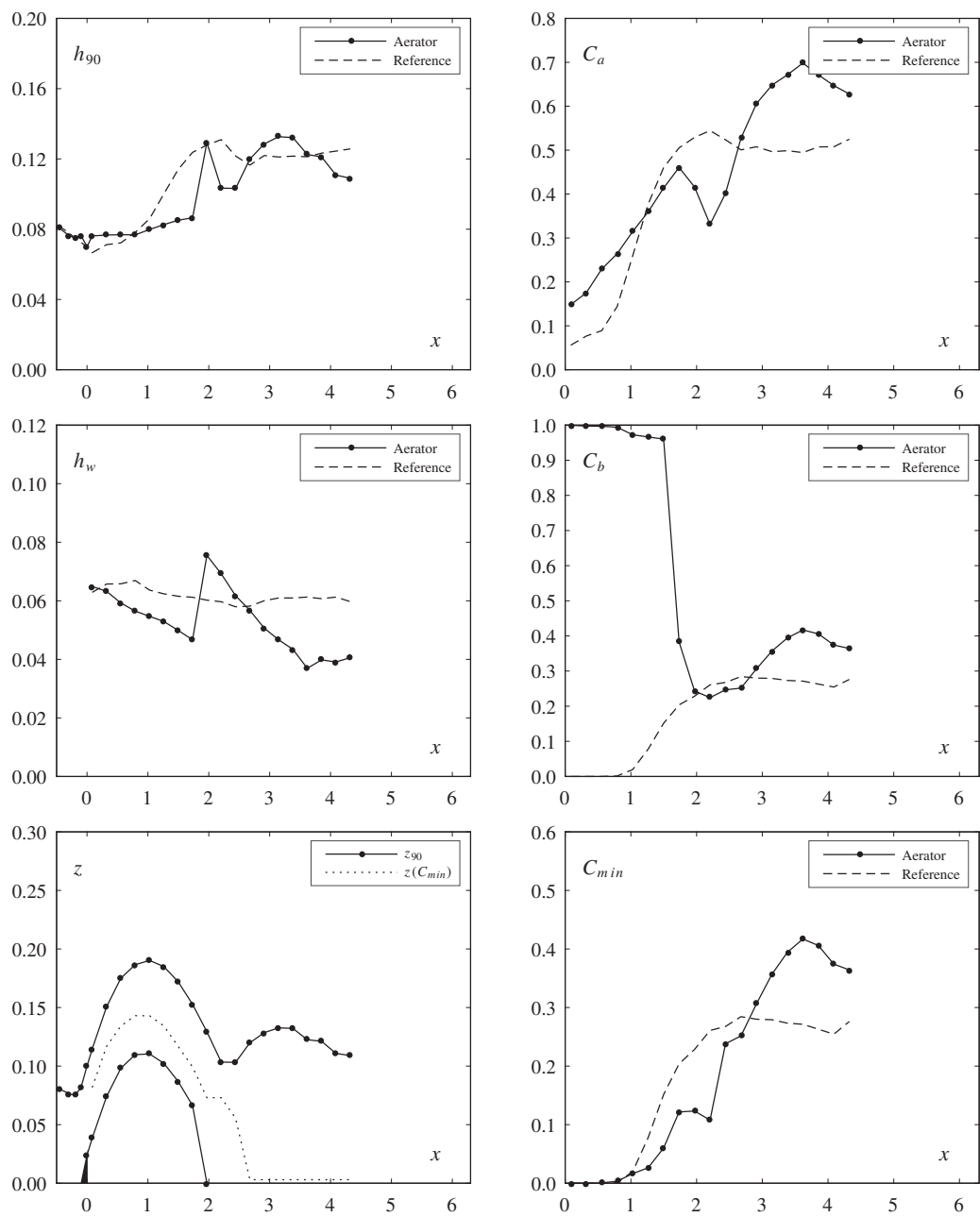
	Aerator	Reference	
Test	34	15	
Parameters			
φ	50	50	[°]
s	0.060	0.060	[m]
F_o	5.52	5.54	[-]
h_o	0.052	0.052	[m]
α	14.04	-	[°]
t	0.030	-	[m]
Flow			
q	0.205	0.206	[m ² /s]
h_c	0.163	0.163	[m]
h_c/s	2.71	2.71	[-]
u_o	3.95	3.95	[m/s]
Pressure			
$p/(\rho g)$	0.074	0.072	[m]
$p'/(\rho g)$	0.0021	0.0020	[m]
Dimensionless numbers			
R	205195	205611	[-]
W_o	106	106	[-]
F_k	9.9	9.9	[-]
F_s	5.1	5.1	[-]
Inception point			
x_i	-	0.59	[m]
h_i	-	0.060	[m]
h_{wi}	-	0.047	[m]
Air entrainment			
β	0.246	-	[-]
q_A	0.050	-	[m ² /s]
$u_{A,max}$	1.70	-	[m/s]
u_A	1.39	-	[m/s]
Jet			
L	1.84	-	[m]
L/h_o	35.4	-	[-]
L_{obs}	1.45	-	[m]
$\Delta p/h$	0.06	-	[-]
h_t	0.048	-	[m]
α_{tu}	13.00	-	[°]
α_{tl}	12.54	-	[°]
γ	8.95	-	[°]
Observation			
-			



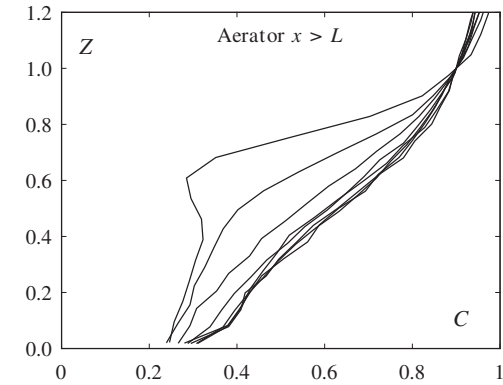
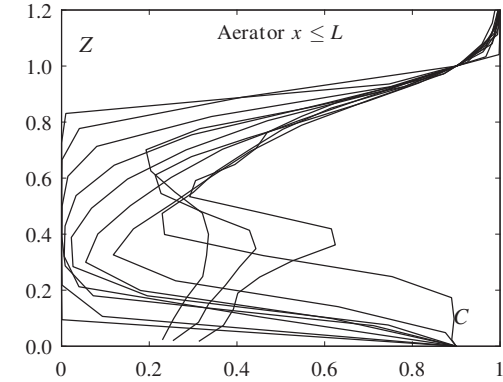
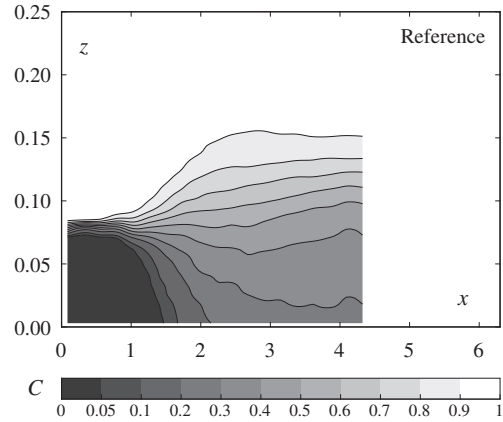
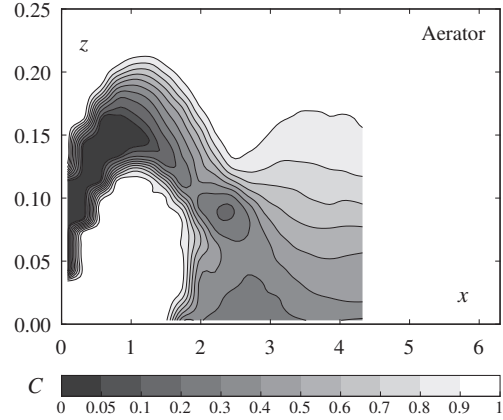


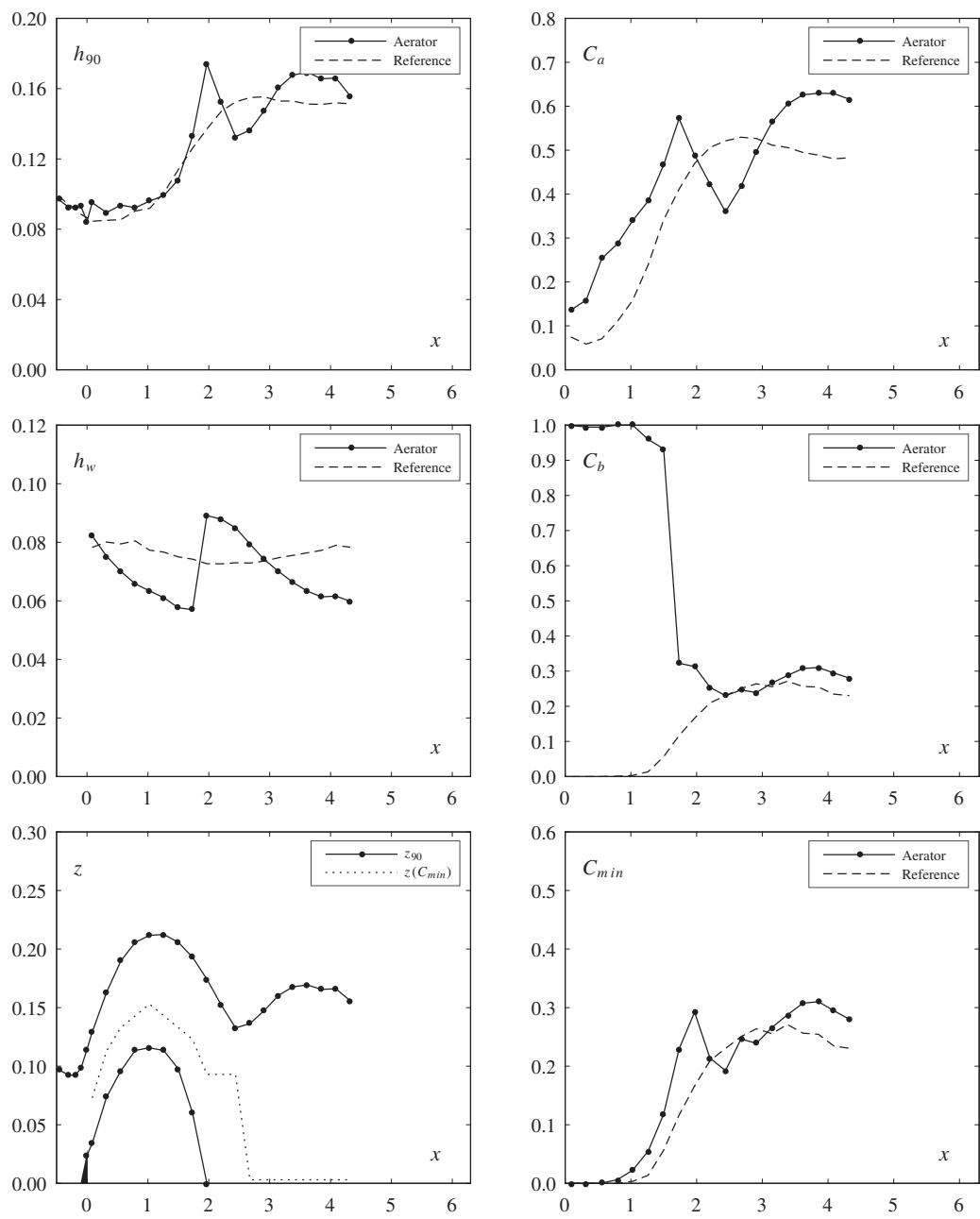
	Aerator	Reference	
Test	35	13	
Parameters			
φ	50	50	[°]
s	0.060	0.060	[m]
F_o	5.55	5.53	[-]
h_o	0.075	0.075	[m]
α	14.04	-	[°]
t	0.030	-	[m]
Flow			
q	0.357	0.356	[m ² /s]
h_c	0.235	0.234	[m]
h_c/s	3.92	3.91	[-]
u_o	4.76	4.74	[m/s]
Pressure			
$p/(\rho g)$	0.119	0.100	[m]
$p'/(\rho g)$	0.0038	0.0038	[m]
Dimensionless numbers			
R	357069	355670	[-]
W_o	154	153	[-]
F_k	17.2	17.1	[-]
F_s	8.9	8.8	[-]
Inception point			
x_i	-	0.90	[m]
h_i	-	0.082	[m]
h_{wi}	-	0.065	[m]
Air entrainment			
β	0.253	-	[-]
q_A	0.090	-	[m ² /s]
$u_{A,max}$	3.01	-	[m/s]
u_A	2.49	-	[m/s]
Jet			
L	2.24	-	[m]
L/h_o	29.9	-	[-]
L_{obs}	1.60	-	[m]
$\Delta p/h$	0.08	-	[-]
h_t	0.070	-	[m]
α_{tu}	12.05	-	[°]
α_{tl}	11.38	-	[°]
γ	8.72	-	[°]
Observation			
-			



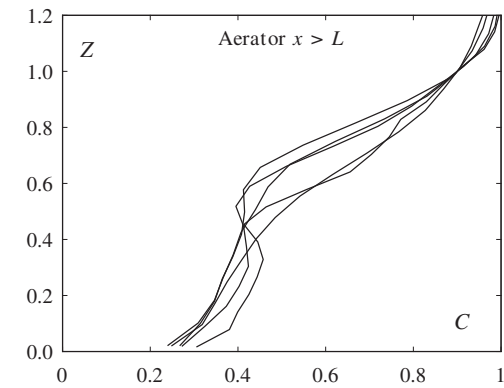
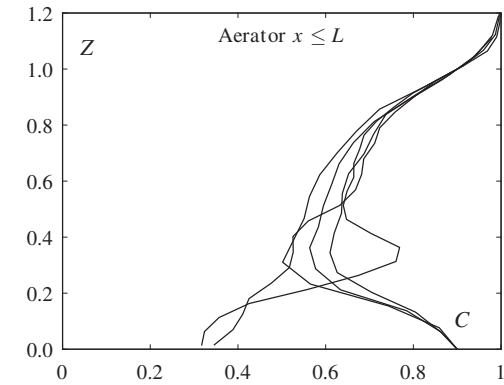
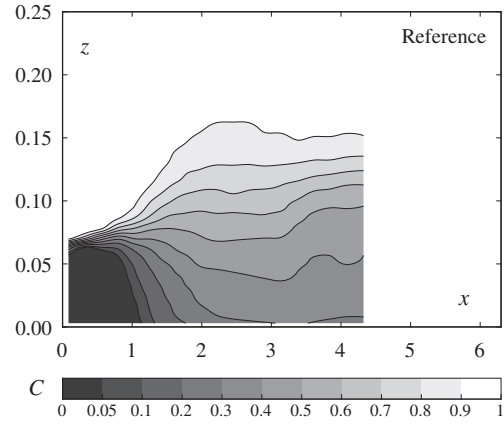
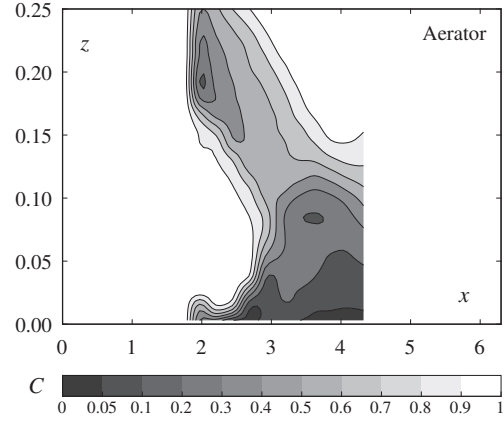


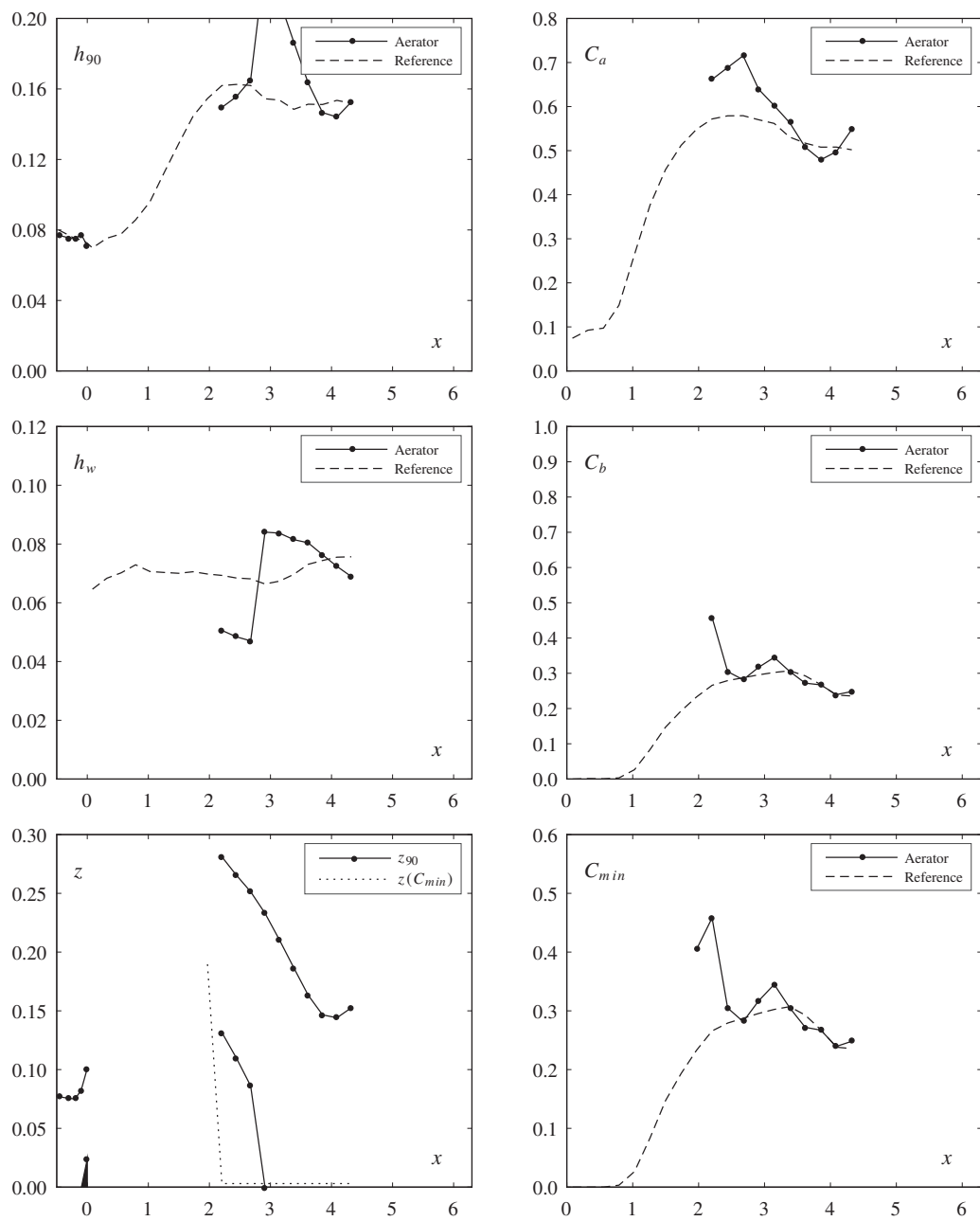
	Aerator	Reference	
Test	36	14	
Parameters			
φ	50	50	[°]
s	0.060	0.060	[m]
F_o	5.50	5.49	[-]
h_o	0.092	0.092	[m]
α	14.04	-	[°]
t	0.030	-	[m]
Flow			
q	0.481	0.480	[m ² /s]
h_c	0.287	0.286	[m]
h_c/s	4.78	4.77	[-]
u_o	5.23	5.22	[m/s]
Pressure			
$p/(\rho g)$	0.156	0.119	[m]
$p'/(\rho g)$	0.0055	0.0057	[m]
Dimensionless numbers			
R	481093	479863	[-]
W_o	187	186	[-]
F_k	23.2	23.1	[-]
F_s	11.9	11.9	[-]
Inception point			
x_i	-	1.18	[m]
h_i	-	0.098	[m]
h_{wi}	-	0.077	[m]
Air entrainment			
β	0.250	-	[-]
q_A	0.120	-	[m ² /s]
$u_{A,max}$	3.98	-	[m/s]
u_A	3.31	-	[m/s]
Jet			
L	2.44	-	[m]
L/h_o	26.5	-	[-]
L_{obs}	1.67	-	[m]
$\Delta p/h$	0.10	-	[-]
h_t	0.085	-	[m]
α_{tu}	11.23	-	[°]
α_{tl}	10.46	-	[°]
γ	8.42	-	[°]
Observation			
I			



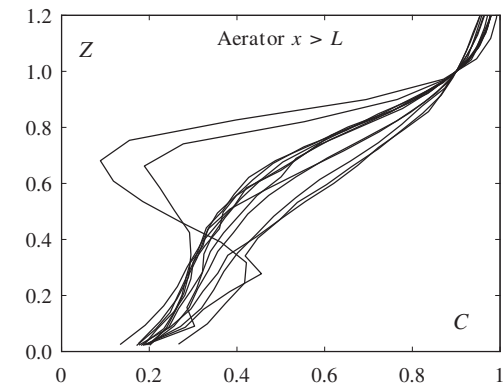
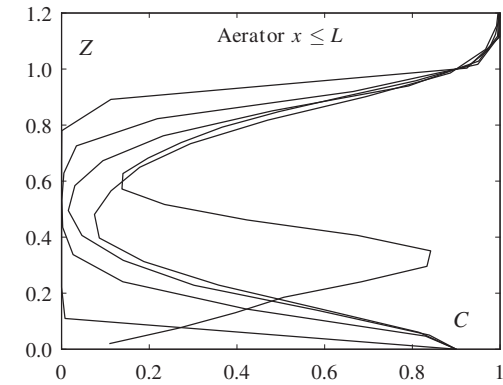
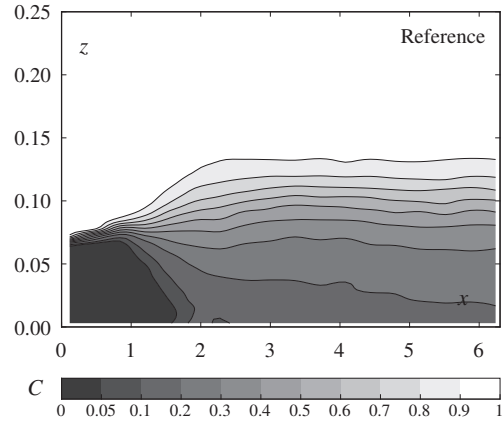
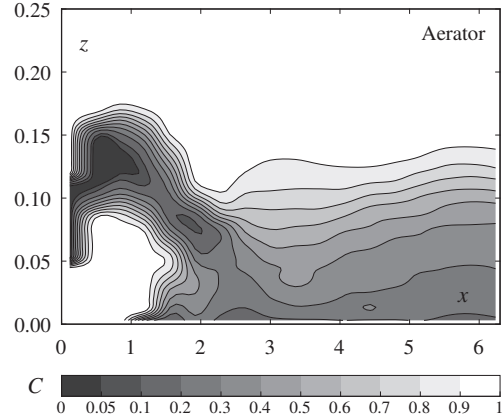


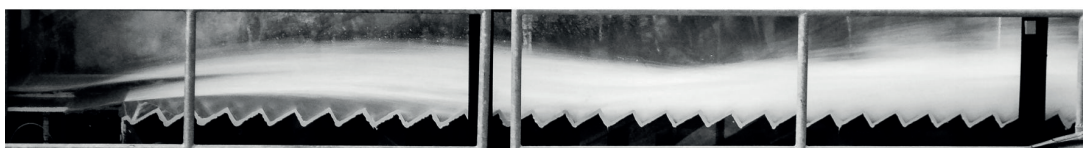
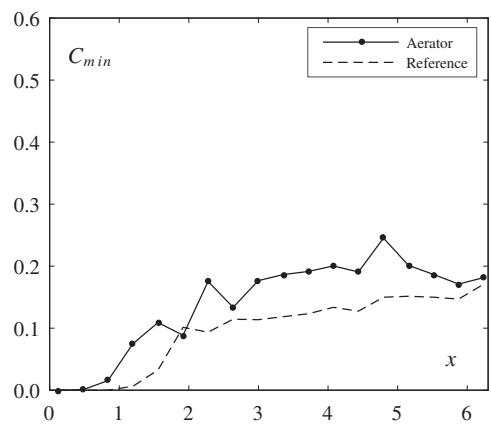
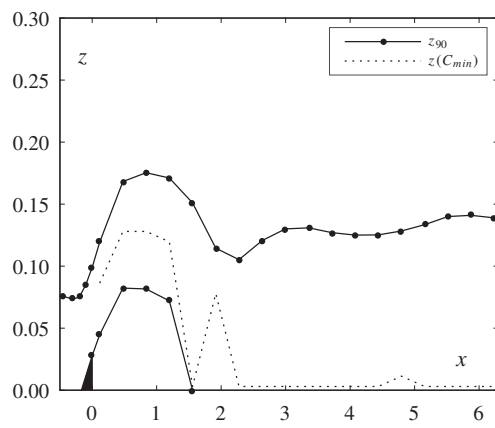
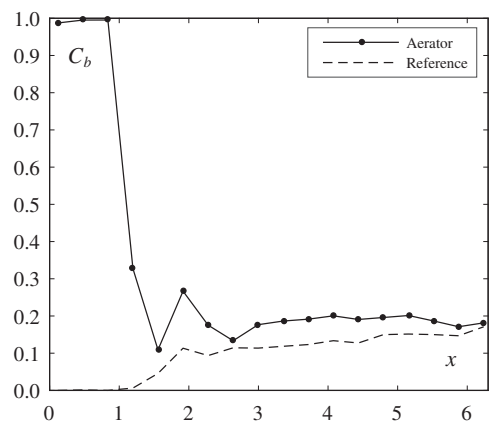
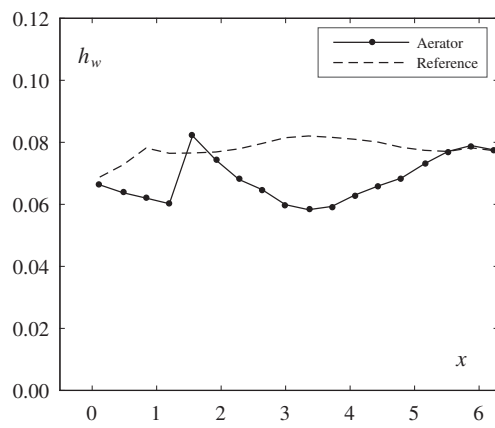
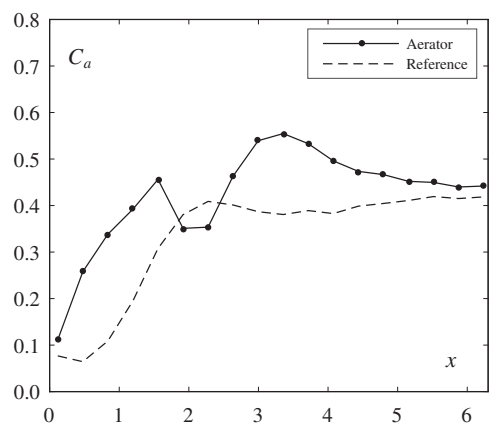
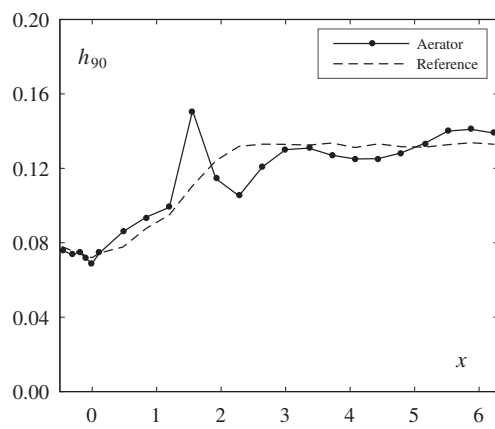
	Aerator	Reference	
Test	37	16	
Parameters			
φ	50	50	[°]
s	0.060	0.060	[m]
F_o	7.55	7.48	[-]
h_o	0.075	0.075	[m]
α	14.04	-	[°]
t	0.030	-	[m]
Flow			
q	0.485	0.481	[m ² /s]
h_c	0.289	0.287	[m]
h_c/s	4.81	4.78	[-]
u_o	6.47	6.41	[m/s]
Pressure			
$p/(\rho g)$	0.180	0.148	[m]
$p'/(\rho g)$	0.0056	0.0058	[m]
Dimensionless numbers			
R	485490	480936	[-]
W_o	209	207	[-]
F_k	23.4	23.2	[-]
F_s	12.1	11.9	[-]
Inception point			
x_i	-	0.86	[m]
h_i	-	0.089	[m]
h_{wi}	-	0.072	[m]
Air entrainment			
β	0.246	-	[-]
q_A	0.119	-	[m ² /s]
$u_{A,max}$	3.95	-	[m/s]
u_A	3.29	-	[m/s]
Jet			
L	3.33	-	[m]
L/h_o	44.4	-	[-]
L_{obs}	2.36	-	[m]
$\Delta p/h$	0.13	-	[-]
h_t	0.071	-	[m]
α_{tu}	12.36	-	[°]
α_{tl}	10.16	-	[°]
γ	8.66	-	[°]
Observation			
-			



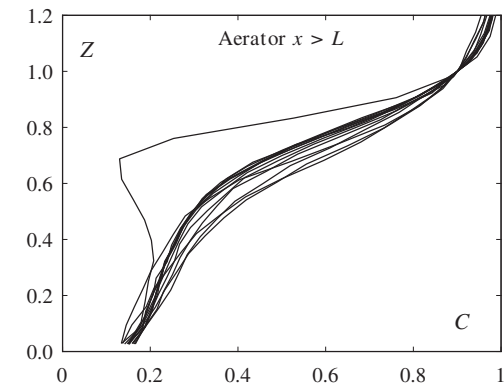
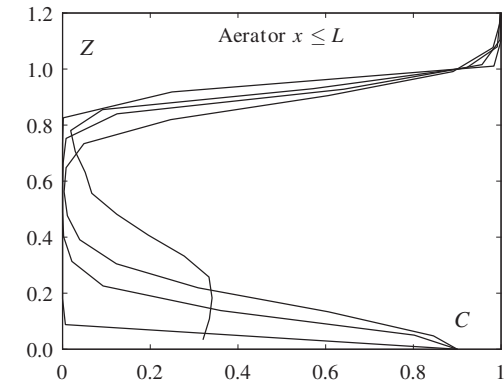
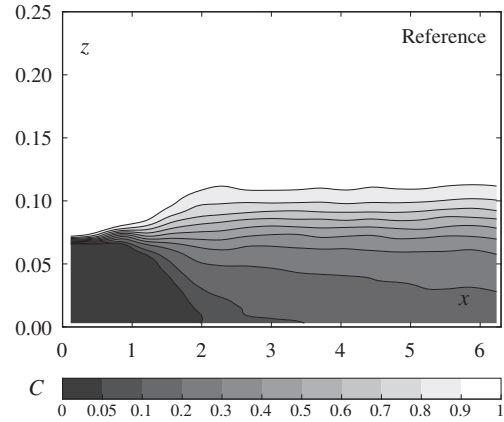
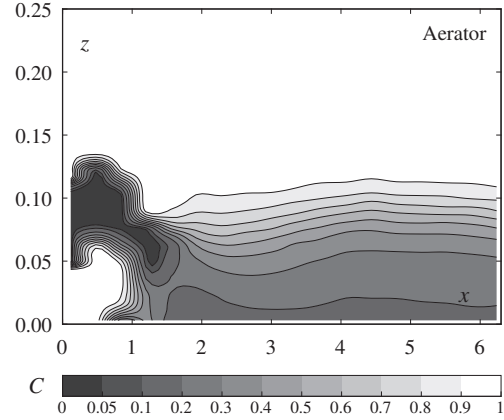


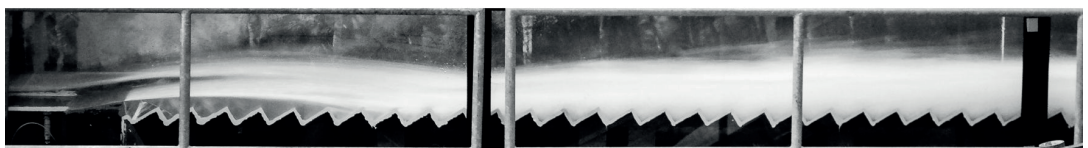
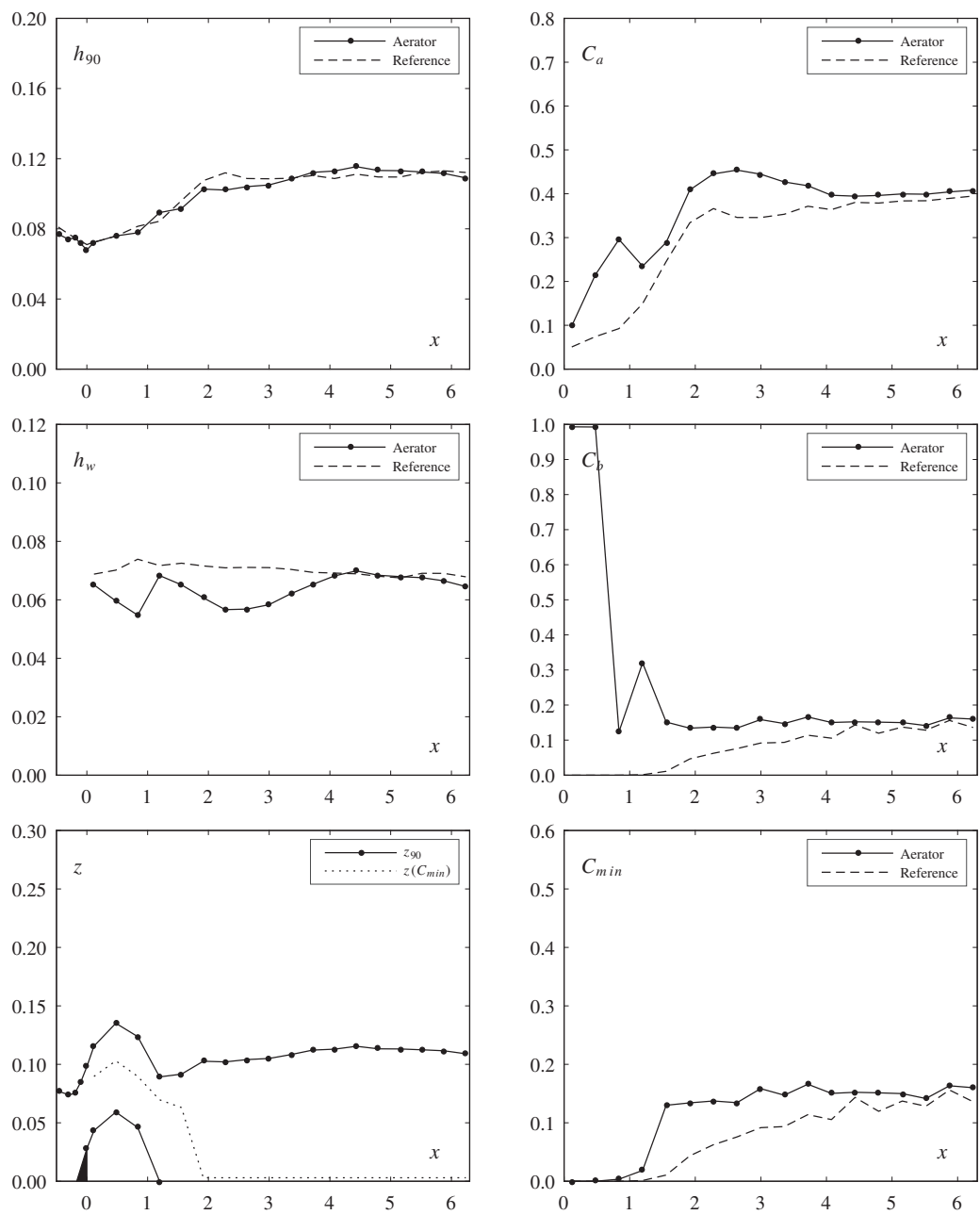
	Aerator	Reference	
Test	43	42	
Parameters			
φ	30	30	[°]
s	0.060	0.060	[m]
F_o	7.45	7.48	[-]
h_o	0.075	0.075	[m]
α	9.46	-	[°]
t	0.030	-	[m]
Flow			
q	0.479	0.481	[m ² /s]
h_c	0.286	0.287	[m]
h_c/s	4.77	4.78	[-]
u_o	6.39	6.41	[m/s]
Pressure			
$p/(\rho g)$	0.238	0.168	[m]
$p'/(\rho g)$	0.0050	0.0054	[m]
Dimensionless numbers			
R	478954	481006	[-]
W_o	206	207	[-]
F_k	18.3	18.3	[-]
F_s	14.7	14.8	[-]
Inception point			
x_i	-	1.23	[m]
h_i	-	0.096	[m]
h_{wi}	-	0.076	[m]
Air entrainment			
β	0.198	-	[-]
q_A	0.095	-	[m ² /s]
$u_{A,max}$	3.15	-	[m/s]
u_A	2.61	-	[m/s]
Jet			
L	1.90	-	[m]
L/h_o	25.3	-	[-]
L_{obs}	1.32	-	[m]
$\Delta p/h$	0.08	-	[-]
h_t	0.069	-	[m]
α_{tu}	9.40	-	[°]
α_{tl}	7.85	-	[°]
γ	8.30	-	[°]
Observation			
-			



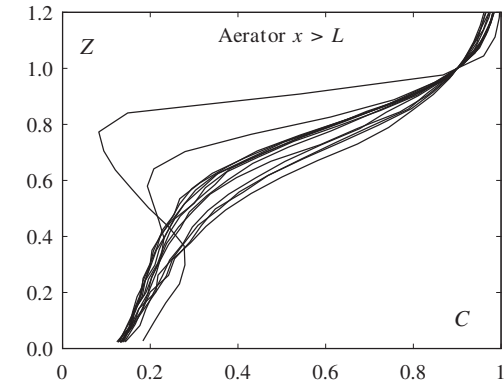
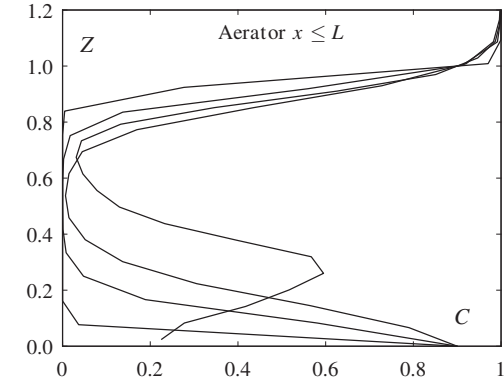
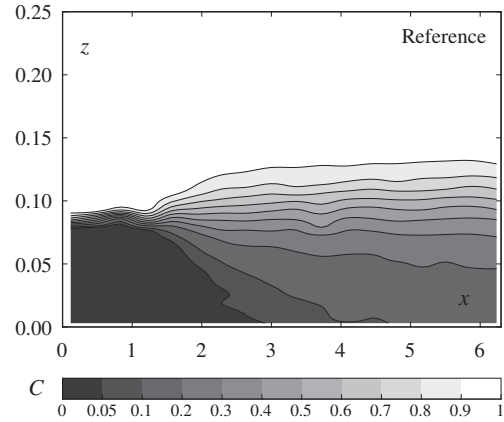
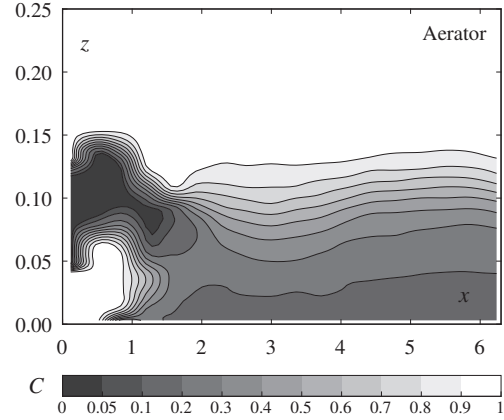


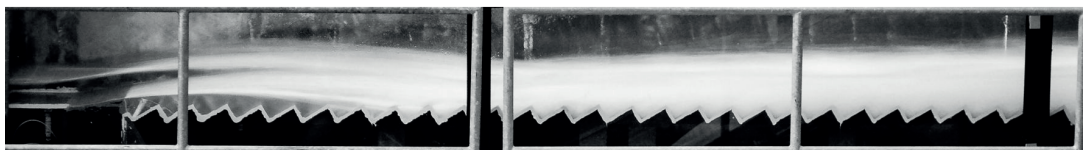
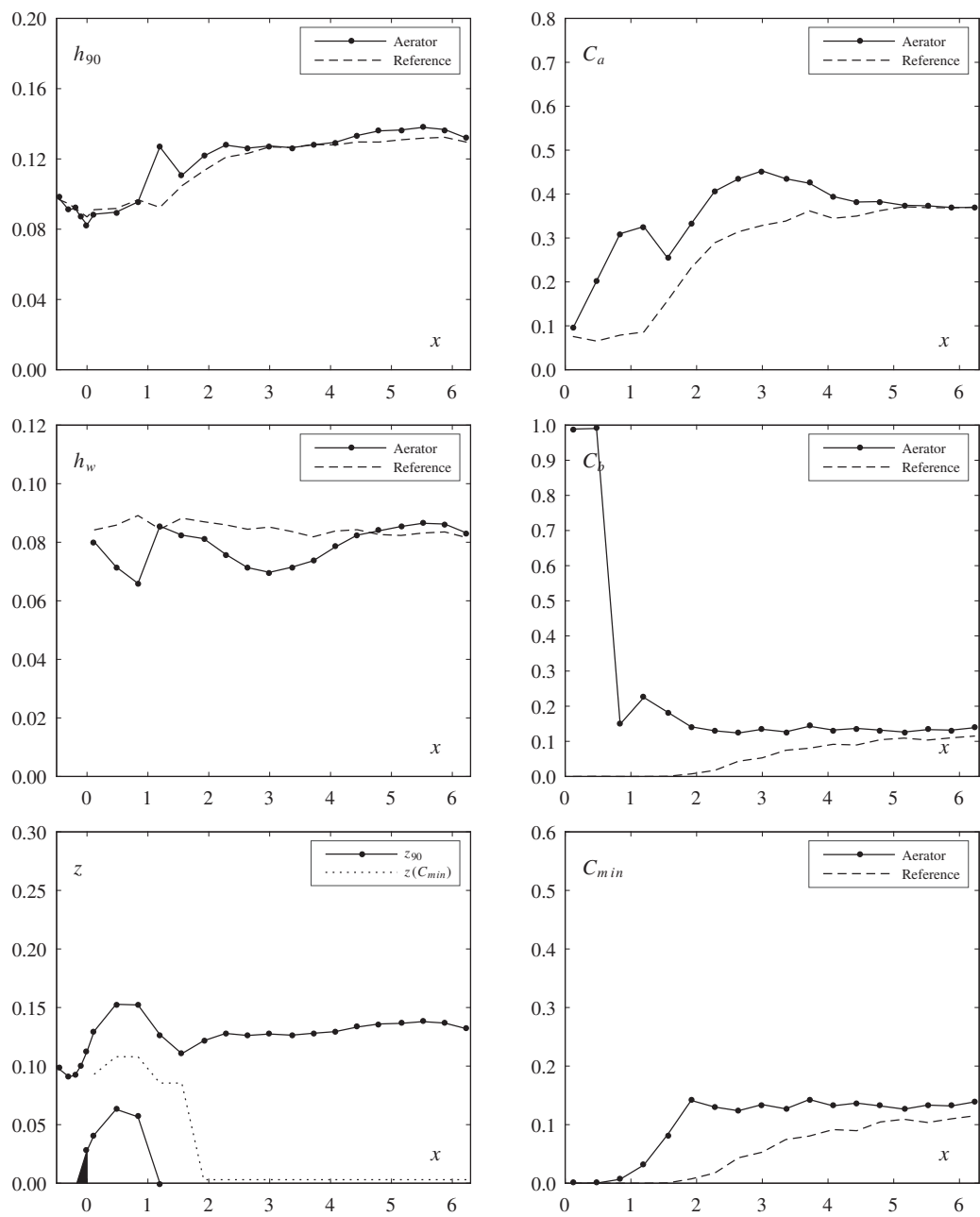
	Aerator	Reference	
Test	44	38	
Parameters			
φ	30	30	[°]
s	0.060	0.060	[m]
F_o	5.54	5.53	[-]
h_o	0.075	0.075	[m]
α	9.46	-	[°]
t	0.030	-	[m]
Flow			
q	0.356	0.356	[m ² /s]
h_c	0.235	0.235	[m]
h_c/s	3.91	3.91	[-]
u_o	4.75	4.74	[m/s]
Pressure			
$p/(\rho g)$	0.160	0.119	[m]
$p'/(\rho g)$	0.0031	0.0033	[m]
Dimensionless numbers			
R	356311	355693	[-]
W_o	153	153	[-]
F_k	13.6	13.6	[-]
F_s	10.9	10.9	[-]
Inception point			
x_i	-	1.52	[m]
h_i	-	0.095	[m]
h_{wi}	-	0.072	[m]
Air entrainment			
β	0.124	-	[-]
q_A	0.044	-	[m ² /s]
$u_{A,max}$	1.50	-	[m/s]
u_A	1.22	-	[m/s]
Jet			
L	1.22	-	[m]
L/h_o	16.2	-	[-]
L_{obs}	0.90	-	[m]
$\Delta p/h$	0.01	-	[-]
h_t	0.068	-	[m]
α_{tu}	9.09	-	[°]
α_{tl}	8.10	-	[°]
γ	8.94	-	[°]
Observation			
-			



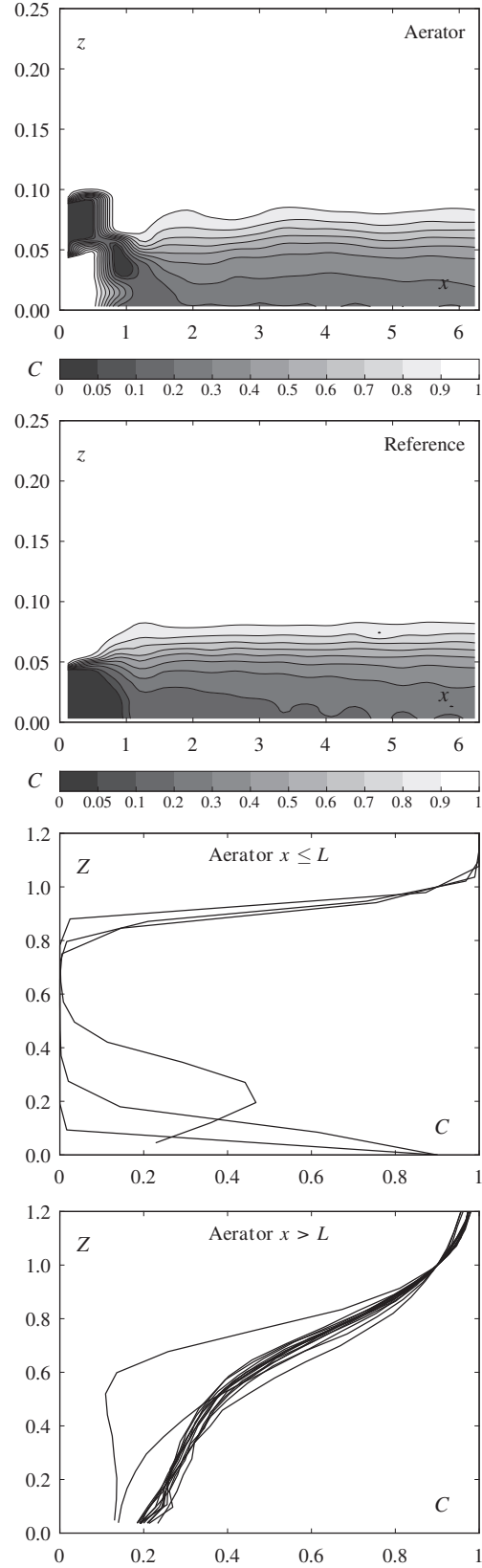


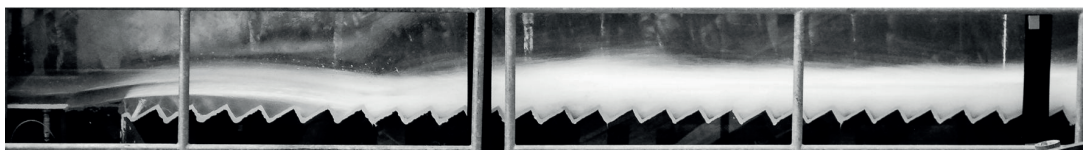
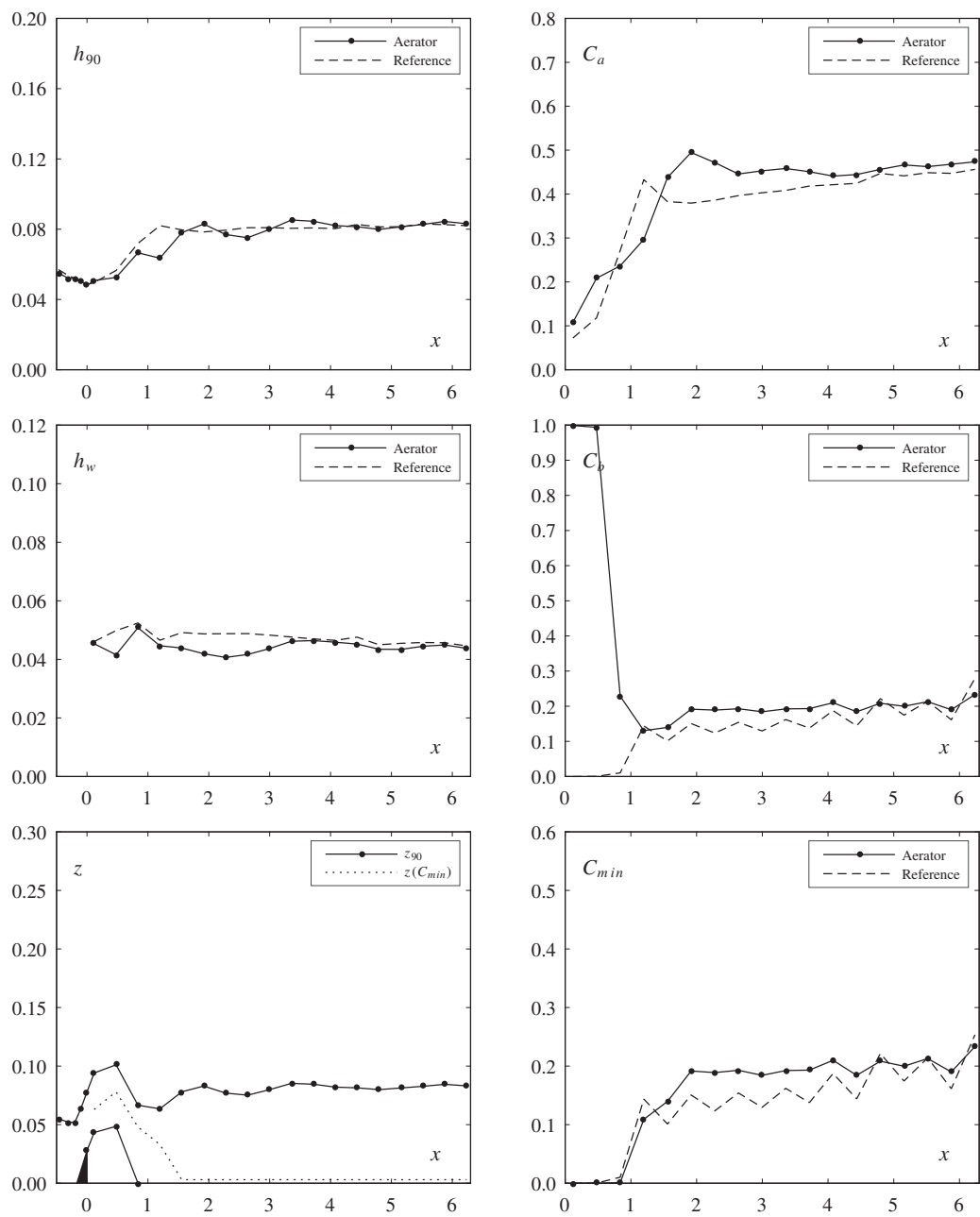
	Aerator	Reference	
Test	45	39	
Parameters			
φ	30	30	[°]
s	0.060	0.060	[m]
F_o	5.50	5.52	[-]
h_o	0.092	0.092	[m]
α	9.46	-	[°]
t	0.030	-	[m]
Flow			
q	0.481	0.483	[m ² /s]
h_c	0.287	0.287	[m]
h_c/s	4.78	4.79	[-]
u_o	5.23	5.25	[m/s]
Pressure			
$p/(\rho g)$	0.210	0.145	[m]
$p'/(\rho g)$	0.0045	0.0045	[m]
Dimensionless numbers			
R	480848	482720	[-]
W_o	187	188	[-]
F_k	18.3	18.4	[-]
F_s	14.8	14.8	[-]
Inception point			
x_i	-	2.01	[m]
h_i	-	0.115	[m]
h_{wi}	-	0.087	[m]
Air entrainment			
β	0.144	-	[-]
q_A	0.069	-	[m ² /s]
$u_{A,max}$	2.32	-	[m/s]
u_A	1.91	-	[m/s]
Jet			
L	1.39	-	[m]
L/h_o	15.1	-	[-]
L_{obs}	0.90	-	[m]
$\Delta p/h$	0.01	-	[-]
h_t	0.083	-	[m]
α_{tu}	8.66	-	[°]
α_{tl}	7.64	-	[°]
γ	8.44	-	[°]
Observation			
-			



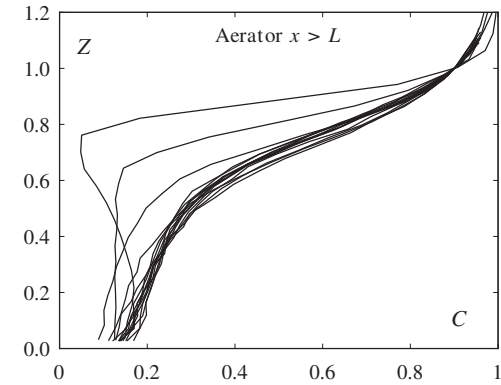
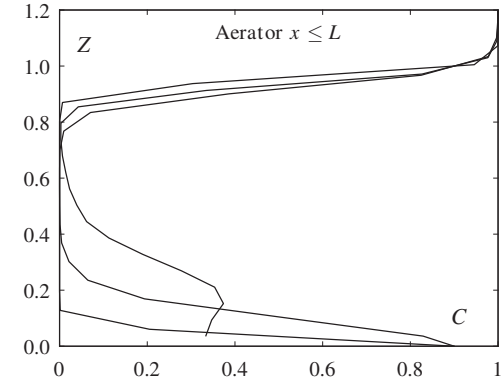
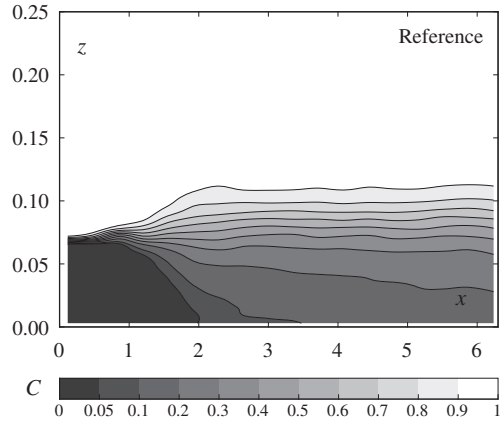
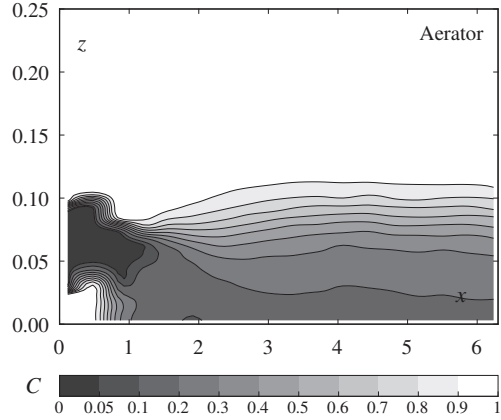


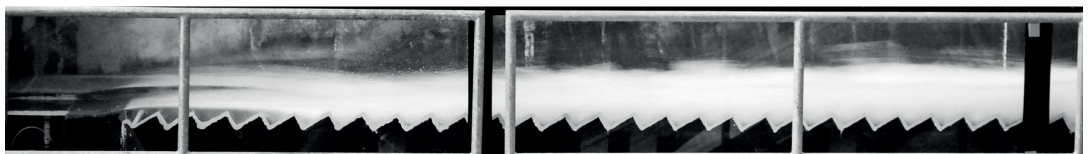
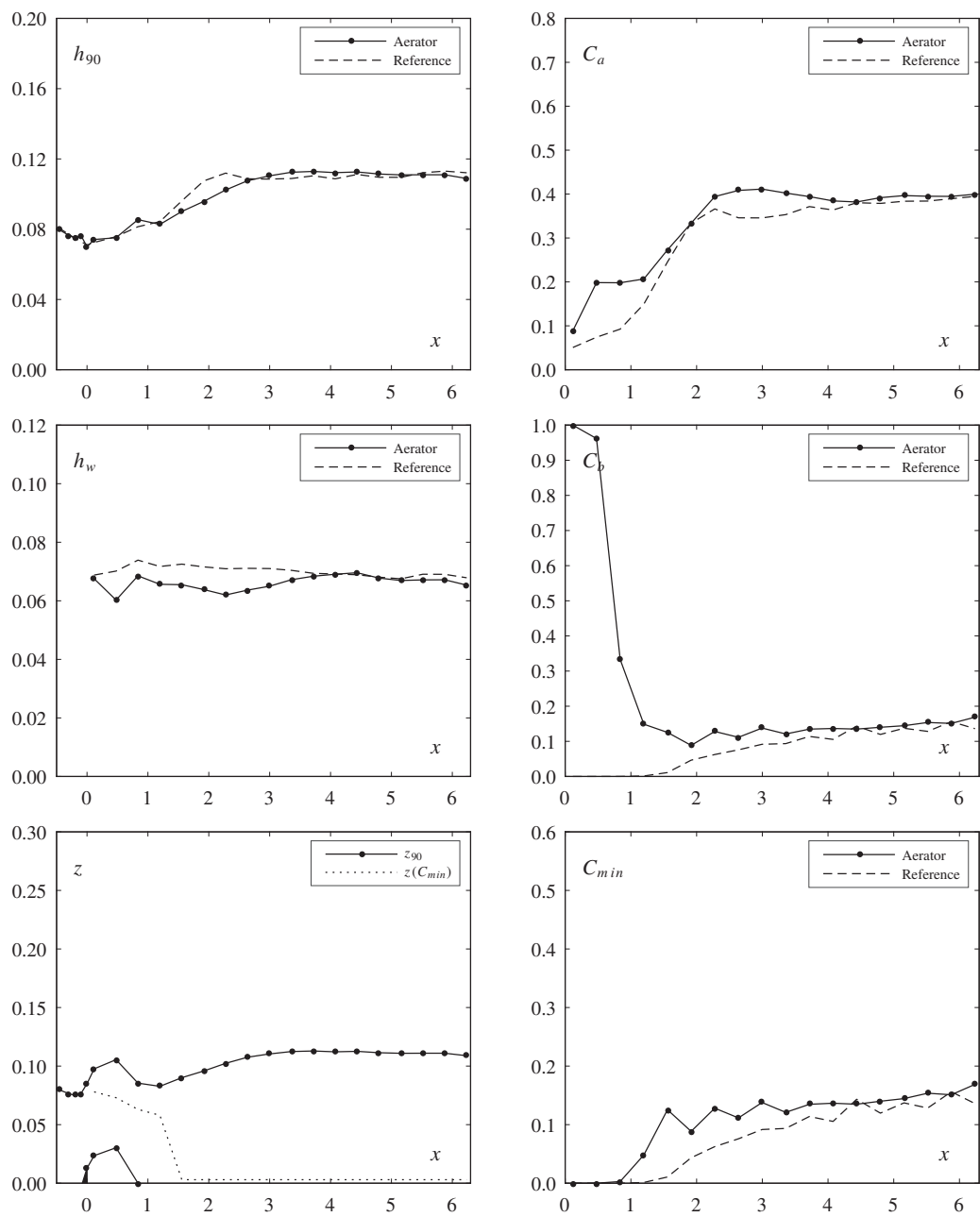
	Aerator	Reference	
Test	46	40	
Parameters			
φ	30	30	[°]
s	0.060	0.060	[m]
F_o	5.53	5.45	[-]
h_o	0.052	0.052	[m]
α	9.46	-	[°]
t	0.030	-	[m]
Flow			
q	0.205	0.202	[m ² /s]
h_c	0.163	0.161	[m]
h_c/s	2.71	2.68	[-]
u_o	3.95	3.89	[m/s]
Pressure			
$p/(\rho g)$	0.096	0.083	[m]
$p'/(\rho g)$	0.0023	0.0020	[m]
Dimensionless numbers			
R	205499	202413	[-]
W_o	106	105	[-]
F_k	7.8	7.7	[-]
F_s	6.3	6.2	[-]
Inception point			
x_i	-	0.83	[m]
h_i	-	0.072	[m]
h_{wi}	-	0.052	[m]
Air entrainment			
β	0.099	-	[-]
q_A	0.020	-	[m ² /s]
$u_{A,max}$	0.70	-	[m/s]
u_A	0.56	-	[m/s]
Jet			
L	0.85	-	[m]
L/h_o	16.3	-	[-]
L_{obs}	0.72	-	[m]
$\Delta p/h$	0.02	-	[-]
h_t	0.048	-	[m]
α_{tu}	9.26	-	[°]
α_{tl}	8.55	-	[°]
γ	10.91	-	[°]
Observation			
-			



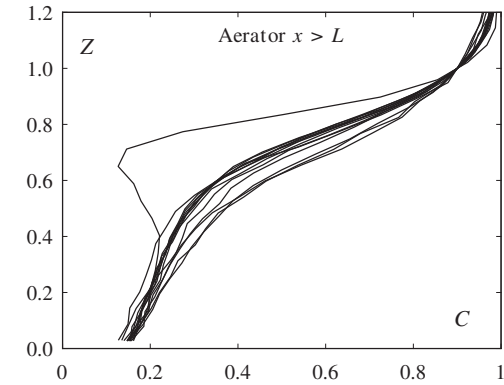
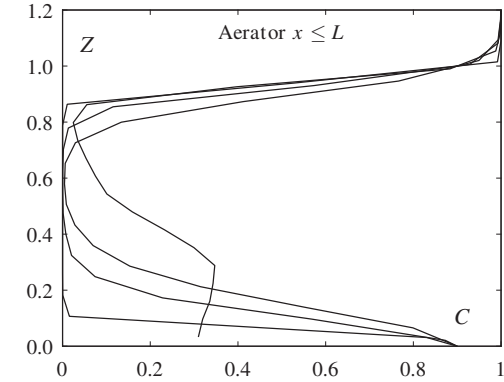
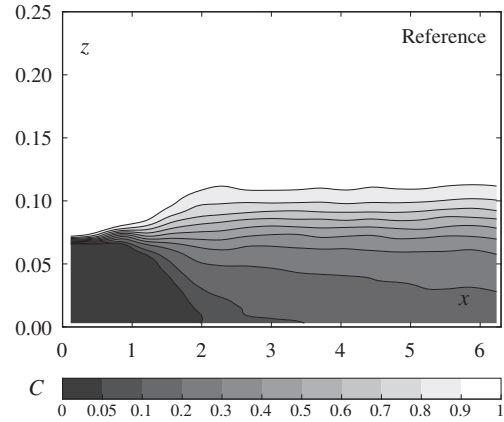
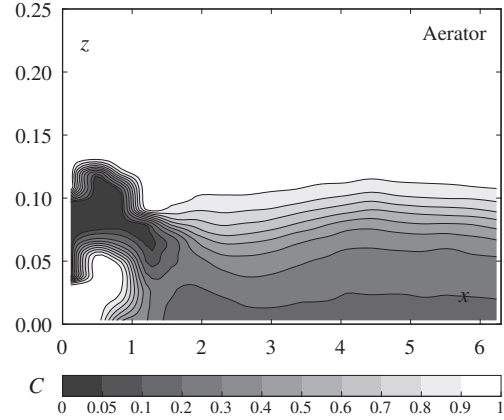


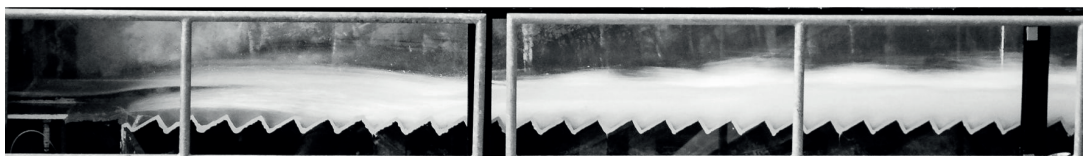
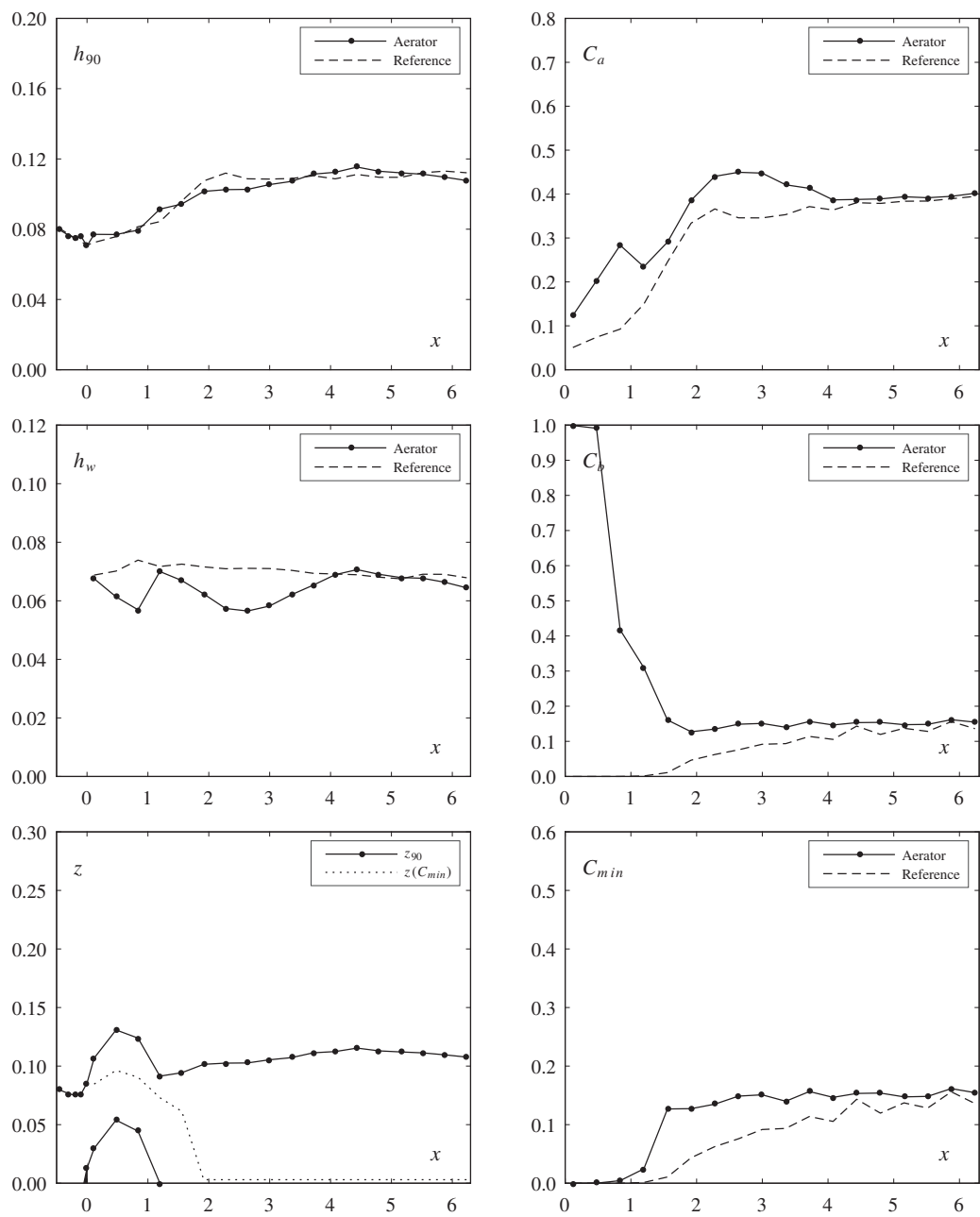
	Aerator	Reference	
Test	47	38	
Parameters			
φ	30	30	[°]
s	0.060	0.060	[m]
F_o	5.52	5.53	[-]
h_o	0.075	0.075	[m]
α	9.46	-	[°]
t	0.015	-	[m]
Flow			
q	0.355	0.356	[m ² /s]
h_c	0.234	0.235	[m]
h_c/s	3.90	3.91	[-]
u_o	4.73	4.74	[m/s]
Pressure			
$p/(\rho g)$	0.124	0.119	[m]
$p'/(\rho g)$	0.0032	0.0033	[m]
Dimensionless numbers			
R	354918	355693	[-]
W_o	153	153	[-]
F_k	13.5	13.6	[-]
F_s	10.9	10.9	[-]
Inception point			
x_i	-	1.52	[m]
h_i	-	0.095	[m]
h_{wi}	-	0.072	[m]
Air entrainment			
β	0.080	-	[-]
q_A	0.028	-	[m ² /s]
$u_{A,max}$	0.97	-	[m/s]
u_A	0.78	-	[m/s]
Jet			
L	0.86	-	[m]
L/h_o	11.5	-	[-]
L_{obs}	0.64	-	[m]
$\Delta p/h$	0.01	-	[-]
h_t	0.070	-	[m]
α_{tu}	7.37	-	[°]
α_{tl}	6.42	-	[°]
γ	7.08	-	[°]
Observation			
-			



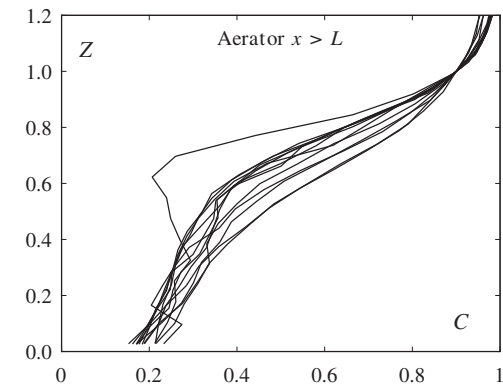
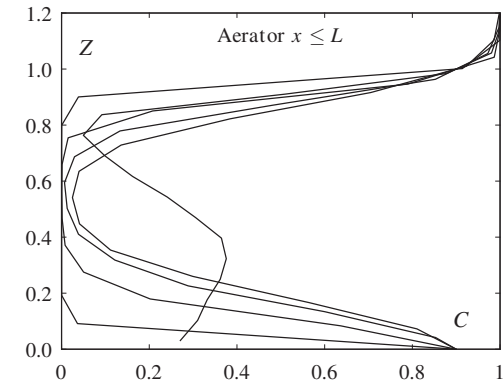
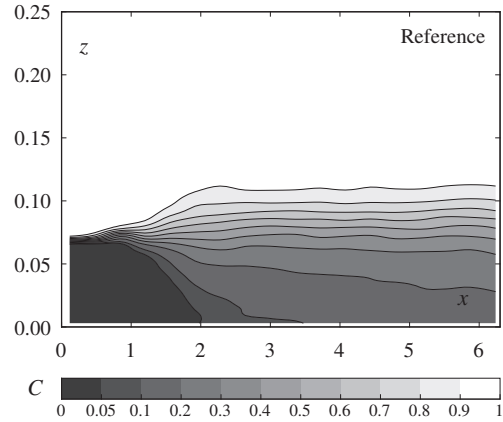
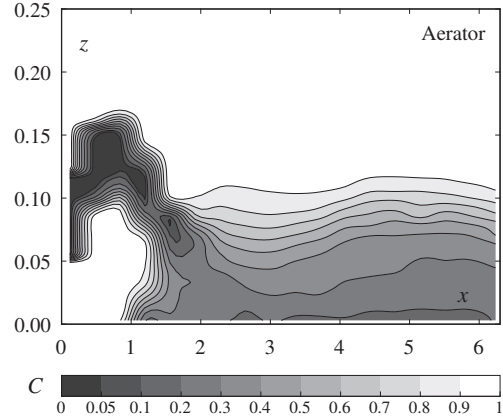


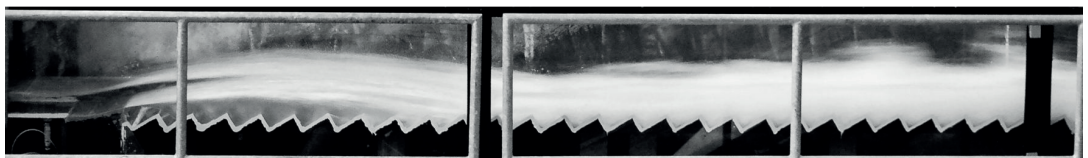
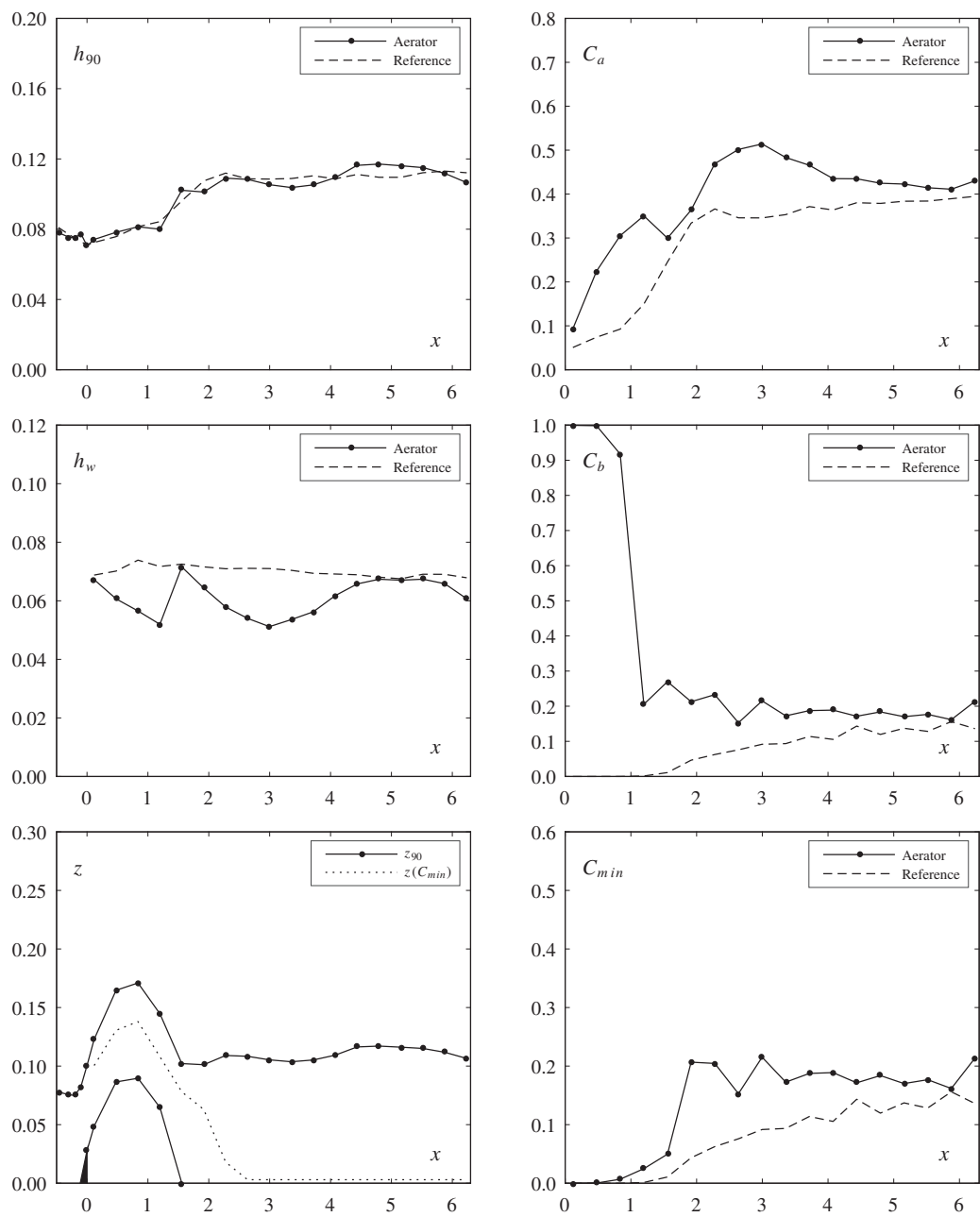
	Aerator	Reference	
Test	48	38	
Parameters			
φ	30	30	[°]
s	0.060	0.060	[m]
F_o	5.50	5.53	[-]
h_o	0.075	0.075	[m]
α	14.04	-	[°]
t	0.015	-	[m]
Flow			
q	0.354	0.356	[m ² /s]
h_c	0.234	0.235	[m]
h_c/s	3.89	3.91	[-]
u_o	4.72	4.74	[m/s]
Pressure			
$p/(\rho g)$	0.123	0.119	[m]
$p'/(\rho g)$	0.0032	0.0033	[m]
Dimensionless numbers			
R	353788	355693	[-]
W_o	152	153	[-]
F_k	13.5	13.6	[-]
F_s	10.9	10.9	[-]
Inception point			
x_i	-	1.52	[m]
h_i	-	0.095	[m]
h_{wi}	-	0.072	[m]
Air entrainment			
β	0.127	-	[-]
q_A	0.045	-	[m ² /s]
$u_{A,max}$	1.52	-	[m/s]
u_A	1.24	-	[m/s]
Jet			
L	1.23	-	[m]
L/h_o	16.4	-	[-]
L_{obs}	0.77	-	[m]
$\Delta p/h$	0.01	-	[-]
h_t	0.071	-	[m]
α_{tu}	10.39	-	[°]
α_{tl}	9.47	-	[°]
γ	8.69	-	[°]
Observation			
-			



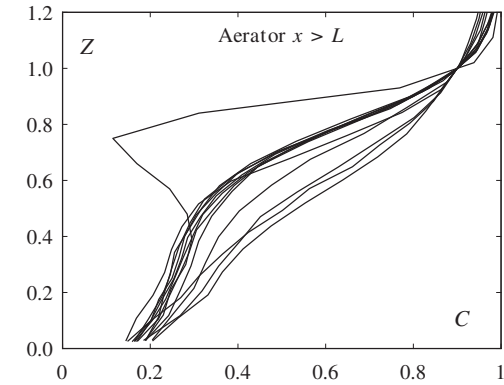
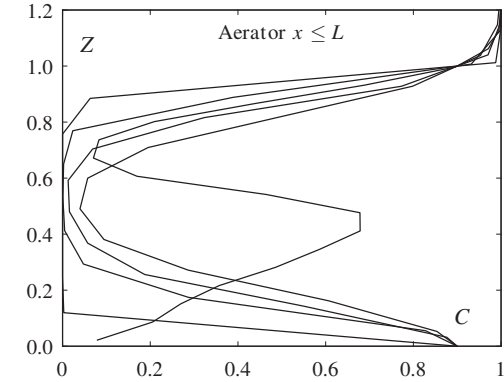
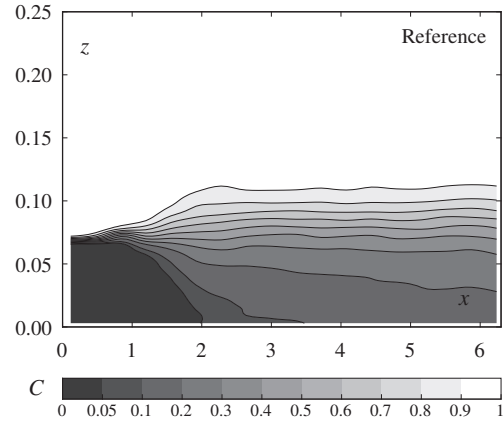
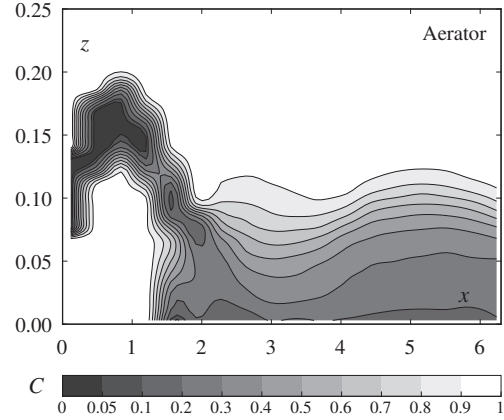


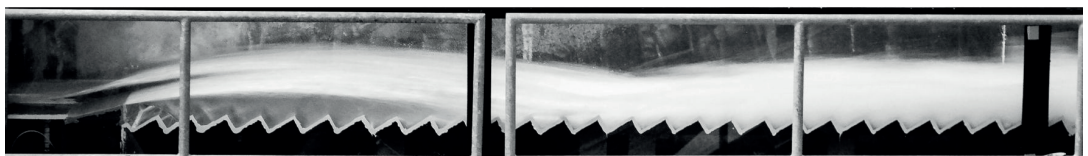
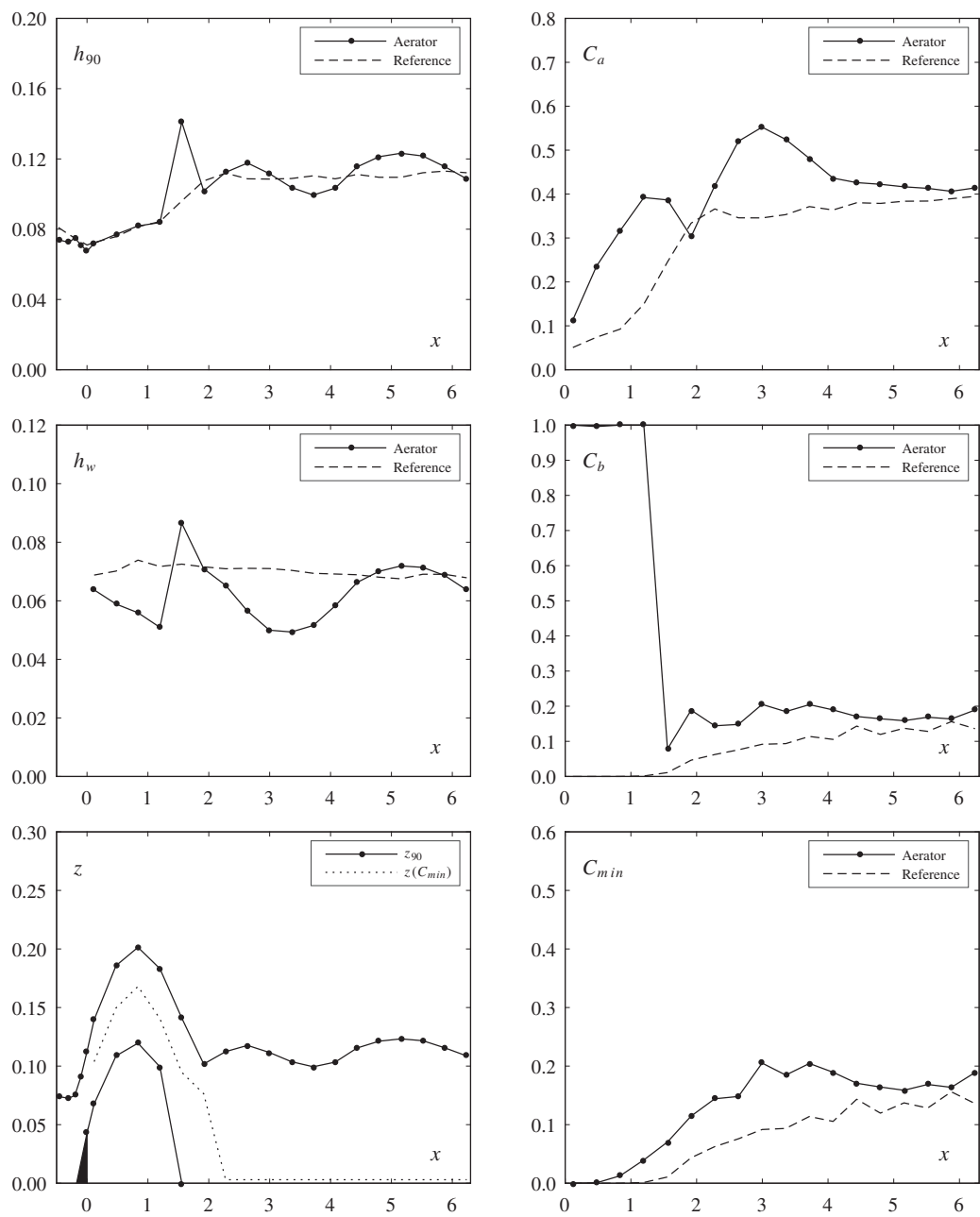
	Aerator	Reference	
Test	49	38	
Parameters			
φ	30	30	[°]
s	0.060	0.060	[m]
F_o	5.55	5.53	[-]
h_o	0.075	0.075	[m]
α	14.04	-	[°]
t	0.030	-	[m]
Flow			
q	0.357	0.356	[m ² /s]
h_c	0.235	0.235	[m]
h_c/s	3.92	3.91	[-]
u_o	4.76	4.74	[m/s]
Pressure			
$p/(\rho g)$	0.138	0.119	[m]
$p'/(\rho g)$	0.0031	0.0033	[m]
Dimensionless numbers			
R	357297	355693	[-]
W_o	154	153	[-]
F_k	13.6	13.6	[-]
F_s	11.0	10.9	[-]
Inception point			
x_i	-	1.52	[m]
h_i	-	0.095	[m]
h_{wi}	-	0.072	[m]
Air entrainment			
β	0.160	-	[-]
q_A	0.057	-	[m ² /s]
$u_{A,max}$	1.92	-	[m/s]
u_A	1.58	-	[m/s]
Jet			
L	1.63	-	[m]
L/h_o	21.8	-	[-]
L_{obs}	1.20	-	[m]
$\Delta p/h$	0.01	-	[-]
h_t	0.070	-	[m]
α_{tu}	12.62	-	[°]
α_{tl}	11.75	-	[°]
γ	10.59	-	[°]
Observation			
-			



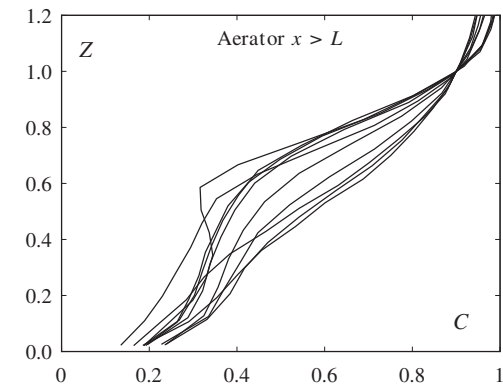
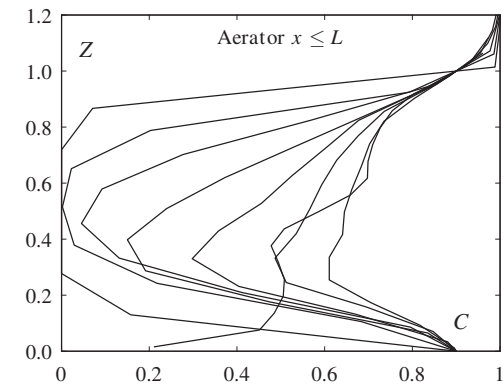
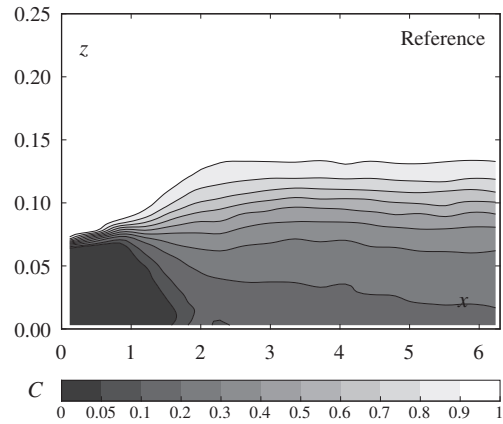
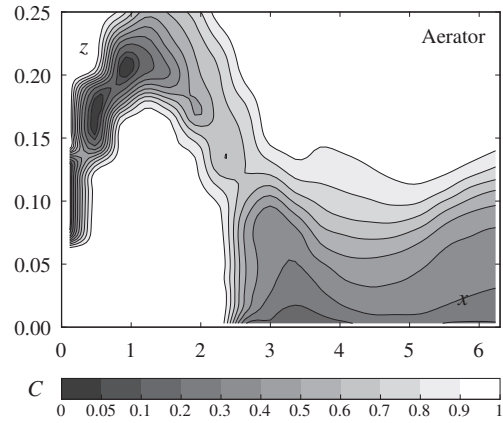


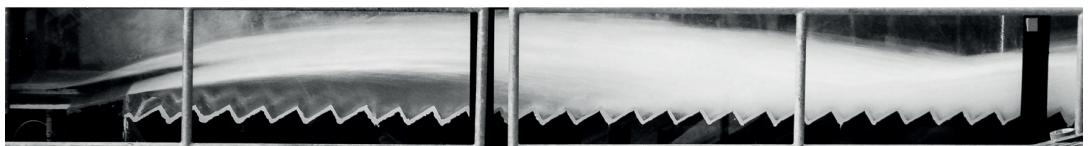
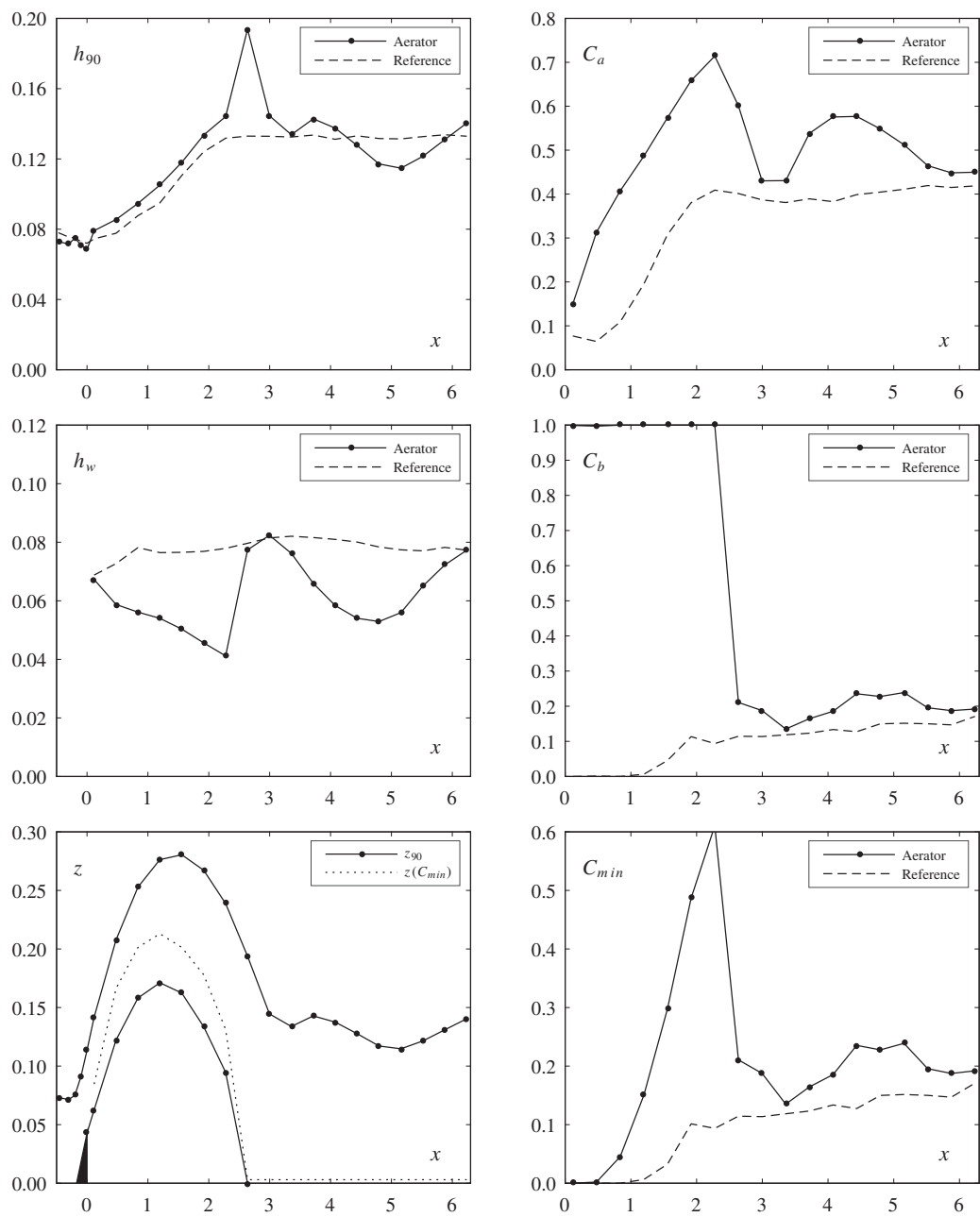
	Aerator	Reference	
Test	50	38	
Parameters			
φ	30	30	[°]
s	0.060	0.060	[m]
F_o	5.53	5.53	[-]
h_o	0.075	0.075	[m]
α	14.04	-	[°]
t	0.045	-	[m]
Flow			
q	0.356	0.356	[m ² /s]
h_c	0.235	0.235	[m]
h_c/s	3.91	3.91	[-]
u_o	4.74	4.74	[m/s]
Pressure			
$p/(\rho g)$	0.183	0.119	[m]
$p'/(\rho g)$	0.0031	0.0033	[m]
Dimensionless numbers			
R	355865	355693	[-]
W_o	153	153	[-]
F_k	13.6	13.6	[-]
F_s	10.9	10.9	[-]
Inception point			
x_i	-	1.52	[m]
h_i	-	0.095	[m]
h_{wi}	-	0.072	[m]
Air entrainment			
β	0.193	-	[-]
q_A	0.069	-	[m ² /s]
$u_{A,max}$	2.30	-	[m/s]
u_A	1.89	-	[m/s]
Jet			
L	1.85	-	[m]
L/h_o	24.6	-	[-]
L_{obs}	1.38	-	[m]
$\Delta p/h$	0.03	-	[-]
h_t	0.068	-	[m]
α_{tu}	13.12	-	[°]
α_{tl}	12.18	-	[°]
γ	11.79	-	[°]
Observation			
-			



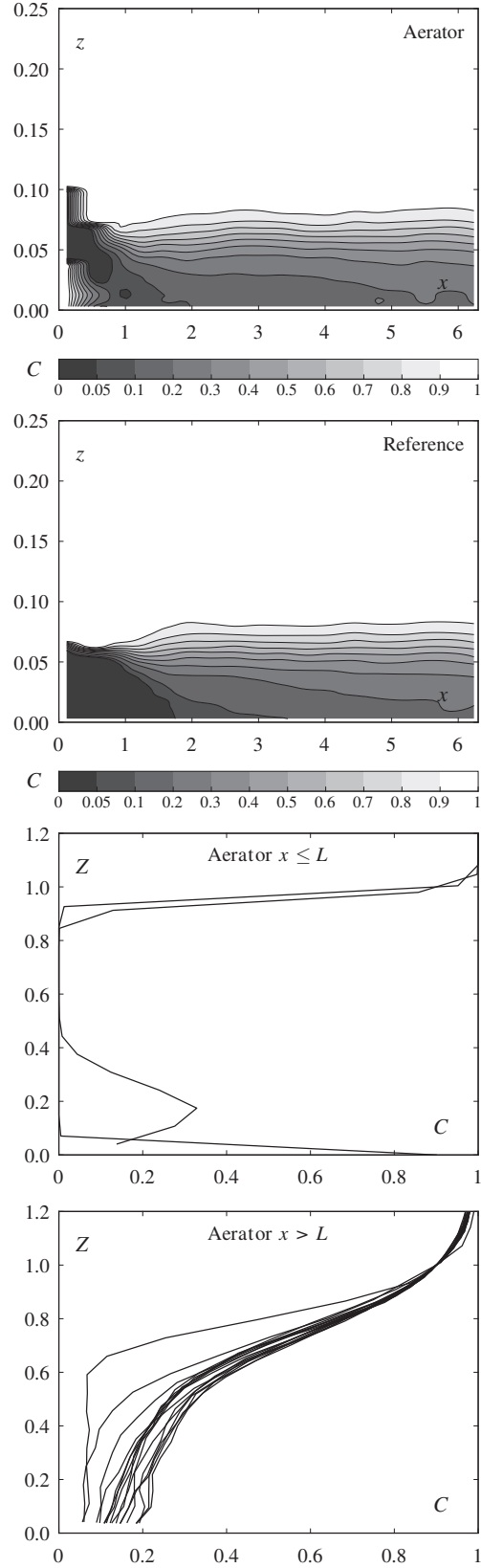


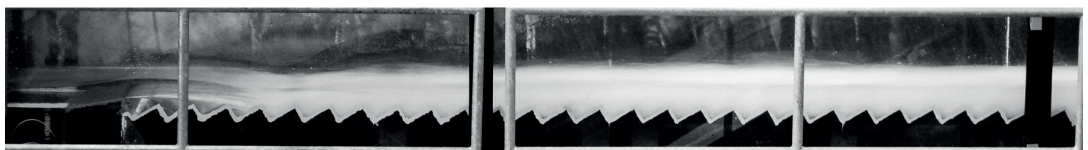
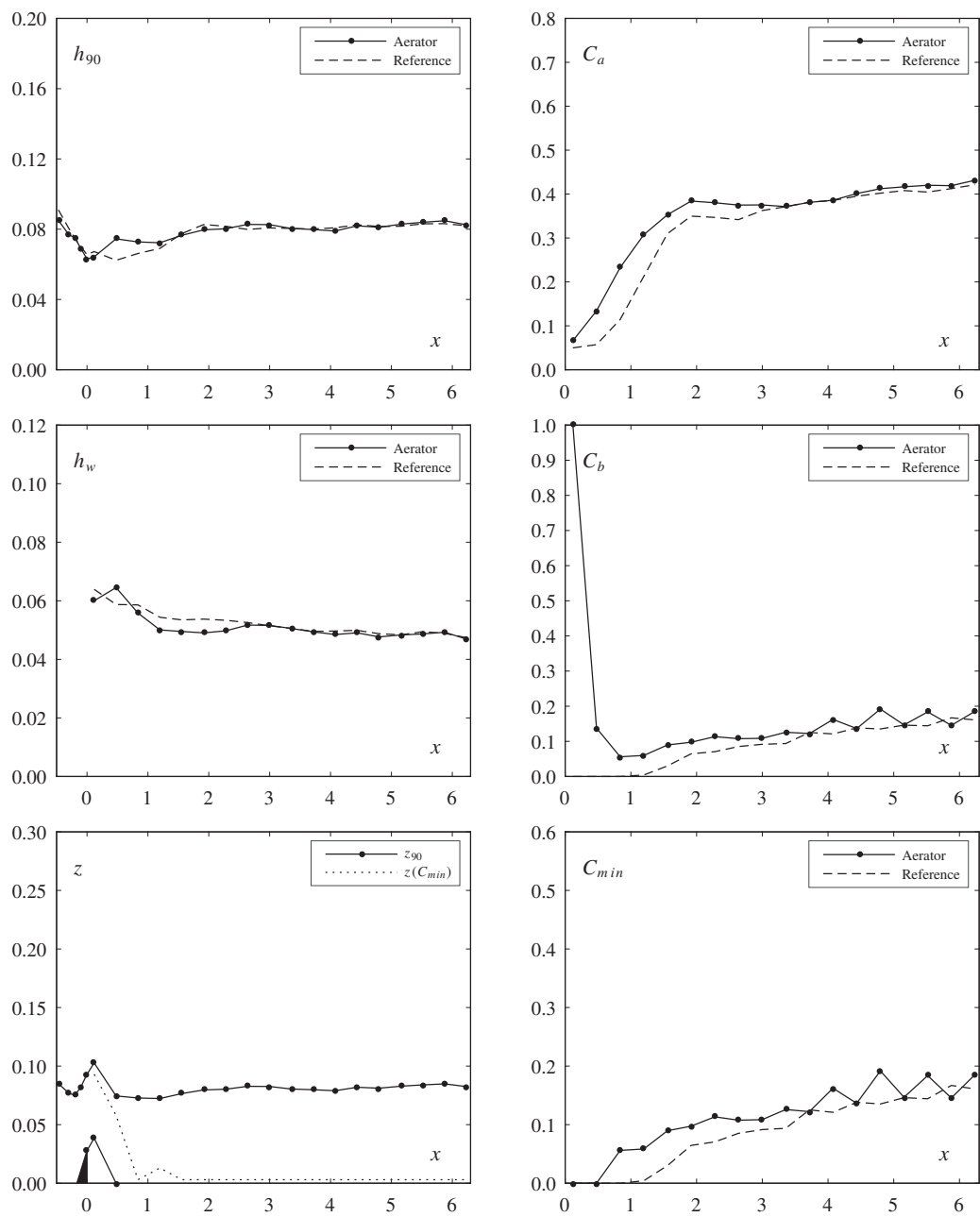
	Aerator	Reference	
Test	51	42	
Parameters			
φ	30	30	[°]
s	0.060	0.060	[m]
F_o	7.46	7.48	[-]
h_o	0.075	0.075	[m]
α	14.04	-	[°]
t	0.045	-	[m]
Flow			
q	0.480	0.481	[m ² /s]
h_c	0.286	0.287	[m]
h_c/s	4.77	4.78	[-]
u_o	6.40	6.41	[m/s]
Pressure			
$p/(\rho g)$	0.283	0.168	[m]
$p'/(\rho g)$	0.0052	0.0054	[m]
Dimensionless numbers			
R	479661	481006	[-]
W_o	206	207	[-]
F_k	18.3	18.3	[-]
F_s	14.7	14.8	[-]
Inception point			
x_i	-	1.23	[m]
h_i	-	0.096	[m]
h_{wi}	-	0.076	[m]
Air entrainment			
β	0.250	-	[-]
q_A	0.120	-	[m ² /s]
$u_{A,max}$	3.97	-	[m/s]
u_A	3.31	-	[m/s]
Jet			
L	2.83	-	[m]
L/h_o	37.8	-	[-]
L_{obs}	1.86	-	[m]
$\Delta p/h$	0.11	-	[-]
h_t	0.069	-	[m]
α_{tu}	13.51	-	[°]
α_{tl}	11.50	-	[°]
γ	11.25	-	[°]
Observation			
-			



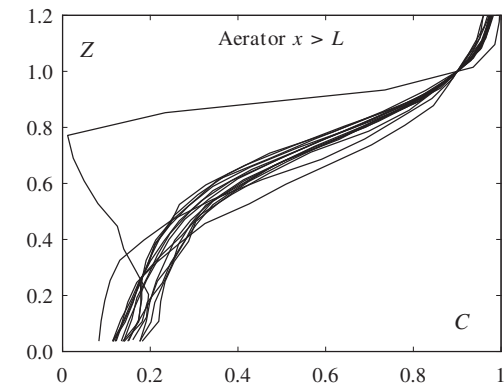
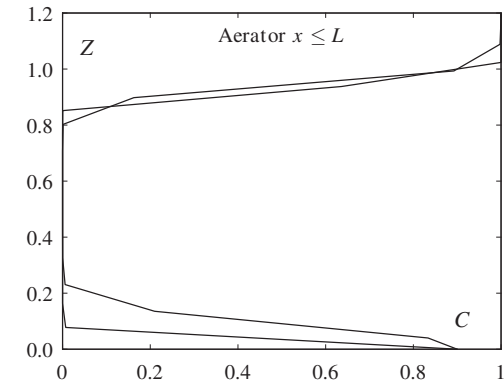
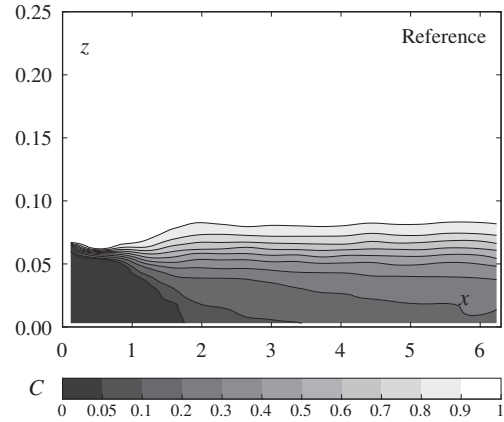
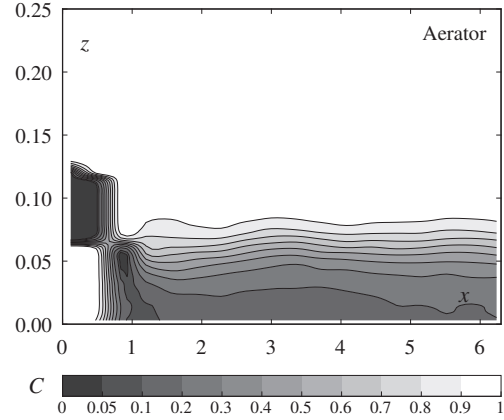


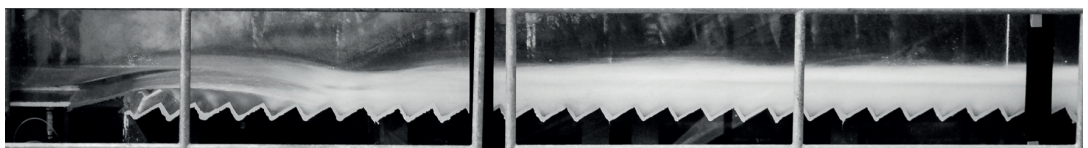
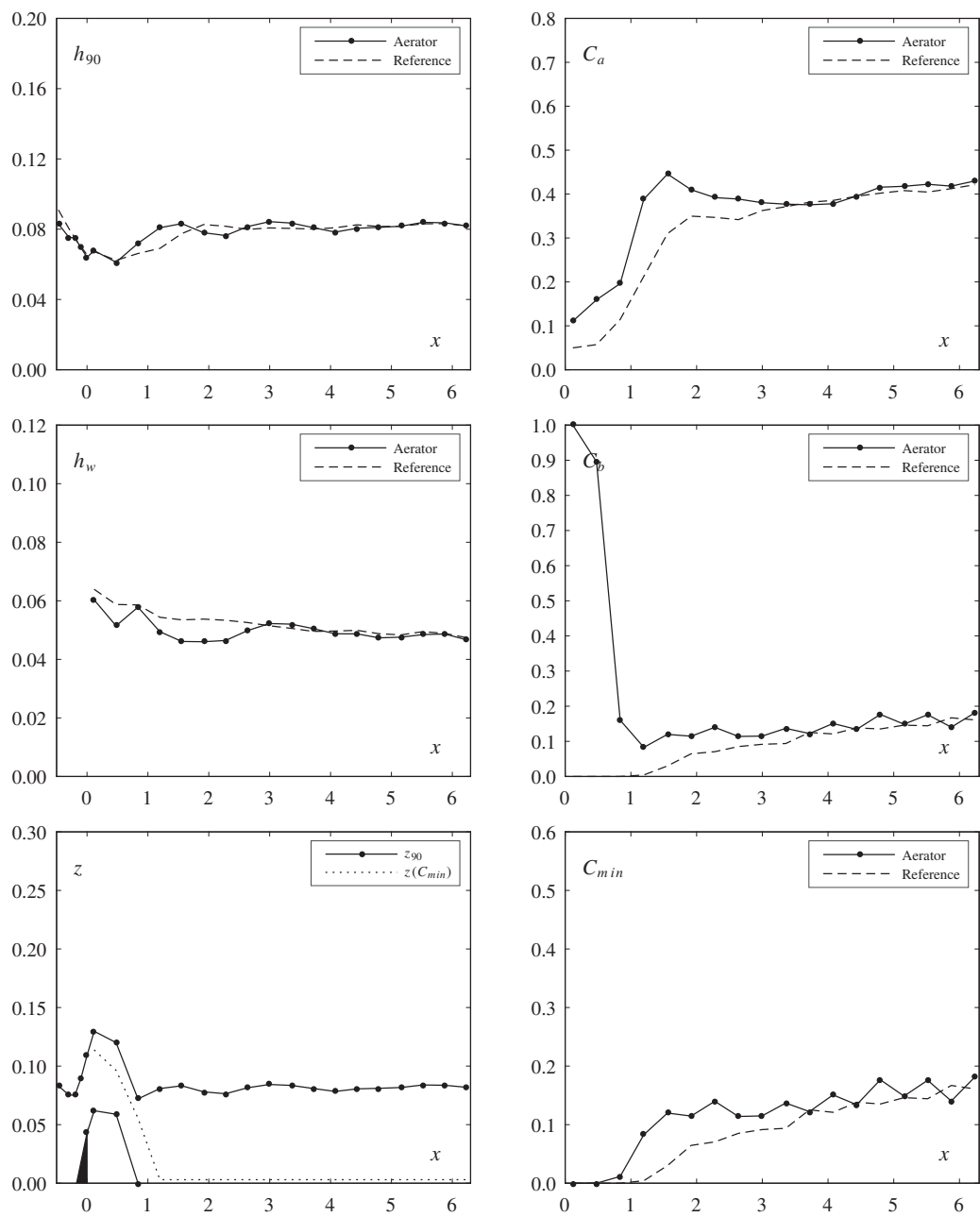
	Aerator	Reference	
Test	52	41	
Parameters			
φ	30	30	[°]
s	0.060	0.060	[m]
F_o	3.22	3.23	[-]
h_o	0.075	0.075	[m]
α	9.46	-	[°]
t	0.030	-	[m]
Flow			
q	0.207	0.208	[m ² /s]
h_c	0.163	0.164	[m]
h_c/s	2.72	2.73	[-]
u_o	2.76	2.77	[m/s]
Pressure			
$p/(\rho g)$	0.097	0.086	[m]
$p'/(\rho g)$	0.0015	0.0016	[m]
Dimensionless numbers			
R	207065	207930	[-]
W_o	89	89	[-]
F_k	7.9	7.9	[-]
F_s	6.4	6.4	[-]
Inception point			
x_i	-	1.28	[m]
h_i	-	0.071	[m]
h_{wi}	-	0.054	[m]
Air entrainment			
β	0.037	-	[-]
q_A	0.008	-	[m ² /s]
$u_{A,max}$	0.59	-	[m/s]
u_A	0.46	-	[m/s]
Jet			
L	0.55	-	[m]
L/h_o	7.4	-	[-]
L_{obs}	0.36	-	[m]
$\Delta p/h$	-0.03	-	[-]
h_t	0.063	-	[m]
α_{tu}	7.56	-	[°]
α_{tl}	-	-	[°]
γ	11.53	-	[°]
Observation			
-			



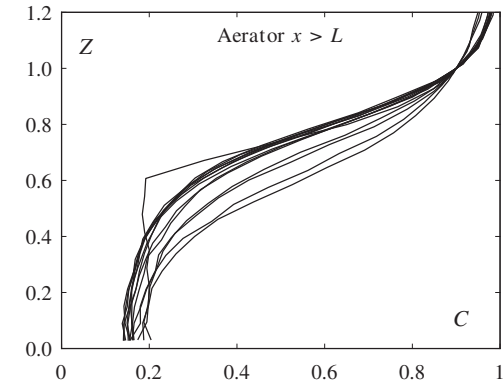
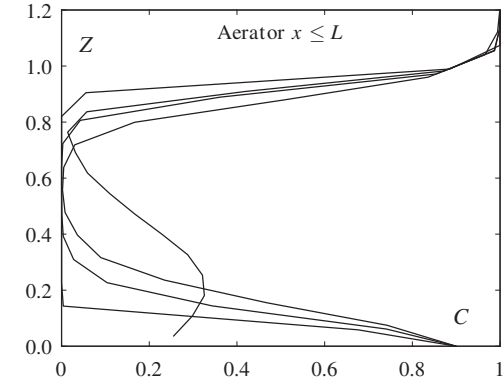
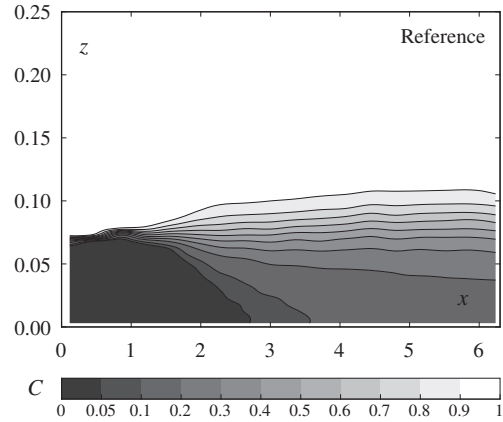
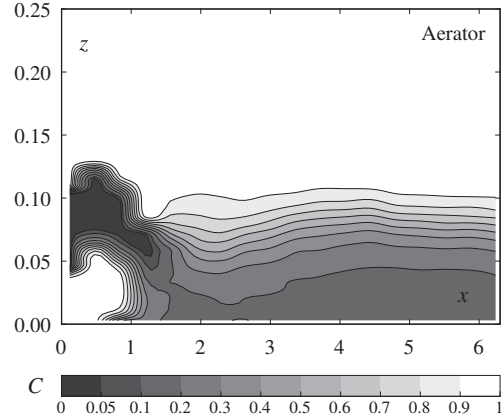


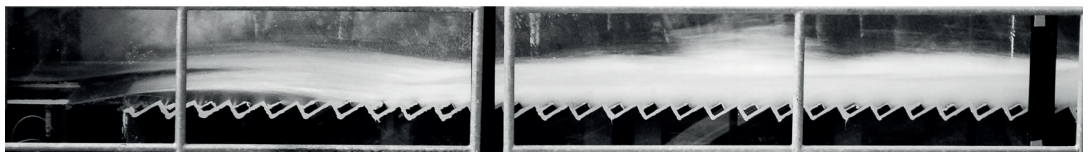
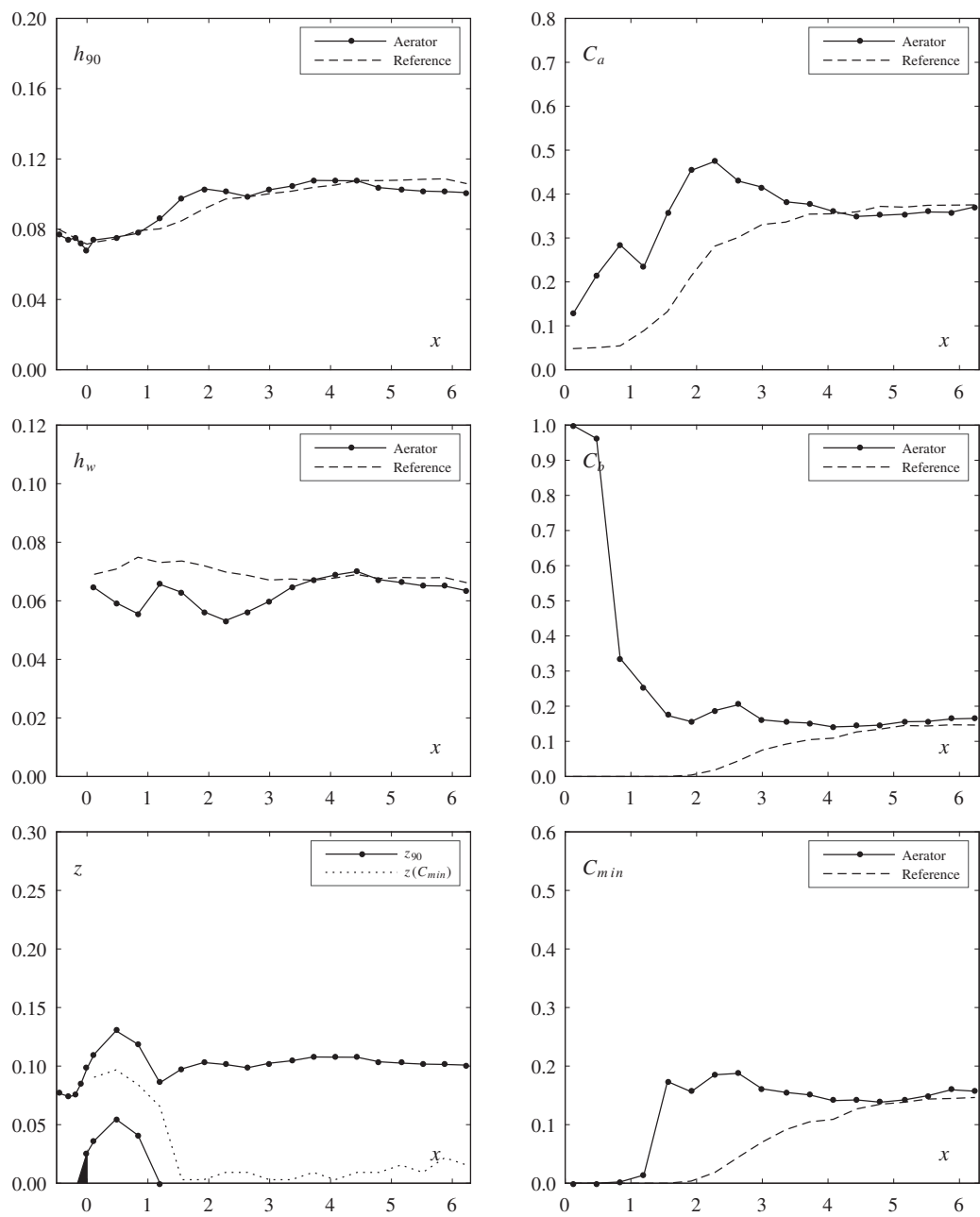
	Aerator	Reference	
Test	53	41	
Parameters			
φ	30	30	[°]
s	0.060	0.060	[m]
F_o	3.21	3.23	[-]
h_o	0.075	0.075	[m]
α	14.04	-	[°]
t	0.045	-	[m]
Flow			
q	0.206	0.208	[m ² /s]
h_c	0.163	0.164	[m]
h_c/s	2.72	2.73	[-]
u_o	2.75	2.77	[m/s]
Pressure			
$p/(\rho g)$	0.105	0.086	[m]
$p'/(\rho g)$	0.0016	0.0016	[m]
Dimensionless numbers			
R	206457	207930	[-]
W_o	89	89	[-]
F_k	7.9	7.9	[-]
F_s	6.3	6.4	[-]
Inception point			
x_i	-	1.28	[m]
h_i	-	0.071	[m]
h_{wi}	-	0.054	[m]
Air entrainment			
β	0.062	-	[-]
q_A	0.013	-	[m ² /s]
$u_{A,max}$	0.97	-	[m/s]
u_A	0.77	-	[m/s]
Jet			
L	0.79	-	[m]
L/h_o	10.5	-	[-]
L_{obs}	0.66	-	[m]
$\Delta p/h$	-0.02	-	[-]
h_t	0.064	-	[m]
α_{tu}	11.69	-	[°]
α_{tl}	11.91	-	[°]
γ	14.44	-	[°]
Observation			
-			



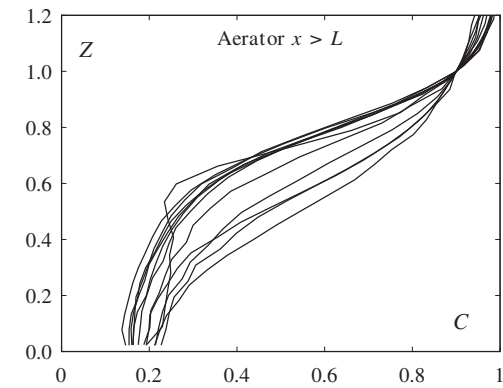
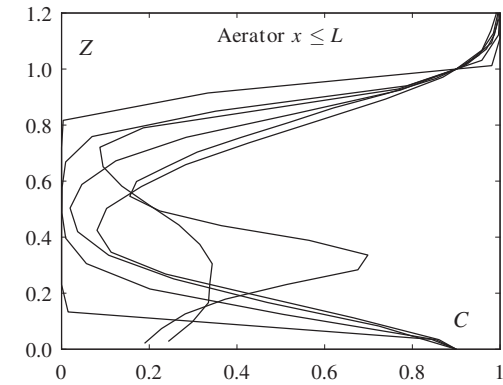
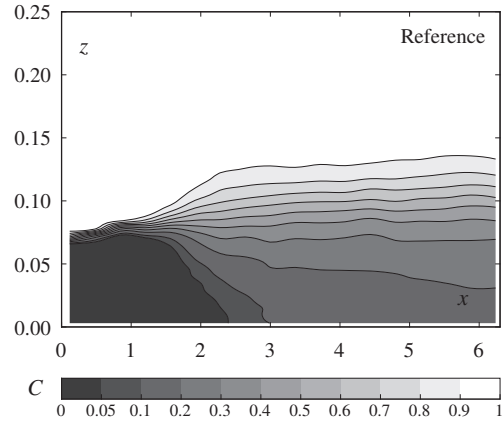
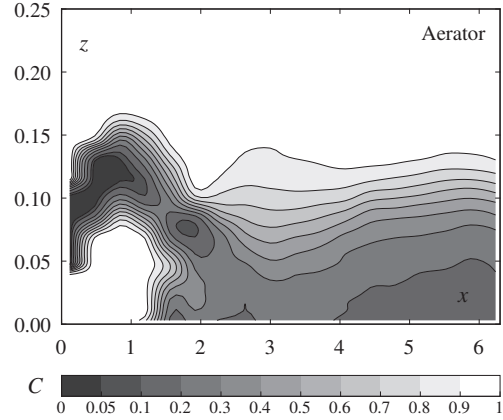


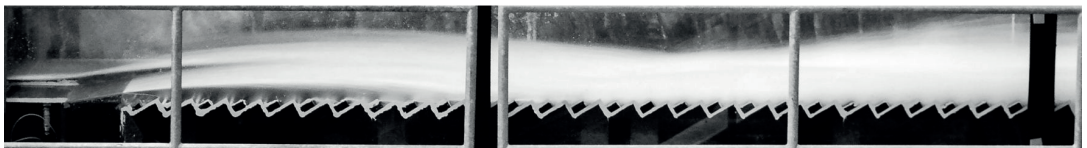
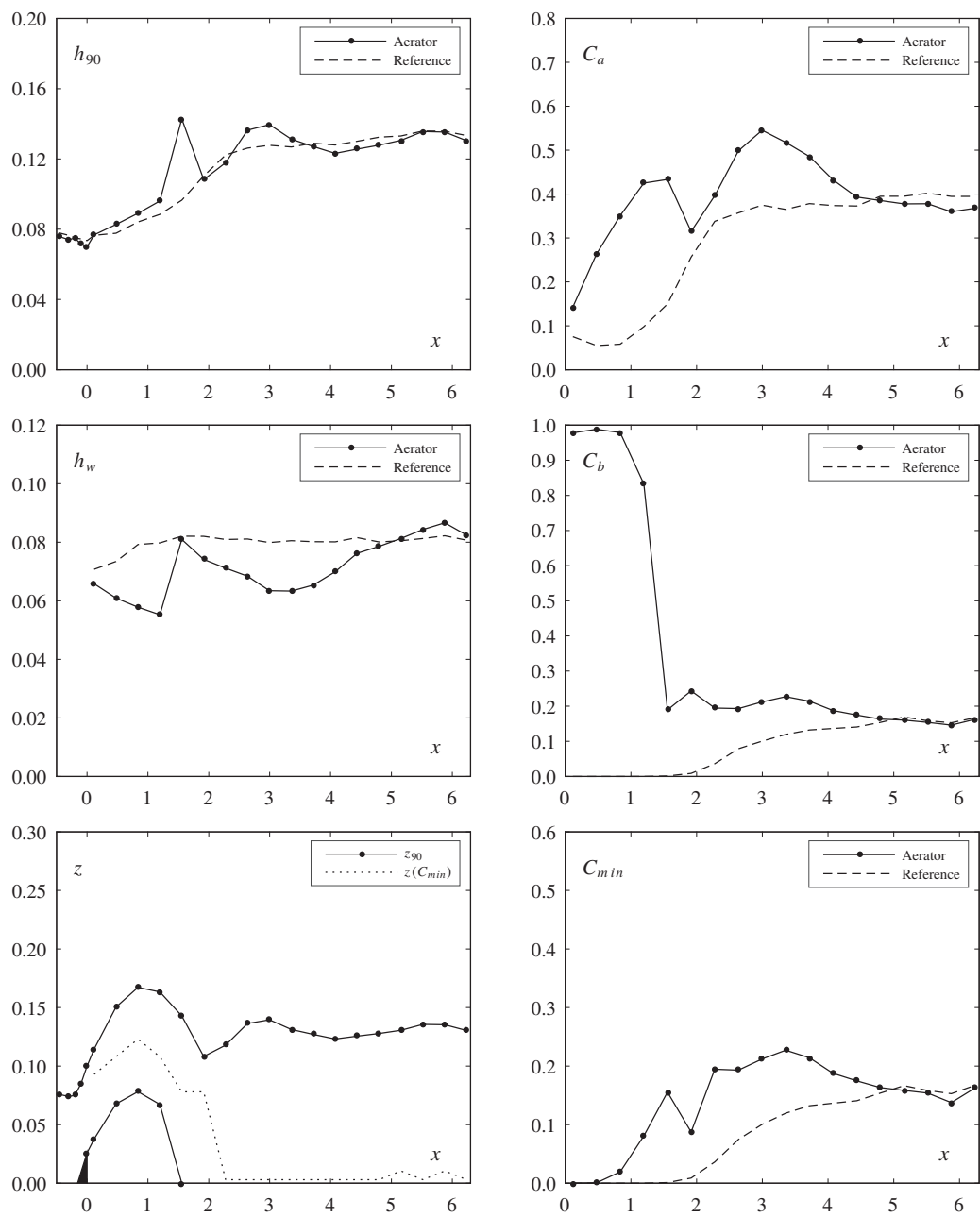
	Aerator	Reference	
Test	57	54	
Parameters			
φ	30	30	[°]
s	0.030	0.030	[m]
F_o	5.49	5.52	[-]
h_o	0.075	0.075	[m]
α	9.46	-	[°]
t	0.030	-	[m]
Flow			
q	0.353	0.355	[m ² /s]
h_c	0.233	0.234	[m]
h_c/s	7.78	7.81	[-]
u_o	4.71	4.74	[m/s]
Pressure			
$p/(\rho g)$	0.159	0.121	[m]
$p'/(\rho g)$	0.0030	0.0033	[m]
Dimensionless numbers			
R	353186	355233	[-]
W_o	152	153	[-]
F_k	38.1	38.3	[-]
F_s	30.7	30.9	[-]
Inception point			
x_i	-	2.07	[m]
h_i	-	0.094	[m]
h_{wi}	-	0.071	[m]
Air entrainment			
β	0.112	-	[-]
q_A	0.040	-	[m ² /s]
$u_{A,max}$	1.34	-	[m/s]
u_A	1.09	-	[m/s]
Jet			
L	1.22	-	[m]
L/h_o	16.3	-	[-]
L_{obs}	0.78	-	[m]
$\Delta p/h$	0.00	-	[-]
h_t	0.068	-	[m]
α_{tu}	9.06	-	[°]
α_{tl}	7.91	-	[°]
γ	7.99	-	[°]
Observation			
-			



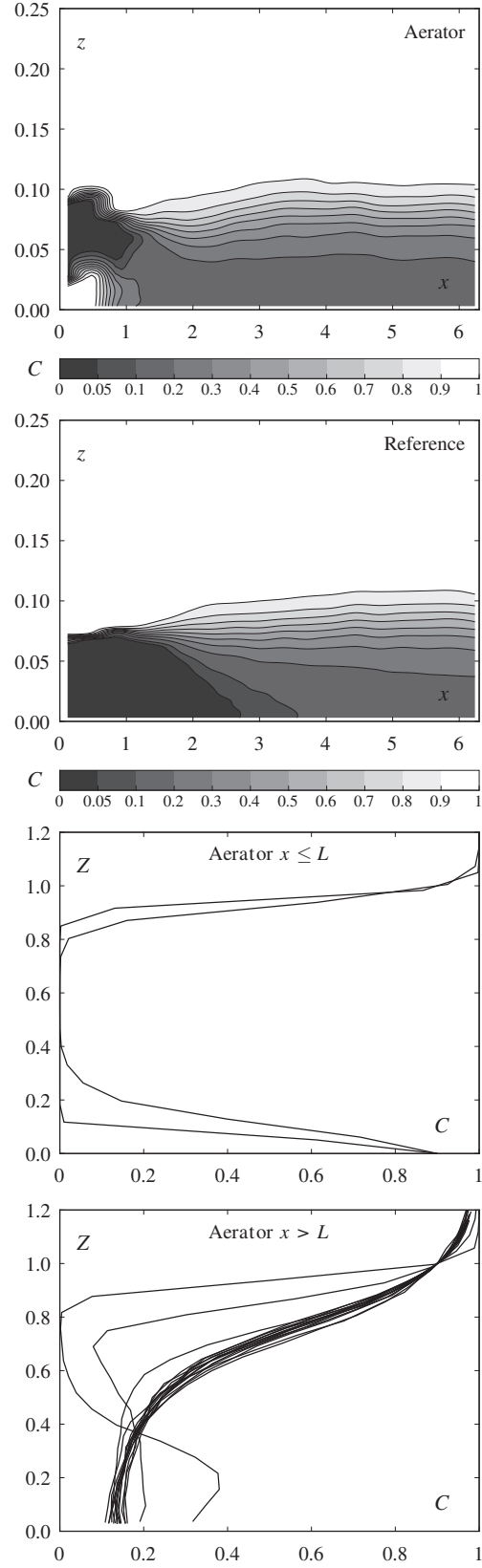


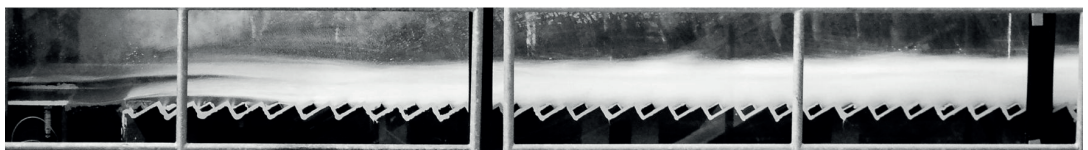
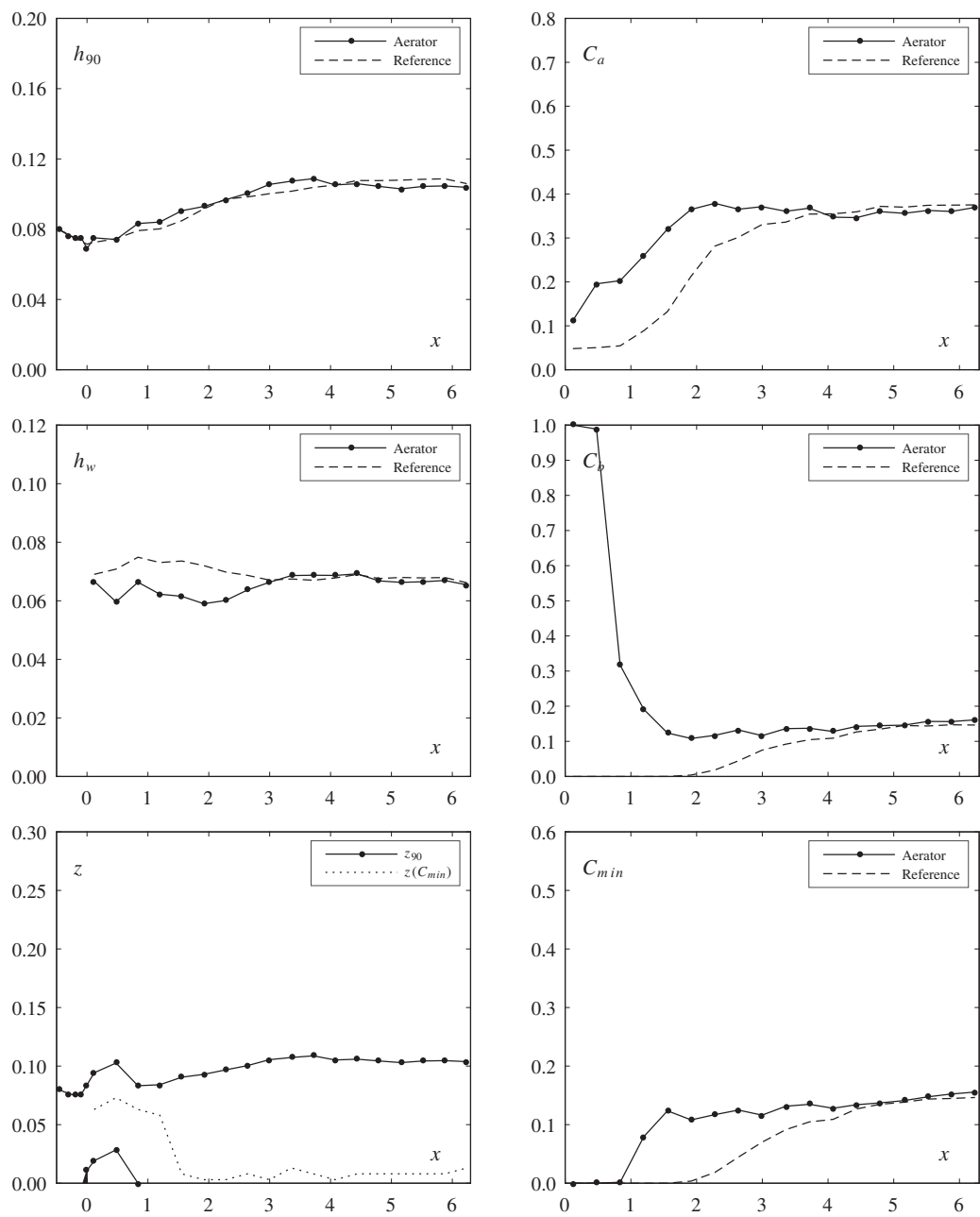
	Aerator	Reference	
Test	58	55	
Parameters			
φ	30	30	[°]
s	0.030	0.030	[m]
F_o	7.51	7.49	[-]
h_o	0.075	0.075	[m]
α	9.46	-	[°]
t	0.030	-	[m]
Flow			
q	0.483	0.482	[m ² /s]
h_c	0.288	0.287	[m]
h_c/s	9.58	9.57	[-]
u_o	6.44	6.42	[m/s]
Pressure			
$p/(\rho g)$	0.239	0.167	[m]
$p'/(\rho g)$	0.0051	0.0053	[m]
Dimensionless numbers			
R	482904	481839	[-]
W_o	208	207	[-]
F_k	52.1	52.0	[-]
F_s	42.0	41.9	[-]
Inception point			
x_i	-	1.93	[m]
h_i	-	0.111	[m]
h_{wi}	-	0.082	[m]
Air entrainment			
β	0.207	-	[-]
q_A	0.100	-	[m ² /s]
$u_{A,max}$	3.31	-	[m/s]
u_A	2.75	-	[m/s]
Jet			
L	1.93	-	[m]
L/h_o	25.7	-	[-]
L_{obs}	1.26	-	[m]
$\Delta p/h$	0.07	-	[-]
h_t	0.070	-	[m]
α_{tu}	9.20	-	[°]
α_{tl}	7.73	-	[°]
γ	7.66	-	[°]
Observation			
-			



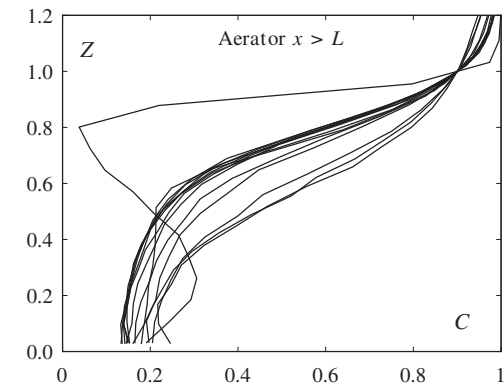
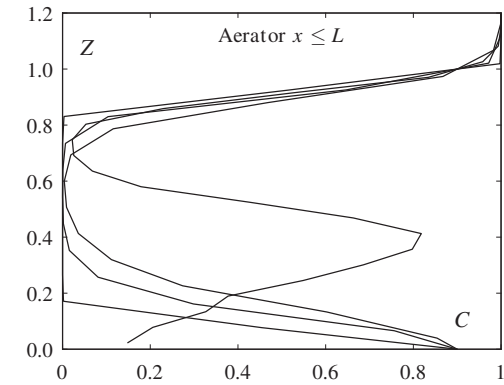
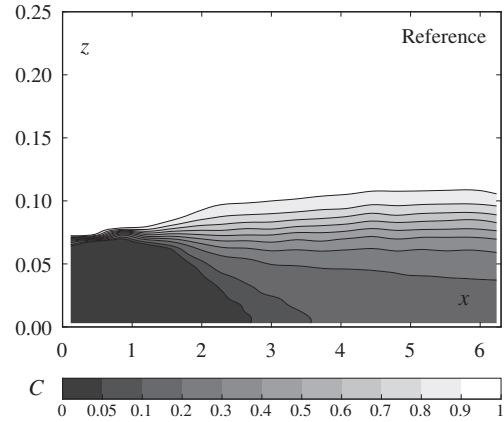
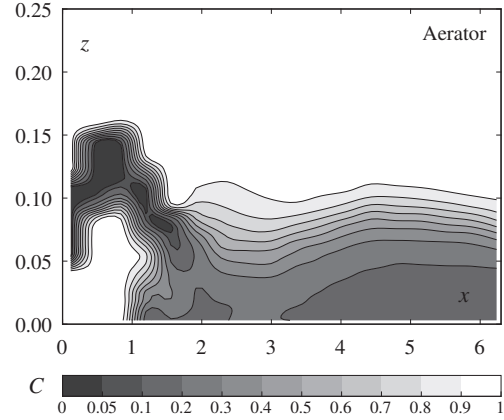


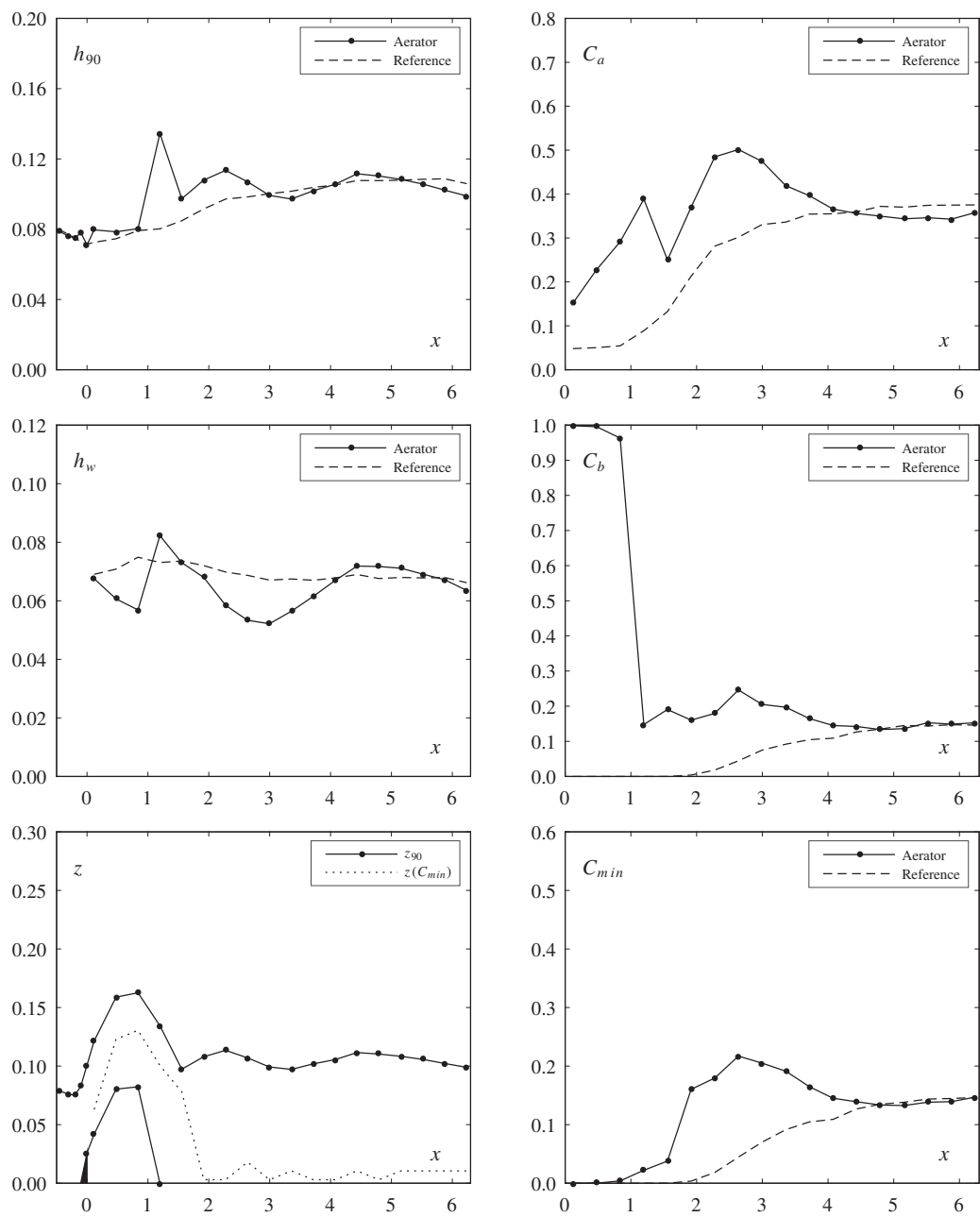
	Aerator	Reference	
Test	59	54	
Parameters			
φ	30	30	[°]
s	0.030	0.030	[m]
F_o	5.52	5.52	[-]
h_o	0.075	0.075	[m]
α	9.46	-	[°]
t	0.015	-	[m]
Flow			
q	0.355	0.355	[m ² /s]
h_c	0.234	0.234	[m]
h_c/s	7.81	7.81	[-]
u_o	4.73	4.74	[m/s]
Pressure			
$p/(\rho g)$	0.126	0.121	[m]
$p'/(\rho g)$	0.0032	0.0033	[m]
Dimensionless numbers			
R	355000	355233	[-]
W_o	153	153	[-]
F_k	38.3	38.3	[-]
F_s	30.8	30.9	[-]
Inception point			
x_i	-	2.07	[m]
h_i	-	0.094	[m]
h_{wi}	-	0.071	[m]
Air entrainment			
β	0.076	-	[-]
q_A	0.027	-	[m ² /s]
$u_{A,max}$	0.93	-	[m/s]
u_A	0.75	-	[m/s]
Jet			
L	0.84	-	[m]
L/h_o	11.2	-	[-]
L_{obs}	0.60	-	[m]
$\Delta p/h$	-0.01	-	[-]
h_t	0.069	-	[m]
α_{tu}	7.23	-	[°]
α_{tl}	-	-	[°]
γ	6.85	-	[°]
Observation			
-			



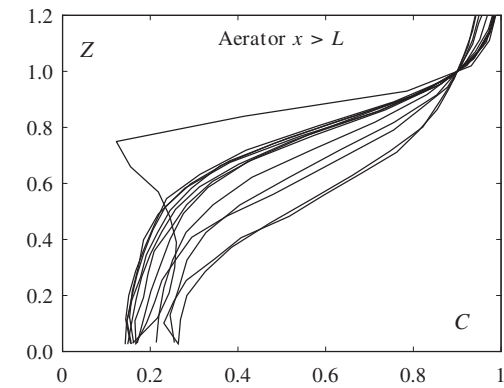
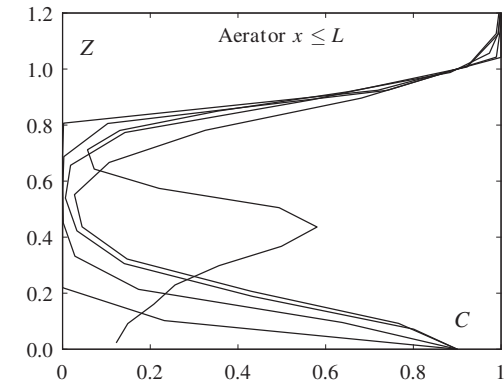
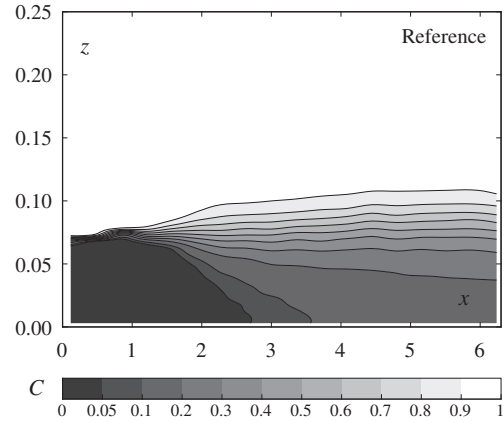
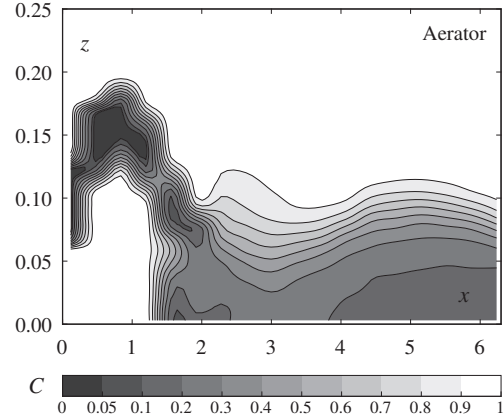


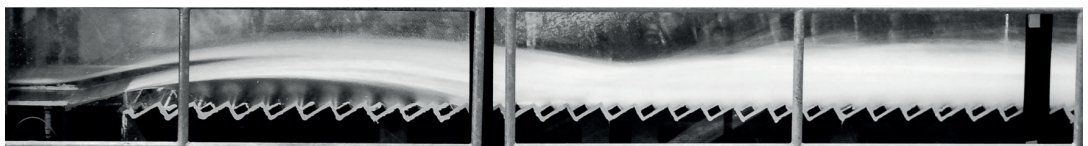
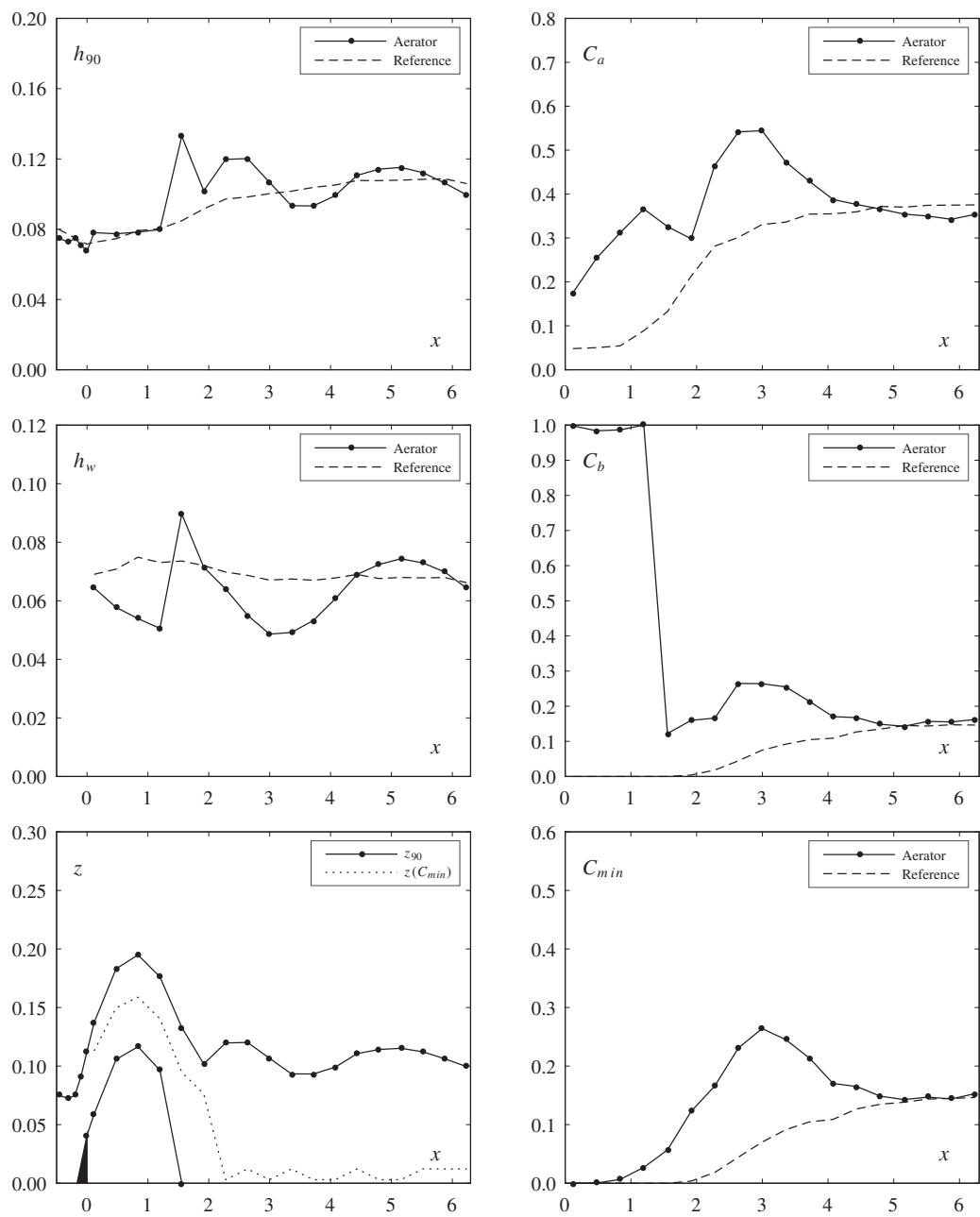
	Aerator	Reference	
Test	60	54	
Parameters			
φ	30	30	[°]
s	0.030	0.030	[m]
F_o	5.51	5.52	[-]
h_o	0.075	0.075	[m]
α	14.04	-	[°]
t	0.030	-	[m]
Flow			
q	0.355	0.355	[m ² /s]
h_c	0.234	0.234	[m]
h_c/s	7.80	7.81	[-]
u_o	4.73	4.74	[m/s]
Pressure			
$p/(\rho g)$	0.138	0.121	[m]
$p'/(\rho g)$	0.0032	0.0033	[m]
Dimensionless numbers			
R	354619	355233	[-]
W_o	153	153	[-]
F_k	38.2	38.3	[-]
F_s	30.8	30.9	[-]
Inception point			
x_i	-	2.07	[m]
h_i	-	0.094	[m]
h_{wi}	-	0.071	[m]
Air entrainment			
β	0.143	-	[-]
q_A	0.051	-	[m ² /s]
$u_{A,max}$	1.70	-	[m/s]
u_A	1.39	-	[m/s]
Jet			
L	1.48	-	[m]
L/h_o	19.8	-	[-]
L_{obs}	1.08	-	[m]
$\Delta p/h$	0.00	-	[-]
h_t	0.071	-	[m]
α_{tu}	12.17	-	[°]
α_{tl}	11.29	-	[°]
γ	10.80	-	[°]
Observation			
-			



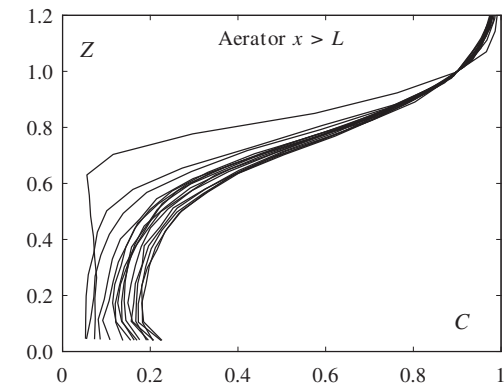
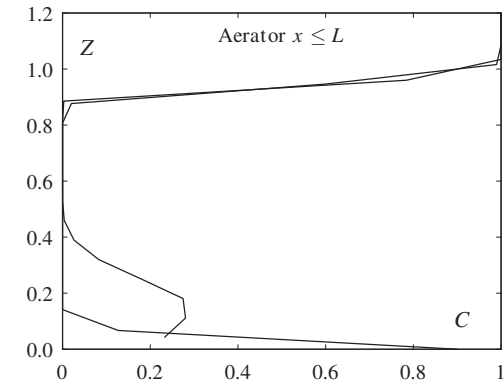
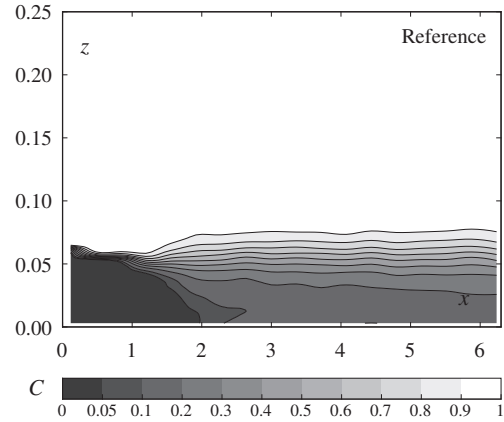
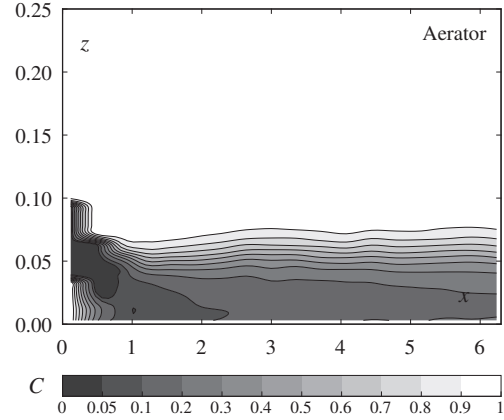


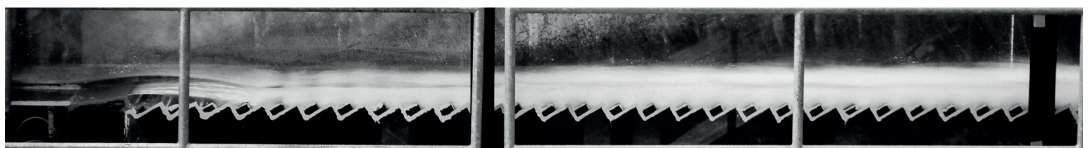
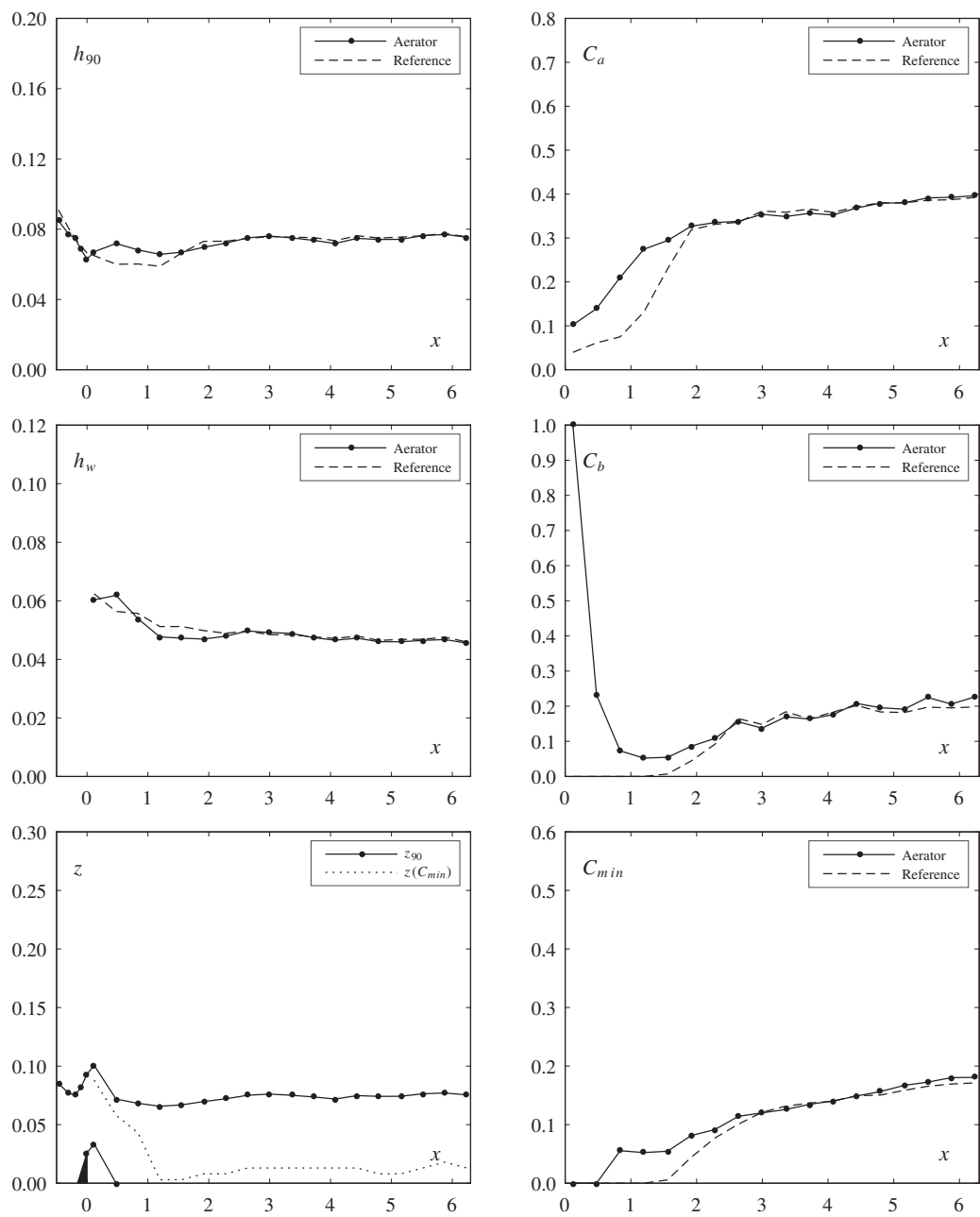
	Aerator	Reference	
Test	61	54	
Parameters			
φ	30	30	[°]
s	0.030	0.030	[m]
F_o	5.47	5.52	[-]
h_o	0.075	0.075	[m]
α	14.04	-	[°]
t	0.045	-	[m]
Flow			
q	0.352	0.355	[m ² /s]
h_c	0.233	0.234	[m]
h_c/s	7.76	7.81	[-]
u_o	4.69	4.74	[m/s]
Pressure			
$p/(\rho g)$	0.182	0.121	[m]
$p'/(\rho g)$	0.0032	0.0033	[m]
Dimensionless numbers			
R	351894	355233	[-]
W_o	151	153	[-]
F_k	37.9	38.3	[-]
F_s	30.6	30.9	[-]
Inception point			
x_i	-	2.07	[m]
h_i	-	0.094	[m]
h_{wi}	-	0.071	[m]
Air entrainment			
β	0.164	-	[-]
q_A	0.058	-	[m ² /s]
$u_{A,max}$	1.94	-	[m/s]
u_A	1.59	-	[m/s]
Jet			
L	1.87	-	[m]
L/h_o	24.9	-	[-]
L_{obs}	1.32	-	[m]
$\Delta p/h$	0.00	-	[-]
h_t	0.068	-	[m]
α_{tu}	13.07	-	[°]
α_{tl}	12.27	-	[°]
γ	11.33	-	[°]
Observation			
-			



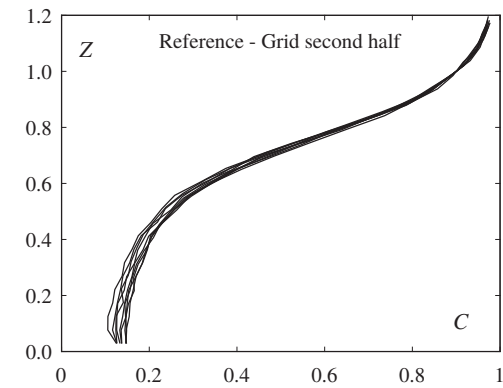
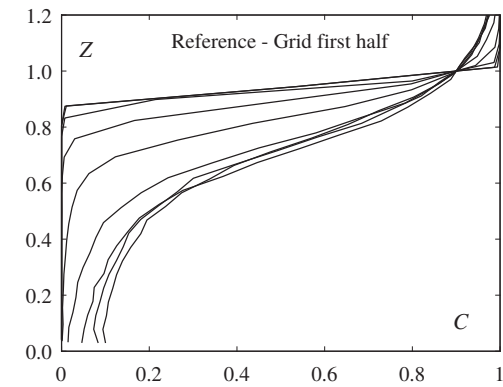
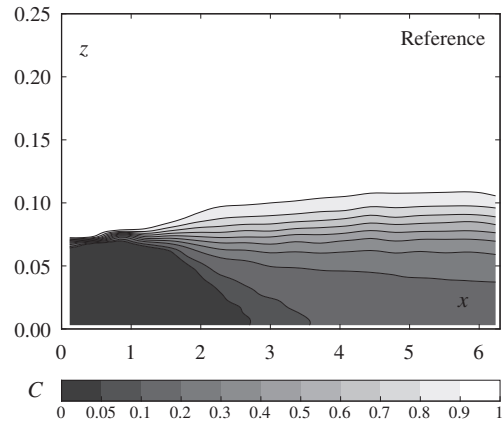
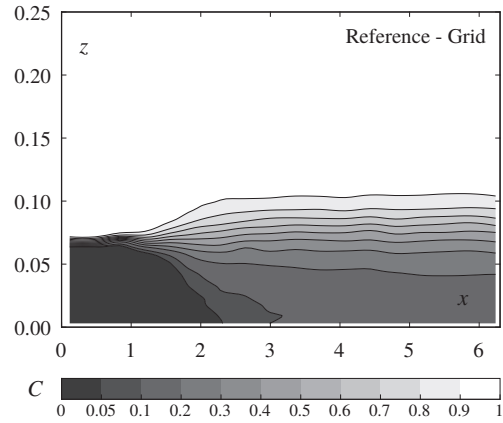


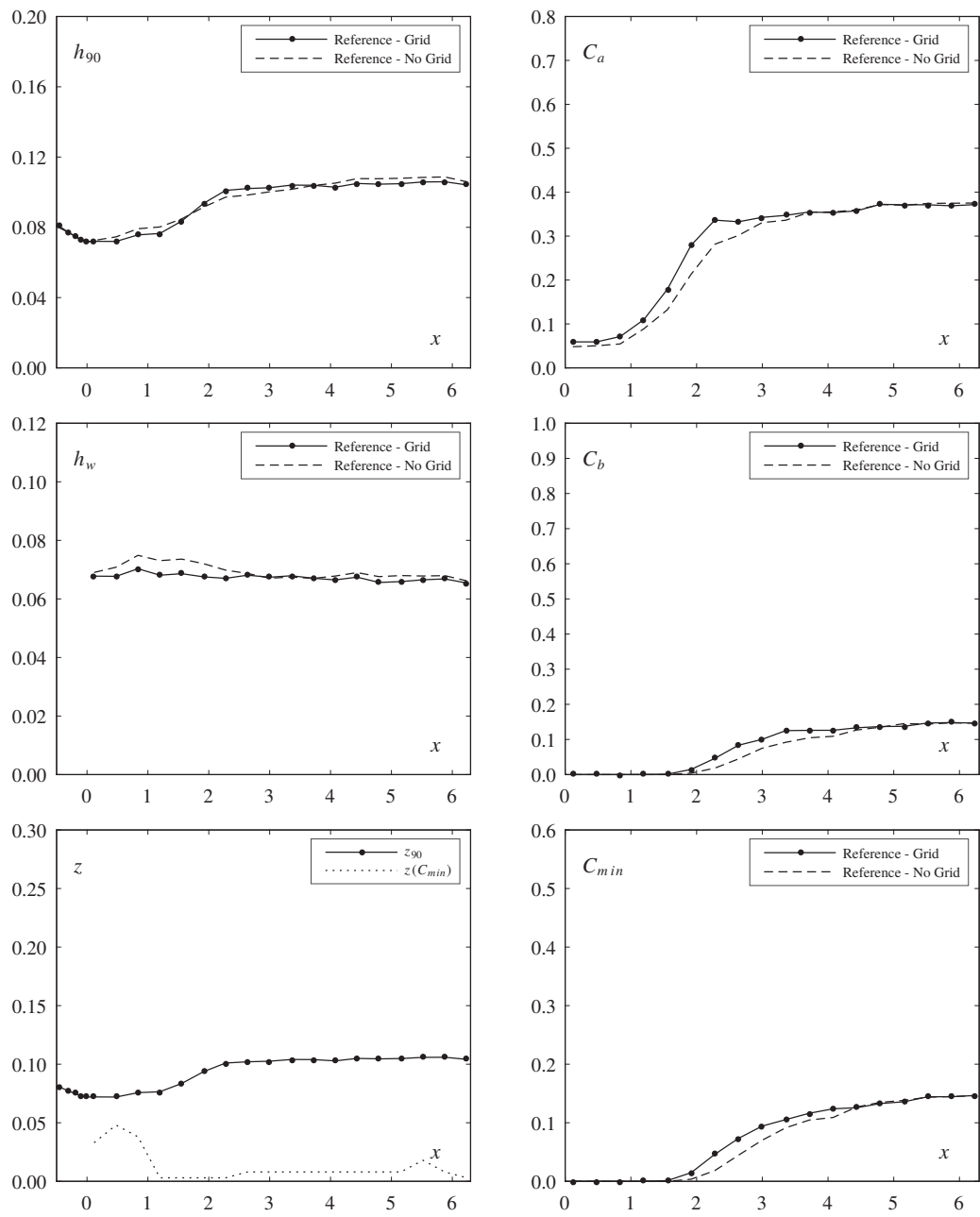
	Aerator	Reference	
Test	62	56	
Parameters			
φ	30	30	[°]
s	0.030	0.030	[m]
F_o	3.22	3.23	[-]
h_o	0.075	0.075	[m]
α	9.46	-	[°]
t	0.030	-	[m]
Flow			
q	0.207	0.208	[m ² /s]
h_c	0.164	0.164	[m]
h_c/s	5.45	5.47	[-]
u_o	2.76	2.77	[m/s]
Pressure			
$p/(\rho g)$	0.099	0.086	[m]
$p'/(\rho g)$	0.0018	0.0016	[m]
Dimensionless numbers			
R	207106	207948	[-]
W_o	89	90	[-]
F_k	22.3	22.4	[-]
F_s	18.0	18.1	[-]
Inception point			
x_i	-	1.58	[m]
h_i	-	0.067	[m]
h_{wi}	-	0.051	[m]
Air entrainment			
β	0.034	-	[-]
q_A	0.007	-	[m ² /s]
$u_{A,max}$	0.55	-	[m/s]
u_A	0.43	-	[m/s]
Jet			
L	0.48	-	[m]
L/h_o	6.4	-	[-]
L_{obs}	0.42	-	[m]
$\Delta p/h$	0.00	-	[-]
h_t	0.063	-	[m]
α_{tu}	7.46	-	[°]
α_{tl}	-	-	[°]
γ	10.83	-	[°]
Observation			
-			



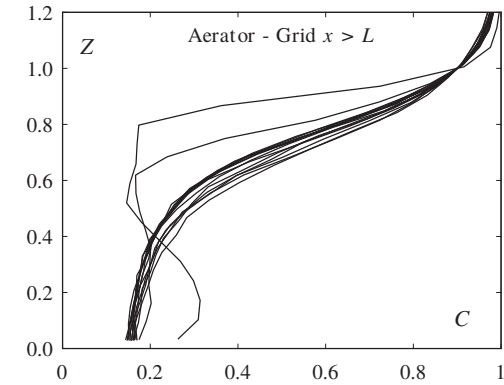
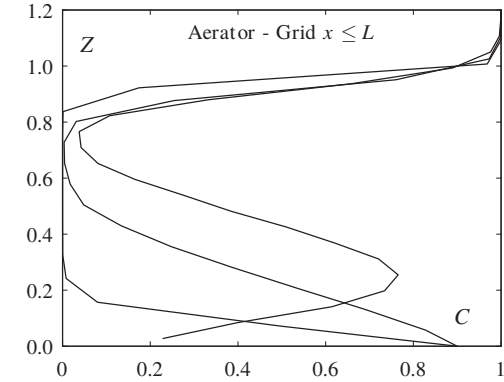
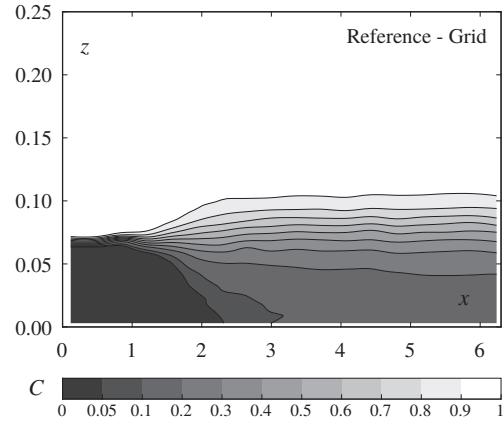
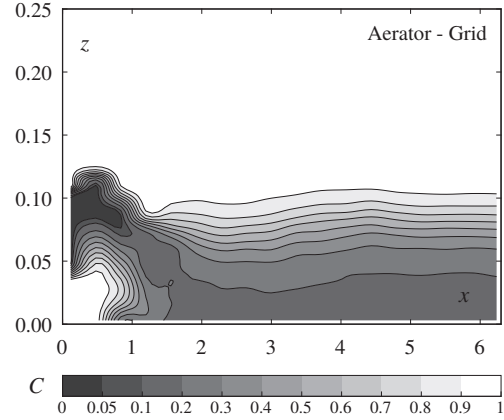


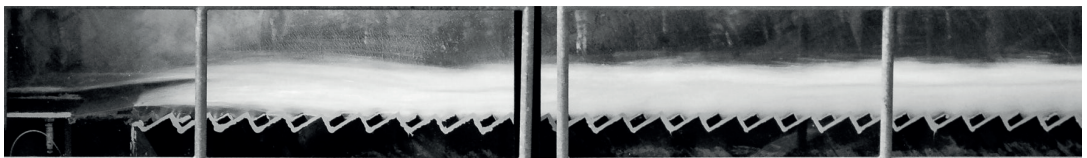
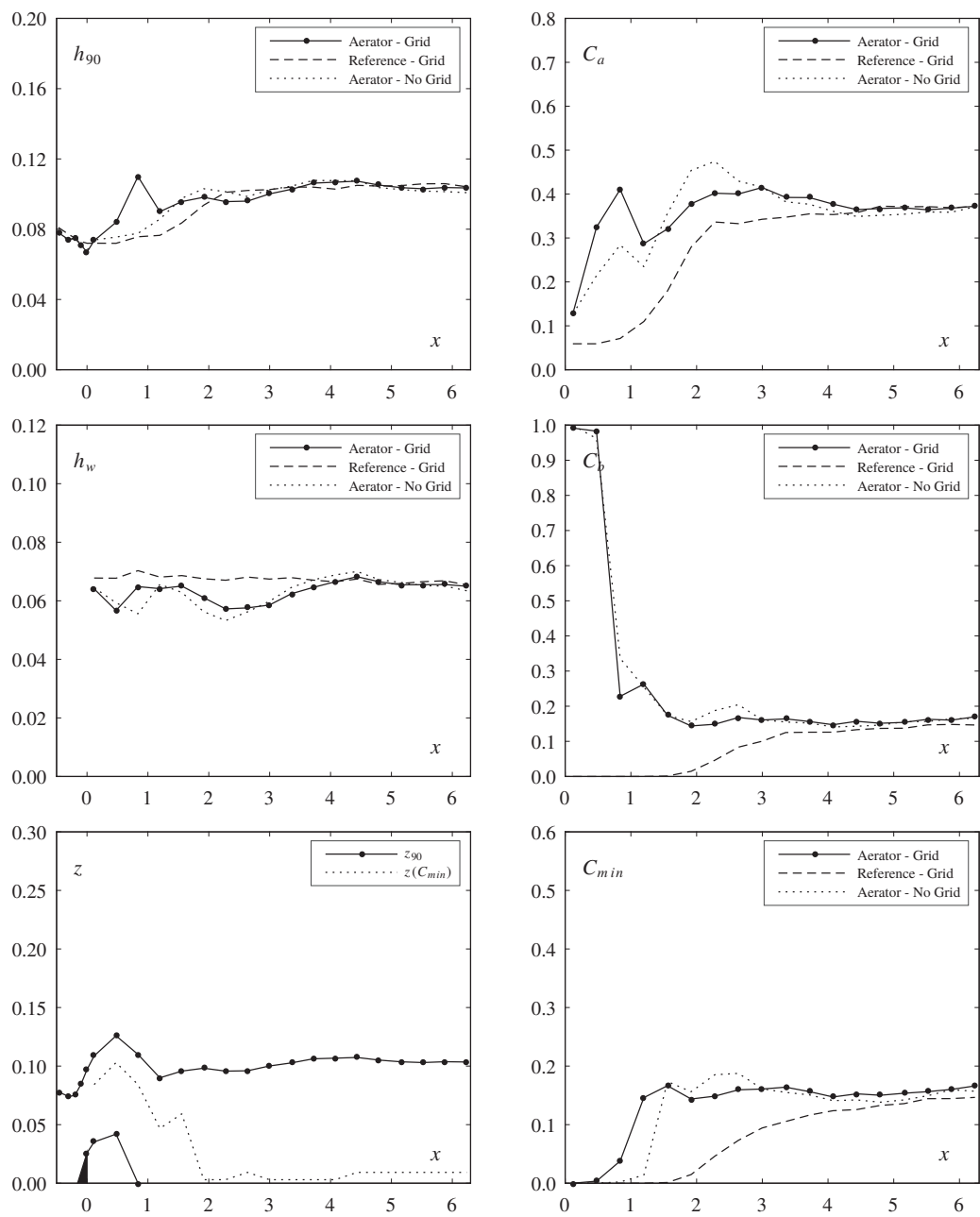
	Grid	Reference	
Test	63	54	
	grid		
Parameters			
φ	30	30	[°]
s	0.030	0.030	[m]
F_o	5.55	5.52	[-]
h_o	0.075	0.075	[m]
α	-	-	[°]
t	-	-	[m]
Flow			
q	0.357	0.355	[m ² /s]
h_c	0.235	0.234	[m]
h_c/s	7.84	7.81	[-]
u_o	4.76	4.74	[m/s]
Pressure			
$p/(\rho g)$	0.103	0.121	[m]
$p'/(\rho g)$	0.0046	0.0033	[m]
Dimensionless numbers			
R	357266	355233	[-]
W_o	154	153	[-]
F_k	38.5	38.3	[-]
F_s	31.0	30.9	[-]
Inception point			
x_i	1.79	2.07	[m]
h_i	0.090	0.094	[m]
h_{wi}	0.068	0.071	[m]
Air entrainment			
β	-	-	[-]
q_A	-	-	[m ² /s]
$u_{A,max}$	-	-	[m/s]
u_A	-	-	[m/s]
Jet			
L	-	-	[m]
L/h_o	-	-	[-]
L_{obs}	-	-	[m]
$\Delta p/h$	-	-	[-]
h_t	-	-	[m]
α_{tu}	-	-	[°]
α_{tl}	-	-	[°]
γ	-	-	[°]
Observation			
-			



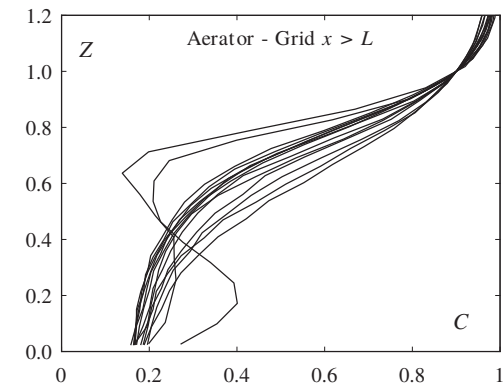
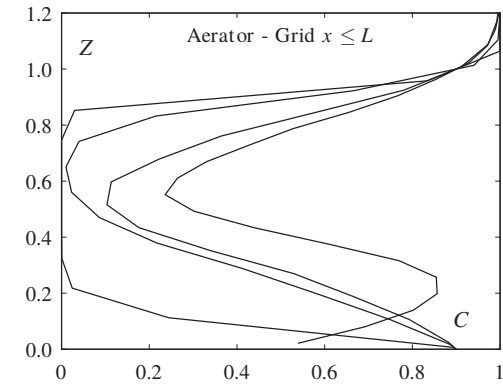
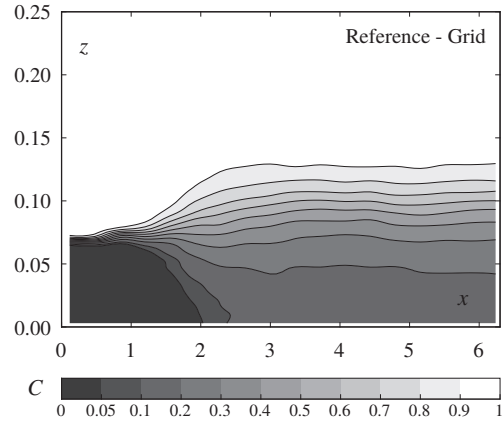
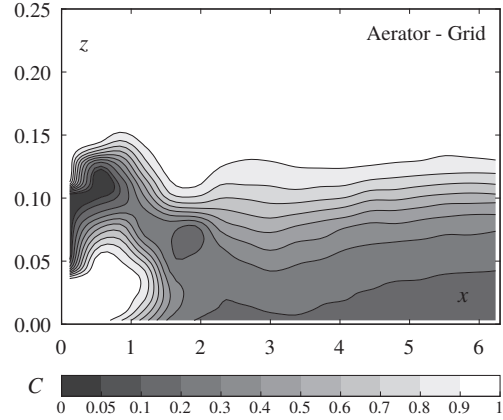


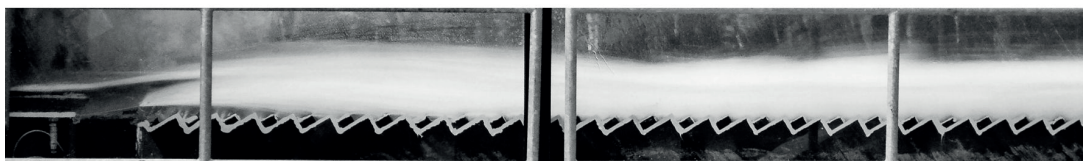
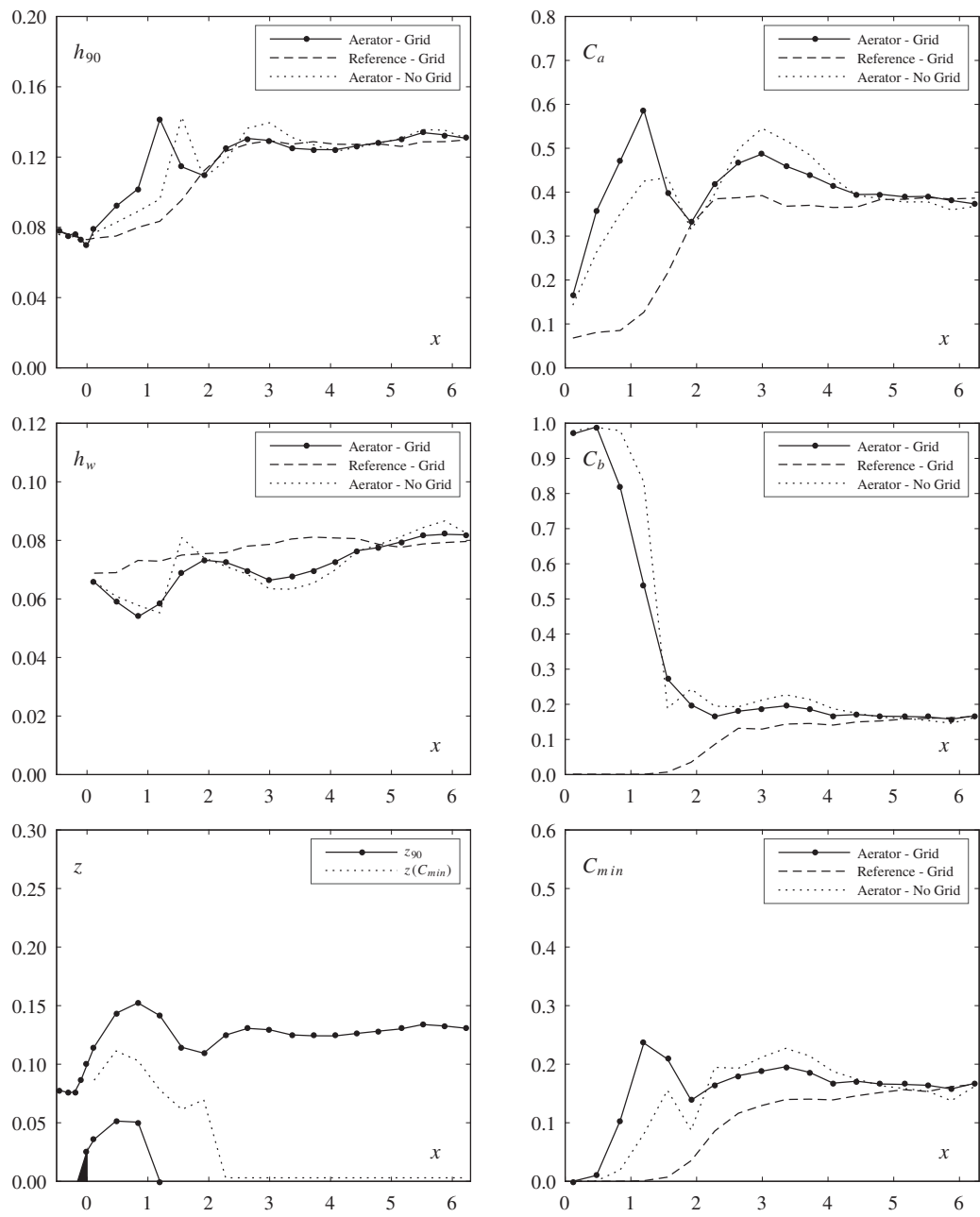
	Aerator	Reference	
Test	64	63	
	grid	grid	
Parameters			
φ	30	30	[°]
s	0.030	0.030	[m]
F_o	5.52	5.55	[-]
h_o	0.075	0.075	[m]
α	9.46	-	[°]
t	0.030	-	[m]
Flow			
q	0.355	0.357	[m ² /s]
h_c	0.234	0.235	[m]
h_c/s	7.81	7.84	[-]
u_o	4.73	4.76	[m/s]
Pressure			
$p/(\rho g)$	0.132	0.103	[m]
$p'/(\rho g)$	0.0047	0.0046	[m]
Dimensionless numbers			
R	355093	357266	[-]
W_o	153	154	[-]
F_k	38.3	38.5	[-]
F_s	30.9	31.0	[-]
Inception point			
x_i	-	1.79	[m]
h_i	-	0.090	[m]
h_{wi}	-	0.068	[m]
Air entrainment			
β	0.216	-	[-]
q_A	0.077	-	[m ² /s]
$u_{A,max}$	2.56	-	[m/s]
u_A	2.12	-	[m/s]
Jet			
L	1.00	-	[m]
L/h_o	13.3	-	[-]
L_{obs}	0.78	-	[m]
$\Delta p/h$	0.04	-	[-]
h_t	0.067	-	[m]
α_{tu}	8.01	-	[°]
α_{tl}	5.90	-	[°]
γ	7.54	-	[°]
Observation			
-			



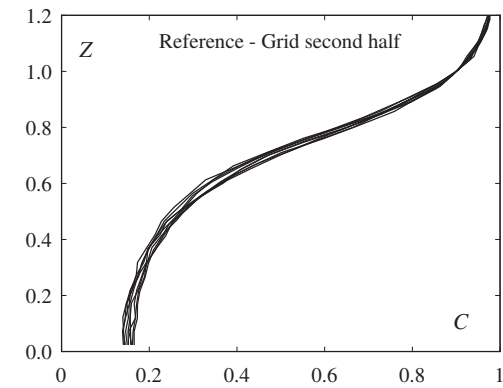
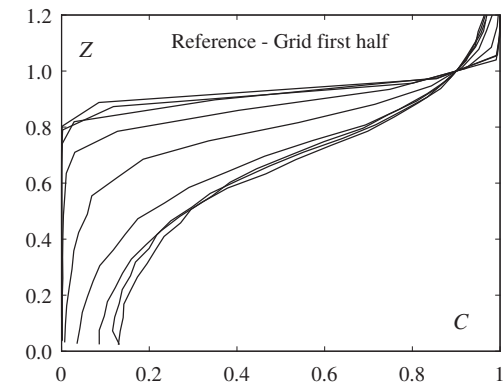
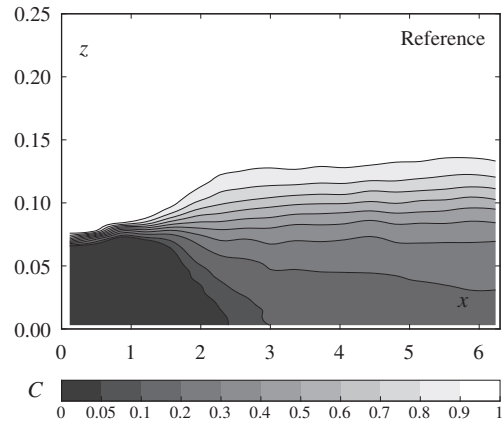
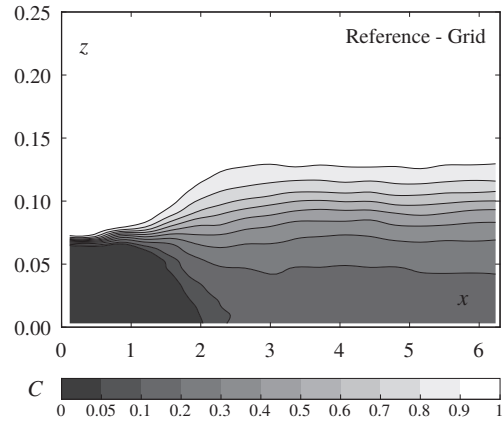


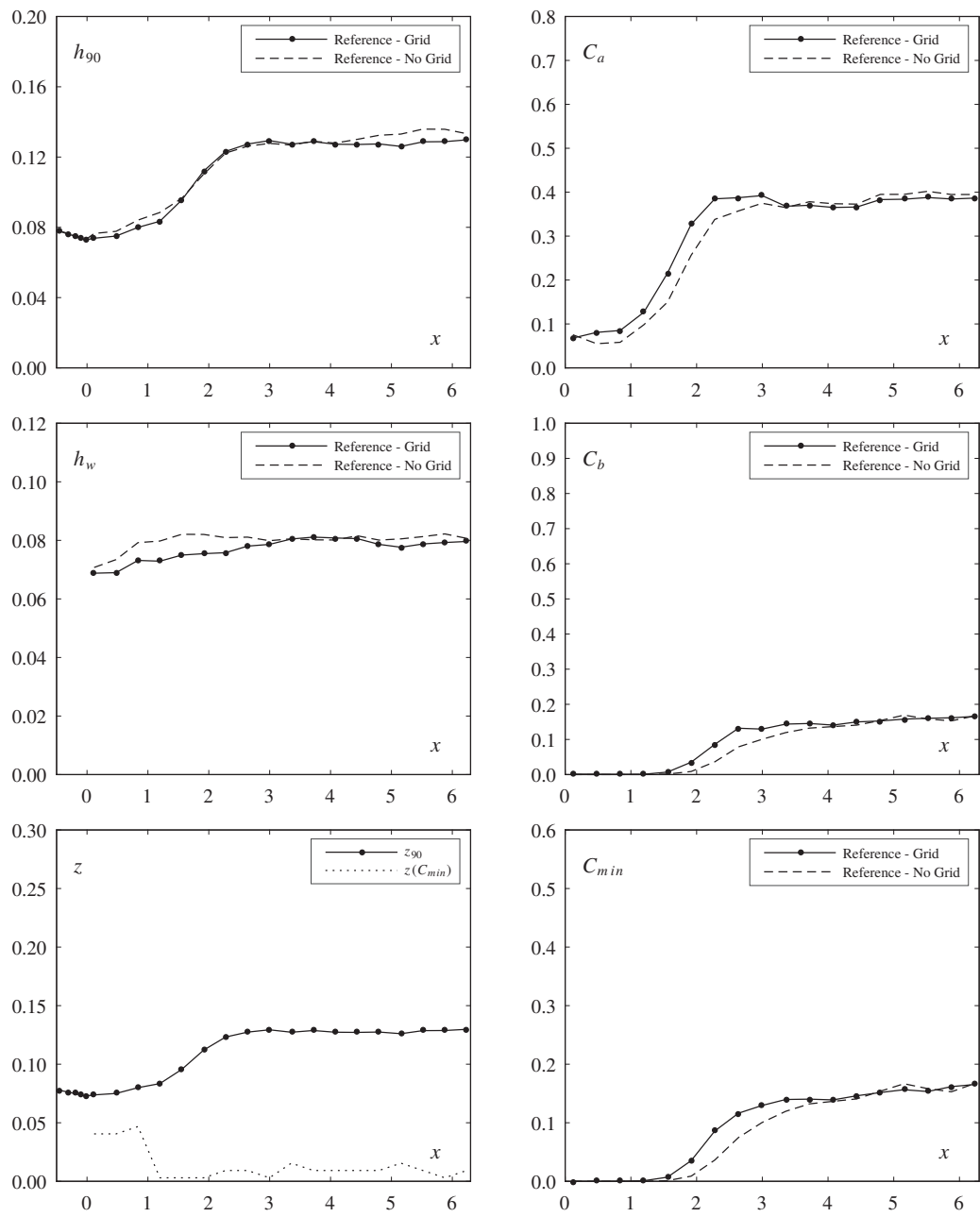
	Aerator	Reference	
Test	65	66	
	grid	grid	
Parameters			
φ	30	30	[°]
s	0.030	0.030	[m]
F_o	7.29	7.46	[-]
h_o	0.076	0.075	[m]
α	9.46	-	[°]
t	0.030	-	[m]
Flow			
q	0.483	0.480	[m ² /s]
h_c	0.288	0.286	[m]
h_c/s	9.59	9.54	[-]
u_o	6.32	6.40	[m/s]
Pressure			
$p/(\rho g)$	0.185	0.111	[m]
$p'/(\rho g)$	0.0081	0.0073	[m]
Dimensionless numbers			
R	483383	479800	[-]
W_o	206	207	[-]
F_k	52.1	51.7	[-]
F_s	42.0	41.7	[-]
Inception point			
x_i	-	1.59	[m]
h_i	-	0.097	[m]
h_{wi}	-	0.075	[m]
Air entrainment			
β	0.297	-	[-]
q_A	0.144	-	[m ² /s]
$u_{A,max}$	4.74	-	[m/s]
u_A	3.96	-	[m/s]
Jet			
L	1.56	-	[m]
L/h_o	20.3	-	[-]
L_{obs}	1.12	-	[m]
$\Delta p/h$	0.16	-	[-]
h_t	0.070	-	[m]
α_{tu}	7.99	-	[°]
α_{tl}	5.65	-	[°]
γ	6.34	-	[°]
Observation			
-			



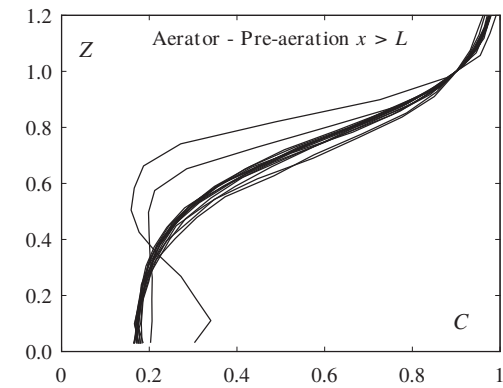
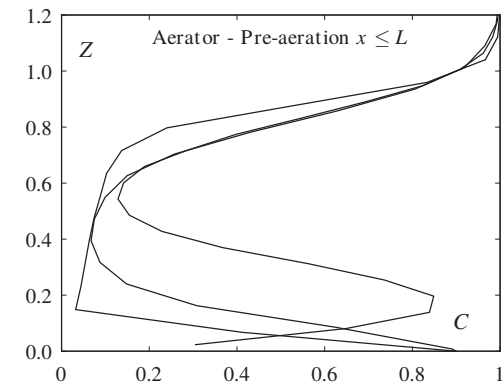
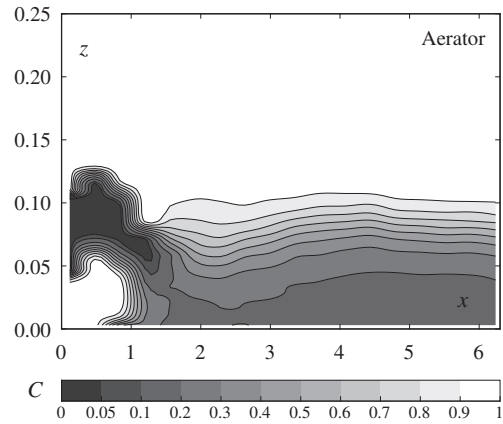
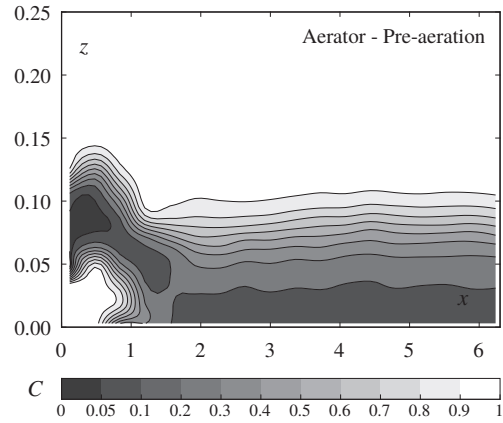


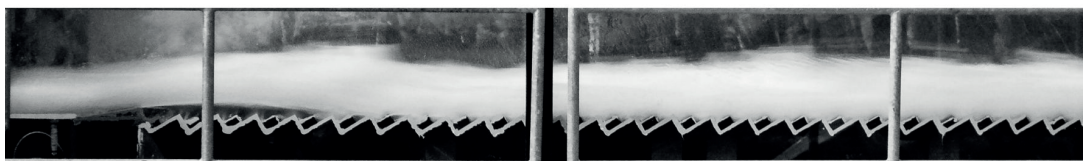
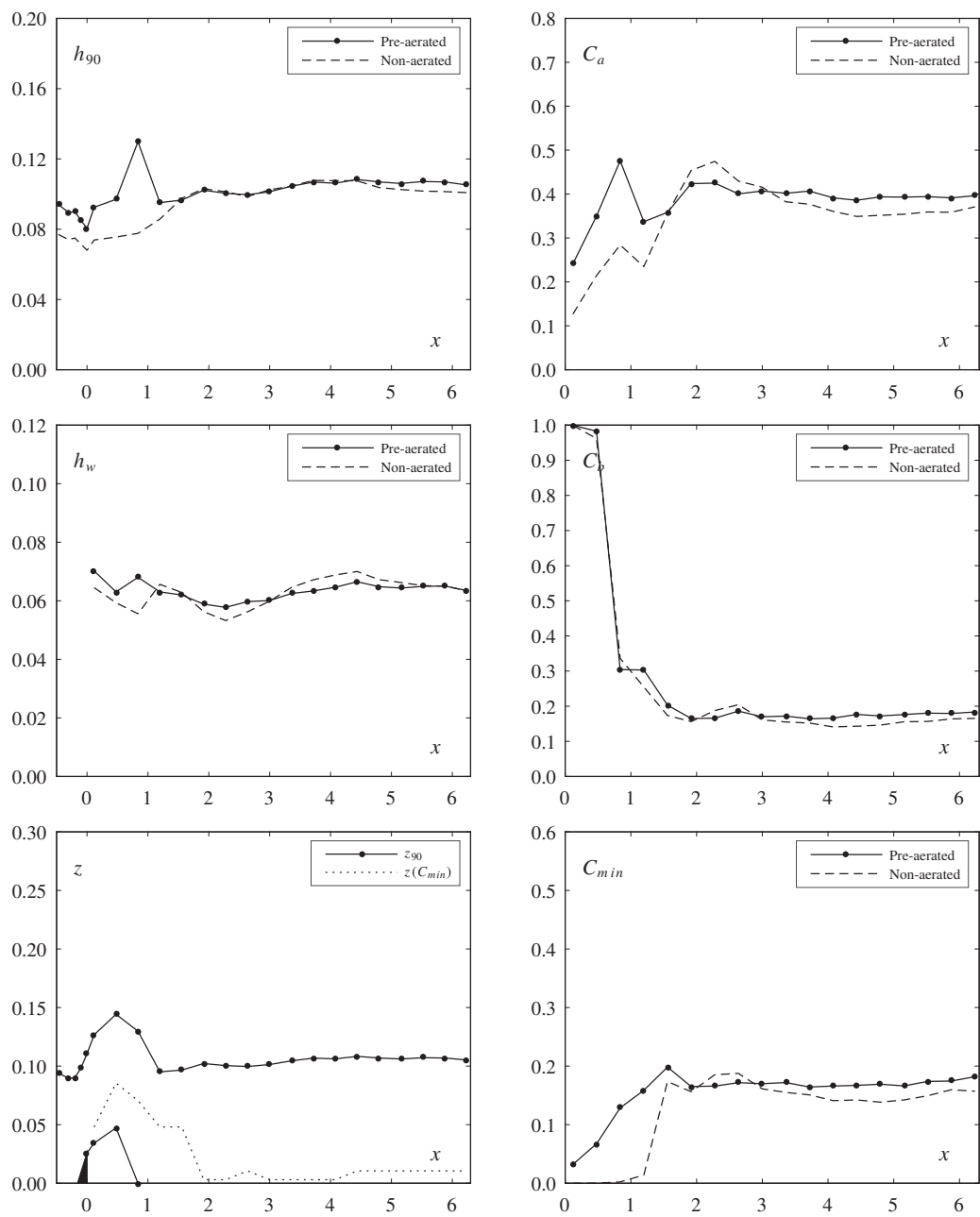
	Grid	Reference	
Test	66	55	
	grid		
Parameters			
φ	30	30	[°]
s	0.030	0.030	[m]
F_o	7.46	7.49	[-]
h_o	0.075	0.075	[m]
α	-	-	[°]
t	-	-	[m]
Flow			
q	0.480	0.482	[m ² /s]
h_c	0.286	0.287	[m]
h_c/s	9.54	9.57	[-]
u_o	6.40	6.42	[m/s]
Pressure			
$p/(\rho g)$	0.111	0.167	[m]
$p'/(\rho g)$	0.0073	0.0053	[m]
Dimensionless numbers			
R	479800	481839	[-]
W_o	207	207	[-]
F_k	51.7	52.0	[-]
F_s	41.7	41.9	[-]
Inception point			
x_i	1.59	1.93	[m]
h_i	0.097	0.111	[m]
h_{wi}	0.075	0.082	[m]
Air entrainment			
β	-	-	[-]
q_A	-	-	[m ² /s]
$u_{A,max}$	-	-	[m/s]
u_A	-	-	[m/s]
Jet			
L	-	-	[m]
L/h_o	-	-	[-]
L_{obs}	-	-	[m]
$\Delta p/h$	-	-	[-]
h_t	-	-	[m]
α_{tu}	-	-	[°]
α_{tl}	-	-	[°]
γ	-	-	[°]
Observation			
-			



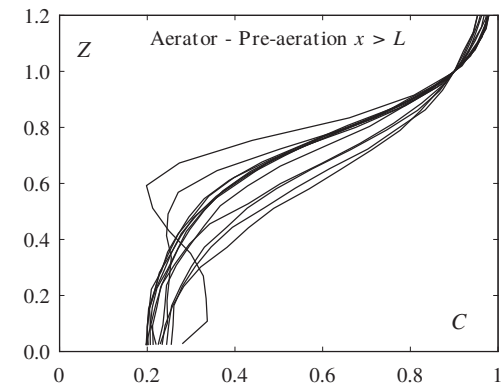
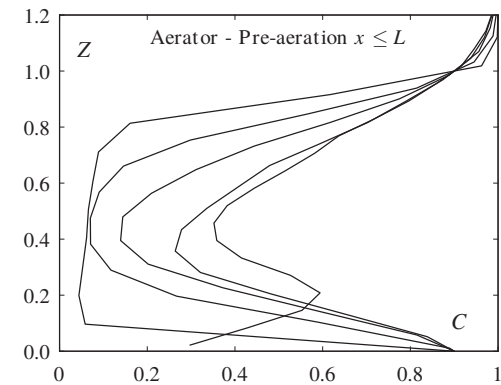
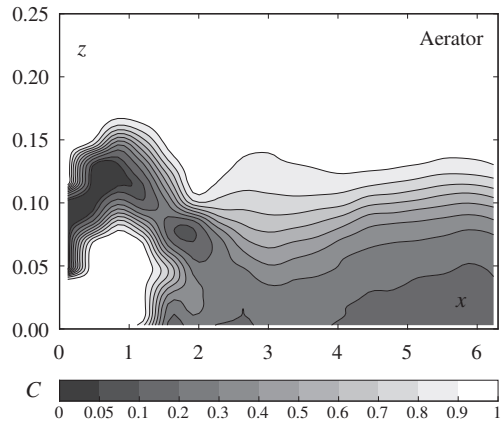
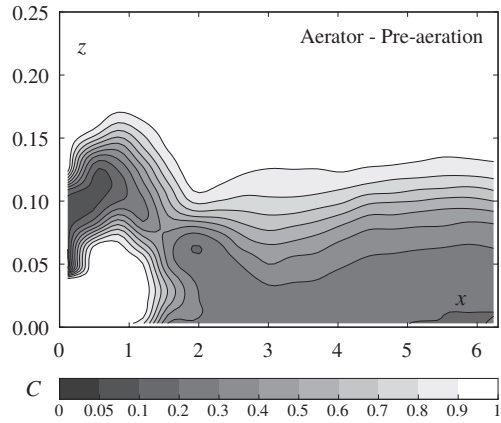


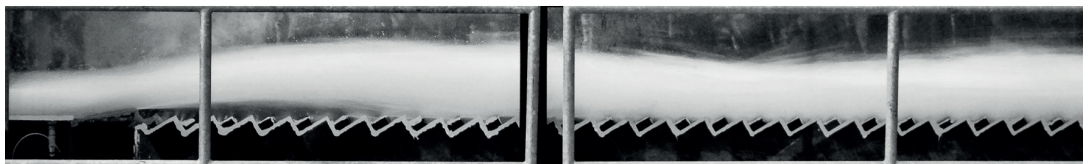
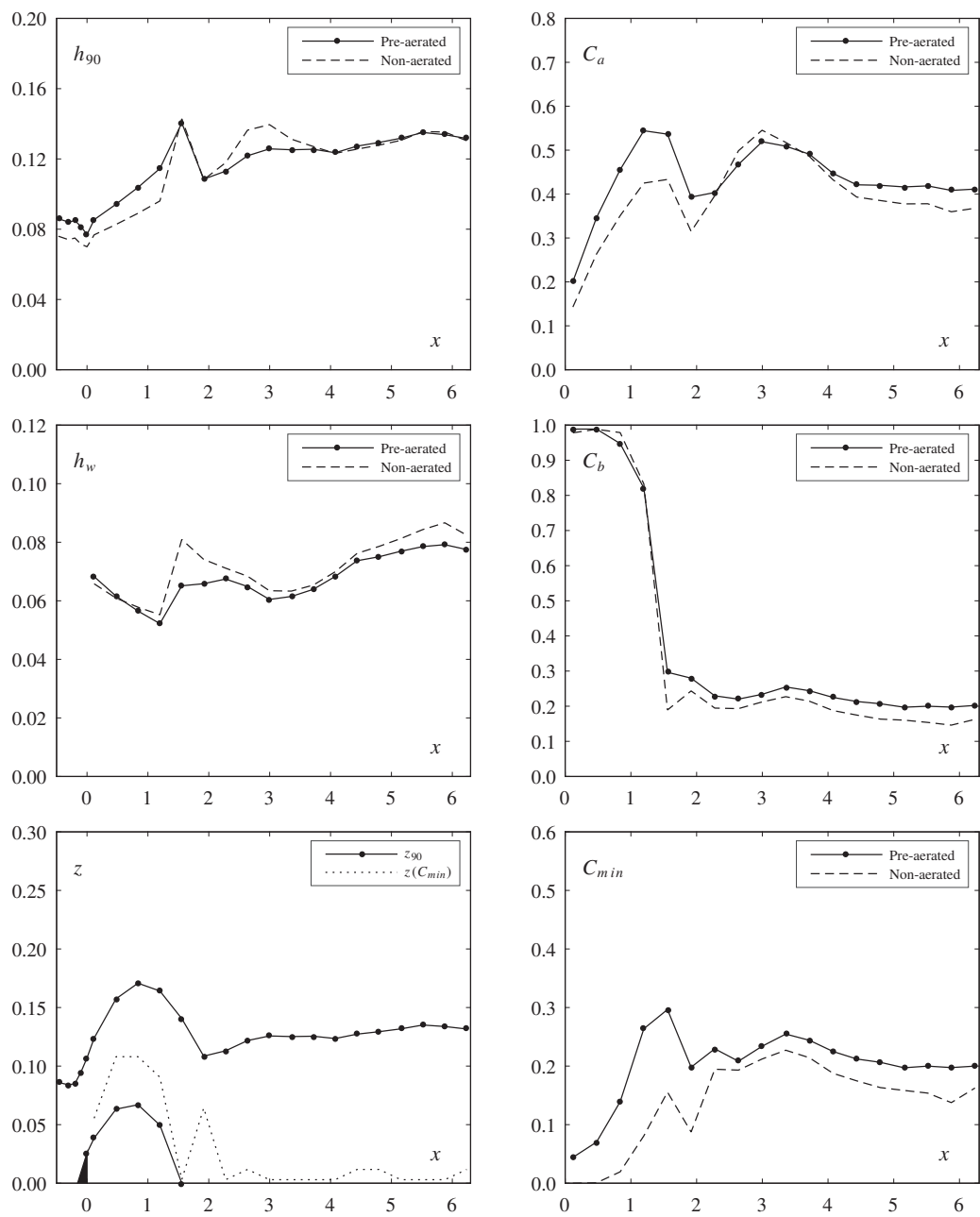
	Pre-aerated	Reference	
Test	67	57	
	pre-aerated		
Parameters			
φ	30	30	[°]
s	0.030	0.030	[m]
F_o	5.53	5.49	[-]
h_o	0.075	0.075	[m]
α	9.46	9.46	[°]
t	0.030	0.030	[m]
Flow			
q	0.356	0.353	[m ² /s]
h_c	0.234	0.233	[m]
h_c/s	7.82	7.78	[-]
u_o	4.74	4.71	[m/s]
Pressure			
$p/(\rho g)$	0.153	0.159	[m]
$p'/(\rho g)$	0.0123	0.0030	[m]
Dimensionless numbers			
R	355659	353186	[-]
W_o	153	152	[-]
F_k	38.3	38.1	[-]
F_s	30.9	30.7	[-]
Inception point			
x_i	-	-	[m]
h_i	-	-	[m]
h_{wi}	-	-	[m]
Air entrainment			
β	0.149	0.112	[-]
q_A	0.053	0.040	[m ² /s]
$u_{A,max}$	1.79	1.34	[m/s]
u_A	1.46	1.09	[m/s]
Jet			
L	0.95	1.22	[m]
L/h_o	12.7	16.3	[-]
L_{obs}	0.84	0.78	[m]
$\Delta p/h$	0.01	0.00	[-]
h_t	0.081	0.068	[m]
α_{tu}	10.35	9.06	[°]
α_{tl}	7.20	7.91	[°]
γ	8.94	7.99	[°]
Observation			
-			



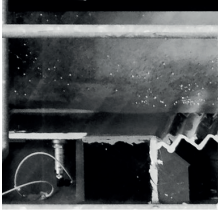
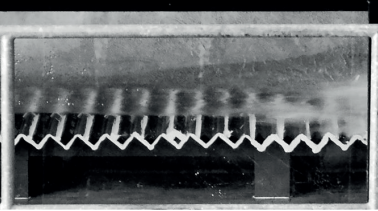
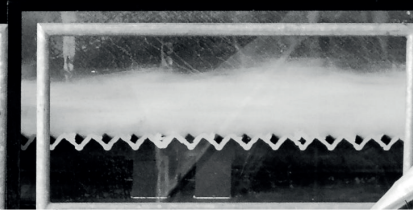
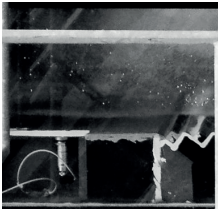
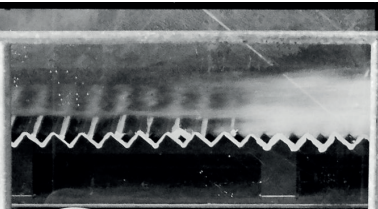
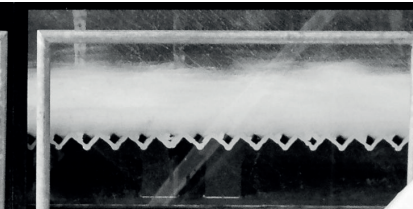
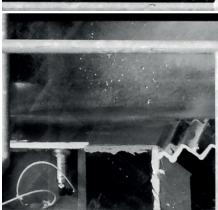
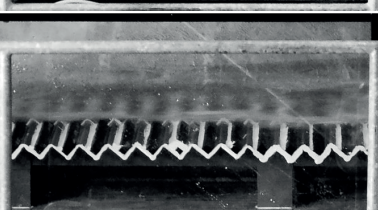
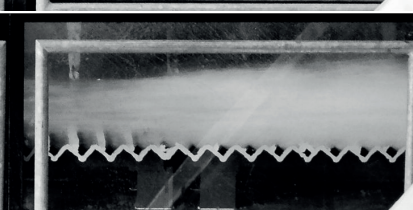
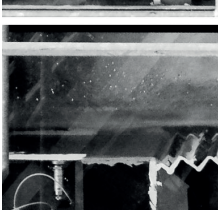
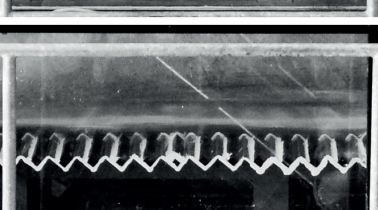
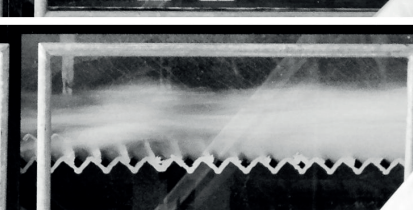
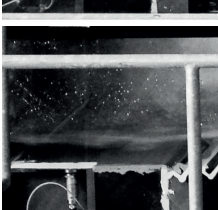
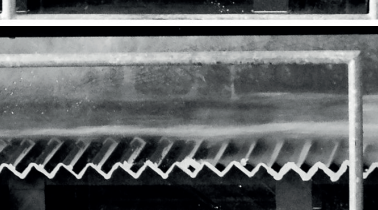
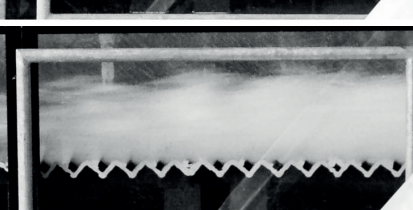


	Pre-aerated	Reference	
Test	68	58	
	pre-aerated		
Parameters			
φ	30	30	[°]
s	0.030	0.030	[m]
F_o	7.46	7.51	[-]
h_o	0.075	0.075	[m]
α	9.46	9.46	[°]
t	0.030	0.030	[m]
Flow			
q	0.480	0.483	[m ² /s]
h_c	0.286	0.288	[m]
h_c/s	9.55	9.58	[-]
u_o	6.40	6.44	[m/s]
Pressure			
$p/(\rho g)$	0.224	0.239	[m]
$p'/(\rho g)$	0.0103	0.0051	[m]
Dimensionless numbers			
R	479959	482904	[-]
W_o	207	208	[-]
F_k	51.7	52.1	[-]
F_s	41.7	42.0	[-]
Inception point			
x_i	-	-	[m]
h_i	-	-	[m]
h_{wi}	-	-	[m]
Air entrainment			
β	0.244	0.207	[-]
q_A	0.117	0.100	[m ² /s]
$u_{A,max}$	3.87	3.31	[m/s]
u_A	3.22	2.75	[m/s]
Jet			
L	1.66	1.93	[m]
L/h_o	22.1	25.7	[-]
L_{obs}	1.32	1.26	[m]
$\Delta p/h$	0.09	0.07	[-]
h_t	0.077	0.070	[m]
α_{tu}	9.45	9.20	[°]
α_{tl}	7.19	7.73	[°]
γ	7.82	7.66	[°]
Observation			
-			





$\varphi = 50^\circ$ and $s = 0.030\text{m}$

Test	Photo		
10			
9			
8			
7			
6			

$\varphi = 50^\circ$ and $s = 0.060\text{ m}$

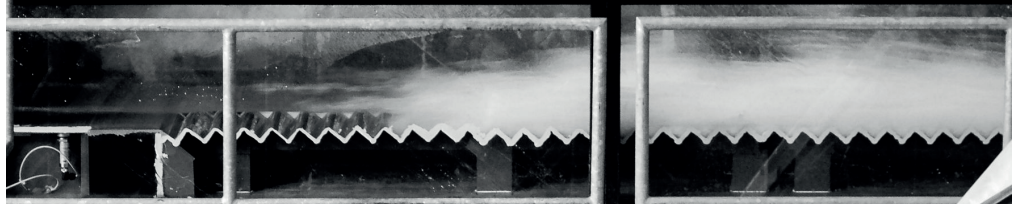
Test

Photo

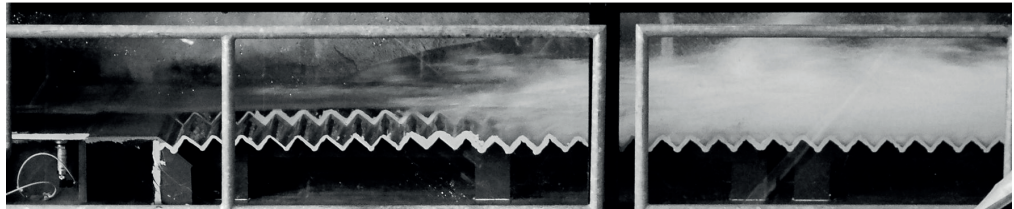
17



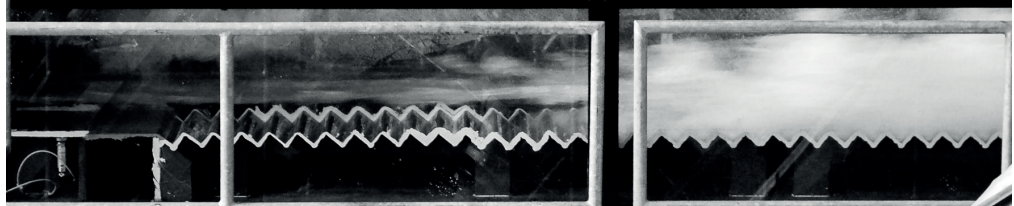
15



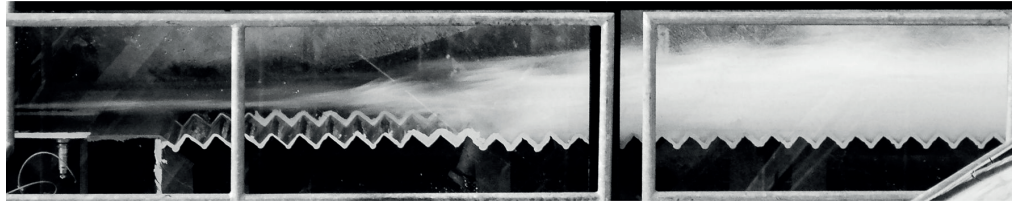
13



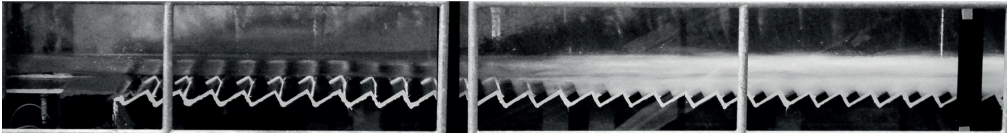
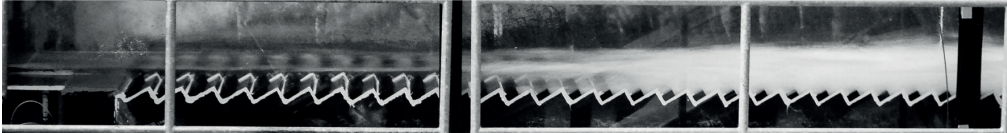
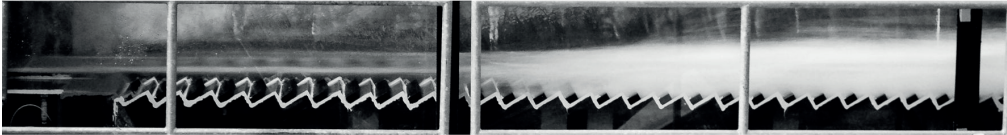
14



16



$\varphi = 30^\circ$ and $s = 0.030\text{ m}$

Test	Photo
56	
-	
54	
-	
55	

$\varphi = 30^\circ$ and $s = 0.060\text{ m}$

Test

Photo

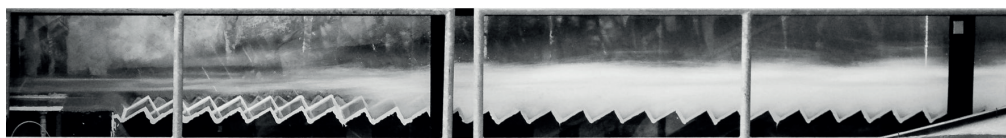
41



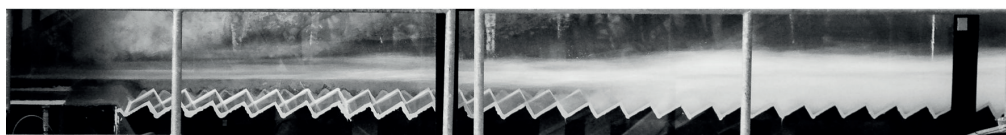
40



38



39



42



References

- Al Harthy, S. H., Hall, J. K., Hieatt, M. J., and Wheelerl, M. (2010). The day Wadi Dayqah roared. *International Water Power & Dam Construction*, 62(12):40–43.
- Amador, A., Sánchez-Juny, M., and Dolz, J. (2005). Discussion of "Two-phase flow characteristics of stepped spillways" by R. M. Boes and W. H. Hager. *Journal of Hydraulic Engineering*, 131(5):421–423.
- Amador, A., Sánchez-Juny, M., and Dolz, J. (2006). Characterization of the nonaerated flow region in a stepped spillway by PIV. *Journal of Fluids Engineering*, 128(6):1266–1273.
- Amador, A., Sánchez-Juny, M., and Dolz, J. (2009). Developing flow region and pressure fluctuations on steeply sloping stepped spillways. *Journal of Hydraulic Engineering*, 135(12):1092–1100.
- André, S. (2004). *High velocity aerated flows on stepped chutes with macro-roughness elements*. In Schleiss, A. J., editor, Communication LCH 20. École Polytechnique Fédérale de Lausanne.
- André, S., Boillat, J.-L., and Schleiss, A. J. (2005). Discussion of "Two-phase flow characteristics of stepped spillways" by R. M. Boes and W. H. Hager. *Journal of Hydraulic Engineering*, 131(5):423–427.
- André, S., Boillat, J.-L., and Schleiss, A. J. (2008a). Ecoulements aérés sur évacuateurs en marches d'escalier équipées de macro-rugosités - Partie I: Caractéristiques hydrauliques. *Houille Blanche*, 2008(1):91–100.
- André, S., Boillat, J.-L., and Schleiss, A. J. (2008b). Ecoulements aérés sur évacuateurs en marches d'escalier équipées de macro-rugosités, Partie II: Dissipation d'énergie. *Houille Blanche*, 2008(1):101–108.
- André, S. and Schleiss, A. J. (2008). Discussion of "Pressures on a stepped spillway" by M. Sánchez-Juny, E. Bladé and J. Dolz. *Journal of Hydraulic Research*, 46(4):574–576.
- Arndt, R. E. A. and Ippen, A. T. (1968). Rough surface effects on cavitation inception. *Journal of Basic Engineering*, 90(6):249.
- Arndt, R. E. A. and Ippen, A. T. (1970). Turbulence measurements in liquids using an improved total pressure probe. *Journal of Hydraulic Research*, 8(2):131–158.

References

- Balaguer, G. (1992). *Sohlenbelüfter in Schussrinnen, Ergänzende Untersuchungen zur Bemessung*. PhD Thesis, Universität Fridericiana, Karlsruhe, Germany.
- Ball, J. W. (1976). Cavitation from surface irregularities in high velocity. *Journal of the Hydraulics Division*, 102(9):1283–1297.
- Bauer, W. J. (1953). Turbulent boundary layer on steep slopes. *ASCE Transactions*, 119(9):1212–1233.
- Boes, R. M. (2000a). Discussion of "Characteristics of skimming flow over stepped spillways" by M. R. Chamani and N. Rajaratnam. *Journal of Hydraulic Engineering*, 126(11):860–862.
- Boes, R. M. (2000b). Scale effects in modelling two-phase stepped spillway flow. In Minor, H.-E. and Hager, W. H., editors, *Hydraulics of stepped spillways*, 53–60, Zürich, Switzerland. Balkema, Rotterdam.
- Boes, R. M. (2000c). *Zweiphasenströmung und Energieumsetzung an Grosskaskaden*. In Minor, H.-E., editor, VAW Mitteilungen 166. ETH Zürich.
- Boes, R. M. and Hager, W. H. (2003a). Hydraulic design of stepped spillways. *Journal of Hydraulic Engineering*, 129(9):671–679.
- Boes, R. M. and Hager, W. H. (2003b). Two-phase flow characteristics of stepped spillways. *Journal of Hydraulic Engineering*, 129(9):661–670.
- Boes, R. M. and Hager, W. H. (2005). Closure to "Two-phase flow characteristics of stepped spillways". *Journal of Hydraulic Engineering*, 131(5):427–429.
- Bradley, J. N. (1945). *Study of air injection into the flow in the Hoover Dam spillway tunnels*. In United States Bureau of Reclamation, editor, Hydraulic Laboratory Report 186. U.S. Dept. of the Interior, Denver, CO.
- Brujan, E. A., Keen, G. S., Vogel, A., and Blake, J. R. (2002). The final stage of the collapse of a cavitation bubble close to a rigid boundary. *Physics of Fluids*, 14(1):85–92.
- Buckingham, E. (1914). On physically similar systems; Illustrations of the use of dimensional equations. *Physical Review*, 4(4):345–376.
- Bung, D. B. (2011). Developing flow in skimming flow regime on embankment stepped spillways. *Journal of Hydraulic Research*, 49(5):639–648.
- Cain, P. and Wood, I. R. (1981). Measurements of self-aerated flow on a spillway. *Journal of the Hydraulics Division*, 107(11):1425–1444.
- Carosi, G. and Chanson, H. (2008). Turbulence characteristics in skimming flows on stepped spillways. *Canadian Journal of Civil Engineering*, 35(9):865–880.

- Chamani, M. R. (2000). Air inception in skimming flow regime over stepped spillways. In Minor, H.-E. and Hager, W. H., editors, *Hydraulics of stepped spillways*, 61–67, Zürich, Switzerland. Balkema, Rotterdam.
- Chamani, M. R. and Rajaratnam, N. (1999). Characteristics of skimming flow over stepped spillways. *Journal of Hydraulic Engineering*, 125(4):361–368.
- Chanson, H. (1988). *Study of air entrainment and aeration devices on a spillway model*. PhD Thesis, University of Canterbury, New Zealand.
- Chanson, H. (1989a). Flow downstream of an aerator - aerator spacing. *Journal of Hydraulic Research*, 27(4):519–536.
- Chanson, H. (1989b). Study of air entrainment and aeration devices. *Journal of Hydraulic Research*, 27(3):301–319.
- Chanson, H. (1991). Aeration of a free jet above a spillway. *Journal of Hydraulic Research*, 29(5):655–667.
- Chanson, H. (1993). Self-aerated flows on chutes and spillways. *Journal of Hydraulic Engineering*, 119(2):220–243.
- Chanson, H. (1994a). Aeration and deaeration at bottom aeration devices on spillways. *Canadian Journal of Civil Engineering*, 21(3):404–409.
- Chanson, H. (1994b). Drag reduction in open channel flow by aeration and suspended load. *Journal of Hydraulic Research*, 32(1):87–101.
- Chanson, H. (1995a). Air bubble diffusion in supercritical open channel flow. In *12th Australasian Fluid Mechanics Conference*, 2, 707–710, Sydney, Australia.
- Chanson, H. (1995b). *Hydraulic design of stepped cascades, channels, weirs, and spillways*. Pergamon, Oxford, UK.
- Chanson, H. (1995c). Predicting the filling of ventilated cavities behind spillway aerators. *Journal of Hydraulic Research*, 33(3):361–372.
- Chanson, H. (2002). *The hydraulics of stepped chutes and spillways*. Balkema, Rotterdam, Lisse, Netherlands.
- Chanson, H. (2005). Discussion of "Two-phase flow characteristics of stepped spillways" by R. M. Boes and W. H. Hager. *Journal of Hydraulic Engineering*, 131(5):419–421.
- Chanson, H. (2006). Hydraulics of skimming flows on stepped chutes: the effects of inflow conditions? *Journal of Hydraulic Research*, 44(1):51–60.
- Chanson, H. (2008). Physical modelling, scale effects and self-similarity of stepped spillway flows. In *World Environmental and Water Resources Congress*, 316, Honolulu, USA.

References

- Chanson, H. (2009). Turbulent air-water flows in hydraulic structures: dynamic similarity and scale effects. *Environmental Fluid Mechanics*, 9(2):125–142.
- Chanson, H. (2015). Discussion of "Cavitation potential of flow on stepped spillways" by K. Warren Frizell, F. M. Renna, and J. Matos. *Journal of Hydraulic Engineering*, 141(5):07014025.
- Chanson, H., Aoki, S., and Hoque, A. (2004). Physical modelling and similitude of air bubble entrainment at vertical circular plunging jets. *Chemical Engineering Science*, 59(4):747 – 758.
- Chanson, H., Bung, D. B., and Matos, J. (2015). Stepped spillways and cascades. In Chanson, H., editor, *Energy Dissipation in Hydraulic Structures*, IAHR Monographs, 45–64. CRC Press.
- Chanson, H. and Toombes, L. (2002a). Air–water flows down stepped chutes: turbulence and flow structure observations. *International Journal of Multiphase Flow*, 28(11):1737–1761.
- Chanson, H. and Toombes, L. (2002b). Experimental investigations of air entrainment in transition and skimming flows down a stepped chute. *Canadian Journal of Civil Engineering*, 29(1):145–156.
- Chanson, H., Yasuda, Y., and Ohtsu, I. (2002). Flow resistance in skimming flows in stepped spillways and its modelling. *Canadian Journal of Civil Engineering*, 29(6):809–819.
- Chow, V. T. (1959). *Open channel hydraulics*. McGraw-Hill Book Company, New York, NY.
- Colgate, D. (1977). Cavitation damage in hydraulic structures. In *Wear of Materials*, St. Louis, Missouri. The American Society of Mechanical Engineers.
- Deng, Y., Lin, K., and Han, L. (2003). Design and prototype test of stepped overflow surface at Dachao Shan hydropower station in China. In *4th Roller Compacted Concrete Dams Symposium*, 431–432, Madrid, Spain.
- Drewes, U. (1988). Oberflächentoleranzen bei Betonschussrinnen im Hinblick auf Kavitation. In Vischer, D., editor, *VAW Mitteilungen*, 99, 11–33. ETH Zürich.
- Ervine, D. A. and Falvey, H. T. (1987). Behaviour of turbulent water jets in the atmosphere and in plunge pools. *Proceedings of the Institution of Civil Engineers*, 83(1):295–314.
- Ervine, D. A., Falvey, H. T., and Kahn, A. R. (1995). Turbulent flow structure and air uptake at aerators. *International Journal on Hydropower and Dams*, 2(5):89–96.
- Ervine, D. A., McKeogh, E., and Elsayy, E. M. (1980). Effect of turbulence intensity on the rate of air entrainment by plunging water jets. *Proceedings of the Institution of Civil Engineers*, 69(2):425–445.
- Estrella, S., Sánchez-Juny, M., Bladé, E., and Dolz, J. (2015). Physical modeling of a stepped spillway without sidewalls. *Canadian Journal of Civil Engineering*, 42(5):311–318.
- Falvey, H. T. (1983). Prevention of cavitation on chutes and spillways. In *Frontiers in Hydraulic Engineering*, 432–437. ASCE.

- Falvey, H. T. (1990). *Cavitation in chutes and spillways*. In United States Bureau of Reclamation, editor, Engineering monographs 42. U.S. Dept. of the Interior, Denver, Colorado.
- Falvey, H. T. and Ervine, D. A. (1988). Aeration in jets and high velocity flows. In Burgi, P. H., editor, *Model-Prototype Correlation of Hydraulic Structures*, 22–55. ASCE.
- Felder, S. and Chanson, H. (2009a). Energy dissipation, flow resistance and gas-liquid interfacial area in skimming flows on moderate-slope stepped spillways. *Environmental Fluid Mechanics*, 9(4):427–441.
- Felder, S. and Chanson, H. (2009b). Turbulence, dynamic similarity and scale effects in high-velocity free-surface flows above a stepped chute. *Experiments in Fluids*, 47(1):1–18.
- Felder, S. and Chanson, H. (2011). Air–water flow properties in step cavity down a stepped chute. *International Journal of Multiphase Flow*, 37(7):732 – 745.
- Felder, S. and Chanson, H. (2014). Air–water flows and free-surface profiles on a non-uniform stepped chute. *Journal of Hydraulic Research*, 52(2):253–263.
- Felder, S. and Chanson, H. (2016). Simple design criterion for residual energy on embankment dam stepped spillways. *Journal of Hydraulic Engineering*, 142:04015062.
- Frizell, K. H. and Mefford, B. W. (1991). Designing spillways to prevent cavitation damage. *Concrete International*, 13(5):58–64.
- Frizell, K. W., Renna, F., and Matos, J. (2015). Closure to "Cavitation potential of flow on stepped spillways". *Journal of Hydraulic Engineering*, 141(8):07015009.
- Frizell, K. W., Renna, F. M., and Matos, J. (2013). Cavitation potential of flow on stepped spillways. *Journal of Hydraulic Engineering*, 139(6):630–636.
- Galperin, R. S., Kuzmin, K. K., Novikova, I. S., Oskolkov, A. G., Semenkov, V. M., and Tsedrov, G. N. (1971). Cavitation in elements of hydraulic structures and methods of controlling it. *Hydrotechnical Construction*, 5(8):726–732.
- Galperin, R. S., Oskolkov, A. G., Semenkov, V. M., and Tsedrov, G. N. (1977). *Cavitation in hydraulic structures*. Energiya, Moscow, Russia.
- Gaskin, S. J., Aubel, T., and Holder, G. (2003). Air demand for a ramp-offset aerator as a function of spillway slope, ramp angle and Froude number. In *30th IAHR Congress*, 719–724, Thessaloniki, Greece.
- Glazov, A. (1984). Calculation of the air-capturing ability of a flow behind an aerator ledge. *Hydrotechnical Construction*, 18(11):554–558.
- Gomes, J., Marques, M., and Matos, J. (2007). Predicting cavitation inception on steeply sloping stepped spillways. In *32nd IAHR Congress*, Venice, Italy.

References

- Gonzalez, C. A. and Chanson, H. (2004). Interactions between cavity flow and main stream skimming flows: an experimental study. *Canadian Journal of Civil Engineering*, 31(1):33–44.
- Gonzalez, C. A. and Chanson, H. (2007). Hydraulic design of stepped spillways and downstream energy dissipators for embankment dams. *Dam Engineering*, 17(4):223–244.
- Gonzalez, C. A. and Chanson, H. (2008). Turbulence and cavity recirculation in air–water skimming flows. *Journal of Hydraulic Research*, 46(1):65–72.
- Gonzalez, C. A., Takahashi, M., and Chanson, H. (2008). An experimental study of effects of step roughness in skimming flows on stepped chutes. *Journal of Hydraulic Research*, 46(Extra Issue 1):24–35.
- Guo, J., Liu, Z., Liu, J., and Lu, Y. (2003). Field observation on the RCC stepped spillways with the flaring pier gate on the Dachaoshan project. In *30th IAHR Congress*, D, 473–478, Thessaloniki, Greece.
- Hager, W. H. (1991). Uniform aerated chute flow. *Journal of Hydraulic Engineering*, 117(4):528–533.
- Hager, W. H. and Blaser, F. (1998). Drawdown curve and incipient aeration for chute flow. *Canadian Journal of Civil Engineering*, 25(3):467–473.
- Hager, W. H. and Boes, R. (2000). Backwater and drawdown curves in stepped spillway flow. In Minor, H.-E. and Hager, W. H., editors, *Hydraulics of stepped spillways*, 129–136, Zürich, Switzerland. Balkema, Rotterdam.
- Hager, W. H. and Pfister, M. (2009). Historical advance of chute aerators. In *33rd IAHR Congress*, 5827–5834, Vancouver, Canada.
- Hager, W. H. and Pfister, M. (2013). Stepped Spillways: technical Advance from 1900. In *35th IAHR Congress*, 1–8, Chengdu, China. Tsinghua University Press.
- Hamilton, W. (1983). Preventing cavitation damage to hydraulic structures. *International Water Power & Dam Construction*, 35(12):48–53.
- Heller, V., Hager, W. H., and Minor, H.-E. (2005). Ski jump hydraulics. *Journal of Hydraulic Engineering*, 131(5):347–355.
- Hunt, S. L. and Kadavy, K. C. (2011). Inception point relationship for flat-sloped stepped spillways. *Journal of Hydraulic Engineering*, 137(2):262–266.
- Hunt, S. L. and Kadavy, K. C. (2013). Inception point for embankment dam stepped spillways. *Journal of Hydraulic Engineering*, 139(1):60–64.
- Hunt, S. L. and Kadavy, K. C. (2014). Flow depth and energy coefficient relationships for stepped spillways. In *5th International Symposium on Hydraulic Structures*, 1–9, Brisbane, Australia. University of Queensland.

- Hunt, S. L., Kadavy, K. C., and Hanson, G. J. (2014). Simplistic design methods for moderate-sloped stepped chutes. *Journal of Hydraulic Engineering*, 140(12):04014062.
- Hunt, S. L., Temple, D. M., Abt, S. R., Kadavy, K. C., and Hanson, G. (2012). Converging stepped spillways: simplified momentum analysis approach. *Journal of Hydraulic Engineering*, 138(9):796–802.
- Kells, J. A. and Smith, C. D. (1991). Reduction of cavitation on spillways by induced air entrainment. *Canadian Journal of Civil Engineering*, 18(3):358–377.
- Kobus, H. (1984a). Local air entrainment and detrainment. In Kobus, H., editor, *Scale Effects in Modelling Hydraulic Structures*, 4.10, 1–10, Esslingen am Neckar, Germany.
- Kobus, H. (1984b). *Proceedings of international symposium on scale effects in modelling hydraulic structures*. IAHR, Esslingen, Germany.
- Kökpınar, M. A. (2004). Flow over a stepped chute with and without macro-roughness elements. *Canadian Journal of Civil Engineering*, 31(5):880–891.
- Kökpınar, M. A. and Göğüş, M. (2002). High-speed jet flows over spillway aerators. *Canadian Journal of Civil Engineering*, 29(6):885–898.
- Koschitzky, H.-P. (1987). *Dimensionierungskonzept für Sohlbelüfter in Schussrinnen zur Vermeidung von Kavitationsschäden*. In Kobus, H., editor, Mitteilung 65. Institut für Wasserbau, TU Stuttgart.
- Kramer, K. (2004). *Development of aerated chute flow*. In Minor, H.-E., editor, VAW Mitteilungen 183. ETH Zürich.
- Kramer, K. and Hager, W. H. (2005). Air transport in chute flows. *International Journal of Multiphase Flow*, 31(10-11):1181–1197.
- Kramer, K., Hager, W. H., and Minor, H.-E. (2006). Development of air concentration on chute spillways. *Journal of Hydraulic Engineering*, 132(9):908–915.
- Lesleighter, E. (1988). Cavitation in hydraulic structures. In *Model-Prototype Correlation of Hydraulic Structures*, 74–94, Colorado Springs, Colorado. ASCE.
- Li, X.-y. and Yin, J.-b. (2016). Study on the damage of stepped spillways combined with flaring gate piers. *Journal Of Yangtze River Scientific Research Institute*, 33(1):61.
- Lin, K. J. and Han, L. (2001). Stepped spillway for Dachaoshan RCC dam. In Burgi, P. H. and Gao, J., editors, *29th IAHR Congress*, 88–93, Beijing, China.
- Lopardo, R. (2002). Contribution of hydraulic models on the safe design of large dams stilling basins. In *Hydraulic and hydrological aspects of reliability and safety assessment of hydraulic structures*, St. Petersburg, Russia.

References

- Low, H. S. (1986). *Model studies of Clyde dam spillway aerators*. Research report 86-6. University of Canterbury, Christchurch, New Zealand.
- Marcano, A. and Castillejo, N. (1984). Model-prototype comparison of aeration devices of Guri Dam spillway. In Kobus, H., editor, *Scale Effects in Modelling Hydraulic Structures*, 4.6, 1–5, Esslingen am Neckar, Germany.
- Marcano, A. and Patiño, A. (1989). Cavitation damage at Chute 3 Stage II of Guri Spillway and solution to the problem. In *Casos e Acidentes em Sistemas Fluidos*, 35–38, São Paulo, Brazil.
- Mason, P. J. (1983). Energy dissipating crest splitters for concrete dams. *International Water Power & Dam Construction*, 35(11):37–40.
- Matos, J. (1997). Discussion of "Model study of a roller compacted concrete stepped spillway" by E. Rice and K. Kadavy. *Journal of Hydraulic Engineering*, 123(10):931–936.
- Matos, J. (1999). *Emulsioneamento de ar e dissipação de energia do escoamento em descarregadores em degraus*. PhD Thesis, Instituto Superior Técnico de Lisboa, Lisbon, Portugal.
- Matos, J. (2000a). Discussion of "Characteristics of skimming flow over stepped spillways" by M. R. Chamani and N. Rajaratnam. *Journal of Hydraulic Engineering*, 126(11):865–869.
- Matos, J. (2000b). Hydraulic design of stepped spillways over RCC dams. In Minor, H.-E. and Hager, W. H., editors, *Hydraulics of stepped spillways*, 187–194, Zürich, Switzerland. Balkema, Rotterdam.
- Matos, J. (2005). Discussion of "Hydraulic design of stepped spillways" by R. M. Boes and W. H. Hager. *Journal of Hydraulic Engineering*, 131(6):525–527.
- Matos, J. and Meireles, I. (2014). Hydraulics of stepped weirs and dam spillways: engineering challenges, labyrinths of research. In *5th International Symposium on Hydraulic Structures*, 1–30, Brisbane, Australia. University of Queensland.
- Matos, J., Quintela, A., Sánchez-Juny, M., and Dolz, J. (2000). Air entrainment and safety against cavitation damage in stepped spillway over RCC dams. In Minor, H.-E. and Hager, W. H., editors, *Hydraulics of stepped spillways*, 69–76, Zürich, Switzerland. Balkema, Rotterdam.
- Meireles, I. and Matos, J. (2009). Skimming flow in the nonaerated region of stepped spillways over embankment dams. *Journal of Hydraulic Engineering*, 135(8):685–689.
- Meireles, I., Renna, F., Matos, J., and Bombardelli, F. (2012). Skimming, nonaerated flow on stepped spillways over roller compacted concrete dams. *Journal of Hydraulic Engineering*, 138(10):870–877.
- Meireles, I., Renna, F., Matos, J., and Bombardelli, F. (2014). Closure to "Skimming, nonaerated flow on stepped spillways over roller compacted concrete dams". *Journal of Hydraulic Engineering*, 140(10):07014013.

- Minor, H.-E. (1987). Erfahrungen mit Schussrinnenbelüftung. *Wasserwirtschaft*, 77(6):292–295.
- Minor, H.-E. (2000). Spillways fir high velocities. In Minor, H.-E. and Hager, W. H., editors, *Hydraulics of stepped spillways*, 3–10, Zürich, Switzerland. Balkema, Rotterdam.
- Ohtsu, I. and Yasuda, Y. (1997). Characteristics of flow conditions on stepped channels. In *27th IAHR Congress*, 583–588, San Francisco, USA. ASCE.
- Ohtsu, I., Yasuda, Y., and Takahashi, M. (2004). Flow characteristics of skimming flows in stepped channels. *Journal of Hydraulic Engineering*, 130(9):860–869.
- Ozturk, M., Aydin, M. C., and Aydin, S. (2008). Damage limitation - A new spillway aerator. *International Water Power & Dam Construction*, 60(5):36–40.
- Pan, S. and Shao, Y. (1984). Scale effects in modelling air demand by a ramp slot. In Kobus, H., editor, *Scale Effects in Modelling Hydraulic Structures*, 4.7, 1–4, Esslingen am Neckar, Germany.
- Pan, S., Shao, Y., Shi, Q., and Dong, X. (1980). Self-aeration capacity of a water jet over an aeration ramp. *Shuili Xuebao*, 5(10):13–22.
- Pegram, G. G. S., Officer, A. K., and Mottram, S. R. (1999). Hydraulics of skimming flow on modeled stepped spillways. *Journal of Hydraulic Engineering*, 125(5):500–510.
- Peterka, A. J. (1953). The effect of entrained air on cavitation pitting. In *Minnesota International Hydraulic Convention*, 507–518, Minneapolis. ASCE, New York.
- Pfister, M. (2002). *Kaskadenbelüfter - Hydraulische Modelluntersuchung*. MSc Thesis, VAW, ETH Zürich, Switzerland.
- Pfister, M. (2008). *Schussrinnenbelüfter Lufttransport ausgelöst durch interne Abflussstruktur*. In Minor, H.-E., editor, VAW Mitteilungen 203. ETH Zürich.
- Pfister, M. (2009). Effect of control section on stepped spillway flow. In *33rd IAHR Congress*, 10229, 1964–1971, Vancouver, Canada.
- Pfister, M. (2011). Chute aerators: steep deflectors and cavity subpressure. *Journal of Hydraulic Engineering*, 137(10):1208–1215.
- Pfister, M. (2012). Jet impact angle on chute downstream of aerator. In *4th International Symposium on Hydraulic Structures*, 1–8, Porto, Portugal.
- Pfister, M. and Boes, R. (2014). Discussion of "Skimming, nonaerated flow on stepped spillways over roller compacted concrete dams" by I. Meireles, F. Renna, J. Matos, and F. Bombardelli. *Journal of Hydraulic Engineering*, 140(10):07014012.
- Pfister, M. and Chanson, H. (2014). Two-phase air-water flows: Scale effects in physical modeling. *Journal of Hydrodynamics, Ser. B*, 26(2):291–298.

- Pfister, M. and Hager, W. H. (2009). Deflector-generated jets. *Journal of Hydraulic Research*, 47(4):466–475.
- Pfister, M. and Hager, W. H. (2010a). Chute Aerators. I: Air transport characteristics. *Journal of Hydraulic Engineering*, 136(6):352–359.
- Pfister, M. and Hager, W. H. (2010b). Chute aerators. II: Hydraulic design. *Journal of Hydraulic Engineering*, 136(6):360–367.
- Pfister, M. and Hager, W. H. (2011). Self-entrainment of air on stepped spillways. *International Journal of Multiphase Flow*, 37(2):99–107.
- Pfister, M. and Hager, W. H. (2012). Deflector-jets affected by pre-aerated approach flow. *Journal of Hydraulic Research*, 50(2):181–191.
- Pfister, M. and Hager, W. H. (2014). History and significance of the Morton number in hydraulic engineering. *Journal of Hydraulic Engineering*, 140(5):02514001.
- Pfister, M., Hager, W. H., and Boes, R. M. (2014). Trajectories and air flow features of ski jump-generated jets. *Journal of Hydraulic Research*, 52(3):336–346.
- Pfister, M., Hager, W. H., and Minor, H.-E. (2006a). Bottom aeration of stepped spillways. *Journal of Hydraulic Engineering*, 132(8):850–853.
- Pfister, M., Hager, W. H., and Minor, H.-E. (2006b). Stepped chutes: Pre-aeration and spray reduction. *International Journal of Multiphase Flow*, 32(2):269–284.
- Pfister, M., Lucas, J., and Hager, W. H. (2011). Chute aerators: preaerated approach flow. *Journal of Hydraulic Engineering*, 137(11):1452–1461.
- Pfister, M. and Schwindt, S. (2014). Air concentration distribution in deflector-jets. In *5th International Symposium on Hydraulic Structures*, 1–8, Brisbane, Australia. University of Queensland.
- Pinto, N. L. (1984). Model evaluation of aerators in shooting flow. In Kobus, H., editor, *Scale Effects in Modelling Hydraulic Structures*, 4.2, 1–6, Esslingen am Neckar, Germany.
- Pinto, N. L., Neidert, S. H., and Ota, J. J. (1982a). Aeration at high velocity flows I. *Water Power & Dam Construction*, 34(2):34–38.
- Pinto, N. L., Neidert, S. H., and Ota, J. J. (1982b). Aeration at high velocity flows II. *Water Power & Dam Construction*, 34(3):42–44.
- Prisk, M., Richards, M., and Hieatt, M. (2009). Delivering Wadi Dayqah, Oman’s tallest dam. *Proceedings of the Institution of Civil Engineers*, 162(6):42–50.
- Pugh, C. A. and Rhone, T. J. (1988). Cavitation in Bureau of Reclamation tunnel spillways. In *Hydraulics for High Dams*, 645–652, Beijing, China. Chinese Hydraulic Engineering Society.

- Rasmussen, R. E. H. (1956). Some experiments on cavitation erosion in water mixed with air. In *International Symposium on Cavitation in Hydrodynamics*, 20, 1–25. National Physical Laboratory, London.
- Russell, S. O. and Sheehan, G. J. (1974). Effect of entrained air on cavitation damage. *Canadian Journal of Civil Engineering*, 1(1):97–107.
- Rutschmann, P. (1988). *Belüftungseinbauten in Schussrinnen*. In Vischer, D., editor, VAW Mitteilungen 97. ETH Zürich.
- Rutschmann, P. and Hager, W. H. (1990). Air entrainment by spillway aerators. *Journal of Hydraulic Engineering*, 116(6):765–782.
- Sánchez-Juny, M., Bladé, E., and Dolz, J. (2007). Pressures on a stepped spillway. *Journal of Hydraulic Research*, 45(4):505–511.
- Sánchez-Juny, M., Bladé, E., and Dolz, J. (2008). Analysis of pressures on a stepped spillway. *Journal of Hydraulic Research*, 46(3):410–414.
- Sánchez-Juny, M. and Dolz, J. (2005). Experimental study of transition and skimming flows on stepped spillways in RCC dams: qualitative analysis and pressure measurements. *Journal of Hydraulic Research*, 43(5):540–548.
- Schiess Zamora, A., Pfister, M., Hager, W. H., and Minor, H.-E. (2008). Hydraulic performance of step aerator. *Journal of Hydraulic Engineering*, 134(2):127–134.
- Schiess Zamora, A., Pfister, M., Hager, W. H., and Minor, H.-E. (2009). Closure to "Hydraulic performance of step-aerator". *Journal of Hydraulic Engineering*, 135(7):621–622.
- Schleiss, A. J. and Pougatsch, H. (2011). *Les barrages: Du projet à la mise en service*. Traité de Génie Civil 17. PPUR, Lausanne.
- Schrader, E. K. (1983). Cavitation resistance of concrete structures. In *Frontiers in Hydraulic Engineering*. ASCE.
- Schwalt, M. and Hager, W. H. (1992). Die Strahlbox. *Schweizer Ingenieur und Architekt*, 110(27-28):547–549.
- Schwartz, H. I. and Nutt, L. P. (1963). Projected nappes subject to transverse pressure. *Journal of the Hydraulics Division*, 89(4):97–104.
- Semenkov, V. M. and Lentyaev, L. D. (1973). Spillway with nappe aeration. *Hydrotechnical Construction*, 7(5):436–441.
- Skipalle, J. (1994). *Zwangsbelüftung von Hochgeschwindigkeitsströmungen an zurückspringenden Stufen im Wasserbau*. Mitteilung 124. Technische Universität, Berlin, Germany.
- Sorensen, R. M. (1985). Stepped spillway hydraulic model investigation. *Journal of Hydraulic Engineering*, 111(12):1461–1472.

References

- Steiner, R., Heller, V., Hager, W. H., and Minor, H.-E. (2008). Deflector ski jump hydraulics. *Journal of Hydraulic Engineering*, 134(5):562–571.
- Straub, L. G. and Anderson, A. G. (1958). Self-aerated flow in open channels. *Journal of the Hydraulics Division*, 84(7):456–486.
- Strobl, T. (2013). Die Trinkwasser-Talsperre Wadi Dayqah im Oman - Erfahrungen aus Planung, Bau und Betrieb. *Wasserwirtschaft*, 103(5):68–71.
- Takahashi, M., Gonzalez, C. A., and Chanson, H. (2006). Self-aeration and turbulence in a stepped channel: Influence of cavity surface roughness. *International Journal of Multiphase Flow*, 32(12):1370–1385.
- Takahashi, M. and Ohtsu, I. (2012). Aerated flow characteristics of skimming flow over stepped chutes. *Journal of Hydraulic Research*, 50(4):427–434.
- Takahashi, M. and Ohtsu, I. (2014). Analysis of nonuniform aerated skimming flows on stepped channels. In *5th International Symposium on Hydraulic Structures*, 1–9, Brisbane, Australia. University of Queensland.
- Takahashi, M., Yasuda, Y., and Ohtsu, I. (2005). Effect of Reynolds number on characteristics of skimming flows in stepped channels. In *31st IAHR Congress*, 2880–2889, Seoul, Korea.
- Tan, T. P. (1984). *Model Studies of Aerators on Spillways*. Research report 84-6. University of Canterbury, Christchurch, New Zealand.
- Terrier, S., Pfister, M., and Schleiss, A. J. (2015). Comparison of chute aerator effect on stepped and smooth spillways. In *36th IAHR Congress*, The Hague, The Netherlands. IAHR.
- Toloshinov, A. V., Volynchikov, A. N., Prokof'ev, V. A., and Sudol'skii, G. A. (2009). Development of the design for the No. 2 spillway at the Boguchany hydroproject. *Power Technology and Engineering*, 43(3):135–142.
- Tozzi, M. J. (1994). Residual energy in stepped spillways. *International Water Power & Dam Construction*, 46(5):32–34.
- U.S. Army Corps of Engineers (1987). *Hydraulic design criteria*. Waterways Experiment Station, Vicksburg, MS.
- Vischer, D., Volkart, P., and Sigenthaler, A. (1982). Hydraulic modelling of air slots in open chute spillways. In *Hydraulic Modelling of Civil Engineering Structures*, 239–252, Coventry, England. BHRA Fluid Engineering.
- Volkart, P. (1984). Sohlenbelüftung gegen Kavitationserosion in Schussrinnen. *Wasserwirtschaft*, 74(9):431–443.
- Volkart, P. and Chervet, A. (1983). *Air slots for flow aeration*. In Vischer, D., editor, VAW Mitteilungen 66. ETH Zürich.

- Volkart, P. and Rutschmann, P. (1984). Rapid flow in spillway chutes with and without deflectors: a model-prototype comparison. In Kobus, H., editor, *Scale Effects in Modelling Hydraulic Structures*, 4.5, 1–8, Esslingen am Neckar, Germany.
- Volkart, P. and Rutschmann, P. (1986). Aerators of spillway chutes: Fundamentals and applications. In *Advancements in Aerodynamics, Fluid Mechanics, and Hydraulics*, 1–15, Minneapolis. ASCE, New York.
- Wahrheit-Lensing, A. (1996). *Selbstbelüftung und Energieumwandlung beim Abfluss über treppenförmige Entlastungsanlagen*. PhD Thesis, University of Karlsruhe, Karlsruhe, Germany.
- Wang, S. Y., Hou, D. M., and Wang, C. H. (2012). Aerator of stepped chute in Murum Hydropower Station. In *2012 International Conference on Modern Hydraulic Engineering*, 28, 803–807, Nanjing, China. Elsevier Procedia.
- Wei, C. and Defazio, F. (1982). Simulation of free jet trajectories for the design of aeration devices on hydraulic structures. In Holz, K., Meissner, U., Zielke, W., Brebbia, C., Pinder, G., and Gray, W., editors, *Finite Elements in Water Resources*, 1039–1048. Springer Berlin Heidelberg.
- Wilhelms, S. C. and Gulliver, J. S. (2005). Bubbles and waves description of self-aerated spillway flow. *Journal of Hydraulic Research*, 43(5):522–531.
- Wiley, J., Ewing, T., Lesleighter, E., and Dymke, J. (2010). Numerical and physical modelling for a complex stepped spillway. *International Journal on Hydropower and Dams*, 17(3):108–113.
- Wood, I. R. (1983). Uniform region of self-aerated flow. *Journal of Hydraulic Engineering*, 109(3):447–461.
- Wood, I. R. (1991). *Air entrainment in free-surface flows*. IAHR Hydraulic Structures Design Manuals 4. A.A. Balkema, Rotterdam, Netherlands.
- Wood, I. R., Ackers, P., and Loveless, J. (1983). General method for critical point on spillways. *Journal of Hydraulic Engineering*, 109(2):308–312.
- Wu, J., Ma, F., and Xu, W. (2013). Bottom roller characteristics in cavity of chute aerators. *Journal of Hydraulic Research*, 51(3):317–321.
- Wu, J. and Ruan, S. (2007). Estimation of cavity length behind aerators. In *32nd IAHR Congress*, Venice, Italy.
- Yasuda, Y. and Ohtsu, I. (2000). Characteristics of plunging flows in stepped channel chutes. In Minor, H.-E. and Hager, W. H., editors, *Hydraulics of stepped spillways*, 147–152, Zürich, Switzerland. Balkema, Rotterdam.
- Yasuda, Y., Ohtsu, I., and Takahashi, M. (2006). Hydraulic characteristics in connections between smooth crest and stepped section. In Marcano, A. and Martinez, E., editors, *2nd International Symposium on Hydraulic Structures*, 507–513, Ciudad Guayana, Venezuela. Venezuelan Society of Hydraulic Engineering.

References

- Zagustin, K., Mantellini, T., and Castillejo, N. (1982). Some experiments on the relationship between a model and a prototype for flow aeration in spillways. In *Hydraulic Modelling of Civil Engineering Structures*, 285–295, Coventry, England. BHRA Fluid Engineering.
- Zare, H. K. and Doering, J. C. (2012). Effect of rounding edges of stepped spillways on the flow characteristics. *Canadian Journal of Civil Engineering*, 39(2):140–153.
- Zhang, G. and Chanson, H. (2015). Broad-crested weir operation upstream of a steep stepped spillway. In *36th IAHR Congress*, 1–11, The Hague, The Netherlands. IAHR.
- Zhang, G. and Chanson, H. (2016). Self-aeration in the rapidly- and gradually-varying flow regions of steep smooth and stepped spillways. *Environmental Fluid Mechanics*, 16:1–20.

Acknowledgments

This PhD research was performed at the Laboratory of Hydraulic Constructions (LCH) of École Polytechnique Fédérale de Lausanne (EPFL). It was supported by the Swiss National Science Foundation project Nos. 200021_137572/1 and 200020_159967/1, as well as the Lombardi Foundation.

I would like to acknowledge people who contributed to this research or supported me in any form during this PhD.

First, I would like to express my gratitude to my thesis director Prof. Anton Schleiss for giving me the opportunity to conduct this research and enrich my knowledge. Since my Master's studies, I considerably benefited from his guidance. He offered an excellent research environment that allowed to fulfill my objectives.

Secondly, I thank my thesis co-director Dr. Michael Pfister for sharing his remarkable knowledge in hydraulics and his experience with chute aerators. His advice, availability and interest were invaluable to the accomplishment of this research. Helpful discussions with Dr. Pedro Manso and Dr. Giovanni De Cesare are also acknowledged.

I would like to thank Prof. Markus Aufleger, Prof. Willi Hager, Prof. Jorge Matos for being part of the jury and Prof. Bertrand Merminod for being the president of the jury.

The physical experiments would not have been possible without the technical assistance of the workshop, and I particularly thank Cédric, Michel and Panpam for their availability to constantly adjust and improve the physical model.

During my years at LCH, I had the pleasure to work with great colleagues and friends. I highly appreciated this scientific, creative, multi-cultural, and most importantly humorous team. The mutual support that resulted was precious. I'm especially thankful for the support, collaborations and friendship of my former officemate Dr. Martin Bieri. As a teaching assistant, I also benefited from the insight and time spent with the students I supervised.

Furthermore, I'm grateful for the time and adventures I shared with Brianna, Florian, Mario and multiple others friends that gave me the motivation and balance I needed to achieve this research.

Finally, my warmest thanks go to my family for their eternal support and confidence in my abilities.

Stéphane TERRIER



Birth 30 June 1986
Nationality Swiss
Contact stephane.terrier@alumni.epfl.ch

Education

2012 - 2016 **PhD in Hydraulic Engineering**,
Laboratory of Hydraulic Constructions (LCH)
École polytechnique fédérale de Lausanne (EPFL), Switzerland

2007 - 2009 **Master of Science (MSc) in Civil Engineering**,
École polytechnique fédérale de Lausanne (EPFL), Switzerland
Focus: Hydraulic and structural engineering

2004 - 2007 **Bachelor of Science (BSc) in Civil Engineering**,
École polytechnique fédérale de Lausanne (EPFL), Switzerland

2001 - 2004 **Matura**,
Gymnase de la Cité, Lausanne, Switzerland
Focus: Biology and chemistry

Professional experience

2011 - 2016 **Laboratory of Hydraulic Constructions, EPFL**
Research assistant and PhD student (since 2012)
Sediment management and delta restoration of Baye de Clarens
Head losses and surge waves propagation in the tailrace channels of the enhanced hydropower plant Hongrin-Léman (FMHL+)

2010 - 2011 **Laboratory of Hydraulic Constructions, EPFL**
Civilian service (13 months)
Hydrological modelling of glacial outflows for various climate scenarios and hydroelectric potential of new lakes uncovered by retreating glaciers

2010 **Stucky Ltd**, Renens, Switzerland
Project Engineer (6 months)
Finite elements verification of the access tunnel to the enhanced hydro-power plant Hongrin-Léman (FMHL+)
Structural design of a large wastewater shaft in Jeddah (Saudi Arabia)
Stability verification of Fionnay reservoir embankment dam

2008 **Stucky Ltd**, Renens, Switzerland
Internship (3.5 months)
Energy production and reservoir management of Inguri (Georgia)
Alternate spillway designs for Baixo Sabor (Portugal)

2006 **Losinger Construction SA**, Bussigny, Switzerland
Internship (4 weeks)
Works supervision of an industrial building in Chavornay

2004 **CSD Ingénieurs Conseils SA**, Lausanne, Switzerland
Internship (2 weeks)

Computer skills

Software	MS Office, AutoCAD, Inventor, Routing System, Hydraulic System, GEO-SLOPE, Z_Soil, Diana
Programming	VBA, Matlab, HTML, PHP, JavaScript

Languages

French	Native language
English	Fluent (CAE)
German	Intermediate

Awards

2010	IM Maggia Award for the Master thesis
------	---------------------------------------

Teaching

Follow-up of 6 Master theses, as well as numerous semester projects and exercises of graduate students of the School of Architecture, Civil and Environmental Engineering (ENAC) of EPFL.

Publications

Terrier, S., Pfister, M., and Schleiss, A. J. (2016). Effect of deflector aerator on stepped spillway flow. *Proc., 6th International Symposium on Hydraulic Structures*, Portland OR, USA.

Terrier, S., Pfister, M., and Schleiss, A. J. (2015). Comparison of chute aerator effect on stepped and smooth spillways. *Proc., 36th IAHR Congress*, The Hague, The Netherlands.

Terrier, S., De Cesare, G., Schleiss, A. J., André, S., Lecomte, E., and De Montmollin, G. (2015). Case study – Delta restoration at a steep river mouth. *Proc., 36th IAHR Congress*, The Hague, The Netherlands.

Terrier, S., Bieri, M., Jordan, Frédéric, and Schleiss, A. J. (2015). Impact du retrait glaciaire et adaptation du potentiel hydroélectrique dans les Alpes suisses. *La Houille Blanche*, (1), 93–101.

Terrier, S., Bieri, M., De Cesare, G., and Schleiss, A. J. (2014). Surge wave propagation in a common tailrace channel for two large pumped-storage plants. *Journal of Hydraulic Engineering*, 140(2), 218–225.

De Cesare, G., Bieri, M., Terrier, S., Candolfi, S., Wickenhäuser, M., and Micoulet, G. (2014). Optimization of a shared tailrace channel of two pumped-storage plants by physical and numerical modeling. *Advances in Hydroinformatics: SIMHYDRO 2012 – New Frontiers of Simulation*, P. Gourbesville, J. Cunge, and G. Caignaert, eds., Springer Singapore, Singapore, 291–305.

Terrier, S., Jordan, F., Schleiss, A. J., Haeberli, W., Huggel, C., and Künzler, M. (2011). Optimized and adapted hydropower management considering glacier shrinkage scenarios in the Swiss Alps. *Proc., International Symposium on Dams and Reservoirs under Changing Challenges*, A. J. Schleiss and R. M. Boes, eds., CRC Press, Taylor & Francis Group, Lucerne, Switzerland, 497–508.

